The University of Nottingham

UNITED KINGDOM · CHINA · MALAYSIA

The School of Pharmacy Journal

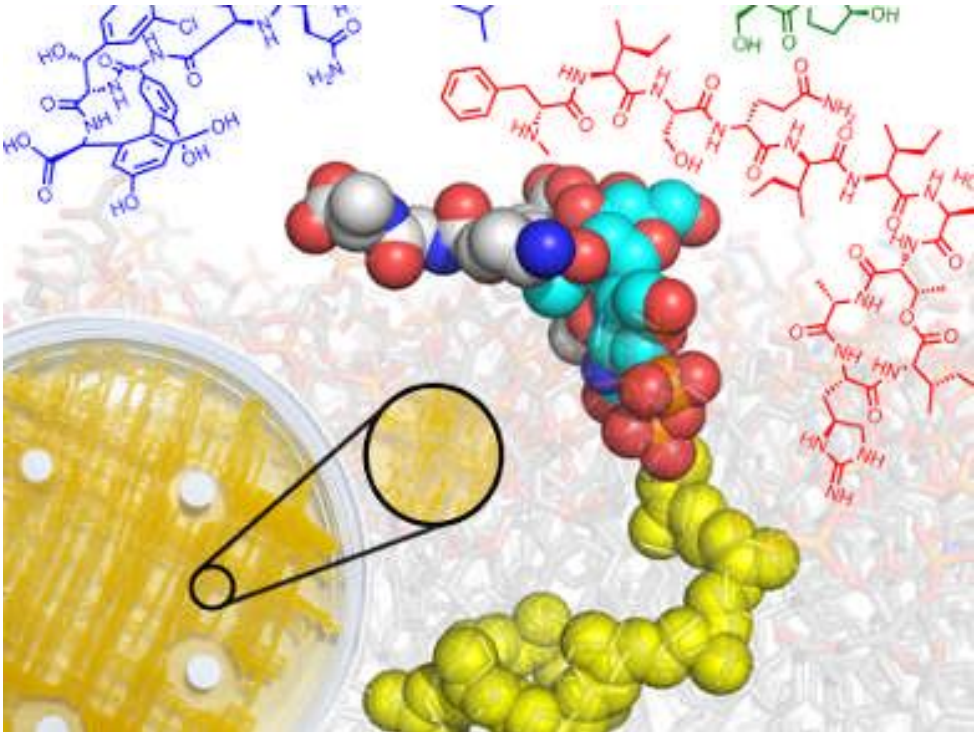

May 2016-July 2016

Foreword

Welcome to our latest edition of the School of Pharmacy Journal, a quarterly collection of publications and press releases from May to July 2016.

Researchers in the School continue to pave the way to tackle the healthcare challenges of the present and future. The advent of personalized medicine, where both the drug and its delivery are tailored to the individual, has created new challenges for the pharmaceutical industry. In June we and our partners were delighted to be awarded a £3.5m grant from the Engineering and Physical Sciences (EPSRC) to develop a library of 3D printing materials. The project, led by Professor Ricky Wildman from the Faculty of Engineering, aims to create 'plug and play' platforms of materials, material combinations and formulations which could be used to develop 3D printed products in fields as diverse as pharmaceuticals, food, agrochemicals and consumer products. Clive Roberts and Morgan Alexander from the School join Ricky, Richard Hague, Ian Ashcroft, Chris Tuck and Derek Irvine, from the Faculty of Engineering; Tim Foster, Professor of Food Manufacturing and director of Centre for Innovative Food Manufacturing; and David Ambilino, Professor of Sustainable Chemistry, and industrial partners GlaxoSmithKline, Unilever, PPG, Syngenta and Malvern Instruments to establish a suite of new materials from which anyone can select to most appropriate 3D printable material for their product. It is our aim to remove the limited palette of materials available to industry and the significant barrier to the wider adoption of the technology will be greatly reduced. Details of this and other awards made during the period are given later.

Our research continues to be published in the leading journals of many fields of pharmacy science and practise, including *ACS Nano*, *Analytical Chemistry*, *Blood*, Nucleic *Acids Research*, and *Scientific Reports*.

This period also saw the launch of our new undergraduate Masters of Science course in 'Pharmaceutical Sciences with a Year in Industry programme'. This course meets the current and future needs of pharmaceutical and biotechnology industries. The course has been designed, together with experts from industry, to prepare graduates for careers in drug discovery, medicines design and development. And we are delighted that the great efforts of all staff and researchers has helped propel the School up the Guardian University Guide league table for Pharmacy and Pharmacology to 4th where we remain the top school of pharmacy in England.

Professor Phil Williams
Phil.Williams@nottingham.ac.uk
Director of Research
(Nottingham)

Professor Nashiru Billa
Nashiru.Billa@nottingham.edu.my
Associate Dean (Research)
(Malaysia)

Contents

- ***Angers Exchange***
- ***Studying in Malaysia***
- ***The Opportunity of a Lifetime while Studying Pharmacy!***
- ***The European Pharmacy Students' Association Annual Congress 2016 in Helsinki***
- ***The importance of history in championing the future prosperity of British Pharmacy***
- ***International Conferences: Beers and Brexit***

- ***Collated Research Papers:***

Dynamic Surfaces for the Study of Mesenchymal Stem Cell Growth through Adhesion Regulation

Jemma N. Roberts, Jugal Kishore Sahoo, Laura E. McNamara, Karl V. Burgess, Jingli Yang, Enateri V. Alakpa, Hilary J. Anderson, Jake Hay, Lesley-Anne Turner, Stephen J. Yarwood, Mischa Zelzer, Richard O. C. Oreffo, Rein V. Ulijn and Matthew J. Dalby
ACS Nano (2016) 10, 6667-6679
DOI: 10.1021/acsnano.6b01765

Length-Selective Chemical Assembly of Vertically Aligned Carbon Nanotubes

Zarrar Hussein, Frankie J. Rawson, Pola G. Oppenheimer, Aaron Acton and Paula M. Mendes
Advanced Materials Interfaces (2016) 3, 1500860
DOI: 10.1002/admi.201500860

LESA FAIMS Mass Spectrometry for the Spatial Profiling of Proteins from Tissue

Rian L. Griffiths, Andrew J. Creese, Alan M. Race, Josephine Bunch and Helen J. Cooper
Analytical Chemistry (2016) 88, 6758-6766
DOI: 10.1021/acs.analchem.6b01060

Investigation of the Impact of Desorption Electrospray Ionization Sprayer Geometry on Its Performance in Imaging of Biological Tissue

Jocelyn Tillner, James S. McKenzie, Emrys A. Jones, Abigail V. M. Speller, James L. Walsh, Kirill A. Veselkov, Josephine Bunch, Zoltan Takats and Ian S. Gilmore
Analytical Chemistry (2016) 88, 4808-4816
DOI: 10.1021/acs.analchem.6b00345

Influence of Polymer Size on Uptake and Cytotoxicity of Doxorubicin-Loaded DNA–PEG Conjugates

Laura Purdie, Cameron Alexander, Sebastian G. Spain and Johannes P. Magnusson
Bioconjugate Chemistry (2016) 27, 1244-1252
DOI: 10.1021/acs.bioconjchem.6b00085

3D chemical characterization of frozen hydrogels using ToF-SIMS with argon cluster sputter depth profiling
Michael Taylor, David Scurr, Matthias Lutolf, Lee Buttery, Mischa Zelzer and Morgan Alexander
Biointerphases (2016) 11, 02A301
DOI: 10.1116/1.4928209

New found hope for antibiotic discovery: lipid II inhibitors
Ng, V and Chan, W.C.
Chem. Eur. J. (2016) 22, 12606-12616
DOI: 10.1002/chem.201601315

Alkylation of Staurosporine to Derive a Kinase Probe for Fluorescence Applications
Alexander J.M. Disney, Barrie Kellam and Lodewijk Dekker
Chem Med Chem (2016) 11, 972-979
DOI: 10.1002/cmdc.201500589

Novel Fused Arylpyrimidinone Based Allosteric Modulators of the M_1 Muscarinic Acetylcholine Receptor
Shailesh N. Mistry, Herman Lim, Manuela Jörg, Ben Capuano, Arthur Christopoulos,J. Robert Lane and Peter J. Scammells
ACS Chemical Neuroscience (2016) 7, 647-661
DOI: 10.1021/acschemneuro.6b00018

Survival of the Fittest: Time-To-Event Modeling of Crystallization of Amorphous Poorly Soluble Drugs
Katarzyna Nurzyńska, Rupert P. Austin, Peter M. Fischer, Jonathan Booth and Frank Gommer
Journal of Pharmaceutical Sciences (2016) 105, 1858-1866
DOI: 10.1016/j.xphs.2016.03.014

Modelling the role of CtfA/B in reverse shift continuous culture experiments of Clostridium acetobutylicum
Graeme J. Thorn and John R. King

Mathematical Biosciences (2016) 276, 101-113
DOI: 10.1016/j.mbs.2016.03.003

Investigating MALDI MSI parameters (Part 1) – A systematic survey of the effects of repetition rates up to 20 kHz in continuous raster mode
Rory T. Steven, Alex Dexter and Josephine Bunch
Methods (2016) 104, 101-110
DOI: 10.1016/j.ymeth.2016.04.010

Investigating MALDI MSI parameters (Part 2) – On the use of a mechanically shuttered trigger system for improved laser energy stability
Rory T. Steven, Alex Dexter and Josephine Bunch
Methods (2016) 104, 111-117
DOI: 10.1016/j.ymeth.2016.04.013

The influence of nanotexturing of poly(lacticco-glycolic acid) films upon human ovarian cancer cell attachment
Gökçen Yaşayan, Xuan Xue, Pamela Collier, Philip Clarke, Morgan R Alexander and Maria Marlow
Nanotechnology (2016) 255102
DOI: 10.1088/0957-4484/27/25/255102

Interfering with the CCL2–glycosaminoglycan axis as a potential approach to modulate neuroinflammation
Martha Gschwandtner, Anna Maria Piccinini, Tanja Gerlza, Tiziana Adage and Andreas J. Kungl
Neuroscience Letters (2016) 626, 164-173
DOI: 10.1016/j.neulet.2016.05.037

Structure and dynamics of DNA loops on nucleosomes studied with atomistic, microsecond-scale molecular dynamics
Marco Pasi and Richard Lavery
Nucleic Acids Research (2016) 44, 5450-5456
DOI: 10.1093/nar/gkw293

Synthesis and In Vitro Evaluation of Polyethylene Glycol-Paclitaxel Conjugates for Lung Cancer Therapy
Tian Luo, Johannes Magnusson, Véronique Préat, Raphael Frédérick, Cameron Alexander, Cynthia Bosquillon and Rita Vanbever

Pharm Res (2016) 33, 1671-1681
DOI: 10.1007/s11095-016-1908-2

Enhanced cytocompatibility and functional group content of poly(L-Lysine) dendrimers by grafting with poly(oxazolines).

England, R. M.; R. M. Hare, J. I.; Kemmitt, P. D.; Treacher, K.; Waring, M. J.; Barry, S. T.; Alexander, C. and Ashford, M.
Polymer Chemistry (2016) *7*, 4609-4617.
DOI: 10.1039/C6YPY00478D

Transcriptome analysis of* Streptococcus pneumoniae *treated with the designed antimicrobial peptides, DM3

Cheng-Foh Le, Ranganath Gudimella, Rozaimi Razali, Rishya Manikam and Shamala Devi Sekaran
Scientific Reports (2016) 6, 26828
DOI: 10.1038/srep26828

A novel DFP tripeptide motif interacts with the coagulation factor XI apple 2 domain

Szu S. Wong, Søren Østergaard, Gareth Hall, Chan Li, Philip M. Williams, Henning Stennicke and Jonas Emsley
Thrombosis and Hemostasis
DOI: 10.1182/blood-2015-10-676122

Consumer Opinions on Existing and Proposed Australian Over-the-Counter Medicine Labeling Strategies in Comparison With the Standardized US Drug Facts Label

Vivien Tong, David K. Raynor, Kim K. Hamrosi, Basoori Acharya, Nisha Panchal and Parisa Aslani
Therapeutic Innovation & Regulatory Science (2016) 50, 427-435
DOI: 10.1177/2168479016628301

Staff Research News

- Professor Cameron Alexander has been elected Chair of the Royal Society of Chemistry/ Society for Chemical Industry Macro Group UK, 2016-2019.

- Professor Cameron Alexander gave the following invited talks:
    - "Polymers for nanomedicine – prospects and challenges" – Warwick International Polymer Conference, 12 July 2016.
    - "Responsive Polymers in Drug Delivery" 14th European Symposium on Controlled Drug Delivery (ESCDD) 2016, Egmond an See, Nederlands, 13-15 April 2016.
    - "Exploiting biological responses with synthetic polymers for diagnosis and therapy", Department of Chemistry, University of Leeds, 8 June 2016.
    - "Synthetic materials and biological responses", School of Clinical Sciences, University of Bristol, 6 May 2016.

- Dr Dong-Hyun Kim was invited to give a talk "Metabolomics: Shedding light on human health and diseases" at Nottingham Pathology 2016, University of Nottingham, 28 June-1 July 2016.

- Dr Roger Knaggs has been awarded a Fellowship by Election of the Faculty of Pain Medicine of the Royal College of Anaesthetists; the first non-medical healthcare professional to receive this award.

- Professor Clive Roberts was invited to give a talk at the 7th Drug Delivery & Formulation Summit & Expo, Berlin, 23-25 May 2016.

- Dr Jim Chai was invited to give a talk "How Do Our Patients Cope with Insulin Treatment" at the Malaysian Pharmaceutical Society-Young Pharmacist Chapter (MPS-YPS), International Medical University Malaysia, on 21 July 2016.

Grants/Studentships Awarded

- A team of scientists at The University of Nottingham have been awarded £3.5m from the Engineering and Physical Sciences Research Council (EPSRC) to develop a new library of 3D printing materials which could accelerate commercial uptake of the technology (Principal Investigator: Professor Ricky Wildman, Engineering, Co-Investigators: Professor Clive Roberts and Professor Morgan Alexander, Pharmacy, et al).

- Professor Cameron Alexander has been awarded an EPSRC Healthcare Technologies Impact Fellowship "Radiotherapy ctivated materials for enhanced cancer treatments" for £540k (with Dr Keith Spriggs, Anna Grabowska and Stewart Martin).

- Professor Claire Anderson is a Co-Investigator on an NIHR Health Services & Delivery Research grant led by Health Sciences: Managing Medicines at the end of life for patients being cared for and dying at home.

- Dr Jon Aylott has been awarded an EPSRC Impact Acceleration Award: Desktop viral diagnostic for the common cold (Co-Investigator: Dr Veeren Chauhan).

- Professor David Barrett is a Co-Investigator on an NERC EVAL-FARMS grant led by Biosciences: evaluating the threat of antimicrobial resistance in agricultural manures and slurries.

- Dr Weng Chan has been awarded an MRC Confidence in Concept grant 'A novel and exquisitely potent antibiotic for the treatment of *Clostridium difficile* infection' for £92k.

- Professor Jonas Emsley has been awarded a BHF Equipment grant.

- Professor Peter Fischer is a Co-Investigator on a Wellcome Trust Early Stage Seeding Drug Discovery grant led by Birmingham: Structure-based discovery of CaMK1D kinase inhibitors with in vivo activity as targeted therapeutics agents for breast cancer.

- Dr Pavel Gershkovich has been awarded a Wellcome Trust Vacation scholarship for Chun Long Lau: in vitro and ex vivo assessment of prodrugs designed to target the lymphatic system for treatment of lymphoma and metastatic cancer

- Professor David Heery is a Co-Investigator on a Prostate Cancer UK Research Innovation award led by Vet School: novel therapeutic targets for the prevention and treatment of hormone refractory prostate cancer

- Dr Felicity Rose is a Co-Investigator on an EPSRC grant led by Glasgow: Engineering growth factor microenvironments - a new therapeutic paradigm for regenerative medicine.

- Dr Felicity Rose is a Co-Investigator on 'Find A Better Way Working together - combined technologies for robust engineering of bone grafts with controlled geometries' led by Birmingham.

- Professor Phil Williams has been awarded a Wellcome Trust Vacation scholarship for Christopher Graham: In vitro cross-species membrane insertion of Neisserial Nalp by Campylobacter jejuni-BamA.

- Dr Mischa Zelzer has been awarded a Leverhulme Trust Project research grant: 'Surfaces, the next frontier in understanding and controlling gel properties' (CoI: Dr Maria Marlow).

Student News

- Muna Adan was invited to give an oral presentation at the British Pain Society's Annual Scientific Conference 2016, Harrogate, following the submission of her abstract "Characteristics of non-cancer pain patients prescribed long-term strong opiods in primary care: a population based study using CPRD". Muna's presentation was awarded a prize as one of the top three best research presentations.

- Shehnaz Ahmed attended the international conference "Advances in Cell and Tissue Culture", Barcelona, 30 May-1 June 2016 and won 1st prize in the scientific poster completion with her poster "Investigating fibroblast response in a 3D *in vitro* lung wound model exposed to interstitial flow conditions".

- Alshaimaa Almehmady took part in Three Minute Thesis (3MT), an academic research communication competition developed by The University of Queensland, Australia. Following the semi-final completion of University of Nottingham graduate students, Alshaimaa was selected to participate in the British Science Association (BSA) Masterclass: Science Communication Primer held in Manchester on 15 June 2016.

- Adam Dundas won the 'Best Poster on Display' award at the Engineering Research Showcase held on 10th May 2016 at the Crowne Plaza Hotel, Nottingham, for his poster "High Throughput Synthesis of Monomers using Microwaves".

- Tamara Mahmood won first prize for best poster presentation for her poster "Characterization of a Bioresorbable Drug-Eluting Scaffold" at the UK Society for Biomaterials 15th Annual Conference, University of Westminster, London, 30 June-1 July 2016

- Congratulations to Gizem Osman who has been awarded a University of Nottingham EPSRC Doctoral prize. This will provide her with 2 years funding to continue her PhD work and start her own project look at correcting cystic fibrosis with gene-editing.

- Michael Taylor has obtained a postdoctoral position at the NESAC/BIO, The National ESCA and Surface Analysis Centre for Biomedical Problems at the University of Washington, Seattle. Michael will work on development and analysis of functional tissue scaffolds, and Time-of-Flight Secondary Ion Mass Spectrometry (ToF-SIMS) of pancreatic tissues to aid the development of an early warning system for cancer.

General News

- Matthew Boyd, Claire Anderson, Vibhu Solanki, Kimberley Sonnex and Sarah Brydges won a Lord Dearing Award 2016 for the development of our new 4th year module, **Pharmacy Leadership and Management (PLM)**, a 12 day team-based student-centred simulation of Pharmacy practice delivered in a dedicated teaching suite. Lord Dearing Awards acknowledge the outstanding achievements of University of Nottingham staff in enhancing the student learning experiment.

- The School has been ranked as 4th in the 2017 Guardian University Guide league table for Pharmacy and Pharmacology, up one place from 2016, and remains the top school of pharmacy in England.

- The School has launched a new undergraduate course 'MSci Pharmaceutical Sciences with a Year in Industry programme' to meet the current and future needs of pharmaceutical and biotechnology sectors. The course is designed, together with experts from industry, to prepare graduates for careers in drug discovery, medicines design and development. In addition to a strong foundation in the chemical and biological sciences, students will also learn about patients, business skills, and medicines regulation.

Highlighted Papers

- ***Enhanced cytocompatibility and functional group content of poly(L-Lysine) dendrimers by grafting with poly(oxazolines).***

  England, R. M.; R. M. Hare, J. I.; Kemmitt, P. D.; Treacher, K.; Waring, M. J.; Barry, S. T.; Alexander, C. and Ashford, M.

  Polymer Chemistry (2016) *7*, 4609-4617.

  DOI: 10.1039/C6YPY00478D

  Selected for cover of journal. First paper from AstraZeneca Post-Doctoral Programme scheme, with Nottingham chosen as the external advisor to the project. This paper describes a new approach to the development of dendrimer-drug conjugates, with enhanced chemistries which allow control of biodistribution and drug release for cancer therapies.

- ***New found hope for antibiotic discovery: lipid II inhibitors***

  Ng, V and Chan, W.C.

  Chem. Eur. J. (2016)

  DOI: 10.1002/chem.201601315

  This paper was the most accessed *Chem. Eur. J.* paper in July 2016 and was highlighted as a Noteworthy paper by Chemistry views.

  http://www.chemistryviews.org/details/ezine/9535721/New_Antibiotics_Against_Resistant_Bacteria.html

ACSNANO www.acsnano.org

ARTICLE

Dynamic Surfaces for the Study of Mesenchymal Stem Cell Growth through Adhesion Regulation

Jemma N. Roberts,[†] Jugal Kishore Sahoo,[‡] Laura E. McNamara,[†] Karl V. Burgess,[§] Jingli Yang,[†] Enateri V. Alakpa,[†] Hilary J. Anderson,[†] Jake Hay,[†] Lesley-Anne Turner,[†] Stephen J. Yarwood,[†] Mischa Zelzer,[∥,⊥] Richard O. C. Oreffo,[#] Rein V. Ulijn,[*,‡,¶,△] and Matthew J. Dalby[*,†]

[†]Centre for Cell Engineering, Institute of Molecular, Cell and Systems Biology, College of Medical, Veterinary and Life Sciences, Joseph Black Building, University of Glasgow, Glasgow G12 8QQ, Scotland, U.K.

[‡]Department of Pure & Applied Chemistry, WestCHEM, Thomas Graham Building, 295 Cathedral Street, Glasgow G1 1XL, Scotland, U.K.

[§]Glasgow Polyomics Facility, Translational Cancer Research Centre, University of Glasgow Garscube Campus, Switchback Road, Glasgow G61 1QH, Scotland, U.K.

[∥]School of Pharmacy, University of Nottingham, Boots Science Building, University Park, Nottingham NG7 2RD, U.K.

[⊥]National Physical Laboratory, Teddington, Middlesex TW11 0LW, U.K.

[#]Bone & Joint Research Group, Centre for Human Development, Stem Cells and Regeneration, Institute of Developmental Sciences, University of Southampton, Southampton SO16 6YD, U.K.

[¶]Advanced Science Research Center (ASRC), City University of New York, New York, New York 10031, United States

[△]Department of Chemistry and Biochemistry, City University of New York—Hunter College, 695 Park Avenue, New York, New York 10065, United States

Supporting Information

ABSTRACT: **Out of their niche environment, adult stem cells, such as mesenchymal stem cells (MSCs), spontaneously differentiate. This makes both studying these important regenerative cells and growing large numbers of stem cells for clinical use challenging. Traditional cell culture techniques have fallen short of meeting this challenge, but materials science offers hope. In this study, we have used emerging rules of managing adhesion/cytoskeletal balance to prolong MSC cultures by fabricating controllable nanoscale cell interfaces using immobilized peptides that may be enzymatically activated to change their function. The surfaces can be altered (activated) at will to tip adhesion/cytoskeletal balance and initiate differentiation, hence better informing biological mechanisms of stem cell growth. Tools that are able to investigate the stem cell phenotype are important. While large phenotypical differences, such as the difference between an adipocyte and an osteoblast, are now better understood, the far more subtle differences between fibroblasts and MSCs are much harder to dissect. The development of technologies able to dynamically navigate small differences in adhesion are critical in the race to provide regenerative strategies using stem cells.**

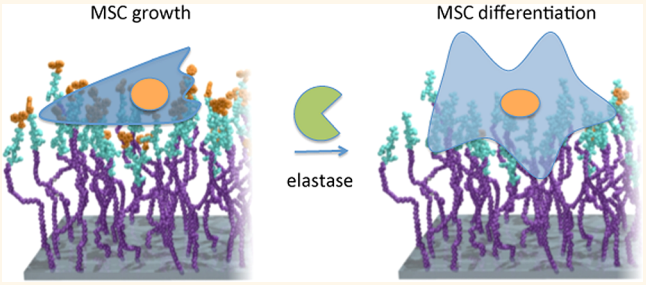

KEYWORDS: *mesenchymal stem cell, stem cell growth, dynamic cell/material interface, metabolomics*

In vivo, adult stem cells reside within a specialized environment known as the niche. The niche is made up of cellular and noncellular components, including resident stem cells, support cells, and extracellular matrix (ECM) that, together, regulate stem cell self-renewal.[1−4]

Traditional culture plastics present a different environment to the *in vivo* niche, and hence mesenchymal stem cells (MSCs) spontaneously differentiate to a heterogeneous population mainly made up of fibroblasts.[5] Thus, understanding and ultimately controlling MSC growth is desirable.

Received: March 13, 2016
Accepted: June 20, 2016
Published: June 20, 2016

DOI: 10.1021/acsnano.6b01765
ACS Nano 2016, 10, 6667−6679

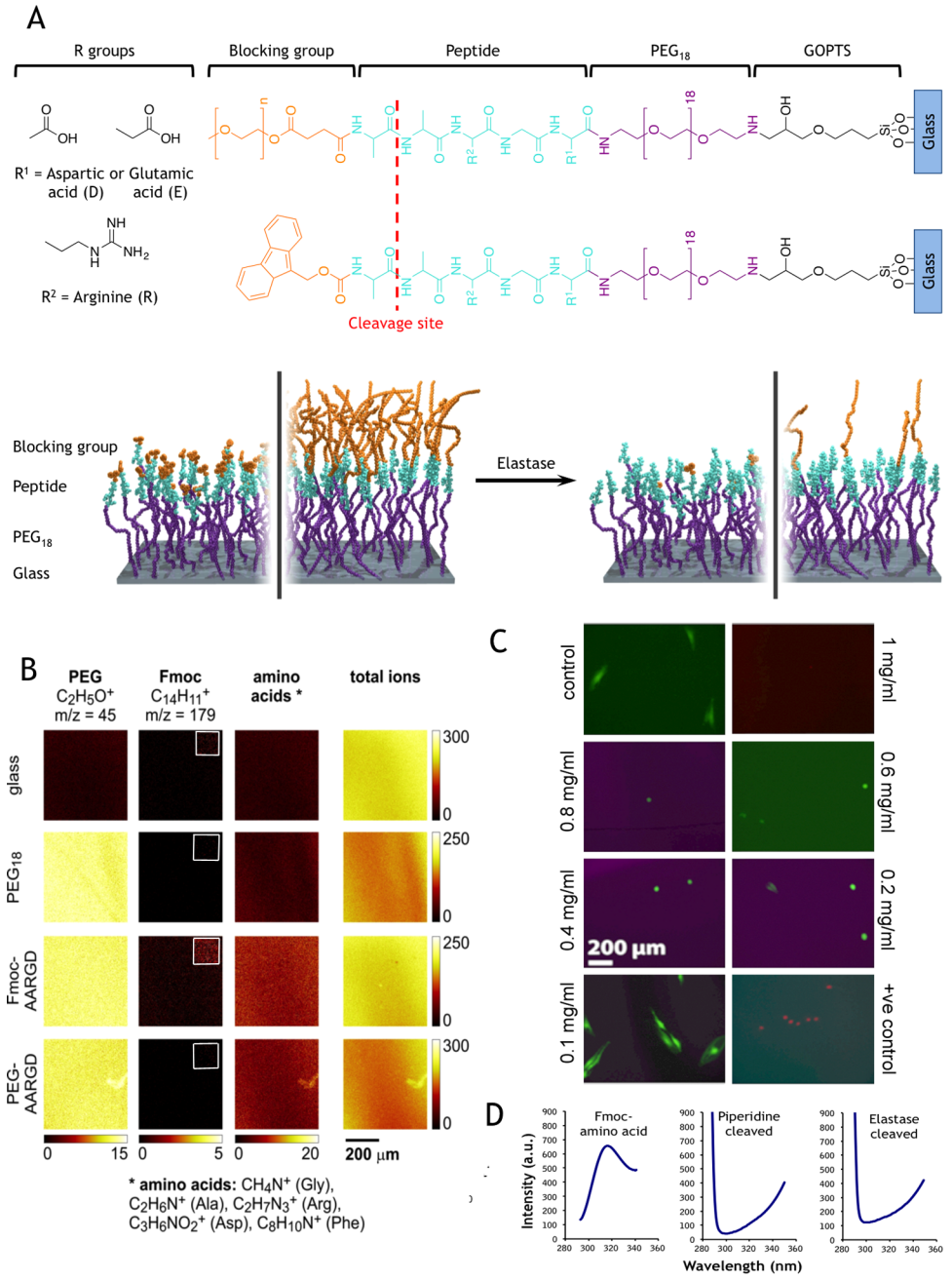

Figure 1. Dynamic, enzyme cleavable surfaces for MSC growth. (A) Cartoon representation of the FMOC and PEG blocked RGD surfaces illustrating the elastase cleavage site. Plain glass coverslips were modified using silanization and PEGylation steps followed by solid-phase peptide synthesis to build up the full structure in a stepwise manner. The incorporation of a dialanine enzyme cleavable linker facilitates the removal of the FMOC/PEG blocking group, thereby forming the basis of the switch. (B) ToF-SIMS image shows a uniform chemical surface composition on the micron scale and confirms that PEG, FMOC, and amino acids (shown as the sum of the indicated representative peaks for each amino acid) are only detected in the analysis where expected; that is, FMOC only seen on the FMOC-D surface and amino acids was only noted when the AARGD sequence was present. Color scales represent ion counts. Images for specific ions are presented on the same scale for all samples; total ion images are scaled to their individual range. Note that inset images in the FMOC column are all similarly brightness-enhanced versions of the main images to show differences more clearly. (C) MSCs were cultured on plain glass coverslips for 48 h and treated with different concentrations of elastase ranging from 1.0 to 0.1 mg/mL (4.60 to 0.460 U) in basal cell culture medium. Live/dead stain for elastase tolerance showed that while cell adhesion was clearly affected at the higher concentrations, few remaining dead cells were noted with any elastase concentration (they may have detached). However, cells incubated with 0.1 mg/mL elastase were indistinguishable from controls, whereas the positive controls (ethanol addition) indicated uptake of the ethidium homodimer; thus these cells were dead. (D) Surface-bound FMOC groups were seen to fluoresce at a wavelength of 315 nm (left-hand spectrum), and piperidine cleavage resulted in a loss of this signal (middle spectrum). At 0.1 mg/mL, it was seen that elastase cleaved surface-bound FMOC (right-hand spectrum); *n* = 3.

In vitro materials-based strategies have been critical for understanding how cells adhere, for example, in showing that MSCs require a minimum patterned area of 69 μm^2 of fibronectin per 1000 μm^2 of surface in order for adhesions to form[6] and that integrin composition and spacing are critical in integrin gathering and adhesion maturation.[7,8] As biomaterials

DOI: 10.1021/acsnano.6b01765
ACS Nano 2016, 10, 6667–6679

can be used to control focal adhesion formation, they can thus be used to tune MSC phenotype.[9,10] It has been shown that if MSCs are allowed to spread, form large adhesions, and develop a highly contractile cytoskeleton, they differentiate into osteoblasts.[11−16] If, however, the MSCs are prevented from spreading, low intracellular tension and resultant adipogenesis follows.[11−16] These rules have been devised using techniques such as microcontact printing of adhesive patterns,[11,17,18] control of stiffness/cross-linking density,[12,13,19] changing grafted chemistries,[20,21] employing stress relaxation,[22,23] and using defined nanotopographies.[24]

Of these, only nanotopography has been shown to also be able to facilitate prolonged MSC growth with retained multipotency.[5] Enhanced MSC self-renewal required a slightly lower level of adhesion and cytoskeletal tension than on controls where spontaneous and untargeted differentiation to fibroblasts was observed.[25] As MSCs have fibroblastic morphology,[26] the morphology/adhesion/tension difference between a fibroblast and a MSC is small. Thus, as it is challenging to control cell tension so subtly, the rules for *in vitro* prolonged MSC growth with multipotency retained remain unclear, and platforms able to achieve this are a scarce resource for the study of how stem cells work.

An optimal cell/material interface would allow dynamic regulation of intracellular tension so that it would be possible to prove that altering the growth adhesion state results in differentiation. While examples of *in situ* change of surface properties exist, these switches involve uncaging and switching between inactive (no adhesion, cell quiescence) and active states (differentiation) and thus are not suited to a more subtle regulation of adhesion required to probe stem cell growth.

Dynamic culture systems are emerging largely based on light-sensitive[27−29] surfaces. Typically, a caging group is removed to reveal the cell adhesive tripeptide RGD (arginine, glycine, aspartic acid), which binds integrins and hence regulates adhesion and intracellular tension.[27,28,30]

The first MSC dynamic system involved MSCs adhering to pendular RGD incorporated within a polyethylene glycol (PEG)-based hydrogel.[31] Photocleavage was used to release the RGDs from the hydrogel, resulting in chondrogenesis as the MSCs rounded up.[31] While clearly demonstrating that it is possible to control cell fate using changes in cell adhesion, this study had limitations as cell viability and expansion were limited in the hydrogels. Another study illustrated the potential for targeting osteogenesis from MSCs in 3D gels over short culture times, but control over cell growth was not achieved.[32]

Electroactive surfaces[33−35] and protein-responsive materials[36] are also of interest in this area. However, these studies rely on nonbiological chemistries and use of conducting materials/electrochemical potentials that may affect cell response, and none demonstrated the ability to support prolonged multipotency or the ability to modulate the environment to allow observation of changes that occur as differentiation is initiated. Recently, mechano-activated surfaces have gained interest based on concepts of opening of cryptic sites in proteins.[37,38]

We, however, chose to employ enzymatic activation to provide a natural stimulus to trigger changes in material properties, with advantages of biocompatibility and selectivity.[39] Here, we present a dynamic surface where both the caging group and the hidden group have discrete and tunable biological roles and show that adhesion can be subtly tuned to turn MSCs from a growth state with multipotency retained to a differentiating state that allows us to elucidate *in vitro* MSC growth mechanisms.

RESULTS AND DISCUSSION

Synthesis of a User-Controlled Nanointerface. Surfaces were synthesized by silanizing glass coverslips and covalently attaching a PEG monolayer onto which fluorenylmethyloxycarbonyl (FMOC)-amino acids were iteratively coupled using solid-phase peptide synthesis directly on the PEGylated glass surface. The complete surface consists of the integrin binding RGD peptide or integrin inactive RGE peptide, followed by an elastase cleavable dialanine (AA) linker and then either FMOC as a steric blocking group, or PEG as an adhesion-reducing blocking group. Hence, the final full sequences were either FMOC-AARGD/E or PEG-AARGD/E, where D/E refers to RGD or RGE constructs. The FMOC protecting moiety sterically prevents cells from fully interacting with the underlying RGD ligands.[40] Elastase removes the FMOC/PEG blocking group exposing RGD, that is, FMOC-A↓ARGD or PEG-A↓ARGD, where ↓ refers to the cleavage point (Figure 1A and Supplementary Figure 1). Using optimized protocols,[41] synthesis was followed using a combination of solid-state fluorescence spectroscopy (SSFS), water contact angle measurements, and time-of-flight secondary ion mass spectrometry (Figure 1B and Supplementary Figures 2 and 3).

In order to activate the surface *in situ*, elastase concentration was optimized so the blocking group could be cleaved from the surface without affecting cell adhesion/viability. MSC adhesion/viability was assessed by incubating the cells with different elastase concentrations (1.0−0.1 mg/mL, 4.60−0.460 U) and using a live/dead stain. Between 1.0 and 0.4 mg/mL, MSCs were rounded up and detached, while at 0.2 mg/mL, some live cells remained attached though poorly spread. At 0.1 mg/mL, cell adhesion/viability was indistinguishable from controls (Figure 1C) and no detrimental affects were identified (Supplementary Figure 4). SSFS confirmed that 0.1 mg/mL elastase could cleave AA and remove FMOC (Figure 1D). ToF-SIMS was employed to indicate that, after FMOC cleavage, RGD was still in place (Supplementary Figure 5). Note that cleavage can be controlled as changing AARGD to phenylalanine (F)ARGD creates a shift from 29 to 50% FMOC cleavage, respectively (Supplementary Figure 6), and this should allow control of how adhesive the surface is or even permit sequential RGD% exposure to the cells.

For FMOC blocking groups, uncleaved substrates are referred to as FMOC-RGD and FMOC-RGE, respectively, and cleaved substrates are referred to as RGD and RGE. Plain glass, PEG_{18}, RGD, and RGE controls were also used, and PEG blocked substrates used in later experiments.

Dynamic Targeting of MSC Adhesions. MSCs were seeded on plain, PEG_{18}, RGD/E controls, FMOC-RGD/E, and surfaces pretreated with 0.1 mg/mL elastase to remove the FMOC blocking group (RGD/E). As expected, poor cell adhesion was observed on PEG_{18}, RGE controls, FMOC-RGD/E, and cleaved RGE substrates. In comparison, cells seeded on plain, RGD controls, and cleaved RGD surfaces adhered well; this is in line with hypothesized adhesion results (*i.e.*, high adhesion on plain glass and surfaces with RGD exposed). Viability assay confirmed that all surfaces supported cell growth (Supplementary Figures 7 and 8).

Seeding density was also optimized and 75, 39, and 7 cells/mm^2 tested. All samples were cultured for 7 days with half of the FMOC-RGD/E substrates cultured as uncleaved (or

DOI: 10.1021/acsnano.6b01765
ACS Nano 2016, 10, 6667−6679

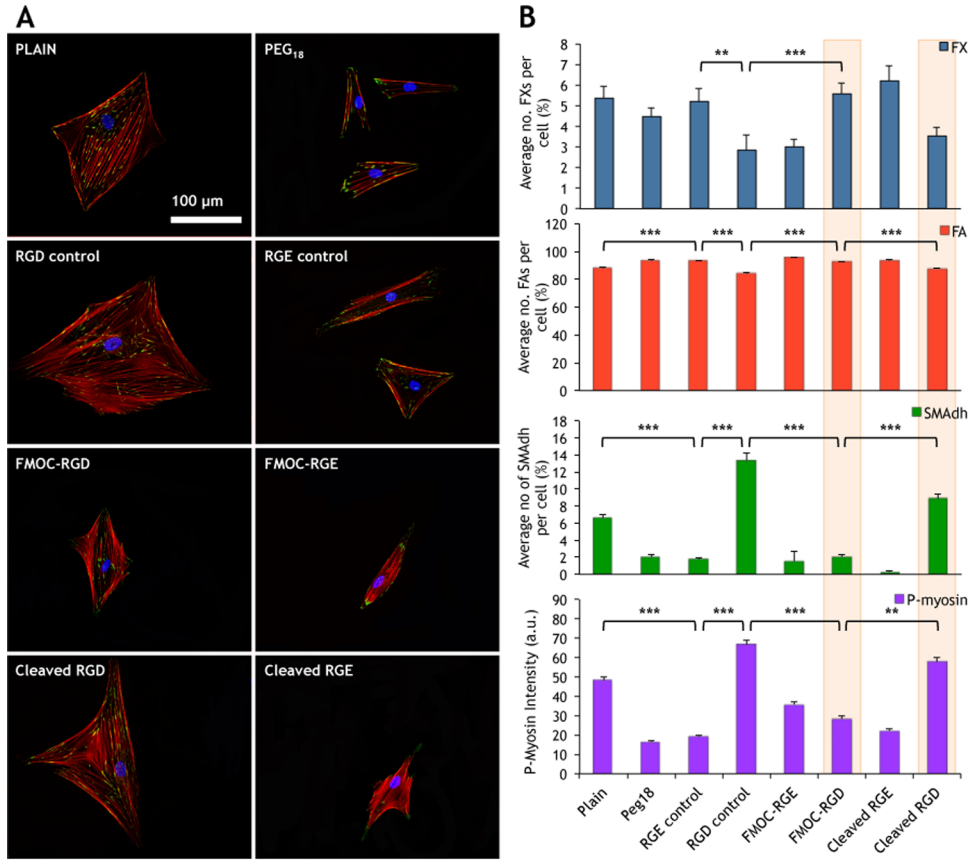

Figure 2. Dynamic control of MSC adhesion and tension. (A) MSCs cultured at 7 cells/mm^2 were seen to spread to a greater degree on plain controls, RGD controls, FMOC-RGD (low), and cleaved RGD (high) surfaces and to a smaller degree on PEG_{18} and all RGE surfaces, creating a pronounced cell size difference between the surfaces. As morphology was altered, adhesion and cytoskeletal arrangement also changed with RGD controls and cleaved RGD (high) surfaces, supporting more organized stress fibers and larger adhesions. Red = actin, green = vinculin, and blue = nuclei. (B) Adhesion subtypes were recorded as a percentage of the average number of adhesions identified per cell. The majority of adhesions were focal adhesions (FAs), with focal complexes (FXs) and supermature adhesions (SMAdhs) making up a much smaller percentage. As a whole, more FXs were observed per cell on plain, PEG_{18}, RGE controls, FMOC-RGD (low), and cleaved RGE substrates, while more SMAdhs were observed on RGD controls and cleaved RGD (high) surfaces. In line with differences in cell size and adhesion length, p-myosin expression, as a measure of cytoskeletal tension, showed the cells were under increased tension on RGD controls and cleaved RGD (high) surfaces. Error bars are standard error of the mean; stars indicate significant difference between groups as determined by one-way ANOVA and Dunn's post-hoc test, where *$P < 0.5$, **$P < 0.01$, and ***$P < 0.001$ - § = plain/PEG different to RGD by $P < 0.05$; $n = 40$ cells per substrate and three material replicates.

adhesion "low") for 48 h before switching to cleaved (or adhesion "high") using elastase (2 days "low" and 5 days "high"). High cell density (75 cells/mm^2) muted the effects of spreading from the "low" to "high" state, while lower cell densities (39 and 7 cells/mm^2) exhibited markedly different degrees of cell spreading between these substrates (Supplementary Figures 8−10). This is in agreement with previous reports illustrating that reduction in cell−cell signaling is important to amplify cell−material signaling.[12] An amount of 7 cells/mm^2 was selected as optimal because, postcleavage, the MSCs acted as if on RGD control.

Adhesion and resultant intracellular tension were further studied through vinculin (present in cell adhesions) and p-myosin (pSer 19 was chosen as it phosphorylates Rho-associated protein kinase involved in cytoskeletal contraction[11]) immunofluorescence. After 7 days of culture (2 days "low" and 5 days "high" for cleaved substrates), adhesions were classified by length[42] as focal complexes (FX, <1 μm), focal adhesions (FA, 1−5 μm), and supermature adhesions (SMAdh, >5 μm). Imaging of vinculin and actin cytoskeleton demonstrated poor adhesion and few stress fibers in cells cultured on PEG_{18}, RGE controls, FMOC-RGE, cleaved RGE, and FMOC-RGD (low) substrates. In contrast, increased adhesion numbers and numerous stress fibers were seen in cells on plain, RGD controls, and cleaved RGD (high) samples (Figure 2A).

All observations thus fit with the hypothesis that FMOC-RGD permitted only cells with a similar adhesion profile to RGE, but as the surfaces were switched from the "low" to the "high" mode, larger cell adhesions became established, similar to RGD controls (Figure 2B and Supplementary Figure 11).

When p-myosin expression was considered, the cells were observed to switch from a lower tension phenotype to a higher one when FMOC-RGD surfaces were enzymatically switched from "low" to "high". MSCs cultured on FMOC-RGD surfaces exhibited p-myosin levels only slightly higher than those of cells cultured on RGE containing substrates, whereas p-myosin expression for MSCs seeded on cleaved RGD surfaces was similar to levels expressed by cells cultured on the RGD control (Figure 2B). Critically, in line with nanotopographical studies, the number of SMAdhs and p-myosin expression was significantly lower on FMOC-RGD substrates than on glass

DOI: 10.1021/acsnano.6b01765
ACS Nano 2016, 10, 6667−6679

controls, supporting that MSC growth requires a lower tensional state than fibroblastic growth.[5,25]

To ascertain if FMOC-RGD substrates do support MSC growth, cell proliferation was assessed on plain, FMOC-RGD, FMOC-RGE, and RGD and RGE controls by analyzing bromodeoxyuridine (BrdU) uptake. Similar numbers of BrdU-positive cells were observed at day 1 of culture, but by day 4, active proliferation was only significantly increased on FMOC-RGD (low) (Supplementary Figure 12A). Furthermore, cell counts over 28 days showed cell expansion was greatest on uncleaved FMOC-RGD (low), in line with MSCs being faster growing than differentiated cells (Supplementary Figure 12B). Moving into functional analysis, we discounted all RGE and PEG_{18} substrates because cell numbers were considered too low to gather meaningful data.

To understand the first stages of differentiation related to adhesion, we examined roles for integrins β_1 (part of the fibronectin (FN) receptor) and β_5 (can form part of the vitronectin (VN) receptor and has been identified previously as being important in MSC osteogenic commitment[43]), the bone morphogenetic protein 2 (BMP2) receptor BMPR1a, and ezrin (anchors stress fibers to the cell membrane). After 48 h of culture, elastase was added to half the cultures to reveal RGD (t_0) and then receptor colocalization followed for 48 h. For MSCs on FMOC-RGD (low) substrates, adhesions were largely punctate and β_1-based, suggesting predominantly FN-receptor-mediated attachments with negligible BMPR1a colocalization or β_5 expression (Figure 3A,B). However, on cleaved RGD (high) surfaces, MSCs were seen to express highly colocalized β_5 and BMPR1a with elongated adhesion morphologies (Figure 3B). These data agree with reports showing that cells bridge adhesions better using VN receptors, allowing larger adhesions to form.[44]

For ezrin, MSCs on FMOC-RGD (low) surfaces had close colocalization of stress fibers and ezrin (Figure 3C). However, on cleaved RGD (high) surfaces, ezrin relocated, becoming associated with cortical actin (Figure 3C). We can postulate that this allows for stress fiber remodeling required as the MSCs adapt to their new environments and increase adhesion. Indeed, if ezrin is knocked down with siRNA, runt-associated transcription factor 2 (RUNX2, an osteogenic transcription regulator) phosphorylation, hence activation, increases (Figure 3C).

Controlling Adhesion Retains MSC Phenotype. Following from observations of adhesion changes, we need to consider if these translate into an ability to control phenotype. Thus, phenotypical analyses of the MSC growth markers STRO-1 and activated leukocyte cell adhesion molecule (ALCAM) and the osteoblast markers osteopontin (OPN) and osteocalcin (OCN) were next used in longer-term cultures. The cells grew to form areas of confluence on glass, RGD controls, FMOC-RGD (low), and cleaved RGD (high) surfaces as could be seen at day 7 (2 days "low" and 5 days "high" for cleaved RGD; Supplementary Figure 13). While MSCs on all surfaces retained expression of STRO-1 and ALCAM, it appeared that MSCs on the RGD controls and cleaved RGD (high) surfaces had started to express OPN and OCN. Image analysis for OCN at days 1, 3, and 5, however, showed negligible OCN at days 1 and 3 and a significant change in osteogenesis only on RGD controls (where cells had been exposed to RGD longest) at day 5 (Supplementary Figure 14).

By day 21 (2 days "low" and 19 days "high" for cleaved RGD), these differences were clear. On RGD controls and

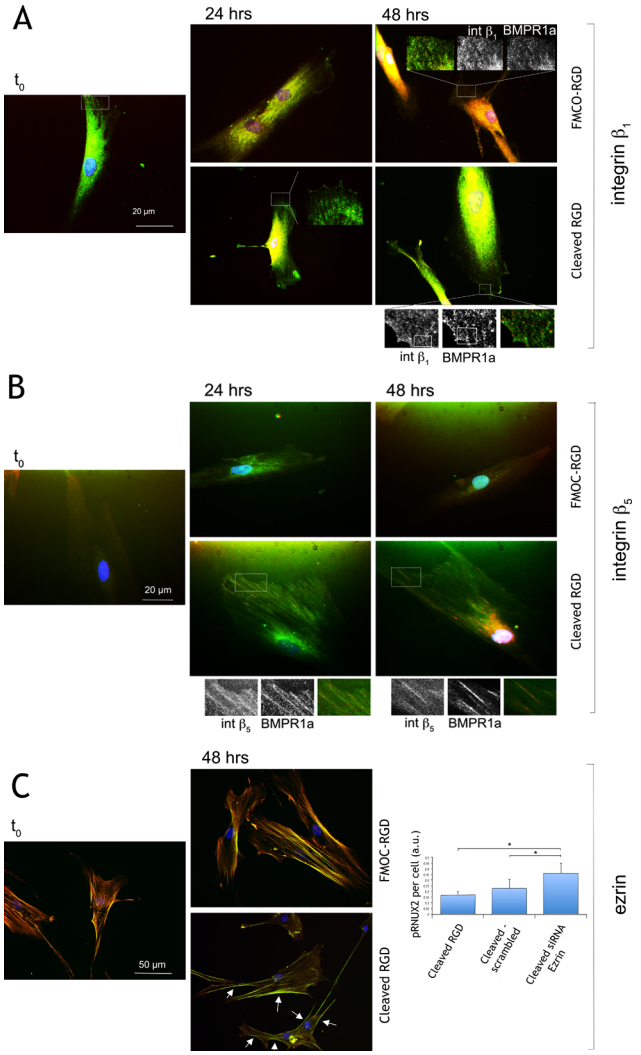

Figure 3. Integrin, BMP2 receptor, and cytoskeletal tethering changes in MSCs on dynamic surfaces. (A) Integrin β_1 and BMPR1a staining in MSCs cultured on FMOC-RGD (low) at t_0 (t_0 is after 48 h of culture immediately before addition of elastase) and then after 24 and 48 h post-elastase treatment (cleaved RGD) or in FMOC-RGD surfaces. β_1 was observed to be found in punctate adhesions, with little BMPR1a colocalization noted (48 h inset). On the cleaved RGD (high) surfaces, BMPR1a was seen with adhesion morphology but in different areas to the regions of β_1 localization (48 h outset). (B) Integrin β_5 and BMPR1a staining in MSCs on FMOC-RGD surfaces at t_0 (immediately before addition of elastase) and then at 24 and 48 h post-elastase (cleaved RGD) or in FMOC-RGD surfaces. On the FMOC-RGD surfaces, little β_5 expression and no BMPR1a colocalization were observed. However, on the cleaved surfaces, strong β_5/BMPR1a colocalization was noted by 24 h (outset images). (C) Actin/ezrin colocalization could be seen at t_0 and on FMOC-RGD. However, for cleaved RGD samples, ezrin appeared to colocalize with cortical actin at the cell periphery (arrows). SiRNA knock-down of ezrin resulted in an increase in pRUNX 2 5 days post-switch. For pRNUX2, in-cell western analysis, $n = 3$, results are mean ± SD, stats by ANOVA and Dunn's post-hoc test where $^*P < 0.05$.

cleaved RGD surfaces, the cells expressed low levels of STRO-1 and ALCAM and high levels of OPN and OCN (Figure 4A). Image analysis of STRO-1 expression at days 7, 14, and 21 illustrated a homogeneous STRO-1 starting population at day 7 on all materials, with STRO-1 levels then falling with time

DOI: 10.1021/acsnano.6b01765
ACS Nano 2016, 10, 6667–6679

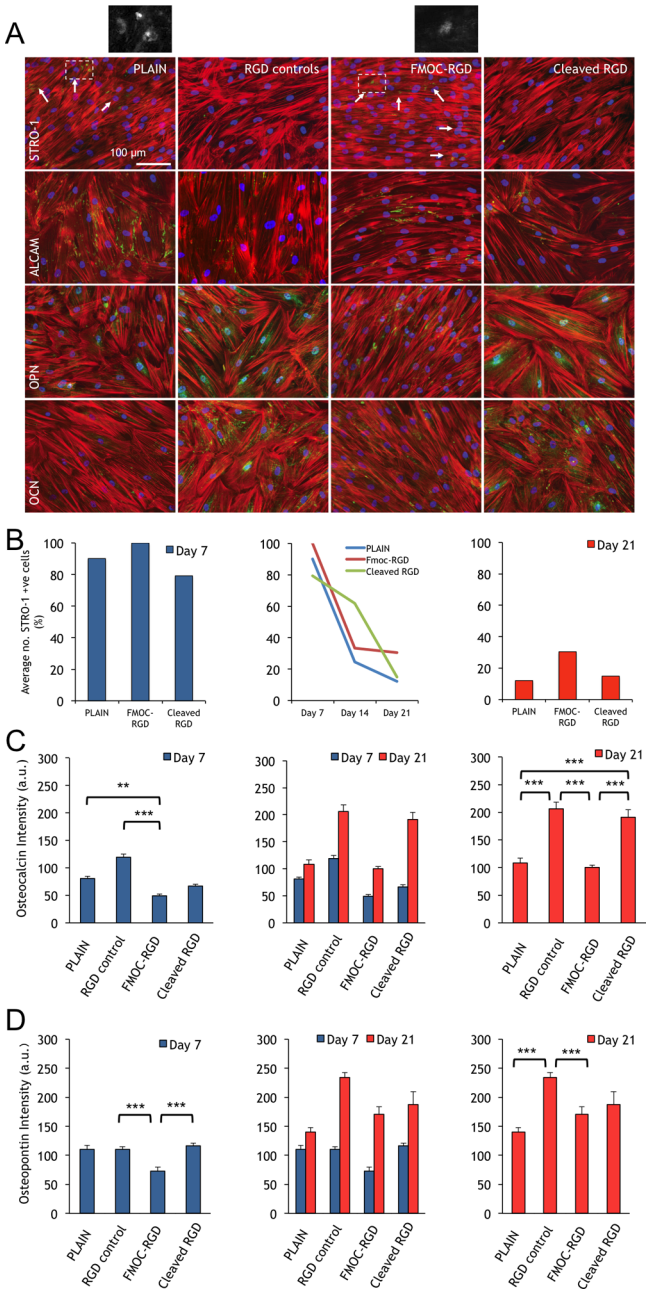

Figure 4. Analysis of MSC growth and differentiation at days 7 and 21. (A) Immunofluorescence images of STRO-1 MSCs at day 21. At this time point, the STRO-1 marker had substantially decreased on all surfaces, remaining only on plain controls and FMOC-RGD (low) surfaces (outset images). ALCAM was still easily detectible on the plain controls and FMOC-RGD but reduced on RGD controls and cleaved RGD (high) surfaces. OPN and OCN levels were increased on RGD controls and cleaved RGD with respect to the other surfaces. Red = actin, green = STRO-1/ALCAM/OPN/OCN, and blue = nuclei; scale bar is 100 μm. (B) Graphs show quantification of STRO-1 expression at 7, 14, and 21 days of culture. At day 7, almost all cells on plain controls, FMOC-RGD, and cleaved RGD surfaces expressed STRO-1. This reduced with time until, at day 21, less that 15% of cells on plain controls and the cleaved RGD surface retained STRO-1 expression, while double this number, >30%, retained STRO-1 expression on FMOC-RGD (approximately 100 cells were included in the quantification; *n* = 2). (C) OCN quantification. Data represent OCN levels expressed by MSCs cultured on plain glass, RGD controls, FMOC-RGD, and cleaved RGD surfaces at days 7 and 21 of culture. OCN expression was observed to increase most on RGD controls and cleaved RGD compared to the other surfaces. (D) OPN quantification. Data represent OPN levels expressed by MSCs seeded on plain glass, RGD controls, FMOC-RGD, and cleaved RGD at days 7 and 21 of culture. OPN expression was observed to increase most on the RGD controls and cleaved RGD surfaces. Statistics carried out by one-way ANOVA and Dunn's post-hoc test, where *$P < 0.05$, **$P < 0.01$, and ***$P < 0.001$, $n = 3$. Note that au = arbitrary units.

(Figure 4B). It is noteworthy that, at day 14, STRO-1 levels were highest on the cleaved RGD (high) surfaces, possibly reflecting a lag due to the switch. However, by day 21, as osteogenic markers were expressed on the cleaved surface, STRO-1 expression was reduced to 15% of cells comparable to 12.2% in cells on the glass control. In contrast, on the FMOC-RGD (low) surface, 30.5% of MSCs retained STRO-1 expression; MSCs could be removed from this surface after 21 day culture and multipotency demonstrated (Supplementary Figure 15).

Quantification of OPN and OCN at 21 days of culture indicated that FMOC-RGD (low) and plain controls had low levels of bone marker expression, wheras significantly elevated levels were observed on the RGD control and cleaved RGD surface (Figure 4C,D). In addition, we checked for the expression of chondrogenic (collagen II) and adipogenic (fatty acid binding protein, FABP) markers. We observed negligible evidence for significant expression of either chondrogenesis or adipogenesis (Supplementary Figure 16), illustrating that targeted differentiation toward a high-tension phenotype, osteogenesis, was achieved on the RGD-exposed surfaces. Osteogenesis for MSCs on the RGD control and cleaved RGD (high) surfaces was confirmed at 28 days (Supplementary Figure 17).

Adhesion/Phenotype Changes Are Reflected in MSC Metabolic Activity. To support phenotypical data, metabolomic analysis was carried out to gain a deeper understanding of MSC metabolism during *in situ* activation as it has been previously shown that the stem cell metabolome becomes activated upon differentiation.[5,25,45,46] Untargeted mass spectrometry analysis of metabolites from MSCs cultured on FMOC-RGD (low) at 2 and 4 days *versus* MSCs on plain controls at similar time points showed only a slight metabolomic change between both time points (Figure 5A,B). However, when FMOC was then cleaved from the surface on day 2 to reveal the RGD ligand (high) and cultured for a further 2 days, changes became highly significant; that is, metabolome activation was observed (Figure 5C). When the culture time was expanded to 7 days (2 days "low" and 5 days "high" for cleaved RGD), metabolic differences increased. Principle component analysis showed that the FMOC-RGD (low) metabolome was more homogeneous than for MSCs on the plain control or cleaved RGD (high) surfaces, where heterogeneous metabolomic profiles were identified (Figure 5D). It has also been proposed that self-renewing embryonic stem cell[45] and MSC[5] populations pool unsaturated metabolites to allow for redox plasticity; this trend is seen in the lipid metabolites in this current study (Figure 5E).

Ingenuity pathway analysis allowed us to observe that fewer metabolic pathways were differentially regulated with less significance in MSCs on the FMOC-RGD (low) surface compared to that on the cleaved RGD (high) surface (Figure

DOI: 10.1021/acsnano.6b01765
ACS Nano 2016, 10, 6667–6679

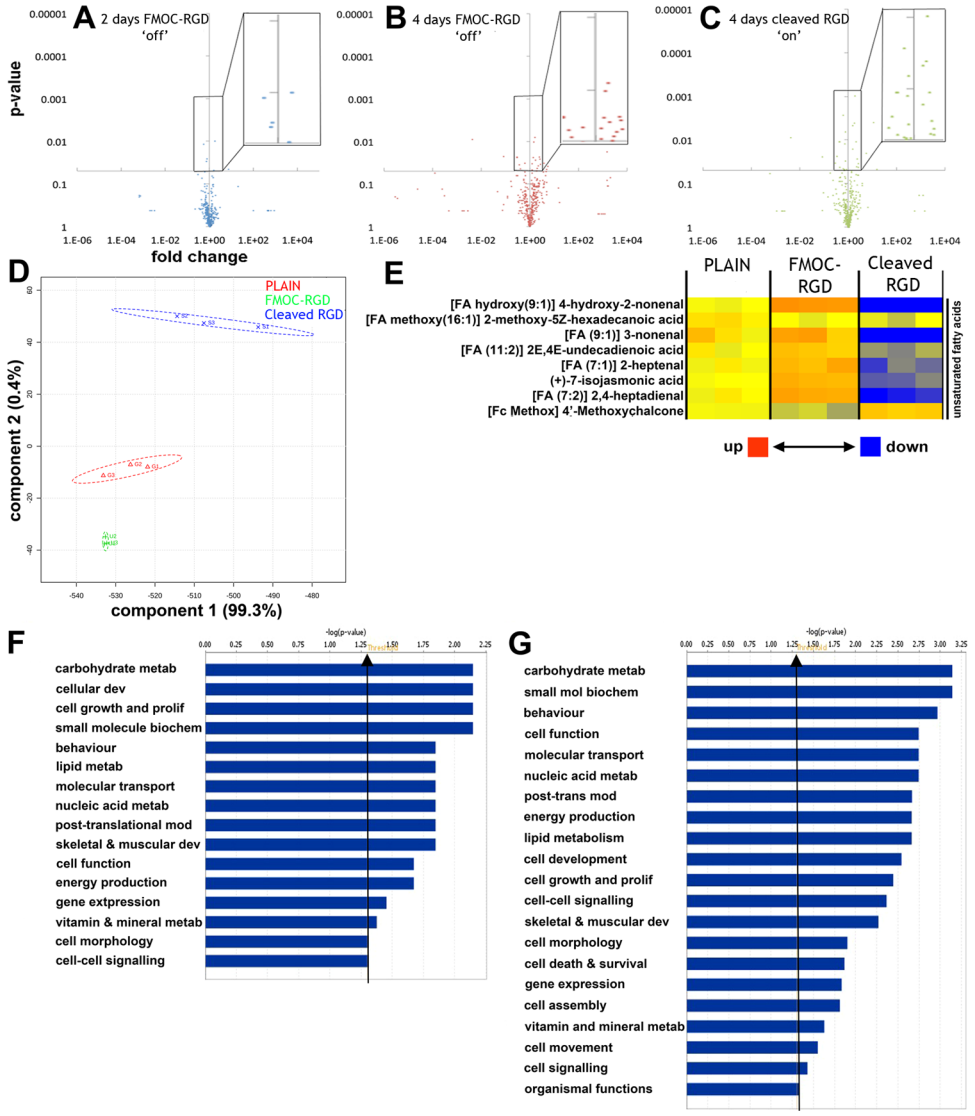

Figure 5. Metabolite analysis of MSCs on dynamic surfaces. (A–C) Putative metabolites were analyzed using MetaboAnalyst 2.0, and the data were displayed as volcano plots relative to D2-plain (plain control at day 2). The *y*-axis refers to the *p* value (determined by two-tailed *t* test), with the *x*-axis intercept set at $P = 0.05$ so that all data points above the *x*-axis represent metabolites that were significantly different from controls. The *x*-axis represents fold change as a measure of the magnitude in difference between samples and the control. Data points to the left of the *y*-axis are metabolites down-regulated with respect to controls, and data points on the right of the *y*-axis were up-regulated ($n = 3$). (D) At 7 days (2 days "low" and 5 days "high" for cleaved RGD), principle component analysis showed very clear metabolomic differences with MSCs on the FMOC-RGD (low) surface having a highly homogeneous metabolome, more so than on the controls, and the cleaved RGD (high) surfaces having a far more heterogeneous metabolome ($n = 3$). (E) Heatmap of putatively detected unsaturated lipids after 7 days culture showing up-regulation in MSCs on the FMOC-RGD surface and down-regulation in MSCs on the cleaved RGD surface ($n = 3$). (F,G) Ingenuity functional pathway analysis illustrating more significantly altered functional pathways in MSCs on the cleaved RGD surface (F) compared to those on FMOC-RGD surfaces (G). Functions include carbohydrate, small molecule, nucleic acid, lipid and vitamin metabolism, cell growth and proliferation, and skeletal development pathways (statistics by Fischer's exact test, $P < 0.05$ represented by bars higher than the threshold arrow, $n = 3$).

5F,G). These include pathways involved in energy (energy production, lipid and carbohydrate metabolism), growth (cell proliferation and nucleic acid metabolism), protein (post-translational modification and cellular development), and skeletal development. Furthermore, most highly modulated networks for MSCs on FMOC-RGD (low) illustrated metabolic regulation linked to cell growth control. When similar networks were considered for cells on cleaved RGD (high), metabolic regulation appeared less significant (Supplementary Figures 18 and 19).

Long-Term MSC Growth Control. Next, we wanted to examine if our "low" maintenance state could work for prolonged cultured before switching to "high", thus further demonstrating that adhesion was responsible for growth/osteogenesis. Thus, we cultured the MSCs for 2 weeks rather than 2 days before adding elastase and then allowed the cells to grow a further 2 weeks before staining for STRO-1. With the longer time to trigger, loss of STRO-1 on the cleaved RGD surface (high) was not seen, suggesting retention of multipotency rather than differentiation (Supplementary Figure 20). Working on the hypothesis that the FMOC group becomes

DOI: 10.1021/acsnano.6b01765
ACS Nano 2016, 10, 6667–6679

coated in ECM proteins reducing elastase efficiency, we substituted the FMOC blocking group for PEG to reduce protein adsorption.

As with FMOC-RGD, MSCs were seen to expand on PEG-RGD and retain STRO-1 expression, which was reduced on plain controls (Figure 6A,B). However, unlike with FMOC, switching from PEG-RGD to its corresponding cleaved counterpart resulted in focal adhesion elongation and reduction in STRO-1, demonstrating that stimulus-initiated cell differentiation with elastase could be achieved with longer culture (Figure 6A,B). Metabolomic analysis after 7 days culture (2 days "low" then 5 days "high" for cleaved RGD) again showed that the inactive RGD surface (PEG-RGD) had the most homogeneous metabolome, while cleaved RGD surfaces had a more heterogeneous metabolome indicative of a change from MSCs to differentiating phenotype (Figure 6C).

SUMMARY AND CONCLUSIONS

This report provides evidence that the MSC adhesion "footprint" permits control of MSC growth and targeted differentiation. Using enzyme cleavable surfaces, it is shown that increasing adhesion causes lineage commitment. This report addresses a major research focus of MSC biology—how do they regulate multipotency. MSCs are shown to walk an extremely fine line between controlled growth with multipotency and spontaneous fibroblast differentiation. We propose from our data that a small reduction in adhesion by controlling the integrin subunit use prevents metabolome activation with associated energy demand required for differentiation; a larger reduction in adhesion and tension would result in adipogenesis.[11,17] On the same surface, we demonstrate that a switch from FN to VN receptor facilitates both adhesion and BMP signaling to switch from stem cell growth to osteogenic commitment through increased levels of intracellular tension. We note that our analysis relies largely on binning adhesion length and that analysis in *X*, *Y*, and *Z* may yield further information.[47,48] However, we show that length gives an effective, easy to use, differentiation between MSC states of self-renewal and osteogenesis. Further, we postulate, from ezrin observations, that potential cytoskeleton decoupling from the membrane during changes in adhesion dynamics can accelerate the commitment to differentiation.

We illustrate that we can refine our protocols by switching from FMOC to PEG to create a surface that is both amenable to longer-term dynamic culture and is made from all biocompatible building blocks. This, and the ability to control degree of cleavage by switching peptide sequence (Supplementary Figure 6), is a clear advantage of our surfaces.

We present a dynamic surface that clearly shows that the adhesion/tension balance relationship between a fibroblast (the "lab weed") and MSCs (a stem cell with major regenerative potential) is small. It is thus exciting that materials can be designed to enhance MSC growth and to study lineage commitment in a dynamic manner.

MATERIALS AND METHODS

Unless otherwise stated, reagents are from Sigma, UK. Raw data can be found at doi.org/10.5525/gla.researchdata.324.

Surface Modification. Substrates were synthesized as previously described[40] using FMOC protected L-amino acids. Glass coverslips were sonicated in acetone, ethanol, methanol, and then deionized water (20 min each). Afterward, coverslips were cleaned for 1 h using a 3:7 piranha solution of 30% hydrogen peroxide and concentrated

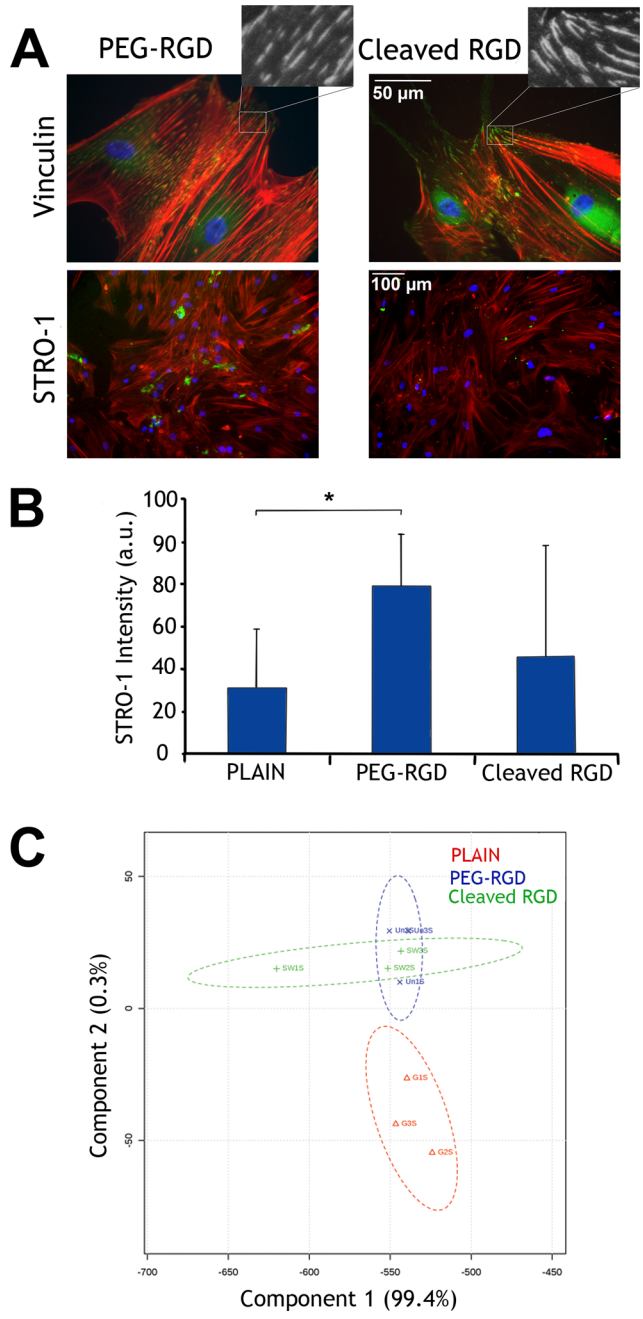

Figure 6. Analysis of MSC adhesion and differentiation on PEG blocked surfaces. (A) Immunofluorescence images of vinculin in adhesions at day 5 and STRO-1 at day 21 of culture. On the PEG-RGD (low) substrates, MSCs were observed to have smaller adhesions and increased expression of the STRO-1 MSC marker (arrows) compared to MSCs seeded on RGD cleaved surfaces (high) where, again, larger adhesions and loss of STRO-1 expression was observed. Red = actin, green = vinculin or STRO-1, and blue = nucleus. (B) Image analysis after 21 days of culture confirmed these results, demonstrating that more MSCs retained STRO-1 expression on PEG-RGD than cells on plain controls and cleaved RGD surfaces which typically lose STRO-1 much faster (results are mean ± SD, statistics by ANOVA, *P < 0.05). (C) Principle component analysis from metabolomics data illustrates most data homogeneity on PEG-RGD surfaces and most heterogeneity on the cleaved RGD surface as with the FMOC blocked samples (n = 3).

DOI: 10.1021/acsnano.6b01765
ACS Nano 2016, 10, 6667–6679

sulfuric acid to remove organic contaminants and then individually washed in copious amounts of deionized water, dried under nitrogen, and left at 75 °C overnight. Once dry, surfaces were functionalized with amine groups as per Piehler *et al.*,[49] to facilitate direct attachment of amino acids during SPPS. To achieve this, surfaces were silanized using (3-glycidyloxypropyl)trimethoxysilane at 37 °C for 1 h and washed with acetone and dried under nitrogen. A diamine-functionalized polyethylene glycol powder (*O*,*O*′-bis(2-aminoethyl)-octadecaethylene glycol, PEG; CAS no. 892154-56-2) was melted onto the surfaces at 75 °C for 48 h to attach the PEG linker through reaction of the epoxy groups on the surface, with the amine groups on the PEG. Surfaces were cleaned in deionized water to wash off the unbound PEG and then dried under nitrogen.

To build up the peptide chain using SPPS, a three-step procedure was applied. In step 1, the first FMOC-protected amino acid (0.2 mmol) was coupled to the PEG monolayer in a solution of ethyl(hydroxyimino)cyanoacetate (0.4 mmol) and *N*,*N*′-diisopropylcarbodiimide (0.4 mmol) per 10 mL of anhydrous *N*,*N*-dimethylformamide (DMF). Samples were submerged in solution for 2 h and gently agitated on an orbital shaker to allow continued mixing of reagents and removal of byproducts from the sample surface. After this time, samples were rinsed in DMF, ethanol, methanol, and DMF (5 min each using agitation). A fresh reaction solution containing the same amino acid was prepared and added to samples, which were then left overnight under the same conditions described above. Washing stages using DMF, ethanol, methanol, and DMF were previously outlined.

For the second step, FMOC groups were removed (deprotected) using piperidine (20% in DMF) for 2 h under agitation, followed by washing steps. Subsequent additions of FMOC-protected amino acids were carried out repeating steps 1 and 2 until the desired peptide sequence was obtained. The terminating FMOC groups were left in place. The final step (step 3) was to remove side-chain protecting groups on aspartic acid and glutamic acid residues (*O*-*tert*-butyl; O*t*Bu) and arginine (pentamethyldihydrobenzofuran-5-sulfonyl; Pbf) with a 90% solution of aqueous trifluoroacetic acid for 4 h. Samples were washed and dried and then stored under vacuum in a desiccator or used straight away. For surfaces terminating in a PEG blocking group (*i.e.*, PEG-AARGD−), the peptide chain was built up as per the method for FMOC surfaces with an additional step to remove the terminating FMOC with piperidine. PEG (*O*-methyl-*O*′-succinyl polyethylene glycol 2000, CAS no. 31961-02-1) was then added to the terminal amino acid prior to the side-chain protecting groups being removed.

FMOC and PEG blocking groups were removed *in situ* by enzymatic cleavage using porcine pancreatic elastase (Worthington Biochemical), which was reconstituted in basic culture media and filtered through 0.22 μm. Throughout this work, the same bottle was used and certified as having an enzymatic activity of 4.61 units/mg, where 1 unit (U) converts 1 μmol of *N*-succinyltrialynyl-*p*-nitroanilide per minute at 25 °C.

Stepwise Monitoring of Solid-Phase Peptide Synthesis. *Water Contact Angle.* Water contact angle was carried out using the sessile drop technique with a KSV CAM 100 contact angle goniometer (KSV Instruments, USA). High contrast images of static water droplets were recorded, and CAM 100 software was used to apply a circular fit to the droplet outline to determine contact angles across a series of measurements. A total of three droplets were recorded per surface (25 frames per droplet) and three of each surface used. Averages were pooled for the main data.

Solid-State Fluorescence Spectroscopy. After each coupling and deprotection stage, samples were taken from the bulk batch after the methanol washing stage and rinsed in distilled water, followed by drying under nitrogen. Samples were analyzed using fluorescence spectroscopy to confirm the attachment of the FMOC-protected amino acids and removal of the FMOC group during coupling and deprotection stages. This technique is as described in literature by Zelzer *et al.*,[50] taking advantage of the fluorescent properties of the FMOC group. Fluorescence spectra were measured at room temperature using a JASCO FP-6500 spectrophotometer (JASCO, JPN) with spectra manager software. Samples were attached to a glass microscope slide inserted into a custom-made rotatable holder within the spectrophotometer chamber. Samples were orientated at 30° to the incident light to limit the amount of reflected excitation light hitting the detector. Excitation of the surface-tethered FMOC groups was carried out using an excitation wavelength of 270 nm with a slit width of 20 nm. Three spectra were recorded at each stage of synthesis using three different samples.

Cell Culture. *STRO-1 Selected MSCs.* Skeletal STRO-1$^+$ MSCs were derived from bone marrow obtained from hematologically normal patients undergoing routine total hip replacement surgery with the approval of Southampton General Hospital Ethics Committee; only tissue that is normally discarded was used. Cells were aspirated from trabecular bone marrow samples and centrifuged at 250*g* for 4 min at 4 °C. The cell pellet was resuspended in α-MEM and passed through a 70 μm pore nylon mesh (BD Biosciences). Red blood cells were removed by centrifugation with lymphoprep gradient solution (Robbins Scientific) and the remaining cells in the buffy layer resuspended in 10 mL of blocking solution (4-(2-hydroxyethyl)-1-piperazine ethanesulfonic acid, HEPES) saline solution with 5% v/v fetal calf serum, 5% v/v human serum, and 1% w/v bovine serum albumin (BSA). Afterward, the cells were incubated with a STRO-1 antibody in hybridoma supernatant (hybridoma courtesy of Dr. Beresford, University of Bath) and flushed with magnetic cell separation buffer (Miltenyi Biotec) to remove any excess antibody. The cells were incubated with human anti-IgM magnetic microbeads (Miltenyi Biotec, UK) and added to a magnetic column; the eluent was collected as the STRO-1$^-$ fraction. After being washed with MACs buffer without the magnetic field, the eluted cell population was collected as the STRO-1$^+$ fraction. Skeletal MSCs purchased from Promocell were used for metabolomics experiments.

MSC Maintenance and Experiment Preparation. MSCs were maintained at 37 °C and 5% CO_2 in α-MEM (PAA Laboratories) supplemented with 10% v/v fetal bovine serum (FBS) and 2% v/v antibiotic mix (60% v/v L-glutamine, 35% v/v penicillin−streptomysin, and 5% v/v ampotericin B). For all experiments, cells were rinsed in HEPES saline solution (150 mM NaCl, 5 mM KCl, 5 mM glucose, 10 mM HEPES, and 0.5% v/v phenol red indicator adjusted to pH 7.5), followed by 4 mL of trypsin−versene solution (0.5% v/v trypsin and versene: 150 mM NaCl, 5 mM KCl, 5 mM glucose, 10 mM HEPES, 1 mM ethylenediaminetetraacetic acid, and 0.5% v/v phenol red indicator adjusted to pH 7.5) until cells were detached from the tissue culture flask. Detached cells were transferred to a sterile falcon tube and centrifuged at 376*g* for 4 min. The supernatant was discarded and the cell pellet resuspended in 5 mL of fresh α-MEMs. Cell numbers were counted using a Neubaur hemocytometer and seeded as per experimental setup. Prior to use, substrates were sterilized with 70% ethanol (3 × 5 min) and then washed with HEPES saline solution and basal α-MEM.

Coomassie Blue Staining. To assess cell adhesion, MSCs were fixed 10% v/v formaldehyde/PBS for 15 min at 37 °C and then stained with coomassie blue protein dye (0.5% w/v coomassie brilliant blue R-250 dissolved in 4:1 methanol/acetic acid and filtered with Whatman filter paper) for 15 min at room temperature. Excess stain was removed by washing samples with water until areas around the cells were clear. Images were taken using a Zeiss Axiovert inverted light microscope at 10× magnification (0.25 NA) with a Qimaging digital CCD camera (Qimaging, Canada) and Qcapture software; $n = 3$.

Elastase Tolerance. For elastase tolerance, MSCs were seeded onto plain glass coverslips and left to adhere for 48 h. Porcine pancreatic elastase was dissolved in α-MEMs at 37 °C as a stock solution and then filter sterilized through a 0.22 μm syringe filter. The stock solution was diluted across a concentration range of 1.0−0.1 mg/mL (4.61−0.461 units) and added to samples in place of α-MEMs (controls were maintained in basic α-MEMs). MSCs were incubated for a further 24 h and examined for detachment using a Zeiss Axiovert inverted light microscope at 10× magnification (0.25 NA) with a Qimaging digital CCD camera (Qimaging, Canada) and Qcapture software; $n = 3$.

DOI: 10.1021/acsnano.6b01765
ACS Nano 2016, 10, 6667−6679

Live/Dead Staining. For live/dead staining during elastase tolerance, cells were seeded onto plain glass coverslips as described in Elastase Tolerance section and cultured for 24 h in α-MEM, followed by a further 24 h of culture in medium containing the titrated concentrations of elastase (4.61−0.461 units and controls). Additional "dead" control cells were cultured in the absence of elastase, and 70% ethanol was added to kill the cells prior to staining. Culture medium was removed, and cells were washed twice in warm phosphate-buffered saline (PBS), which was then replaced with live/dead assay reagents (2 μM calcein AM and 4 μM ethidium homodimer-1 in PBS) and incubated at room temperature until color development occurred (approximately 15 min in the dark). The stain was removed, and the cells were rinsed twice in warm PBS and imaged using a Zeiss Axiovert fluorescence microscope.

For live/dead staining of cells cultured on the panel of surfaces, cells were cultured on plain controls, PEG_{18}, RGD, and RGE controls, FMOC-RGD, and FMOC-RGE (see Supplementary Figure 2 for corresponding peptide sequences) for 24 h in α-MEM. Dead control cells were prepared by adding 70% ethanol to cells cultured on plain coverslips after 24 h. The cells were stained and imaged as described above.

Proliferation Assay. Cells were cultured on plain glass coverslips, plain controls, PEG_{18}, RGD, and RGE controls, FMOC-RGD, and FMOC-RGE substrates in α-MEM and pulse-labeled with 10 μM 5-bromo-2-deoxyuridine (BrdU) for 4 h prior to fixation for 1 day and 4 day time points. BrdU-positive MSCs were visualized as described in Immunocytochemistry.

Phenotype Characterization Pre- and Post-trigger. Cells were seeded onto plain glass coverslips, RGD controls, and FMOC-RGD surfaces and cultured in standard α-MEM (see MSC Maintenance and Experiment Preparation for culture media composition). To cleave the FMOC blocking group, the culture medium was replaced with medium containing 0.1 mg/mL elastase for 2 days and then replaced with standard α-MEM for the remaining length of the culture. The cells were cultured for a total of 2 weeks.

Induction Medium Experiment. Cells were cultured for 2 weeks on plain controls and FMOC-RGD surfaces in standard α-MEM. After this time, samples were divided into three groups: control groups cultured in standard α-MEM, osteogenic cultures incubated with osteogenic induction media (350 μM ascorbate-2-phosphate, 0.1 μM dexamethasone in DMEM with 10% FBS), and adipogenic cultures that were alternated between adipogenic induction media (1 μM dexamethasone, 1.7 nM insulin, 200 μM indomethacin, 500 μM isobutylmethylxanthine in DMEM with 10% FBS, L-glutamine and antibiotics) and maintenance medium (1.7 nM insulin in DMEM with 10% FBS, 200 mM L-glutamine and antibiotics). The three groups were cultured for 4 weeks before fixation; n = 3 replicates of each surface per group.

Cell Population Marker Analysis. Cells were seeded onto plain controls, RGD controls, and FMOC-RGD substrates. Half of the FMOC-RGD surfaces were cleaved by replacing the culture medium with medium containing 0.1 mg/mL elastase after 2 days of culture. Cells were fixed after 24 h, 3 days, and 5 days of culture as per the method described in Immunocytochemistry.

Immunocytochemistry. Samples were washed with PBS and fixed with 10% v/v formaldehyde/PBS for 15 min at 37 °C. Cells were permeabilized at 4 °C for 5 min (30 mM sucrose, 50 mM NaCl, 3 mM $MgCl_2 \cdot 6H_2O$, 20 mM HEPES, and 0.5% v/v Triton X-100 in PBS adjusted to pH 7.2), and nonspecific binding epitopes were blocked with 1% w/v BSA/PBS for 15 min at 37 °C (this step was omitted for anti-BrdU staining). Primary antibodies were made up in PBS/BSA with rhodamine−phalloidin (1:500; Molecular Probes) with either

1. Mouse monoclonal antivinculin IgG (1:150; Sigma) for adhesion analysis.
2. Mouse monoclonal anti-phosphomyosin IgG (1:200; Cell Signaling Technology) for phosphomyosin studies.
3. Mouse monoclonal anti-STRO-1/OPN/OCN IgG (1:50; Insight Biotechnology) or rabbit polyclonal anti-ALCAM IgG (1:50; Epitomics) for phenotype analysis and cell population marker analysis.
4. Mouse monoclonal anti-BrdU (clone BU-1, 1:100 in nuclease solution, prepared according to the manufacturer's instructions in kit RPN202; GE Healthcare) for proliferation studies. Rhodamine−phalloidin was added with the secondary rather than the primary antibody.
5. Rabbit polyclonal anti-fatty acid binding protein (FABP; 1:50; Abcam) or rabbit polyclonal anti-collagen II (COL2A, 1:50; Insight Bio) for cell phenotype pre- and post-trigger. Rhodamine−phalloidin was added with the secondary antibody for collagen II.
6. Rabbit polyclonal anti-RUNX2 (1:50; Insight Bio) or mouse monoclonal anti-vimentin (1:50; Sigma) for elastase experiments.
7. Rabbit polyclonal anti-ezrin/radixin/moesin (Cell Signaling Technology; 1:50) for ezrin expression.

Samples were incubated for 1 h (1.5 h for anti-BrdU) at 37 °C, after which time they were washed in 0.5% v/v Tween 20/PBS (PBST, 3 × 5 min under gentle agitation) to minimize background labeling. Horse biotinylated anti-mouse IgG (1:50; Vector Laboratories) or horse biotinylated anti-rabbit IgG (Vector Laboratories) BSA/PBS was added to samples and incubated for 1 h at 37 °C. After the washing stages, samples were incubated for 30 min at 4 °C with fluorescein isothiocyanate streptavidin (FITC; 1:50; Vector Laboratories) in BSA/PBS followed by a final washing stage. Coverslips were placed on glass slides in 4′6-diamidino-2-phenylindole mountant (Vector Laboratories).

Cells imaged for adhesions analysis were visualized using a Zeiss Axiophot fluorescence microscope at 20× magnification (0.40 NA). Images were captured using an Evolution QEi digital monochromatic CCD camera (Media Cybernetics, USA) with Qcapture imaging software. Cells imaged for phosphomyosin and phenotype analysis were imaged with a Zeiss Axiovert fluorescence microscope at 20× magnification (0.50 NA) and studies at 40× (0.40 NA). Axiovert images were taken using an Evolution QEi digital monochromatic CCD camera (Media Cybernetics, USA) with ImagePro software.

Double Immunostaining for Colocalization Studies. Cells seeded on FMOC-RGD substrates were cultured for 2 days. After this time, control cells were cultured in standard culture media while test samples were incubated with 0.1 mg/mL elastase for 24 and 48 h. Colocalization of BMPR1A with the integrins β1 and β5 was performed using immunocytochemistry in the previous section. After fixation, samples were incubated with a primary antibody cocktail consisting of rabbit polyclonal anti-BMPR1A (Thermo Scientific; 1:50), mouse monoclonal anti-integrin β1 (Thermo Scientific; 1:50), and mouse anti-integrin $\alpha v\beta 5$ (R&D system, 1:50) in 1% of BSA/PBS. Secondary antibodies were Texas red anti-mouse (Vector Laboratories; 1:50) for integrin β1 and β5 and biotinylated anti-rabbit (Vector laboratories) conjugated with FITC for BMPR1A.

Cells imaged for colocalization of BMPR1A with integrin β1 and β5 were visualized using a Zeiss Axiophot fluorescence microscope at 40× magnification (0.75 NA). Images were captured using an Evolution QEi digital monochromatic CCD camera (Media Cybernetics, USA) with Qcapture imaging software.

RNA Interference. RNA interference was performed using non-targeting siRNA (cat no. D001810-01-05) and human ezrin−siRNA (cat no. L-017370-00) purchased from GE Healthcare. Transfections were carried out using DharmaFECT Transfection Reagents (GE Healthcare) according to the manufacturer's instructions.

In Cell Western. Cells on substrates were washed with PBS and fixed with 10% v/v formaldehyde/PBS for 15 min at 37 °C. Cells were permeabilized using precooled methanol at 4 °C for 10 min, and nonspecific binding epitopes were blocked with 1% milk protein in 0.1% Tween 20/PBS (PBST) for 1 h at room temperature. Cells were then washed three times (3 × 5 min) with 0.1% PBST. Primary antibodies diluted in 1% milk/PBST containing cell tag 700CW stain (1:500; LI-COR, cat no. 926-41090) with either

DOI: 10.1021/acsnano.6b01765
ACS Nano 2016, 10, 6667−6679

1. Rabbit polyclonal anti-ezrin/radixin/moesin (Cell Signaling Technology; 1:50) for ezrin knock-down efficiency measurement.
2. Rabbit polyclonal RUNX2 (Santa Cruz; 1:50) expression in ezrin knock-down cells.
3. Rabbit polyclonal phospho-RUNX2 pSer465 (Thermo Scientific; 1:50) for phospho-UNX2 expression in ezrin knock-down cells.

Cells with primary antibodies were incubated at room temperature for 1 h and then washed with 0.1% PBST three times. After being washed, cells with secondary antibody—either IRDye 800CW, goat anti-mouse (LI-COR, cat no. 926-32210), or donkey anti-rabbit (LI-COR, cat no. 926-32213) diluted in 1% milk/PBST at 1:1000 were incubated at room temperature for 1 h or at 4 °C for overnight. After the washing stage, cells were subjected to a LI-COR Odyssey Sa (0157) scanner. The protein of interest was scanned at channel 800 and CellTag at channel 700 (scan parameters: focus offset = 2.0 mm, scan resolution = 100 μm, intensity = 12). Data were collected in integrated intensity (IntegInten) and analyzed by one-way analysis of variance (ANOVA) and Dunn's post-hoc test applied where significance was determined as $P < 0.05$.

Image Analysis. Fluorescence microscopy images were exported to Adobe Photoshop for the purpose of labeling and superimposing color channels. For size analysis, actin images were exported to ImageJ (http://rsbweb.nih.gov/ij/download.html) to calculate cell area using the threshold tool. For adhesion analysis, vinculin images were exported to Adobe Photoshop, and each individual adhesion was traced with a 1 pixel width line to create an adhesion mask superimposed over the background image. ImageJ was then used to determine total adhesion numbers and length; individual subtypes were plotted as a percentage of the overall number of adhesions recorded. For the proliferation analysis, the percentage of BrdU-positive cells was quantified for at least 150 cells per sample type and normalized to determine the percentage change relative to the glass controls. Analysis of the maintenance of STRO-1$^+$ expression of staining over time was performed by allocating cells into categories (at least 50 cells per surface type), indicating the features of the staining.

In order to determine phosphomyosin expression, or STRO-1$^+$ expression for cell population analysis (at least 50 cells per sample type), grayscale images were exported into ImageJ and individual cells were selected with the polygon tool. Using the method described in Burgess *et al.*,[51,52] phosphomyosin expression was calculated using integrated density (ID) values where ID = (area × mean gray value). Calculations were then corrected for background fluorescence using the formula ID − (cell area × ID of background fluorescence). In order to quantify the expression of phenotypic markers, fluorescence images were exported to ImageJ and highlighted with the threshold tool. Integrated density values (area × mean gray value) were recorded, and these values were divided by the number of nuclei to average fluorescence across the number of cells in the same field of view. As the background fluorescence could not be recorded because of cell confluency, only images taken at similar exposure levels were used.

Data were analyzed by ANOVA and Dunn's post-hoc test applied or *t*-tests to identify any significant differences between the groups, where significance was determined as $P < 0.5$.

MTT Assay. After 5 days, 100 μL of 5 mg/mL MTT (methylthiazolyldiphenyl tetrazolium bromide) solution in complete cell culture media was added to the cells for 2 h. After this time, the medium was removed and replaced with DMSO for 5 min. Liquid from each well was then analyzed at 570 nm (background set to 670 nm) and optical density reported.

Metabolomics. For metabolomic analysis, substrates were removed from the well plates and transferred to new sterile plates so that only cells that were attached to the substrates were used in the analysis. Substrates were washed once with warmed PBS, and then 0.5 mL of ice-cold extraction solvent (chloroform/methanol/water at 1:3:1 v/v) was added to the wells. Plates were sealed with parafilm to minimize evaporation and placed on a rotary shaker for 1 h at 4 °C. After this time, the extraction solvent was transferred to sterile 0.5 mL Eppendorf tubes and centrifuged at 13 000*g* for 5 min to remove cell debris. The supernatant was transferred to LC vials; otherwise, samples were stored at −80 °C in Eppendorf tubes until use. For elastase studies, all samples were processed in-well with 150 μL of extraction solvent added to each well. Samples were then processed as above.

All samples were diluted 1 in 2 with acetonitrile prior to being aspirated to HPLC vials; an additional 5 μL of each sample was combined into a single aliquot to be used as a quality control sample. This pooled sample was injected several times throughout the duration of each run in order to monitor metabolite quality and sample degradation. Three standards containing a number of known metabolites were also run alongside unknown samples for the purpose of identifying all other metabolites. Chromatographic separation of metabolites was performed using an UltiMate 3000 RS-LC (Thermo Fisher) with a zwitterionic hydrophilic interaction liquid chromatography (ZIC-HILIC) column (C18 150 × 4.6 mm; Merck Sequant) as the stationary phase, 1% v/v formic acid in acetonitrile as the organic mobile phase, and 1% v/v aqueous formic acid as the aqueous mobile phase. The mobile phase was run as a gradient over 46 min (Table 1). Injection volumes were 10 μL, and a ZIC-HILIC C8 20 × 2.0 guard column was used to protect the main column from impurities; chromatography columns were maintained at 25 °C.

Table 1. LC−MS Mobile Phase Parameters[a]

time (min)	aqueous (%)	organic (%)	flow rate (mL/min)	gradient curve
0	20	80	0.3	1
30	20	80	0.3	6
32	80	20	0.3	6
40	95	5	0.3	6
42	95	5	0.3	6

[a]Chromatographic separation of metabolites was carried out using an organic (1% v/v formic acid in acetonitrile)/aqueous (1% v/v aqueous formic acid) mobile phase run over a period of 46 min. Table data show the percentage of each mobile phase at particular time points, flow rate, and gradient curve conditions.

MS was performed using an Orbitrap Exactive accurate mass mass spectrometer (Thermo Fisher Scientific). Scans were conducted at a mass resolution of 50 000 in both positive and negative ion modes across a range of 70−1400 *m*/*z*. Prior to data acquisition, mass calibration was performed in positive and negative modes using a calibration mix containing a number of compounds with known masses across the acquisition range. Data conversion, chromatographic peak selection, and metabolite identification were carried out using the IDEOM/MzMatch Excel interface,[53,54] and chromatographic peak intensities (peak area under the curve) were normalized against calculated protein content. Known standards were used to define both mass and retention times of analytes. Putative metabolites were also identified on this basis using predicted retention times as described in Creek *et al.*[55] MetaboAnalyst[56] and Ingenuity pathway analysis were used to generate illustrations.

Time-of-Flight Secondary Ion Mass Spectrometry (ToF-SIMS). ToF-SIMS analysis was carried out with a ToF-SIMS IV time-of-flight instrument (ION-ToF GmbH). Secondary ions were generated using a primary ion beam from a 25 kV Bi_3^+ liquid metal ion source with a 1 pA pulsed target current. The primary ion dose was kept below the static limit (less than 2.45×10^{12} ions/cm^2). Built-up surface charge was compensated using an electron gun, producing a flux of low-energy electrons (20 eV). Secondary ions were subjected to a post-acceleration voltage of 10 kV and analyzed with positive polarity with a single stage reflectron analyzer. Images were acquired by rastering the primary ion beam across the sample surface. On each sample, two small scale (500 μm × 500 μm; 2 μm resolution) and one large scale (3 mm × 3 mm; 10 μm resolution) areas were imaged.

DOI: 10.1021/acsnano.6b01765
ACS Nano 2016, 10, 6667−6679

The data were processed using Surface Lab 6. Mass spectra were calibrated to known reference peaks from H^+, CH_3^+, $C_2H_5^+$, $C_3H_7^+$, and $C_4H_9^+$. Peaks from the samples were assigned to PEG, FMOC, and the amino acids according to reference data from the literature.[40,57,58] Ion intensity images were generated from these ions of interest by the software.

For qualitative assessment of sample uniformity and presence of chemical functionalities, small-scale images (500 μm × 500 μm) were used and the ions associated with amino acids were summed up and combined in a single image. The ion count scale for specific ion images (PEG, FMOC, amino acids) was manually adjusted to the same range for each sample to allow direct comparison. Total ion images were scaled individually.

For semiquantitative assessment of the relative amount of FMOC removed from the surface, the large-scale images (3 mm × 3 mm; one per sample type) were normalized to the total ion counts and divided into four regions of interest (ROI) that correspond to four equally sized, non-overlapping quadrants (1.5 mm × 1.5 mm) of the image. Normalized ion intensities for an FMOC-related ion ($C_{14}H_{11}^+$, m/z = 179) were generated for each ROI by the software to provide four data sets for each sample that were used to calculate a mean and standard deviation for the FMOC ion intensities before and after exposure of FMOC-AARGD and FMOC-FARGD to elastase. These normalized intensities were used to calculate a percentage decrease of FMOC on the two sample types. It should be noted that this method to generate numeric data of surface densities of chemical compounds is sensitive to small amounts of material on the surface but not fully quantitative due to a variety of factors affecting measured ion intensities from ToF-SIMS.

ASSOCIATED CONTENT

Supporting Information

The Supporting Information is available free of charge on the ACS Publications website at DOI: 10.1021/acsnano.6b01765.

Supplementary figures and references (PDF)

AUTHOR INFORMATION

Corresponding Authors

*E-mail: rein.ulijn@asrc.cuny.edu.

*E-mail: matthew.dalby@glasgow.ac.uk.

Notes

The authors declare no competing financial interest.

ACKNOWLEDGMENTS

J.N.R., H.A., and J.H. are funded by EPSRC DTC scholarships. M.J.D. and R.V.U. are funded by BBSRC Grant BB/K006908/1. R.V.U. is funded by an ERC starting grant (EMERgE/ERC No. 258775). R.O.C.O. is funded by BBSRC (BB/G010579/1). We thank Carol-Anne Smith and Kate White for technical assistance, and David J. Scurr for helping with ToF-SIMS measurements.

REFERENCES

(1) Ehninger, A.; Trumpp, A. The Bone Marrow Stem Cell Niche Grows Up: Mesenchymal Stem Cells And Macrophages Move. *J. Exp. Med.* **2011**, *208*, 421−428.

(2) Bianco, P. Bone And The Hematopoietic Niche: A Tale Of Two Stem Cells. *Blood* **2011**, *117*, 5281−5288.

(3) Watt, F. M.; Hogan, B. L. Out Of Eden: Stem Cells And Their Niches. *Science* **2000**, *287*, 1427−1430.

(4) Bianco, P.; Cao, X.; Frenette, P. S.; Mao, J. J.; Robey, P. G.; Simmons, P. J.; Wang, C. Y. The Meaning, The Sense And The Significance: Translating The Science Of Mesenchymal Stem Cells Into Medicine. *Nat. Med.* **2013**, *19*, 35−42.

(5) Mcmurray, R. J.; Gadegaard, N.; Tsimbouri, P. M.; Burgess, K. V.; Mcnamara, L. E.; Tare, R.; Murawski, K.; Kingham, E.; Oreffo, R. O.; Dalby, M. J. Nanoscale Surfaces For The Long-Term Maintenance Of Mesenchymal Stem Cell Phenotype And Multipotency. *Nat. Mater.* **2011**, *10*, 637−644.

(6) Giam, L. R.; Massich, M. D.; Hao, L.; Shin Wong, L.; Mader, C. C.; Mirkin, C. A. Scanning Probe-Enabled Nanocombinatorics Define The Relationship Between Fibronectin Feature Size And Stem Cell Fate. *Proc. Natl. Acad. Sci. U. S. A.* **2012**, *109*, 4377−4382.

(7) Huang, J.; Grater, S. V.; Corbellini, F.; Rinck, S.; Bock, E.; Kemkemer, R.; Kessler, H.; Ding, J.; Spatz, J. P. Impact Of Order And Disorder In RGD Nanopatterns On Cell Adhesion. *Nano Lett.* **2009**, *9*, 1111−1116.

(8) Frith, J. E.; Mills, R. J.; Cooper-White, J. J. Lateral Spacing Of Adhesion Peptides Influences Human Mesenchymal Stem Cell Behaviour. *J. Cell Sci.* **2012**, *125*, 317−327.

(9) Dalby, M. J.; Gadegaard, N.; Oreffo, R. O. Harnessing Nanotopography And Integrin-Matrix Interactions To Influence Stem Cell Fate. *Nat. Mater.* **2014**, *13*, 558−569.

(10) Murphy, W. L.; Mcdevitt, T. C.; Engler, A. J. Materials As Stem Cell Regulators. *Nat. Mater.* **2014**, *13*, 547−557.

(11) Mcbeath, R.; Pirone, D. M.; Nelson, C. M.; Bhadriraju, K.; Chen, C. S. Cell Shape, Cytoskeletal Tension, And Rhoa Regulate Stem Cell Lineage Commitment. *Dev. Cell* **2004**, *6*, 483−495.

(12) Engler, A. J.; Sen, S.; Sweeney, H. L.; Discher, D. E. Matrix Elasticity Directs Stem Cell Lineage Specification. *Cell* **2006**, *126*, 677−689.

(13) Trappmann, B.; Gautrot, J. E.; Connelly, J. T.; Strange, D. G.; Li, Y.; Oyen, M. L.; Cohen Stuart, M. A.; Boehm, H.; Li, B.; Vogel, V.; Spatz, J. P.; Watt, F. M.; Huck, W. T. Extracellular-Matrix Tethering Regulates Stem-Cell Fate. *Nat. Mater.* **2012**, *11*, 642−649.

(14) Huebsch, N.; Arany, P. R.; Mao, A. S.; Shvartsman, D.; Ali, O. A.; Bencherif, S. A.; Rivera-Feliciano, J.; Mooney, D. J. Harnessing Traction-Mediated Manipulation Of The Cell/Matrix Interface To Control Stem-Cell Fate. *Nat. Mater.* **2010**, *9*, 518−526.

(15) Swift, J.; Ivanovska, I. L.; Buxboim, A.; Harada, T.; Dingal, P. C.; Pinter, J.; Pajerowski, J. D.; Spinler, K. R.; Shin, J. W.; Tewari, M.; Rehfeldt, F.; Speicher, D. W.; Discher, D. E. Nuclear Lamin-A Scales With Tissue Stiffness And Enhances Matrix-Directed Differentiation. *Science* **2013**, *341*, 1240104.

(16) Khetan, S.; Guvendiren, M.; Legant, W. R.; Cohen, D. M.; Chen, C. S.; Burdick, J. A. Degradation-Mediated Cellular Traction Directs Stem Cell Fate In Covalently Crosslinked Three-Dimensional Hydrogels. *Nat. Mater.* **2013**, *12*, 458−465.

(17) Kilian, K. A.; Bugarija, B.; Lahn, B. T.; Mrksich, M. Geometric Cues For Directing The Differentiation Of Mesenchymal Stem Cells. *Proc. Natl. Acad. Sci. U. S. A.* **2010**, *107*, 4872−7.

(18) Lee, J.; Abdeen, A. A.; Tang, X.; Saif, T. A.; Kilian, K. A. Geometric Guidance Of Integrin Mediated Traction Stress During Stem Cell Differentiation. *Biomaterials* **2015**, *69*, 174−1183.

(19) Wen, J. H.; Vincent, L. G.; Fuhrmann, A.; Choi, Y. S.; Hribar, K. C.; Taylor-Weiner, H.; Chen, S.; Engler, A. J. Interplay Of Matrix Stiffness And Protein Tethering In Stem Cell Differentiation. *Nat. Mater.* **2014**, *13*, 979−987.

(20) Curran, J. M.; Chen, R.; Hunt, J. A. The Guidance Of Human Mesenchymal Stem Cell Differentiation *In Vitro* By Controlled Modifications To The Cell Substrate. *Biomaterials* **2006**, *27*, 4783−4793.

(21) Benoit, D. S.; Schwartz, M. P.; Durney, A. R.; Anseth, K. S. Small Functional Groups For Controlled Differentiation Of Hydrogel-Encapsulated Human Mesenchymal Stem Cells. *Nat. Mater.* **2008**, *7*, 816−823.

(22) Chaudhuri, O.; Gu, L.; Klumpers, D.; Darnell, M.; Bencherif, S. A.; Weaver, J. C.; Huebsch, N.; Lee, H. P.; Lippens, E.; Duda, G. N.; Mooney, D. J. Hydrogels With Tunable Stress Relaxation Regulate Stem Cell Fate And Activity. *Nat. Mater.* **2016**, *15*, 326−334.

(23) Das, R. K.; Gocheva, V.; Hammink, R.; Zouani, O. F.; Rowan, A. E. Stress-Stiffening-Mediated Stem-Cell Commitment Switch In Soft Responsive Hydrogels. *Nat. Mater.* **2016**, *15*, 318−325.

(24) Dalby, M. J.; Gadegaard, N.; Tare, R.; Andar, A.; Riehle, M. O.; Herzyk, P.; Wilkinson, C. D. W.; Oreffo, R. O. C. The Control Of

Human Mesenchymal Cell Differentiation Using Nanoscale Symmetry And Disorder. *Nat. Mater.* **2007**, *6*, 997−1003.
(25) Tsimbouri, P. M.; Mcmurray, R. J.; Burgess, K. V.; Alakpa, E. V.; Reynolds, P. M.; Murawski, K.; Kingham, E.; Oreffo, R. O.; Gadegaard, N.; Dalby, M. J. Using Nanotopography And Metabolomics To Identify Biochemical Effectors Of Multipotency. *ACS Nano* **2012**, *6*, 10239−10249.
(26) Friedenstein, A. J. Precursor Cells Of Mechanocytes. *Int. Rev. Cytol.* **1976**, *47*, 327−359.
(27) Lee, T. T.; Garcia, J. R.; Paez, J. I.; Singh, A.; Phelps, E. A.; Weis, S.; Shafiq, Z.; Shekaran, A.; Del Campo, A.; Garcia, A. J. Light-Triggered *In Vivo* Activation Of Adhesive Peptides Regulates Cell Adhesion, Inflammation And Vascularization Of Biomaterials. *Nat. Mater.* **2015**, *14*, 352−360.
(28) Liu, D.; Xie, Y.; Shao, H.; Jiang, X. Using Azobenzene-Embedded Self-Assembled Monolayers To Photochemically Control Cell Adhesion Reversibly. *Angew. Chem., Int. Ed.* **2009**, *48*, 4406−4408.
(29) Deforest, C. A.; Polizzotti, B. D.; Anseth, K. S. Sequential Click Reactions For Synthesizing And Patterning Three-Dimensional Cell Microenvironments. *Nat. Mater.* **2009**, *8*, 659−664.
(30) Petersen, S.; Alonso, J. M.; Specht, A.; Duodu, P.; Goeldner, M.; Del Campo, A. Phototriggering Of Cell Adhesion By Caged Cyclic RGD Peptides. *Angew. Chem., Int. Ed.* **2008**, *47*, 3192−3195.
(31) Kloxin, A. M.; Kasko, A. M.; Salinas, C. N.; Anseth, K. S. Photodegradable Hydrogels For Dynamic Tuning Of Physical And Chemical Properties. *Science* **2009**, *324*, 59−63.
(32) Deforest, C. A.; Tirrell, D. A. A Photoreversible Protein-Patterning Approach For Guiding Stem Cell Fate In Three-Dimensional Gels. *Nat. Mater.* **2015**, *14*, 523−531.
(33) Yeo, W. S.; Mrksich, M. Electroactive Substrates That Reveal Aldehyde Groups For Bio-Immobilization. *Adv. Mater.* **2004**, *16*, 1352−1356.
(34) Mendes, P. M. Cellular Nanotechnology: Making Biological Interfaces Smarter. *Chem. Soc. Rev.* **2013**, *42*, 9207−9218.
(35) Weis, S.; Lee, T. T.; Del Campo, A.; Garcia, A. J. Dynamic Cell-Adhesive Microenvironments And Their Effect On Myogenic Differentiation. *Acta Biomater.* **2013**, *9*, 8059−8066.
(36) Maitz, M. F.; Freudenberg, U.; Tsurkan, M. V.; Fischer, M.; Beyrich, T.; Werner, C. Bio-Responsive Polymer Hydrogels Homeostatically Regulate Blood Coagulation. *Nat. Commun.* **2013**, *4*, 2168.
(37) Bacharouche, J.; Badique, F.; Fahs, A.; Spanedda, M. V.; Geissler, A.; Malval, J. P.; Vallat, M. F.; Anselme, K.; Francius, G.; Frisch, B.; Hemmerle, J.; Schaaf, P.; Roucoules, V. Biomimetic Cryptic Site Surfaces For Reversible Chemo- And Cyto-Mechanoresponsive Substrates. *ACS Nano* **2013**, *7*, 3457−3465.
(38) Davila, J.; Chassepot, A.; Longo, J.; Boulmedais, F.; Reisch, A.; Frisch, B.; Meyer, F.; Voegel, J. C.; Mesini, P. J.; Senger, B.; Metz-Boutigue, M. H.; Hemmerle, J.; Lavalle, P.; Schaaf, P.; Jierry, L. Cyto-Mechanoresponsive Polyelectrolyte Multilayer Films. *J. Am. Chem. Soc.* **2012**, *134*, 83−86.
(39) Zelzer, M.; Todd, S. J.; Hirst, A. R.; Mcdonald, T. O.; Ulijn, R. V. Enzyme Responsive Materials: Design Strategies And Future Developments. *Biomater. Sci.* **2013**, *1*, 11−39.
(40) Todd, S. J.; Scurr, D. J.; Gough, J. E.; Alexander, M. R.; Ulijn, R. V. Enzyme-Activated RGD Ligands On Functionalized Poly(Ethylene Glycol) Monolayers: Surface Analysis And Cellular Response. *Langmuir* **2009**, *25*, 7533−7539.
(41) Zelzer, M.; Scurr, D. J.; Alexander, M. R.; Ulijn, R. V. Development And Validation Of A Fluorescence Method To Follow The Build-Up Of Short Peptide Sequences On Solid 2D Surfaces. *ACS Appl. Mater. Interfaces* **2012**, *4*, 53−58.
(42) Bershadsky, A. D.; Tint, I. S.; Neyfakh, A. A., Jr.; Vasiliev, J. M. Focal Contacts Of Normal And RSV-Transformed Quail Cells. Hypothesis Of The Transformation-Induced Deficient Maturation Of Focal Contacts. *Exp. Cell Res.* **1985**, *158*, 433−444.
(43) Yang, J.; Mcnamara, L. E.; Gadegaard, N.; Alakpa, E. V.; Burgess, K. V.; Meek, R. M.; Dalby, M. J. Nanotopographical Induction Of Osteogenesis Through Adhesion, Bone Morphogenic Protein Cosignaling, And Regulation Of Micrornas. *ACS Nano* **2014**, *8*, 9941−9953.
(44) Malmstrom, J.; Lovmand, J.; Kristensen, S.; Sundh, M.; Duch, M.; Sutherland, D. S. Focal Complex Maturation And Bridging On 200 Nm Vitronectin But Not Fibronectin Patches Reveal Different Mechanisms Of Focal Adhesion Formation. *Nano Lett.* **2011**, *11*, 2264−2271.
(45) Yanes, O.; Clark, J.; Wong, D. M.; Patti, G. J.; Sanchez-Ruiz, A.; Benton, H. P.; Trauger, S. A.; Desponts, C.; Ding, S.; Siuzdak, G. Metabolic Oxidation Regulates Embryonic Stem Cell Differentiation. *Nat. Chem. Biol.* **2010**, *6*, 411−417.
(46) Reyes, J. M.; Fermanian, S.; Yang, F.; Zhou, S. Y.; Herretes, S.; Murphy, D. B.; Elisseeff, J. H.; Chuck, R. S. Metabolic Changes In Mesenchymal Stem Cells In Osteogenic Medium Measured By Autofluorescence Spectroscopy. *Stem Cells* **2006**, *24*, 1213−1217.
(47) Case, L. B.; Waterman, C. M. Integration Of Actin Dynamics And Cell Adhesion By A Three-Dimensional, Mechanosensitive Molecular Clutch. *Nat. Cell Biol.* **2015**, *17*, 955−963.
(48) Kanchanawong, P.; Shtengel, G.; Pasapera, A. M.; Ramko, E. B.; Davidson, M. W.; Hess, H. F.; Waterman, C. M. Nanoscale Architecture Of Integrin-Based Cell Adhesions. *Nature* **2010**, *468*, 580−584.
(49) Piehler, J.; Brecht, A.; Valiokas, R.; Liedberg, B.; Gauglitz, G. A High-Density Poly(Ethylene Glycol) Polymer Brush For Immobilization On Glass-Type Surfaces. *Biosens. Bioelectron.* **2000**, *15*, 473−481.
(50) Zelzer, M.; Scurr, D. J.; Alexander, M. R.; Ulijn, R. V. Development And Validation Of A Fluorescence Method To Follow The Build-Up Of Short Peptide Sequences On Solid 2D Surfaces. *ACS Appl. Mater. Interfaces* **2012**, *4*, 53−58.
(51) Burgess, A. Measuring Cell Fluorescence Using Imagej. *Science Techblog Science* **2011**, https://sciencetechblog.com/2011/05/24/measuring-cell-fluorescence-using-imagej/.
(52) Burgess, A.; Vigneron, S.; Brioudes, E.; Labbe, J.-C.; Lorca, T.; Castro, A. Loss Of Human Greatwall Results In G2 Arrest And Multiple Mitotic Defects Due To Deregulation Of The Cyclin B-Cdc2/PP2A Balance. *Proc. Natl. Acad. Sci. U. S. A.* **2010**, *107*, 12564−12569.
(53) Creek, D. J.; Jankevics, A.; Burgess, K. E. V.; Breitling, R.; Barrett, M. P. IDEOM: An Excel Interface For Analysis Of LC-MS-Based Metabolomics Data. *Bioinformatics* **2012**, *28*, 1048−1049.
(54) Scheltema, R. A.; Jankevics, A.; Jansen, R. C.; Swertz, M. A.; Breitling, R. Peakml/Mzmatch: A File Format, Java Library, R Library, And Tool-Chain For Mass Spectrometry Data Analysis. *Anal. Chem.* **2011**, *83*, 2786−2793.
(55) Creek, D. J.; Jankevics, A.; Breitling, R.; Watson, D. G.; Barrett, M. P.; Burgess, K. E. Toward Global Metabolomics Analysis With Hydrophilic Interaction Liquid Chromatography-Mass Spectrometry: Improved Metabolite Identification By Retention Time Prediction. *Anal. Chem.* **2011**, *83*, 8703−8710.
(56) Xia, J.; Psychogios, N.; Young, N.; Wishart, D. S. Metaboanalyst: A Web Server For Metabolomic Data Analysis And Interpretation. *Nucleic Acids Res.* **2009**, *37*, W652−660.
(57) Zelzer, M.; Mcnamara, L. E.; Scurr, D. J.; Alexander, M. R.; Dalby, M. J.; Ulijn, R. V. Phosphatase Responsive Peptide Surfaces. *J. Mater. Chem.* **2012**, *22*, 12229−12237.
(58) Lhoest, J. B.; Wagner, M. S.; Tidwell, C. D.; Castner, D. G. Characterization Of Adsorbed Protein Films By Time Of Flight Secondary Ion Mass Spectrometry. *J. Biomed. Mater. Res.* **2001**, *57*, 432−440.

DOI: 10.1021/acsnano.6b01765
ACS Nano 2016, 10, 6667−6679

ADVANCED MATERIALS INTERFACES
www.advmatinterfaces.de

Length-Selective Chemical Assembly of Vertically Aligned Carbon Nanotubes

*Zarrar Hussein, Frankie J. Rawson, Pola G. Oppenheimer, Aaron Acton, and Paula M. Mendes**

Many potential applications of carbon nanotubes (CNTs), ranging from electronics and optoelectronics to biology and medicine, require length-controlled and well-aligned CNTs on surfaces. In this work, the length selectivity behavior of wet-dispersed CNTs on gold functionalized surfaces is investigated, providing new mechanistic insights into the length-selective process that occurs upon chemical assembly. A combination of experimental evidence derived from atomic force microscopy and plane and cross-sectional transmission electron microscopy implies a length-selective deposition of CNTs on the functionalized gold surface. All the solutions containing either a high distribution of longer or shorter CNTs lead to the selective formation of vertically aligned carbon nanotubes with average lengths of 10.6 ± 3.1 nm. It is postulated that such length-selective phenomenon is not only driven by diffusion mechanisms but also is governed by the interactions between the CNTs and the chemically functionalized surfaces. The orientation of the initial attached nanotubes, which act as nucleation sites in the CNT assembly process, is proposed to dictate the CNT length distribution on the surface and be dependent on the packing and ordering of the molecules on the functionalized surface.

1. Introduction

Vertically aligned carbon nanotubes (VACNTs) have attracted significant recent attention due to their wide-ranging applications from electronics and optoelectronics through to biology and medicine.[1–4] Owing to their 3D highly oriented structures and remarkable physical and chemical properties, VACNTs are currently regarded as superior materials for field emitters[5] and optoelectronic devices[3] as well as highly sensitive platforms for chemical and biological sensing.[6,7] With such applications in mind, VACNTs have been successfully prepared using either direct growth by chemical vapor deposition[5,8] or chemical assembly of resynthesized CNTs.[9,10] The chemical assembly route taken to vertically align CNTs is more cost-effective and allows for greater flexibility in selecting the CNT–substrate interactions and the substrate used. In this regard, vertical self-assembly of CNTs have been achieved on different substrates, including ITO, gold, silver, silicon, glass and Nafion films, through metal-assisted chelation,[11] electrostatic interactions,[12] π–π interactions,[13] and different covalent bonds.[2,14–18]

A key issue for chemical assembly of VACNTs is to gain a full understanding and control over the assembly behavior since the properties of the VACNTs are intimately related with, among others, their assembly density, location, average length, and length distribution on the substrate.[10,14,15] For example, advantages in electrical behavior of the unselective vertical alignment of random geometries of CNTs, over random dispersed CNTs on conducting surfaces, has been established.[15] However, to the best of our knowledge no finite control length and/or orientation of alignment of chemically assembled CNTs has been presented.

CNT density studies have demonstrated that CNT surface coverage is a time-dependent process with two distinctive kinetic stages: one fast stage that can last from 2 to 4 h depending on the assembly approach, followed by a relatively slow stage that can take up to 10 h or longer.[11,14,16,19] Research work has been also devoted to the site-selective assembly of vertically aligned CNTs on patterned surfaces, which have been achieved through different lithographic techniques, such as microcontact printing,[20] photolithography,[21] and electron-beam lithography.[22] However, while CNT density and spatial positioning can be achieved with relative ease, understanding and controlling the average length and length distribution of the standing CNTs via chemical assembly remains elusive. The formation of VACNTs via chemical assembly relies on the use of shortened CNTs with a broad length distribution ranging from a few to hundreds of nanometers. Previous investigations have revealed that such uneven distribution is partially reflected in the corresponding VACNT-functionalized surfaces.[16,17,19] Along this line, Yu et al.[17] for example, reported aligned CNTs formed by self-assembly on a silicon surface using shortened CNTs having an average length of 380 nm and a maximum

Z. Hussein, Dr. P. G. Oppenheimer, Dr. A. Acton, Prof. P. M. Mendes
School of Chemical Engineering
University of Birmingham
Edgbaston, Birmingham B15 2TT, UK
E-mail: p.m.mendes@bham.ac.uk
Dr. F. J. Rawson
Laboratory of Biophysics & Surface Analysis
School of Pharmacy
University of Nottingham
University Park
Nottingham NG7 2RD, UK

DOI: 10.1002/admi.201500860

length of about 850 nm. The average and maximum lengths of the CNTs on the surface were shown to progressively increase with surface reaction time, of which were 3 nm and 28 nm, respectively, for 4 h reaction and 65 nm and 204 nm, respectively, for a 48 hour reaction. As in other studies,[16,19] the heights observed for the protruding nanotubes were considerably shorter than the known distribution of lengths of the cut nanotubes. These studies underpin unresolved issues regarding the length-selective process that occurs upon chemical assembly including, which parameters can influence the length selectivity pattern, to which extent the solution length distribution can affect the surface and, ultimately, can such selective process lead to a very narrow length distribution of aligned CNTs on surfaces. Only by addressing these aforementioned issues can chemical assembly-based VACNT technology move forward, expand their functionality and performance and ultimately realize their true potential.

For these reasons, we set out to investigate the length selectivity behavior of dispersed CNTs on gold-functionalized surfaces. The approach we have taken is to assess how different length distribution regimes can alter the length selection pattern on the surface. To assemble the CNTs on the gold surface, a 4-aminothiophenol (ATP) self-assembled monolayer (SAM) was prepared on gold, which can then be used to orchestrate the immobilization of shortened CNTs. Pristine single-walled CNTs were shortened by sonication-assisted oxidative cutting to obtain open-ended nanotubes with terminal carboxylic acid groups.[23] Different cutting times were employed (4–10 h) in order to generate CNTs with different length distributions. The assembly was based on the condensation reaction between the carboxylic acid moieties of the CNTs and the amino groups on the SAM surface.

2. Results and Discussion

The formation of the ATP SAM on gold was studied by means of ellipsometry and contact angle. The clean bare gold substrates displayed low H_2O advancing (θ_{Adv}) and receding (θ_{Rec}) contact angles (22 ± 1° and 16 ± 1°, respectively), which increased to 72 ± 1° and 63 ± 1°, respectively, after 24 h SAM formation. Note that the hysteresis (θ_{Adv}–θ_{Rec}) value of 9° suggests the presence of a well-ordered monolayer. Ellipsometry revealed that the average film thickness was 0.45 ± 0.05 nm, which is less than the theoretical molecular length of the molecules (0.7 nm). The discrepancy between molecular length and SAM thickness is ascribed to the tilt angle of the SAM molecules.[24,25]

Pristine single-walled CNTs purchased from NanoLab (USA) were grown via chemical vapor deposition yielding CNTs between 1 and 5 µm in length with an approximate diameter of 1.4 nm. They were cut by being exposed to ultrasonication and simultaneous oxidative acid treatment and we investigated the cutting procedure applied at varying times (from 4 to 10 h). Consistent with previous studies,[23,26] the length of the shortened CNTs varies as a function of cutting time, wherein a high percentage of shorter nanotubes can be achieved by increasing the CNT cutting time. In order to determine the average degree of CNT length distribution following the cutting procedure, we have performed a quantitative analysis of the transition electron microscopy (TEM) images (**Figure 1**a–h). While for each cutting time, the samples were polydispersed, 23 ± 5% of the CNTs were in the range of 500–600 nm (Figure 1a,b), 20 ± 3% were in the range of 250–300 nm (Figure 1c,d), 21 ± 5% fell in the range between 120 and 150 nm (Figure 1e,f) and 23 ± 2% were found in the range of 60–90 nm (Figure 1g,h), with it representing the majority of the CNTs population in each case. The longest CNTs present in each sample post-sonication also followed similar patterns, with 4, 6, 8, and 10 h of cutting times resulting in maximum lengths of 700, 500, 250, and 210 nm, respectively.

The assembly of the CNTs was achieved by immersing the ATP SAM surfaces for 16 h on the different CNT suspensions with dicyclohexylcarbodiimide (DCC) as a coupling agent. Based on previous research work,[14,16,19] this time of incubation (16 h) was selected to ensure higher packing density and coverage of the CNTs on the ATP SAM-modified gold surface. Atomic force microscopy (AFM) was used to probe the morphology of the surfaces before and after CNTs assembly. In contrast, with a smooth flat ATP SAM surface, closely packed needle-like protrusions were clearly observed for the different CNT cutting times (**Figure 2**). Surprisingly, there was no trend toward variations of CNT length distributions on the surfaces with decreasing cutting time. The distribution of lengths on the surface, obtained from the mean height roughness, for each treatment time was very similar, 10.8 ± 3.0, 10.4 ± 3.2, 10.5 ± 3.4, 10.7 ± 3.0 nm for 4, 6, 8, and 10 h, respectively, with the majority of the nanotubes being between 5 and 10 nm in height. For comparison, control surfaces, i.e., i) clean gold surfaces and gold surfaces ii) without ATP SAM and exposed to CNTs with DCC as a coupling agent and iii) with ATP SAM and exposed to CNTs without DCC as coupling agent, were also analyzed by AFM (Figure S1, Supporting Information). All the control surfaces were essentially smooth and featureless as observed for the AFM images of the ATP SAM (Figure 2a).

The maximum lengths of the protrusions for the different CNT cutting times were about 20 nm (Figure 2b–e), which were significantly shorter than that of the suspension forms. The surface roughness for the ATP SAM was determined by AFM to be 0.99 ± 0.01 nm, which increased upon CNT assembly but largely unchanged for the different CNT cutting times (2.33 ± 0.05, 2.66 ± 0.16, 2.36 ± 0.14, and 2.26 ± 0.03 nm for 4, 6, 8, and 10 h cutting time, respectively). These findings further indicate similar morphological characteristics among the modified gold substrates with VACNTs. The apparent widths of the needle-like protrusions (from the AFM images, Figure 2) are about tens of nanometers, which are significantly larger than the diameter of the single CNTs. This difference is believed to arise from CNTs aggregation in the assembly process due to the strong van der Waals interactions between the sidewalls of the nanotubes.

Another feature to note in the AFM images is that all CNTs are vertically aligned and not lying horizontally on the substrate. This element of orientation control is attributed to a high concentration of carboxyl groups on the severed edges of the CNTs, allowing a high number of amide bonds to be formed between each nanotube and the ATP SAM on the gold surface. The preferred vertical conformation of the CNTs on the surface can also be explained by the hydrophilic nature of the amino-terminated gold substrate that makes interactions with

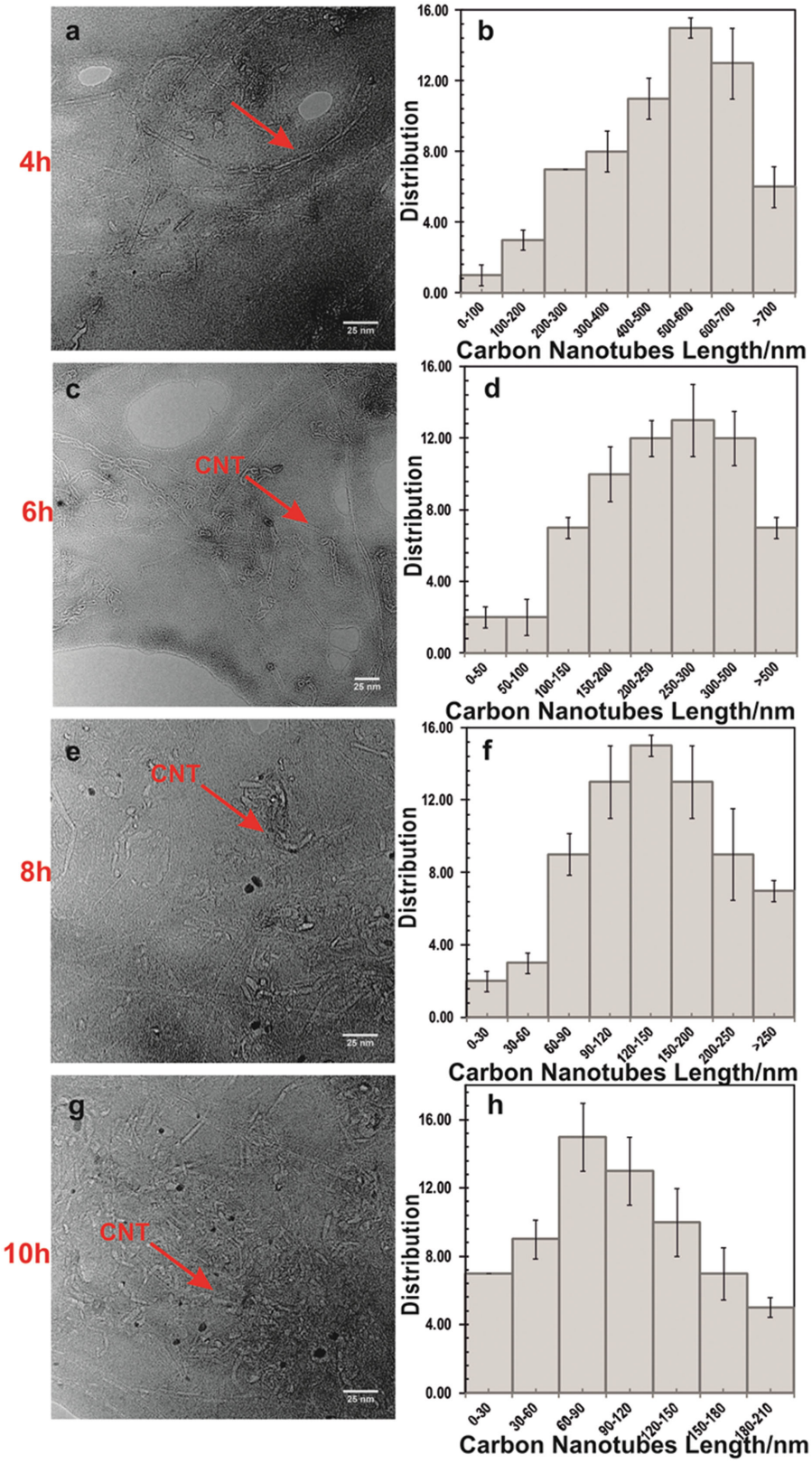

Figure 1. Representative a,c,e,g) TEM images of the dispersed CNTs as function of the cutting times ranging from 4 to 10 h. The arrows indicate the CNTs. The b,d,f,h) histograms show the distribution of the CNTs lengths as function of the various cutting times as extracted from TEM images (n = 18 micrographs).

the hydrophobic sidewalls of the nanotubes very unfavorable.

A microtomed cross section examined by TEM yields additional insight into the CNTs orientation and lengths attached to the surface. **Figure 3** reveals that the CNTs are vertically assembled on the ATP SAM surface with nanotube lengths in good agreement with those measured by AFM. Shorter (4 h) and longer cutting times (10 h) yielded average VACNT lengths of 10.5 ± 0.4 nm and 10.9 ± 0.6 nm, respectively.

Electrochemical studies provided additional evidence of surface functionalization and homogeneity of the different VACNT-functionalized surfaces. **Figure 4** shows cyclic voltammograms (CVs) obtained in the presence of 1×10^{-3} M solution of ferricyanide at unmodified gold, surface functionalized with the ATP SAM and modified ATP SAM with CNTs derived from the different cutting time points. In CVs obtained at gold (Figure 4a), a redox couple was observed associated with the Fe^{2+}/Fe^{3+} and was characterized by a mean anodic peak potential (Figure 4a Inset) of 0.346 ± 0.014 V and a cathodic peak potential of 0.02 V. When CVs were obtained at surfaces modified with ATP SAM, an anodic peak potential of 0.488 ± 0.022 V was obtained and a mean cathodic peak potential of –0.028 ± 0.041 V. The peak separation measured from CVs logged at ATP-modified surfaces yielded a peak separation of 0.516 V versus 0.326 V obtained from CVs generated at unmodified gold, which indicates sluggish electron transfer and is consistent with the blocking nature of ATP films previously reported on gold.[27] If we compare the peak potentials obtained from CVs generated at the gold-modified ATP SAM surface to peak potentials obtained from CVs logged using surfaces functionalized with VACNTs (Figure 4b inset) exposed to acid treatment for varying times of 4, 6, 8, and 10 h, mean peak separation values of 0.168, 0.172, 0.164, 0.170 V were obtained, respectively. The significant difference between peak separation in CVs logged using ATP modified gold and those functionalized with CNTs arises from the fact that the ATP monolayer slows the

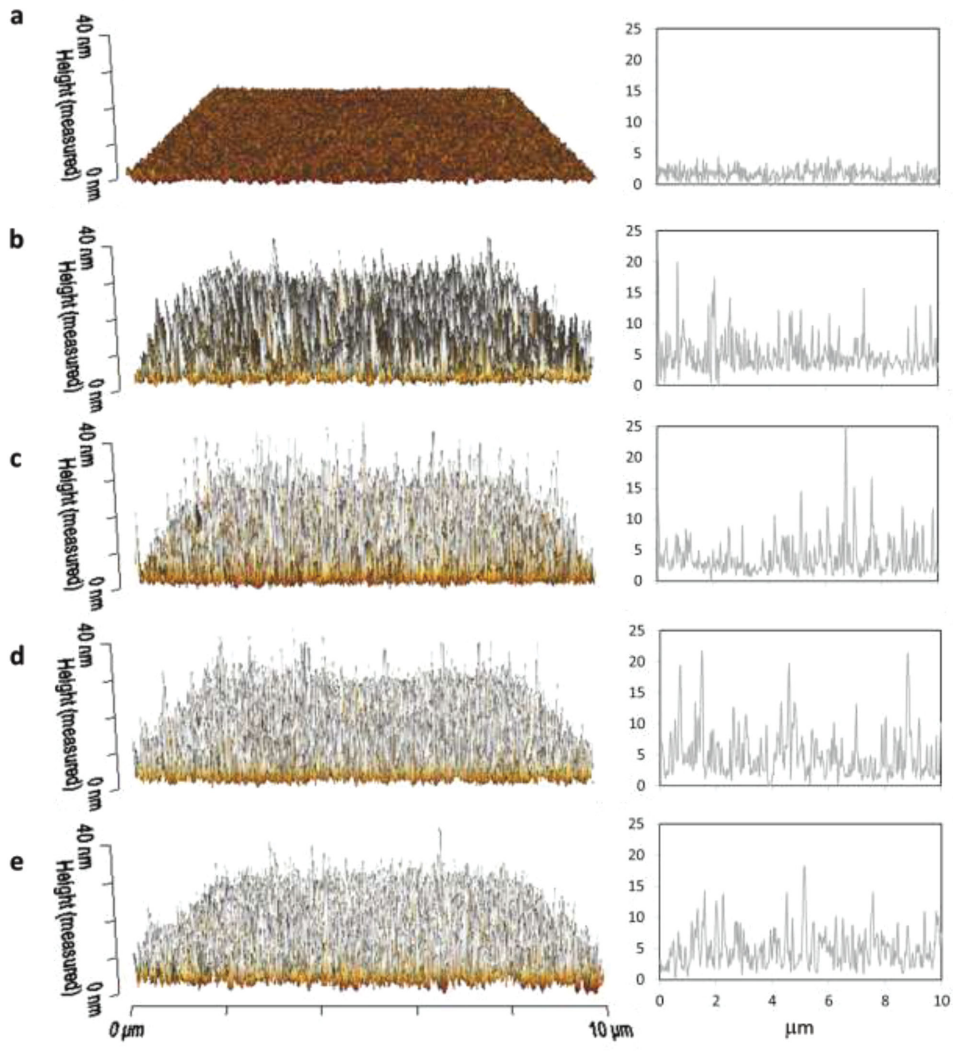

Figure 2. Representative tapping mode AFM images and height profiles of gold surfaces modified with a) ATP SAM and ATP SAM with CNTs derived from the different cutting time points: b) 4 h, c) 6 h, d) 8 h, and e) 10 h.

electron transfer process and this behavior has previously been observed.[27] We can rule out that the difference observed in the cyclic voltammetric behavior between ATP-modified surfaces and those further modified with CNTs is due to ohmic drop for a number of reasons. First, the positioning of the electrodes was consistent between experiments due to the cell design. We used a relatively slow sweep rate of 100 mV s^{-1}. Moreover, if cyclic voltammetry is performed at a relatively fast sweep rate there is a current transient due to the charging and discharging of the electrochemical double layer, which is displayed in the cyclic voltammograms, by a lagging in the true potential, and therefore the peak separation becomes larger. In particular, when the electrodes area is larger the contribution of this transient from charging the double layer increases and therefore an even bigger shift in increased peak separation would be observed. Therefore, we learn from AFM data that the electrode area becomes more-rough and consequently the charge associated with the

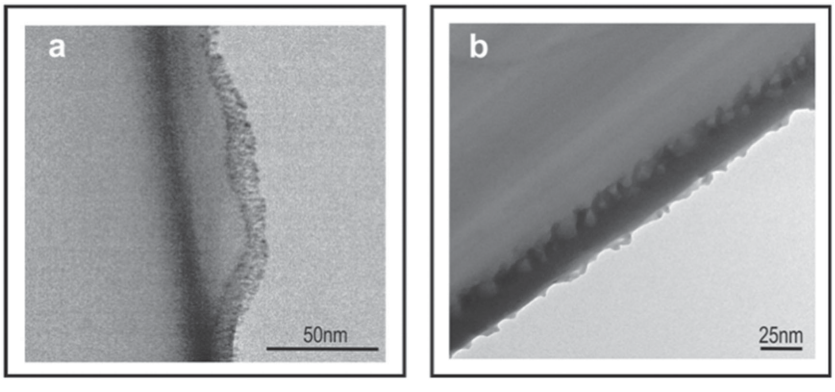

Figure 3. Cross-sectional TEM micrographs of VACNTs organization on the ATP SAMs on gold substrates after cutting for a) 4 and 10 h.

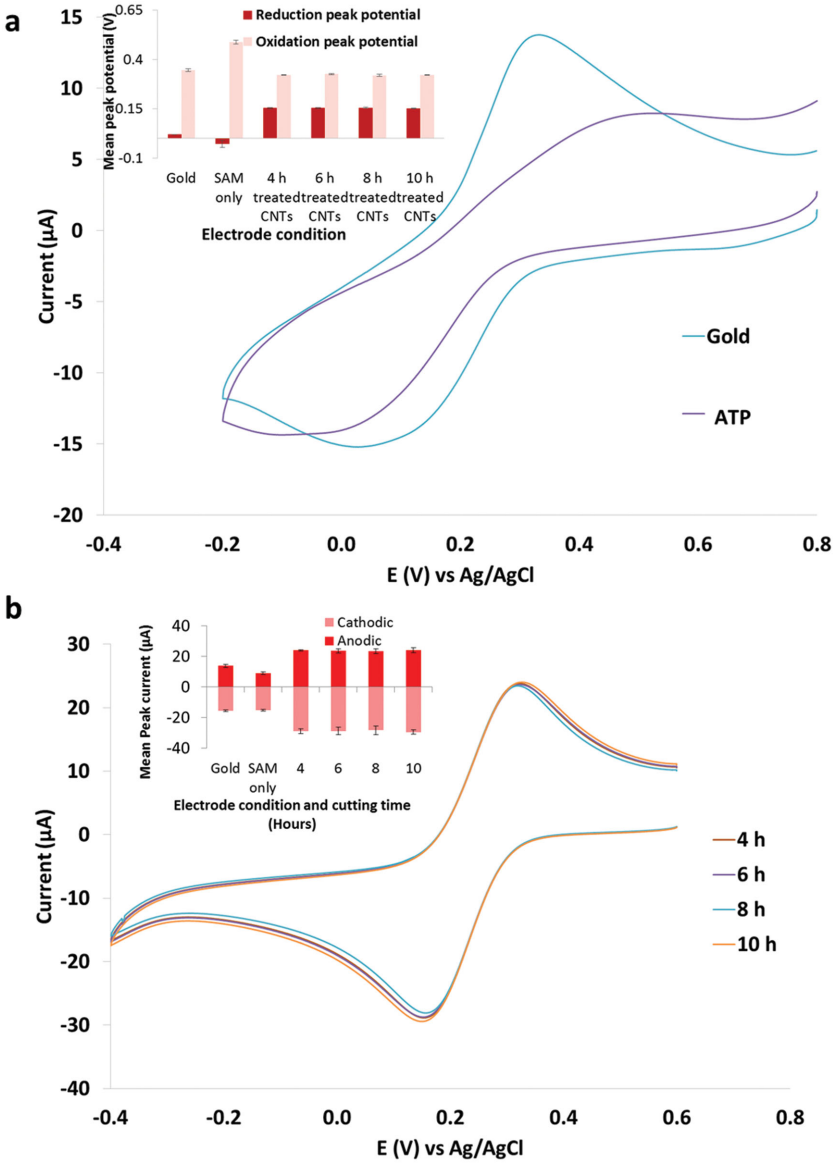

Figure 4. a) Mean CV ($n = 5$) obtained for solutions of 1×10^{-3} M ferricyanide in 50×10^{-3} M phosphate buffered saline (PBS) at bare gold, gold electrodes modified with SAMs formed with ATP. Insets are the mean peak potentials obtained from CV in Figure a for bare gold, gold modified with ATP SAM and working electrodes modified with acid treated CNTs at varying times of 4, 6, 8, and 10 h obtained from means CVs in Figure b. b) Mean CVs ($n = 5$) obtained for solutions of 1×10^{-3} M ferricyanide in 50×10^{-3} M PBS at working electrodes modified with acid treated CNTs at varying times of 4, 6, 8, and 10 h at a scan rate of 100 mV s^{-1}. Inset represents the measured mean peak cathodic and anodic currents at bare gold, ATP modified and surfaces modified with the CNTs exposed to acid for varying times. Error bars represent ±1 standard deviation of the mean.

setting up of the double layer would be greater. Consequently, it would be expected if ohmic loss was the reason for the change in behavior then the peak separation for cyclic voltammograms generated at CNTs surfaces would be large than when compared to the ATP-modified surface. On the contrary, this was not the case, and therefore all of the above indicates the difference in peak potentials arises from electron transfer rate differences between the surfaces. The magnitude of the peak current obtained for an electrochemical reversible (1) and for an irreversible (2) process in a CV is defined by the Randles–Sevcik equation:

$$i_p = (269000)\, n^{3/2} A C D^{1/2} \upsilon^{1/2} \quad (1)$$

$$i_p = (299000)\, n(\alpha n_a)^{1/2} A C D^{1/2}\, \upsilon^{1/2} \quad (2)$$

where i_p is current (A), n is the number of electrons involved in the charge transfer step, α is the transfer coefficient, n_a is the number of electrons involved in the charge-transfer step, A is the electroactive area (cm^2), D is the diffusion coefficient of species of interest (cm^2 s^{-1}) (in this case, ferricyanide), and C is the bulk concentration of ferricyanide (mol cm^{-3}).

Thus, it would be envisaged that if there was a correlation between acid treatment and population differences in heights of CNTs that tethered to the surfaces, then the electrochemical active area would be different between samples prepared with the CNTs cut with acid at varying times. If this was the case, it would be expected that we would observe CVs with significantly different magnitudes in peak current as defined by the Randles–Sevcik equations due the electrochemical active area differing. On the contrary, from Figure 4b (Inset), which shows a plot of mean peak current versus time at which the CNTs were acid treated prior to coupling, the peak currents observed were not significantly different. This lack of difference in the magnitude of the peak current obtained indicates that the electrochemically active area was approximately the same between the surfaces grafted with CNTs that were treated with acid at varying times. These results support the findings that the population of VACNTs, in terms of height that attaches to the SAM, is no different when compared to the cutting times.

Some features of these VACNTs provide information about their assembly behavior. The length distribution of the VACNTs is independent of the CNT length distributions under which the chemical assembly was performed. The studies also established that it was favorable for the short (5–10 nm) CNTs to assemble on the ATP SAM selectively to the longer (i.e., >20 nm) CNTs. These findings provide evidence that the chemical assembly process is dependent on the diffusional characteristics of the CNTs. Previous studies on the motional dynamics of CNTs have demonstrated that they undergo both translation and rotation motion in solution,[28,29] allowing them to be redistributed in space and over various orientations. Since a CNT can be defined as a prolate ellipsoid,[30] the dependence of the

translational (D_{trans}) and rotational (D_{rot}) diffusion coefficients on carbon nanotube length can be described by the Stokes–Einstein relation:[31]

$$D_{trans} = \frac{k_B T}{6\pi\eta a} G(p)$$

and the Stokes–Einstein–Debye relation:

$$D_{rot} = \frac{k_B T}{8\pi\eta a^3} \left(G(p)\right)^3$$

In these relations, T is the temperature, η is the solution viscosity, k_B is the Boltzmann constant, a is the nanotube radius and $G(p)$ a function that depends only on the axial ratio (half-length (b)/ radius (a)) of the nanotube:

$$G(p) = \left(p^2 - 1\right)^{-1/2} \ln\left(p + \left(p^2 - 1\right)^{1/2}\right)$$

With a mean nanotube diameter of about 1.4 nm, $G(p)$ assumes values of 0.38 and 0.07 for a nanotube length of 10 and 100 nm, respectively. Thus, 100 nm nanotubes exhibit a translational diffusion five times slower than 10 nm nanotubes, implying a sluggish diffusion rate for the longest CNTs. The rotational motion is even more sensitive to changes in nanotube length than the translational motion. Rotational diffusion is about 150 times faster for 10 than 100 nm, allowing for the shortest nanotubes to be more easily oriented for vertical assembly on the surface. Following the above considerations, the diffusion-controlled transport mechanism to the surface can thus introduce a screening length, wherein the shortest carbon nanotubes are selected to be incorporated onto the surface.

Bearing in mind the diffusion-controlled transport of the CNTs that preferentially deliver the shorter CNTs to the surface of interest, a possible mechanisms is likely to lie at the origin of the observed vertical CNTs orientation with the selective lengths of 10.6 ± 3.1 nm: Highly uniform ATP SAM acting as nucleation sites for the shorter CNTs, yielding the ultimate packing conformation of the VACNTs. While the ATP-terminated surface on gold has led to a narrow distribution of CNTs of about 10 nm, previous work by Gooding and co-workers[15] using a different amine thiol—mercaptoethylamine—has resulted in tethered CNTs with length distributions in the hundreds of nanometers. Additionally, our previous work[2] utilizing an electrografted arylamine onto indium tin oxide has produced surfaces with a variety of lengths ranging from 10 to 60 nm. Similar lengths and length distribution to the latter have been observed for electrografted arylamine onto a pyrolyzed photoresist film.[16] This difference in length-selective capabilities cannot be explained based on the reactivity of the amino groups. ATP comprises an aromatic amine, conjugation of the amine lone pair with the aromatic group reduces the nucleophilicty of the amine and hence ATP is less reactive toward amide formation compared to an aliphatic amine such as mercaptoethylamine. If reactivity was a key factor on the selectivity, the mercaptoethylamine would have reacted faster with the shortest CNTs (first to reach the surface) and led to these surfaces displaying selectivity for the shortest CNTs. Also, if reaction kinetics was to play a major role in such process, both ATP surfaces and electrografted amino-terminated surfaces would have presented similar length trends—both contain aromatic amino groups. Since this is not the case, other factors should be considered such that the chemical assembly process depends sensitively on the details of the molecular interactions between the CNTs and the substrate surface. Most notably, the orientation and arrangement of the molecules on the surface appears to account for the differences in length control. ATP SAM provides better close-packing and well-ordered layer structures when compared to electrografted amino-terminated surfaces since the latter grow as a multilayer structure on the surface.[2] Based on the calculations above, the shortest nanotubes are the ones to reach the surface first and due to the highest rotational diffusion rate have the highest probability to react with the surface. It is reasonable to postulate that the presentation of the amino groups in a defined density and orientation allows the shortest functionalized carbon nanotube carboxylic acids to bind to several nearby amino groups, form amide bonds and align perpendicular to the surface (**Figure 5**a). Other amino-terminated surfaces might prevent the nanotube carboxylic acids from interacting with the required amino groups in an optimal fashion, so nanotubes can adopt different upright orientations (Figure 5b). These initial nanotubes act as "nucleation" sites for subsequent tubes to bond to the surface.[17] That is, once a nanotube is coupled to the surface, subsequent nanotubes rearrange themselves to allow high degrees of van der Waals interactions with the tethered nanotubes. The presence of only the shortest nanotubes on the ATP surfaces can plausibly be attributed to the restricted, specific conformations that the newcomers need to adopt to maximize van der Waals contacts and align perpendicular to the surface. The shortest nanotubes are expected to more easily take such specific conformations due to their high rotational diffusion rates and limited steric hindrance from the tethered CNTs. We postulate that nucleation sites with nanotubes exhibiting a degree of tilting allow for more flexible nanotube lengths to interact with the tethered CNTs.

3. Conclusion

In summary, we investigated the relationship between the lengths of single-walled carbon nanotubes (CNTs) chemically assembled on gold surfaces, and CNT lengths of solutions from which they were formed and did not observe any obvious correlation. Furthermore, relative to previous research work, our standing CNTs had smaller heights and a narrower length distribution. The ATP SAM is shown to be a very useful surface system for controlling the assembly of very short CNTs. Based on the present and previous findings, we hypothesized that the length-selective process is not only driven by the diffusion mechanisms but also governed by the interactions between the CNTs and the chemically functionalized surfaces. These studies are the initial and necessary steps towards a better understanding of the length-selective process that occurs upon chemical assembly. Furthermore, this work opens up the possibility of using substrate interfaces with tailored properties to create CNTs of uniform lengths on surfaces. This should ensure the

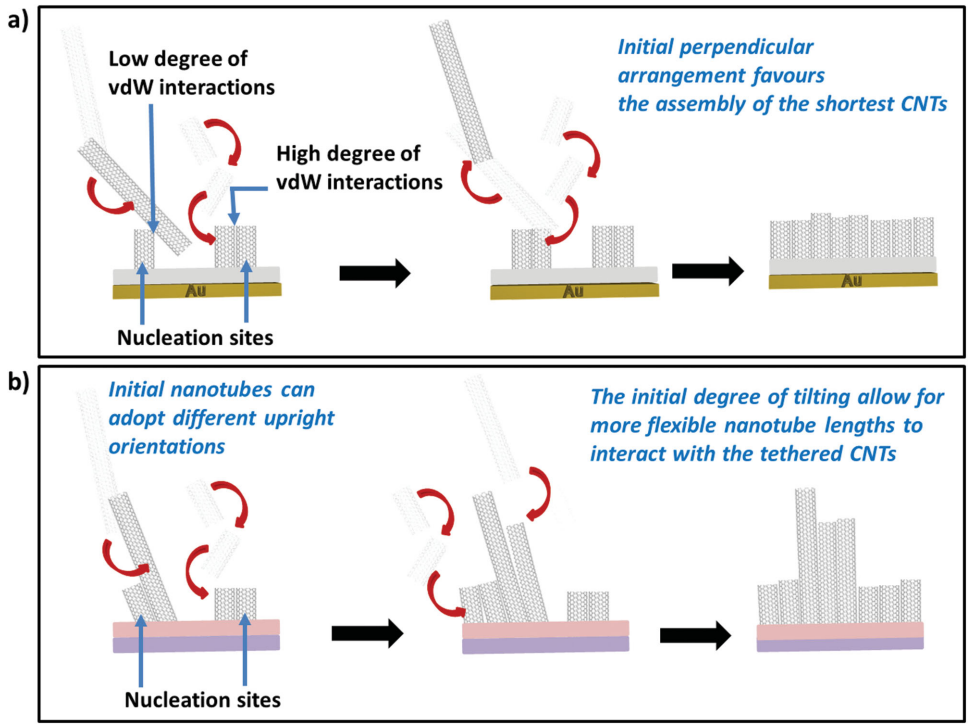

Figure 5. Schematic showing the dynamic process involved in the chemical assembly of CNTs as postulated to occur when initial nanotubes, which act as nucleation sites, are arranged a) perpendicular (ATP SAM) or b) tilted on the substrate surface.

chemical assembly route for functionalizing surfaces with VACNTs can now match and offer more suitable surfaces depending on the application than CVD CNT-functionalized surfaces. Importantly, this will provide a much high resolution in terms of nanoscale control of short vertically aligned CNTs which, we envisage will open up the technology to a plethora of applications from biosensing to electronics through to actuating surfaces.

4. Experimental Section

Chemicals and Materials: Commercially available chemicals and solvents were purchased from Aldrich Chemicals and Fisher Chemicals and were used as received. The single-walled carbon nanotubes were obtained from NanoLab Inc., with a diameter of ≈1.4 nm, length of 1–5 μm, purity of >95% and surface area of 1020.48 m^2 g^{-1}. Polycrystalline gold substrates were purchased from George Albert PVD, Germany and consisted either of a 50 nm gold layer deposited onto glass covered with a thin layer of chromium as the adhesion layer (used for contact angle) or 100 nm gold layer on 100-4 in. silicon wafer, precoated with titanium as the adhesion layer (for ellipsometry analysis).

Preparation of Self-Assembled Monolayers: The Au substrates were cleaned by immersion in piranha solution (3:1, H_2SO_4 : 30% H_2O_2) at room temperature for 10 min, rinsing with ultra high pure (UHP) H_2O and then HPLC-grade EtOH thoroughly for 1 min. (*Caution: Piranha solution reacts violently with all organic compounds and should be handled with care*). Subsequently, the clean Au substrates were immersed in 1×10^{-3} M ethanolic solutions of 4-aminothiophenol to form the SAMs on the Au surfaces. After the desired immersion time, Au substrates were removed from the SAM solution and rinsed with HPLC EtOH.

CNT Cutting Procedure: CNT cutting was carried out by sonication in a mixture of sulfuric and nitric acids. Pristine (uncut) CNTs (25 mg) were added to 27 mL of a 3:1 mixture of concentrated H_2SO_4 and HNO_3 for the selected time points of 4, 6, 8, and 10 h. Following sonication, the contents were poured into 500 mL of distilled water and left to settle overnight. The CNTs were then filtered through a 0.22 μm hydrophilic PVDF filter (Millipore) under vacuum suction, with washing until the rinse water was close to pH 7. The filters containing the mats of CNTs were oven dried at 65 °C overnight. Suspensions of cut CNTs were prepared by sonication of dried CNTs mats in dimethyl sulfoxide (DMSO), making up stocks of 2 mg mL^{-1} solutions.

CNT Coupling and Assembly to the SAM on Gold: CNTs were coupled to the 4-aminothiophenol-modified gold surfaces by submerging the modified gold surfaces in a 0.2 mg mL^{-1} DMSO suspension of cut CNTs containing 0.5 mg mL^{-1} of dicyclohexylcarbodiimide (DCC). The reactants were sonicated for 30 min and then left for 16 h at room temperature. The resulting CNTs modified gold surfaces were sonicated for 5 min in acetone and 10 s in isopropyl alcohol. The surfaces were dried with argon gas between each washing step.

Contact Angle: Contact angles were determined using a home-built contact angle apparatus, equipped with a charged coupled device (CCD) KP-M1E/K camera (Hitachi) that was attached to a personal computer for video capture. The dynamic contact angles were recorded as a microsyringe was used to quasi-statically add water to or remove water from the drop. The drop was shown as a live video image on the PC screen and the acquisition rate was 10 frames per second. FTA Video Analysis software v1.96 (First Ten Angstroms) was used for the analysis of the contact angle of a droplet of UHP H_2O at the three-phase intersection. The averages and standard deviation of contact angles were determined from five different measurements made for each SAM.

Ellipsometry: The thickness of the deposited monolayers was determined by spectroscopic ellipsometry. A Jobin-Yvon UVISEL ellipsometer with a xenon light source was used for the measurements. The angle of incidence was fixed at 70°. A wavelength range of 280–820 nm was used. The DeltaPsi software was employed to determine the thickness values and the calculations were based on a three-phase ambient/SAM/Au model, in which the SAM was assumed to be isotropic and assigned a refractive index of 1.50. The thickness

reported is the average of five measurements, with the errors reported as standard deviation.

Atomic Force Microscopy: AFM images were recorded using the Nanowizard II atomic force microscope (JPK instruments, Germany), operating in tapping mode. CSC17 silicon cantilevers were employed, exhibiting ≈10 nm diameter pyramidal tips (MikroMasch, Tallinn, Estonia). An area of 10 µm x 10 µm was scanned. Five surface roughness measurements (R_a) were made per sample on five samples, including the control substrates. Since the VACNTs exhibit local differences in height, it can be denoted as CNTs having a (local) rough surface. Here the mean height roughness was used, which is defined as the difference in height between the average of *n* highest CNTs and *n* lowest valleys, in the evaluation profile/surface,[32–34] where *n* is the number of sampling points along the assessment length, which is 50 in this study. The errors reported are the standard deviation.

Transmission Electron Microscopy: Dispersed solutions of carbon nanotubes, which were exposed to different cutting times, were deposited on Cu grids with carbon coating on one side. The dispersion of the CNTs was carried out in cetyl trimethyl ammonium bromide (CTAB) (1%) and then centrifuged at 16 000 rpm to remove excess and clumped CNTs. This centrifuging method was repeated five times for each sample. For TEM cross-sectional imaging, the gold covered substrates with CNTs (4 and 10 h) were embedded into a Spurr epoxy resin (either top or bottom side). The substrates were subsequently removed and the films were sectioned using a diamond knife in a Leica Ultracut Microtome, yielding sections with a thickness of 50 nm. The samples were analyzed in an FEI Tecnai 12 TEM at an acceleration voltage of 120 kV. The errors reported are the standard deviation.

Electroanalytical Chemistry: All electrochemical studies were carried out with a Gamry 600 potentiostat and data acquisition software (Gamry electrochemistry software version 5.61a) and a three-electrode cell consisting of a silver/silver chloride reference electrode, Pt counter electrode, and then the working electrode of either bare gold, gold modified with SAM, and gold modified with SAM and functionalized with SWCNTs. The electrochemical area was controlled via use of a O-ring with a diameter of 4 mm. Cyclic voltammetry was performed with 1×10^{-3} M solution of ferricyanide in 50×10^{-3} M PBS (0.1 M KCl) from a starting potential of 0.6 V and a switching potential of –0.4 V and an end potential of 0.6 V. Experiments were replicated five times, with the errors reported as standard deviation.

Supporting Information

Supporting Information is available from the Wiley Online Library or from the author.

Acknowledgement

The authors acknowledge financial support of this work by the EPSRC (EP/K027263/1), ERC (Consolidator Grant 614787) and Leverhulme Trust (ECF/2013-306).

Received: December 28, 2015
Revised: February 2, 2016
Published online: February 29, 2016

[1] P. M. Mendes, *Chem. Soc. Rev.* **2013**, *42*, 9207.
[2] F. J. Rawson, C. L. Yeung, S. K. Jackson, P. M. Mendes, *Nano Lett.* **2013**, *13*, 1.
[3] Y. Kim, S. Lee, K. Lee, S. Shim, J. Y. Kim, H. W. Lee, D. Choi, *ACS Appl. Mater. Interfaces* **2014**, *6*, 20423.
[4] F. J. Rawson, D. J. Garrett, D. Leech, A. J. Downard, K. H. R. Baronian, *Biosens. Bioelectron.* **2011**, *26*, 2383.
[5] S. S. Fan, M. G. Chapline, N. R. Franklin, T. W. Tombler, A. M. Cassell, H. J. Dai, *Science* **1999**, *283*, 512.
[6] J. J. Gooding, R. Wibowo, J. Liu, W. Yang, D. Losic, S. Orbons, F. J. Mearns, J. G. Shapter, D. B. Hibbert, *J. Am. Chem. Soc.* **2003**, *125*, 9006.
[7] P. Goldberg-Oppenheimer, T. Hutter, B. A. Chen, J. Robertson, S. Hofmann, S. Mahajan, *J. Phys. Chem. Lett.* **2012**, *3*, 3486.
[8] S. Park, D. W. Park, C. S. Yang, K. R. Kim, J. H. Kwak, H. M. So, C. W. Ahn, B. S. Kim, H. Chang, J. O. Lee, *ACS Nano* **2011**, *5*, 7061.
[9] Z. Liu, Z. Shen, T. Zhu, S. Hou, L. Ying, Z. Shi, Z. Gu, *Langmuir* **2000**, *16*, 3569.
[10] P. Diao, Z. Liu, *Adv. Mater.* **2010**, *22*, 1430.
[11] D. Chattopadhyay, I. Galeska, F. Papadimitrakopoulos, *J. Am. Chem. Soc.* **2001**, *123*, 9451.
[12] Z. Chen, Y. L. Yang, Z. Y. Wu, G. Luo, L. M. Xie, Z. F. Liu, S. J. Ma, W. L. Guo, *J. Phys. Chem. B* **2005**, *109*, 5473.
[13] T. Ferri, D. Frasca, O. A. de Fuentes, R. Santucci, M. Frasconi, *Angew. Chem.-Int. Ed.* **2011**, *50*, 7074.
[14] P. Diao, Z. F. Liu, *J. Phys. Chem. B* **2005**, *109*, 20906.
[15] J. J. Gooding, A. Chou, J. Liu, D. Losic, J. G. Shapter, D. B. Hibbert, *Electrochem. Commun.* **2007**, *9*, 1677.
[16] D. J. Garrett, B. S. Flavel, J. G. Shapter, K. H. R. Baronian, A. J. Downard, *Langmuir* **2010**, *26*, 1848.
[17] J. Yu, D. Losic, M. Marshall, T. Bocking, J. J. Gooding, J. G. Shapter, *Soft Matter* **2006**, *2*, 1081.
[18] B. S. Flavel, J. X. Yu, A. V. Ellis, J. S. Quinton, J. G. Shapter, *Nanotechnology* **2008**, *19*, 12.
[19] F. Patolsky, Y. Weizmann, I. Willner, *Angew. Chem.-Int. Ed.* **2004**, *43*, 2113.
[20] X. L. Nan, Z. N. Gu, Z. F. Liu, *J. Colloid Interface Sci.* **2002**, *245*, 311.
[21] M. S. Jung, S. O. Jung, D. H. Jung, Y. K. Ko, Y. W. Jin, J. Kim, H. T. Jung, *J. Phys. Chem. B* **2005**, *109*, 10584.
[22] H. Y. Wei, S. N. Kim, H. L. Marcus, F. Papadimitrakopoulos, *Chem. Mater.* **2006**, *18*, 1100.
[23] M. W. Marshall, S. Popa-Nita, J. G. Shapter, *Carbon* **2006**, *44*, 1137.
[24] A. Ulman, *Chem. Rev.* **1996**, *96*, 1533.
[25] H. L. Zhang, J. Zhang, H. Y. Li, Z. F. Liu, H. L. Li, *Mater. Sci. Eng. C* **1999**, *8–9*, 179.
[26] J. Liu, A. G. Rinzler, H. J. Dai, J. H. Hafner, R. K. Bradley, P. J. Boul, A. Lu, T. Iverson, K. Shelimov, C. B. Huffman, F. Rodriguez-Macias, Y. S. Shon, T. R. Lee, D. T. Colbert, R. E. Smalley, *Science* **1998**, *280*, 1253.
[27] V. Ganesh, R. R. Pandey, B. D. Malhotra, V. Lakshminarayanan, *J. Electroanal. Chem.* **2008**, *619–620*, 87.
[28] D. A. Tsyboulski, S. M. Bachilo, A. B. Kolomeisky, R. B. Weisman, *ACS Nano* **2008**, *2*, 1770.
[29] R. Duggal, M. Pasquali, *Phys. Rev. Lett.* **2006**, *96*, 4.
[30] J. Gigault, B. Grassl, I. Le Hecho, G. Lespes, *Microchim. Acta* **2011**, *175*, 265.
[31] R. Borsali, R. Pecora, *Soft Matter Characterization*, Springer, Netherlands **2008**.
[32] G. Huber, S. N. Gorb, N. Hosoda, R. Spolenak, E. Arzt, *Acta Biomater.* **2007**, *3*, 607.
[33] B. Zappone, K. J. Rosenberg, J. Israelachvili, *Tribol. Lett.* **2007**, *26*, 191.
[34] B. G. Chen, G. F. Zhong, P. G. Oppenheimer, C. Zhang, H. Tornatzky, S. Esconjauregui, S. Hofmann, J. Robertson, *ACS Appl. Mater. Interfaces* **2015**, *7*, 3626.

analytical chemistry

Article

pubs.acs.org/ac

LESA FAIMS Mass Spectrometry for the Spatial Profiling of Proteins from Tissue

Rian L. Griffiths,[†] Andrew J. Creese,[†] Alan M. Race,[‡] Josephine Bunch,[‡,§] and Helen J. Cooper*[,†]

[†]School of Biosciences, University of Birmingham, Edgbaston, Birmingham B15 2TT, U.K.

[‡]National Physical Laboratory, Hampton Road, Teddington, Middlesex, TW11 0LW, U.K.

[§]School of Pharmacy, University of Nottingham, University Park, Nottingham NG7 2RD, U.K.

Supporting Information

ABSTRACT: We have shown previously that coupling of high field asymmetric waveform ion mobility spectrometry (FAIMS), also known as differential ion mobility, with liquid extraction surface analysis (LESA) mass spectrometry of tissue results in significant improvements in the resulting protein mass spectra. Here, we demonstrate LESA FAIMS mass spectrometry imaging of proteins in sections of mouse brain and liver tissue. The results are compared with LESA mass spectrometry images obtained in the absence of FAIMS. The results show that the number of different protein species detected can be significantly increased by incorporating FAIMS into the workflow. A total of 34 proteins were detected by LESA FAIMS mass spectrometry imaging of mouse brain, of which 26 were unique to FAIMS, compared with 15 proteins (7 unique) detected by LESA mass spectrometry imaging. A number of proteins were identified including α-globin, 6.8 kDa mitochondrial proteolipid, macrophage migration inhibitory factor, ubiquitin, β-thymosin 4, and calmodulin. A total of 40 species were detected by LESA FAIMS mass spectrometry imaging of mouse liver, of which 29 were unique to FAIMS, compared with 24 proteins (13 unique) detected by LESA mass spectrometry imaging. The spatial distributions of proteins identified in both LESA mass spectrometry imaging and LESA FAIMS mass spectrometry imaging were in good agreement indicating that FAIMS is a suitable tool for inclusion in mass spectrometry imaging workflows.

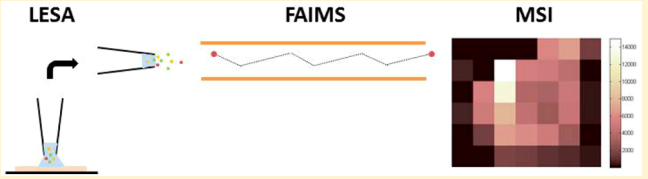

Spatial profiling of solid substrates via mass spectrometry imaging (MSI) can provide insight into biological systems. MSI techniques such as secondary ionization mass spectrometry (SIMS) can provide spatial resolution on the order of nm;[1,2] however, only relatively low molecular weight species (below ~1000 Da) can be detected owing to the destructive nature of the technique. Matrix-assisted laser desorption/ionization (MALDI) provides softer ionization and the ability to ionize larger species such as proteins. Previous MALDI MSI reports have described the detection of numerous protein species from various tissues samples, such as liver[3] and brain[4] in mouse and rat models. The spatial distribution of protein species in bacterial colonies[5] and plant matter[6] have also been probed by MALDI MSI. The detection of high molecular mass protein species has also been reported: Franck et al. reported the detection of protein species up to 50 kDa from rat brain tissue sections and up to 70 kDa from ovarian cancer biopsy tissue sections.[7] Nevertheless, MALDI typically leads to the formation of singly charged ions; hence the analysis of such large species is limited to time-of-flight mass analysers with the associated compromise in resolving power. Other limitations of MALDI MSI include lengthy sample preparation and matrix interference.[8−10]

Electrospray-based MSI methods have been shown to provide complementary data to MALDI MSI. Desorption electrospray ionization (DESI), which involves the desorption of projectile droplets which have been electrosprayed onto a sample surface, was introduced by Cooks et al. in 2004.[11] Eberlin et al. reported analysis of the same tissue section, first by desorption electrospray ionization (DESI) imaging for lipid analysis followed by MALDI imaging for protein analysis, enabling correlation of lipid distributions with those of protein species.[12] Although DESI has been shown to be suitable for the analysis of protein species up to ~17 kDa from (solid) solutions on a surface,[13] the detection of such protein species directly from thin tissue sections has not been reported. A variant of DESI which involves liquid based samples (known as liquid DESI) has enabled the detection of protein species up to ~150 kDa.[14]

Liquid extraction surface analysis (LESA), which enables the extraction of analytes from solid substrates via the formation of a liquid microjunction between a pipet tip and the sample surface,[15−17] has been shown to be suitable for the analysis of intact proteins from a variety of sample substrates. Previously, we have shown that intact protein species can be extracted from substrates including dried blood spots on filter paper,[18−20] thin tissue sections thaw-mounted onto glass[21] and *Escherichia coli* colonies growing on agar.[22] Moreover, intact protein complexes can be sampled by LESA.[23,24] LESA MSI has been used as a high sensitivity profiling technique for the determination of

Received: March 17, 2016
Accepted: May 26, 2016
Published: May 26, 2016

DOI: 10.1021/acs.analchem.6b01060
Anal. Chem. 2016, 88, 6758−6766

drug distributions, as a precursor tool to high spatial resolution MALDI MSI experiments of smaller tissue areas, and in the analysis of various drug dosed animal studies.[25,26] Randall et al. applied LESA MSI to the simultaneous analysis of lipids, proteins and a drug compound in mouse brain tissue sections.[27] In addition, Wisztorski et al. have recently described the use of LESA as an extraction protocol to provide spatially resolved proteomics data.[28] LESA MSI suffers from low spatial resolution, typically 500 μm to 1 mm, but has the advantages of sensitivity, ability to be coupled with high resolution mass analysers and potential for native MSI. It can therefore be considered to be complementary to high spatial resolution imaging techniques. Recent work by Hsu et al. showed imaging of proteins up to 15 kDa in brain tissue by nanospray desorption electrospray ionization (nanoDESI) at approximately 200 μm lateral resolution.[29] NanoDESI is somewhat of a misnomer as it is a variant of liquid microjunction surface sampling in which a continuous solvent stream replaces the discrete liquid microjunction, similar to the technology developed by Van Berkel et al.[30] and now commercialized as the flowprobe system by Prosolia.

Previously, we have shown that coupling of LESA to a high-field asymmetric ion mobility spectrometry (FAIMS, also known as differential ion mobility spectrometry) device,[31] after extraction/ionization and before mass spectrometric analysis, provides significant improvements in the analysis of complex biological samples.[32,33] The inclusion of FAIMS results in improved signal-to-noise ratios, shorter acquisition times, and separation of molecular classes, that is, proteins and lipids. FAIMS enables gas phase separation of ions at atmospheric pressure based on differences in their mobility in high and low electric fields. Ions are passed between two electrodes by a carrier gas (air in this case) and an asymmetric waveform is applied to the electrodes such that the ions are exposed to alternating high and low electric fields perpendicular to their trajectory. Ions diverge from the original trajectory due to their differential mobility, and would discharge on the electrode if a dc compensation field (CF) were not superimposed. It is possible to selectively transmit different ions, or subsets of ions, by careful selection of CF. The benefits afforded by FAIMS suggest that the technique could find applications in LESA MSI protocols.

The inclusion of ion mobility spectrometry has previously been shown to offer advantages for MSI. McLean et al. demonstrated that inclusion of drift tube ion mobility spectrometry in MALDI MSI on a time-of-flight mass spectrometer[34] enabled imaging of isobaric lipid and peptide species from mouse liver tissue sections. Bennett et al. coupled FAIMS to DESI for mass spectrometry imaging of lipids in sections of rat brain and 4-hydroxybenzoic acid in sea algae.[35] Inclusion of the ion mobility device in the MSI workflow was shown to improve signal-to-noise ratios of lipid analytes in rat brain, providing greater insight as to the true spatial distributions of these molecular species in the tissue sections and improving image contrast.

Here, we demonstrate LESA FAIMS mass spectrometry imaging of proteins in tissue sections of mouse brain and liver and compare the results with LESA MSI in the absence of FAIMS. FAIMS was operated in static mode, i.e., the dispersion field and compensation field were kept constant throughout the analysis. The DF and CF values applied are optimum for transmission of proteins with molecular weight >30 kDa.[32] The results show an increase in number of protein species detected: 34 species in the mass range 4−17 kDa were detected and imaged in LESA FAIMS MSI of mouse brain compared with 15 species in LESA MSI. Forty proteins were detected in LESA FAIMS MSI of mouse liver compared with 24 in LESA MSI.

METHODS

Materials. *Thin Tissue Sections.* Brain and liver from wild-type mice (extraneous tissue from culled animals) were the gift of Prof Steve Watson (University of Birmingham). Organs were frozen on dry ice prior to storage at −80 °C. Sections of murine liver tissue and brain tissue of area ∼1.5 cm^2 were obtained at a thickness of 10 μm using a CM1810 Cryostat (Leica Microsystems, Wetzlar, Germany) and thaw mounted onto glass slides.

Solvents. The following solvents were used: acetonitrile (J. T. Baker, The Netherlands), ethanol (Fisher Scientific, Loughborough, UK), HPLC grade water (J. T. Baker, The Netherlands), and formic acid (Sigma-Aldrich Company Ltd., Dorset, U.K.).

LESA. Thin tissue section samples of mouse brain were washed in 80% ethanol for 10 s (to remove abundant lipid species from the sample) and then left to air-dry. Thin tissue sections of mouse liver were not washed. Samples were loaded onto a universal LESA adapter plate. The plate was placed into the TriVersa Nanomate chip-based electrospray device (Advion, Ithaca, NY) coupled to the Thermo Fisher Scientific Orbitrap Elite (Thermo Fisher Scientific, Bremen, Germany). The solvent system used for LESA extraction/electrospray was 40:60 acetonitrile:water with the addition of 1% formic acid.

LESA and LESA FAIMS MSI and Optimization Experiments. 1.5 μL samples were aspirated from the solvent well. The robotic arm relocated to a position above the tissue and descended to a height 0.8 mm above the surface of the sample. 1.0 μL of the solution was dispensed onto the sample surface to form a liquid microjunction. The liquid microjunction was maintained for 10 s; then 1.1 μL were reaspirated into the pipet tip. The sample solvent was mixed once for mouse liver experiments. All MSI experiments were acquired at 2 mm × 2 mm spacing. The LESA Points software in which sampling locations are selected is limited to 1 mm spacing increments; 2 mm spacing was chosen to prevent overlapping of sampled areas from location to location.

LESA and LESA FAIMS MS/MS Experiments. Four microliters were aspirated from the solvent well before the robotic arm relocated to a position 0.8 mm above the surface of the tissue sample. 1.0 μL of the solution was dispensed onto the sample surface, forming a liquid microjunction that was maintained for 10 s, before 1.5 μL was reaspirated. The sample was mixed twice (redispensed and held for a further 10 s). Samples were introduced into the mass spectrometer via the TriVersa NanoMate, with gas pressure 0.3 psi, a tip voltage of 1.70 kV, and a capillary temperature of 250 °C for experiments conducted without the FAIMS device coupled to the mass spectrometer and 350 °C when the FAIMS device was coupled.

FAIMS. The Triversa Nanomate was coupled to a miniaturized ultra-FAIMS device (Owlstone, Cambridge, UK) which was coupled to an Orbitrap Elite mass spectrometer (Thermo Fisher Scientific, Bremen Germany). FAIMS separation was carried out in positive ion mode using an NC chip (Owlstone) with trench length 78.1 mm, gap width 101.3 μm and total thickness 700 μm. The FAIMS device was operated either in static or 1D mode. In static mode, the dispersion field (DF) and compensation field (CF) were 270

DOI: 10.1021/acs.analchem.6b01060
Anal. Chem. 2016, 88, 6758−6766

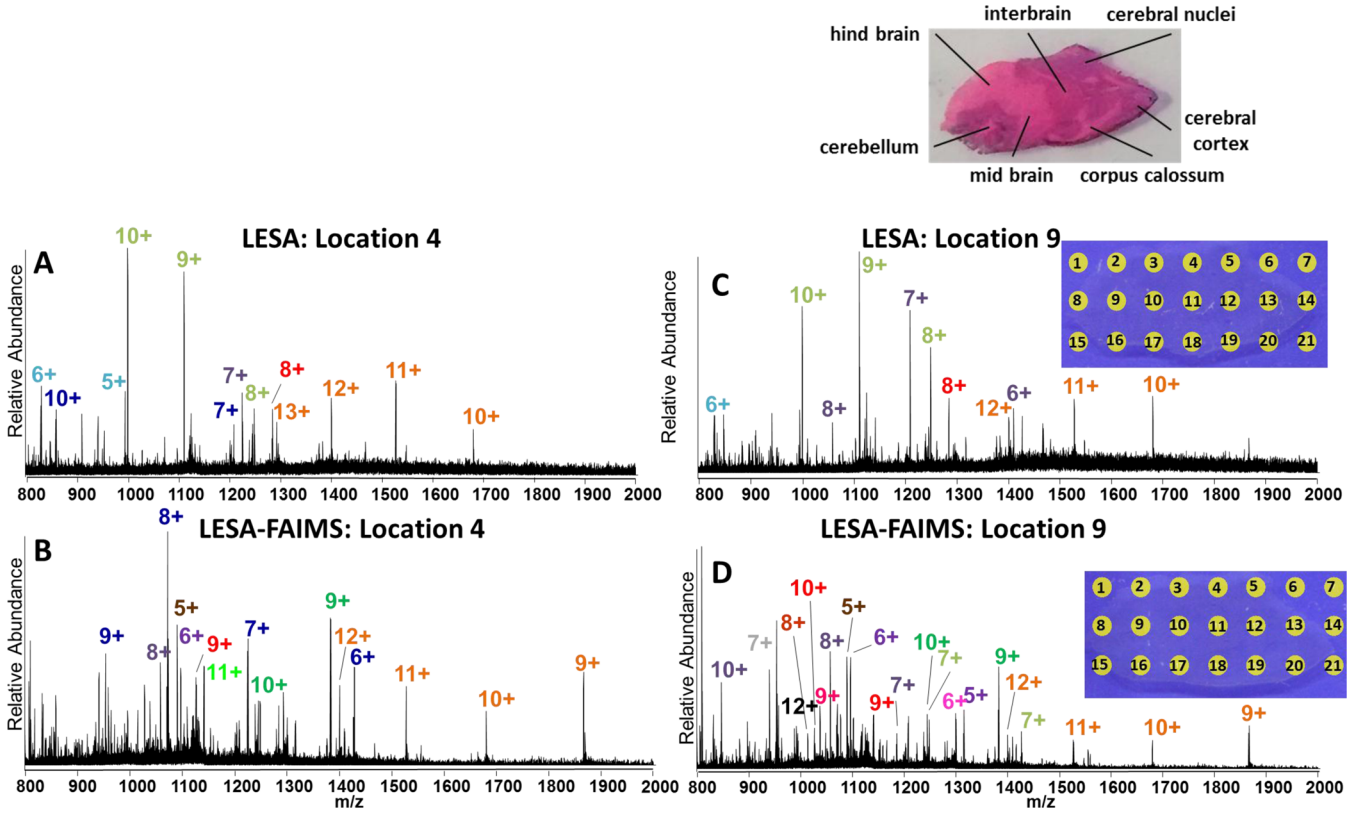

Figure 1. LESA and LESA-FAIMS profiling: (A) mass spectrum acquired at tissue location 4 following LESA profiling; (B) mass spectrum acquired at tissue location 4 following LESA-FAIMS profiling; (C) mass spectrum acquired at tissue location 9 following LESA profiling; (D) mass spectrum acquired at tissue location 9 following LESA-FAIMS profiling. Colors indicate multiple charge states of individual proteins. Photographs inset show the LESA sampling positions in the two tissue sections, and the H&E stained serial section.

and 2.6 Td, respectively (brain), and 270 and 2.68 Td, respectively (liver). In 1D mode, the dispersion field was fixed at 270 Td and the compensation field was varied from −1 to 4 Td over 180 s.

Mass Spectrometry. Experiments were performed on a Thermo Fisher Orbitrap Elite mass spectrometer.

MSI. Mass spectra were recorded in full scan mode (m/z 600−2000) at a resolution of 120 000 at m/z 200. Automatic gain control (AGC) was turned off for spatial profiling experiments. The fill time was optimized prior to analysis (by sampling serial tissue sections at a central location) by acquiring data with the AGC on with extended maximum injection times. Subsequent interrogation of those data revealed the actual approximate fill times required to accumulate 1×10^6 charges. The following fill times were optimal: 2 or 5 ms (mouse brain and liver respectively) for LESA experiments with no FAIMS device attached to the mass spectrometer, 20 ms for LESA experiments with the FAIMS device attached (no field applied), and 150 or 100 ms (mouse brain and liver respectively) for LESA (static) FAIMS experiments. Data were acquired for 2 min at each location.

MS/MS. LESA FAIMS (DF = 270 Td, CF = 2.6 Td) tandem mass spectrometry experiments were conducted via collision induced dissociation (CID). For these experiments, AGC was used with a target of 1×10^6 charges and a maximum injection time of 1000 ms. CID was performed in the ion trap at a normalized collision energy between 20% and 23% and fragments were detected in the orbitrap. The isolation width was between 3.0 and 5.0 Th. Each scan comprised of 1 microscan. Data were recorded for between 2 and 7 min (~245−475 scans).

Data Analysis. *Protein Identification.* Data were analyzed using Xcalibur version 3.0.63 software. All mass spectra were deconvoluted using the Xtract function in Xcalibur to obtain monoisotopic masses of species detected in each experiment. Mass spectra were processed with a signal-to-noise ratio of 2. Identity was confirmed by manual analysis using Protein Prospector (http://prospector.ucsf.edu/prospector/mshome.htm).

Imaging. Single location data were saved as a single mass spectrum using the write to raw file function in the Xcalibur software. These new single mass spectrum.raw files were converted to the mzML format using msconvert as part of ProteoWizard[36] and then to the imzML format using imzMLConverter.[37] Data in imzML format were then loaded into MATLAB (version 2013a, The MathWorks Inc., Natick, Massachusetts) using imzMLConverter and in house software.

Staining. Serial tissue sections were stained with H&E as follows: tissue was twice washed in water for 2 min before immersing in Harris's hematoxylin for 4 min. The tissue was then washed in water (2 min), Scott's Tap Water Substitute (0.5 min) and water (2 min) before immersing in Eoisin for 1 min. Finally, the tissue was washed in water (2 × 2 min), alcohol (4 × 2 min), and xylene (3 × 2 min). Anatomical features were manually assigned by visual inspection and correlation to the sagittal Allen Mouse Brain Atlas.[38]

DOI: 10.1021/acs.analchem.6b01060
Anal. Chem. 2016, 88, 6758−6766

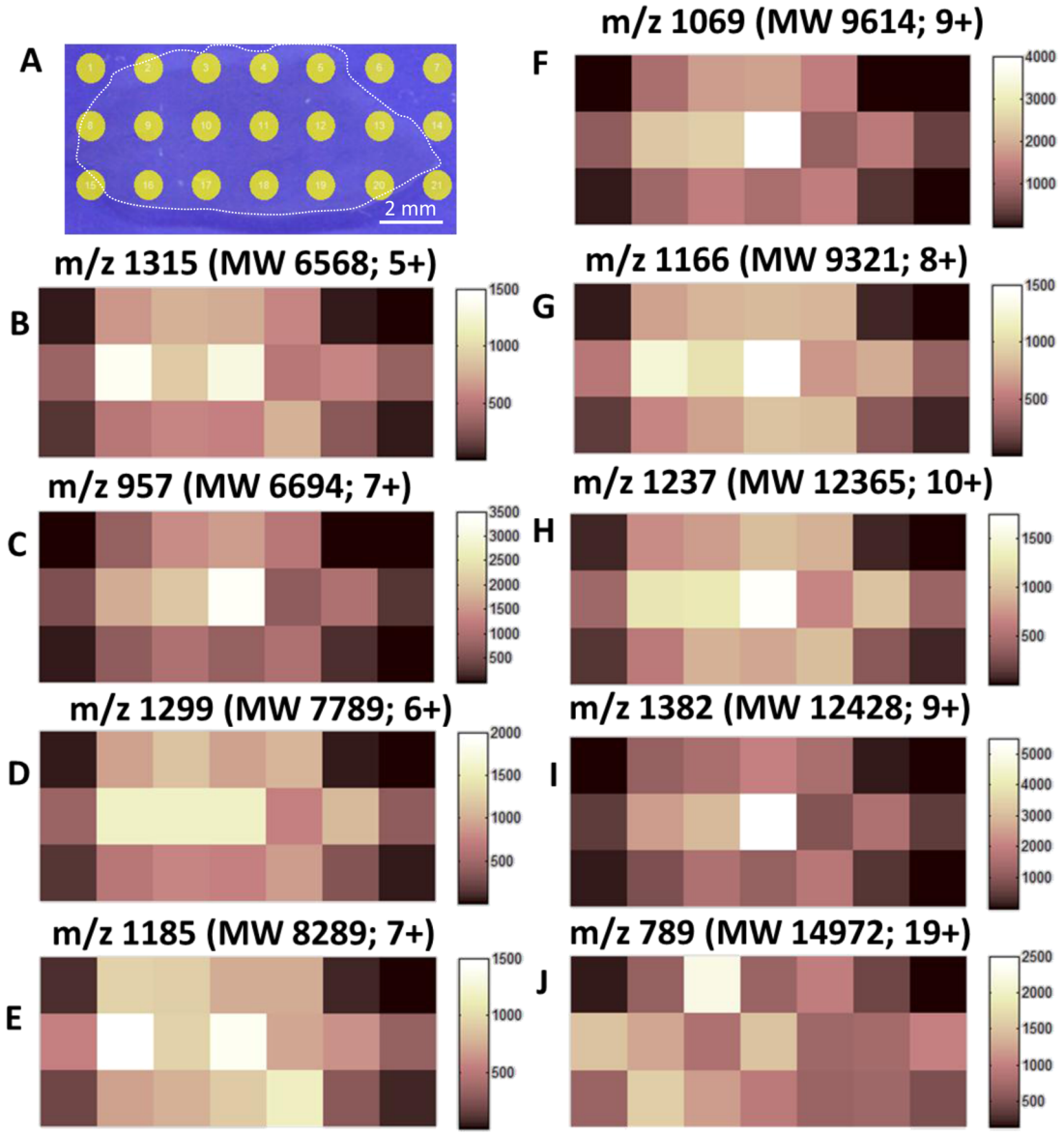

Figure 2. LESA FAIMS MSI of mouse brain tissue at DF = 270 Td, CF = 2.6 Td. (A) LESA sampling positions. LESA FAIMS MS ion images of (B) m/z 1315 (MW 6568 Da; 5+), (C) m/z 957 (MW 6694 Da; 7+, 6.8 kDa proteolipid), (D) m/z 1299 (MW 7789 Da; 6+), (E) m/z 1185 (MW 8289 Da; 7+), (F) m/z 1069 (MW 9614 Da; 9+), (G) m/z 1166 (MW 9321 Da; 8+), (H) m/z 1237 (MW 12365 Da; 10+, macrophage migration inhibitory factor), (I) m/z 1382 (MW 12428 Da; 9+), and (J) m/z 789 (MW 14792 Da; 19+, α-globin).

RESULTS AND DISCUSSION

Mouse Brain Tissue Sections. Serial sections of mouse brain tissue were sampled in a sequential fashion by LESA or LESA coupled to (static) FAIMS, allowing the spatial mapping of detected species, as shown in the photographs inset in Figure 1. Previously we reported that protein species in mouse brain were optimally transmitted through the chip-based FAIMS device at a dispersion field of 270 Td and a compensation field 2.6 Td,[32] hence those conditions were employed here for data acquisition via LESA (static) FAIMS. Data were acquired at 2 mm spacing in order to prevent any oversampling between sampling locations. Oversampling is often used in MSI to improve spatial resolution; however, that approach is only applicable for methods in which the surface is fully ablated. LESA does not result in complete ablation and previous work in our laboratory[39] has shown that resampling a tissue location alters the subsequent mass spectrum, possibly due to washing effects or degradation of the wetted surface. For the sampling volumes used here, the sampling area has diameter ~1.8 mm. (The LESA points software allows sampling locations to be spaced at increments of 1 mm only). Data were acquired with the automatic gain control (AGC) switched off, using a defined fill time which had been optimized prior to full tissue profiling experiments, see above. Automatic gain control governs the number of charges accumulated in the linear ion trap prior to transmission to the orbitrap. To allow comparisons of the relative abundances of species at different sampling locations, AGC was not used and instead the fill time was given a defined value.

Profiling of mouse brain tissue by LESA and LESA FAIMS led to the detection of a number of multiply charged protein species. Figure 1A shows the summed mass spectrum from a specific location (location 4 on the inset photograph) sampled by LESA (no FAIMS device coupled). A variety of multiply charged protein species were detected, corresponding to several

DOI: 10.1021/acs.analchem.6b01060
Anal. Chem. 2016, 88, 6758−6766

different protein species; however, a greater number of protein species were detected from the equivalent location on the serial section when LESA was coupled to FAIMS, as shown in Figure 1B. Deconvolution of the mass spectra, using the Xtract function in Xcalibur, shows that 11 separate protein species (4−17 kDa) were detected in the LESA experiment compared to 14 protein species in the LESA (static) FAIMS experiment. A similar analysis of the mass spectra obtained at a different location (location 9, Figure 1 inset photographs) reveals detection of 10 separate protein species in the LESA experiment and 19 separate species between 4−17 kDa in the LESA (static) FAIMS experiment. The spatial distributions of a selection of the species unique to the LESA (static) FAIMS experiment are shown in Figure 2. (Figure 1 inset shows an H&E stained serial section for comparison). As described above, the spatial resolution afforded by the LESA sampling regime is low; nevertheless it is possible to profile multiple protein species by LESA FAIMS.

A summary of all protein species detected in the LESA and LESA FAIMS MSI experiments according to location, as indicated in the H&E stained section Figure 1 inset, is given in Supporting Information Tables 1 and 2. A total of 34 separate protein species were detected in the mass range 4 to 17 kDa across the tissue section profiled by LESA (static) FAIMS, 26 of which were not detected in the LESA analysis. Note that we previously reported that surface sampling of mouse brain tissue at a specific discrete location via LESA (static) FAIMS experiments (at DF = 270 Td and CF = 2.6 Td) led to the detection of 29 different protein species in the mass range ∼5 to ∼37 kDa.[32] Clearly different species were detected in the current experiment. This observation is not unexpected: There will be differences in the anatomical regions being sampled, which naturally vary in protein composition. In addition, the smaller extraction volumes used for here for optimized spatial resolution may result in reduced extraction efficiency.

To identify some of the protein species unique to the FAIMS MSI experiment, top-down collision induced dissociation (CID) analysis was performed in a further experiment. LESA (static) FAIMS CID MS/MS of the 20+ ions centered at m/z 749.99 (MW_{meas} 14970.71 Da, MW_{calcd} 14971.82, Δ 5.6 ppm) resulted in identification of α-globin with 22% sequence coverage, see Figure 3A. This protein was detected in most of the on-tissue locations (9/21, see Supporting Information Table 2).The ion distribution of the 19+ charge state of the same protein (detected at m/z 789) is shown in Figure 2 Panel J. The 7+ precursor ion at m/z 957.80 (MW_{meas} 6693.58 Da, MW_{calcd} 6693.58) was identified as 6.8 kDa mitochondrial proteolipid with a sequence coverage of 24%, see Figure 3B. This is the first reported identification of this protein from brain tissue by LESA. Finally, the 9+ precursor ion m/z 1375.69 (MW_{meas} 12365.18 Da, MW_{calcd} 12365.14, Δ 3.2 ppm) was identified as macrophage migration inhibitory factor, see Figure 3C. Although the sequence coverage achieved was low (7%), this protein has previously been reported by surface sampling (coupled to LC-MS) of mouse brain tissue sections by Schey et al.[40]

A number of species (MW = 2105.07, 2401.19, 2404.18, 2475.27, 3215.59, 3343.65, 4744.39, 4979.27, 5368.70, 5455.79, 5703.08, 8976.23, and 10069.75 Da) were detected in the LESA profiling experiment that were not detected in the LESA (static) FAIMS experiment. Six of these species were in the mass range 2−4 kDa whereas the remainder fell within the mass range detected in the FAIMS experiment (4−17 kDa).

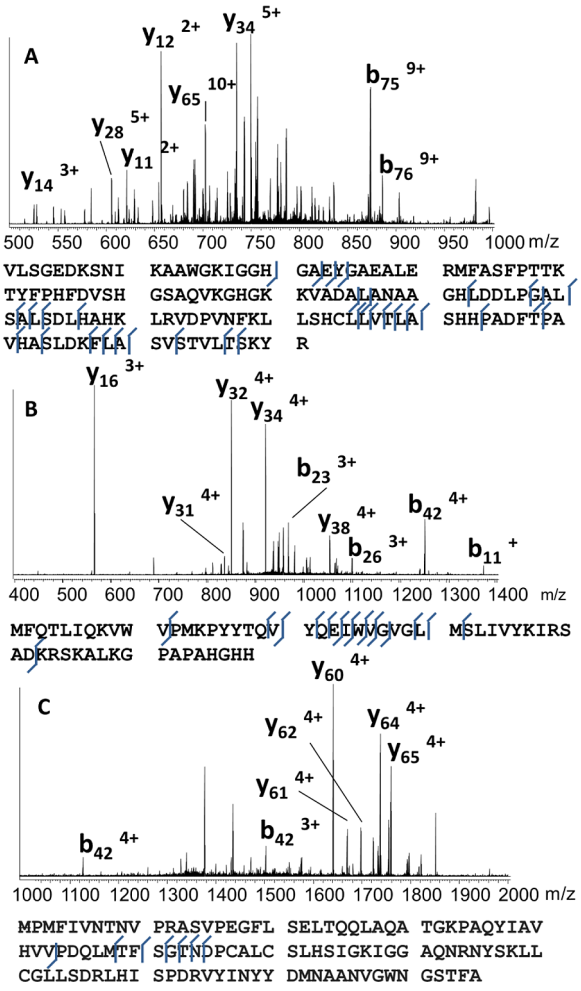

Figure 3. LESA FAIMS CID MS/MS of (A) m/z 749^{20+} (MW 14 972 Da) identified as α-globin; (B) m/z 987^{7+} (MW 6693 Da) identified as 6.8 kDa proteolipid; (C) m/z 1375^{8+} (MW 12365 Da) identified as macrophage migration inhibitory factor.

The charge states varied from 3+ to 10+, see Supporting Information Table 3. The absence of these species in the FAIMS data set may be the result of low abundance (FAIMS is associated with a reduction in absolute sensitivity despite the improvements in signal-to-noise[32]) or that the static FAIMS conditions used here are not suitable for their transmission. Similarly, the species with MW 4960 Da (assigned as β-thymosin 4, see below) was detected in most (10/12) on-tissue locations in which protein signals were detected in the LESA experiment, but in only two locations in the LESA (static) FAIMS experiment. Supporting Information Figure 1C shows the spatial mapping (ion image) of m/z 828 (6+ charge state) together with the corresponding LESA sampling method (Supporting Information Figure 1B). To determine whether the static FAIMS conditions were limiting transmission of these ions, a LESA 1D FAIMS MSI experiment was performed in which the dispersion field was fixed at 270 Td and the compensation field was varied from −1 to 4 Td. (Note that this experiment was performed on a nonserial section of mouse brain tissue). β-Thymosin 4 was detected at each tissue location; however, the optimum CF field for its transmission was 3.6 Td. That observation explains the inconsistent results from the static FAIMS analysis, that is, the static FAIMS

DOI: 10.1021/acs.analchem.6b01060
Anal. Chem. 2016, 88, 6758−6766

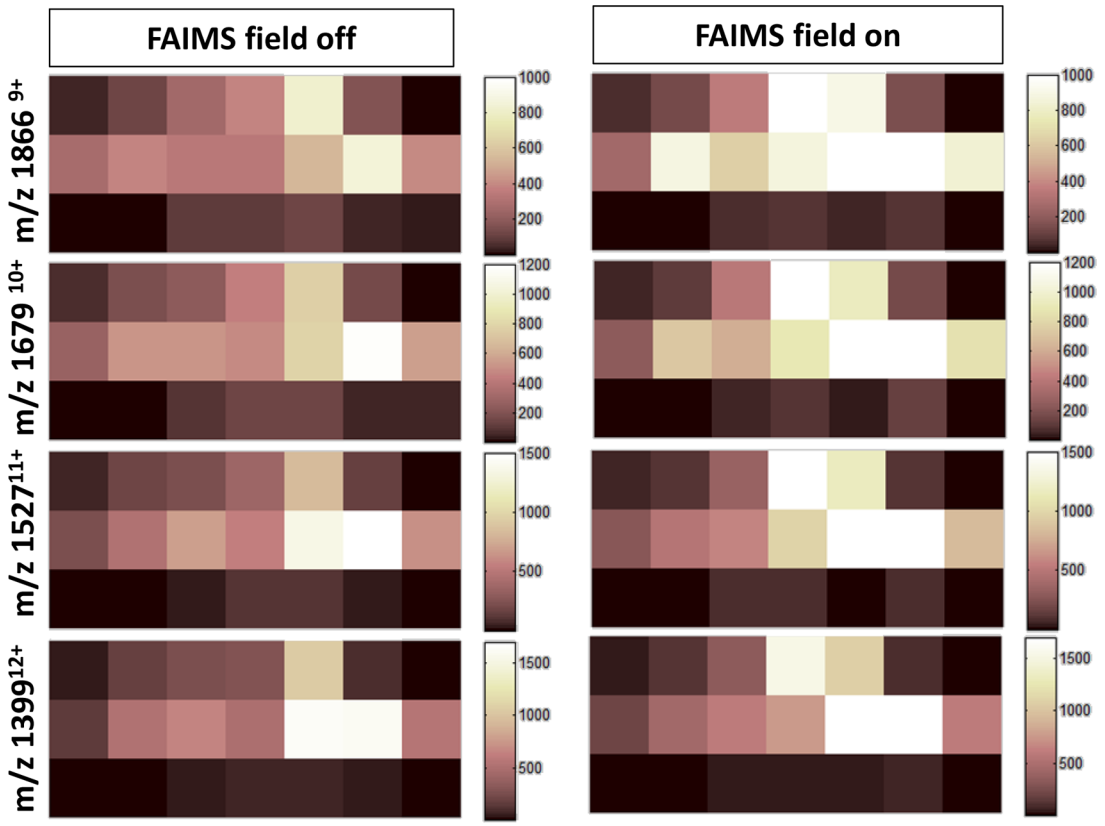

Figure 4. LESA MSI and LESA (static) FAIMS MSI of mouse brain acquired following single extractions from the same tissue section. The spatial distributions of the 9+ to 12+ charge states of calmodulin (MW 16780 Da) are shown (left) in the absence of FAIMS field and (right) in static FAIMS field (DF = 270 Td, CF = 2.6 Td).

conditions (DF = 270 Td, CF = 2.6 Td) were not optimum for transmission of β-thymosin 4 ions.

β-Thymosin 4 was identified following LESA CID MS/MS of the 5+ ions at m/z 993.70 (MW_{meas} 4960.47 Da, MW_{calcd} 4960.49 Da, Δ 2.7 ppm, 61% sequence coverage), see Supporting Information Figure 2A. In addition, the species with MW 8559 Da, which was detected in both the LESA and the LESA (static) FAIMS experiment, was identified as ubiquitin (MW_{meas} 8559.59, MW_{calcd} 8559.62, Δ 3.0 ppm, 27% coverage) following LESA CID MS/MS of the 7+ ions at m/z 1224.50, see Supporting Information Figure 2B. The 12+ ions observed at m/z 1400.33 were identified as calmodulin acetylated at position 95 (MW_{meas} 16779.80, MW_{calcd} 16779.81, Δ 0.7 ppm, 13% coverage), see Supporting Information Figure 2C.

Recently, Hsu et al. reported nanoDESI mass spectrometry imaging of proteins from coronal sections of mouse brain.[29] In their study, ubiquitin was described to be homogeneously distributed across the tissue whereas β-thymosin 4 was detected in greater intensity in the hippocampus. We detected β-thymosin 4 and ubiquitin across the tissue section (Supporting Information Figure 1C and D); however, both proteins were detected in greater intensity in the cerebral nuclei. The hippocampus was not sampled in the tissue sections analyzed here; the hippocampus is a small anatomical feature which is not consistently present in sagittally sectioned brain. Hsu et al. also reported that α-globin was present in high abundance in certain locations, possibly corresponding to vasculature features. In this work, α-globin was only detected when FAIMS was incorporated in the MSI workflow, see Figure 2J. The signal intensity is particularly high in location 3 which could be due to similar vasculature features, although no such features were visible to the naked eye.

The protein calmodulin (MW 16780 Da) was detected in both the LESA experiment and the LESA (static) FAIMS experiments. Monitoring of the various charge states of this species shows that the spatial distributions and relative abundances of the 9+ through 12+ charge states *within* each experiment are in good agreement with one another, see Supporting Information Figure 3; however, comparison of the spatial distributions of ions detected *between* each experiment is hindered by the fact that the LESA sampling locations are not identical in the two serial sections. This variation is a consequence of the LESA software which requires manual positioning of the sampling locations. For example, in the photographs inset in Figure 1, the bottom row of the LESA image has sampled the edge of the tissue whereas the equivalent row in the LESA (static) FAIMS image has sampled on tissue. In order to ensure that the presence of the FAIMS field does not affect the spatial distribution of detected analytes, an imaging experiment was performed on a single tissue section in which each individual LESA sample was analyzed both with the FAIMS field off and on. As the LESA extraction was performed as a single step in each experiment, any differences in location and extraction efficiency are controlled for and the spatial distributions in LESA MSI and LESA (static) FAIMS MSI can be directly compared. Figure 4 shows the spatial distributions of the 9^+ (m/z 1866), 10^+ (m/z 1679), 11^+ (m/z 1527), and 12^+ (m/z 1399) charge states of calmodulin with and without the FAIMS field applied. The spatial distributions

DOI: 10.1021/acs.analchem.6b01060
Anal. Chem. 2016, 88, 6758−6766

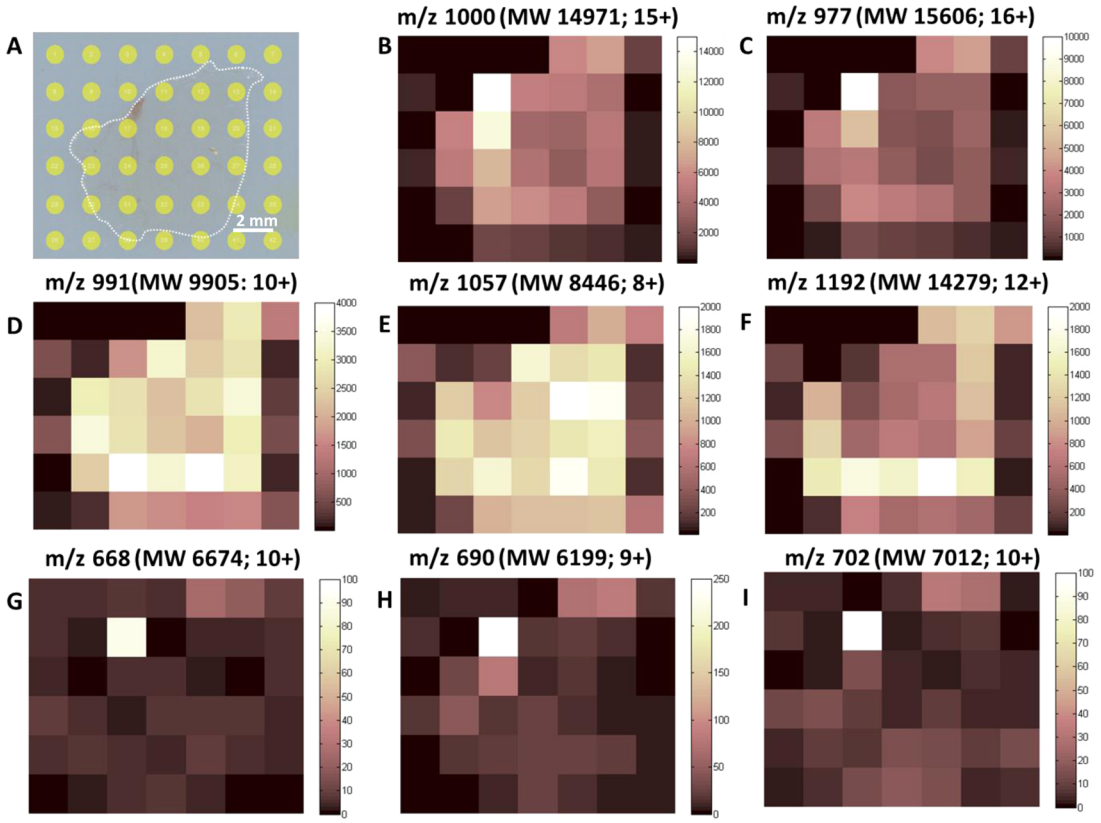

Figure 5. LESA FAIMS MSI of mouse liver tissue at DF = 270 Td, CF = 2.68 Td. (A) LESA sampling positions, (B) m/z 1000 (MW 14971 Da; 15+; α-globin), (C) m/z 977 (MW 15606 Da; 16+; β-globin), (D) m/z 9791 (MW 9905 Da; 10+), (E) m/z 1057 (MW 8446 Da; 7+), (F) m/z 1192 (MW 14279 Da; 12+; FABP1), (G) m/z 668 (MW 6674 Da; 10+), (H) m/z 690 (MW 6199 Da; 9+), and (I) m/z 702 (MW 7012 Da; 10+).

observed in the LESA MSI and LESA FAIMS MSI are in agreement. The differences in absolute intensity between the two ion maps are the result of improved S/N observed with FAIMS. Similar data are shown for the 6^+ (m/z 1409), 7^+ (m/z 1208), and 8^+ (m/z 1057) charge states of the protein with MW 8446 Da in Supporting Information Figure 4. Again, the spatial distributions of these ions are in agreement.

Mouse Liver Tissue Sections. In further experiments, serial sections of mouse liver were sampled by LESA and LESA (static) FAIMS (DF = 270 Td; CF = 2.68 Td). A summary of all protein species detected in the LESA and LESA FAIMS experiments according to location, as indicated in Figure 5A and Supporting Information Figure 5A, is given in Supporting Information Tables 4 and 5. Again, a greater number of protein species were detected from an equivalent location on the serial section when LESA was coupled with (static) FAIMS. A total of 40 separate protein species in the mass range 4−16 kDa were detected across the tissue section profiled by LESA (static) FAIMS, 29 of which were not detected in the LESA analysis. Tissue profiling by LESA revealed 24 protein species in that mass range, 13 of which were unique to that data set.

Figures 5B−F show the spatial distributions of a selection of protein species detected in the LESA (static) FAIMS experiment. A vascular feature can be seen in the tissue sections, see Figure 5A, and the location of α- and β-globin clearly correspond with that feature (Figure 5B and 5C, respectively). Interestingly, the protein species unique to the LESA (static) FAIMS experiment were predominantly detected in pixel locations corresponding to the vascular feature. For example, see Figure 5G, 5H, and 5I. Figure 5F shows the spatial distribution of liver fatty acid binding protein FABP1 within the section. FABP1 appears to be predominantly located toward the outer of the section. For comparison, the spatial distributions of α-globin, β-globin and FABP1 detected in the LESA experiment are shown in Supporting Information Figure 5. Again, the globin chains correlate with the position of the vascular feature and the FABP1 is distributed toward the outer of the section.

CONCLUSIONS

The results show that inclusion of FAIMS in the LESA MSI workflow increases the number of protein species detected. For the mouse brain sample studied here, 15 proteins (in mass range 4−17 kDa) were detected by LESA MSI compared with 34 proteins detected by LESA (static) FAIMS MSI. In total, 41 protein species were detected in the range 4−17 kDa. Twenty-six of those proteins were unique to LESA (static) FAIMS MSI. Seven proteins in that mass range were unique to LESA MSI. A further six species in the mass range 2−4 kDa were observed in LESA MSI only. For the mouse liver sample studied, 24 species (in the mass range 4−16 kDa) were detected by LESA MSI compared with 40 species detected by LESA (static) FAIMS MSI. In total, 53 protein species were detected in the range 4−16 kDa. Twenty-nine of those proteins were unique to LESA (static) FAIMS MSI. Thirteen proteins in that mass range were unique to LESA MSI. The static FAIMS conditions used here were optimized for higher molecular weight species thus preventing transmission of the lower molecular weight species (<4 kDa). In addition, although the static FAIMS conditions (DF = 270 Td, CF = 2.6 Td) were broadly optimized for

DOI: 10.1021/acs.analchem.6b01060
Anal. Chem. 2016, 88, 6758−6766

proteins of MW> 4 kDa, there are some outliers such as β-thymosin 4 (CF = 3.6 Td), or species of very low abundance, which were not transmitted by FAIMS.

A number of proteins in mouse brain were identified by collision-induced dissociation: LESA (static) FAIMS CID MS/MS resulted in the identification of α-globin (MW 14972 Da), 6.8 kDa mitochondrial proteolipid (MW 6693 Da) and macrophage migration inhibitory factor (MW 12665 Da). LESA CID MS/MS resulted in identification of ubiquitin (MW 8560 Da), β-thymosin 4 (MW 4960 Da), and calmodulin (MW 16780 Da), all of which were also observed in the FAIMS data set.

Eight protein species were detected in both the LESA MSI and LESA (static) FAIMS MSI analysis of mouse brain. The presence of these allowed comparisons of the spatial distributions measured with and without FAIMS. The good agreement between the two distributions confirms the suitability of FAIMS as a useful tool in mass spectrometry imaging.

■ ASSOCIATED CONTENT

Supporting Information

The Supporting Information is available free of charge on the ACS Publications website at DOI: 10.1021/acs.analchem.6b01060.

Tables of protein masses detected in LESA MSI and LESA FAIMS MSI of mouse brain, unique species detected in LESA MSI of mouse brain, and protein masses detected in LESA MSI and LESA FAIMS MSI of mouse liver (PDF)

Figures showing ion images obtained following LESA MSI of mouse brain, LESA CID MS/MS spectra of proteins detected following LESA of mouse brain, spatial distribution of a protein in various charge states in the presence and absence of FAIMS field, and ion images obtained following LESA MSI of mouse liver (PDF)

■ AUTHOR INFORMATION

Notes

The authors declare no competing financial interest.

Supplementary data supporting this research is openly available from the University of Birmingham data archive at http://findit.bham.ac.uk/.

■ ACKNOWLEDGMENTS

H.J.C., R.L.G., and A.J.C. are funded by EPSRC (EP/L023490/1). The Advion Triversa Nanomate and Thermo Fisher Orbitrap Elite mass spectrometer used in this research were funded through Birmingham Science City Translational Medicine, Experimental Medicine Network of Excellence Project with support from Advantage West Midlands.

■ REFERENCES

(1) Benabdellah, F.; Seyer, A.; Quinton, L.; Touboul, D.; Brunelle, A.; Laprévote, O. *Anal. Bioanal. Chem.* **2010**, *396*, 151−162.
(2) Passarelli, M. K.; Newman, C. F.; Marshall, P. S.; West, A.; Gilmore, I. S.; Bunch, J.; Alexander, M. R.; Dollery, C. T. *Anal. Chem.* **2015**, *87*, 6696−6702.
(3) Seeley, E. H.; Oppenheimer, S. R.; Mi, D.; Chaurand, P.; Caprioli, R. M. *J. Am. Soc. Mass Spectrom.* **2008**, *19*, 1069−1077.
(4) Lemaire, R.; Wisztorski, M.; Desmons, A.; Tabet, J.; Day, R.; Salzet, M.; Fournier, I. *Anal. Chem.* **2006**, *78*, 7145−7153.
(5) Blaze, M.; Aydin, B.; Carlson, R. P.; Hanley, L. *Analyst* **2012**, *137*, 5018−5025.
(6) Cavatorta, V.; Sforza, S.; Mastrobuoni, G.; Pieraccini, G.; Francese, S.; Moneti, G.; Dossena, A.; Pastorello, E. A.; Marchelli, R. *J. Mass Spectrom.* **2009**, *44*, 891−897.
(7) Franck, J.; Longuespee, R.; Wisztorski, M.; Van Remoortere, A.; Van Zeijl, R.; Deelder, A.; Salzet, M.; McDonnell, L.; Fournier, I. *Annals of Transplantation* **2010**, *16*, BR293−BR299.
(8) Cohen, S. L.; Chait, B. T. *Anal. Chem.* **1996**, *68*, 31−37.
(9) Figueroa, I. D.; Torres, O.; Russell, D. H. *Anal. Chem.* **1998**, *70*, 4527−4533.
(10) Jackson, S. N.; Wang, H.-Y. J.; Woods, A. S.; Ugarov, M.; Egan, T.; Schultz, J. A. *J. Am. Soc. Mass Spectrom.* **2005**, *16*, 133−138.
(11) Takáts, Z.; Wiseman, J. M.; Gologan, B.; Cooks, R. G. *Science* **2004**, *306*, 471−473.
(12) Eberlin, L. S.; Liu, X.; Ferreira, C. R.; Santagata, S.; Agar, N. Y.; Cooks, R. G. *Anal. Chem.* **2011**, *83*, 8366−8371.
(13) Shin, Y.-S.; Drolet, B.; Mayer, R.; Dolence, K.; Basile, F. *Anal. Chem.* **2007**, *79*, 3514−3518.
(14) Ferguson, C. N.; Benchaar, S. A.; Miao, Z.; Loo, J. A.; Chen, H. *Anal. Chem.* **2011**, *83*, 6468−6473.
(15) Wachs, T.; Henion, J. *Anal. Chem.* **2001**, *73*, 632−638.
(16) Kertesz, V.; Ford, M. J.; Van Berkel, G. J. *Anal. Chem.* **2005**, *77*, 7183−7189.
(17) Kertesz, V.; Van Berkel, G. J. *J. Mass Spectrom.* **2010**, *45*, 252−260.
(18) Edwards, R.; Griffiths, P.; Bunch, J.; Cooper, H. *J. Am. Soc. Mass Spectrom.* **2012**, *23*, 1921−1930.
(19) Edwards, R. L.; Creese, A. J.; Baumert, M.; Griffiths, P.; Bunch, J.; Cooper, H. J. *Anal. Chem.* **2011**, *83*, 2265−2270.
(20) Edwards, R. L.; Griffiths, P.; Bunch, J.; Cooper, H. J. *Proteomics* **2014**, *14*, 1232−1238.
(21) Sarsby, J.; Martin, N. J.; Lalor, P. F.; Bunch, J.; Cooper, H. J. *J. Am. Soc. Mass Spectrom.* **2014**, *25*, 1953−1961.
(22) Randall, E. C.; Bunch, J.; Cooper, H. J. *Anal. Chem.* **2014**, *86*, 10504−10510.
(23) Griffiths, R. L.; Cooper, H. J. *Anal. Chem.* **2016**, *88*, 606−609.
(24) Martin, N. J.; Griffiths, R. L.; Edwards, R. L.; Cooper, H. J. *J. Am. Soc. Mass Spectrom.* **2015**, *26*, 1320.
(25) Swales, J. G.; Tucker, J. W.; Strittmatter, N.; Nilsson, A.; Cobice, D.; Clench, M. R.; Mackay, C. L.; Andren, P. E.; Takáts, Z.; Webborn, P. J.; et al. *Anal. Chem.* **2014**, *86*, 8473−8480.
(26) Nilsson, A.; Goodwin, R. J. A.; Swales, J. G.; Gallagher, R.; Shankaran, H.; Sathe, A.; Pradeepan, S.; Xue, A.; Keirstead, N.; Sasaki, J.; Andrén, P. E.; Gupta, A. *Chem. Res. Toxicol.* **2015**, *28*, 1823.
(27) Randall, E. C.; Race, A. M.; Cooper, H. J.; Bunch, J. 2016, submitted for publication.
(28) Wisztorski, M.; Desmons, A.; Quanico, J.; Fatou, B.; Gimeno, J.-P.; Franck, J.; Salzet, M.; Fournier, I. *Proteomics* **2016**, DOI: 10.1002/pmic.201500508.
(29) Hsu, C.-C.; Chou, P.-T.; Zare, R. N. *Anal. Chem.* **2015**, *87*, 11171−11175.
(30) Van Berkel, G. J.; Sanchez, A. D.; Quirke, J. M. E. *Anal. Chem.* **2002**, *74*, 6216−6223.
(31) Cooper, H. J. *J. Am. Soc. Mass Spectrom.* **2016**, *27*, 566.
(32) Sarsby, J.; Griffiths, R. L.; Race, A. M.; Bunch, J.; Randall, E. C.; Creese, A. J.; Cooper, H. J. *Anal. Chem.* **2015**, *87*, 6794−6800.
(33) Griffiths, R. L.; Dexter, A.; Creese, A. J.; Cooper, H. J. *Analyst* **2015**, *140*, 6879−6885.
(34) McLean, J. A.; Ridenour, W. B.; Caprioli, R. M. *J. Mass Spectrom.* **2007**, *42*, 1099−1105.
(35) Bennett, R. V.; Gamage, C. M.; Galhena, A. S.; Fernández, F. M. *Anal. Chem.* **2014**, *86*, 3756−3763.
(36) Chambers, M. C.; Maclean, B.; Burke, R.; Amodei, D.; Ruderman, D. L.; Neumann, S.; Gatto, L.; Fischer, B.; Pratt, B.; Egertson, J.; Hoff, K.; Kessner, D.; Tasman, N.; Shulman, N.; Frewen, B.; Baker, T. A.; Brusniak, M.-Y.; Paulse, C.; Creasy, D.; Flashner, L.; Kani, K.; Moulding, C.; Seymour, S. L.; Nuwaysir, L. M.; Lefebvre, B.; Kuhlmann, F.; Roark, J.; Rainer, P.; Detlev, S.; Hemenway, T.;

DOI: 10.1021/acs.analchem.6b01060
Anal. Chem. 2016, 88, 6758−6766

Huhmer, A.; Langridge, J.; Connolly, B.; Chadick, T.; Holly, K.; Eckels, J.; Deutsch, E. W.; Moritz, R. L.; Katz, J. E.; Agus, D. B.; MacCoss, M.; Tabb, D. L.; Mallick, P. *Nat. Biotechnol.* **2012**, *30*, 918−920.
(37) Race, A. M.; Styles, I. B.; Bunch, J. *J. Proteomics* **2012**, *75*, 5111−5112.
(38) Allen Institute for Brain Science. Mouse, P56, Sagittal, Interactive Atlas Viewer, 2016. http://atlas.brain-map.org/atlas?atlas=2.
(39) Sarsby, J. Liquid microjunction surface sampling and MALDI imaging of small and large molecules in human liver disease. PhD Thesis, University of Birmingham, 2016.
(40) Schey, K. L.; Anderson, D. M.; Rose, K. L. *Anal. Chem.* **2013**, *85*, 6767−6774.

DOI: 10.1021/acs.analchem.6b01060
Anal. Chem. 2016, 88, 6758−6766

analytical chemistry

Article

pubs.acs.org/ac

Investigation of the Impact of Desorption Electrospray Ionization Sprayer Geometry on Its Performance in Imaging of Biological Tissue

Jocelyn Tillner,[†,‡] James S. McKenzie,[†] Emrys A. Jones,[†,∥] Abigail V. M. Speller,[†] James L. Walsh,[§] Kirill A. Veselkov,[†] Josephine Bunch,[*,‡,⊥] Zoltan Takats,[*,†] and Ian S. Gilmore[*,‡]

[†]Biomolecular Medicine, Department of Surgery and Cancer, Faculty of Medicine, Imperial College London, Sir Alexander Fleming Building, South Kensington, London SW7 2AZ, United Kingdom

[‡]NiCE-MSI, National Physical Laboratory (NPL), Hampton Road, Teddington, Middlesex TW11 0LW, United Kingdom

[§]Department of Electrical, Engineering and Electronics, University of Liverpool, Brownlow Hill, Liverpool L69 3GJ, United Kingdom

[⊥]School of Pharmacy, University of Nottingham, University Park, Nottingham NG7 2RD, United Kingdom

Supporting Information

ABSTRACT: In this study, the impact of sprayer design and geometry on performance in desorption electrospray ionization mass spectrometry (DESI-MS) is assessed, as the sprayer is thought to be a major source of variability. Absolute intensity repeatability, spectral composition, and classification accuracy for biological tissues are considered. Marked differences in tissue analysis performance are seen between the commercially available and a lab-built sprayer. These are thought to be associated with the geometry of the solvent capillary and the resulting shape of the primary electrospray. Experiments with a sprayer with a fixed solvent capillary position show that capillary orientation has a crucial impact on tissue complex lipid signal and can lead to an almost complete loss of signal. Absolute intensity repeatability is compared for five lab-built sprayers using pork liver sections. Repeatability ranges from 1 to 224% for individual sprayers and peaks of different spectral abundance. Between sprayers, repeatability is 16%, 9%, 23%, and 34% for high, medium, low, and very low abundance peaks, respectively. To assess the impact of sprayer variability on tissue classification using multivariate statistical tools, nine human colorectal adenocarcinoma sections are analyzed with three lab-built sprayers, and classification accuracy for adenocarcinoma versus the surrounding stroma is assessed. It ranges from 80.7 to 94.5% between the three sprayers and is 86.5% overall. The presented results confirm that the sprayer setup needs to be closely controlled to obtain reliable data, and a new sprayer setup with a fixed solvent capillary geometry should be developed.

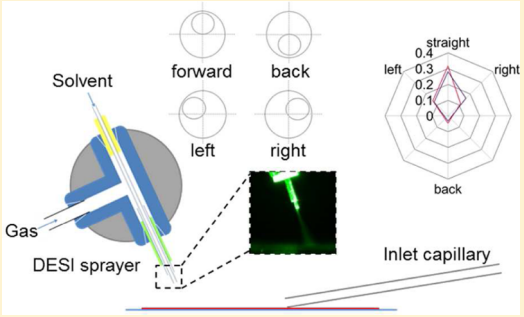

Desorption electrospray ionization (DESI) is an ambient ionization technique first described in 2004.[1] Since then it has rapidly gained popularity and found a large array of applications in environmental chemistry,[2] analysis of pharmaceuticals,[3,4] forensics,[5] food chemistry,[6] and histopathology through mass spectrometric imaging (MSI) of tissues.[7,8] Its minimal sample preparation and ESI-like spectra make DESI a strong contender in the emerging field of molecular pathology.[9] Integration into everyday clinical workflows, however, necessitates a high level of robustness and reproducibility.

In a recent study, the repeatability and reproducibility of DESI were examined by imaging human esophageal cancer tissue sections.[10] Both were calculated as the variation in normalized intensities of 25 lipid species in the mass range of 600 to 900 *m*/*z*. After careful optimization of the setup, a repeatability (same instrument, same operator) of 22% and (different instrument, different operator) of 20% could be achieved. However, a larger scale VAMAS interlaboratory study conducted by the National Physical Laboratory[11] using rhodamine-coated slides and double-sided tape as reference standards, illustrated that DESI-MS can show substantial interlaboratory variability. Day-to-day absolute intensity variability ranged from 14 to 140% for rhodamine B, and spectral constancy, i.e. the relative intensity between different regions of the mass spectrum, ranged from 9 to 83% for the adhesive tape.

A large part of the variability in DESI is thought to be associated with the sprayer. Ionization has been shown to occur through solubilization of ions into a thin film of solvent on the sample surface, charge build-up on the surface, and subsequent formation of secondary droplets through the impact of the primary droplets facilitated by the nebulizing gas.[12,13] The size, velocity, solvent composition, and impact angle of the primary droplets is known to have a significant effect on desorption efficiency.[14] Changes in the nature of the primary electrospray can thus have a direct impact on ionization efficiency.

Received: January 26, 2016
Accepted: March 25, 2016
Published: March 25, 2016

DOI: 10.1021/acs.analchem.6b00345
Anal. Chem. 2016, 88, 4808−4816

The sprayer setup used for the initial DESI experiments was originally developed as a simple sonic spray ionization source,[15] which uses a supersonic nebulizing gas and no high voltage. An identical sprayer equipped with variable spray potential capability was used for subsequent electrosonic spray ionization (ESSI) studies.[16] Since the original publication of DESI, the design of the sprayer has remained virtually unchanged, apart from the commercially available sprayer, which is marketed by Prosolia Inc. The majority of research laboratories still assemble their own DESI sources[11], and most studies on biological tissue have been performed using in-house built sprayers (see Supplementary Table S1[17−28]).

While a number of studies have examined the influence of geometrical (distances, angles) and operating (flow rates, solvent composition, voltages) parameters on DESI performance,[10,19,20,29−31] the impact of the sprayer design itself is poorly understood. Like most relatively new methods, optimization of DESI-MS experiments commonly rely on trial and error and empirical testing of parameters, without an understanding of the underlying mechanisms. In this study, we compare different sprayers built according to the same design in order to identify uncontrolled sprayer parameters and illuminate their effect on the quality and reproducibility of DESI-MS data in a tissue imaging setting.

EXPERIMENTAL SECTION

Materials. Methanol and water were Chromasolv LC-MS grade purchased from Sigma-Aldrich (St. Louis, MO, USA). Dilauroylphosphatidyl choline was obtained from Avanti Polar Lipids (Alabaster, AL, USA). Rhodamine-coated slides were the same as those used in the VAMAS interlaboratory study.[11] Food grade pork liver was bought at a local supermarket (Sainsbury's, London, UK). The liver was cut into small blocks and frozen on dry ice. Human colorectal samples were obtained from patients undergoing colorectal tumor resection at St. Mary's Hospital, Paddington, London as part of a larger study that has received favorable opinion from Cambridge East REC, and patients consented for the study prior to surgical intervention. Both the pork liver and the colorectal samples were sectioned to a thickness of 10 μm using a Microm HM 550 cryomicrotome (Thermo Fisher Scientific Inc., Waltham, MA, USA), and sections were stored at −80 °C until analysis. Sections were removed from the freezer 10 min prior to analysis and allowed to stabilize at room temperature.

DESI Sprayers. Nine DESI sprayers were used in this study: seven conventional in-house built sprayers (denoted Sp 1−7), an altered in-house built sprayer with a fixed capillary (Sp 8), and a commercial sprayer (Sp 9) obtained from Prosolia Inc. (Indianapolis, IN, USA). In-house built sprayers were composed of a 1/16″ stainless steel tee (Swagelok, Kings Langley UK) with a fused silica gas capillary (363 μm outer diameter, 220 μm inner diameter), and a fused silica solvent capillary (150 μm outer diameter, 50 μm inner diameter) (both from SGE analytical, Milton Keynes, UK), held in place using NanoTight sleeves (Idex, Lake Forest, IL, USA). Observation during operation using an optical microscope showed that the initial alignment of the inner capillary was variable between sprayers and often changed once the gas was flowing. We therefore also produced a modified sprayer, where cyanoacrylate glue (Loctite, Henkel, Aachen, Germany) was used to attach the inner solvent capillary to the outer gas capillary, in order ensure consistent alignment (for optical images see Supplementary Figure S1). For the experiments with the fixed sprayer, the sprayer holder of the 2D DESI stage was altered so that the sprayer was fully rotational around the central axis of the sprayer body and different orientations could be studied (see Figure 1).

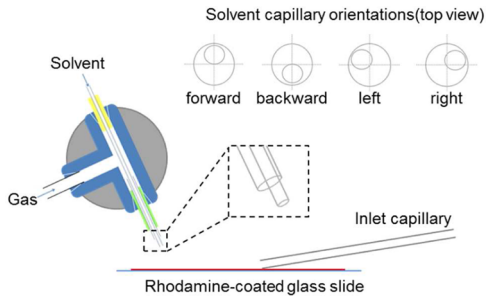

Figure 1. Schematic of the DESI sprayer setup and the geometric parameters examined. Solvent capillary positions are relative to the central axis of the gas capillary as viewed when looking down the sprayer at the sample.

Mass Spectrometry Instrumentation. Comparisons of the in-house built and commercial sprayer on pork liver were performed on an LTQ Orbitrap mass spectrometer (Thermo Fisher Scientific Inc., Waltham, MA, USA), equipped with a 2D sample stage from Prosolia Inc. (Indianapolis, IN, USA) and on a Xevo G2-XS QToF (Waters Corporation, Milford, MA) also equipped with 2D sample stage from Prosolia Inc. (Indianapolis, IN, USA). The latter was used when high scan rates were required. All comparisons of in-house built sprayers were performed on an Exactive Orbitrap mass spectrometer (Thermo Fisher Scientific Inc., Waltham, MA, USA) equipped with a customized 2D sample stage (Newmark Systems Incorporated, Rancho Santa Margarita, CA, USA). Details of instrumental parameters can be found in Table 1.

Optical Equipment. For laser light sheet visualization, a laser sheet was created using a 532 nm continuous wave DPSS laser (CNI Optoelectronics Technology Co., Changchun, China) at 50 mW and a cylindrical lens (Thorlabs Inc., Newton, NJ, USA). The mass spectrometer inlet was emulated with a stainless steel capillary of the same dimensions and a pumping rate to give the same pressure difference, although no voltage was applied to the simulated inlet capillary.

Sprayer tips and rhodamine traces were examined using an optical microscope (Leica, Wetzlar, Germany). Positioning of the fixed sprayer during DESI-MS analysis was monitored using a Dino-Lite digital microscope (Dino-Lite Europe, Naarden, Netherlands).

Data Acquisition and Data Processing. The commercially available sprayer from Prosolia Inc. and the original, in-house built sprayer design (see Figure 2 A and B) were compared for their performance in DESI-MS using a neat lipid standard deposited on a glass slide, rhodamine-coated glass slides, and pork liver sections. Spectral data with individual peak intensities was extracted directly from the instrument software.

To examine the impact of solvent capillary orientation, the sprayer with the fixed solvent capillary was mounted in four different orientations (see schematic Figure 1). The orientations tested were as follows: forward, directed toward the mass spectrometer inlet, which was expected to be the best orientation; 45° left and 45° right, which corresponded with the positions observed for the sprayers used in the sprayer comparison; backward, directed away from the mass

DOI: 10.1021/acs.analchem.6b00345
Anal. Chem. 2016, 88, 4808−4816

Table 1. Experimental Parameters for DESI-MS Analyses

experiment	lab-built vs commercial sprayer experiment 1 - coated rhodamine and pork liver	lab-built vs commercial sprayer experiment 2 - coated rhodamine and pork liver	comparison of 4 lab-built sprayers (pork liver); comparison of 3 lab-built sprayers (colorectal samples)
mass spectrometer	LTQ Orbitrap (Thermo Fisher Scientific Inc., Waltham, MA, USA)	Xevo G2-XS QToF (Waters Corporation, Milford, MA)	Exactive (Thermo Fisher Scientific Inc., Waltham, MA, USA)
mass spectrometric parameters	scan time: 1 s; sampling cone voltage: 50 V; source T: 100 °C; source offset: 80 V	scan time: 0.033 s	scan time: 1 s
2D sample stage	2D sample stage from Prosolia Inc. (Indianapolis, IN, USA)	2D sample stage from Prosolia Inc. (Indianapolis, IN, USA)	custom-built 2D sample stage ((Newmark Systems Incorporated, Rancho Santa Margarita, CA, USA)
solvent composition	methanol/water, 90:10, v:v	methanol/water, 95:5, v:v	methanol/water, 95:5, v:v
solvent flow rate	1.5 μL/min	1.5 μL/min	1.5 μL/min
high voltage	4.5 kV	4.5 kV	4.5 kV
gas inlet pressure	7 bar	7 bar	7 bar
sprayer-to surface distance	1.5 mm	1.5 mm	1.5 mm
sprayer-to-inlet distance	variable; optimal distance for lab-built sprayer: 12 mm; optimal distance for commercial sprayer: 10 mm	8 mm	12 mm
sprayer incidence angle	70°	70°	70°

spectrometer inlet. All orientations were tested on the same three pork liver sections with two line scans per orientation and scan direction. For repeatability measurements, the forward orientation and a left-to-right scanning pattern (standard operating conditions) were used, and three line scans were acquired per section.

The resulting raw files were cropped using the recalibrate offline tool in Excalibur (v2.2 SP1.48; Thermo Fisher Scientific Inc.) and converted into mzML files using the ProteoWizard msConvertGUI (Vanderbilt University, Nashville, TN, USA) and then into an imzML image file using imzML Converter v1.3.[32] The imzML file was imported into MatLab (R2014a; MathWorks, Natick, MA, USA) environment using an in-house written function. For the investigation of the impact of sprayer orientation on intensity, the mean spectrum for the standard orientation was calculated, and peaks were ranked with regard to their intensities. The top 5 fatty acid-related ions and top 10 phospholipid ions were selected. Identification was performed using the Lipid Maps database (http://www.lipidmaps.org/) with an m/z tolerance of 5 ppm for accurate mass data. The presence and correct abundance of the ^{13}C isotope peak was also verified. The list of selected peaks can be found in Supplementary Table S2.

For the first sprayer comparison experiment, four in-house built sprayers (Sp1−4) were compared using 12 adjacent sections from the same pork liver sample analyzed in randomized order in negative ion mode. Three sections were analyzed with each sprayer. Five lines were scanned across each section at a speed of 200 μm/s and with a line-to-line distance of 500 μm to avoid overlap. For principal component analysis (PCA), the data were preprocessed including peak detection, alignment, and quantile normalization[33] using the mean spectrum, binning to m/z-dependent 10 ppm bins, and log transformation for variance stabilization[34] using the Matlab-based toolbox.[34] Multivariate analyses and cross-validations were performed using the same toolbox. The full acquired m/z range from 150 to 1500 and two smaller mass ranges from 150 to 350 m/z and from 600 to 1000 m/z were analyzed. The lower m/z range in DESI-MS is dominated by fatty acids, both from the tissue and from contamination of the solvent, as well as other solvent-related peaks. It is therefore subject to higher variability as it is strongly impacted by small changes in solvent quality or composition. The m/z region from 600 to 1000 contains phospholipids and triglycerides, which are commonly used for tissue identification and classification.

For repeatability measurements, the mean spectrum across all four conventional sprayers was calculated, and the region from 50 to 950 m/z was segmented into 50 m/z sections. From each section, one high intensity peak, one midintensity peak, and one low intensity peak relative to the highest peak in that region were selected and tentatively assigned an identity using the Lipid Maps database (http://www.lipidmaps.org/) and the Metlin Scripps database (https://metlin.scripps.edu/index.php). A summary can be found in Supplementary Table S3. Relative standard deviations (RSDs) of absolute intensity were calculated for all selected peaks. Peaks were grouped according to their relative intensity in the overall mean spectrum, with >40% being classed as high relative abundance (5 peaks), 3 to 40% medium relative abundance (10 peaks), 1 to 3% low relative abundance (8 peaks), and <1% very low relative abundance (25 peaks), and RSDs were averaged for each group. The same peak list was used for the fixed capillary sprayer, though not all peaks could be detected.

To assess the relative magnitude of instrument-related and biological variability of the data (adenocarcinoma versus adjacent stroma), three in-house built sprayers (Sp5−7) were used. Nine adjacent sections from the same sample of human colorectal tissue, containing regions of adenocarcinoma and neighboring healthy tissue, were analyzed in negative ion mode. Three sections were imaged with each sprayer, using a pixel size of 100 × 100 μm. Sections were then H&E stained, and approximately 100 to 150 pixels per section and tissue type were annotated by a histopathologist. The raw data was converted into imzML format using imzML Converter v1.1.4.5i beta[35] and processed as for the PCA above.

RESULTS AND DISCUSSION

Comparison of the Commercial and the in-House Built Sprayer. The performance of an in-house built sprayer (Sp 7) and a commercially available sprayer from Prosolia Inc. were initially compared using a neat lipid standard deposited on a glass slides. Similar performance was exhibited with regard to

DOI: 10.1021/acs.analchem.6b00345
Anal. Chem. 2016, 88, 4808−4816

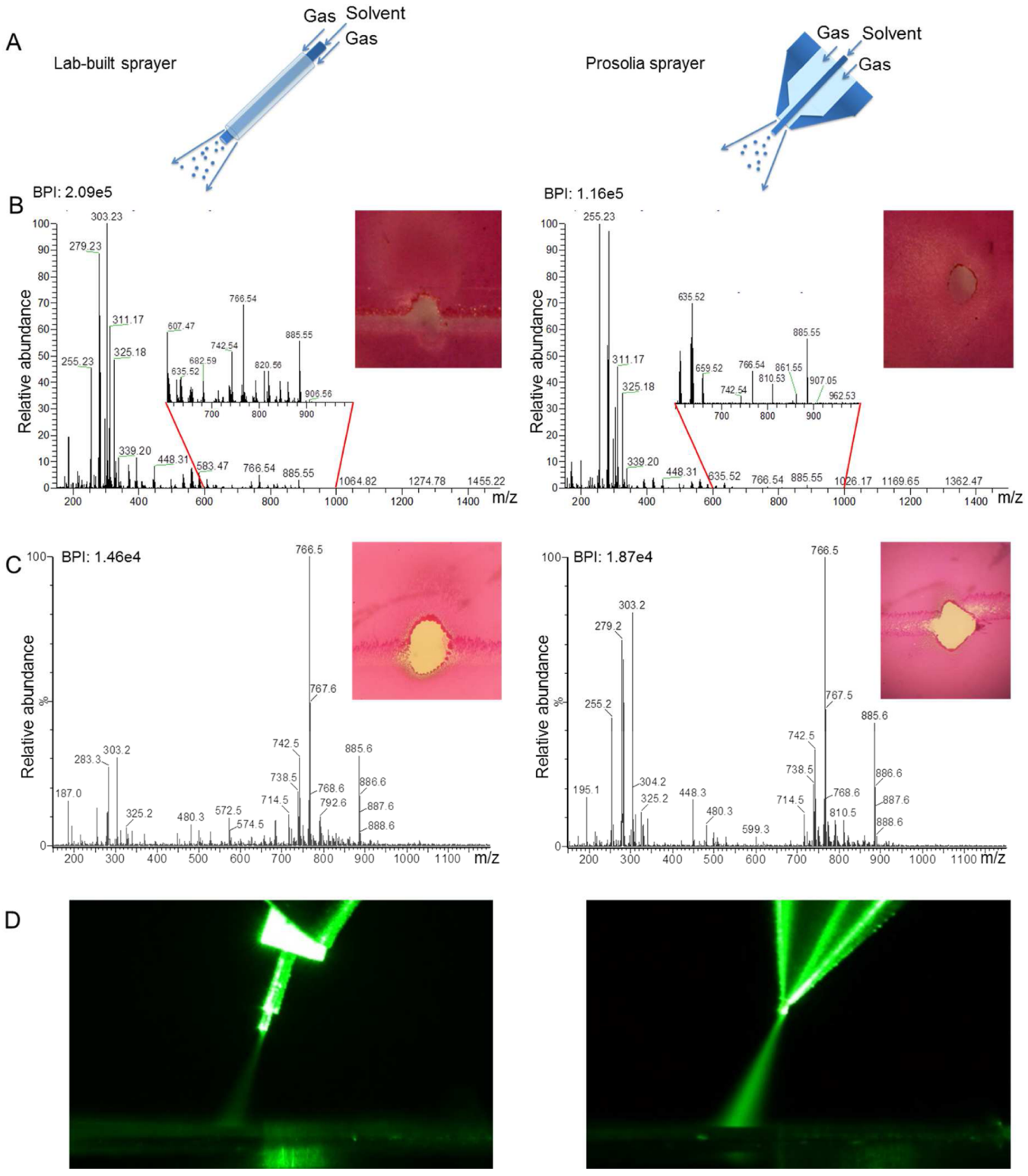

Figure 2. Comparison of the in-house built and commercial DESI sprayers. A: schematic diagram of the in-house built sprayer, consisting of two fused silica capillaries and the commercial sprayer, consisting of a stainless steel gas nozzle and a fused silica solvent capillary; B,C: Negative ion spectra from pork liver and corresponding desorption areas for 30 s dwell time on coated rhodamine for the in-house built and commercial sprayer for the first and second experiment; BPI: base peak intensity; D: laser sheet visualization of the electrospray emitted by the in-house built and commercial sprayers, respectively.

spectral intensity and composition (see Supplementary Figure S2). However, their performance for analysis of a pork liver section was markedly different as shown in Figure 2 B. The in-house sprayer provided mass spectra with a high abundance of phospholipids in contrast to the commercial sprayer, which showed very low abundance of phospholipids and tissue-related fatty acids (e.g., m/z 303.23 - fatty acid 20:5). Surprisingly, subsequent repeat experiments with the commercial sprayer

DOI: 10.1021/acs.analchem.6b00345
Anal. Chem. 2016, 88, 4808−4816

resulted in similar spectra to the in-house sprayers, as shown in Figure 2 C. We later propose a possible explanation for this extreme variability.

In order to deconstruct the sources of variance, the desorption rate and desorption footprint of both sprayers were studied on deposited rhodamine films as done previously by Green et al.[31] and Gurdak et al.[11] The desorption rate was measured as time dependence of spectral intensity and was found to be similar for both sprayers (see Supplementary Figure S3). However, the desorption footprint left behind on the rhodamine surface was markedly different. The footprint of the in-house built sprayer showed a clear directionality, with rhodamine being redeposited on the upper edge facing the mass spectrometer inlet capillary and a diffuse ring from the outer droplet of the electrospray forming mainly in that same direction, similar to that described by Green et al.[31] The footprint of the commercial sprayer showed a homogeneous edge all around with a diffuse ring in all directions with only a slight sideways bias, which suggests a less directional and less focused electrospray (see Figure 2 B). Such differences could potentially have an impact on desorption efficiency of molecules from tissue and spatial resolution during DESI-MS imaging.

Laser light sheet visualization was used to investigate the primary electrospray of each sprayer, and images are shown in Figure 2 D. It was observed that the droplet emission from the inner capillary is similar for both, with the emission concentrated toward the edge furthest from the spectrometer inlet (or, in this case, the simulated inlet) and closer to the surface (right edge in Figure 2 B). For the in-house sprayer, the inner capillary is set in the forward direction, which is presumably enhanced by the gas flow. Since the capillary is asymmetrically aligned, there is a higher gas flow along the far edge. This has the effect of pushing in, or focusing, the edge of the emission cone. In contrast, the commercial source has a smaller diameter nebulizing gas exit orifice and has a more symmetric alignment and consequently a more symmetric emission cone but also a broader spray cone. The experiments were performed at relatively low solvent flow rate (1.5 μL/min) and high gas pressure (7 bar). The spreading effect is likely to be enhanced if the solvent flow rate is increased or the gas pressure is lowered.

Examination of the Impact of Sprayer Capillary Orientation on Tissue Complex Lipid Signal. In order to study the effect of capillary orientation asymmetry on the lipid spectra from the pork liver sections, an in-house sprayer with a fixed solvent capillary geometry (as described above) was tested in four different orientations (see Figure 1). The obstructed gas flow was found to reduce the total ion intensity to around 50% to 65% of the intensity provided by the unmodified sprayer. The phenomenon was associated with the change in the gas flow pattern introduced by fixing the solvent capillary to the gas capillary. The mounting point blocks the gas flow, so that the electrospray is no longer surrounded by the nebulizing gas. This presumably leads to a formation of larger, slower droplets and lower desolvation and desorption in that part of the primary electrospray, as observed by Venter et al. for low nebulizing gas pressures.[13]

The summed signal intensities for the top 5 fatty acid peaks and top 10 phospholipid peaks, normalized to the forward orientation, are shown on the spider plot diagram in Figure 3, with axes set at the sprayer rotation angles. Absolute values can be found in Supplementary Figure S4. The results of this study

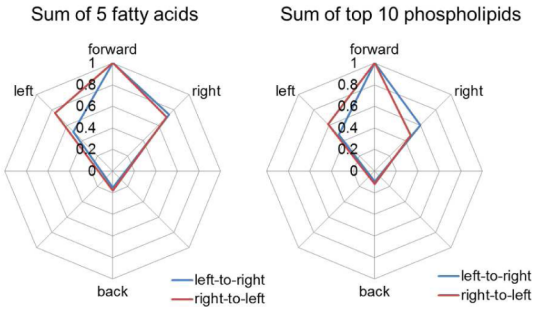

Figure 3. Relative intensities for four orientations of the fixed sprayer and two different scan directions. All intensities are normalized to the TIC of the full m/z range of the sprayer when oriented forward and scanning left-to-right, as these are the standard conditions used for imaging. For a schematic of the sprayer orientation see Figure 1.

are striking with an extreme difference between the forward and backward orientations. Both the fatty acid and the phospholipid signal is optimal in the forward direction and almost zero in the backward direction. It would therefore appear that any asymmetric design in the forward orientation is most effective. Any design where the capillary orientation is easily shifted could result in radical changes to the lipid spectrum by small deviations of the capillary in the forward or backward direction, with the latter decreasing the signal dramatically. We believe that this is the reason why the commercial source exhibited high variability in performance, as the large inner diameter of the gas nozzle means that the capillary is considerably easier to move aside from its symmetrical starting position. Consequently, it is subject to variations in capillary orientation, which can have a deleterious effect on the lipid signal.

A correlation was also found between the sprayer orientation, the scanning direction and intensity, with signal intensity. According to Pasilis et al., when analyzing drug compounds, highest intensity could be achieved by moving the sample toward the jet emitted by the DESI sprayer.[36] This was found to hold true not only for the left and right orientations with left-to-right and right-to-left scanning patterns but also for top-to-bottom and bottom-to-top scanning when using the forward pointing orientation (see Supplementary Figure S4). However, the differences were not always significant compared to the standard deviation of measurements across sections.

Comparison of in-House Built Sprayers on Pork Liver. To study the effect of unmounting and remounting a sprayer on the desorption footprint, Sp2 was tested multiple times with deinstallation and reinstallation between measurements on the rhodamine sample. These results are summarized in the Supplementary Table S6 and show that solvent capillary positioning can change between measurements, which leads to changes in the size and shape of the desorption area. This observation further underpins the conclusion that this parameter needs to be closely controlled, either by fixing or by monitoring, during the DESI experiment.

A comparison of four in-house built sprayers, Sp1−4, on pork liver was performed to examine the variability of DESI-MS for tissue analysis, both in terms of absolute intensity using selected ions and pattern level reproducibility using principal component analysis (PCA). Absolute intensity repeatability was also compared to the results for the fixed capillary sprayer (see Table 2).

Line-to-line variability with the same sprayer on the same section (five lines per section) was found to be good but varied

DOI: 10.1021/acs.analchem.6b00345
Anal. Chem. 2016, 88, 4808−4816

Table 2. Absolute Intensity Variability for DESI-MSI of Pork Liver Sections for the Fixed Capillary Sprayers and Conventional Lab-Built Sprayers Sp1−4[a]

	HA	MA	LA	VLA
Fixed Capillary Sprayer				
Line-to-Line Variability (Within Sections)				
mean RSD	38%	30%	37%	28%
min RSD	7%	3%	4%	10%
max RSD	78%	69%	81%	56%
Section-to-Section Variability				
RSD	25%	24%	24%	27%
Line-to-Line Variability (Across Sections)				
	43%	43%	49%	56%
Conventional Sprayers Sp1−4				
	HA	MA	LA	VLA
Line-to-Line Variability (Same Sprayer, Same Section)				
mean RSD	6%	7%	11%	49%
min RSD	1%	2%	3%	3%
max RSD	22%	45%	27%	224%
Section-to-Section Variability (Same Sprayer)				
mean RSD	11%	8%	9%	28%
min RSD	1%	2%	1%	1%
max RSD	31%	56%	35%	173%
Line-to-Line Variability (Across Sprayers)				
RSD	19%	13%	25%	71%
Section-to-Section Variability (Across Sprayers)				
RSD	18%	11%	23%	51%
Sprayer-to-Sprayer				
RSD	16%	9%	23%	34%

[a]Relative standard deviations (RSD) for selected peaks of high (HA), medium (MA), low (LA), and very low (VLA) relative abundance in the mean spectrum.

widely between sprayers, with the best sprayer achieving RSDs of 1 to 3% across the intensity range and the worst 45% for medium abundance peaks and 224% for very low abundance peaks. Line-to-line variability across all sprayers was 25% or less for all but very low abundance peaks. Section-to-section variability differed greatly between sprayers, ranging from 1% for some peaks to over 50% for others. Section-to-section repeatability across sprayers ranged from 11 to 51%. Repeatability was best for medium abundance peaks and, as would be expected, worst for lowest abundance peaks. Overall, these results support the hypothesis that DESI performance can vary considerably between sprayers, making the sprayer an important source of variability. The repeatability for the fixed capillary sprayer, surprisingly, was found to be poorer than that of the best performing conventional sprayer and also the mean of Sp1−4. We hypothesize that although the solvent capillary position can have a major impact on signal intensity, fixing the solvent capillary to the gas capillary introduces further turbulence in the proximity of the spray tip, which contributes to the poor reproducibility of results. The application of glue is a rather crude method used here to simply test the effect of asymmetry. Of course, a more carefully engineered source is required that does not disrupt the gas flow.

Although the most abundant peaks were the same for all four sprayers, PCA showed that sprayers can be separated based on their overall spectral patterns (see Supplementary Figure S5). The respective loadings plots (see Supplementary Figure S6) show that this is due mainly to the ratio of lower to higher m/z peaks and the relative abundance of phospholipids below 800 m/z (primarily phosphatidyl ethanolamines) and above 800 m/z (primarily phosphatidyl inositols and phosphatidyl serines).

Since the orientation of the inner capillary can have a significant effect on both absolute and relative intensities, all sprayers were examined under an optical microscope to measure the protrusion of the solvent capillary from the gas capillary and its orientation within the gas capillary relative to the central axis of the gas capillary (see schematic in Figure 1). The shape and size of the desorption footprint for each sprayer were evaluated using rhodamine-coated glass slides. Results of these experiments are summarized in the Supporting Information in Tables S4−S6. However, no direct correlation of solvent capillary protrusion and positioning and the resulting desorption footprint with signal intensity or repeatability could be found.

Comparison of Sprayers on Colorectal Tissue. To evaluate the variability of DESI in the context of tissue imaging, its impact on tissue differentiation using multivariate tools was tested.

To do this, a set of nine colorectal samples containing regions of adenocarcinoma and neighboring stroma was analyzed using three of the in-house built sprayers, Sp 5−7. Ion images were aligned with optical images of the same section after H&E staining, and three regions of 100 to 150 pixels per tissue type and sample were annotated by a histopathology professional. Example images can be found in Figure 4. The

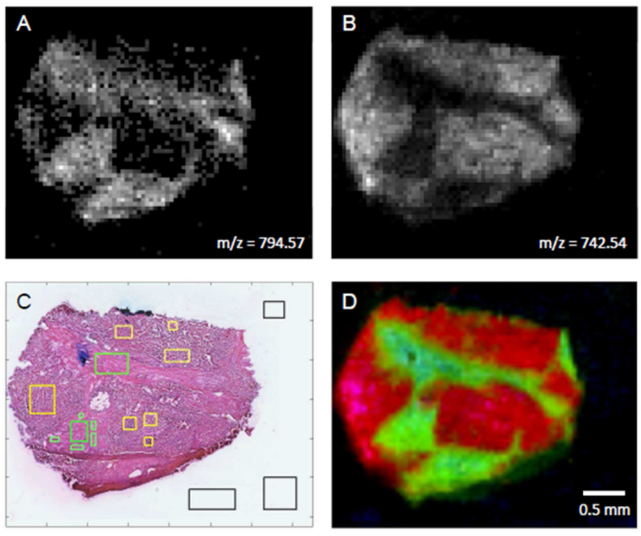

Figure 4. Single ion images, annotated optical image, and RGB image 3 PCs for one of the human colorectal adenocarcinoma samples analyzed. A,B: Single ion images for m/z = 794.570 and m/z = 742.539, respectively; C: optical image of the hematoxylin and eosin stained section with histological annotations - yellow: tumor, green - stroma, black - background; D: RGB image for principal components 1, 2, and 5.

pixels from the annotated regions were combined for each sprayer and tissue type and submitted to multivariate analysis, as this is a commonly applied tool for tissue classification using mass spectrometry imaging.[34] Principal component analysis (PCA) was performed as described earlier, and the scores plots are shown in Figure 5, with each data point representing one pixel. Corresponding loadings can be found in Supplementary Figure S7. In Figure 5 A the data points are colored according to tissue type, and in Figure 5 B they are colored by sprayer. It

DOI: 10.1021/acs.analchem.6b00345
Anal. Chem. 2016, 88, 4808−4816

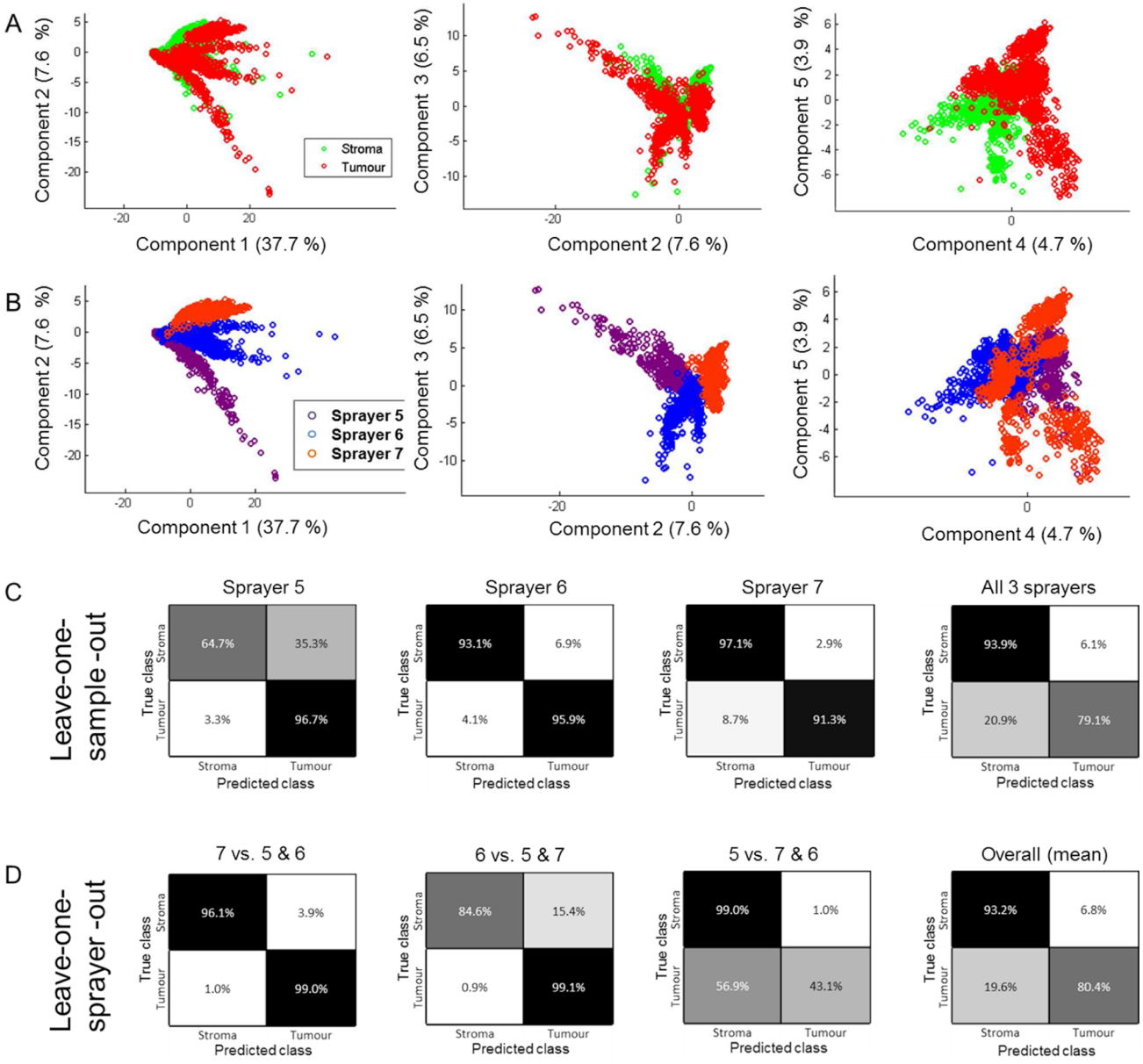

Figure 5. PCA and cross-validations for histologically annotated pixels from colorectal samples analyzed with three different DESI sprayers. A: PCA with data points colored according to tissue type; B: PCA with pixels colored according to sprayer; C: leave-one-sample-out cross-validation for each sprayer individually and all sprayers combined; D: leave-one-sprayer-out cross-validation.

is quite clear that separation of the tumor and stroma is only, to some extent, achieved in the fourth and fifth principal components, corresponding to 4.7% and 3.9% of the variance, respectively. By contrast, principal component 2 clearly separates out the three sprayers capturing 7.6% of the variance. Therefore, with these sprayers, the variance from the DESI source itself is >1.8 times the variance originating from the tissue type. This clearly shows that for reliable application in clinical diagnostics the repeatability needs to be significantly improved.

To evaluate the impact of sprayers of classification accuracy of tissue types, PCA-LDA (linear discriminant analysis) was used to construct a classification model. Classification of tissue pixels as tumor and stroma was assessed using leave-one-sample-out cross-validation for each sprayer individually and for all samples put together and using leave-one-sprayer-out cross-validation, i.e. using the data from two sprayers as a training set and that from the third as a test set. While overall classification accuracies of more than 90% were achieved with sprayers 6 and 7, the accuracy with sprayer 5 was only 80%. The leave-one-sprayer-out cross-validation using the samples from sprayer 5 as a test set also showed the lowest classification accuracy at only 71%. This suggests that the data from sprayer 5 were markedly different from those acquired with the other two sprayers.

Overall, this comparison shows that the sprayer used can have a substantial impact on tissue classification accuracy. Although all three sprayers were optimized using pork liver before the analysis and the spectra from sprayer 5 were judged to be acceptable, the data quality was inferior to that of the other sprayers. This emphasizes the need for an improved sprayer design and a standardized tool (and reference material) for sprayer evaluation. In a clinical setting, where samples would be classified using a central database, potentially acquired

DOI: 10.1021/acs.analchem.6b00345
Anal. Chem. 2016, 88, 4808−4816

using different sprayer, both intersprayer reproducibility and sprayer stability over time would be crucial.

CONCLUSIONS

This study illustrates that the sprayer is a major source of variability in DESI-MS analysis of biological tissues and that it is important to use an appropriate sprayer design for biological tissue imaging.

Based on our results, variations in absolute and relative intensities can be caused by changes in the orientation of the solvent capillary within the gas capillary. Orientation of the solvent capillary toward the inlet of the mass spectrometer (forward) can improve the signal, while orientation away from the mass spectrometer inlet (backward) can lead to an almost complete loss of signal. Capillary positions vary between sprayers and can change when a gas flow is applied, which means that spectral and intensity reproducibility varies between sprayers.

In our study using pork liver, absolute intensity repeatability varied from 1 to 224% for different sprayers and peaks of different abundance. Analysis of a small clinical sample set showed that variability between sprayers was 1.8 larger than spectral variability between tissue types, which can impede classification accuracy. In studies using multivariate tools to classify samples based on small changes in the spectral profile, the sprayer geometry therefore needs to be closely controlled, in order to provide reliable mass spectrometry data.

We therefore propose that the position of the solvent capillary needs to be fixed within the gas capillary, in order to obtain reproducible sprayer geometry. However, fixing the solvent capillary directly to the gas capillary was shown to impact negatively on ionization, presumably because the flow path of the nebulizing gas is altered and droplet formation was impeded. The solvent capillary should therefore be fixed without obstructing the nebulizing gas flow, with a forward orientation promising a high and less variable lipid signal.

ASSOCIATED CONTENT

Supporting Information

The Supporting Information is available free of charge on the ACS Publications website at DOI: 10.1021/acs.analchem.6b00345.

Additional information, figures, and tables as described in the text (PDF)

AUTHOR INFORMATION

Corresponding Authors

*J.B. Josephine.bunch@npl.co.uk.
*Z.T. z.takats@imperial.ac.uk.
*I.S.G. Ian.gilmore@npl.co.uk. Fax: 020 86140573.

Present Address

[‖]Waters Corporation, Altrincham Rd, Wilmslow, Cheshire East SK9 4AX, United Kingdom.

Notes

The authors declare no competing financial interest.

ACKNOWLEDGMENTS

This research was funded by NPL Strategic Research Programme 116301 and supported by the European Union Seventh Frame-work Programme (FP7/2007-2013 under Grant Agreement No. 297499/305940), the European Research Council Consolidator Grant, Grant Agreement No. 617896, and the National Institute for Health Research (NIHR) Biomedical Research Centre based at Imperial College Healthcare NHS Trust and Imperial College London. The views expressed are those of the author(s) and not necessarily those of the NHS, the NIHR, or the Department of Health.

REFERENCES

(1) Takats, Z.; Wiseman, J. M.; Gologan, B.; Cooks, R. G. *Science* **2004**, *306*, 471−473.
(2) Strittmatter, N.; During, R. A.; Takats, Z. *Analyst* **2012**, *137*, 4037−4044.
(3) Kauppila, T. J.; Wiseman, J. M.; Ketola, R. A.; Kotiaho, T.; Cooks, R. G.; Kostiainen, R. *Rapid Commun. Mass Spectrom.* **2006**, *20*, 387−392.
(4) Chen, H. W.; Talaty, N. N.; Takats, Z.; Cooks, R. G. *Anal. Chem.* **2005**, *77*, 6915−6927.
(5) Takats, Z.; Cotte-Rodriguez, I.; Talaty, N.; Chen, H. W.; Cooks, R. G. *Chem. Commun.* **2005**, 1950−1952.
(6) Berchtold, C.; Muller, V.; Meier, L.; Schmid, S.; Zenobi, R. *J. Mass Spectrom.* **2013**, *48*, 587−593.
(7) Wiseman, J. M.; Ifa, D. R.; Song, Q.; Cooks, R. G. *Angew. Chem., Int. Ed.* **2006**, *45*, 7188−7192.
(8) Wiseman, J. M.; Ifa, D. R.; Venter, A.; Cooks, R. G. *Nat. Protoc.* **2008**, *3*, 517−524.
(9) Pol, J.; Strohalm, M.; Havlicek, V.; Volny, M. *Histochem. Cell Biol.* **2010**, *134*, 423−443.
(10) Abbassi-Ghadi, N.; Jones, E. A.; Veselkov, K. A.; Huang, J. Z.; Kumar, S.; Strittmatter, N.; Golf, O.; Kudo, H.; Goldin, R. D.; Hanna, G. B.; Takats, Z. *Anal. Methods* **2015**, *7*, 71−80.
(11) Gurdak, E.; Green, F. M.; Rakowska, P. D.; Seah, M. P.; Salter, T. L.; Gilmore, I. S. *Anal. Chem.* **2014**, *86*, 9603−9611.
(12) Costa, A. B.; Cooks, R. G. *Chem. Phys. Lett.* **2008**, *464*, 1−8.
(13) Venter, A.; Sojka, P. E.; Cooks, R. G. *Anal. Chem.* **2006**, *78*, 8549−8555.
(14) Green, F. M.; Salter, T. L.; Gilmore, I. S.; Stokes, P.; O'Connor, G. *Analyst* **2010**, *135*, 731−737.
(15) Takats, Z.; Nanita, S. C.; Cooks, R. G.; Schlosser, G.; Vekey, K. *Anal. Chem.* **2003**, *75*, 1514−1523.
(16) Takats, Z.; Wiseman, J. M.; Gologan, B.; Cooks, R. G. *Anal. Chem.* **2004**, *76*, 4050−4058.
(17) Agar, N. Y. R.; Golby, A. J.; Ligon, K. L.; Norton, I.; Mohan, V.; Wiseman, J. M.; Tannenbaum, A.; Jolesz, F. A. *Neurosurgery* **2011**, *68*, 280−290.
(18) Bodzon-Kulakowska, A.; Cichon, T.; Golec, A.; Drabik, A.; Ner, J.; Suder, P. *Cytotechnology* **2015**, *67*, 1085−1091.
(19) Bodzon-Kulakowska, A.; Drabik, A.; Ner, J.; Kotlinska, J. H.; Suder, P. *Rapid Commun. Mass Spectrom.* **2014**, *28*, 1−9.
(20) Campbell, D. I.; Ferreira, C. R.; Eberlin, L. S.; Cooks, R. G. *Anal. Bioanal. Chem.* **2012**, *404*, 389−398.
(21) Dill, A. L.; Ifa, D. R.; Manicke, N. E.; Costa, A. B.; Ramos-Vara, J. A.; Knapp, D. W.; Cooks, R. G. *Anal. Chem.* **2009**, *81*, 8758−8764.
(22) Eberlin, L. S.; Ifa, D. R.; Wu, C.; Cooks, R. G. *Angew. Chem., Int. Ed.* **2010**, *49*, 873−876.
(23) Eberlin, L. S.; Ferreira, C. R.; Dill, A. L.; Ifa, D. R.; Cheng, L.; Cooks, R. G. *ChemBioChem* **2011**, *12*, 2129−2132.
(24) Eberlin, L. S.; Tibshirani, R. J.; Zhang, J.; Longacre, T. A.; Berry, G. J.; Bingham, D. B.; Norton, J. A.; Zare, R. N.; Poultsides, G. A. *Proc. Natl. Acad. Sci. U. S. A.* **2014**, *111*, 2436−2441.
(25) Ferreira, C. R.; Pirro, V.; Eberlin, L. S.; Hallett, J. E.; Cooks, R. G. *Anal. Bioanal. Chem.* **2012**, *404*, 2915−2926.
(26) Gerbig, S.; Golf, O.; Balog, J.; Denes, J.; Baranyai, Z.; Zarand, A.; Raso, E.; Timar, J.; Takats, Z. *Anal. Bioanal. Chem.* **2012**, *403*, 2315−2325.
(27) Meetani, M. A.; Shin, Y. S.; Zhang, S. F.; Mayer, R.; Basile, F. *J. Mass Spectrom.* **2007**, *42*, 1186−1193.

DOI: 10.1021/acs.analchem.6b00345
Anal. Chem. 2016, 88, 4808−4816

(28) Kerian, K. S.; Jarmusch, A. K.; Pirro, V.; Koch, M. O.; Masterson, T. A.; Cheng, L.; Cooks, R. G. *Analyst* **2015**, *140*, 1090−1098.
(29) Kertesz, V.; van Berkel, G. J. *Anal. Chem.* **2008**, *80*, 1027−1032.
(30) Kertesz, V.; Van Berkel, G. J. *Rapid Commun. Mass Spectrom.* **2008**, *22*, 2639−2644.
(31) Green, F. M.; Stokes, P.; Hopley, C.; Seah, M. P.; Gilmore, I. S.; O'Connor, G. *Anal. Chem.* **2009**, *81*, 2286−2293.
(32) Race, A. M.; Styles, I. B.; Bunch, J. *J. Proteomics* **2012**, *75*, 5111−5112.
(33) Veselkov, K. A.; Vingara, L. K.; Masson, P.; Robinette, S. L.; Want, E.; Li, J. V.; Barton, R. H.; Boursier-Neyret, C.; Walther, B.; Ebbels, T. M.; Pelczer, I.; Holmes, E.; Lindon, J. C.; Nicholson, J. K. *Anal. Chem.* **2011**, *83*, 5864−5872.
(34) Veselkov, K. A.; Mirnezami, R.; Strittmatter, N.; Goldin, R. D.; Kinross, J.; Speller, A. V. M; Abramov, T.; Jones, E. A.; Darzi, A.; Holmes, E.; Nicholson, J. K.; Takats, Z. *Proc. Natl. Acad. Sci. U. S. A.* **2014**, *111*, 1216−1221.
(35) Schramm, T.; Hester, A.; Klinkert, I.; Both, J. P.; Heeren, R. M.; Brunelle, A.; Laprevote, O.; Desbenoit, N.; Robbe, M. F.; Stoeckli, M.; Spengler, B.; Rompp, A. *J. Proteomics* **2012**, *75*, 5106−5110.
(36) Pasilis, S. P.; Kertesz, V.; Van Berkel, G. J. *Anal. Chem.* **2007**, *79*, 5956−5962.

DOI: 10.1021/acs.analchem.6b00345
Anal. Chem. 2016, 88, 4808−4816

Bioconjugate Chemistry

Article

pubs.acs.org/bc

Influence of Polymer Size on Uptake and Cytotoxicity of Doxorubicin-Loaded DNA–PEG Conjugates

Laura Purdie, Cameron Alexander, Sebastian G. Spain,*,† and Johannes P. Magnusson*

School of Pharmacy, University of Nottingham, University Park, Nottingham, United Kingdom NG7 2RD

Supporting Information

ABSTRACT: Intercalation of drugs into assembled DNA systems offers versatile new mechanisms for controlled drug delivery. However, current systems are becoming increasingly complex, reducing the practicality of large scale production. Here, we demonstrate a more pragmatic approach where a short DNA sequence was modified with poly(ethylene glycol) (PEG) of various lengths at both 5′-termini to provide serum stability and compatibility. The anticancer drug doxorubicin was physically loaded into two designed binding sites on the dsODN. The polymer conjugation improved the stability of the dsODN toward serum nucleases while its doxorubicin binding affinity was unaffected by the presence of the polymers. We examined the effects of polymer size on the dsODN carrier characteristics and studied the resulting DOX@DNA–PEG systems with respect to cytotoxicity, cellular uptake, and localization in A549 and MCF7 cell lines. For the A549 cell line the DOX@DNA-PEG1900 exhibited the best dose response of the conjugates while DOX@DNA-PEG550 was the least potent. In MCF-7, a more doxorubicin sensitive cell line, all conjugates exhibited similar dose response to that of the free drug. Confocal microscopy analysis of doxorubicin localization shows that conjugates successfully deliver doxorubicin to the cell nucleus and also the lysosome. These data provide a valuable insight into the complexities of designing an oligonucleotide based drug delivery system and highlight some practical issues that need to be considered when doing so.

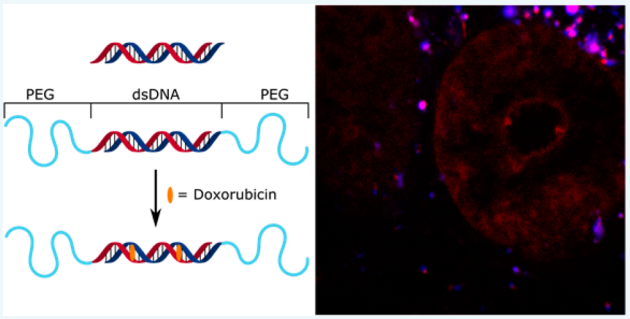

INTRODUCTION

In recent decades DNA-based materials have revolutionized the scope and complexity of nanomaterials that can be produced. Exploiting the specificity of Watson–Crick base pairing has produced complex dynamic structures such as molecular computers,[1] motors,[2] nanoreactors,[3] as well as sensors and diagnostics.[4−10] More recently, the ability of certain drugs to intercalate within the DNA double helix and form strong physical complexes has been utilized to form physical prodrugs for cytotoxics. Farokhzad et al. first demonstrated that a DNA aptamer could be loaded with doxorubicin (DOX), allowing targeted uptake into cells presenting the aptamer target.[11] This was extended to aptamer-targeted quantum dots[12] and polymer particles[13] allowing the addition of detection and delivery. Dabrowiak et al. have demonstrated several systems based upon gold nanoparticles (AuNPs) coated with DNA. Both DOX and actinomycin D (ActD) were intercalated into the helix, and targeting was achieved by introduction of folic acid onto one of the DNA strands.[14−16] "DNA origami" has also been used for intercalated delivery. Ahn et al. have demonstrated that a DNA tetrahedron, formed by annealing 4 strands, can be used to deliver DOX to cells, overcoming resistance in a multidrug resistant cell line.[17] Leong et al. have used similar tetrahedra, decorated with AuNPs and loaded with ActD, for theranostic delivery to bacteria.[18] Högberg et al. have taken the origami approach a step further and designed large DNA bundles that can twist upon intercalation of DOX. Drug release kinetics, and thus cytotoxicity, can be modulated by varying the induced twist.[19]

Although these systems have demonstrated the feasibility of using DNA intercalation as a drug delivery mechanism, problems still remain. First, none have the shielding components required to prevent degradation and reduce potential immunogenic interactions in vivo, although some of the non-natural DNA conformations have been shown to be resistant to degradation.[20] Second, the systems being developed are displaying increasing complexity, in one case requiring over 200 short DNA "staples" to hold the drug delivery system together, where each has to be synthesized and purified. PEG polymers have been extensively used to improve the pharmacokinetics of biologics.[21] Despite recent concerns about potential immunogenicity of PEG,[22] this remains controversial,[23] and they are still the polymer of choice for in vivo applications.

Herein we describe a more pragmatic approach to intercalating drug delivery. A simple, short, double-stranded DNA was assembled from complementary oligonucleotides, modified with poly(ethylene glycol) (PEG) at both 5′

Received: February 16, 2016
Revised: April 10, 2016
Published: April 14, 2016

DOI: 10.1021/acs.bioconjchem.6b00085
Bioconjugate Chem. 2016, 27, 1244−1252

positions. The effects of PEG polymer size on the ODN carrier delivery characteristics were examined. DOX was physically conjugated by intercalation into a pair of binding sites designed into the oligonucleotide sequence forming the DOX@DNA–PEG delivery system (Figure 1).

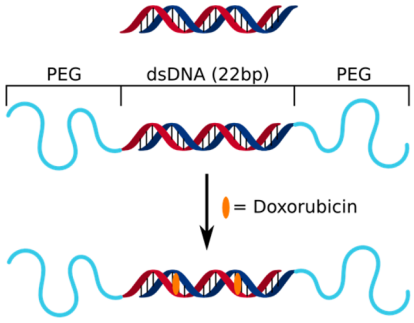

Figure 1. Schematic representation of intercalating DOX@DNA delivery system described herein.

RESULTS AND DISCUSSION

Synthesis and Analysis of PEG–DNA Conjugates. PEG–DNA conjugates were synthesized in a similar manner to that described previously.[10] Polyethylene glycol monomethyl ether (mPEG, M_n 550, 1900, and 5000 Da) was activated with *N,N*-disuccinimidyl carbonate to form amino-reactive mPEG-succinimidyl carbonates (PEG-SC). The PEG-SCs were subsequently conjugated to 5′-aminohexyl modified single-stranded oligonucleotides to form a small library of PEG–ssDNA conjugates with three different PEG lengths, and consisting of two complementary DNA sequences (Oligo A: TAA CAG GAT TAG CAG AGC GAG G and Oligo B: CCT CGC TCT GCT AAT CCT GTT A). Conjugates were purified by semipreparative HPLC with typical isolated yields of 50–80% independent of mPEG length. HPLC and PAGE analysis (Figure 2A and S1) confirmed no residual unmodified oligonucleotides in any of the conjugate samples. Molecular masses from MALDI-ToF mass spectrometry were generally in good agreement with theoretical values; however, slight deviation from theoretical values was observed. This is not unexpected as mPEG is a disperse polymer and some molecular weight enrichment is likely to occur during HPLC purification, i.e., polymer fractionation.

Lyophilized conjugates were dissolved in DNase-free annealing buffer and hybridized with the appropriate complementary strands (e.g., PEG550-A and PEG550-B) to form dsDNA conjugates with mPEG chains at both 5′-termini. Consequently, a series of three PEG DNA conjugates was produced, DNA–PEG550, DNA–PEG1900, and DNA–PEG5K, as well as the unPEGylated, "unmodified" DNA. After annealing, the conjugates were analyzed by PAGE to ensure that no single-stranded ODNs were remaining after the annealing (Figure 2A and Figure S1A). PAGE analysis revealed that the PEG-ODNs had successfully formed the double-stranded structures. Weak high molecular weight bands were observed for the single strands in all of the gels which arose from self-association of the unhybridized strands under the nondenaturing conditions.

Stability of DNA–PEG Conjugates. To determine the effect of PEG on DNA stability toward nucleases, DNA–PEG conjugates and unmodified DNA were incubated in the presence of fetal calf serum. The conditions were chosen to

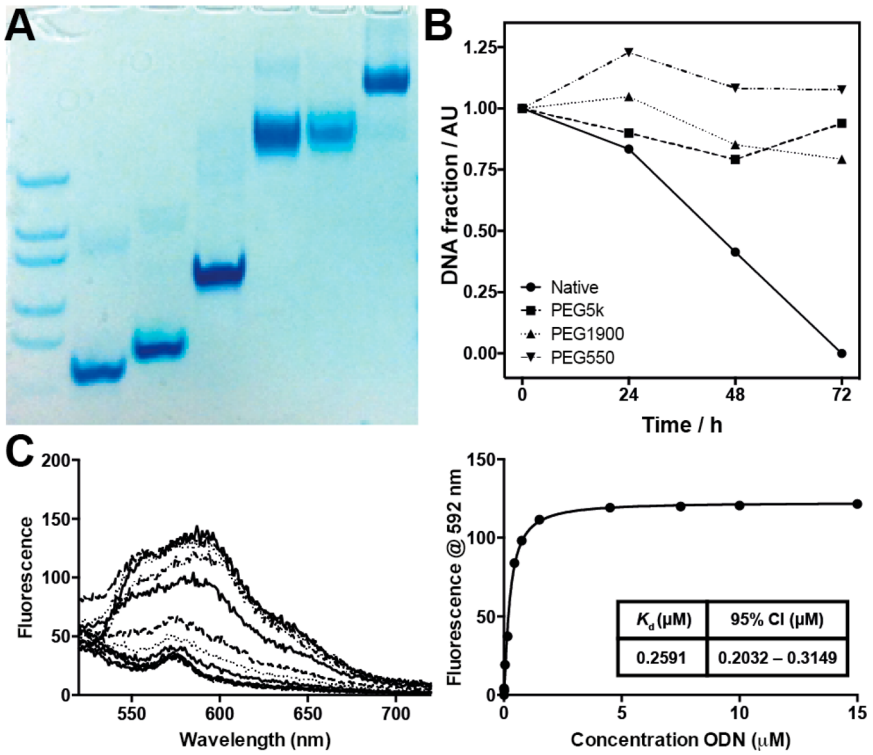

Figure 2. (A) PAGE analysis of PEG5K-oligos and DNA–PEG5K conjugates. Lanes, L–R: (1) IDT Ladder 10/60, (2) Oligo A, (3) Oligo B, (4) dsDNA, (5) PEG5K-A, (6) PEG5K–B, (7) DNA–PEG5K. (B) Stability of DNA conjugates in serum. (C) Affinity of doxorubicin for DNA–PEG1900 carriers. Fluorescence spectra of DOX with increasing ODN concentrations with corresponding Hill plots and calculated K_d values.

DOI: 10.1021/acs.bioconjchem.6b00085
Bioconjugate Chem. 2016, 27, 1244–1252

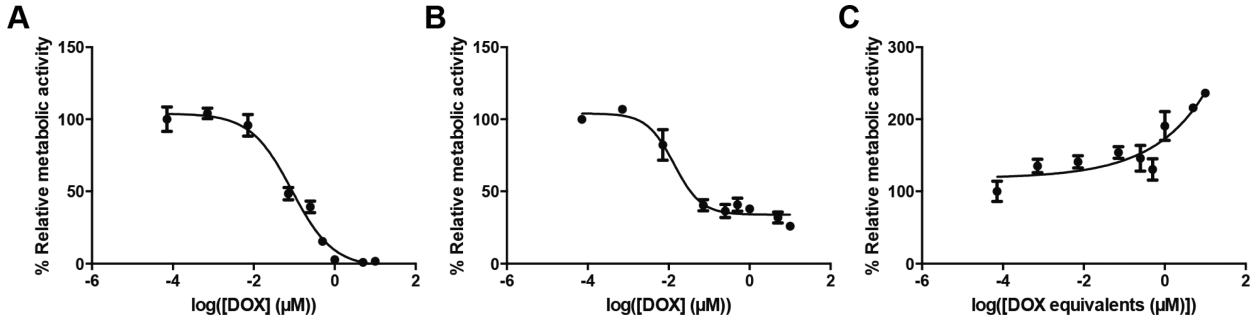

Figure 3. Cytotoxicity of A, doxorubicin; B, DOX@DNA−PEG1900; and C, DNA−PEG1900 dsODN in the A549 cell line.

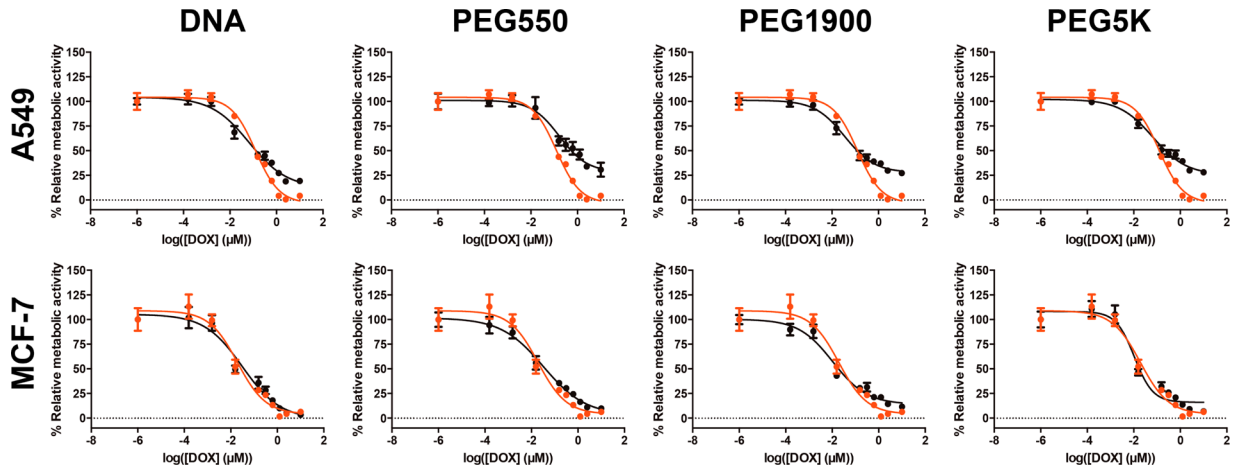

Figure 4. Cytotoxicity of DOX@DNA−PEG in A549 and MCF-7 cell lines. Cells were cultured in the presence of free nucleosides. Samples (black) are as labeled. Free DOX (red) is shown for comparison. Lines are calculated four-parameter logistic fits.

mimic as closely as possible those used for later in vitro experiments to ensure that any effects that arose from differential degradation could be accounted for. The samples were analyzed by native PAGE and individual band intensity estimated using image analysis software. The band intensity of each conjugate at the start of the experiment (0 h) was set as 100%. All DNA−PEG conjugates were stable for the duration of the experiment with 80−90% remaining after 72 h. Conversely, the unmodified DNA had completely degraded after 72 h and was reduced to approximately 40% after 48 h (Figures 2B and S2). The conjugation of the PEG polymers to each terminus of the DNA therefore improved its stability significantly and provided protection against the nucleases. However, no effect of polymer molecular weight on stability was observed under these conditions.

Doxorubicin-Loading and Affinity. The affinity of doxorubicin (DOX) to the DNA carriers was examined in order to determine the binding of the drug and if this was affected by PEGylation. Doxorubicin binds preferentially to 5′-GC-3′ and 5′-CG-3′ double-stranded sequences;[24] thus, it is expected that the sequence used here would have two preferential binding sites. Affinity measurements were performed by a previously established fluorescence quenching protocol.[11] The fluorescence of doxorubicin was plotted as a function of the oligonucleotide concentration to produce a Hill plot from which dissociation constants (K_d) were calculated (Figures 2C and S3). Comparison of the calculated K_d values showed no difference beyond experimental error between the PEGylated and non-PEGylated DNA, with all being 200 ± 60 nM.

In Vitro Cytotoxicity Studies of DNA−PEG and DOX@DNA−PEG Conjugates. *DNA Conjugates Promote Cell Proliferation.* To determine if the DNA−PEG conjugates were capable of delivering DOX they were assessed in vitro in A549 cells (lung adenocarcinoma epithelial cells). Carriers were loaded at a 1/10 (w/w) with DOX based on their oligonucleotide content (i.e., 1 mg DOX per 10 mg of ODN) forming the DOX@DNA−PEG conjugates. Cells were incubated with free DOX, DOX@DNA−PEG, and empty DNA−PEG carriers for 72 h. DOX concentrations ranged 0.15 nM−10 μM and were maintained across groups. For the unloaded conjugates the concentrations were matched to the oligonucleotide concentrations used in the DOX@DNA−PEG group. Metabolic activity was assessed by MTT assay; untreated cells were normalized as 100% metabolic activity.

As expected, free DOX resulted in complete suppression of metabolic activity at higher concentrations (≳1 μM), with a calculated IC_{50} of 89 nM (95% CI 57−131 nM, Figure 3A). However, for DOX@DNA−PEG conjugates complete suppression was not seen even at very high concentrations of DOX (10 μM), with approximately 30% metabolic activity remaining compared to untreated cells (Figures 3B and S3). Although intercalation of the DOX within a carrier is expected to affect cell entry, and thus cytotoxicity, this should be compensated for at the higher concentrations. When considered with the effect of the unloaded DNA−PEG (Figure 3C) it is clear that the carriers alone promote metabolic activity/cell growth, and this promotion is also dose dependent. Visual inspection during the course of the experiment revealed that the cell density increased as a function of DNA concentration which was in an agreement

DOI: 10.1021/acs.bioconjchem.6b00085
Bioconjugate Chem. 2016, 27, 1244−1252

Table 1. Cytotoxicity Data for Doxorubicin and DOX@DNA Complexes in A549 and MCF7 Cells

		curve Fit[a]		interpolated[b]		
treatment	cells	IC_{50}[a] (nM)	95% CI (nM)	IC_{50}[a] (nM)	95% CI (nM)	$vial_{max}$[c] (% ± SD)
DOX	A549	124	102−151	126	109−144	4.2 ± 0.3
DOX@DNA	A549	67	43−104	132	104−165	19.3 ± 2.0
DOX@DNA−PEG550	A549	167	105−265	541	411−718	30.8 ± 7.0
DOX@DNA−PEG1900	A549	35	26−48	122	98−151	27.3 ± 1.8
DOX@DNA−PEG5K	A549	66	47−92	232	189−282	28.0 ± 1.9
DOX	MCF7	19	12−29	27	20−37	6.4 ± 0.6
DOX@DNA	MCF7	31	19−52	37	27−49	3.4 ± 0.5
DOX@DNA−PEG550	MCF7	32	21−50	40	31−50	9.8 ± 1.2
DOX@DNA−PEG1900	MCF7	11	7−17	19	14−26	11.5 ± 1.7
DOX@DNA−PEG5K	MCF7	10	8−15	17	13−24	4.2 ± 0.3

[a]Calculated using the four-parameter variable slope log(inhibitor) vs response model in Graphpad Prism 6.0. As incomplete inhibition was achieved for some treatments, these values are relative to the achieved maximum inhibition. [b]Calculated by interpolation of the fitted curve at 50% relative metabolic activity. [c]Viability at maximum DOX concentration.

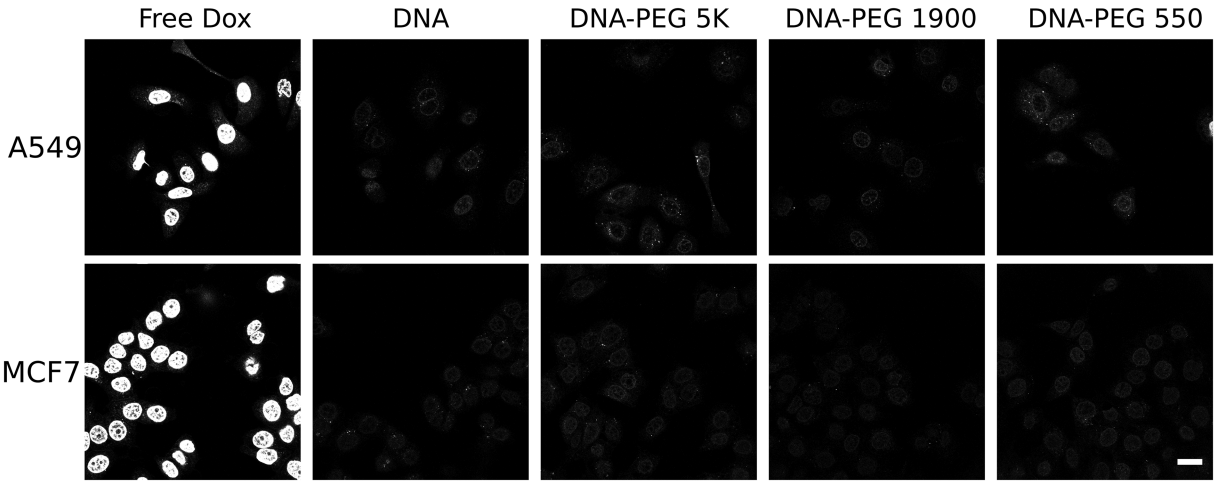

Figure 5. Cellular uptake DOX@DNA samples. Cells were incubated with doxorubicin loaded conjugates for 3 h. Intrinsic doxorubicin fluorescence was visualized by confocal microscopy. Bar = 20 μm.

with the MTT results. It has previously been shown that pyrimidine nucleosides are growth promoting when they are present in media at a concentration of 1 μg/mL with endothelial cells.[22] Cells which are proliferating rapidly require a high rate of DNA synthesis. For those cells the rate of DNA synthesis can become the growth limiting factor. To administer 10 μM DOX, 58 μg/mL of the dsODN carrier was required. The proliferation of the A549 cell line was thus promoted by degradation of the dsODN carrier and subsequent release of free nucleosides. The dsODN carrier was not shown to promote the proliferation of a MCF-7 breast cancer cell line.

Cytotoxicity of DOX@DNA−PEG and DNA−PEG. To counteract enhanced cell proliferation in the presence of oligonucleotide carriers, further in vitro studies were performed in media supplemented with free nucleosides (A, C, G, and T; 10 μg/mL each) for both cell lines. Cytotoxicity experiments were performed with A549 cells as before. With the addition of free nucleosides to the media no enhancement in cell proliferation was observed in the presence of unloaded dsODN carriers when compared to untreated cells (Figure S4). For free DOX, complete suppression of metabolic activity was observed at high concentrations as before (Figure 4). However, the calculated IC_{50} value increased to 124 nM (95% CI 102−151 nM) indicating that a higher dose of DOX is required to inhibit cell growth in the presence of nucleosides, further supporting our previous conclusions. The half maximal inhibitory concentration (IC_{50}) is derived as the midpoint between the maximum and minimum of the dose response curve. However, since the maximal inhibition response varies between DOX@DNA carriers and compared to that of the free drug, direct IC_{50} comparison between the groups was difficult. Consequently, IC_{50} values were also calculated by interpolation of the fitted curve at 50% viability. In the case of free DOX, where the maximum inhibition nears 100%, this has little effect on the calculated IC_{50} (126 nM c.f. 124 nM); however, it provides a more realistic value for the DOX@DNA samples. Values calculated by both methods are contained with Table 1.

For non-PEGylated DOX@DNA, an IC_{50} of 132 nM (95% CI 104−165 nM) is comparable to that of free DOX. This is not unexpected considering that the unshielded DNA is readily degraded in the presence of serum and this is likely to be exacerbated in the presence of cells or if internalized. However, even at the highest non-PEGylated DOX@DNA concentration (1 μM) cell viability remains at ∼20% compared to the untreated control. For the DOX@DNA−PEG samples IC_{50} values are strongly dependent on the molecular weight of the shielding polymer. DOX@DNA− PEG5K and DOX@DNA−PEG550, with IC_{50}s of 232 nM (95% CI 189−282) and 541 nM (95% CI 411−718), respectively, are approximately 2- and 4-fold less toxic than DOX@DNA. DOX@DNA−PEG1900

DOI: 10.1021/acs.bioconjchem.6b00085
Bioconjugate Chem. 2016, 27, 1244−1252

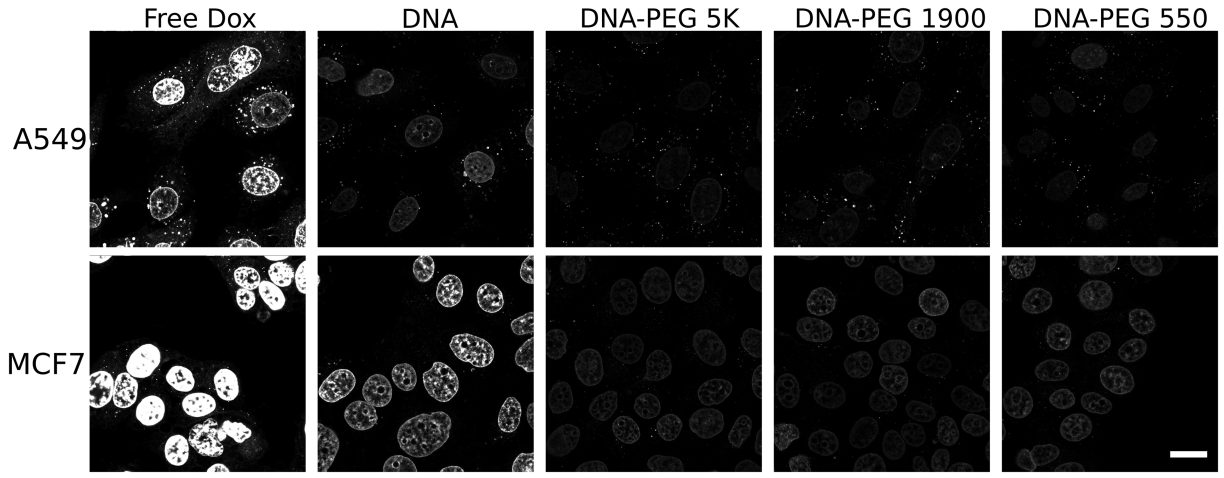

Figure 6. Cellular uptake DOX@DNA samples. Cells were incubated with doxorubicin loaded conjugates for 18 h. Intrinsic doxorubicin fluorescence was visualized by confocal microscopy. Bar = 20 μm.

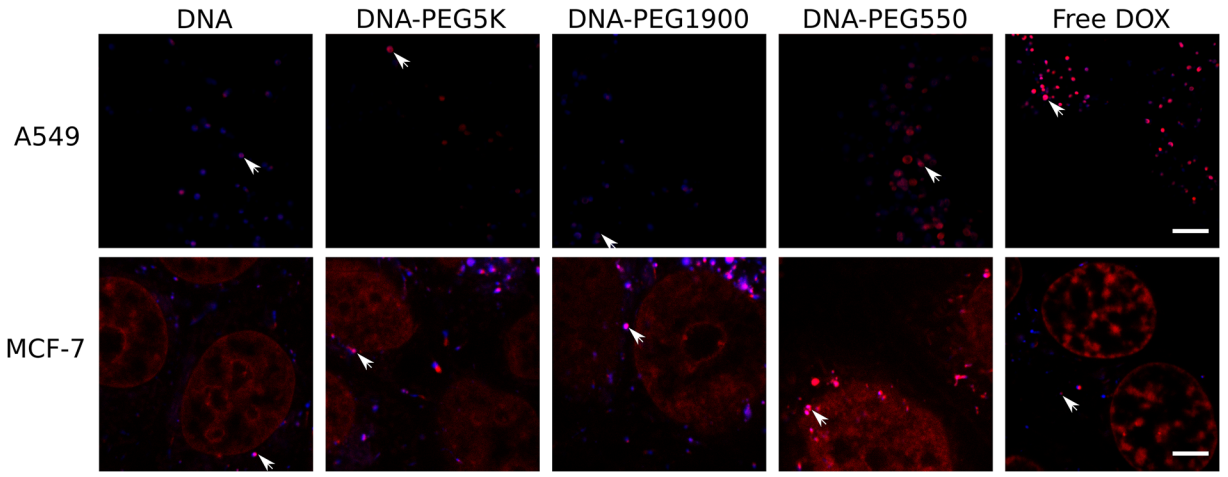

Figure 7. Doxorubicin colocalizes with a lysosomal marker. MCF-7 and A549 cells were incubated with DOX@DNA-PEG for 18 h then counterstained for lysosomes with CytoPainter Lysosome Blue. Doxorubicin (red) and lysosomal (blue) staining was visualized by confocal microscopy. Arrows: areas of colocalization. Bar = 5 μm.

maintains an IC_{50} similar to that of DOX@DNA and free drug with an IC_{50} of 122 nM (95% CI 98−151). The DOX@DNA−PEG conjugates all exhibited dose saturation at highest DOX@DNA concentrations and inhibition was limited to approximately 70% in comparison to 95% inhibition for the free drug.

In vitro studies were extended to a MCF7 cell line (breast adenocarcinoma epithelial cells) to determine if the limiting toxicity was cell line specific. MCF7 cells were more sensitive to DOX with an IC_{50} of 27 nM (95% CI 20−37) for free drug and all systems were capable of ∼90−95% inhibition at the highest concentrations. The greater sensitivity results in less pronounced effects seen with polymer molecular weight, with little variation between treatments, particularly when the large confidence intervals are considered.

Confocal Microscopy Analysis of Cells Treated with DOX@DNA. *DOX@DNA Systems Display Cell Line Dependent Localization.* To further understand the cytotoxicity data DOX@DNA systems were studied by confocal microscopy in A549 and MCF7 cells. Cells were incubated with DOX@DNA carriers and free DOX and the localization studied at various time points using the inherent fluorescence of the drug for detection. Due to sensitivity requirements the drug concentration was fixed at 3 μM in all cases. After 3 h (Figure 5), free DOX showed intense staining in the nucleus in both cell lines indicating rapid uptake, while in all DOX@DNA nuclear staining was considerably less intense. DOX@DNA samples contain punctate regions within the cytoplasm and in the perinuclear region; this was particularly pronounced in A549 cells. This demonstrates that dsODN are readily internalized into both A549 and MCF7 cells, albeit at lower levels than free drug, and allow trafficking into the target organelle. By 18 h (Figure 6) nuclear staining in MCF7 cells remains intense for both free drug and dsODN-DNA, while other conjugates have lower levels. In contrast, A549 cells have lower levels of nuclear staining compared to MCF7 cells but retain staining in cytoplasmic regions for all DOX@DNA samples and free DOX.

Intracellular Localization after 18 h. In order to investigate the intracellular localization of internalized DOX, cells were incubated for 18 h with free DOX or DOX@DNA and the lysosomal compartments were counterstained (Figures 7 and S6 for nonmerged images). In MCF7 cells, intense doxorubicin staining was observed in the nucleus for all dsODN and free DOX. Furthermore, punctate doxorubicin positive regions colocalized with the lysosomal marker. In contrast,

DOI: 10.1021/acs.bioconjchem.6b00085
Bioconjugate Chem. 2016, 27, 1244−1252

A549 cells showed no detectable nuclear staining at 18 h, even for free DOX, while retaining cytoplasmic doxorubicin positive lysosomal staining. This contrasts with the findings of the previous experiment (Figure 6) where some low-level signal was still detected in nucleus of A549 cells at 18 h. However, due to the broad excitation/emission spectra of both doxorubicin and the lysosomal marker, the collection range and signal gain for doxorubicin had to be narrowed to prevent signal bleed through. The colocalization assay (Figure 7) therefore only visualized the most intense regions of doxorubicin staining, i.e., the punctate cytoplasmic regions. Lower levels of doxorubicin fluorescence may reflect increased efflux of doxorubicin from A549 cell nuclei in comparison to MCF7 cells which could explain the cell lines elevated resistance to the drug. Both cell lines have been shown to express multidrug resistance associated-proteins (MRP) which can limit the efficiency of chemotherapy.[25] Encapsulation of doxorubicin in dsODN allows the drug to traffic into the nucleus and lysosome; however, it does not alter the final destination of the doxorubicin nor prevent drug efflux. However, replacement of the oligonucleotide segment with one that exerts its own therapeutic effect, e.g., siRNA or T-oligos,[26,27] may provide a synergistic effect.

CONCLUSIONS

We have described the synthesis and in vitro biological activity of a series of oligonucleotide-based carriers for doxorubicin. Carriers were synthesized by conjugation of PEG to the 5′ termini of ODN and hybridization by Watson−Crick base pairing. As expected, PEGylation was found to enhance stability to serum nucleases compared to an unPEGylated control. DOX was successfully bound to the carriers with high affinity (K_d ∼ 200 nM) in all cases.

Initial in vitro assays with A549 cells revealed that the carriers promoted cell growth compared to untreated control, with later experiments requiring supplementation with free nucleosides to enable comparison. Comparisons of the metabolic activity, uptake, and localization of DOX@DNA systems in A549 and MCF7 cells demonstrated several differences. In MCF7 cells, metabolic activity and uptake were comparable to that of free DOX. Conversely, in A549 cell line DOX@DNA systems had a lesser effect on metabolic activity than free DOX with no system able to achieve more than 70% inhibition. Uptake studies determined that DOX@DNA systems were taken up to a lower extent than free DOX, and that DOX levels in nuclei reduced with time in A549 cells compared to MCF7 cells.

Our findings highlight the issues that need to be addressed when designing and evaluating oligonucleotide based drug delivery systems. The vast difference observed between the two cell lines underlines the importance of adopting appropriate in vitro models early on and supplementing tissue culture medium with free nucleosides. Our results suggest that our PEG-based system could be used to treat doxorubicin sensitive cancer cells in instances where adverse drug effects are limiting. The data derived from A549 cell line also accentuates the fact that PEGylated-dsODN system would be not suitable to treat drug resistance cells; in those circumstances, amphiphilic polymers and known inhibitors of multidrug resistance protein (MRP) should be considered instead.[28,29] We are currently evaluating alternative dsODN-derived systems to address this issue of drug resistance.

MATERIALS AND METHODS

Materials. All oligonucleotides (HPLC purified) were purchased from Biomers.net GmbH (Ulm, Germany) and used without further purification. MCF-7 and A549 cell lines were received from CRN NCI-60 cell bank.

Polyethylene glycol monomethyl ether (mPEG, M_n 5000, 1900, and 550 Da) were purchased from Polysciences Inc. CytoPainter lysosomal staining kit blue fluorescence was purchased from Abcam. *N*,*N*′-Disuccinimidyl carbonate (DSC, ≥95.0%), triethylamine (Et_3N, ≥99%), thiazolyl blue tetrazolium bromide (MTT, 98%), water (BPC grade), diammonium hydrogen citrate (DAHC, ≥99%), Stains-All (95%), 3-hydroxypicolinic acid (3-HPA, (≥99%)), methylene blue hydrate (>97%), tris-borate-EDTA buffer (TBE, 10× concentrate), ammonium persulfate (≥98%), *N*,*N*,*N*′,*N*′-tetramethylethylenediamine (TEMED, 99%), ethylenediaminetetraacetic acid disodium salt (EDTA, >99%), glycerol anhydrous (Fluka), bromophenol blue solution (0.04 wt % H_2O), acrylamide:*N*,*N*′-methylenebis(acrylamide) (29:1) 40% solution and Dulbecco's PBS (Modified, without calcium chloride and magnesium chloride) were purchased from Sigma-Aldrich.

All other solvents and reagents were of analytical or HPLC grade and purchased from Sigma-Aldrich unless otherwise specified.

NMR Spectroscopy. NMR spectra were recorded on a Bruker Avance 400 spectrometer at 400.13 MHz (^1H) and 100.62 MHz (^{13}C, ^1H decoupled at 400.13 MHz) in chloroform-*d*. All chemical shifts are reported in ppm relative to the signal for tetramethylsilane.

HPLC Analysis and Purification of DNA Strands. Reverse phase high performance liquid chromatography (RP-HPLC) was performed on a Shimadzu Prominence UPLC system fitted with a DGU-20A5 degasser, LC-20AD low-pressure gradient pump, CBM-20A LITE system controller, SIL-20A autosampler, and an SPD-M20A diode array detector. Analytical separations were performed on a Phenomenex Clarity 3 μm Oligo-RP C18 column (4.6 × 50 mm) with a gradient of MeOH (10−70% for PEG5K and PEG1900 ODNs and 10−50% for PEG550 ODNs over 20 min) in 0.1 M triethylammonium acetate (TEAA, pH 7.5)/MeCN (95/5) as the mobile phase at a flow rate of 1.0 mL/min. Semipreparative separations were performed on a Phenomenex Clarity 3 μm Oligo-RP C18 column (10 × 50 mm) under the same conditions at a flow rate of 5.0 mL/min.

MALDI-ToF Mass Spectrometry. Matrix-assisted laser desorption/ionization time-of flight (MALDI-ToF) mass spectrometry was performed on a Bruker MALDI-ToF Ultra Flex III spectrometer operated in linear, positive ion mode. 3-HPA containing DAHC was used as the matrix for oligonucleotide analysis. Briefly, a saturated solution of 3-HPA (50 mg/mL) was prepared by adding 25 μg of 3-HPA to 500 μL of 50% MeCN/water. 25 μL of DAHC solution (100 mg/mL) was added to 225 μL of the 3-HPA solution, to give a final DAHC concentration of 10 mg/mL. ODN solutions were desalted prior to mixing with matrix using C18 Ziptips. Equal volumes of matrix solution and ODN solution (0.2 mM) were mixed and 2 μL of the mixture was spotted onto the MALDI plate and allowed to dry.

Polyacrylamide Gel Electrophoresis. Polyacrylamide gel electrophoresis (PAGE) analysis was performed at 160 mV using a 15% acrylamide running gel. Native gels were prepared

DOI: 10.1021/acs.bioconjchem.6b00085
Bioconjugate Chem. 2016, 27, 1244−1252

using acrylamide−bis-acrylamide (29:1) and TBE (Tris-borate-EDTA) solutions. Samples were prepared by dilution in native loading buffer containing glycerol and bromophenol blue. 5 μg of oligonucleotide was loaded per well. IDT Oligo Length Standard 10/60 was used a size marker for the gels. The oligonucleotide/polymer bands were visualized using methylene blue staining.

Synthesis of α-Methoxy-ω-succinimidyl carbonate poly[ethylene glycol] (mPEG-SC). mPEG550-SC. mPEG (M_n 550 Da, 1.39 g, 2.5 mmol) was dried by azeotropic distillation with toluene. The residue was dissolved in THF (100 mL) and the solution cooled to 0 °C with an ice bath. DSC (1.89 g, 7.4 mmol) and TEA (0.745 g, 7.4 mmol) were added and the solution allowed to warm to room temperature then stirred overnight (16 h). The resulting suspension was filtered and volatiles removed under reduced pressure. The residue was dissolved in toluene and any insoluble material removed by filtration. Toluene was removed under reduced pressure and the residue redissolved in chloroform. In order to remove any unreacted DSC Wang resin/TEA was added to the solution and allowed to react overnight. The resin was removed by centrifugation and the supernatant was washed with 0.1 M HCl. The organic layer was dried over $MgSO_4$, filtered, and volatiles removed under reduced pressure. The product was dried under vacuum and isolated as yellowish oil (400 mg, 20% yield).

^{1}H NMR (CDCl3, 400 MHz): δ 4.49−4.47 (t, 2H), 3.82−3.56 (m, 50H), 3.40 (s, 3H), 2.86 (s, 4H).

mPEG1900-SC. mPEG (M_n 1900 Da, 3 g, 1.6 mmol) was dried by azeotropic distillation with toluene. The residue was dissolved in MeCN (70 mL) and the solution cooled to 0 °C with an ice bath. DSC (1.01 g, 4 mmol) and TEA (0.4 g, 4 mmol) were added and the solution allowed to warm to room temperature, then stirred overnight (16 h). The resulting suspension was filtered and concentrated under reduced pressure. The crude product was precipitated into Et_2O and collected by vacuum filtration. The product was purified by twice redissolving in $CHCl_3$ and precipitating into Et_2O. After drying under vacuum the product was recovered as white powder (1.5 g, 47% yield).

^{1}H NMR ($CDCl_3$, 400 MHz): δ 4.49−4.47 (t, 2H), 3.84−3.48 (m, 206H), 3.40 (s, 3H), 2.86 (s, 4H).

mPEG5000-SC. mPEG5000-SC was synthesized by the same protocol as mPEG1900-SC starting for mPEG (M_n 5 kDa). Isolated 7 g, 68% yield.

^{1}H NMR ($CDCl_3$, 400 MHz): δ 4.49−4.47 (t, 2H), 3.85−3.48 (m, 522H), 3.40 (s, 3H), 2.86 (s, 4H).

General Procedure for the Synthesis of PEGylated Oligonucleotides. PEGylated oligonucleotides were synthesized as previously described.[10] Specific reaction conditions are detailed in Table 2. Briefly, 5′-aminohexyl oligonucleotide (1 equiv) was dissolved in DPBS to a concentration of 2.5 mg/mL. A solution of mPEG-SC (5 equiv) was added with gentle agitation and the reaction allowed to proceed for up to 72 h. Conversion was monitored by HPLC and additional mPEG-SC added if required. PEGylated oligonucleotides were purified by semipreparative HPLC and lyophilized. Lyophilized materials were redissolved in DNase free water and concentration determined by measurement of optical density at 260 nm (1 OD = 20 μg/mL). Solutions were then aliquoted and lyophilized before storage at −20 °C.

Hybridization of DNA Strands. Strands were hybridized in annealing buffer which consisted of 10 mM Tris, 50 mM NaCl, and 1 mM EDTA, pH 7.5. For the hybridization the strands were mixed in equimolar quantities to give a final concentration of 75 μM of each strand and placed in a water bath at 95 °C for 5 min. The water bath was then turned off and allowed to cool slowly to room temperature. Annealed strands were desalted using a PD SpinTrap G-25 column (GE Healthcare) and oligonucleotide concentration determined by optical density @ 260 nm (1 OD = 30 ug/mL). Annealing was verified using PAGE gel under nondenaturing conditions. Solutions were aliquoted, lyophilized, and stored at −20 °C until needed.

Table 2. Conditions and Analytical Data for the PEGylation of Oligonucleotides

oligo[a]	PEG	equiv	solvent[b]	yield[c]	MALDI[d]
A	550	5	THF	66	7729/7633
B	550	5	THF	54	7484/7386
A	1900	5	DMSO	75	9079/9076
B	1900	5	THF	56	8834/9271
A	5000	5	DMSO	54	12189/12189
B	5000	6.7	DMSO	84	11934/12006

[a]Sequences. Oligo A: TAA CAG GAT TAG CAG AGC GAG G; Oligo B: CCT CGC TCT GCT AAT CCT GTT A. [b]For dissolution of mPEG-SC. [c]Calculated from measured OD values. [d]Theoretical/found.

Drug Loading of DNA Carriers. Doxorubicin HCl (Dox HCl) (1 mg) was dissolved in UHQ water (1 mL). The solution was filtered through a 0.22 μm PES syringe filter and stored at 4 °C until use. DNA carriers were dissolved in sterile DPBS. Dox HCl was added to the DNA solution in order to achieve a 10% (w/w) Dox HCl to DNA drug loading. The DOX@DNA complexes were allowed to form for 30 min and used without further purification. For in vitro experiments the DOX@DNA complexes were diluted 25-fold with media to a DOX concentration of 10 μM (5.8 μg/mL of DOX, 58 μg/mL ODN).

Stability of Oligonucleotides. DOX@DNA systems were incubated at an oligonucleotide concentration of 0.63 μg/mL in DPBS containing 10% fetal calf serum (FCS). Solutions were incubated at 37 °C with mild agitation. At each time point (0, 24, 48, 72 h) a sample (10 μL) was removed, flash frozen in liq. N_2, and stored at −20 °C until analysis by PAGE. The samples were diluted with 10 μL of loading buffer and 10 μL of the diluted sample loaded per well. PAGE was carried out at 160 mV using a 15% acrylamide gel. The oligonucleotide/polymer bands were visualized using methylene blue. Intensity of gel bands was estimated by image analysis using Scion Image (Macro: Gelplot2).

Affinity of Doxorubicin HCl to Hybridized Oligonucleotide Strands. A fluorescence spectroscopy method[11] was used to assess the binding affinity of DOX for DNA systems. The assay was performed with a constant DOX concentration (1.5 μM) while DNA carrier was titrated from 0 to 15 molar (DNA concentrations: 15, 10, 7.5, 4.5, 1.5, 0.75, 0.45, 0.15, 0.045, 0.015, 0.005, and 0 μM). A Hill plot was used to determine the binding affinity of the double stranded oligonucleotide sequence to doxorubicin HCl (Y: ($F_0 - F$), X: Concentration ODN μM). All analyses were performed in Graphpad Prism 6.0.

In Vitro Assays. *General.* The MCF-7 cells were grown in standard T75 flasks. A549 cells were grown in T75 flasks treated for optimal attachment (Corning T75 Cat no 430641).

DOI: 10.1021/acs.bioconjchem.6b00085
Bioconjugate Chem. 2016, 27, 1244−1252

Both cell lines were grown in Minimum Essential Medium Eagle (MEM) media containing 4 mM L-glutamine, penicillin/streptomycin, and 10% FCS. The media was supplemented with nucleosides (G, C, T, A) at the later stages of the cell work, each nucleoside was added at a final concentration of 10 μg/L.

Cytotoxicity Assays. Cells were allowed to reach confluence in the T75 flasks before being seeded onto 96-well plates. Cells were seeded at 5×10^3 cells/well for both cell lines (100 μL, 5×10^4 cells/mL). Cells were allowed to attach for 24 h before the media was removed and replaced with 100 μL of media containing the appropriate DOX concentration. For experiments with carrier alone, an equivalent concentration of DNA (without drug) was used. Six wells were used for each concentration. Cells were treated for 72 h before metabolic activity was determined using an MTT assay. MTT solution (10 μL of 5 mg/mL) in media was added to each well and allowed to develop for 75 min. The media was then carefully aspirated and wells washed with PBS (100 μL). The formazan crystals were finally dissolved by adding DMSO (100 μL) to each well. The plate was read using a Tecan M200 platereader at 562 nm and the MTT response compared to untreated cells. Untreated cells were normalized as 100% metabolic activity.

Toxicity curves were fitted with Graphpad Prism 6.0 using the four-parameter variable slope log(inhibitor) vs response model. Due to incomplete inhibition IC_{50} calculated are considered as relative. Real IC_{50} values were calculated by interpolation of the fitted curve within the same software.

Confocal Microscopy. Cells were seeded on Nunc LabTekII coverglass 8 well slides at 20 000 cells/well and incubated overnight. Conjugates were loaded with drug as described above and added to cells at a final doxorubicin concentration of 3 μM. After the required incubation time cells were fixed in cold 4% paraformalydehyde in PBS for 10 min. Samples were stored at 4 °C and imaged by laser scanning confocal microscopy (LSCM) within 24 h. Settings were excitation 532 nm laser, emission 552−654 nm. Lysosomal staining was conducted using CytoPainter Lysosomal staining kit (blue, Abcam, ab112135) following the manufacturer's instructions with an incubation time of 20 min. Cells were imaged immediately by LSCM using settings excitation 405 nm, emission 430−480 nm and excitation 532 nm, emission 553−672.

■ ASSOCIATED CONTENT

Supporting Information

The Supporting Information is available free of charge on the ACS Publications website at DOI: 10.1021/acs.bioconjchem.6b00085.

PAGE analysis of annealed strands and degradation study. HPLC traces of purified PEG−ODN conjugates. Doxorubicin−ODN affinity plots. MTT cytotoxicity assays in absence of nucleosides and doxorubicin (ODN-carrier only). Additional colocalization images. (PDF)

■ AUTHOR INFORMATION

Corresponding Authors

*E-mail: s.g.spain@sheffield.ac.uk.
*E-mail: johannespall@gmail.com.

Present Address

†Department of Chemistry, University of Sheffield, Brook Hill, Sheffield, S3 7HF, United Kingdom.

Author Contributions

L.P., S.G.S., and J.P.M. performed experiments. All authors contributed to experimental design. The manuscript was written through contributions of all authors. All authors have given approval to the final version of the manuscript.

Notes

The authors declare no competing financial interest.

■ ACKNOWLEDGMENTS

All work was funded by the UK EPSRC (Grants EP/H005625/1, EP/G042462/1) awarded to C.A. The authors thank Christine Grainger-Boultby, Tom Booth, and Paul Cooling for technical support.

■ ABBREVIATIONS

PEG, polyethylene glycol; DOX, doxorubicin; DNA, deoxyribonucleic acid; ODN, oligonucleotide; dsODN, double-stranded oligonucleotide; DOX@DNA-PEG, pegylated double-stranded oligonucleotide physically complexed with doxorubicin; DOX@DNA, double-stranded oligonucleotide physically complexed with doxorubicin; IC, inhibitory concentration; CI, confidence interval; MTT, Thiazolyl Blue Tetrazolium Blue; HPLC, high performance liquid chromatography; MALDI-ToF, matrix-assisted laser desorption/ionization time-of flight mass spectroscopy; NMR, nuclear magnetic resonance; PAGE, polyacrylamide gel electrophoresis

■ REFERENCES

(1) Chakraborty, B., Jonoska, N., and Seeman, N. C. (2012) A programmable transducer self-assembled from DNA. *Chem. Sci. 3*, 168−176.

(2) Bath, J., Green, S. J., and Turberfield, A. J. (2005) A free-running DNA motor powered by a nicking enzyme. *Angew. Chem., Int. Ed. 44*, 4358−4361.

(3) McKee, M. L., Milnes, P. J., Bath, J., Stulz, E., Turberfield, A. J., and O'Reilly, R. K. (2010) Multistep DNA-Templated Reactions for the Synthesis of Functional Sequence Controlled Oligomers. *Angew. Chem., Int. Ed. 49*, 7948−7951.

(4) Roh, Y. H., Lee, J. B., Kiatwuthinon, P., Hartman, M. R., Cha, J. J., Um, S. H., Muller, D. A., and Luo, D. (2011) DNAsomes: Multifunctional DNA-Based Nanocarriers. *Small 7*, 74−78.

(5) Roh, Y. H., Ruiz, R. C. H., Peng, S., Lee, J. B., and Luo, D. (2011) Engineering DNA-based functional materials. *Chem. Soc. Rev. 40*, 5730−5744.

(6) Chien, M.-P., Thompson, M. P., and Gianneschi, N. C. (2011) DNA-nanoparticle micelles as supramolecular fluorogenic substrates enabling catalytic signal amplification and detection by DNAzyme probes. *Chem. Commun. 47*, 167−169.

(7) Chien, M.-P., Rush, A. M., Thompson, M. P., and Gianneschi, N. C. (2010) Programmable Shape-Shifting Micelles. *Angew. Chem., Int. Ed. 49*, 5076−5080.

(8) Cutler, J. I., Auyeung, E., and Mirkin, C. A. (2012) Spherical Nucleic Acids. *J. Am. Chem. Soc. 134*, 1376−1391.

(9) Cutler, J. I., Zhang, K., Zheng, D., Auyeung, E., Prigodich, A. E., and Mirkin, C. A. (2011) Polyvalent Nucleic Acid Nanostructures. *J. Am. Chem. Soc. 133*, 9254−9257.

(10) Magnusson, J. P., Fernandez-Trillo, F., Sicilia, G., Spain, S. G., and Alexander, C. (2014) Programmed assembly of polymer-DNA conjugate nanoparticles with optical readout and sequence-specific activation of biorecognition. *Nanoscale 6*, 2368−74.

DOI: 10.1021/acs.bioconjchem.6b00085
Bioconjugate Chem. 2016, 27, 1244−1252

(11) Bagalkot, V., Farokhzad, O. C., Langer, R., and Jon, S. (2006) An aptamer-doxorubicin physical conjugate as a novel targeted drug-delivery platform. *Angew. Chem., Int. Ed. 45*, 8149−8152.
(12) Bagalkot, V., Zhang, L., Levy-Nissenbaum, E., Jon, S., Kantoff, P. W., Langer, R., and Farokhzad, O. C. (2007) Quantum Dot−Aptamer Conjugates for Synchronous Cancer Imaging, Therapy, and Sensing of Drug Delivery Based on Bi-Fluorescence Resonance Energy Transfer. *Nano Lett. 7*, 3065−3070.
(13) Zhang, L., Radovic-Moreno, A. F., Alexis, F., Gu, F. X., Basto, P. A., Bagalkot, V., Jon, S., Langer, R. S., and Farokhzad, O. C. (2007) Co-Delivery of Hydrophobic and Hydrophilic Drugs from Nanoparticle−Aptamer Bioconjugates. *ChemMedChem 2*, 1268−1271.
(14) Alexander, C. M., Maye, M. M., and Dabrowiak, J. C. (2011) DNA-capped nanoparticles designed for doxorubicin drug delivery. *Chem. Commun. 47*, 3418−3420.
(15) Alexander, C. M., Dabrowiak, J. C., and Maye, M. M. (2012) Investigation of the drug binding properties and cytotoxicity of DNA-capped nanoparticles designed as delivery vehicles for the anticancer agents doxorubicin and actinomycin D. *Bioconjugate Chem. 23*, 2061−70.
(16) Alexander, C. M., Hamner, K. L., Maye, M. M., and Dabrowiak, J. C. (2014) Multifunctional DNA-Gold Nanoparticles for Targeted Doxorubicin Delivery. *Bioconjugate Chem. 25*, 1261−1271.
(17) Kim, K. R., Kim, D. R., Lee, T., Yhee, J. Y., Kim, B. S., Kwon, I. C., and Ahn, D. R. (2013) Drug delivery by a self-assembled DNA tetrahedron for overcoming drug resistance in breast cancer cells. *Chem. Commun. 49*, 2010−2.
(18) Setyawati, M. I., Kutty, R. V., Tay, C. Y., Yuan, X., Xie, J., and Leong, D. T. (2014) Novel Theranostic DNA Nanoscaffolds for the Simultaneous Detection and Killing of Escherichia coli and Staphylococcus aureus. *ACS Appl. Mater. Interfaces 6*, 21822.
(19) Zhao, Y.-X., Shaw, A., Zeng, X., Benson, E., Nyström, A. M., and Högberg, B. (2012) DNA Origami Delivery System for Cancer Therapy with Tunable Release Properties. *ACS Nano 6*, 8684−8691.
(20) Seferos, D. S., Prigodich, A. E., Giljohann, D. A., Patel, P. C., and Mirkin, C. A. (2009) Polyvalent DNA nanoparticle conjugates stabilize nucleic acids. *Nano Lett. 9*, 308−11.
(21) Duncan, R. (2003) The dawning era of polymer therapeutics. *Nat. Rev. Drug Discovery 2*, 347−360.
(22) Knop, K., Hoogenboom, R., Fischer, D., and Schubert, U. S. (2010) Poly(ethylene glycol) in Drug Delivery: Pros and Cons as Well as Potential Alternatives. *Angew. Chem., Int. Ed. 49*, 6288−6308.
(23) Schellekens, H., Hennink, W. E., and Brinks, V. (2013) The Immunogenicity of Polyethylene Glycol: Facts and Fiction. *Pharm. Res. 30*, 1729−1734.
(24) Frederick, C. A., Williams, L. D., Ughetto, G., Vandermarel, G. A., Vanboom, J. H., Rich, A., and Wang, A. H. J. (1990) Structural comparison of anticancer drug DNA complexes - adriamycin and daunomycin. *Biochemistry 29*, 2538−2549.
(25) Abdallah, H. M., Al-Abd, A. M., El-Dine, R. S., and El-Halawany, A. M. (2015) P-glycoprotein inhibitors of natural origin as potential tumor chemo-sensitizers: A review. *J. Adv. Res. 6*, 45−62.
(26) Sarkar, S., and Faller, D. V. (2011) T-Oligos Inhibit Growth and Induce Apoptosis in Human Ovarian Cancer Cells. *Oligonucleotides 21*, 47−53.
(27) Resnier, P., Montier, T., Mathieu, V., Benoit, J.-P., and Passirani, C. (2013) A review of the current status of siRNA nanomedicines in the treatment of cancer. *Biomaterials 34*, 6429−6443.
(28) Batrakova, E. V., Dorodnych, T. Y., Klinskii, E. Y., Kliushnenkova, E. N., Shemchukova, O. B., Goncharova, O. N., Arjakov, S. A., Alakhov, V. Y., and Kabanov, A. V. (1996) Anthracycline antibiotics non-covalently incorporated into the block copolymer micelles: in vivo evaluation of anti-cancer activity. *Br. J. Cancer 74*, 1545−1552.
(29) Guo, Y., Luo, J., Tan, S., Otieno, B. O., and Zhang, Z. (2013) The applications of Vitamin E TPGS in drug delivery. *Eur. J. Pharm. Sci. 49*, 175−186.

DOI: 10.1021/acs.bioconjchem.6b00085
Bioconjugate Chem. 2016, 27, 1244−1252

Biointerphases
A Journal of Biomaterials and Biological Interfaces

3D chemical characterization of frozen hydrated hydrogels using ToF-SIMS with argon cluster sputter depth profiling

Michael Taylor, David Scurr, Matthias Lutolf, Lee Buttery, Mischa Zelzer, and Morgan Alexander

Citation: Biointerphases **11**, 02A301 (2016); doi: 10.1116/1.4928209
View online: http://dx.doi.org/10.1116/1.4928209
View Table of Contents: http://scitation.aip.org/content/avs/journal/bip/11/2?ver=pdfcov
Published by the AVS: Science & Technology of Materials, Interfaces, and Processing

3D chemical characterization of frozen hydrated hydrogels using ToF-SIMS with argon cluster sputter depth profiling

Michael Taylor[a] and David Scurr
School of Pharmacy, University of Nottingham, University Park, Nottingham NG7 2RD, United Kingdom

Matthias Lutolf
Laboratory of Stem Cell Bioengineering, École Polytechnique Fédérale de Lausanne, Lausanne CH-1015, Switzerland

Lee Buttery, Mischa Zelzer, and Morgan Alexander
School of Pharmacy, University of Nottingham, University Park, Nottingham NG7 2RD, United Kingdom

(Received 8 May 2015; accepted 24 June 2015; published 7 August 2015)

Hydrogels have been used extensively in bioengineering as artificial cell culture supports. Investigation of the interrelationship between cellular response to the hydrogel and its chemistry ideally requires methods that allow characterization without labels and can map species in three-dimensional to follow biomolecules adsorbed to, and absorbed into, the open structure before and during culture. Time-of-flight secondary ion mass spectrometry (ToF-SIMS) has the potential to be utilized for through thickness characterization of hydrogels. The authors have established a simple sample preparation procedure to successfully achieve analysis of frozen hydrated hydrogels using ToF-SIMS without the need for dry glove box entry equipment. They demonstrate this on a poly(2-hydroxyethyl methacrylate) (pHEMA) film where a model protein (lysozyme) is incorporated using two methods to demonstrate how protein distribution can be determined. A comparison of lysozyme incorporation is made between the situation where the protein is present in a polymer dip coating solution and where lysozyme is in an aqueous medium in which the film is incubated. It is shown that protonated water clusters $H(H_2O)_n^+$ where $n = 5–11$ that are indicative of ice are detected through the entire thickness of the pHEMA. The lysozyme distribution through the pHEMA hydrogel films can be determined using the intensity of a characteristic amino acid secondary ion fragment. [http://dx.doi.org/10.1116/1.4928209]

I. INTRODUCTION

Three-dimensional polymer networks that hold large quantities of water are termed hydrogels.[1] This class of materials has been investigated extensively in biomedical research over the past decade due to their attractive properties and biophysical similarities to soft biological tissues.[2] Certain synthetic hydrogels have been proposed to be similar in composition and structure to the native extracellular matrix of the stem cell niche, their *in vivo* cell habitat, which is a powerful component in controlling stem cell fate.[3] Ease of chemical modification, biocompatibility, gas permeability, and the ability to deliver functional compounds are some of the attractive properties that may be exploited to instruct stem cell development on hydrogel substrates.[4–7] In many hydrogel culture substrates, bioactive compounds are incorporated to illicit control of stem cell regulatory mechanisms. The choice of cell developmental pathway taken can be strongly dependent on the 3D hydrogel chemistry, which plays a significant role in determining hydrogel–cell interactions[8] in addition to their physical properties.[9–11] Promotion of osteogenesis, adipogenesis, and chondrogenesis of human mesenchymal stem cells on poly(ethylene glycol) (PEG) based hydrogels has been described through simple functional group modifications to hydrogel chemistry.[8]

Stem cells cultured upon or within biologically derived hydrogels such as Matrigel™ actively remodel the hydrogel, exuding extracellular proteins and soluble factors that create a favorable niche environment in which to reside.[12,13] Synthetic hydrogel chemistry can be designed to respond to remodeling. PEG hydrogels have been reported where severable matrix metalloproteinase (MMP) responsive peptide linkages are incorporated into the polymer backbone, allowing active remodeling by MMP hydrolysis of the responsive peptide fragments.[14] This illustrates the characterization challenge to gaining a complete understanding of the chemical processes involved in stem cell culture on hydrogels.

Previous work in surface characterization has shown time-of-flight secondary ion mass spectrometry (ToF-SIMS) to be a powerful tool in material characterization, particularly in understanding the complex surface chemistry of extracellular matricies.[13] Subsurface chemical characterization of such organic systems is now possible using polyatomic sputtering beams such as Ar cluster ions beams in combination with a focused liquid metal ion analysis source. Ejected secondary ions from the materials are analyzed as a function of etch time creating a depth profile of the material.[15–17] Bailey *et al.* recently demonstrated the Ar cluster source's capacity to reliably sputter through multilayer

[a]Author to whom correspondence should be addressed; electronic mail: pazma1@exmail.nottingham.ac.uk

polymer films of varying thickness ($\leq 15\,\mu$m).[18] Through thickness chemical characterization of hydrogels will ideally be able to minimize changes associated with dehydration or the increase complexity of chemical fixation.[19]

The preparatory of a frozen hydrated sample is not trivial; it must be suitable to both retain water in the vacuum environment and limit ice formation on the sample surface.[20–25] We describe a preparation procedure for introducing hydrogels into a ToF-SIMS instrument for frozen hydrated 3D chemical analysis that employs a gas to remove crystals of frozen, condensed water from the sample surface prior to evacuation of the instrument load lock. In this study, we compare the results of cryodepth profiling of a simple polymer hydrogel system of poly(2-hydroxyethyl methacrylate) (pHEMA) with a model protein (lysozyme) either premixed with the polymer or immersed in a solution to allow it to diffuse into the hydrogel film. This simple method of preparing pHEMA hydrogel films and introducing them into the ultrahigh vacuum instrument provides high quality ToF-SIMS depth profiles.

II. EXPERIMENT

A. Materials

Poly(2-hydroxyethylmethacrylate) (6% wt/v, $M_n \sim 20\,000$, Sigma Aldrich) was dissolved in ethanol by sonication overnight at 20 °C. A silicon wafer substrate (5 × 5 mm) was prepared by first sonicating with water, acetone, and finally with ethanol. The wafer was dip coated in the pHEMA solution at a retraction speed of 2 mm/s three times and allowed to dry for 1 h. To investigate the ingress of protein into the films, the polymer dip coated wafer was immersed in a lysozyme (1% wt/v, Sigma Aldrich)/Milli-Q grade deionized water solution at room temperature for 16 h. A pHEMA (6% wt/v) and lysozyme (1% wt/v) ethanol solution was also prepared and dip coated onto silicon wafers. Similarly, the silicon wafers was immersed in deionized water for 16 h. Ellipsometric measurements of the films before analysis indicated an average dry film thickness of 300 nm for the hydrated pHEMA hydrogel in the absence of lysozyme. Measurement of film thickness of the pHEMA/lysozyme hydrogels was unavailable due to the opaque nature of the films.

B. Frozen hydrated sample preparation

For ToF-SIMS analysis, hydrated films were mounted onto an ION TOF cryostage, one sample at a time *(of dimensions* 5 × 5 mm*)* followed by plunging into liquid nitrogen for 5 min. The sample stage was removed from the liquid nitrogen and placed onto the precooled sample transfer arm in the entry chamber under nitrogen flow (T ∼ − 70 °C). A high flow of argon gas (3 bars) was immediately used to remove ice (frost), which formed on the sample stage in an "air gun" fashion, which accumulated upon transfer through the ambient air to the loadlock. Upon reaching a pressure of 2×10^{-6} mbar, the entry door to the main chamber was opened and the cryostage introduced for analysis. Sample temperature did not exceed −70 °C in the entry chamber, maintaining at −110 °C under a 2×10^{-6} mbar vacuum. Analysis was performed at −120 °C in the main chamber; the sample was maintained below this temperature when depth profiled to reduce the possibility of surface ice crystallization.

C. Instrumentation

ToF-SIMS data were collected using a ToF-SIMS IV instrument (Münster, Germany) equipped with a bismuth liquid metal ion gun and argon cluster sputter gun. The analysis beam for this study was generated by the liquid metal ion gun, specifically a 25 keV bismuth source, utilizing a Bi_3^{++} rastered over an area of $100 \times 100\,\mu$m with 128 × 128 pixels. The target current was measured as 0.3 pA with a total primary ion dose of 9.2×10^{10} ions/cm^2. A 10 keV Ar_{1455} cluster ion source was employed to etch through the sample over a $400 \times 400\,\mu$m area. Rastering was performed in a noninterlaced mode with 1 frame of analysis and 3 s for sputtering per cycle. The corresponding beam dose was determined to be 6.84×10^{12} ions/cm^2. An argon beam target current of 9 nA was employed for all samples analyzed allowing comparison of sample thicknesses from time taken to reach the hydrogel–silicon wafer interface. Postprofiling crater analysis was attempted with the aim of determining the crater depth for each sample, however, on warming the films to room temperature topography developed, likely indicating delamination of the films, preventing accurate film thickness analysis. A low energy electron flood gun was employed for charge neutralization. Data processing was done with the commercial ION-TOF software, SURFACELAB6. Secondary ion assignments were selected by referring to a reference database of secondary ions related to the components of the material analyzed.[26]

III. RESULTS

The process of analyzing frozen hydrated pHEMA samples by ToF-SIMS involves plunge freezing in liquid nitrogen, which then leads to the accumulation of surface frost during the short transfer in the ambient laboratory atmosphere. Etching of these samples provides very poor depth profiles since the spectra are taken from the rough surface of ice accumulated on the flat sample. While dry box entry is a solution to this problem, we investigated the simpler approach of removing the frost from the surface of the sample using pressurized gas and immediately evacuating the entry lock.

Three frozen hydrated samples are compared in this study, including a pHEMA film, a pHEMA film immersed in lysozyme solution, and lysozyme mixed with the pHEMA dip solution used to form a film. The positive polarity secondary ion spectra acquired using Bi_3^{++} from the surface of the samples are presented in Fig. 1. All the spectra are dominated by secondary ion peaks characteristic of pHEMA, such as at m/z = 39, 41, 43, 45, and 69 (labeled with red markers in Fig. 1), the corresponding formulas for which are shown in Table I. Protonated water clusters at m/z = 91, 109, 127, 145, and 199 representative of $H(H_2O)_5^+$, $H(H_2O)_6^+$, $H(H_2O)_7^+$, $H(H_2O)_8^+$, and $H(H_2O)_{11}^+$, respectively, were additionally observed (highlighted with blue markers in Fig. 1). Histidine is also indicated as a marker for lysozyme by the $C_4H_6N_2^+$ peak at m/z = 82 (green marker in Fig. 1).[26] A

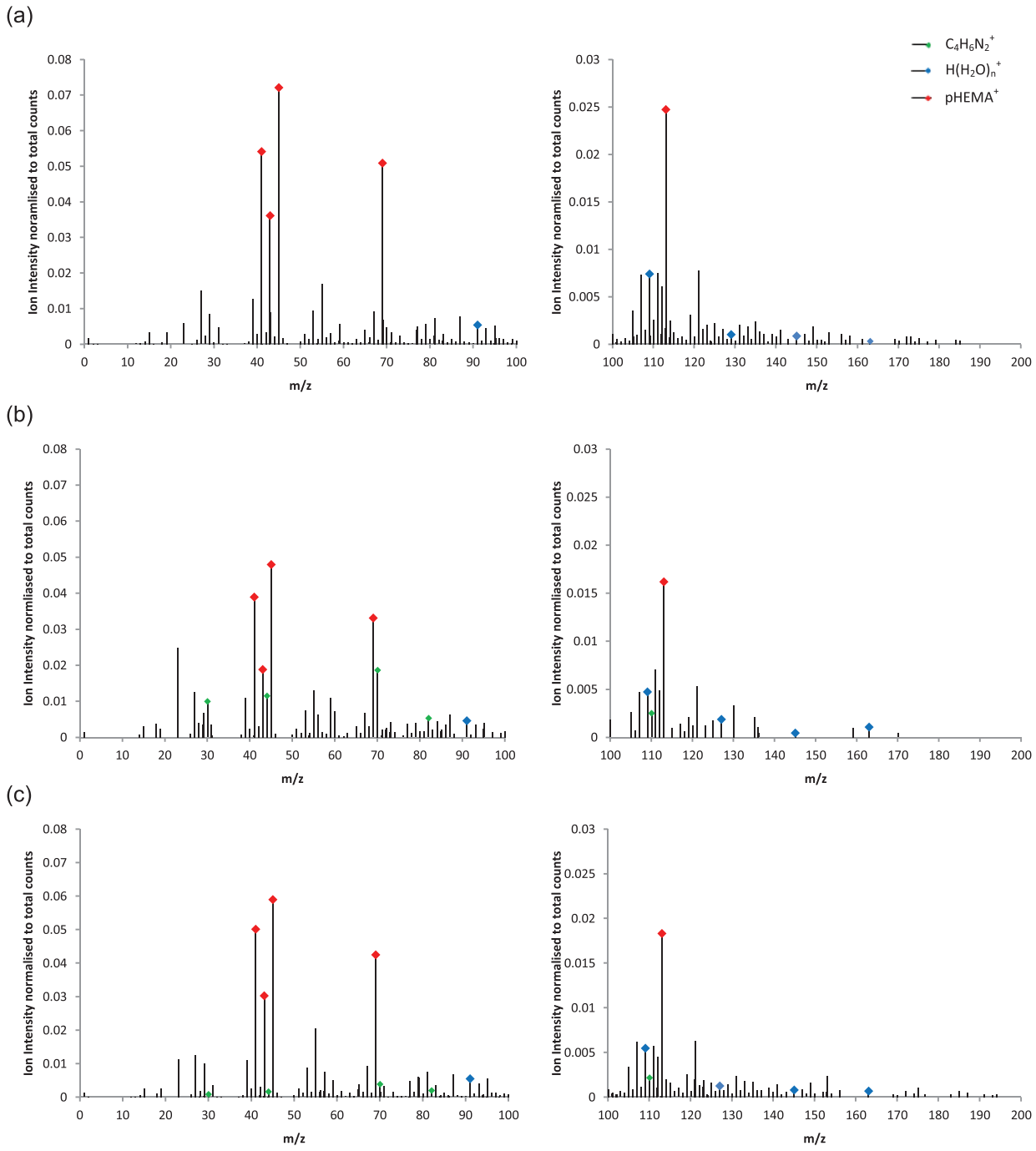

FIG. 1. Positive polarity ToF-SIMS spectra acquired from five scans of the hydrogel surface followed by incubating in water for 16 h at 20 °C for (a) a pHEMA film, (b) a pHEMA hydrogel incubated in 1% wt/v lysozyme in water for 16 h at 20 °C, and (c) a silicon wafer dip coated in an ethanoic solution of 6% wt/v pHEMA/1% wt/v lysozyme.

peak at m/z = 82.182 was detected in the pure pHEMA sample; however, this was reflective of polymer. The mass peak at m/z = 82.047 was absent from this control sample.

A representative secondary ion diagnostic of each component of the sample was selected to represent pHEMA ($C_6H_9O_2^+$), lysozyme ($C_4H_6N_2^+$), protonated water signifying ice ($H(H_2O)_6^+$) and the silicon substrate (Si^+). Depth profiles were observed for the pHEMA film, a pHEMA film incubated in lysozyme solution and a pHEMA/lysozyme film produced by dip coating into a combined lysozyme/pHEMA coating solution shown in Figs. 2(a), 2(b), and 2(c), respectively. The depth profile of the pHEMA film with water [Fig. 2(a)] suggests a surface enrichment of water and depletion of pHEMA evident in the ion intensity shifts from the first five scans. The intensity of the fragment representing these components then remains constant until the relatively sharp pHEMA-silicon interface observed after 120 s of sputtering. Beyond this point, the spectrum is dominated by the Si^+ peak of the silicon wafer substrate at much lower overall intensity compared to the polymer film.

TABLE I. Positive secondary ions reported from depth profiling pHEMA hydrogels. The shading denotes each component of the hydrogel. Silicon is shown in grey, protein in green, water in blue and pHEMA in red.

			Assignment deviation (ppm)		
	m/z	Structure	pHEMA	(pHEMA/lysozyme)	pHEMA/lysozyme
	18.038	NH_4^+	28.2	32.2	40.1
	19.020	$H(H_2O)^+$	39.8	35.2	33.5
	22.999	Na^+	27.0	83.7	61.1
	27.034	$C_2H_3^+$	14.8	10.8	13.9
Silicon wafer	27.987	Si^+	−22.9	−36.4	—
	29.047	$C_2H_5^+$	2.7	32.2	77.3
	30.023	CH_4N	—	12.4	11.9
	39.030	$C_3H_3^+$	5.7	5.4	20.5
	41.041	$C_3H_5^+$	26.5	4.3	50.0
	43.022	$C_2H_3O^+$	28.5	27.6	52.3
	44.218	$C_2H_6N^+$	—	−2.2	−4.6
	45.040	$C_2H_5O^+$	39.3	33.0	67.8
	53.043	$C_4H_5^+$	22.2	18.5	14.4
	55.069	$C_4H_7^+$	34.3	33.3	35.6
	69.044	$C_4H_5O^+$	43.4	32.2	68.9
	70.712	$C_4H_8N^+$	—	10.7	21.1
Protein (His)	82.047	$C_4H_6N_2^+$	—	−61.5	−48.5
	87.051	$C_4H_7O_2^+$	37.4	31.2	59.9
	91.688	$H(H_2O)_5^+$	−48.2	−56.3	−34.6
Water (n = 6)	109.086	$H(H_2O)_6^+$	8.7	−2.0	24.0
	110.08	$C_5H_8N_3^+$	—	17.4	31.2
pHEMA	113.089	$C_6H_9O_2^+$	51.2	39.4	73.3
	127.096	$H(H_2O)_7^+$	4.3	0.2	4.4
	145.113	$H(H_2O)_8^+$	64.5	52.0	65.8
	182.123	$H(H_2O)_{10}^+$	−29.3	−36.6	−37.4
	199.130	$H(H_2O)_{11}^+$	0.9	6.3	−7.8

As can be seen in Fig. 2, the depth profile for the hydrogel film incubated in a lysozyme solution, both the $C_6H_9O_2^+$ and $H(H_2O)_6^+$ ion intensities significantly increase from the surface compared to the bulk of the film. The $C_4H_6N_2^+$ ion, however, displays relatively a steady state ion intensity throughout the profile until reaching the interface between silicon wafer and hydrogel after 110 s of sputtering. A gradual decrease in the $C_6H_8O_2^+$ ion intensity is observed, with no steady state being achieved. A decreasing ion intensity was observed over five comparative samples, demonstrating that this effect is repeatable (Fig. 3).

The depth profile for the hydrogel film produced from dip coating a silicon wafer in a pHEMA/Lysozyme dip solution displays a more pronounced increase in the lysozyme secondary ion marker ($C_4H_6N_2^+$) at the surface [Fig. 2(c)]. This surface enrichment effect was observed over five samples, suggesting repeatability. The relative intensities of the $C_6H_8O_2^+$ and $H(H_2O)_6^+$ ions increase from the surface, reaching a steady state intensity after 60 s of sputtering. The relative ion intensity of the $C_4H_6N_2^+$ ion at (400 counts) at the surface reduced to a steady state intensity (200 counts) in the bulk of the film.

IV. DISCUSSION

This study aims to develop a simple sample preparation procedure for ToF-SIMS to achieve a frozen hydrated hydrogel for analysis without dry box sample entry facilities. The method is anticipated to be equally applicable to other vacuum based analytical techniques. We determined that water was retained in all samples by detection of $H(H_2O)_n^+$ secondary ions signifying a frozen hydrated state. Previous studies have reported ToF-SIMS molecular depth profiling of ice indicated by the detection of these clusters in a histadine/ice film.[16,27] The spectra from depth profiling each of the three hydrogel sample compositions show evidence of water cluster secondary ions beginning at n = 5 (m/z = 91.688) to n = 11 (m/z = 199.130), which shows a similarity to the spectra observed previously for pure ice films.[16]

Frost build up was removed with a high flow rate of argon to clear the surface of ice crystals, which were accumulated during the transfer between plunging with liquid nitrogen to the precooled sample entry chamber. A time of 4 s argon flow over the sample surface was found to be sufficient to remove surface ice without inducing visible changes in the sample surface. Purging of the entry chamber was also employed with nitrogen to eliminate the condensation of species on the sample surface. Maintaining a frozen sample state between the liquid nitrogen plunge and the analysis chamber via the precooled sample entry chamber was a significant consideration as the sublimation rate of ice in the vacuum chamber increases as sample temperature rises. Sample mounting onto the IonTOF cryostage was time

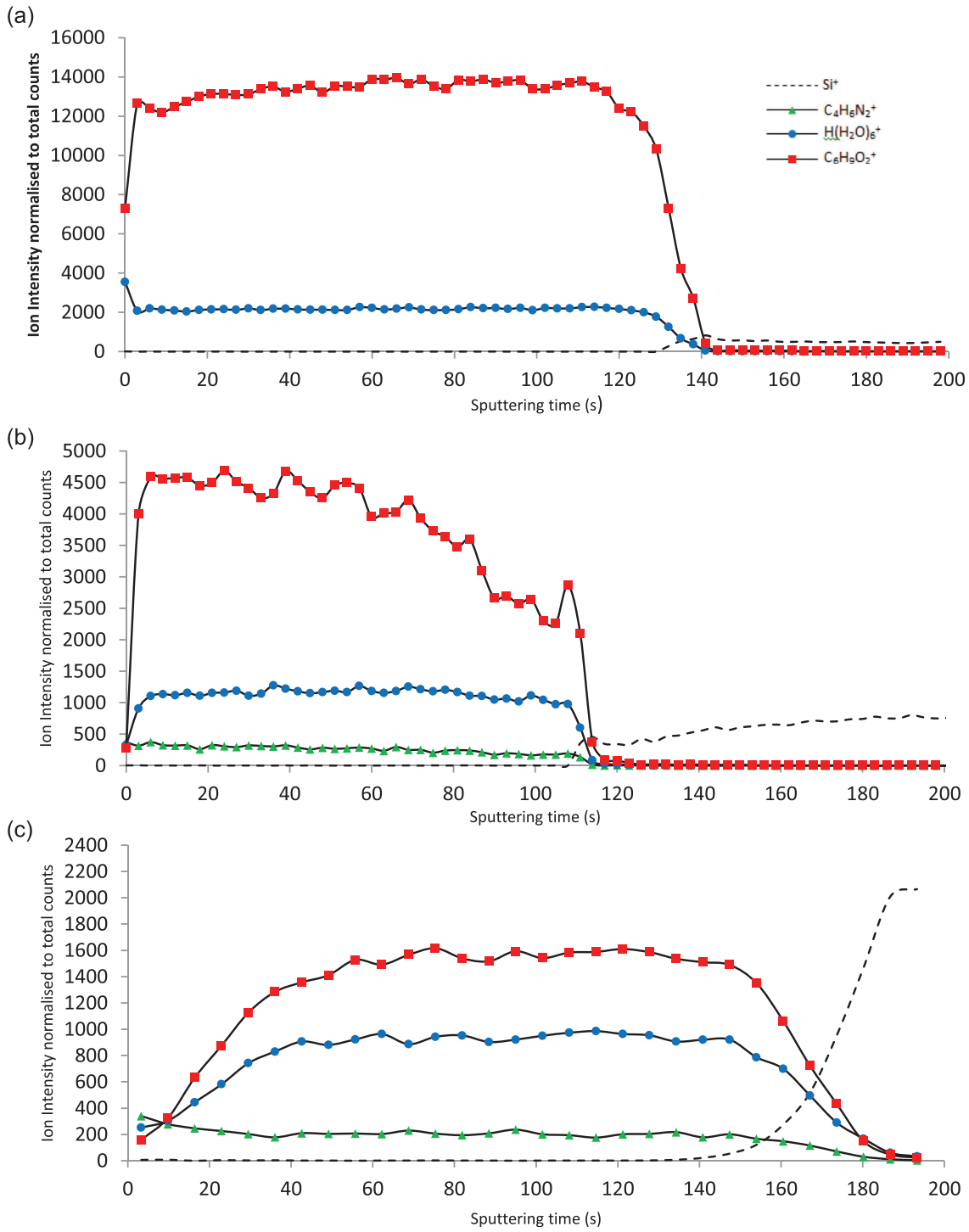

FIG. 2. ToF-SIMS depth profiles of pHEMA hydrogels incubated in water of water/lysozyme for 16 h at 20 °C. (a) A pHEMA film, (b) a pHEMA hydrogel incubating the pHEMA films in 1% wt/v lysozyme in water for 16 h at 20 °C, and (c) a silicon wafer dip coated with a 6% wt/v pHEMA/1% wt/v lysozyme.

consuming; thus, plunge freezing the whole stage assembly allowed immediate transfer of samples to the precooled entry chamber as this did not have any measureable detrimental effect on the instrument vacuum. Previous works by Gemmei-Ide *et al.* among others report a target temperature range of −70 to −110 °C for sample preparation of frozen samples for vacuum analysis, and state that if the sample temperature exceeds −70 °C ice crystallization can occur.[28,29] Furthermore, the sample transfer time from liquid nitrogen immersion to the entry chamber was also performed rapidly; otherwise, the accumulation of frost on the sample surface occurs when the sample is exposed to the ambient atmosphere. The entry chamber cold finger was precooled to liquid nitrogen temperature, and upon entry of the precooled sample, the cold finger was immediately connected with the sample stage. The attached thermocouple temperature reading

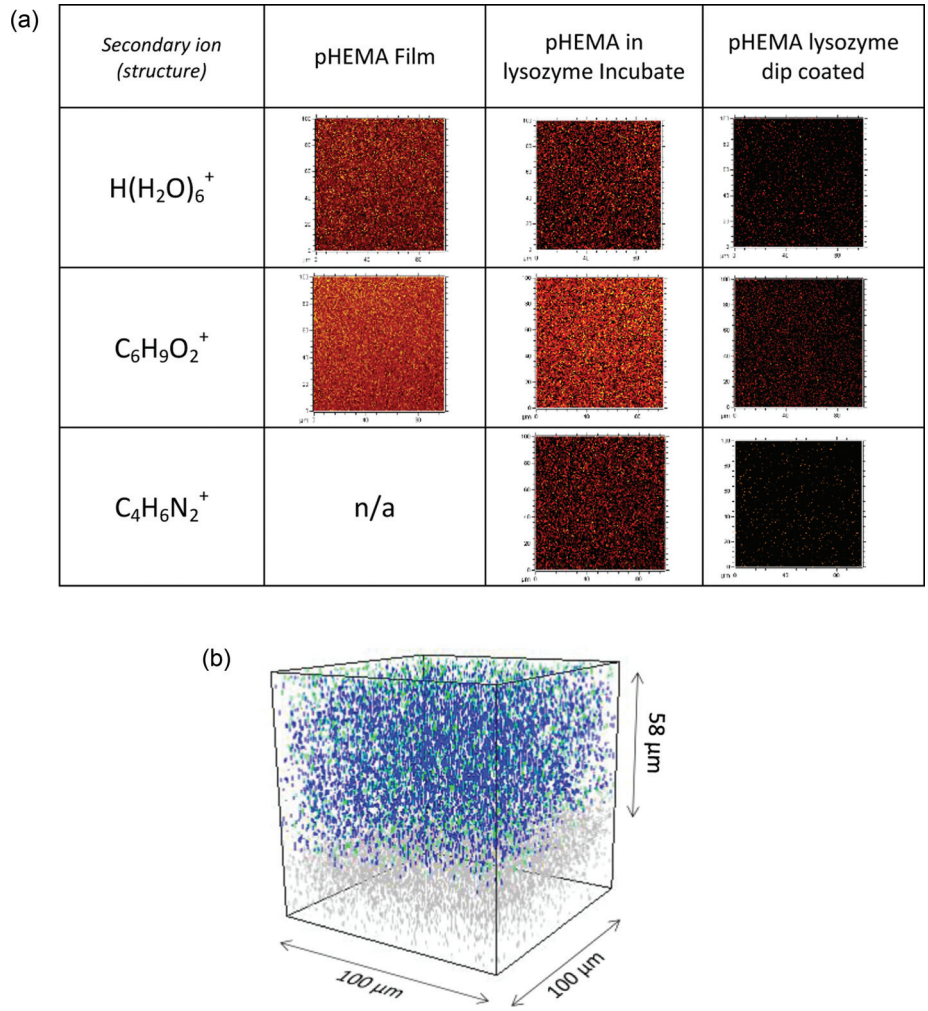

FIG. 3. (a) Positive secondary ion maps from depth profiles of pHEMA hydrogels showing lateral distribution (X/Y coordinates) acquired at 60 s of sputtering. (b) Three-dimensional render of pHEMA/lysozyme film prepared by dip coating in lysozyme/pHEMA solution. $C_4H_6N_2^+$ (Lysozyme) is represented in green, $H(H_2O)_6^+$ (ice) in blue, and Si^+ (silicon wafer) in gray. The hydrogel z thickness represents the gel in a dry state, therefore will be an underestimate of the true thickness.

from the cold finger was reflective of the actual sample temperature, therefore could be used to ensure the sample was below −70 °C. The following low temperature analysis of each of the sample formats was effective to produce a full through-thickness chemical map. This method has been employed across three differing sample formats showing the versatility of the preparatory procedure in high vacuum frozen hydrated hydrogel analysis.

Additionally, this study aimed to characterize biomolecule distribution within hydrogels using the method developed. A model biomolecule, lysozyme, was used and incorporated within the hydrogel either by diffusion into the pHEMA film during incubation in an aqueous solution or by mixing with the polymer with the pHEMA solution prior to depositing the film. In both cases, lysozyme was detected throughout the film. Using the relative $C_4H_6N_2^+$ ion intensities within a sample of constant water and polymer content is thought to be valid to characterize the protein distribution as a function of depth, but between samples of composition, the mass spectrometry matrix effect needs to be considered. The most marked difference in secondary ion intensities is the decrease of the intensity of both the characteristic polymer and water upon lysozyme incorporation (Fig. 2). This suggests that the change in chemistry of the sample associated with the introduction of lysozyme suppresses secondary ion emission (Table II) since we know that the molar

TABLE II. Ion intensity ratios at steady state intensity in depth profile, n = 5. Standard deviations presented in parentheses.

	$H(H_2O)_6^+/C_6H_9O_2^+$	$C_4H_6N_2^+/H(H_2O)_6^+$	$C_4H_6N_2^+/C_6H_9O_2^+$
(1) pHEMA	0.18 (0.013)	—	—
(2) Lysozyme incubated pHEMA	0.29 (0.025)	0.32 (0.038)	0.094 (0.038)
(3) pHEMA mixed with lysozyme before film formation	0.47 (0.076)	0.39 (0.89)	0.19 (0.068)

reduction in the constituents (0.06% pHEMA) could not account for the near tenfold decrease in $C_6H_9O_2^+$ ion intensity from Figs. 2(a)–2(c). Quantitative comparisons between samples are therefore not readily possible.

An enriched lysozyme surface layer is observed when lysozyme is combined as a component of the dip coating solution signifying that lysozyme diffuses toward the hydrogel–water interface, presumably as a result of leaching into the water.

In the pure pHEMA sample, complementary pHEMA depletion and water enrichment is indicated by the characteristic ion trends with etch time [Fig. 2(a)]. Such complementary and self-consistent trends are not seen in from the samples with lysozyme [Figs. 2(b) and 2(c)], suggesting that this incorporation induces "surface transience" supporting the view of a significant role for the matrix effect related to lysozyme presence. Recent studies using ToF-SIMS depth profiling illustrate the complexity of this effect when depth profiling organic materials.[30]

V. CONCLUSION

A sample preparation procedure using argon gas in an "air gun" style to remove the surface frost accumulated on the cooled sample surface on exposure to ambient atmosphere yielded interesting results. It has been demonstrated that poly(2-hydroxyethyl methacrylate) hydrogels incorporating lysozyme can be successfully chemically characterized as frozen hydrated films by utilizing 10 keV Ar_{1500}^+ cluster sputtering by ToF-SIMS. The methodology allows full through-thickness chemical characterization of the pHEMA hydrogel by ToF-SIMS using the $C_4H_6N_2^+$ secondary ion to track lysozyme distribution through the hydrogels.

Lysozyme was found to be sufficiently mobile within the hydrated hydrogel film to diffuse into the films from solution. When lysozyme is combined with pHEMA into the dip coating solution, it diffuses out of the hydrogel resulting in an increased loading at the surface.

This method of 3D chemical characterization of frozen hydrated samples is of particular importance as it provides a way of effective full through-thickness chemical characterization of hydrogels, which is of importance to the biomedical research field.

ACKNOWLEDGMENTS

This work was supported by the EPSRC CTD in Regenerative Medicine. The authors thank Taranjit Singh and Sebastiaan Van Nuffel for consultation on film preparation and ToF-SIMS, as well as Sunil Rajput for editing of the preparatory methodology. Finally, they thank Nottingham University and The Laboratory of Biophysics and Surface analysis for their support.

[1]M. P. Lutolf, Nat. Mater. **8**, 451 (2009).
[2]S. C. Lee, I. K. Kwon, and K. Park, Adv. Drug Delivery Rev. **65**, 17 (2013).
[3]S. Kobel and M. P. Lutolf, Curr. Opin. Biotechnol. **22**, 690 (2011).
[4]Y. Mei, Nat. Mater. **9**, 768 (2010).
[5]M. P. Lutolf, P. M. Gilbert, and H. M. Blau, Nature **462**, 433 (2009).
[6]S. Khetan, M. Guvendiren, W. R. Legant, D. M. Cohen, C. S. Chen, and J. A. Burdick, Nat. Mater. **12**, 458 (2013).
[7]J. Zhu, Biomaterials **31**, 4639 (2010).
[8]D. S. W. Benoit, M. P. Schwartz, A. R. Durney, and K. S. Anseth, Nat. Mater. **7**, 816 (2008).
[9]W. L. Murphy, T. C. Mcdevitt, and A. J. Engler, Nat. Mater. **13**, 547 (2014).
[10]M. J. Dalby, N. Gadegaard, and R. O. C. Oreffo, Nat. Mater. **13**, 558 (2014).
[11]A. D. Celiz, Nat. Mater. **13**, 570 (2014).
[12]C. A. DeForest and K. S. Anseth, Annu. Rev. Chem. Biomol. Eng. **3**, 421 (2012).
[13]B. N. Brown, C. A. Barnes, R. T. Kasick, R. Michel, T. W. Gilbert, D. Beer-Stolz, D. G. Castner, B. D. Ratner, and S. F. Badylak, Biomaterials **31**, 428 (2010).
[14]A. Ranga, S. Gobaa, Y. Okawa, K. Mosiewicz, A. Negro, and M. P. Lutolf, Nat. Commun. **5**, 1 (2014).
[15]N. Winograd, Surf. Interface Anal. **45**, 3 (2013).
[16]D. Rading, S. Ray, L. Yang, and A. G. Shard, Phys. Chem. **114**, 769 (2010).
[17]A. G. Shard *et al.*, Anal. Chem. **84**, 7865 (2012).
[18]J. Bailey, R. Havelund, A. G. Shard, I. S. Gilmore, M. R. Alexander, J. S. Sharp, and D. J. Scurr, ACS Appl. Mater. Interfaces **7**, 2654 (2015).
[19]M. A. Robinson and D. G. Castner, Biointerphases **8**, 15 (2013).
[20]A. Piwowar, J. Fletcher, N. Lockyer, and J. Vickerman, Surf. Interface Anal. **43**, 207 (2011).
[21]M. Dickinson, P. J. Heard, J. H. A. Barker, A. C. Lewis, D. Mallard, and G. C. Allen, Appl. Surf. Sci. **252**, 6793 (2006).
[22]T. Masumi, Y. Matsushita, D. Aoki, R. Takama, K. Saito, K. Kuroda, and K. Fukushima, Appl. Surf. Sci. **289**, 155 (2014).
[23]K. Kuroda, T. Fujiwara, T. Imai, R. Takama, K. Saito, Y. Matsushita, and K. Fukushima, Surf. Interface Anal. **45**, 215 (2013).
[24]A. P. Nair, B. J. Tyler, and R. E. Peterson, Appl. Surf. Sci. **231–232**, 538 (2004).
[25]A. M. Piwowar, J. S. Fletcher, J. Kordys, N. P. Lockyer, N. Winograd, and J. C. Vickerman, Anal. Chem. **82**, 8291 (2010).
[26]J. Lhoest, M. S. Wagner, C. D. Tidwell, and D. G. Castner, Biomed. Mater. **57**, 432 (2001).
[27]C. Bradish, C. Brain, J. Messrs, and E. Hall, Nature **159**, 28 (1947).
[28]M. Gemmei-Ide and H. Kitano, J. Phys. Chem. B **112**, 13499 (2008).
[29]K. Lewis and B. Ratner, J. Colloid Interface Sci. **159**, 77 (1993).
[30]A. G. Shard, S. J. Spencer, S. A. Smith, R. Havelund, and I. S. Gilmore, Int. J. Mass Spectrom. **377**, 599 (2015).

New Antibiotics Against Resistant Bacteria

Author: Ruben Ragg
Published Date: 19 July 2016
Source / Publisher: Chemistry – A European Journal/Wiley-VCH

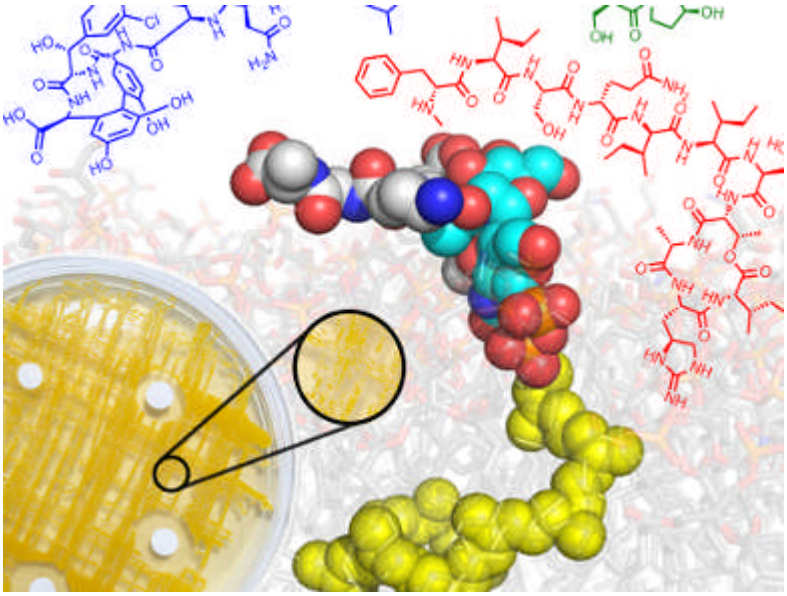

Related Articles

Magazine: Fight Multiresistant Bacteria
News: One Step Ahead of Antibiotic Resistances
Magazine: Modified Quinolines Kill Resistant Bacteria
News: Redesigned Antibiotic for Antibiotic-Resistent Bacteria

Related Societies

ChemPubSoc Europe

The discovery of the first antibiotic penicillin by Alexander Fleming in the 1930s saved millions of lives. However, in recent years, the widespread overuse of antibiotics, even for the treatment of harmless diseases, has contributed to the emergence of numerous antibiotic-resistant bacterial strains. The quest to find new potent antibacterial agents against such strains is a pressing demand now more than ever.

Weng C. Chan and colleagues, University of Nottingham, UK, have summarized the recent advances in the discovery of antibiotics with a focus on novel lipid II inhibitors. These antibiotics prevent the bacterial cell-wall synthesis of gram-positive bacteria. They bind to precursor molecules and inhibit the production of the peptidoglycan layer of the cell wall. Examples of this type of compound are teixobactin (an 11-residue macrocyclic depsipeptide discovered in 2015) and mannopeptimycin (a complex cyclic glycopeptide discovered in 2003).

According to the researchers, these inhibitors may solve the global infection crisis that is associated with the emergence of a high number of resistant bacterial strains.

New Found Hope for Antibiotic Discovery: Lipid II Inhibitors,
Vivian Ng, Weng C. Chan,
Chem. Eur. J. **2016**.
DOI: 10.1002/chem.201601315

Sign in Area

Please note that to comment on an article you must be registered and logged in.
Registration is for free, you may already be registered to receive, e.g., the newsletter. When you register on this website, please ensure you view our terms and conditions. All comments are subject to moderation.

Article Comments - To add a comment please sign in

CONNECT:

ChemPubSoc Europe

DOI: 10.1002/chem.201601315

CHEMISTRY
A European Journal
Minireview

Medicinal Chemistry

New Found Hope for Antibiotic Discovery: Lipid II Inhibitors

Vivian Ng and Weng C. Chan*[a]

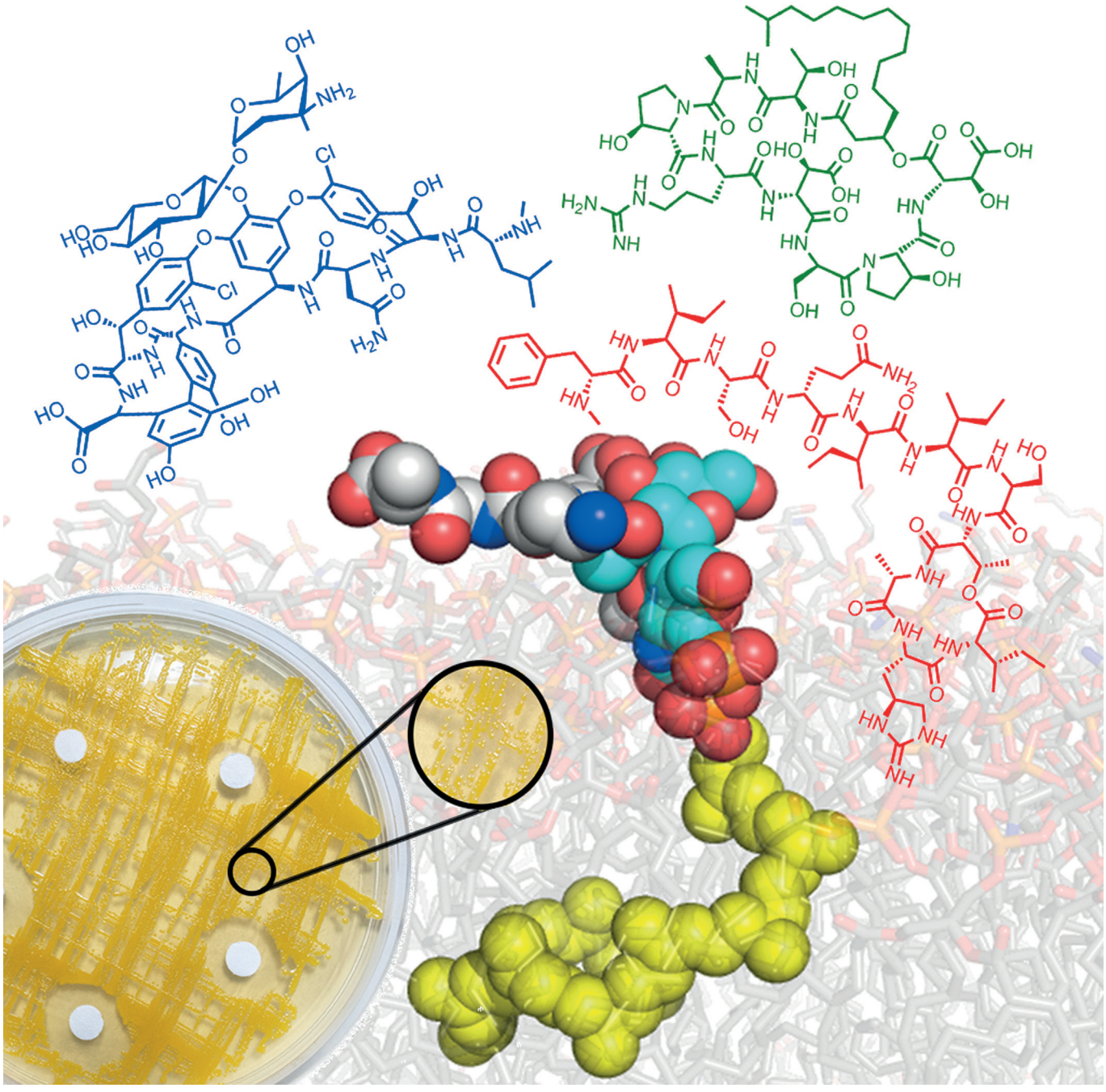

Abstract: Research into antibacterial agents has recently gathered pace in light of the disturbing crisis of antimicrobial resistance. The development of modern tools offers the opportunity of reviving the fallen era of antibacterial discovery through uncovering novel lead compounds that target vital bacterial cell components, such as lipid II. This paper provides a summary of the role of lipid II as well as an overview and insight into the structural features of macrocyclic peptides that inhibit this bacterial cell wall component. The recent discovery of teixobactin, a new class of lipid II inhibitor has generated substantial research interests. As such, the significant progress that has been achieved towards its development as a promising antibacterial agent is discussed.

Introduction

Past, present and future of antibiotics

For centuries, bacterial infections have troubled mankind and their history could be traced all the way back to ancient Egypt. Mouldy jam and bread were often used in folk medicine as poultice on wounds without understanding the antibacterial nature of moulds.[1] In the 1930s, the discovery of penicillin by Alexander Fleming heralded the dawn of a new era for controlling previously fatal bacterial infections, saving numerous lives.[2] Intensive research soon followed that led to the discovery of other antibiotics, such as streptomycin and tetracycline.[3–5] However, as predicted by Paul Ehrlich, resistance tends to follow a medicine development like a "faithful shadow".[6] The widespread misuse of antibacterial agents have contributed to the emergence of resistant bacterial strains within just a few years after their clinical introduction.[5–8]

Antimicrobial resistance (AMR), which could be either intrinsic or acquired, remains an increasingly serious global threat with far-reaching clinical and cost implications.[3,9] Clinically important antibiotic-resistant pathogens include *Staphylococcus aureus*, *Pseudomonas aeruginosa* and *Enterococcus faecium*.[10] Treatment failure and prolonged illnesses inevitably lead to greater healthcare expenditure and higher mortality rate.[11] On top of that, significant medical breakthroughs such as organ transplantation and invasive surgeries that rely heavily on the use of antibiotics are now threatened by AMR.[12] A recent evaluation of this crisis has estimated that AMR would lead to 300 million premature deaths and a global economic cost of $100 trillion over the next three decades.[13,14]

Unfortunately, the situation is further complicated by a decline in the introduction of novel antibiotics (Figure 1). The "golden age" (1940–1960s) saw the discovery of most of the antibiotics in clinical use today through the exploitation of cultivable soil microbes (Waksman platform).[15,16] However, this era crumbled by the end of 1960s as no new compounds with significantly different molecular scaffold and/or mechanism-of-action from existing agents were uncovered from this limited resource of soil bacteria.[14,17] Scientists began to employ synthetic approaches but bacterial cell envelopes have proven to be a huge hurdle for the synthetic compounds.[16,18] Attempts to overcome cell-membrane penetration and efflux issues by formulating sophisticated drug-delivery systems have not yielded satisfactory clinical results.[12] The unfavourable financial return eventually caused pharmaceutical companies to shift their research focus to other diseases.[10,14] As feared by scientific community and healthcare professionals, the post-antibiotic age may now be upon us with the detection of pathogenic bacterial strains being resistant to colistin, the last antibiotic on the shelf.[12]

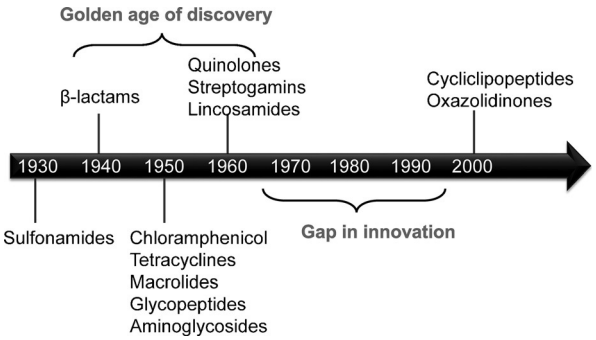

Figure 1. Antibiotic discovery timeline showing the golden era and the gap where no new structurally or functionally distinct antibiotics were found.[7,18]

Despite the seemingly discouraging circumstances, Ling et al. brought exciting news to address this global predicament through their work on uncultured bacteria.[16] Over 99% of soil bacteria in nature are uncultured which reflects their inability to grow on laboratory media.[19] These microbes thus represent an untapped reservoir of valuable compounds.[18,20] A multichannel device known as the isolation chip (iChip)[21] was utilised by the research group to isolate and grow individual bacterial cells in miniature chambers. Prior to returning it to the soil, the device was covered with two semi-permeable membranes so that the cells could receive the environmental nutrients and growth factors needed for viability. Following incubation, the bacterial colonies were grown in vitro and their extracts were screened for antibacterial activity. The hard work paid off with the discovery of teixobactin which is isolated from a newly identified Gram-negative β-proteobacteria, *Eleftheria terrae*.[14,16,20,22,23] Significantly, teixobactin is a potent inhibitor of lipid II, an essential component for the bacterial biosynthesis of cross-linked peptidoglycan.[16]

Therefore, all is not lost in the battle against bacterial infections as modern tools offer great opportunities to revive the old ways of discovering therapeutic compounds from the huge diversity of soil microorganisms.[18,21] This Minireview thus

[a] *V. Ng, Dr. W. C. Chan*
School of Pharmacy, Centre of Biomolecular Sciences
University of Nottingham, University Park
Nottingham, NG7 2RD (UK)
E-mail: weng.chan@nottingham.ac.uk

provides an overview and an update on different classes of lipid II-targeting peptide antibiotics, particularly their chemical and structural aspects, as they are likely to revolutionise the treatment of bacterial infections.

Targeting the Central Component of Peptidoglycan Synthesis

Bacterial cell wall synthesis

Bacterial cell wall, a unique structure crucial for cell survival and integrity, has long been validated as a prominent target for antimicrobials.[24,25] Its main structural component known as peptidoglycan provides bacteria with the mechanical strength to withstand high intracellular osmotic pressure.[26,27] Peptidoglycan is a polymer made up of linear chains of alternating *N*-acetylglucosamine (GlcNAc) and *N*-acetylmuramic acid (MurNAc) amino sugars coupled together by a β-1,4-glycosidic bond.[28] A pentapeptide domain, the sequence of which depends on the species of bacteria, is attached at the N-terminal to the carboxyl moiety of the MurNAc sugar.[29–31] The pentapeptide L-Ala-D-γ-Glu-L-Lys-D-Ala-D-Ala is typically present in most Gram-positive pathogens.[30,32,33] Cross-linking of the glycan chains is then achieved through side-chain-to-backbone amide bond formation between strands of pentapeptide domains.[34–36]

Bacterial cell wall biosynthesis is highly complex, with multiple components and numerous tightly coordinated enzymatic reactions (Figure 2).[34] The two-stage process of peptidoglycan subunit synthesis begins with the assembly of UDP-MurNAc-pentapeptide precursor from UDP-GlcNAc through a series of steps catalysed by MurA-F synthetases in cytoplasmic side.[29] UDP-MurNAc-pentapeptide is then transferred by MraY translocase to the 11-subunit membrane-embedded undecaprenyl phosphate, thereby producing an intermediate called lipid I. Following the coupling of GlcNAc to lipid I, lipid II is formed which carries the complete peptidoglycan subunit (GlcNAc-MurNAc-pentapeptide) that is attached to undecaprenyl phosphate by a pyrophosphate moiety.[27,30,34] During the second stage, lipid II is flipped by MurJ or FtsW flippase to the periplasmic side of inner membrane.[29,37,38] Subsequently, lipid II is incorporated into growing cell wall through transglycosylation and transpeptidation reactions catalysed by the two catalytic domains of penicillin-binding proteins (PBPs).[35,39] The released undecaprenyl pyrophosphate is then shuttled back to the cytosolic face where it is dephosphorylated back into its monophosphate form to be recycled for the next synthesis cycle.[27,34,40]

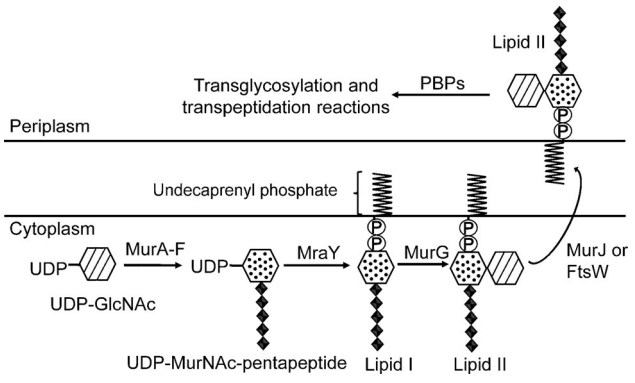

Figure 2. Bacterial cell wall synthesis involves a complex series of enzymatic reactions. Lipid I is produced when the assembled UDP-MurNAc-pentapeptide is attached to the membrane-embedded undecaprenyl phosphate. Another UDP-GlcNAc molecule is transferred to lipid I, thus forming lipid II which is then flipped across the membrane to the periplasmic face where it can be incorporated into the peptidoglycan layer through transglycosylation and transpeptidation reactions.

Lipid II as the therapeutic target

Among the cell wall components, lipid II is one of the most highly sought-after targets for antimicrobials (Figure 3).[34,41] Despite being an essential peptidoglycan precursor, a limited

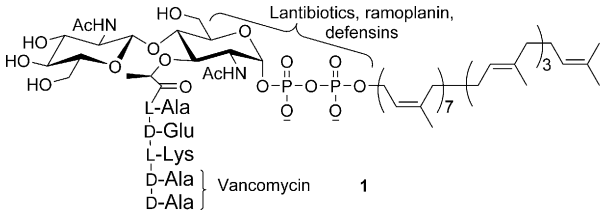

Figure 3. The chemical structure of lipid II (**1**) and binding sites of several lipid II inhibitors. The pentapeptide sequence in Gram-positive bacteria is shown.

Vivian Ng *received her Masters in Pharmacy degree from the University of Nottingham in 2015. She is currently pursuing her Ph.D. degree under the supervision of Dr Weng Chan with research interests focusing on macrocyclic peptides as antibacterial agents.*

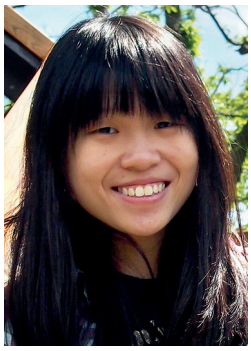

Weng C. Chan *received his Ph.D. degree from the University of Nottingham in 1988, followed by postdoctoral training (1988–1992) under the guidance of Professors Barrie Bycroft and Gordon Roberts. He is currently Associate Professor and Reader in Chemical Biology and has published extensively in the area of solid-phase peptide chemistry, chemical biology and antibacterial agents, with over 85 papers, book chapters and patents. His research themes are focused on medicinal chemistry of macrocyclic antimicrobials and the development of chemical tools for the biological studies of Gram-positive quorum sensing systems.*

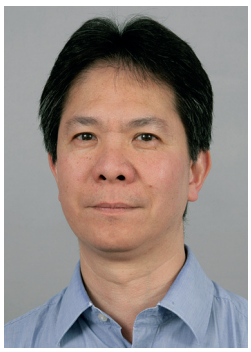

amount of lipid II can be synthesised at a time since there are only approximately 2×10^5 undecaprenyl phosphate molecules present in each cell.[30,42,43] To keep up with the rapid growth of peptidoglycan layer, each lipid II molecule must have a high turnover rate.[44] The lipid II cycle is thus considered to be the rate-limiting step in peptidoglycan biosynthesis, thereby making this lipid intermediate an attractive antibiotic target.[30,45]

The localisation of lipid II on the outside of bacterial cytoplasmic membrane allows it to be easily targeted by antimicrobial agents. In addition, its structural complexity offers several potential binding sites for antibiotics.[27] The pentapeptide domain apparently adopts an upright position and points away from the surface of phospholipid bilayer.[44] Meanwhile, the anchoring of its undecaprenyl phosphate in the membrane strategically places the negatively charged pyrophosphate at the bilayer interface where ionic interactions with positively charged residues or compounds can be easily formed.[17] These groups therefore serve as attractive binding motifs for lipid II inhibitors.[44] Furthermore, lipid II composition is unique within the bacterial kingdom, thereby preventing possible toxic effect of lipid II binders on mammalian cells.[27,46,47]

Research with lipid II was initially restricted by its low abundance and the laborious isolation and purification processes involved.[48,49] However, the availability of membrane enzymes and the attractiveness of lipid II as an antimicrobial target have driven the development of chemical, chemoenzymatic and enzymatic strategies to prepare lipid II.[50–53] The enzymatic approach utilises MraY and MurG activities of membrane preparations to synthesise lipid II in the presence of undecaprenyl phosphate, UDP-MurNAC-pentapeptide and UDP-GlcNAc. As both enzymes have narrow substrate specificity, this method is highly effective and can be easily scaled up.[50,53,54] On the other hand, chemical synthesis enables various structural alterations of lipid II that cannot be achieved with MraY and MurG.[51,52] Its main drawback is the costly chemical reagents. Alternatively, a combination of chemical and enzymatic procedures can be utilised whereby purified MurG is used to convert chemically-synthesised lipid I to lipid II.[54,55] The development of these methods for the preparation of lipid II facilitates the identification and detailed studies of lipid II inhibitors; the choice of preparation of lipid II relies primarily on the lipid II variant that is needed.[54] The interaction of antibacterial agents with lipid II can then be investigated via co-incubation of these compounds with the purified lipid II, followed by extraction and analysis using thin-layer chromatography.[16,56]

Lipid II Inhibitors as Therapeutic Agents

Progress over the last 60 years

The highly dynamic lipid II is the target of several classes of antibiotics that home in on different parts of the molecule.[25,30,34,57] The first discovered example of lipid II inhibitor is vancomycin **2**, a glycopeptide which is used as the last-line treatment for problematic Gram-positive organisms, such as methicillin-resistant *S. aureus* (MRSA).[58] As shown in Figure 4,

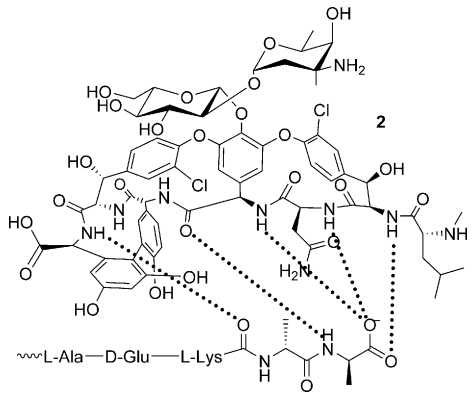

Figure 4. Hydrogen bonds (dotted lines) between vancomycin (**2**) and D-Ala-D-Ala of lipid II.[62]

it binds to the C-terminal D-Ala-D-Ala of the pentapeptide.[59,60] By forming a stable complex with lipid II through five hydrogen bonds and hydrophobic interactions, vancomycin sterically shields this lipid intermediate from PBPs and prevents its subsequent incorporation into the growing peptidoglycan network.[61,62] Bacteria eventually succumb to the high internal osmotic pressure due to weakened cell wall.[17] However, despite the initial excitement of vancomycin being effective against resistant bacteria when it was introduced in 1953, vancomycin-insensitive strains have now surfaced through horizontal gene transfer.[22,63] The clinical resistance can be attributed to operons encoding proteins that mediate the enzymatic replacement of terminal D-Ala with D-Lac or D-Ser, producing low-affinity peptidoglycan building blocks.[63,64] The resulting D-Ala-D-Lac and D-Ala-D-Ser dipeptide motifs reduce the affinity of vancomycin through the loss of a crucial hydrogen bond and the formation of steric hindrance, respectively.[34,62,65,66]

The clinical challenges of vancomycin-resistant staphylococci and enterococci raised research interests into semi-synthetic glycopeptide variants, such as oritavancin and telavancin, which also bind to the C-terminus dipeptide.[67,68] These agents, however, contain extra hydrophobic residues which increase their amphiphilicity.[34] For example, oritavancin **3** carries both 4-epi-vancosamine and 4′-chlorobiphenyl methyl moieties that form additional interactions with the peptidyl cross bridge and D-γ-Gln of lipid II, thus compensating for the lost hydrogen bond observed in vancomycin-resistant strains

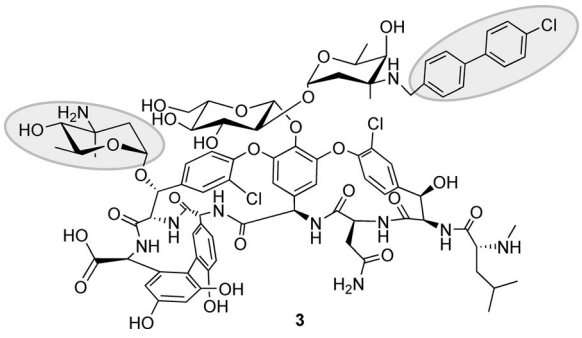

Figure 5. Chemical structure of oritavancin (**3**), with its extra hydrophobic side chains.

(Figure 5).[62,69] As such, oritavancin showed enhanced antibacterial potency against MRSA and other vancomycin-insensitive bacteria.[70,71]

Besides that, the issue with vancomycin resistance revealed binding sites that are prone to mutations and highlighted the need for antibiotics that exploit other less modifiable domains of lipid II.[72] One important class of such agents is the lantibiotics, a group of peptides with the characteristic lanthionine and/or methyllanthionine moieties.[73–75] They can be further divided into two subtypes. Type A lantibiotics are elongated and positively charged whereas type B agents are globular compounds which are either slightly negatively charged or non-charged under neutral conditions.[76,77]

Nisin, a type A lantibiotic produced by *Lactococcus lactis*, has been used as a natural food preservative for decades.[40,78] Hsu et al.[26] have shown that the first ten N-terminal amino acid residues of its rings A and B form a cage that envelopes the pyrophosphate linkage of lipid II instead of the vancomycin-targeted pentapeptide domain. Intermolecular hydrogen bonds between the pyrophosphate and the amide backbone of the rings lock lipid II in a stable complex, thus halting the entire peptidoglycan synthesis.[26,34,56] The primary structure of nisin and its structure–activity relationship (SAR) with lipid II are depicted in Figure 6. However, rings A–B are inactive on their own.[79] It is suggested that upon pyrophosphate cage formation, the rings C–E (C-terminus) of nisin insert into the lipid bilayer, thereby facilitating the assembly of nisin-lipid II pore complex which leads to the lysis of bacteria.[40,80–82] This dual mechanism-of-action makes nisin a very potent Gram-positive antibacterial agent. Unfortunately, the poor pharmaceutical properties of native nisin, such as sensitivity to proteolytic enzymes and poor solubility beyond pH 6, limit its clinical uses.[73,77] Semisynthetic analogues have been developed

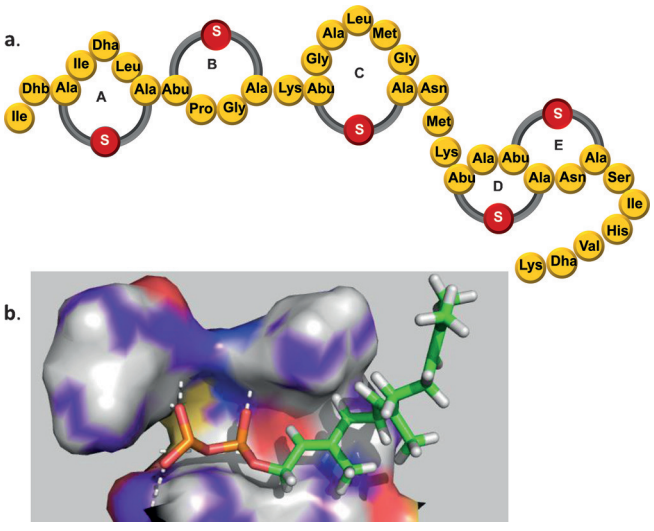

Figure 6. a) Primary structure of nisin. b) The residues of rings A and B of the nisin envelope the pyrophosphate group of a lipid II variant, with intermolecular hydrogen bonds illustrated as white dashes.[26] The solution-structure of nisin–lipid II complex was obtained from Research Collaboratory for Structural Bioinformatics (RCSB) Protein Data Bank (PDB ID: 1WCO) and the figure was generated using PyMOL (http://www.pymol.org/). Abu, aminobutyric acid; Dha, didehydroalanine; Dhb, didehydrobutyrine.

whereby the C–E domain of the natural product was replaced with various lipid substituents. Several of these derivatives that showed enhanced proteolytic stability and potent antibacterial activity hold great therapeutic promise.[82]

The modes of action of other lantibiotics and cyclic peptides, such as ramoplanin and enduracidin, have been extensively reviewed in various literature.[17,34,83–88]

Lipid II inhibition is also achieved by defensins, a large group of endogenous peptides expressed in a wide range of organisms. They form the host epithelial defense system.[89,90] For instance, Schneider et al. demonstrated that plectasin, a defensin isolated from a saprophytic fungus *Pseufoplectania nigrella*, disrupts cell wall biosynthesis through binding to lipid II.[91,92] Defensins from fungi, invertebrates such as maggots and mussels, and humans have shown similar antimicrobial activity.[46,93,94] These studies not only firmly support lipid II as a valuable therapeutic target, but also suggest alternative resources of discovering novel antibacterial agents.

Teixobactin as a promising lipid II inhibitor

The aforementioned teixobactin has been reported to be the first of a new class of lipid II inhibitors that interacts mainly with the pyrophosphate and first sugar moiety of the molecule. Although lipid II is its predominant target, teixobactin also acts on lipid III (undecaprenyl-pyrophosphate-GlcNAc), which plays a pivotal role in the synthesis of another cell wall component called teichoic acid.[3,16] This may lead to the release of autolysins that are anchored by teichoic acid under normal circumstances.[95] Autolysin-mediated digestion of peptidoglycan layers that eventually results in bacterial lysis has, therefore, been proposed as another mode of action of this antibacterial agent.[16,96] As such, teixobactin has demonstrated potent in vitro and in vivo bactericidal activity.[16]

Structural studies have revealed teixobactin (**4**) as a cyclic tetradepsipeptide that comprises 11 amino acids, four of which are of a D-configuration (Figure 7). Apart from *N*-methyl-D-phenylalanine, it contains an unusual amino acid known as L-*allo*-enduracididine. The variants of this amino acid can also be found in enduracidin and mannopeptimycin.[16,87,97,98] The SARs

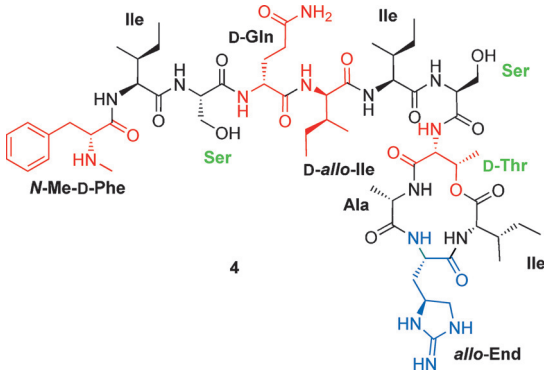

Figure 7. Chemical structure of teixobactin (**4**), with D-amino acids (red), β-hydroxy amino acids (green) and the unusual enduracididine highlighted (blue).

of teixobactin and its lipid targets, however, remain to be addressed. Also, there are still very few preclinical investigations to date for this cyclic depsipeptide and so these preliminary results should be interpreted with caution to avoid possible bias.

Its excellent activity against resistant bacterial strains and the lack of resistance have stimulated tremendous research interests in developing teixobactin into a therapeutic agent.[16] In less than a year after its discovery, the first total synthesis of its analogue by solid-phase peptide synthesis has been successfully executed. Here, the L-*allo*-enduracididine residue found in teixobactin is replaced with the readily available L-Arg.[99] Intramolecular cyclisation, an intrinsically slow process susceptible to side-reactions such as dimerisation and epimerisation of α-C on the C-terminus, is the main synthetic hurdle for all cyclic peptides.[100,101] Following careful consideration of cyclisation position and coupling reagents, Albericio and his co-workers accomplished macrolactamisation of the protected peptide in just one day by using PyAOP/OxymaPure/DIEA without side reactions (Figure 8). However, their synthetic attempt was not

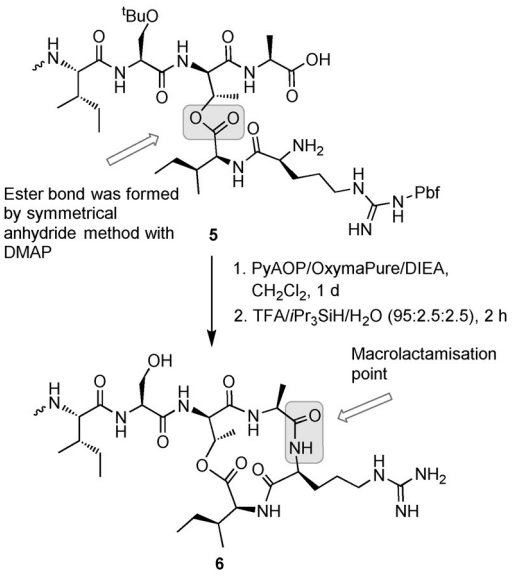

Figure 8. Esterification and macrolactamisation performed by Albericio and his co-workers to obtain a teixobactin analogue. DIEA = *N*,*N*-diisopropylethylamine; DMAP = 4-dimethylaminopyridine; PyAOP = (7-azabenzotriazol-1-yloxy)tripyrrolidinophosphonium hexafluorophosphate; TFA = trifluoroacetic acid.

without setback. The symmetrical anhydride method employed for the esterification between D-Thr and L-Ile required several couplings to attain 97% conversion. Nevertheless, several problems were avoided with the realisation that it was necessary to couple two additional amino acids onto D-Thr prior to the esterification of its hydroxyl group, in order to prevent O→N acyl migration during deprotection of fluorenylmethyloxycarbonyl (Fmoc) from D-Thr. Undesirable formation of diketopiperazine was also prevented by protecting the N-terminus of both L-Ile and L-Arg with an Alloc protecting group instead of Fmoc.[99] With further optimisation of the esterification step, this synthetic strategy would represent a significant advancement. Importantly, the Arg-analogue obtained displayed similar antibacterial activity as teixobactin.[99] Its slight inferior potency against *S. aureus* and *B. subtilis* compared to teixobactin must then be attributed to the L-Arg residue, implying that a constrained guanidino-based side chain with additional chirality is better than its flexible counterpart.

The remaining hurdle to the total synthesis of the natural product is then the availability of the unusual amino acid L-*allo*-enduracididine. The presence of enduracididine in several prominent peptides has inspired efforts to devise its synthesis from simple precursors.[102–104] Achieving the correct chirality at C4 is the primary difficulty in synthesising this amino acid.[103] The earliest reported strategy utilised Bamberger cleavage of methyl L-histidinate and subsequent hydrogenation to give a 1:1 mixture of (2*S*,4*R*)-enduracididine and its (2*S*,4*S*)-diastereomer.[105] Other research groups undertook alternative methods of synthesising the amino acid from commercially available allylglycine, namely, one-pot iminoiodane-mediated tandem aziridation and ring-opening reactions, as well as the Rh-catalysed approach. However, neither diasteroselectivity nor yield was satisfactory.[102,104] The situation may have been turned around as Craig et al. have succeeded in developing a method with desirable stereoselectivity (d.r. > 50:1) and scalability. The required chirality of C4 was obtained through inversion of the hydroxyl group of *trans*-hydroxyproline **7** by mesylation and azide substitution to afford the azido-derivative **8** as shown in Figure 9. Although 10 steps were involved, the high diastereoselectivity ensured that the yield of the desired diastereomer was not compromised.[103]

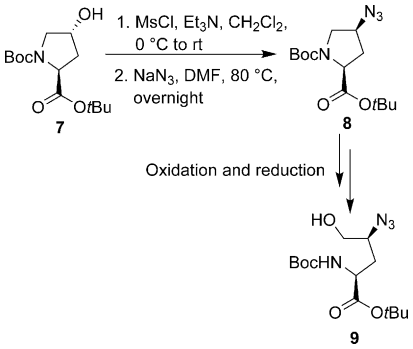

Figure 9. The key mesylation and azide substitution steps that established the chirality of C4. Boc = *tert*-butoxycarbonyl.

With tremendous progress in the synthetic strategies for enduracididine and teixobactin analogue, the total synthesis of the naturally occurring teixobactin would soon be within the grasp of the scientific community.

An insight into the structures of teixobactin and other lipid II binders

Until recently, the different classes of lipid II binders have been regarded as having no significant structural similarities.[17,58] However, a closer examination of the chemical structures of teixobactin (Figure 7) and other lipid II binders including ramo-

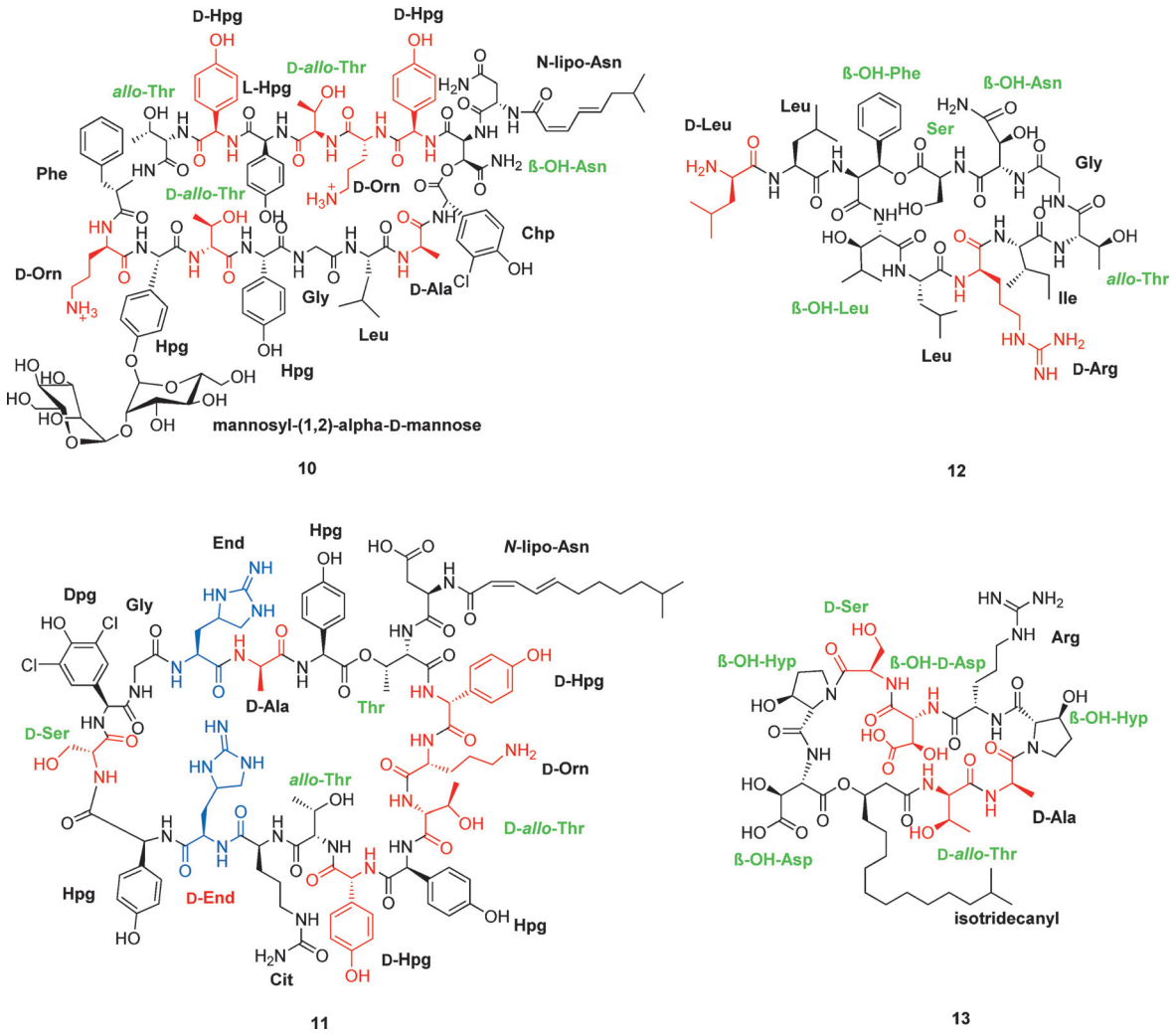

Figure 10. Chemical structures of ramoplanin A2 (**10**), enduracidin A (**11**), katanosin B (**12**) and plusbacin A3 (**13**), with D-amino acids (red), β-hydroxy amino acids (green), and enduracididine (blue) highlighted. Orn, ornithine; Hpg, 4-hydroxyphenylglycine; Dpg, 3,5-dichloro-4-hydroxyphenylglycine; Cit, citrulline.

planin A2, enduracidin A, katanosin B and plusbacin A3 (Figure 10) showed that lipid II is generally favoured by cyclic peptides.[30,87,88,106,107] In contrast to linear peptides, the conformational restriction of cyclic structures contributes to better metabolic stability and improved target binding affinity.[108] Also, the macrocyclic peptides **10**, **11** and **13** (Figure 10) possess lipophilic side chains that are vital for their antimicrobial activities, possibly through membrane insertion or hindering PBPs from reaching lipid II.[17,107] A noticeable structural difference is the unique dimannosyl group that is present only in ramoplanin A2 (**10**), which is likely to provide enhanced hydrolytic stability and solubility.[87,109,110]

Interestingly, in the case of mannopeptimycins, a class of cyclic glycopeptide isolated from *Streptomyces hygroscopicus LL-AC98*,[111] an acyl dissaccharide moiety O-tethered to a tyrosine residue appeared to be crucial for antibacterial activity. Its most potent member, mannopeptimycin ε consists of a cyclic hexapeptide core. Importantly, its D-Tyr residue is O-glycosylated with a dimannosyl moiety carrying an isovaleryl group at the C4-position of the terminal mannose ring while its β-OH-D-*allo*-enduracididine residue has an N-linked mannose group (Figure 11).[98,112–114] Singh et al. demonstrated that mannopeptimycin β which lacks both the isovaleryl and dissacharide displayed poor in vitro and in vivo activity.[111] Further investigations revealed that the isovaleryl moiety is also vital for antibacterial activity.[115] Research began to focus on preparation of semi-synthetic analogues with modifications mainly on this disaccharide side chain.[113–117] Moreover, the replacement of both

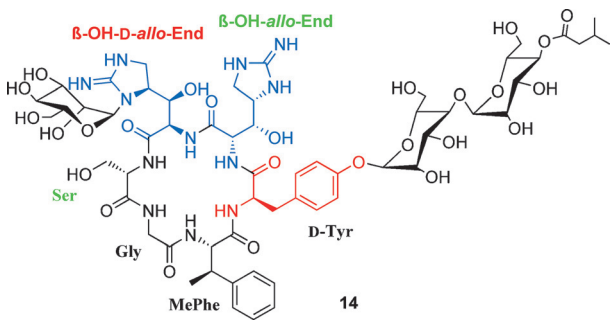

Figure 11. Chemical structure of mannopeptimycin ε (**14**), showing D-amino acid (red), β-hydroxy amino acids (green) and enduracididine (blue).

enduracididine residues of a mannopeptimycin aglycone analogue with L- and D-Arg demonstrated a notable reduction in antimicrobial effect;[118] a similar detrimental effect was observed when the enduracididine residue in teixobactin was replaced with Arg.[99] As limited SAR studies are currently available, the key structural requirements of lipid II inhibitors remain to be established.

Nevertheless, other common structural features can still be seen in these peptides. As the lipid components of bacterial cell walls are negatively charged, antibacterial agents are typically cationic and amphiphilic to facilitate effective charged-mediated binding interactions.[34,119] For instance, the guanidine side chain of teixobactin and katanosin B as well as the ornithine residue of ramoplanin are positively charged.[83,106,120] Another evidence came from a study by Fletcher et al. which demonstrated that the positively charge pyrylium moiety of a small molecule inhibitor BAS00127538 **15** (Figure 12) was essential in forming ionic interactions with the phosphate group.[58] Apart from the pyrylium ring, its indolene and two phenyl rings are predicted to interact with the hydrophobic undecaprenyl residues and the MurNAc of lipid II, respectively.[58,121]

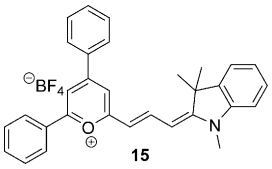

Figure 12. BAS00127538, a small molecule lipid II inhibitor (**15**).

Recently, in an attempt to identify transglycosylase inhibitors through in silico followed by in vitro biochemical screens, a lipid II inhibitor was unexpectedly discovered.[122] This lipid II inhibitor is a tryptamine-containing molecule **16** (Figure 13). Biological evaluation on a subset of related analogues showed that the replacement of the amine group with a guanidine moiety improved their lipid II-binding ability.[123] These compounds thus serve as valuable leads for further optimisation and development of novel low molecular weight lipid II inhibitors. Over the years, there has been a growing interest in peptide antibacterial agents over small molecules as peptides generally exhibit better target specificity and a lower risk of systemic toxicity.[124,125]

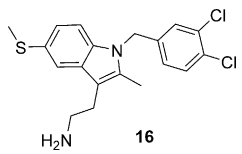

Figure 13. The tryptamine-containing lead compound discovered through in silico screening that binds to lipid II (**16**).

Besides that, all of the lipid II inhibitors discussed above contain D-amino acids and/or non-proteinogenic amino acids that are often synthesised by bacteria.[126] Their presence confers improved in vivo protease stability to these antimicrobial peptides, thereby overcoming pharmacokinetic issues, such as short half-life and poor oral bioavailability that often thwart the therapeutic applications of peptides with only naturally occurring amino acids.[127,128]

Interestingly, as pointed out by von Nussbaum et al.,[106] teixobactin (**4**) is structurally similar to hypeptin **17**, an octapeptide isolated in 1989 from a strain of *Pseudomonas sp*. Hypeptin also showed good antibacterial activity against *S. aureus*.[129] Apart from the same 13-membered ring size, hypeptin possesses similar shape and amino acid composition as teixobactin, with three L-amino acids and one D-amino acid involved in the formation of the cyclic ring.[106] The only major difference is that hypeptin has a shorter exocyclic linear peptide chain. Nev-

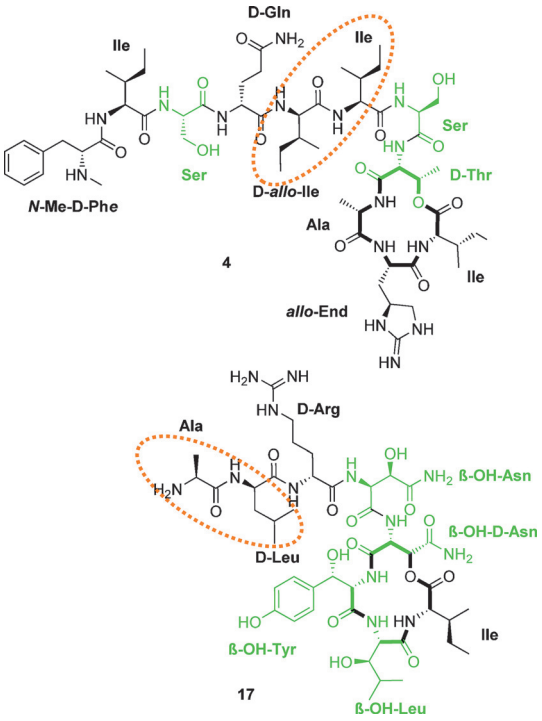

Figure 14. Structural resemblances between teixobactin (**4**) and hypeptin (**17**) with the same ring size as well as similar alipathic dipeptides (circle) and β-hydroxy amino acids (green).

ertheless, it can be seen from Figure 14 that the first two amino acids of hypeptin (Ala-D-Leu) are both aliphatic, which are comparable to the aliphatic dipeptide in teixobactin (D-*allo*-Ile-Ile), thereby suggesting their role in forming hydrophobic interactions with lipid II. β-Hydroxy amino acids are also a characteristic feature of these cyclic peptides. In fact, half of the amino acids of hypeptin are β-hydroxylated. These structural resemblances have led to the suggestion that hypeptin might also interact with lipid II.[106]

Amidst the excitement around teixobactin (**4**), there are concerns that resistance would ultimately emerge especially if the trend of inappropriate antimicrobial use remained widespread. Possible resistance mechanisms include secretion of antibiotic-modifying enzymes and thickening of the bacterial cell wall that impedes the access of teixobactin to its lipid II target.[23] It is also uncertain if resistance is already in existence in nature.[16] However, this should not be a major concern since the producer of teixobactin is a Gram-negative pathogen and so it is unlikely to have transferred its intrinsic resistance mechanisms to its Gram-positive counterparts.[20,23] Additionally, it has been proposed that unlike other resistance mechanisms that involve efflux pumps and enzymes mutations, resistance to lipid II binders does not occur readily due to the difficulty in

modifying a component that is biosynthesised in multiple steps.[30,130,131] As lipid II is a unique non-protein target that cannot be easily altered by simple gene mutations especially at its pyrophosphate and lipid portions, resistance towards teixobactin is unlikely to develop at least for the next few decades.[20,23,47]

Summary and Outlook

AMR is a prevalent global issue that has significant human and financial implications. Apart from curbing the misuse of antibiotics, intensive research into finding new antibiotics is of utmost importance to address the current unmet treatment needs for resistant bacterial strains. The enhanced appreciation of the molecular basis of cell wall biosynthetic pathways and the development of modern tools to explore uncultured soil bacteria provides hope for discovering novel antibacterial agents.

Lipid II has been validated as a prominent molecular target and various lipid II binders with substantial structural diversity have emerged. As great progress has been made and more medicinal chemistry research projects would soon unfold, the battle against bacterial infections might not be lost. The antibacterial efficacy of teixobactin especially against resistant strains offers promise of further clinical applications once proper validation studies have been carried out. However, its current lack of resistance could not be taken for granted and the power of evolution should not be underestimated as resistance might surface during its clinical usage period.[132]

Acknowledgements

We would like to acknowledge financial support from Vice-Chancellor's Scholarship for Research Excellence, University of Nottingham (to VN). We thank Dr Anton Chugunov for the structure file of lipid II which we used to generate the Figure (using PyMOL) in the frontispiece and the graphical abstract (table of contents).

Keywords: antibiotics · lipid II inhibitors · macrocyclic peptides · mannopeptimycin · teixobactin

[1] M. Wainwright, *Mycologist* **1989**, *3*, 21 – 23.
[2] S. A. Alharbi, M. Wainwright, T. A. Alahmadi, H. Bin Salleeh, A. A. Faden, A. Chinnathambi, *Saudi J. Biol. Sci.* **2014**, *21*, 289 – 293.
[3] A. Penesyan, M. Gillings, I. T. Paulsen, *Molecules* **2015**, *20*, 5286 – 5298.
[4] N. Kardos, A. L. Demain, *Appl. Microbiol. Biotechnol.* **2011**, *92*, 677 – 687.
[5] C. M. Kunin, *Ann. Intern. Med.* **1993**, *118*, 557.
[6] G. J. Ebrahim, *J. Trop. Pediatr.* **2010**, *56*, 141 – 143.
[7] C. T. Walsh, T. A. Wencewicz, *J. Antibiot. (Tokyo).* **2014**, *67*, 7 – 22.
[8] M. L. Cohen, *Science* **1992**, *257*, 1050 – 1055.
[9] A. J. Alanis, *Arch. Med. Res.* **2005**, *36*, 697 – 705.
[10] H. W. Boucher, G. H. Talbot, D. K. Benjamin, J. Bradley, R. J. Guidos, R. N. Jones, B. E. Murray, R. A. Bonomo, D. Gilbert, *Clin. Infect. Dis.* **2013**, *56*, 1685 – 1694.
[11] F. C. Tenover, *Am. J. Med.* **2006**, *119*, S3 – 10; discussion S62 – 70.
[12] E. D. Brown, G. D. Wright, *Nature* **2016**, *529*, 336 – 343.
[13] J. O'Neill, *Rev. Antimicrob. Resist.* **2014**, 1 – 16.
[14] C. A. Arias, B. E. Murray, *N. Engl. J. Med.* **2015**, *372*, 1168 – 1170.
[15] R. I. Aminov, *Front. Microbiol.* **2010**, *1*, 134.
[16] L. L. Ling, T. Schneider, A. J. Peoples, A. L. Spoering, I. Engels, B. P. Conlon, A. Mueller, D. E. Hughes, S. Epstein, M. Jones, *Nature* **2015**, *517*, 455 – 459.
[17] J. B. Hamburger, A. J. Hoertz, A. Lee, R. J. Senturia, D. G. McCafferty, P. J. Loll, *Proc. Natl. Acad. Sci. USA* **2009**, *106*, 13759 – 13764.
[18] K. Lewis, *Nature* **2012**, *485*, 439 – 440.
[19] Y. Wang, Y. Chen, Q. Zhou, S. Huang, K. Ning, J. Xu, R. M. Kalin, S. Rolfe, W. E. Huang, *PLoS One* **2012**, *7*, e47530.
[20] C. T. Kåhrström, *Nat. Rev. Microbiol.* **2015**, *13*, 126 – 127.
[21] D. Nichols, N. Cahoon, E. M. Trakhtenberg, L. Pham, A. Mehta, A. Belanger, T. Kanigan, K. Lewis, S. S. Epstein, *Appl. Environ. Microbiol.* **2010**, *76*, 2445 – 2450.
[22] G. Wright, *Nature* **2015**, *517*, 442 – 444.
[23] A. Kali, *J. Clin. Diagn. Res.* **2015**, *9*, DL01.
[24] A. L. Koch, *Clin. Microbiol. Rev.* **2003**, *16*, 673 – 687.
[25] A. Chugunov, D. Pyrkova, D. Nolde, A. Polyansky, V. Pentkovsky, R. Efremov, *Sci. Rep.* **2013**, *3*, 1678.
[26] S.-T. D. Hsu, E. Breukink, E. Tischenko, M. A. G. Lutters, B. de Kruijff, R. Kaptein, A. M. J. J. Bonvin, N. A. J. van Nuland, *Nat. Struct. Mol. Biol.* **2004**, *11*, 963 – 967.
[27] B. de Kruijff, V. van Dam, E. Breukink, *Prostaglandins. Leukot. Essent. Fatty Acids* **2008**, *79*, 117 – 121.
[28] H. Harz, K. Burgdorf, J.-V. Höltje, *Anal. Biochem.* **1990**, *190*, 120 – 128.
[29] J. van Heijenoort, L. Gutmann, *Proc. Natl. Acad. Sci. USA* **2000**, *97*, 5028 – 5030.
[30] E. Breukink, B. de Kruijff, *Nat. Rev. Drug Discov.* **2006**, *5*, 321 – 332.
[31] S. O. Meroueh, K. Z. Bencze, D. Hesek, M. Lee, J. F. Fisher, T. L. Stemmler, S. Mobashery, *Proc. Natl. Acad. Sci. USA* **2006**, *103*, 4404 – 4409.
[32] A. J. F. Egan, J. Biboy, I. van't Veer, E. Breukink, W. Vollmer, *Philos. Trans. R. Soc. B Biol. Sci.* **2015**, *370*, 20150031.
[33] J. Humann, L. L. Lenz, *J. Innate Immun.* **2008**, *1*, 88 – 97.
[34] D. Münch, H.-G. Sahl, *Biochim. Biophys. Acta* **2015**, *1848*, 3062 – 3071.
[35] D.-J. Scheffers, M. G. Pinho, *Microbiol. Mol. Biol. Rev.* **2005**, *69*, 585 – 607.
[36] J. L. Strominger, D. J. Tipper, *Am. J. Med.* **1965**, *39*, 708 – 721.
[37] L.-T. Sham, E. K. Butler, M. D. Lebar, D. Kahne, T. G. Bernhardt, N. Ruiz, *Science* **2014**, *345*, 220 – 222.
[38] T. Mohammadi, V. van Dam, R. Sijbrandi, T. Vernet, A. Zapun, A. Bouhss, M. Diepeveen-de Bruin, M. Nguyen-Distèche, B. de Kruijff, E. Breukink, *EMBO J.* **2011**, *30*, 1425 – 1432.
[39] H.-W. Shih, Y.-F. Chang, W.-J. Li, F.-C. Meng, C.-Y. Huang, C. Ma, T.-J. R. Cheng, C.-H. Wong, W.-C. Cheng, *Angew. Chem. Int. Ed. Engl.* **2012**, *51*, 10123 – 10126.
[40] E. Breukink, B. de Kruijff, *Biochim. Biophys. Acta - Biomembr.* **1999**, *1462*, 223 – 234.
[41] S. F. Oppedijk, N. I. Martin, E. Breukink, *Biochim. Biophys. Acta - Biomembr.* **2016**, *1858*, 947 – 957.
[42] N. E. Kramer, E. J. Smid, J. Kok, B. de Kruijff, O. P. Kuipers, E. Breukink, *FEMS Microbiol. Lett.* **2004**, *239*, 157 – 161.
[43] D. R. Storm, J. L. Strominger, *J. Biol. Chem.* **1974**, *249*, 1823 – 1827.
[44] D. N. Ganchev, H. E. Hasper, E. Breukink, B. de Kruijff, *Biochemistry* **2006**, *45*, 6195 – 6202.
[45] T. Mascher, S. L. Zimmer, T.-A. Smith, J. D. Helmann, *Antimicrob. Agents Chemother.* **2004**, *48*, 2888 – 2896.
[46] A. Essig, D. Hofmann, D. Münch, S. Gayathri, M. Künzler, P. T. Kallio, H.-G. Sahl, G. Wider, T. Schneider, M. Aebi, *J. Biol. Chem.* **2014**, *289*, 34953 – 34964.
[47] B. B. Bonev, E. Breukink, E. Swiezewska, B. De Kruijff, A. Watts, *FASEB J.* **2004**, *18*, 1862 – 1869.
[48] T.-J. R. Cheng, M.-T. Sung, H.-Y. Liao, Y.-F. Chang, C.-W. Chen, C.-Y. Huang, L.-Y. Chou, Y.-D. Wu, Y.-H. Chen, Y.-S. E. Cheng, *Proc. Natl. Acad. Sci. USA* **2008**, *105*, 431 – 436.
[49] H.-W. Shih, K.-T. Chen, T.-J. R. Cheng, C.-H. Wong, W.-C. Cheng, *Org. Lett.* **2011**, *13*, 4600 – 4603.
[50] E. Breukink, H. E. van Heusden, P. J. Vollmerhaus, E. Swiezewska, L. Brunner, S. Walker, A. J. R. Heck, B. de Kruijff, *J. Biol. Chem.* **2003**, *278*, 19898 – 19903.
[51] B. Schwartz, J. A. Markwalder, Y. Wang, *J. Am. Chem. Soc.* **2001**, *123*, 11638 – 11643.

[52] M. S. VanNieuwenhze, S. C. Mauldin, M. Zia-Ebrahimi, B. E. Winger, W. J. Hornback, S. L. Saha, J. A. Aikins, L. C. Blaszczak, *J. Am. Chem. Soc.* **2002**, *124*, 3656 – 3660.
[53] L.-Y. Huang, S.-H. Huang, Y.-C. Chang, W.-C. Cheng, T.-J. R. Cheng, C.-H. Wong, *Angew. Chem. Int. Ed. Engl.* **2014**, *53*, 8060 – 8065.
[54] J. van Heijenoort, *Microbiol. Mol. Biol. Rev.* **2007**, *71*, 620 – 635.
[55] M. C. Lo, H. Men, A. Branstrom, J. Helm, N. Yao, R. Goldman, S. Walker, *J. Am. Chem. Soc.* **2000**, *122*, 3540 – 3541.
[56] H. Brötz, M. Josten, I. Wiedemann, U. Schneider, F. Götz, G. Bierbaum, H. G. Sahl, *Mol. Microbiol.* **1998**, *30*, 317 – 327.
[57] T. Schneider, H.-G. Sahl, *Int. J. Med. Microbiol.* **2010**, *300*, 161 – 169.
[58] S. Fletcher, W. Yu, J. Huang, S. M. Kwasny, J. Chauhan, T. J. Opperman, A. D. MacKerell, E. P. H. de Leeuw, *Drug Des. Devel. Ther.* **2015**, *9*, 2383 – 2394.
[59] B. P. Howden, J. K. Davies, P. D. R. Johnson, T. P. Stinear, M. L. Grayson, *Clin. Microbiol. Rev.* **2010**, *23*, 99 – 139.
[60] J. C. Barna, D. H. Williams, *Annu. Rev. Microbiol.* **1984**, *38*, 339 – 357.
[61] P. E. Reynolds, *Eur. J. Clin. Microbiol. Infect. Dis.* **1989**, *8*, 943 – 950.
[62] D. Münch, I. Engels, A. Müller, K. Reder-Christ, H. Falkenstein-Paul, G. Bierbaum, F. Grein, G. Bendas, H.-G. Sahl, T. Schneider, *Antimicrob. Agents Chemother.* **2015**, *59*, 772 – 781.
[63] C. G. Marshall, I. A. Lessard, I. Park, G. D. Wright, *Antimicrob. Agents Chemother.* **1998**, *42*, 2215 – 2220.
[64] P. Courvalin, *Clin. Infect. Dis.* **2006**, *42*, S25 – S34.
[65] C. T. Walsh, S. L. Fisher, I.-S. Park, M. Prahalad, Z. Wu, *Chem. Biol.* **1996**, *3*, 21 – 28.
[66] T. D. H. Bugg, G. D. Wright, S. Dutka-Malen, M. Arthur, P. Courvalin, C. T. Walsh, *Biochemistry* **1991**, *30*, 10408 – 10415.
[67] F. Van Bambeke, *Curr. Opin. Investig. Drugs* **2006**, *7*, 740 – 749.
[68] P. K. Linden, *Expert Rev. Anti. Infect. Ther.* **2008**, *6*, 917 – 928.
[69] S. J. Kim, L. Cegelski, D. Stueber, M. Singh, E. Dietrich, K. S. E. Tanaka, T. R. Parr, A. R. Far, J. Schaefer, *J. Mol. Biol.* **2008**, *377*, 281 – 293.
[70] L. D. Saravolatz, J. Pawlak, L. B. Johnson, *Int. J. Antimicrob. Agents* **2010**, *36*, 69 – 72.
[71] F. F. Arhin, D. C. Draghi, C. M. Pillar, T. R. Parr, G. Moeck, D. F. Sahm, *Antimicrob. Agents Chemother.* **2009**, *53*, 4762 – 4771.
[72] S.-T. D. Hsu, E. Breukink, G. Bierbaum, H.-G. Sahl, B. de Kruijff, R. Kaptein, N. A. J. van Nuland, A. M. J. J. Bonvin, *J. Biol. Chem.* **2003**, *278*, 13110 – 13117.
[73] M. R. Islam, J.-I. Nagao, T. Zendo, K. Sonomoto, *Biochem. Soc. Trans.* **2012**, *40*, 1528 – 1533.
[74] A. Guder, I. Wiedemann, H. G. Sahl, *Biopolymers* **2000**, *55*, 62 – 73.
[75] N. Schnell, K.-D. Entian, U. Schneider, F. Götz, H. Zähner, R. Kellner, G. Jung, *Nature* **1988**, *333*, 276 – 278.
[76] G. Jung, *Angew. Chemie Int. Ed. English* **1991**, *30*, 1051 – 1068.
[77] A. Arguelles Arias, M. Ongena, B. Devreese, M. Terrak, B. Joris, P. Fickers, *PLoS One* **2013**, *8*, e83037.
[78] C. van Kraaij, W. M. de Vos, R. J. Siezen, O. P. Kuipers, *Nat. Prod. Rep.* **1999**, *16*, 575 – 587.
[79] W. C. Chan, M. Leyland, J. Clark, H. M. Dodd, L.-Y. Lian, M. J. Gasson, B. W. Bycroft, G. C. K. Roberts, *FEBS Lett.* **1996**, *390*, 129 – 132.
[80] H. E. Hasper, B. de Kruijff, E. Breukink, *Biochemistry* **2004**, *43*, 11567 – 11575.
[81] I. Wiedemann, E. Breukink, C. van Kraaij, O. P. Kuipers, G. Bierbaum, B. de Kruijff, H. G. Sahl, *J. Biol. Chem.* **2001**, *276*, 1772 – 1779.
[82] T. Koopmans, T. M. Wood, P. 't Hart, L. H. J. Kleijn, A. P. A. Hendrickx, R. J. L. Willems, E. Breukink, N. I. Martin, *J. Am. Chem. Soc.* **2015**, *137*, 9382 – 9389.
[83] A. Ruzin, G. Singh, A. Severin, Y. Yang, R. G. Dushin, A. G. Sutherland, A. Minnick, M. Greenstein, M. K. May, D. M. Shlaes, *Antimicrob. Agents Chemother.* **2004**, *48*, 728 – 738.
[84] R. Bauer, L. M. T. Dicks, *Int. J. Food Microbiol.* **2005**, *101*, 201 – 216.
[85] Y. Hu, J. S. Helm, L. Chen, X.-Y. Ye, S. Walker, *J. Am. Chem. Soc.* **2003**, *125*, 8736 – 8737.
[86] X. Yin, T. M. Zabriskie, *Microbiology* **2006**, *152*, 2969 – 2983.
[87] X. Fang, K. Tiyanont, Y. Zhang, J. Wanner, D. Boger, S. Walker, *Mol. Biosyst.* **2006**, *2*, 69 – 76.
[88] P. Cudic, J. K. Kranz, D. C. Behenna, R. G. Kruger, H. Tadesse, A. J. Wand, Y. I. Veklich, J. W. Weisel, D. G. McCafferty, *Proc. Natl. Acad. Sci. USA* **2002**, *99*, 7384 – 7389.
[89] T. Ganz, *Nat. Rev. Immunol.* **2003**, *3*, 710 – 720.
[90] E. de Leeuw, C. Li, P. Zeng, C. Li, M. Diepeveen-de Buin, W.-Y. Lu, E. Breukink, W. Lu, *FEBS Lett.* **2010**, *584*, 1543 – 1548.
[91] T. Schneider, T. Kruse, R. Wimmer, I. Wiedemann, V. Sass, U. Pag, A. Jansen, A. K. Nielsen, P. H. Mygind, D. S. Raventós, *Science* **2010**, *328*, 1168 – 1172.
[92] P. H. Mygind, R. L. Fischer, K. M. Schnorr, M. T. Hansen, C. P. Sönksen, S. Ludvigsen, D. Raventós, S. Buskov, B. Christensen, L. De Maria, *Nature* **2005**, *437*, 975 – 980.
[93] J. S. Oeemig, C. Lynggaard, D. H. Knudsen, F. T. Hansen, K. D. Nørgaard, T. Schneider, B. S. Vad, D. H. Sandvang, L. A. Nielsen, S. Neve, *J. Biol. Chem.* **2012**, *287*, 42361 – 42372.
[94] M. Wilmes, B. P. A. Cammue, H.-G. Sahl, K. Thevissen, *Nat. Prod. Rep.* **2011**, *28*, 1350 – 1358.
[95] G. Bierbaum, H. G. Sahl, *Arch. Microbiol.* **1985**, *141*, 249 – 254.
[96] H. J. Rogers, C. W. Forsberg, *J. Bacteriol.* **1971**, *108*, 1235 – 1243.
[97] L. Han, A. W. Schwabacher, G. R. Moran, N. R. Silvaggi, *Biochemistry* **2015**, *54*, 7029 – 7040.
[98] H. He, R. T. Williamson, B. Shen, E. I. Graziani, H. Y. Yang, S. M. Sakya, P. J. Petersen, G. T. Carter, *J. Am. Chem. Soc.* **2002**, *124*, 9729 – 9736.
[99] Y. E. Jad, G. A. Acosta, T. Naicker, M. Ramtahal, A. El-Faham, T. Govender, H. G. Kruger, B. G. De La Torre, F. Albericio, *Org. Lett.* **2015**, *17*, 6182 – 6185.
[100] L. M. De Leon Rodriguez, A. J. Weidkamp, M. A. Brimble, *Org. Biomol. Chem.* **2015**, *13*, 6906 – 6921.
[101] C. J. White, A. K. Yudin, *Nat. Chem.* **2011**, *3*, 509 – 524.
[102] L. Sanière, L. Leman, J.-J. Bourguignon, P. Dauban, R. H. Dodd, *Tetrahedron* **2004**, *60*, 5889 – 5897.
[103] W. Craig, J. Chen, D. Richardson, R. Thorpe, Y. Yuan, *Org. Lett.* **2015**, *17*, 4620 – 4623.
[104] D. E. Olson, J. Y. Su, D. A. Roberts, J. Du Bois, *J. Am. Chem. Soc.* **2014**, 1 – 4.
[105] S. Tsuji, K. Shoichi, T. Shiba, *Chem. Lett.* **1975**, 1281 – 1284.
[106] F. von Nussbaum, R. D. Süssmuth, *Angew. Chemie - Int. Ed.* **2015**, *54*, 6684 – 6686.
[107] S. J. Kim, M. Singh, A. Wohlrab, T.-Y. Yu, G. J. Patti, R. D. O'Connor, M. VanNieuwenhze, J. Schaefer, *Biochemistry* **2013**, *52*, 1973 – 1979.
[108] A. Thakkar, T. B. Trinh, D. Pei, *ACS Comb. Sci.* **2013**, *15*, 120 – 129.
[109] P. Cudic, D. C. Behenna, J. K. Kranz, R. G. Kruger, A. J. Wand, Y. I. Veklich, J. W. Weisel, D. G. McCafferty, *Chem. Biol.* **2002**, *9*, 897 – 906.
[110] M.-C. Wu, M. Q. Styles, B. J. C. Law, A.-W. Struck, L. Nunns, J. Micklefield, *Microbiology* **2015**, *161*, 1338 – 1347.
[111] M. P. Singh, P. J. Petersen, W. J. Weiss, J. E. Janso, S. W. Luckman, E. B. Lenoy, P. A. Bradford, R. T. Testa, M. Greenstein, *Antimicrob. Agents Chemother.* **2003**, *47*, 62 – 69.
[112] M. Adinolfi, D. Giacomini, A. Iadonisi, A. Quintavalla, S. Valerio, *European J. Org. Chem.* **2008**, *2008*, 2895 – 2899.
[113] R. S. Babu, S. R. Guppi, G. A. O'Doherty, *Org. Lett.* **2006**, *8*, 1605 – 1608.
[114] K. S. Olivier, M. S. Van Nieuwenhze, *Org. Lett.* **2010**, *12*, 1680 – 1683.
[115] R. G. Dushin, T.-Z. Wang, P.-E. Sum, H. He, A. G. Sutherland, J. S. Ashcroft, E. I. Graziani, F. E. Koehn, P. A. Bradford, P. J. Petersen, *J. Med. Chem.* **2004**, *47*, 3487 – 3490.
[116] P.-E. Sum, D. How, N. Torres, H. Newman, P. J. Petersen, T. S. Mansour, *Bioorg. Med. Chem. Lett.* **2003**, *13*, 2607 – 2610.
[117] P. J. Petersen, T. Z. Wang, R. G. Dushin, P. A. Bradford, *Antimicrob. Agents Chemother.* **2004**, *48*, 739 – 746.
[118] S. Fuse, H. Koinuma, A. Kimbara, M. Izumikawa, Y. Mifune, H. He, K. Shin-ya, T. Takahashi, T. Doi, *J. Am. Chem. Soc.* **2014**, *136*, 12011 – 12017.
[119] D. G. Brown, T. L. May-Dracka, M. M. Gagnon, R. Tommasi, *J. Med. Chem.* **2014**, *57*, 10144 – 10161.
[120] M. Cheng, J. X. Huang, S. Ramu, M. S. Butler, M. A. Cooper, *Antimicrob. Agents Chemother.* **2014**, *58*, 6819 – 6827.
[121] K. M. Varney, A. M. J. J. Bonvin, M. Pazgier, J. Malin, W. Yu, E. Ateh, T. Oashi, W. Lu, J. Huang, M. Diepeveen-de Buin, et al., *PLoS Pathog.* **2013**, *9*, e1003732.
[122] A. Derouaux, S. Turk, N. K. Olrichs, S. Gobec, E. Breukink, A. Amoroso, J. Offant, J. Bostock, K. Mariner, I. Chopra, *Biochem. Pharmacol.* **2011**, *81*, 1098 – 1105.
[123] I. Sosič, M. Anderluh, M. Sova, M. Gobec, I. Mlinarič RaŠčan, A. Derouaux, A. Amoroso, M. Terrak, E. Breukink, S. Gobec, *J. Med. Chem.* **2015**, *58*, 9712 – 9721.

[124] D. J. Craik, D. P. Fairlie, S. Liras, D. Price, *Chem. Biol. Drug Des.* **2013**, *81*, 136 – 147.
[125] K. Fosgerau, T. Hoffmann, *Drug Discov. Today* **2015**, *20*, 122 – 128.
[126] A. D. Radkov, L. A. Moe, *Appl. Microbiol. Biotechnol.* **2014**, *98*, 5363 – 5374.
[127] L. Gentilucci, R. De Marco, L. Cerisoli, *Curr. Pharm. Des.* **2010**, *16*, 3185 – 3203.
[128] D. P. McGregor, *Curr. Opin. Pharmacol.* **2008**, *8*, 616 – 619.
[129] H. Hinoo, T. Hattori, Y. Kimura, T. Yoshida, J. Shoji, K. Hirooka, *J. Antibiot. (Tokyo).* **1989**, *42*, 1460 – 1464.
[130] T. J. Oman, T. J. Lupoli, T. S. A. Wang, D. Kahne, S. Walker, W. a. Van Der Donk, *J. Am. Chem. Soc.* **2011**, *133*, 17544 – 17547.
[131] T. Schneider, H.-G. Sahl, *Curr. Opin. Investig. Drugs* **2010**, *11*, 157 – 164.
[132] **Note added in proof**: Since the completion of this article, two new reports have been published on the total synthesis of teixobactin and its analogues, as well as limited SAR: a) A. M. Giltrap, L. J. Dowman, G. Nagalingam, J. L. Ochoa, R. G. Linington, W. J. Britton, R. J. Payne, *Org. Lett.* **2016**, *18*, 2788 – 2791; b) H. Yang, K. H. Chen, J. S. Nowick, *ACS Chem. Biol.* **2016**, DOI: 10.1021/acschembio.6b00295.

Received: March 18, 2016
Published online on July 8, 2016

ChemPubSoc Europe

DOI: 10.1002/cmdc.201500589

CHEMMEDCHEM Full Papers

Alkylation of Staurosporine to Derive a Kinase Probe for Fluorescence Applications

Alexander J. M. Disney, Barrie Kellam, and Lodewijk V. Dekker*[a]

The natural product staurosporine is a high-affinity inhibitor of nearly all mammalian protein kinases. The labelling of staurosporine has proven effective as a means of generating protein kinase research tools. Most tools have been generated by acylation of the 4′-methylamine of the sugar moiety of staurosporine. Herein we describe the alkylation of this group as a first step to generate a fluorescently labelled staurosporine. Following alkylation, a polyethylene glycol linker was installed, allowing subsequent attachment of fluorescein. We report that this fluorescein–staurosporine conjugate binds to cAMP-dependent protein kinase in the nanomolar range. Furthermore, its binding can be antagonised with unmodified staurosporine as well as ATP, indicating it targets the ATP binding site in a similar fashion to native staurosporine. This reagent has potential application as a screening tool for protein kinases of interest.

Introduction

The natural product staurosporine, first described in 1977,[1] has been demonstrated to be a high-affinity inhibitor of nearly all mammalian protein kinases.[2,3] Staurosporine binds to the ATP binding site of the kinase, making multiple contacts with the hinge region and the N- and C-terminal lobes of the catalytic domain. Staurosporine itself is not used as a therapeutic agent, but has proven invaluable in the discovery of novel anticancer drugs based on kinase inhibition.[4,5] Furthermore, it has been modified to generate functionalised molecular tools such as immobilised staurosporine to capture kinases,[6] a staurosporine-based photoaffinity probe,[7] a cell-permeable affinity-based probe for kinome labelling,[8] a highly selective bivalent staurosporine-tethered peptide ligand,[9] and a fluorescent staurosporine conjugate.[10]

The molecular interactions between staurosporine and numerous protein kinase catalytic domains have been determined in great detail in co-crystallisation experiments.[11–16] The main polar interaction points on staurosporine involve the lactam oxygen and nitrogen atoms, the tetrahydropyran moiety, as well as the 3′-methoxy and 4′-methylamine side groups (see Supporting Information for numbering). Interactions at the 4′-methylamine contribute to binding, and the number of interactions taking place at this group appears to correlate with affinity. Both hydrogen bond and ionic interactions of this group have been implicated in binding, with different kinases engaging it in a different fashion.[17] For example, cAMP-dependent protein kinase (PKA) is predicted to make a hydrogen bond as well as an ionic interaction, whilst the EGF receptor kinase relies on an ionic interaction and Fyn kinase on a hydrogen bond interaction with this group.

To derivatise staurosporine, most strategies have relied upon modification of this 4′-methylamine group, usually involving an acylation step. The resulting amide may be predicted to display decreased basicity with respect to the nitrogen atom, affecting its ability to act as hydrogen bond acceptor. As such, the acyl-based chemical modification may result in some loss of affinity of the probe relative to staurosporine itself. This has indeed been suggested as one of the reasons why, compared with staurosporine, a probe obtained by acylation of the secondary amine showed decreased affinity to the kinase ASK1.[10] However, acylated tools have been shown to retain kinase binding and in some cases even showed a slight increase in affinity (e.g., Ref. [8]). As an alternative to the acylation modification, we have sought to derivatise staurosporine using alkylation of the 4′-methylamine, which does not lead to formation of an amide. We report a high-affinity fluorescent ligand, consisting of staurosporine linked to fluorescein via a polyethylene glycol linker and show that this can be used to interrogate the ATP binding site by simple fluorescence polarisation detection. We show that the ligand is useful to predict compound interactions at the ATP binding site of PKA and that the ligand is viable for the exploration of a wide range of different kinases.

Results

Synthesis

Staurosporine (**1**) (Scheme 1) was 4′-N alkylated with a variety of alkyl halides of which methyl bromoacetate was found to

[a] *Dr. A. J. M. Disney, Prof. B. Kellam, Dr. L. V. Dekker*
School of Pharmacy, Centre for Biomolecular Sciences
University of Nottingham, Nottingham NG7 2RD, Nottinghamshire (UK)
E-mail: lodewijk.dekker@nottingham.ac.uk

Supporting information and the ORCID identification number(s) for the author(s) of this article can be found under http://dx.doi.org/10.1002/cmdc.201500589.

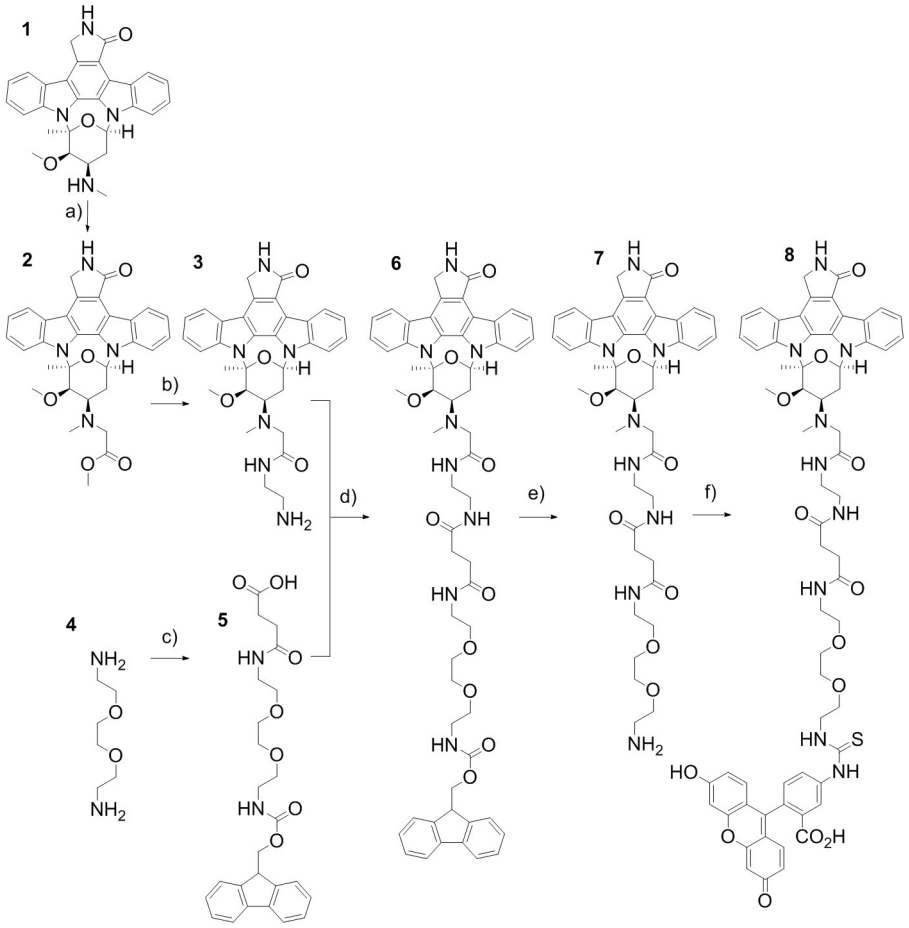

Scheme 1. *Reagents and conditions*: a) methyl bromoacetate, potassium carbonate, THF, RT, 48 h; b) ethylenediamine, RT, 48 h; c) 1. succinic anhydride, MeCN, RT, 12 h, 2. Fmoc-Cl, $NaHCO_3$, MeCN, H_2O, RT, 12 h; d) HBTU, DIPEA, DMF, RT, 12 h; e) diethylamine, THF, RT, 4 h; f) fluorescein isothiocyanate, DIPEA, DMF, RT, 48 h.

afford the *N*-acetyl methyl ester **2** in quantitative yield. Compound **2** was sufficiently pure to use without further purification so was aminolysed directly using ethylenediamine to give compound **3** in quantitative yield. Compound **3** provided a suitable moiety for further derivatisation of staurosporine with dyes, linkers or potentially other functionalities.

To derivatise compound **3**, we chose one of the shortest and simplest commercially available polyethylene glycol linkers available. Shorter linker strategies were attempted, but did not yield product with viable solubility and optical properties (not shown). Compound **3** was acylated using a fluorenylmethoxycarbonyl (Fmoc)-protected diamino-diethylene glycol linker capped at the other amino terminus with a succinic acid group (**5**) to afford **6**. Compound **5** was originally prepared by reacting commercially available 2,2-(ethylenedioxy)bisethylamine (**4**) with succinic anhydride and Fmoc-Cl, with a yield of 41%.[18] Compound **5** was subsequently acylated to the primary amine of **3** using *O*-(benzotriazol-1-yl)-*N*,*N*,*N*′,*N*′-tetramethyluronium hexafluorophosphate (HBTU) as the coupling agent, followed by preparative HPLC, affording **6** in a yield of 47%.

Compound **6** was deprotected using diethylamine, releasing the free amine **7**, which was again purified by RP-HPLC. The overall yield of 43% was somewhat disappointing, so the final step was repeated as a two-step one-pot procedure. Compound **6** was deprotected and then immediately coupled with fluorescein isothiocyanate to generate compound **8** with a slightly improved yield of 52%. The overall yield for the preparation of compound **8** from staurosporine (**1**) was 24%. NMR analysis demonstrated that the tethering point for the linker was indeed the 4′-methylamine.

Optical properties

Absorption and emission spectra of compound **8** and fluorescein isothiocyanate were compared. Figure 1 demonstrates that **8** displayed similar absorbance and emission profiles to those of fluorescein isothiocyanate itself. Thus the basic spectral behaviour of the fluorophore was not affected by attachment of the modified staurosporine. Next we evaluated the anisotropic properties of **8** and compared these again to those of fluorescein isothiocyanate. Fluorescein isothiocyanate provoked a full depolarisation of incident polarised light at a concentration of 10 nM (Figure 1c). Compound **8** also depolarised the incident polarised light; however, the concentration required was higher. The minimum concentration of **8** resulting

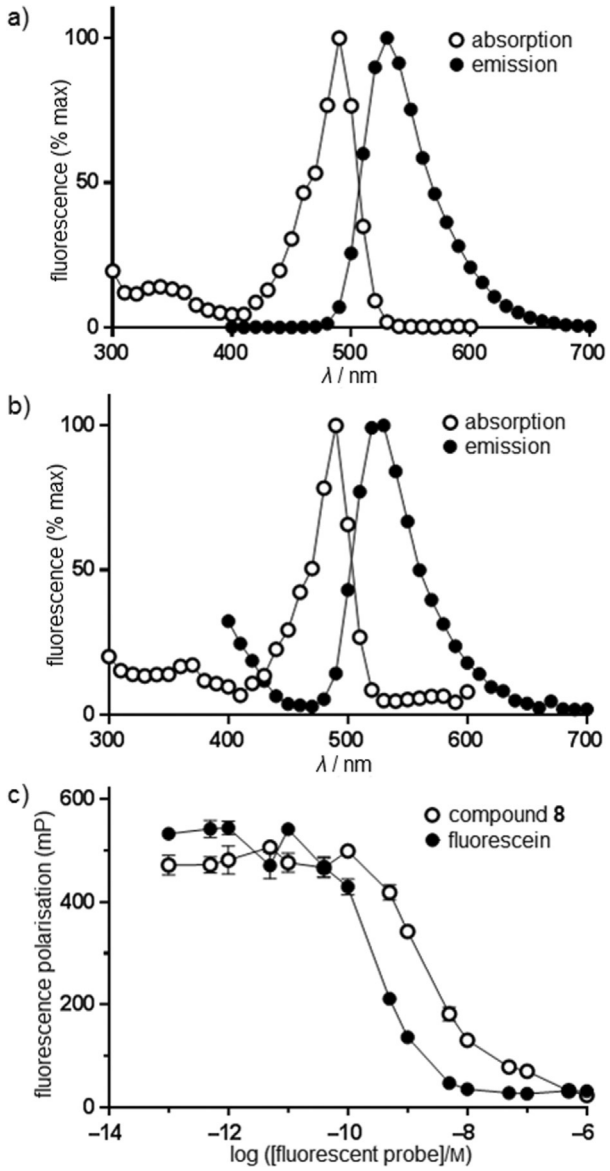

Figure 1. Spectral behaviour of compound **8** in comparison with fluorescein isothiocyanate. Solutions of a) fluorescein isothiocyanate and b) compound **8** were prepared at a concentration of 10 μM. Absorption and emission spectra were recorded by measuring emission at 650 nm with excitation over 300–600 nm, and by measuring emission over 400–700 nm with excitation at 350 nm, respectively. c) Fluorescence polarisation in response to fluorescein isothiocyanate and compound **8**. A set of serially diluted wells were prepared in triplicate for each of these, and fluorescence polarisation was measured as described in the Experimental Section.

in near complete depolarisation was 50 nM (Figure 1c). This concentration was used to measure kinase binding in subsequent assays.

Evaluation of kinase binding

It is predicted that if compound **8** can bind to PKA, the depolarisation observed above (Figure 1c) will be reversed. Figure 2a shows that the fluorescence polarisation signal of 50 nM compound **8** was reversed upon incubation with a preparation of tetrameric PKA enzyme (Figure 2a, 'total'), indicating that the kinase bound the probe. Because this PKA preparation is semi-pure, it could be hypothesised that the reversal was not due to binding to PKA, but to nonspecific binding to non-PKA proteins in the preparation. To assess this, a parallel incubation was carried out with excess unmodified ('cold') staurosporine which would prevent specific binding of the probe. As expected, excess staurosporine did not affect the polarisation signal in the absence of PKA (as this is a signal derived from the probe itself). In the presence of PKA, some reversal of the polarisation signal was observed even in the presence of excess 'cold' staurosporine (Figure 2a, 'nonspecific'), which we attributed to a certain level of nonspecific interaction of the probe. The difference between the total and nonspecific was then taken as specific binding to PKA. This was used throughout the study to assess probe binding. The specific binding of **8** to PKA was time dependent (Figure 2b). Increased incubation times were associated with a decrease in the variability of the signal. To estimate the binding constant, the probe was incubated with increasing concentrations of PKA. Specific binding of compound **8** to PKA was saturable in a way that is compatible with a one-site binding event at the kinase (Figure 2c). The binding constant observed for binding of compound **8** was 44 nM. This is compatible with the K_d value recorded previously for unmodified staurosporine binding to PKA.[3,17,19]

To verify that **8** could be displaced from PKA, it was incubated at a concentration of 50 nM with PKA in the presence of increasing concentrations of unmodified staurosporine. As shown in Figure 2d, staurosporine inhibits the binding of compound **8** to PKA in the low nanomolar range with a pIC_{50} value of 8.0 ± 0.1 ($IC_{50} = 11$ nM). Similarly, binding of **8** to PKA was antagonised by ATP in the presence of $MgCl_2$, indicating it interacted with the ATP binding site of PKA (Figure 2e).

Reversible binding with purified PKA catalytic subunit

The above-mentioned experiments were conducted using a semi-pure preparation which used the whole PKA tetramer of two catalytic subunits and two regulatory subunits bound together. The binding characteristics of compound **8** indicate binding to a bona fide ATP binding site. However, as shown in Figure 2a, a degree of nonspecific binding decreased the antagonisable window. We measured the binding of compound **8** to a purer PKA catalytic subunit preparation. The binding window for specific binding (as assessed using the procedure in Figure 2a) increased from 10–20 mP units using semi-pure PKA tetramer to ~50 mP units for the purer PKA catalytic subunit (Figure 3a).

The above data indicate that compound **8** can be used to identify compounds that bind to the ATP binding site of PKA. To confirm this further, H-7, a known ATP binding site blocker unrelated to staurosporine was tested in the fluorescence polarisation binding assay described in Figure 3a. As shown in Figure 3b, H-7 antagonised the binding of compound **8** to PKA in a concentration-dependent fashion, with an IC_{50} value of 3.9 μM. This value is similar to the K_i reported for antagonism of PKA enzyme activity.[20]

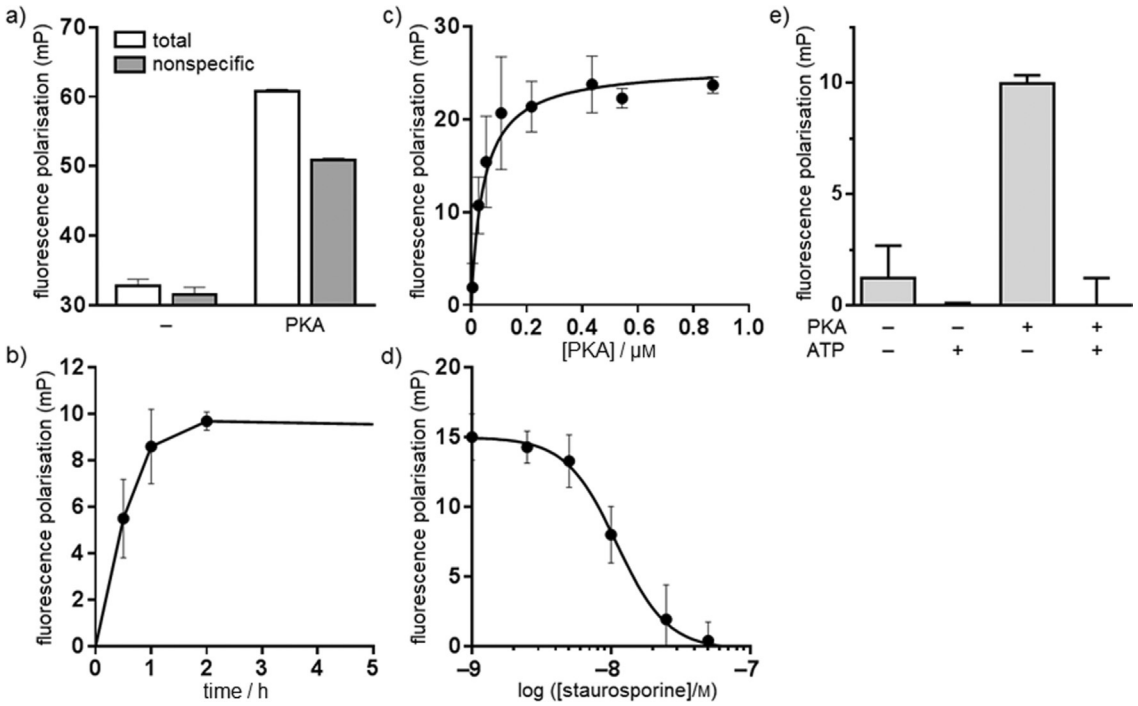

Figure 2. Binding of compound **8** to PKA. a) PKA (200 nM) was incubated with compound **8** (50 nM) for 120 min at 20 °C in the presence (nonspecific) or absence (total) of excess unmodified staurosporine, after which the fluorescence polarisation signal was determined (mean ± SEM, $n = 2–3$). b) Time dependence of specific binding of compound **8** to 200 nM PKA (mean ± SEM, $n = 3$). c) Concentration dependence of specific binding of PKA to 50 nM compound **8** (mean ± SEM, $n = 3$); nonlinear regression (one-site binding site algorithm) was performed in Prism (version 6.04, GraphPad Software, La Jolla, CA, USA). d) Competition of binding of compound **8** (50 nM) to 200 nM PKA with unlabelled staurosporine (mean ± SEM, $n = 3$); nonlinear regression [log(agonist) vs. response, variable slope (four parameters)] was performed in Prism. e) Compound **8** binds to the ATP binding site of PKA: compound **8** (50 nM) was incubated with 200 nM PKA in the presence or absence of $MgCl_2$ [1 mM] with ATP [1 mM], and specific binding was measured as described in panel a) (mean ± SEM, $n = 2–3$).

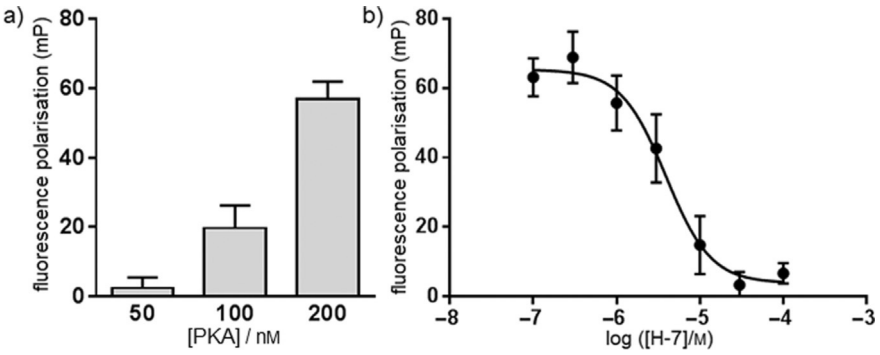

Figure 3. Antagonism of compound **8** binding to PKA by known kinase inhibitor H-7. a) Binding of compound **8** to pure PKA catalytic domain. Three concentrations of the catalytic subunit from bovine PKA were incubated with 50 nM compound **8** for 120 min in the presence or absence of excess unmodified staurosporine, after which the specific fluorescence polarisation signal was determined as described in Figure 2a (mean ± SEM, $n = 2–3$). b) Compound **8** (50 nM) was incubated with 200 nM PKA in the presence of increasing concentrations of H-7, and specific binding was measured as described in Figure 2a (mean ± SEM, $n = 6$). Data were fitted in GraphPad Prism (version 6.04) [log(agonist) vs. response, variable slope (four parameters)].

Interaction of compound 8 with other kinases

Whilst the experiments above indicate that compound **8** is a useful probe to identify binding of compounds to the ATP binding site of PKA, the promiscuous nature of staurosporine from which compound **8** was derived suggests that compound **8** could be a more universal kinase probe. Using the ability of the staurosporine moiety of compound **8** to inhibit kinase activity, we tested this notion by evaluating the inhibition of a range of kinases by compound **8** and comparing this with PKA inhibition.

Table 1 shows the inhibition of 50 kinases (including PKA) by compound **8** at both 100 nM and 1 μM. It can be observed that compound **8** at a concentration of 100 nM inhibited PKA by about 60%. Given that compound **8** is a good fluorescence

Table 1. Inhibitory activity of compound **8** against a range of serine/threonine and tyrosine kinases.[a]

Kinase	[**8**]/M		Kinase	[**8**]/M	
	10^{-6}	10^{-7}		10^{-6}	10^{-7}
MKK1	44±1	64±2	CK2	117±1	115±10
JNK1	83±3	82±4	DYRK1A	10±1	55±12
p38a MAPK	121±6	98±11	NEK6	82±35	84±12
RSK1	3±1	6±3	TBK1	3±2	7±2
PDK1	4±1	24±8	PIM1	20±1	70±3
PKBα	42±1	75±2	SRPK1	25±1	85±4
SGK1	34±1	77±9	EF2K	97±12	94±1
S6K1	5±1	59±16	HIPK2	74±2	93±1
PKA	8±0	40±2	PAK4	12±6	40±15
ROCK 2	4±0	54±3	MST2	4±1	10±4
PRK2	35±19	98±16	MLK3	13±1	23±5
PKCα	8±1	40±0	TAK1	4±1	53±9
PKD1	16±1	59±6	IRAK4	13±0	37±3
MSK1	6±1	49±13	RIPK2	90±2	93±9
CAMKKb	6±0	60±2	TTK	18±0	54±5
CAMK1	18±2	87±6	Src	2±1	20±14
SmMLCK	49±2	91±7	Lck	13±2	40±1
CHK2	20±0	56±5	BTK	13±2	47±1
GSK3β	11±0	47±11	JAK2	3±0	4±0
PLK1	101±1	101±4	SYK	26±5	49±9
Aurora B	11±1	24±2	EPHA2	91±8	101±5
LKB1	101±1	116±2	HER4	88±8	92±16
AMPK	1±0	1±0	IGF-1R	56±5	116±5
MARK3	1±0	13±11	TrkA	4±0	6±1
CK1δ	118±10	109±2	VEGFR	7±1	25±4

[a] Compound **8** was tested at 10^{-6} and 10^{-7} M, and values are the percent kinase activity remaining. Data are the average of duplicate observations, with error bars indicating the spread between the duplicates. A repeat experiment was conducted with the same results.

polarisation probe for PKA, this suggests that a kinase that is inhibited by compound **8** to a similar extent could be detected by compound **8** using fluorescence polarisation.

Kinases that were inhibited by compound **8** to a similar extent as PKA include RSK1, PDK1, ROCK 2, PKCα, MSK1, GSK3β, Aurora B, AMPK (hum), MARK3, TBK1, PAK4, MST2, MLK3, IRAK4, Src, Lck, BTK, JAK2, TrkA, and VEG-FR. Therefore, compound **8** would be predicted to be suitable to assay these kinases by fluorescence polarisation. Kinases that were clearly not inhibited by compound **8** at the concentrations tested include JNK1, p38a MAPK, PLK1, LKB1, CK1δ, CK2, EF2K, NEK6, HIPK2, EPH-A2, and HER4; therefore, this probe would not appear to be suitable to assay these kinases. Some of these kinases (p38a MAPK, CK1δ, NEK6, CK2, EPH-A2, EF2K and to a large extent JNK1) are, in fact, not sensitive to staurosporine itself (not shown), and for others it appears that the modification has led to a loss of binding. A number of kinases appeared to be inhibited by compound **8** but to a lesser extent than PKA, and for these kinases it would need to be established individually whether compound **8** would make a viable tool to interrogate the ATP binding site using fluorescence polarisation.

Discussion

A fluorescein-labelled staurosporine derivative (**8**) has been prepared by alkylation in five steps with an overall yield of 24%. Fluorescein is widely used as fluorophore in fluorescence polarisation assays. The coupling of staurosporine to the fluorophore did not affect the basic fluorescent characteristics of the fluorophore, and the resulting probe was capable of depolarising plane-polarised light, indicating its potential application in fluorescence polarisation assays. Using fluorescence polarisation, compound **8** was shown to bind to PKA in the nanomolar range. Compound **8** binding was successfully antagonised using unmodified staurosporine as well as ATP and H-7, indicating it interacted with the ATP binding site of the kinase and could monitor inhibitor binding.

The most frequently employed method for attachment to staurosporine has been acylation of the 4′-methylamine. Although the 4′-methylamine is oriented towards solvent-accessible space, it is involved in binding to the protein. In many crystal structures the 4′-methylamine can be seen to be binding to acidic side chain residues in the kinase; for example, Glu127 and Glu170 in the case of PKA,[21] and Asp807 in the case of ASK1.[22] For kinases that hydrogen bond via aspartate or glutamate to the 4′-methylamine nitrogen of staurosporine, a 7- to 80-fold decrease in affinity was observed upon acylation of this moiety to introduce a PEG linker.[9] However, acylation did not affect the inhibition of c-Src by a recently developed covalently binding affinity probe.[8] The role of the 4′-methylamine and tetrahydropyran functionality of staurosporine may be inferred when comparing the IC_{50} values for staurosporine and K252c (staurosporine aglycone) which for PKC were 9 and 680 nM, respectively.[23] A similar but larger difference was observed for PKA (40 and $>10\,000$ nM).[23] This difference in IC_{50} suggests the importance of the tetrahydropyran functionality that bears the 4′-methylamine with respect to retaining its bonding interactions with the target protein. The tetrahydropyran ring of staurosporine is documented as being flexible, and conformational changes have been observed which include movement of the 4′-methylamine.[24] This flexibility of the tetrahydropyran may be partly responsible for the broad-ranging affinity of staurosporine.

Acylation of the amine introduces an electron-withdrawing carbonyl group that greatly decreases the basicity of the nitrogen. In alkylating rather than acylating the 4′-methylamine, the basicity of the nitrogen is predicted to be preserved, while also maintaining the nitrogen atom's ability to act as a hydrogen bond acceptor.[25] In the work presented herein, alkylation of the 4′-methylamine has successfully generated a functional probe that has retained high affinity. As compound **8** has been demonstrated to bind reversibly to the ATP binding site of PKA, it could be employed to demonstrate whether a known inhibitor binds in a competitive or allosteric manner, as only competitive blockers are expected to displace compound **8**. This was confirmed using H-7, a competitive blocker of the ATP binding site on PKA. Additionally, the fact that H-7 displaced the probe from PKA indicates that the fluorescence po-

larisation format used for compound **8** could be readily used in the screening of ATP-competitive inhibitors.

Conclusions

Staurosporine was derivatised successfully via a five-step alkylation route to yield a fluorescein-based fluorescent tool. The linking and labelling strategy could be readily modified to introduce a wide range of other fluorophores or other moieties to staurosporine. The tool developed here interacted with PKA at the ATP binding site and was shown to be useful to monitor inhibitor binding at this site. We established for a large number of kinases whether or not the tool developed in this study is predicted to interact. This suggests that it is useful as probe for the identification of ATP-competitive blockers for numerous kinases.

Experimental Section

General: Solvents were obtained from Fisher and used without further purification. Reagents were obtained from Sigma–Aldrich unless otherwise stated. ^{1}H and ^{13}C NMR spectra were obtained with Bruker AV(I) 400 MHz, Bruker AV(III) 400 MHz, and Bruker AV(III) 500 MHz instruments. Mass spectra (ToF ES±) were recorded on a micromass LCT. Reversed-phase HPLC was performed on a Waters 2525 gradient module coupled with a Waters 2487 dual absorbance detector set at λ 254 and 366 nm. A linear gradient was run over 35 min, from 100/0 phase 1 (deionised and degassed H_2O with 0.05% trifluoroacetic acid) to 100/0 phase 2 (90% MeCN, 10% H_2O with 0.05% trifluoroacetic acid). The analytical column used was a Phenominex Luna C_8, 150×4.6 mm, 5 μm, at a flow rate of 1 mL min^{-1}. The semipreparative column was a YMC C_8 150×10 mm, 5 μm, at a flow rate of 3.00 mL min^{-1}. The preparative column was a Phenominex Luna C_8, 150×30 mm, 5 μm, at a flow rate of 20 mL min^{-1}. Retention times (t_R) are given in minutes.

PKA was used in two forms: semi-pure PKA from bovine heart as a whole tetramer (Sigma–Aldrich P5511), and PKA catalytic subunit purified from P5511 by column chromatography (Sigma–Aldrich P2645). PKA was added to the assay at the required number of enzyme units, and this was converted into a molar value using the specific activity of the P2645 preparation as a guide (10 units per μg protein, one unit of PKA being equivalent to 2.3 pmol of kinase).

Fluorescence polarisation assays were performed in 384-well plates in a final volume of 50 μL at RT in 0.01 M phosphate buffer, 0.0027 M potassium chloride, and 0.137 M sodium chloride, pH 7.4. Fluorescence polarisation was measured on a PerkinElmer Wallac Envision 2104 Multilabel plate-reading spectrophotometer using 485 nm excitation and 535 nm emission filters, suitable for measurement of fluorescein. Fluorescence polarisation was determined by measuring the parallel and perpendicular fluorescence emission intensity with respect to the polarised excitation light and is expressed in millipolarisation (mP) units following Equation (1):

$$\text{mP value} = 1000 \times (S - G \times P)/(S + G \times P) \quad (1)$$

in which S is the parallel and P is the perpendicular fluorescence signal, and G is the gain factor, which was set prior to the assay so that 1 nM fluorescein isothiocyanate gives a reading of 27 mP units. For fluorescence spectra in Figure 1, all solutions tested were made up in phosphate-buffered saline (PBS) 0.01 M phosphate buffer, 0.0027 M potassium chloride, and 0.137 M sodium chloride, pH 7.4, at 25 °C with 2% DMSO final well concentration. The wells were prepared in triplicate or quadruplicate.

Kinase profiling (Table 1) was performed in the Express Screen at the University of Dundee International Centre for Kinase Profiling using a radiolabel filter binding assay.[26]

Methyl *N*-((5*R*,7*R*,8*R*,9*S*)-8-methoxy-9-methyl-16-oxo-6,7,8,9,15,16-hexahydro-5*H*,14*H*-17-oxa-4*b*,9*a*,15-triaza-5,9-methanodibenzo[*b*,*h*]cyclonona[*jkl*]cyclopenta[*e*]-*as*-indacen-7-yl)-*N*-methylglycinate (2). Staurosporine (LC Labs; 5 mg, 1.07×10^{-5} M) was dissolved in tetrahydrofuran (THF, 0.5 mL) and to this solution was added potassium carbonate (30 mg, 2.17×10^{-4} M, 20 equiv). Methyl bromoacetate (20 μL, 32 mg, 2.11×10^{-4} M, 20 equiv) was then added, and the mixture was stirred at room temperature (RT) for 48 h. The solvent was removed under vacuum, and the resulting solid was resuspended in THF, and the mixture was centrifuged (5 min, 8100x*g*). The supernatant was then removed under vacuum to afford a white amorphous powder (5.6 mg, 97% yield). Purity: >99% by HPLC, t_R=16.85 min; ^{1}H (400 MHz, [D$_6$]DMSO, 348 K): δ=9.32 (1H, d, J=7.7 Hz, H4), 8.24 (1H, s, H6), 8.05–8.00 (2H, m, H1 and H11), 7.57–7.55 (1H, m, H8), 7.51–7.46 (2H, m, H2 and H10), 7.37–7.27 (2H, m, H3 and H9), 6.82 (1H, dd, J=4.76, 3.15 Hz, H6′), 4.98 (2H, s, H7), 4.34 (1H, d, J=1.6 Hz, H3′), 3.71 (1H, m, H4′), 3.56 (3H, s, H4″) 3.23 (2H, m, H1″), 2.89 (1H, m, H5′), 2.77 (3H, s, OCH$_3$3′), 2.45 (1H, m, H5′), 2.40 (3H, s, NCH$_3$4′), 2.18 ppm (3H, s, CH$_3$2′); ^{13}C (101 MHz, [D$_6$]DMSO, 293 K): δ=171.9, 138.3, 136.3, 132.3, 129.8, 126.3, 125.7, 125.2 125.1, 123.9, 122.6, 121.5, 120.4, 119.5, 114.7, 114.0, 113.30, 113.27, 108.9, 93.6, 81.3, 79.3, 67.0, 59.0, 53.9, 51.9, 45.4, 34.4, 30.4, 27.9 ppm; HRMS: calcd for $C_{31}H_{30}N_4O_5$ $[M+H]^+$ 539.2250, found 539.2250.

***N*-(2-Aminoethyl)-2-(((5*R*,7*R*,8*R*,9*S*)-8-methoxy-9-methyl-16-oxo-6,7,8,9,15,16-hexahydro-5*H*,14*H*-17-oxa-4*b*,9*a*,15-triaza-5,9-methanodibenzo[*b*,*h*]cyclonona[*jkl*]cyclopenta[e]-*as*-indacen-7-yl)(methyl)amino)acetamide (3)**. Compound **2** (5 mg, 9.29×10^{-6} M) was dissolved in ethylenediamine (1 mL, 899 mg, 1.50×10^{-2} M, 1700 equiv), and the resulting reaction mixture was stirred at RT for 48 h. Deionised water was added (2 mL), and the product was extracted into ethyl acetate, washed with deionised water (2×2 mL) and then dried using $MgSO_4$ then concentrated under nitrogen. This afforded an off-white amorphous powder (5.2 mg, 99% yield). Purity: >99% by HPLC, t_R=12.53 min; ^{1}H NMR (400 MHz, [D$_6$]DMSO, 363 K): δ=9.34 (1H, d, J=8.0 Hz, H4), 8.22 (1H, s, H6), 8.07 (1H, d, J=8.0 Hz H11), 8.02 (1H, d, J=8.5 Hz, H1), 7.76 (1H, br s, H3″) 7.55–7.47 (3H, m, H2, H8 and H10), 7.37 (1H, t, J=7.5 Hz, H9), 7.31 (1H, t, J=8.0 Hz, H3), 6.88 (1H, dd, J=5.29, 3.59 Hz, H6′), 4.99 (2H, s, H$_2$7), 4.42 (1H, d, J=0.3 Hz, H3′), 3.67–3.64 (1H, m, H4′), 3.41–3.23 (4H, m, H$_2$1″ and H$_2$4″) 3.05–2.98 (1H, m, H5′), 2.86 (2H, t, J=6.2 Hz, H$_2$5″), 2.51 (3H, s, OCH$_3$3′), 2.45 (3H, s, NCH$_3$4′), 2.41 (3H, s, CH$_3$2′) 2.40–2.33 ppm (1H, m, H5′); ^{13}C NMR (101 MHz, [D$_6$]DMSO, 293 K): δ=172.4, 158.6, 158.4, 138.4, 136.7, 132.7, 130.3, 126.7, 126.2, 125.8, 124.3, 123.1, 122.2, 121.1, 120.0, 115.2, 114.5, 113.3, 109.6, 94.6 82.3, 59.2, 45.8, 41.1, 40.8, 38.9, 36.8, 28.1, 27.3 ppm; HRMS: calcd for $C_{32}H_{34}N_6O_4$ $[M+H]^+$ 567.2675, found 567.2733.

1-(9*H*-Fluoren-9-yl)-3,14-dioxo-2,7,10-trioxa-4,13-diazaheptadecan-17-oic acid (5). 2,2,-(Ethylenedioxy)bisethylamine (1.48 mL, 10 mM) was dissolved in acetonitrile (50 mL). To this was added dropwise a solution of succinic anhydride (1.00 g, 10 mM) in acetonitrile (25 mL) over 90 min with stirring at RT.[18] The mixture was allowed to stir for a further 90 min by which time a waxy solid had

precipitated out of solution. The solvent was decanted off, and the solid was dissolved in a 1:1 mixture of acetonitrile and deionised water (100 mL). The solution was cooled in an ice bath, and to this was added dropwise a solution of Fmoc chloride (3.37 g, 13 mM, 1.3 equiv) in acetonitrile (25 mL) over 60 min. The solution was adjusted to pH 7–8 with a 5% aqueous solution of sodium hydrogen carbonate. The mixture was left to stand overnight. The mixture was concentrated under vacuum. The solids were dissolved in 5% sodium hydrogen carbonate (100 mL) and washed with ethyl acetate (4×75 mL). The aqueous phase was then acidified with hydrochloric acid 1 M, to between pH 2 and 3. The aqueous phase was then extracted with ethyl acetate (4×100 mL). The combined ethyl acetate extracts were washed with deionised water (2×100 mL), dried over $MgSO_4$, filtered and concentrated under vacuum to afford the product as a colourless oil (1.932 g, 41.1%). The oil was further purified by loading onto Isolute sorbent and run on silica using ethyl acetate as an eluent. This gave the light-yellow oil that crystallised on standing (750 mg, 16.0% yield); mp 98–100 °C. Purity: >99% by HPLC, t_R=17.37 min; ^{1}H NMR (400 MHz, $CDCl_3$, 293 K): δ=7.76 (2H, d, J=7.4 Hz), 7.56 (2H, d, J=7.4 Hz), 7.40 (2H, t, J=7.4 Hz), 7.31 (2H, t, J=7.4 Hz), 4.52–4.39 (2H, m) 4.28–4.18 (1H, m), 3.61 (4H, s), 3.59–3.53 (2H, m), 3.49–3.41 (4H, m), 3.41–3.31 (2H, m), 2.72–2.64 (2H, m), 2.53–2.45 ppm (2H, m); ^{13}C NMR (101 MHz, [D_6]DMSO, 293 K): δ=174.0, 171.3, 156.3, 144.0, 140.9, 127.2, 125.3, 120.2, 69.6, 65.5, 46.9, 38.7, 30.1, 29.3 ppm; HRMS: calcd for $C_{25}H_{30}N_2O_7$ $[M+H]^+$ 471.2087, found 471.2151, HRMS: calcd for $C_{25}H_{30}N_2O_7$ $[M-H]^-$ 469.1980, found 469.1860.

Fluoren-9-ylmethyl (2-((5*R*,7*R*,8*R*,9*S*)-8-methoxy-9-methyl-16-oxo-6,7,8,9,15,16-hexahydro-5*H*,14H-17-oxa-4b,9a,15-triaza-5,9-methanodibenzo[*b,h*]cyclonona[*jkl*]cyclopenta[*e*]-as-indacen-7-yl)-4,9,12-trioxo-16,19-dioxa-2,5,8,13-tetraazahenicosan-21-yl)-carbamate (6). Compound **3** (9.40 mg, 1.66×10^{-5} M) was dissolved in DMF (100 μL) and to this solution was added DIPEA (3.2 μL, 2 equiv). A separate solution of **5** (9.37 mg, 1.2 equiv), HBTU (7.55 mg, 1.2 equiv), and DIPEA (3.2 μL, 2 equiv) was prepared in DMF (100 μL). The two solutions were stirred for 1 min and then combined. The resulting reaction mixture was stirred for a further 12 h. The solvent was removed under vacuum and the reaction product purified by semi-preparative RP-HPLC to afford an amorphous white powder (8 mg, 47% yield). Purity: >99% by HPLC, t_R=18.12 min; ^{1}H NMR (500 MHz, [D_6]DMSO, 298 K): δ=9.32 (1H, d, J=8.0 Hz), 8.63 (1H, s), 8.09 (1H, d, J=8.0 Hz), 8.05 (1H, d, J=8.5 Hz), 7.89–7.86 (4H, m), 7.68–7.63 (2H, m), 7.56–7.49 (3H, m), 7.39 (3H, t, J=7.1 Hz), 7.34–7.30 (3H, m), 6.99–6.97 (1H, m), 5.00 (2H, s), 4.29–4.27 (2H, m), 4.21–4.18 (1H, m), 3.47 (4H s), 3.40–3.34 (5H, m), 3.17 (6H, s), 3.15–3.10 (6H, m), 2.48 (2H, s), 2.32–2.28 (4H, m), 2.25 ppm (2H, br s); ^{13}C NMR (126 MHz, [D_6]DMSO, 293 K): δ= 206.5, 171.9, 171.8, 171.5, 156.2, 143.9, 140.7, 137.8, 136.3, 132.3, 129.7, 127.6, 127.0, 126.2, 125.8, 125.4, 125.4, 125.2, 124.9, 123.9, 122.7, 121.8, 120.8, 120.1, 119.8, 119.7, 118.1, 117.8, 115.5, 114.9, 114.2, 112.7, 109.2, 94.1, 81.6, 79.1, 69.5, 69.5, 69.1 65.3, 59.0, 54.7, 48.6, 46.7, 45.4, 40.5, 38.8, 38.5, 37.9, 30.8, 30.5, 29.1, 27.4, 26.1, 22.5, 1.2 ppm; HRMS: calcd for $C_{57}H_{62}N_8O_{10}$ $[M+H]^+$ 1019.4622, found 1019.4639.

***N*^{1}-(2-(2-(2-Aminoethoxy)ethoxy)ethyl)-*N*^{4}-(2-(2-(((5*R*,7*R*,8*R*,9*S*)-8-methoxy-9-methyl-16-oxo-6,7,8,9,15,16-hexahydro-5*H*,14*H*-17-oxa-4*b*,9*a*,15-triaza-5,9-methanodibenzo[*b,h*]cyclonona[*jkl*]-cyclopenta[*e*]-*as*-indacen-7-yl)(methyl)amino)acetamido)ethyl)succinimide (7)**. Diethylamine (200 μL) was added to a stirred solution of **6** (4 mg, 3.93×10^{-6} M) in THF (800 μL) and the mixture was stirred for 4 h; completion was assessed by mass spectrometry. The solvent and excess diethylamine were removed under vacuum. The remaining solids were triturated with THF and petroleum ether and then dried under high vacuum for 6 h to afford an off-white powder. Half of this material was then purified for analysis by semi-preparative RP-HPLC to afford an amorphous white powder **7** (0.7 mg, 45% yield). Purity: >99% by HPLC, t_R= 12.03 min; ^{1}H NMR (400 MHz, [D_6]DMSO/D_2O 9:1, 293 K): δ=9.20 (1H, d, J=8.1 Hz, H4), 8.04–7.99 (2H, m, H1 and H11), 7.54–7.46 (3H, m, H2, H8 and H10), 7.36 (1H, t, J=7.4 Hz, H9), 7.31–7.27 (1H, m, H3), 6.81–6.78 (1H, m, H6′), 4.98 (2H, s, $H_2$7), 4.22 (1H, s, H3′), 3.53 (2H, t, J=5.1 Hz, CH_2), 3.50–3.46 (4H, m, $2CH_2$) 3.41–3.39 (1H, m, CH), 3.35 (2H, t, J=5.9 Hz, CH_2), 3.31–3.27 (1H, m, H4′), 3.15 (2H, t, J=5.8 Hz, CH_2), 3.06–2.81 (8H, m, H5′, $H_2$1″, $H_2$4″, and 3CH), 2.53 (3H, s, $OCH_3$3′), 2.36 (3H, s, $NCH_3$4′), 2.33–2.28 (1H, m, H5′), 2.27–2.21 (4H, m, $2CH_2$), 2.00 ppm (3H, s, $CH_3$2′); ^{13}C NMR (101 MHz, [D_6]DMSO, 293 K): δ=139.2, 136.3, 132.3, 129.8, 128.0, 126.2, 124.9, 123.9, 122.7, 114.8, 94.2, 72.3, 69.6, 69.4, 69.0, 66.6, 60.0, 58.8, 38.6, 38.4, 34.4, 30.7, 30.5, 30.4, 21.0, 16.7 ppm; HRMS: calcd for $C_{42}H_{52}N_8O_8$ $[M+H]^+$ 797.39417, found 797.3945

2-(6-Hydroxy-3-oxo-3*H*-xanthen-9-yl)-5-(3-(2-((5*R*,7*R*,8*R*,9*S*)-8-methoxy-9-methyl-16-oxo-6,7,8,9,15,16-hexahydro-5*H*,14*H*-17-oxa-4b,9a,15-triaza-5,9-methanodibenzo[*b,h*]cyclonona[*jkl*]-cyclopenta[*e*]-*as*-indacen-7-yl)-4,9,12-trioxo-16,19-dioxa-2,5,8,13-tetraazahenicosan-21-yl)thioureido)benzoic acid (8). The remaining half of the deprotected material described above for the preparation of compound **7** was dissolved in DMF (100 μL) and added to a solution of fluorescein isothiocyanate (1 mg, 1.3 equiv) in DMF (100 μL). This was left to stir at RT in the dark for 12 h. Monitoring by mass spectrometry indicated unreacted precursor; therefore, further fluorescein isothiocyanate (0.76 mg, 1 equiv) was added and left to stir for a further 24 h. At this point there was little or no detectable precursor remaining, so the solvent was removed under vacuum and the material was purified by HPLC to afford an amorphous dark-orange powder (1.2 mg, 52% yield). Purity: >99% by HPLC, t_R-15.60 min; ^{1}H NMR (500 MHz, [D_6]DMSO/D_2O 9:1, 298 K): δ=9.25 (1H, d, J=8.1 Hz), 8.26 (1H, br s), 8.07 (1H, d J=7.9 Hz), 8.02 (1H, d, J=8.3 Hz), 7.70 (1H, d, J=7.6 Hz), 7.52 (3H, quintet, J=8.0 Hz), 7.31 (1H, t, J=7.7 Hz), 7.14 (1H, d, J=7.9 Hz), 6.93 (1H, d, J=8.8 Hz), 6.68–6.67 (2H, m), 6.59–6.57 (2H, m), 6.56–6.53 (2H, m), 4.98 (2H, s), 4.64 (1H, s), 3.65 (2H, s), 3.56 (2H, t, J=5.1 Hz), 3.50, (4H, dd, J=4.0, 10.6 Hz), 3.34 (2H, t, J=5.4 Hz), 3.13–3.11 (6H, m), 2.84 (3H, s), 2.45 (2H, s) 2.36 (1H, s) 2.27 (4H, q, J= 6.5 Hz), 2.19 (3H, s), 2.07–2.06 ppm (1H, m); HRMS: calcd for $C_{63}H_{63}N_9O_{13}S$ $[M+H]^+$ 1186.4300, found 1186.3001.

Acknowledgements

A.J.M.D. was funded by a Biotechnology and Biological Sciences Research Council studentship (grant ref. BB/F016867/1). The authors are grateful for additional financial support from the School of Pharmacy, University of Nottingham.

Keywords: alkylation · fluorescein · fluorescent probes · kinases · screening

[1] S. Omura, Y. Iwai, A. Hirano, A. Nakagawa, J. Awaya, H. Tsuchiya, Y. Takahashi, R. Masuma, *J. Antibiot.* **1977**, *30*, 275–282.
[2] H. Nakano, S. Omura, *J. Antibiot.* **2009**, *62*, 17–26.
[3] M. W. Karaman, S. Herrgard, D. K. Treiber, P. Gallant, C. E. Atteridge, B. T. Campbell, K. W. Chan, P. Ciceri, M. I. Davis, P. T. Edeen, R. Faraoni, M. Floyd, J. P. Hunt, D. J. Lockhart, Z. V. Milanov, M. J. Morrison, G. Pallares, H. K. Patel, S. Pritchard, L. M. Wodicka, P. P. Zarrinkar, *Nat. Biotechnol.* **2008**, *26*, 127–132.

[4] C. Lipinski, A. Hopkins, *Nature* **2004**, *432*, 855 – 861.
[5] S. Atwell, J. M. Adams, J. Badger, M. D. Buchanan, I. K. Feil, K. J. Froning, X. Gao, J. Hendle, K. Keegan, B. C. Leon, H. J. Muller-Dieckmann, V. L. Nienaber, B. W. Noland, K. Post, K. R. Rajashankar, A. Ramos, M. Russell, S. K. Burley, S. G. Buchanan, *J. Biol. Chem.* **2004**, *279*, 55827 – 55832.
[6] J. J. Fischer, C. Dalhoff, A. K. Schrey, O. Y. G. N. Baessler, S. Michaelis, K. Andrich, M. Glinski, F. Kroll, M. Sefkow, M. Dreger, H. Koester, *J. Proteomics* **2011**, *75*, 160 – 168.
[7] H. B. Shi, X. M. Cheng, S. K. Sze, S. Q. Yao, *Chem. Commun.* **2011**, *47*, 11306 – 11308.
[8] X. Cheng, L. Li, M. Uttamchandani, S. Q. Yao, *Chem. Commun.* **2014**, *50*, 2851 – 2853.
[9] C. D. Shomin, S. C. Meyer, I. Ghosh, *Bioorg. Med. Chem.* **2009**, *17*, 6196 – 6202.
[10] M. Kawaguchi, T. Terai, R. Utata, M. Kato, K. Tsuganezawa, A. Tanaka, H. Kojima, T. Okabe, T. Nagano, *Bioorg. Med. Chem. Lett.* **2008**, *18*, 3752 – 3755.
[11] T. J. Zhou, L. G. Sun, Y. Gao, E. J. Goldsmith, *Acta Biochim. Biophys. Sin.* **2006**, *38*, 385 – 392.
[12] T. J. Boggon, Y. Li, P. W. Manley, M. J. Eck, *Blood* **2005**, *106*, 996 – 1002.
[13] L. Jin, S. Pluskey, E. C. Petrella, S. M. Cantin, J. C. Gorga, M. J. Rynkiewicz, P. Pandey, J. E. Strickler, R. E. Babine, D. T. Weaver, K. J. Seidl, *J. Biol. Chem.* **2004**, *279*, 42818 – 42825.
[14] T. Kinoshita, M. Matsubara, H. Ishiguro, K. Okita, T. Tada, *Biochem. Biophys. Res. Commun.* **2006**, *346*, 840 – 844.
[15] M. B. Lamers, A. A. Antson, R. E. Hubbard, R. K. Scott, D. H. Williams, *J. Mol. Biol.* **1999**, *285*, 713 – 725.
[16] L. M. Toledo, N. B. Lydon, *Structure* **1997**, *5*, 1551 – 1556.
[17] D. Tanramluk, A. Schreyer, W. R. Pitt, T. L. Blundell, *Chem. Biol. Drug Des.* **2009**, *74*, 16 – 24.
[18] A. Soriano, R. Ventura, A. Molero, R. Hoen, V. Casado, A. Cortes, F. Fanelli, F. Albericio, C. Lluis, R. Franco, M. Royo, *J. Med. Chem.* **2009**, *52*, 5590 – 5602.
[19] J. M. Herbert, E. Seban, J. P. Maffrand, *Biochem. Biophys. Res. Commun.* **1990**, *171*, 189 – 195.
[20] H. Hidaka, M. Inagaki, S. Kawamoto, Y. Sasaki, *Biochemistry* **1984**, *23*, 5036 – 5041.
[21] L. Prade, R. A. Engh, A. Girod, V. Kinzel, R. Huber, D. Bossemeyer, *Structure* **1997**, *5*, 1627 – 1637.
[22] O. Singh, A. Shillings, P. Craggs, I. Wall, P. Rowland, T. Skarzynski, C. I. Hobbs, P. Hardwick, R. Tanner, M. Blunt, D. R. Witty, K. J. Smith, *Prot. Sci.* **2013**, *22*, 1071 – 1077.
[23] J. Kleinschroth, J. Hartenstein, C. Rudolph, C. Schachtele, *Bioorg. Med. Chem. Lett.* **1993**, *3*, 1959 – 1964.
[24] P. D. Davis, C. H. Hill, W. A. Thomas, I. W. A. Whitcombe, *J. Chem. Soc. Chem. Commun.* **1991**, 182 – 184.
[25] K. V. Zaitseva, M. A. Varfolomeev, V. B. Novikov, B. N. Solomonov, *J. Chem. Thermodyn.* **2011**, *43*, 1083 – 1090.
[26] C. J. Hastie, H. J. McLauchlan, P. Cohen, *Nat. Protoc.* **2006**, *1*, 968 – 971.

Received: December 18, 2015
Published online on March 23, 2016

ACS Chemical Neuroscience

Research Article

pubs.acs.org/chemneuro

Novel Fused Arylpyrimidinone Based Allosteric Modulators of the M_1 Muscarinic Acetylcholine Receptor

Shailesh N. Mistry,[†,§] Herman Lim,[‡,§] Manuela Jörg,[†] Ben Capuano,[†] Arthur Christopoulos,[‡] J. Robert Lane,[*,‡] and Peter J. Scammells[*,†]

[†]Medicinal Chemistry and [‡]Drug Discovery Biology, Monash Institute of Pharmaceutical Sciences, Monash University, Parkville 3052, Victoria Australia

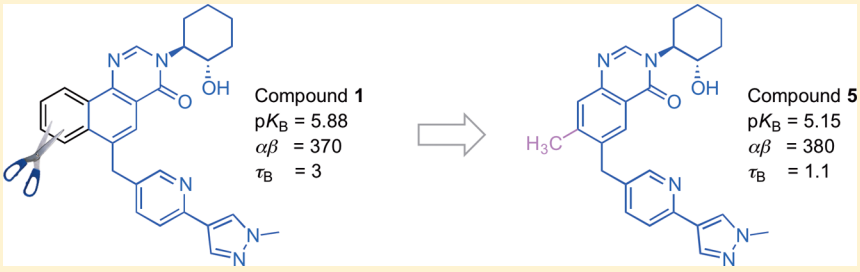

ABSTRACT: Benzoquinazolinone **1** is a positive allosteric modulator (PAM) of the M_1 muscarinic acetylcholine receptor (mAChR), which is significantly more potent than the prototypical PAM, 1-(4-methoxybenzyl)-4-oxo-1,4-dihydroquinoline-3-carboxylic acid (BQCA). In this study, we explored the structural determinants that underlie the activity of **1** as a PAM of the M_1 mAChR. We paid particular attention to the importance of the tricyclic scaffold of compound **1**, for the activity of the molecule. Complete deletion of the peripheral fused benzene ring caused a significant decrease in affinity and binding cooperativity with acetylcholine (ACh). This loss of affinity was rescued with the addition of either one or two methyl groups in the 7- and/or 8-position of the quinazolin-4(3*H*)-one core. These results demonstrate that the tricyclic benzo[*h*]quinazolin-4(3*H*)-one core could be replaced with a quinazolin-4(3*H*)-one core and maintain functional affinity. As such, the quinazolin-4(3*H*)-one core represents a novel scaffold to further explore M_1 mAChR PAMs with improved physicochemical properties.

KEYWORDS: *M_1 muscarinic acetylcholine receptor, positive allosteric modulator*

Alzheimer's disease is a progressive and irreversible neurodegenerative disorder affecting around 25 million people worldwide.[1] The disorder is primarily observed in the aging population, and characteristic symptoms of the disease include memory loss, confusion, and dementia.[2,3] Currently, pharmacological interventions for Alzheimer's disease remain limited, and provide only symptomatic relief to patients.[4,5]

The reduction of cholinergic neurons in the basal nuclear complex is associated with the cognitive deficits observed in patients with Alzheimer's disease.[6,7] A link between mAChR function and disease pathology has been suggested, with the M_1 mAChR subtype particularly highlighted for a role in cognition.[7,8]

Acetylcholinesterase inhibitors are currently used to treat the cognitive deficits associated with Alzheimer's disease, but this approach is limited by the moderate improvement in the cognitive function of patients, as well as debilitating side effects including nausea, diarrhea, hypotension and vomiting.[9] However, they exert a nonselective effect at all muscarinic receptor subtypes, because acetylcholine esterase inhibitors act to inhibit acetylcholine breakdown. It is likely that such side-effects are due activation of M_2 and M_3 mAChRs expressed in the periphery.[7]

Accordingly, there has been considerable focus upon the design of ligands that selectively activate the M_1 mAChR. However, the design of selective orthosteric agonists for the M_1 mAChR has proven difficult, due to the highly conserved orthosteric pocket of all the mAChRs (M_1–M_5).[10] However, efforts to target the less-conserved, and topographically distinct allosteric site of the receptor have proven more fruitful.[11−14] Ligands that target such allosteric sites may act to potentiate the binding and signaling activity of an orthosteric receptor agonist (positive allosteric modulators, PAM) and/or activate the receptor themselves (allosteric agonists). Allosteric ligands of the M_1 mAChR have been recognized as a potentially promising novel drug class for the treatment of Alzheimer's disease.[14]

BQCA was reported as the first highly selective PAM for the M_1 mAChR.[15] Structure–activity relationship (SAR) studies around BQCA have revealed structurally related compounds with higher affinity and potency.[16−18] Furthermore, our group has reported an enriched SAR study that used analytical modeling of pharmacological data, to relate structural modification to BQCA analogues, with variations in binding affinity (pK_B), binding (α) and functional ($\alpha\beta$) cooperativity,

Received: January 21, 2016
Accepted: February 18, 2016
Published: February 18, 2016

DOI: 10.1021/acschemneuro.6b00018
ACS Chem. Neurosci. 2016, 7, 647−661

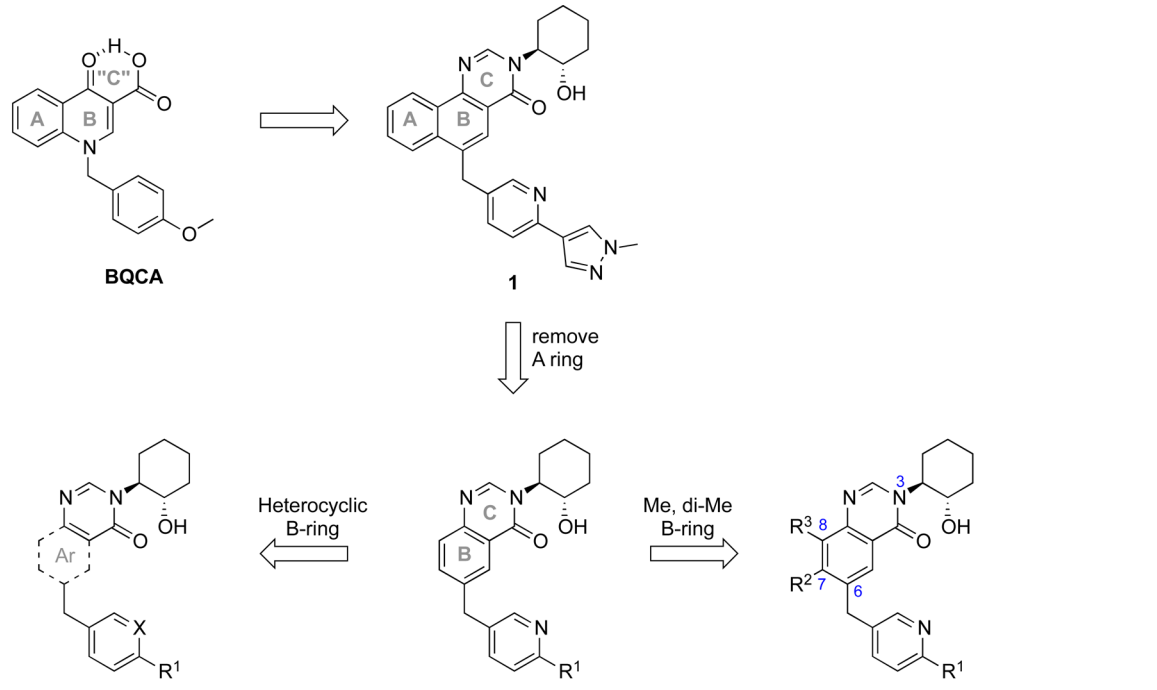

Figure 1. Top: Chemical structure of lead compounds 1-(4-methoxybenzyl)-4-oxo-1,4-dihydroquinoline-3-carboxylic acid (BQCA) and 3-((1*S*,2*S*)-2-hydroxycyclohexyl)-6-((6-(1-methyl-1*H*-pyrazol-4-yl)pyridin-3-yl)methyl)benzo[*h*]quinazolin-4(3*H*)-one (**1**). Bottom: Overview of the structures and design strategy behind the novel analogues derived from compound **1**. The numbering of the atoms in the quinazolinone ring bearing substituents is shown in blue.

Scheme 1. Synthesis of Compound 1[a]

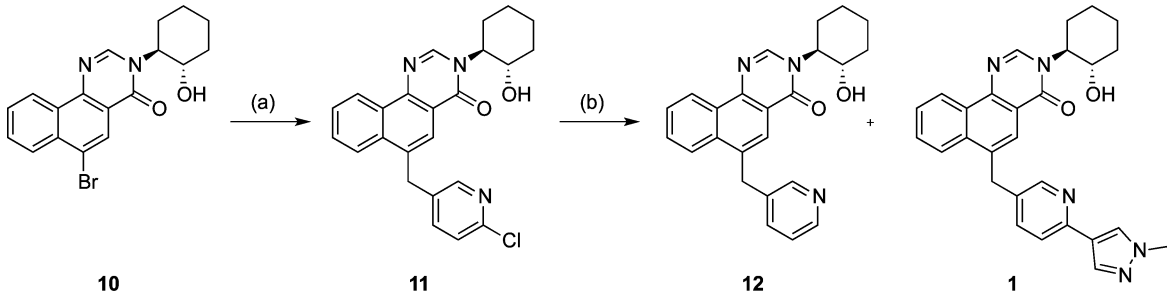

[a]Reagents and conditions: (a) (i) cat. $Pd(P(^tBu)_3)_2$, degassed anhydrous THF, 0 °C; (ii) 0.5 M (2-chloro-5-pyridyl)methylzinc chloride/THF, 0 °C to rt, 79%; (b) 1-methyl-4-(4,4,5,5-tetramethyl-1,3,2-dioxaborolan-2-yl)-1*H*-pyrazole, cat. $PdCl_2(PPh_3)_2$, 1 M $Na_2CO_{3(aq)}$/THF 1:3 degassed, 100 °C, 64% (59% **1**: 5% **12**).

and intrinsic efficacy (τ_B).[19] 3-((1*S*,2*S*)-2-Hydroxycyclohexyl)-6-((6-(1-methyl-1*H*-pyrazol-4-yl)pyridin-3-yl)methyl)benzo-[*h*]quinazolin-4(3*H*)-one (**1**), is a significantly more potent M_1 mAChR PAM with a structural ancestry originating from BQCA and related compounds (Figure 1).[17,20] We recently used a combination of site-directed mutagenesis, modeling of pharmacological data and molecular dynamics simulations to propose a binding mode for **1** at the M_1 mAChR, similar to that predicted for BQCA. In particular, residues $Y85^{2.64}$ and $Y82^{2.61}$ in transmembrane (TM) bundle 2, Y179 in extracellular loop (ECL) 2, and $W400^{7.35}$ in TM 7 were shown to be important for the binding and function of both BQCA and compound **1**.[21] This approach also revealed that the higher potency of **1** was predominantly driven by an increase in affinity, rather than cooperativity with ACh, for the M_1 mAChR allosteric site. The current study aimed to explore the structural determinants that underlie the activity of **1** as a PAM of the M_1 mAChR and, in particular, those that are responsible for its superior potency. Furthermore, we aimed to move away from the tricyclic scaffold of compound **1** and determine the importance of this moiety for the activity of the molecule (Figure 1), using approaches such as core trimming (compounds **2**–**9**). An enriched SAR profile was compiled to explore the important features of these novel compounds to maintain high affinity, cooperativity, and intrinsic efficacy.

DOI: 10.1021/acschemneuro.6b00018
ACS Chem. Neurosci. 2016, 7, 647–661

Scheme 2. Synthesis of Analogues 2−7[a]

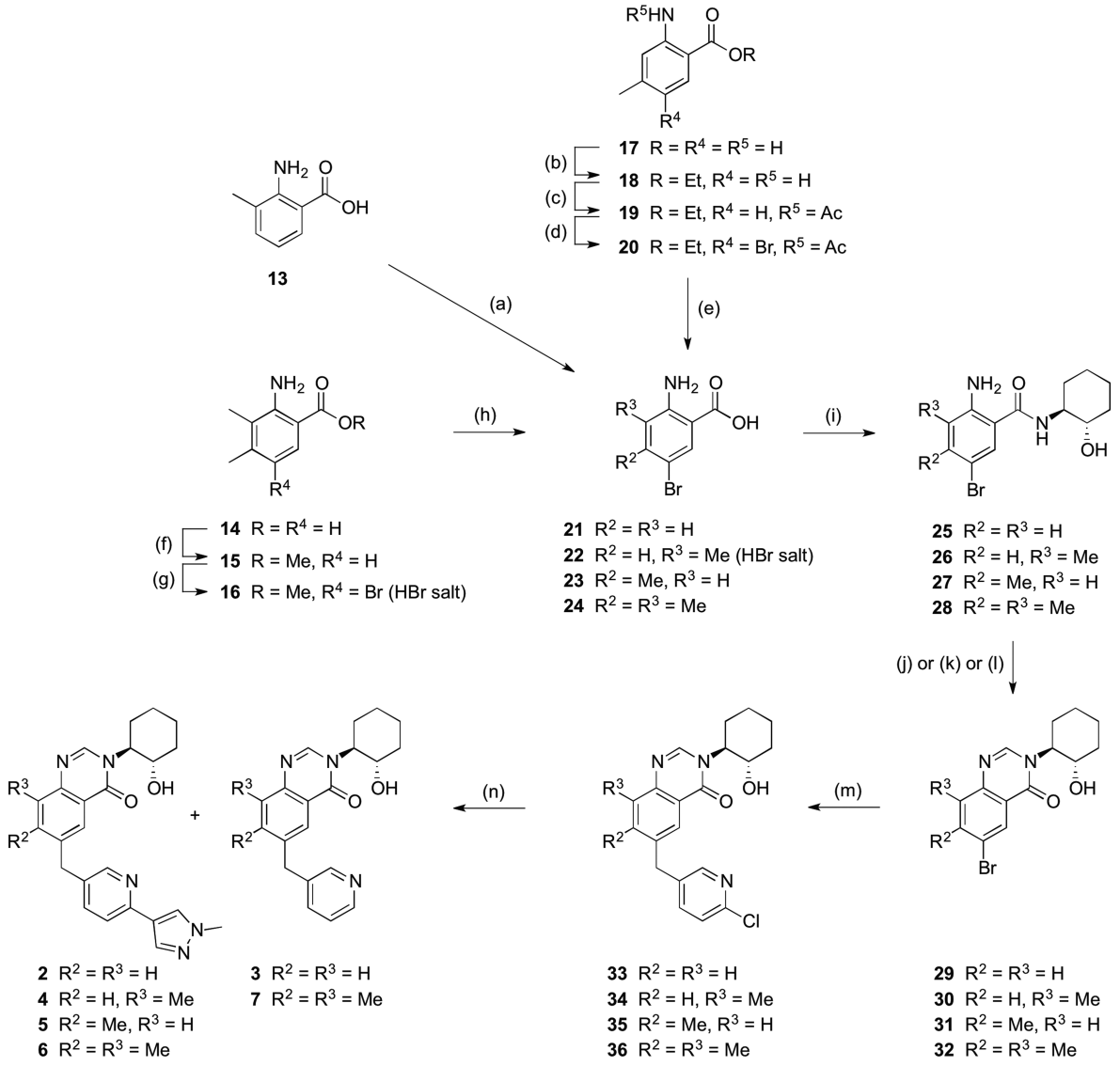

[a]Reagents and conditions: (a) Br_2, AcOH, DCM, rt, 95%; (b) cat. conc. $H_2SO_{4(aq)}$, EtOH, reflux, 75%; (c) acetyl chloride, TEA, DCM, 0 °C to rt, 100%; (d) Br_2, AcOH, rt, 23% (brsm); (e) 5 M $NaOH_{(aq)}$, EtOH, 90 °C, 81%; (f) cat. $H_2SO_{4(aq)}$, MeOH, reflux, 83%; (g) (i) 1,4-dioxane/CCl_4 1:1, 0 °C; (ii) Br_2, 1,4-dioxane/CCl_4 1:1, dropwise, 0 °C, 93%; (h) LiOH·H_2O, THF, water, rt, 94%; (i) HCTU, (1*S*,2*S*)-2-aminocyclohexanol hydrochloride, DIPEA, DMF, rt, 77−95%; (j) DMF-DMA, 85 or 115 °C, 63−95%; (k) formamide, 150 or 180 °C, 44−69%; (l) triethylorthoformate, 100−150 °C, 65%; (m) (i) cat. $Pd(P(^tBu)_3)_2$, dry THF, 0 °C; (ii) 0.5 M (2-chloro-5-pyridylmethyl)zinc chloride/THF, 0 °C to RT or 55 °C, 14−90%; (n) 1-methyl-4-(4,4,5,5-tetramethyl-1,3,2-dioxaborolan-2-yl)-*1H*-pyrazole, cat. $PdCl_2(PPh_3)_2$, 1 M $Na_2CO_{3(aq)}$/THF 1:3 degassed, 100 °C, Suzuki product 15−96%, dehalogenation product 0−14%.

RESULTS AND DISCUSSION

Chemistry. The synthesis of lead compound **1**, though previously reported in patent literature,[20] has only recently been fully optimized and characterized in our hands.[21] Seeking to understand the basis for the PAM activity of compound **1**, we initially decided to pharmacologically characterize key synthetic intermediates. Compound **10** was synthesized as previously described, with subsequent Negishi coupling carried out according to established methodology,[20,21] affording intermediate **11** in good yield. After the final Suzuki coupling of **11** with commercially available 1-methyl-4-(4,4,5,5-tetramethyl-1,3,2-dioxaborolan-2-yl)-*1H*-pyrazole, we were able to isolate and characterize both the desired Suzuki product **1**, and corresponding dehalogenated product **12** (Scheme 1).[21]

Aside from pharmacological characterization of compounds **10**, **12**, and **1**, which represent a stepwise buildup of the (pyridin-3-yl)methyl pendant group, we also sought to investigate the nature of the polyaromatic core. Given the precedence for polyaromatic heterocycles potentially imparting toxic DNA-chelation behavior to a scaffold,[22] investigation of related heteroaromatics seemed a prudent avenue of investigation. Initially we envisaged generating comparable analogues of **1**, incorporating gradual deletion of the benzo[*h*]-quinazolin-4(3*H*)-one core toward a quinazolin-4(3*H*)-one core. The deletion of the fused benzene ring was also anticipated to make these analogues more "druglike", through reductions in lipophilicity (assessed through calculated log *P*), topological polar surface area (tPSA), and molecular weight.[23] With this strategy in mind, we synthesized analogues with

DOI: 10.1021/acschemneuro.6b00018
ACS Chem. Neurosci. 2016, 7, 647−661

Scheme 3. Synthesis of Compound 8 Containing a Pyrido[2,3-*d*]pyrimidinone Core[a]

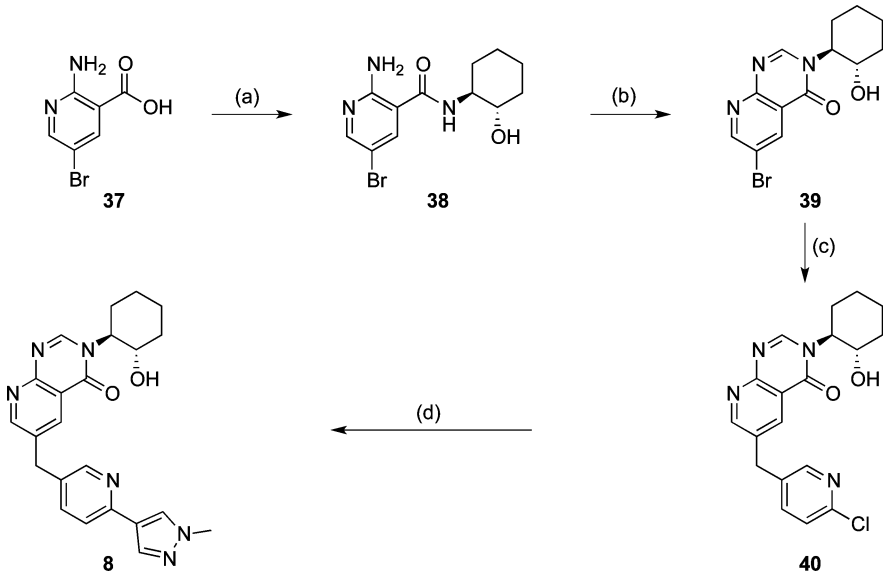

[a]Reagents and conditions: (a) HCTU, (1*S*,2*S*)-2-aminocyclohexanol hydrochloride, DIPEA, DMF, rt, 94%; (b) formamide, 150 or 180 °C, 69%; (c) (i) cat. $Pd(P(^tBu)_3)_2$, dry THF, 0 °C; (ii) 0.5 M (2-chloro-5-pyridylmethyl)zinc chloride/THF, 0 °C to RT or 55 °C, 90%; (d) 1-methyl-4-(4,4,5,5-tetramethyl-1,3,2-dioxaborolan-2-yl)-*1H*-pyrazole, cat. $PdCl_2(PPh_3)_2$, 1 M $Na_2CO_{3(aq)}$/THF 1:3 degassed, 100 °C, 24%.

either complete deletion of the peripheral fused benzene ring (**2**), or the presence of one or two methyl groups in the 7/8 positions of the quinazolin-4(3*H*)-one core, to give **4**, **5** and **6**. Evaluation of these compounds was anticipated to address whether the peripheral fused benzene ring of literature compound **1**, could be replaced by the steric presence of either one or two methyl groups.

Our recent work determining the structural nature of the interaction of compound **1** with the allosteric binding site at the M_1 mAChR, highlighted the importance of Y179 in ECL2, making aromatic edge-face interactions with both the benzylic pendant group and benzo[*h*]quinazolin-4(3*H*)-one core.[21] In addition, the proximity of the phenol moiety of Y179 could facilitate additional polar interactions with an appropriately positioned heteroatom incorporated into the ligand. With this in mind, we also synthesized **8**, the pyrido[2,3-*d*]pyrimidin-4(3*H*)-one analogue of **2**.

Synthesis of these analogues was carried out in a similar manner to that of lead compound **1**. In the case of **2**, commercially available 2-amino-5-bromobenzoic acid (**21**) was employed, while the remaining substituted 2-amino-5-bromobenzoic acid intermediates (**22**−**24**), required synthesis from unbrominated starting materials.

2-Amino-3,4-dimethylbenzoic acid (**14**) underwent initial Fischer esterification to give the corresponding methyl ester **15**, followed by selective bromination of the 5-position to give intermediate **16** as the hydrobromide salt, in excellent yield. Subsequent basic hydrolysis afforded the desired 2-amino-5-bromo-3,4-dimethylbenzoic acid (**24**). In the case of 2-amino-3-methylbenzoic acid (**13**), we were able to directly brominate in acetic acid at room temperature, to give **22**, without the need for esterification of the carboxylic acid moiety (Scheme 2). Finally, in the case of 2-amino-4-methylbenzoic acid (**23**), our attempts at direct bromination in the same manner as for **22**, gave a mixture of mono- and dibrominated products, in addition to unreacted starting material, which proved difficult to separate. However, selective bromination in the 5-postion was achieved through esterification of the carboxylic acid moiety, and acetylation of the aniline group. The acetanilide derivative **19** facilitated selective monobromination of the 5-position, allowing the isolation of **23** following the saponification of the ester in the modest yield of 19% over these two steps.

Subsequent synthetic steps proceeded in accordance with our reported synthesis of lead compound **1**.[21] Briefly, the 2-amino-5-bromobenzoic acid (**21**−**24**) intermediates first underwent *O*-(1*H*-6-chlorobenzotriazole-1-yl)-1,1,3,3-tetramethyluronium hexafluorophosphate (HCTU)-mediated coupling with (1*S*,2*S*)-2-aminocyclohexanol hydrochloride in the presence of DIPEA, in DMF at room temperature, furnishing the corresponding amides (**25**−**28**) in good to excellent yield. Cyclisation of these 2-amino arylcarboxamide derivatives was achieved through heating in *N*,*N*-dimethylformamide-dimethylacetal (DMF-DMA), formamide or triethylorthoformate, affording **29**-**32**. The more forcing conditions (150 or 180 °C in formamide) were found to prevent formation of stable 2-(dimethylamino)-2,3-dihydroquinazolin-4(1*H*)-one-type intermediates, which occurred in the presence of DMF-DMA. In some cases, these intermediates failed to undergo elimination of *N*,*N*-dimethylamine to furnish the desired product, necessitating the use of more forcing conditions.

Installation of the (pyridin-3-yl)methyl pendant group was achieved as described for lead compound **1**, through a sequence of Negishi and Suzuki reactions, to give the desired compounds **2** and **4**-**6**, bearing the (6-(1-methyl-1*H*-pyrazol-4-yl)pyridin-3-yl)methyl group. During Suzuki coupling of final compounds **2** and **6**, appreciable amounts of the dehalogenation side-product, **3** and **7** were also isolated, and deemed of interest for pharmacological evaluation.

As part of the strategy to develop fused heteroaromatic analogues of lead compound **1**, the investigation of alternative cores was also of interest. The pyrido[2,3-*d*]pyrimidinone analogue of **2** (compound **8**) was prepared using an analogous

DOI: 10.1021/acschemneuro.6b00018
ACS Chem. Neurosci. 2016, 7, 647−661

Scheme 4. Synthesis of Analogue 9 Containing a Thienopyrimidinone Core[a]

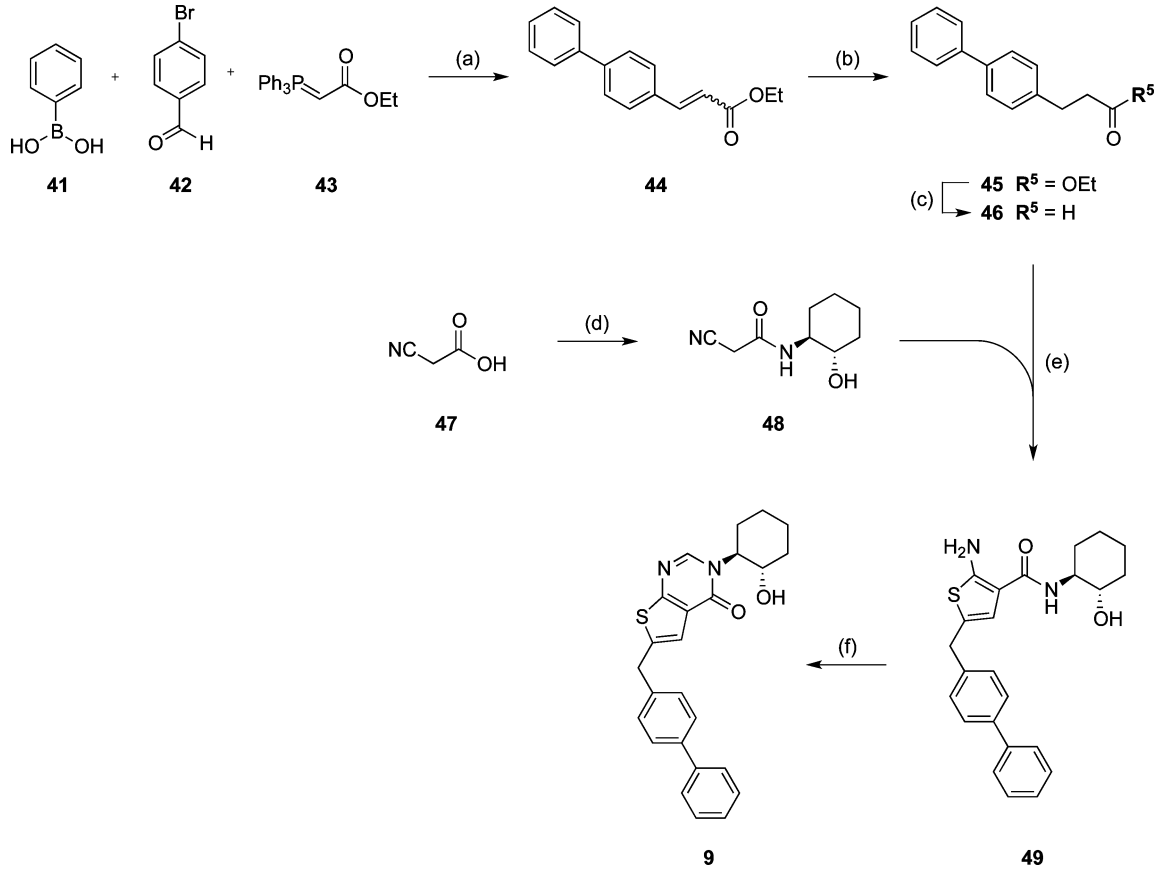

[a]Reagents and conditions: (a) (i) cat. PPh_3, cat. $PdCl_2(PPh_3)_2$, degassed DME/2 M $Na_2CO_{3(aq)}$, 70 °C; (ii) 100 °C; (iii) 85 °C, 84% (*E*/*Z* 4:1); (b) H_2, wet 10% Pd/C, EtOAc, rt, 99%; (c) (i) anhydrous toluene, −78 °C; (ii) 1 M DIBAL-H in toluene, dropwise, −78 °C; (iii) MeOH quench, −78 °C; 88%; (d) (1*S*,2*S*)-2-aminocyclohexanol hydrochloride, HCTU, DIPEA, DMF, rt, 71%; (e) sulfur, TEA, EtOH, 60 °C, 57%; (f) formamide, 180 °C, 56%.

approach starting from 2-amino-5-bromonicotinic acid (**37**) (Scheme 3).

Having synthesized the pyrido[2,3-*d*]pyrimidin-4(3*H*)-one analogue **8**, we turned our attention to 5−6 fused heterocyclic scaffolds. The thieno[2,3-*d*]pyrimidin-4(3*H*)-one core was of interest, since spatially isosteric replacements for the quinazolin-4(3*H*)-one core have been reported in a number of medicinal chemistry lead optimization campaigns, possessing "drug-like" properties and biological activity.[24−26]

The thieno[2,3-*d*]pyrimidin-4(3*H*)-one core was accessible through synthesis of the appropriately substituted 2-amino-thiophene-3-carboxamide, which in turn was assembled in a one-pot Gewald synthesis based on literature precedent.[5] Components for the Gewald reaction were readily synthesized from commercially available reagents (Scheme 4). Cyanoacetamide **48**, was obtained through HCTU-mediated coupling of cyanoacetic acid and (1*S*,2*S*)-2-aminocyclohexanol hydrochloride in the presence of DIPEA and DMF at room temperature. A one-pot Wittig-Suzuki reaction was employed to construct ester **44**, from phenylboronic acid (**41**), 4-bromobenzaldehyde (**42**), and (ethoxycarbonylmethylene)-triphenylphosphorane (**43**), according to previously described methodology.[6] Though intermediate **44** was isolated as both the *E*- and *Z*-isomers, these were combined before hydrogenation of the double bond, to give saturated ester **45**. Reduction of **45** in the presence of DIBAL-H at −78 °C, afforded the desired aldehyde **46** in excellent yield.

The combination of **46**, **48**, and sulfur in the presence of TEA and ethanol at 60 °C (one-pot Gewald conditions) gave the substituted 2-aminothiophene-3-carboxamide **49** in moderate yield. Finally cyclization of **49** was achieved by heating in formamide at 180 °C, affording the desired thieno[2,3-*d*]pyrimidin-4(3*H*)-one derivative **9**. We elected to synthesize **9** bearing the biphenylmethyl pendant group, for initial ease of access and to establish synthetic methodology. Furthermore, this moiety has been shown to impart good affinity and cooperativity on the BQCA scaffold (an early precursor of lead compound **1** and related structures).[7]

PHARMACOLOGY

We recently published an SAR study of the M_1 mAChR PAM, BQCA.[19] By incorporating modeling into our pharmacological analysis, we were able to relate modifications of the structural features of BQCA, to changes in parameters that describe allosteric ligand action. These comprise the affinity of the modulator for the free receptor (K_B), its modulatory effects on the binding and efficacy of acetylcholine (α and β, respectively), and its intrinsic efficacy (direct allosteric agonism) in the system (τ_B). In particular, alternative substitution of the quinolone ring in the 5- and 8-positions modulated intrinsic efficacy; isosteric replacement of the carboxylic acid moiety or

DOI: 10.1021/acschemneuro.6b00018
ACS Chem. Neurosci. 2016, 7, 647−661

Table 1. Binding and Functional Parameters of 4-Phenylpyridin-2-one Analogues 2−12 at the M_1 mAChR

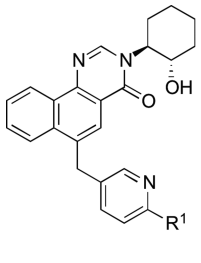

1, 11, 12

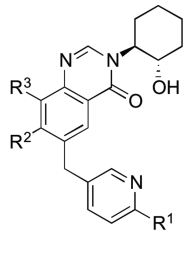

2-7

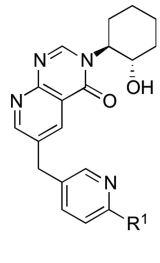

8

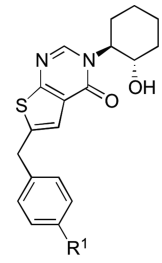

9

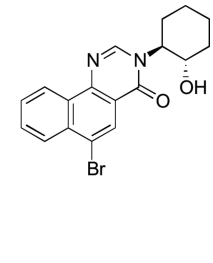

10

				Radioligand binding ([^{3}H]NMS)			IP$_1$ accumulation	
	R^1	R^2	R^3	pK_B (K_B, μM)	Log α' [a]	Log α (α) [b]	Log $\alpha\beta$ ($\alpha\beta$) [c]	Log τ_B (τ_B) [d]
BQCA				4.78 ± 0.06 (17)*	-3	1.77 ± 0.13 (58)*	1.84 ± 0.13 (69)*	-0.60 ± 0.10 (0.2)
1		–	–	5.88 ± 0.02 (1.3)	-3	2.84 ± 0.13 (692)	2.57 ± 0.15 (370)	0.44 ± 0.07 (3)
2		H	H	4.28 ± 0.13 (52)*	-3	1.96 ± 0.17 (91)*	2.29 ± 0.07 (195)	0.60 ± 0.02 (4)
3	H	H	H	4.21 ± 0.06 (61)*	-3	1.01 ± 0.26 (10)*	1.24 ± 0.07 (17)*	-3
4		Me	H	4.98 ± 0.11 (10)*	-3	2.32 ± 0.09 (209)	2.42 ± 0.10 (263)	0.44 ± 0.04 (2.8)
5		H	Me	5.15 ± 0.18 (7.1)	-3	2.58 ± 0.16 (380)	2.66 ± 0.05 (457)	0.05 ± 0.03 (1.1)*
6		Me	Me	5.14 ± 0.13 (7.2)*	-3	2.41 ± 0.21 (257)	2.69 ± 0.11 (490)	0.81 ± 0.05 (6.5)*
7	H	Me	Me	4.76 ± 0.14 (17)*	-3	2.34 ± 0.17 (219)	2.86 ± 0.09 (776)	1.06 ± 0.02 (11)*
8		–	–	4.10 ± 0.07 (79)*	-3	1.84 ± 0.16 (69)*	1.82 ± 0.04 (66)*	-3
9	Ph	–	–	4.66 ± 0.20 (22)	-0.32 ± 0.12	-0.04 ± 0.09 (0.91)	n/a	n/a
10	–	–	–	4.99 ± 0.22 (10)*	0.08 ± 0.05	0.60 ± 0.08 (4)*	0.67 ± 0.09 (5)*	-3
11	Cl	–	–	4.06 ± 0.08 (87)*	-0.55 ± 0.18	0.67 ± 0.08 (5)*	1.12 ± 0.11 (13)*	-0.36 ± 0.11 (0.4)*
12	H	–	–	5.29 ± 0.09 (5)	-3	2.35 ± 0.18 (223)	2.64 ± 0.13 (436)	1.14 ± 0.02 (14)*

[a]Binding cooperativity with [^{3}H]NMS; for instances where a complete inhibition of [^{3}H]NMS binding by the allosteric modulator was observed (consistent with a high level of negative cooperativity), log α' was fixed to −3. [b]Binding cooperativity with ACh. [c]Functional cooperativity with ACh. [d]Intrinsic efficacy of the modulator; for instances where no intrinsic efficacy was observed, log τ_B was fixed to −3. *Significant difference ($p < 0.05$) relative to same parameter determined for **1**, one-way ANOVA with Tukeys's post-test. Values represent the mean ± SEM from at least three experiments performed in duplicate.

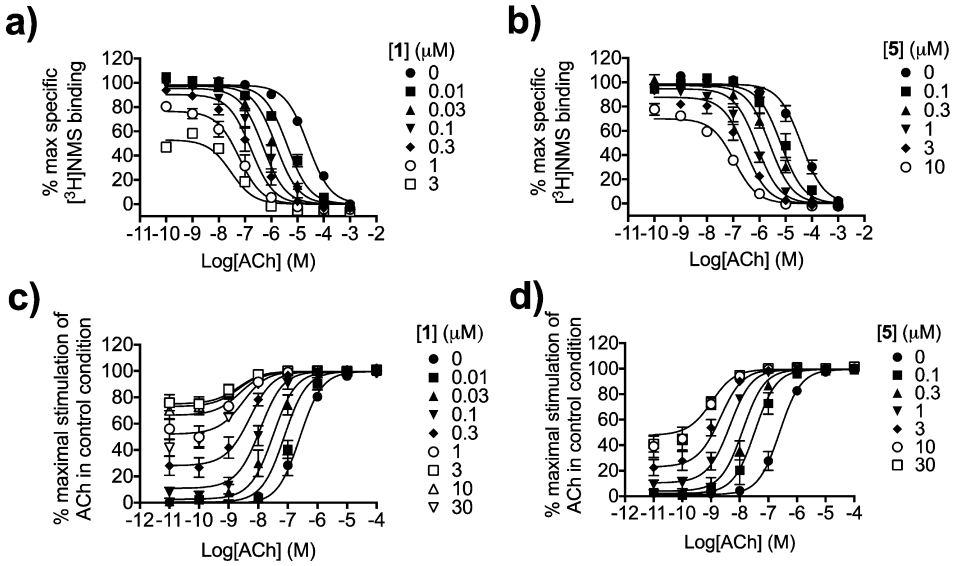

Figure 2. (a−d) Pharmacological characterization of **1** and **5** in binding and function at the M_1 mAChR. (a,b) Radioligand binding experiments were performed using FlpIn-CHO cells expressing the M_1 mAChR, 0.1 nM of the radiolabeled antagonist [^{3}H]NMS, increasing concentrations of ACh, with or without increasing concentrations of either **1** (a) or **5** (b). (c,d) IP$_1$ accumulation experiments were performed using FlpIn-CHO cells expressing the M_1 mAChR and increasing concentrations of ACh with or without increasing concentrations of either compound **1** (c) or **5** (d). 100% represents the maximal stimulation of ACh in the absence of test compound.

DOI: 10.1021/acschemneuro.6b00018
ACS Chem. Neurosci. 2016, 7, 647−661

amide derivatives of the acid function was important in determining cooperativity, and replacement of the *N*-alkyl group modulated ligand affinity.[19] More recently, we focused on the binding mode of 3-((1*S*,2*S*)-2-hydroxycyclohexyl)-6-((6-(1-methyl-1*H*-pyrazol-4-yl)pyridin-3-yl)methyl)benzo[*h*]-quinazolin-4(3*H*)-one (**1**), a significantly more potent M_1 mAChR PAM with a structural ancestry originating from BQCA.[21] To understand the structural determinants that underlie the superior PAM activity of **1**, we applied the same approach as described above for BQCA for all ligands described in this study. Competition binding studies between ACh and the radiolabeled antagonist [^{3}H]NMS at the M_1 mAChR expressed in FlpIN CHO cells were performed in the absence and presence of increasing concentrations of each test compound. Data were analyzed with an allosteric ternary complex,[27] to determine the K_B of the test compound for the allosteric site on the unoccupied M_1 mAChR, and its binding cooperativity (α) with ACh. To assess the ability of our test compounds to modulate ACh function, we used myoinositol-1-phosphate (IP_1) accumulation as a measure of M_1 mAChR activation. Concentration curves of ACh were generated in the presence of increasing concentrations of test compound, and an operational model of allostery was applied to the data with the K_B fixed to that determined in the binding studies, thus allowing an overall estimate of both functional cooperativity with ACh ($\alpha\beta$) and the intrinsic efficacy of the allosteric ligand. Values of α or $\beta > 1$ describe a positive modulatory effect upon ACh, whereas values between 0 and 1 describe a negative modulatory effect. It should be noted that because the logarithms of affinity and cooperativity values are normally distributed, whereas the corresponding absolute (antilogarithms) are not,[28] all statistical comparisons were performed on the logarithmic values (Table 1).

As described before, **1** displays a significant 13-fold higher affinity (K_B = 1.3 μM) for the M_1 mAChR as compared to BQCA. In addition, in comparison to BQCA, **1** displays a 12-fold increase in binding cooperativity (α = 692) and a 5-fold increase in functional cooperativity ($\alpha\beta$ = 370) with ACh (Figure 2, Table 1). Finally, **1** displays superior intrinsic efficacy compared to BQCA with a 15-fold increase in τ_B (τ_B = 3). Complete deletion of the peripheral fused benzene ring, as in **2**, caused a 40-fold decrease in affinity (K_B = 52) and an 8-fold decrease in binding cooperativity with ACh (α = 91). However, no change in intrinsic efficacy was observed (τ_B = 4). Further deletion of the 4-(1-methylpyrazole-4-yl) substitution of the (pyridin-3-yl)methyl pendant group to give **3**, caused no change in affinity relative to **2**, but caused a significant 9-fold loss of binding cooperativity, a significant 11-fold loss of functional cooperativity, and a complete loss of observed intrinsic efficacy. The addition of a methyl group at the 8- or 7-positions of the quinazolin-4(3*H*)-one core (compounds **4** and **5**, respectively) caused a significant 5- to 7-fold increase in affinity compared to **2**, but with no significant change in cooperativity with ACh. While methyl substitution at the 8-position (**4**) resulted in similar intrinsic activity relative to **2**, the addition of methyl at the 7-position (**5**) caused a significant 4-fold decrease in intrinsic efficacy (Figure 2). The addition of a methyl group at both the 7- and 8-positions in compound **6** caused a 7-fold increase in affinity, and no significant change in cooperativity with ACh or intrinsic efficacy relative to **2**. Indeed this analogue displayed a 2-fold higher intrinsic efficacy than **1**. Together these data reveal that the benzo[*h*]quinazolin-4(3*H*)-one core is an important determinant of the affinity of **1**. Deletion of the fused benzene ring of this core (**2**) was associated with a significant loss of affinity that was partly rescued with the addition of methyl groups in the 7 and/or 8 position of a quinazolin-4(3*H*)-one core (**5** and **6**). Indeed, compound **5** displayed no significant difference in affinity compared to **1** ($p > 0.05$, one-way ANOVA with Tukey's post-test). In our recent SAR study,[19] we observed that the replacement of the *N*-alkyl group of the quinolone core of BQCA modulated ligand affinity. In particular, changing the *N*-(4-methoxy)benzyl group to *N*-(4-phenyl)benzyl tended to improve affinity for the receptor without improving cooperative binding with ACh. In contrast, the absence of a 4-(1-methylpyrazole-4-yl) substituent from the (pyridin-3-yl)methyl pendant group of **2** (with a quinazolin-4(3*H*)-one core) had no effect upon affinity but instead caused a decrease in intrinsic activity (compare compounds **2** and **3**). However, when two methyl groups were present on the quinazolin-4(3*H*)-one core, the absence of the 4-(1-methylpyrazole-4-yl) moiety caused no change in affinity, cooperativity or intrinsic activity (**6** compared to **7**, Table 1).

To further explore the role of the (pyridin-3-yl)methyl pendant group in the determination of the activity of **1**, we characterized the synthetic intermediates **10** and **11** and synthetic byproduct **12**. Replacement of the (6-(1-methyl-1*H*-pyrazol-4-yl)pyridin-3-yl)methyl group with a bromo-substituent (**10**) caused an 8-fold loss of affinity, a 170-fold and 70-fold loss in binding and functional cooperativity with ACh, respectively. In addition, a complete loss of intrinsic efficacy was observed. Compound **12**, which possessed an unsubstituted (pyridin-3-yl)methyl group, displayed an affinity for the M_1 mAChR that was not significantly different from **1** and had similar binding and functional cooperativity with ACh (α = 223, $\alpha\beta$ = 436). Furthermore, **12** displayed 5-fold higher intrinsic efficacy than **1** (τ_B = 14). In contrast, the (6-chloropyridin-3-yl)methyl derivative **11** displayed 66-fold lower affinity than **1**, 140-fold and 30-fold lower binding and functional cooperativity with ACh and 8-fold lower intrinsic efficacy. Together these data illustrate the importance of the benzylic pendant group for the activity of **1**. In contrast to our findings with BQCA, we found that this moiety was not only important for affinity, but also for the cooperativity with ACh and intrinsic efficacy displayed by **1**. However, removal of the 4-(1-methylpyrazole-4-yl) substitution of the (pyridin-3-yl)methyl pendant group of **1** was tolerated both in terms of affinity, cooperativity with ACh and intrinsic efficacy.

The pyrido[2,3-*d*]pyrimidin-4(3*H*)-one analogue (**8**: α = 69, $\alpha\beta$ = 66) displayed attenuated binding and functional cooperativity with ACh relative to compound **2** (**2**: α = 91, $\alpha\beta$ = 195). Finally, the thieno[2,3-*d*]pyrimidin-4(3*H*)-one **9** showed negligible binding cooperativity with ACh.

CONCLUSIONS

We have recently reported that 3-((1*S*,2*S*)-2-hydroxycyclohexyl)-6-((6-(1-methyl-1*H*-pyrazol-4-yl)pyridin-3yl)methyl)benzo-[*h*]quinazolin-4(3*H*)-one (**1**), while structurally related to BQCA, is a significantly more potent PAM of the M_1 mAChR, driven both by an increased affinity for the M_1 mAChR and an increased level of positive cooperativity with ACh.[21] In addition, **1** displays higher intrinsic efficacy than BQCA. Furthermore, we recently proposed a binding mode of **1** within the M_1 mAChR that is similar to that predicted for BQCA.[21] In this study, we wanted to explore the structural determinants that underlie the activity of **1** as a PAM of the M_1

DOI: 10.1021/acschemneuro.6b00018
ACS Chem. Neurosci. 2016, 7, 647−661

mAChR. We have previously demonstrated that changing the *N*-alkyl group of the quinolone core of BQCA modulated ligand affinity but not cooperativity with ACh.[19] In this study, we demonstrate that the (pyrid-3-yl)methyl pendant group of **1** is not only important for affinity, but has an additional role in determining cooperativity with ACh. In addition, we found that removal of the 1-methyl-1*H*-pyrazol-4-yl moiety of **1** was well tolerated in terms of both affinity and cooperativity with ACh and generated a PAM (**7**) with superior intrinsic efficacy. We paid particular attention to the importance of the tricyclic scaffold of compound **1** for the activity of the molecule. Complete deletion of the peripheral fused benzene ring caused a significant decrease in affinity and binding cooperativity with ACh, but no change in intrinsic activity. However, this loss of affinity was partially rescued with the addition of methyl groups in the 7- and/or 8-position of the quinazolin-4(3*H*)-one core (compounds **4**, **5** and **6**). Indeed, compound **5** with the addition of a methyl group in the 8-position displayed no significant difference in affinity for the M_1 mAChR compared to **1**, but lower intrinsic activity (Figure 2). The addition of methyl groups at the 7- and 8-positions (**6**) maintained this affinity and rescued intrinsic efficacy. These results demonstrate that the tricyclic benzo[*h*]quinazolin-4(3*H*)-one core could be replaced with a quinazolin-4(3*H*)-one core. This may be important, given the precedence of polyaromatic heterocycles as DNA chelators. In addition, the quinazolin-4(3*H*)-one core represents a novel scaffold to explore further M_1 mAChR PAMs with improved physicochemical properties.

METHODS

Synthesis of Compounds. Chemicals and solvents were purchased from standard suppliers and used without further purification. Davisil silica gel (40−63 μm), for flash column chromatography (FCC), was supplied by Grace Davison Discovery Sciences (Victoria, Australia), and deuterated solvents were purchased from Cambridge Isotope Laboratories, Inc. (distributed by Novachem PTY. Ltd., Victoria, Australia).

Unless otherwise stated, reactions were carried out at ambient temperature. Reactions were monitored by thin layer chromatography on commercially available precoated aluminum-backed plates (Merck Kieselgel 60 F_{254}). Visualization was by examination under UV light (254 and 366 nm). General staining was carried out with $KMnO_4$ or phosphomolybdic acid. A solution of Ninhydrin (in ethanol) was used to visualize primary and secondary amines. All organic extracts collected after aqueous workup procedures were dried over anhydrous $MgSO_4$ or Na_2SO_4 before gravity filtering and evaporation to dryness. Organic solvents were evaporated in vacuo at ≤40 °C (water bath temperature). Purification using preparative layer chromatography (PLC) was carried out on Analtech preparative TLC plates (200 mm × 200 mm × 2 mm).

^{1}H NMR and ^{13}C NMR spectra were recorded on a Bruker Avance Nanobay III 400 MHz Ultrashield Plus spectrometer at 400.13 and 100.62 MHz, respectively. Chemical shifts (δ) were recorded in parts per million (ppm) with reference to the chemical shift of the deuterated solvent. Coupling constants (J) and carbon−fluorine coupling constants (J_{CF}) were recorded in Hz, and the significant multiplicities described by singlet (s), doublet (d), triplet (t), quadruplet (q), broad (br), multiplet (m), doublet of doublets (dd), and doublet of triplets (dt). Spectra were assigned using appropriate COSY, distortionless enhanced polarization transfer (DEPT), HSQC and HMBC sequences. Specific optical rotation was determined using a Jasco P-2000 polarimeter.

LC-MS were run to verify reaction outcome and purity using following system: Agilent 6120 Series Single Quad coupled to an Agilent 1260 Series HPLC. The following buffers were used; buffer A, 0.1% formic acid in H_2O; buffer B, 0.1% formic acid in MeCN. The following gradient was used with a Poroshell 120 EC-C18 50 × 3.0 mm 2.7 μm column, and a flow rate of 0.5 mL/min and total run time of 5 min; 0−1 min 95% buffer A and 5% buffer B, from 1 to 2.5 min up to 0% buffer A and 100% buffer B, held at this composition until 3.8 min, 3.8−4 min 95% buffer A and 5% buffer B, held until 5 min at this composition. Mass spectra were acquired in positive and negative ion mode with a scan range of 100−1000 m/z. UV detection was carried out at 214 and 254 nm. All retention times (t_R) are quoted in minutes. High resolution mass spectra (HRMS) were obtained from a Waters LCT Premier XE (TOF) mass spectrometer fitted with an ESI ion source, coupled to a 2795 Alliance Separations Module.

Preparative HPLC was performed using an Agilent 1260 infinity coupled with a binary preparative pump and Agilent 1260 FC-PS fraction collector, using Agilent OpenLAB CDS software (Rev C.01.04), and an Altima 5 μM C8 22 × 250 mm column. The following buffers were used: buffer A, H_2O; buffer B, MeCN, with sample being run at a gradient of 5% buffer B to 100% buffer B over 20 min, at a flow rate of 20 mL/min All screening compounds were of >95% purity unless stated otherwise.

General Procedure A: HCTU-Mediated Amide Bond Formation. Carboxylic acid (1 equiv), HCTU (1.1 equiv), and amine or amine salt (1.1 equiv) were dispersed or dissolved in DMF (∼2 mL/mmol) at RT. To this was added DIPEA (2.5 eq, for amine salts, an additional 1.0 equiv per salt form was also added), and the mixture allowed to stir at RT overnight. LC-MS analysis was used to confirm reaction completion. The mixture was diluted with water/sat. $NaHCO_{3(aq)}$ (1:1, ∼20 mL/mmol) and stirred for 30 min at RT. Where a solid precipitate formed, this was collected by filtration (vacuum) and washed with water. Where no solid could be isolated in this manner, the aqueous slurry was extracted with EtOAc (3 times) and the combined organic layers washed with brine, then concentrated under reduced pressure. Where necessary, further purification was carried out by FCC.

General Procedure B: Negishi Coupling of Aryl Bromides with (2-Chloro-5-pyridylmethyl)zinc Chloride. Aryl bromide (1.0 equiv) was dissolved in dry THF (2 mL/mmol), under an atmosphere of nitrogen, and degassed for 5 min under a stream of nitrogen. $Pd(P(^tBu)_3)_2$ (0.03 equiv) was added and then vessel was evacuated and refilled with nitrogen, before cooling to 0 °C over an ice bath. A solution of 2-chloro-5-pyridylmethyl)zinc chloride (0.5 M in THF, 1.25 equiv) was added in a dropwise fashion, and stirring continued over the ice bath for a further 5 min, before allowing the mixture to warm to RT. Reactions were monitored by LC-MS analysis and generally left to stir overnight. To quench, the mixture was cooled to 0 °C over an ice bath and a small amount of water added with care. The quenched mixture was diluted with water, then washed three times with equal volumes of EtOAc. The combined organic layers were washed with brine, before drying over $MgSO_4$, and concentrating under reduced pressure. The crude product was further purified by FCC (eluent EtOAc/PE 50:50 to 100:0).

General Procedure C: Suzuki Coupling of Substituted 2-Chloropyridines with 1-Methyl-4-(4,4,5,5-tetramethyl-1,3,2-dioxaborolan-2-yl)-1H-pyrazole. Substituted 2-chloropyridine (1.0 equiv) and 1-methyl-4-(4,4,5,5-tetramethyl-1,3,2-dioxaborolan-2-yl)-1*H*-pyrazole (1.5 equiv) were dispersed in 1 M $Na_2CO_{3(aq)}$/THF (1:3, ∼ 10 mL/mmol) in a 10 mL microwave tube. The mixture was sonicated for 5 min, then degassed under a stream of nitrogen. $PdCl_2(PPh_3)_2$ (0.1 equiv) was added, and the tube sealed, before heating (hot plate) at 100 °C for 2 h. The mixture was cooled to RT, then diluted with water (20 mL), before extracting with EtOAc (3 × 20 mL). The combined organic extracts were washed with brine (20 mL), then concentrated under reduce pressure. The crude product was purified by normal phase silica chromatography as specified under each monologue.

*3-((1S,2S)-2-Hydroxycyclohexyl)-6-((6-(1-methyl-1H-pyrazol-4-yl)pyridin-3-yl)methyl)quinazolin-4(3H)-one (**2**) and 3-((1S,2S)-2-Hydroxycyclohexyl)-6-(pyridin-3-ylmethyl)quinazolin-4(3H)-one (**3**).* 6-((6-Chloropyridin-3-yl)methyl)-3-((1*S*,2*S*)-2-hydroxycyclohexyl)-quinazolin-4(3*H*)-one (**33**) (70 mg, 0.19 mmol) underwent Suzuki coupling according to General Procedure C. The crude product was purified by PLC (MeOH/EtOAc 6:94, plate run three times). The

DOI: 10.1021/acschemneuro.6b00018
ACS Chem. Neurosci. 2016, 7, 647−661

higher running band was found to be dehalogenated starting material: 3-((1*S*,2*S*)-2-Hydroxycyclohexyl)-6-(pyridin-3-ylmethyl)quinazolin-4(3*H*)-one (**3**), isolated as 9 mg (14%) of a white solid. ^{1}H NMR ($CDCl_3$) δ 8.62−8.41 (m, 2H), 8.09 (s, 1H), 8.04 (d, J = 1.8 Hz, 1H), 7.68 (d, J = 7.9 Hz, 1H), 7.59 (d, J = 8.3 Hz, 1H), 7.49 (dd, J = 8.4/2.0 Hz, 1H), 7.45−7.32 (m, 1H), 4.74−4.40 (m, 1H), 4.13 (s, 2H), 4.08−3.85 (m, 1H), 2.30−2.17 (m, 1H), 2.03−1.77 (m, 4H), 1.58−1.35 (m, 3H); ^{13}C NMR ($CDCl_3$) δ 161.8, 147.2, 146.4, 145.2, 144.9, 139.4, 138.2, 137.6, 135.1, 128.1, 126.7, 124.7, 122.2, 70.4, 38.8, 35.7, 31.0, 25.4, 24.5; m/z MS (TOF ES$^+$) 336.2 [MH]$^+$; HRMS - $C_{20}H_{22}N_3O_2$ [MH]$^+$ calcd 336.1712; found 336.1716; LC-MS t_R: 2.76 min; $[\alpha]_D^{27}$ = +5.10° (0.11, DMSO).

The lower running band was found to be 3-((1*S*,2*S*)-2-hydroxycyclohexyl)-6-((6-(1-methyl-1*H*-pyrazol-4-yl)pyridin-3-yl)-methyl)quinazolin-4(3*H*)-one (**2**, isolated as 42 mg (53%) of a glassy solid. ^{1}H NMR ($CDCl_3$) δ 8.39 (d, J = 1.7 Hz, 1H), 8.08 (s, 1H), 8.05 (s, 1H), 8.00 (d, J = 1.6 Hz, 1H), 7.88 (s, 1H), 7.53 (d, J = 8.3 Hz, 1H), 7.51−7.42 (m, 2H), 7.39 (d, J = 8.2 Hz, 1H), 4.51 (s, 1H), 4.06−3.85 (m, 6H), 2.29−2.15 (m, 1H), 2.01−1.73 (m, 4H), 1.58−1.33 (m, 3H); ^{13}C NMR ($CDCl_3$) δ 161.8, 149.5, 148.1, 146.2, 144.6, 139.0, 138.6, 137.7, 135.1, 133.6, 129.6, 127.8, 126.5, 122.1, 120.0, 113.6, 71.6, 39.4, 38.5, 35.6, 31.0, 25.4, 24.6; m/z MS (TOF ES$^+$) 416.3 [MH]$^+$; HRMS - $C_{24}H_{26}N_5O_2$ [M-Na]$^+$ calcd 438.1906; found 438.1872; LC-MS t_R: 2.85 min; $[\alpha]_D^{27}$ = −1.04° (0.26, DMSO).

*3-((1S,2S)-2-Hydroxycyclohexyl)-8-methyl-6-((6-(1-methyl-1H-pyrazol-4-yl)pyridin-3-yl)methyl)quinazolin-4(3H)-one (**4**).* 6-((6-Chloropyridin-3-yl)methyl)-3-((1*S*,2*S*)-2-hydroxycyclohexyl)-8-methylquinazolin-4(3*H*)-one (**34**) (200 mg, 0.52 mmol) underwent Suzuki coupling according to General Procedure C. The crude product was purified by FCC (eluent MeOH/DCM 0:100 to 10:90) to give 214 mg (96%) of pale yellow glassy solid. ^{1}H NMR (DMSO-d_6) δ 8.46 (d, J = 1.6 Hz, 1H), 8.38 (s, 1H), 8.22 (s, 1H), 7.93 (d, J = 0.6 Hz, 1H), 7.84 (d, J = 1.6 Hz, 1H), 7.61 (dd, J = 8.1/2.3 Hz, 1H), 7.58 (dd, J = 1.9/0.7 Hz, 1H), 7.55 (dd, J = 8.1/0.7 Hz, 1H), 4.90 (d, J = 5.4 Hz, 1H), 4.39 (s, 1H), 4.05 (s, 2H), 3.93 (s, 1H), 3.86 (s, 3H), 2.50 (s, 3H), 2.14−1.50 (m, 5H), 1.50−1.21 (m, 3H); ^{13}C NMR (DMSO-d_6) δ 160.6, 149.8, 149.4, 144.9, 144.4, 139.1, 137.0, 136.9, 135.4, 135.2, 133.5, 129.6, 123.2, 122.7, 121.6, 119.1, 69.0, 38.7, 37.4, 35.2, 30.3, 25.0, 24.0, 17.0; m/z MS (TOF ES$^+$) 430.3 [MH]$^+$; HRMS - $C_{25}H_{28}N_5O_2$ [MH]$^+$ calcd 430.2243; found 430.2248; LC-MS t_R: 3.29 min; $[\alpha]_D^{27}$ = +6.93° (0.29, DMSO).

*3-((1S,2S)-2-Hydroxycyclohexyl)-7-methyl-6-((6-(1-methyl-1H-pyrazol-4-yl)pyridin-3-yl)methyl)quinazolin-4(3H)-one (**5**).* 6-((6-Chloropyridin-3-yl)methyl)-3-((1*S*,2*S*)-2-hydroxycyclohexyl)-7-methylquinazolin-4(3*H*)-one (**35**) (328 mg, 0.97 mmol) underwent Suzuki coupling according to General Procedure C. The crude product was purified by FCC (eluent EtOAc/PE 50:50 to 100:0) to give 334 mg (90%) of an off-white solid. ^{1}H NMR (DMSO-d_6) δ 8.38 (d, J = 1.6 Hz, 1H), 8.34 (s, 1H), 8.23 (s, 1H), 7.94 (d, J = 0.7 Hz, 1H), 7.84 (s, 1H), 7.56 (dd, J = 8.1/0.6 Hz, 1H), 7.53−7.42 (m, 2H), 4.90 (d, J = 5.4 Hz, 1H), 4.37 (s, 1H), 4.11 (s, 2H), 3.94 (s, 1H), 3.87 (s, 3H), 2.39 (s, 3H), 2.11−1.49 (m, 5H), 1.46−1.13 (m, 3H); ^{13}C NMR (DMSO-d_6) δ 160.2, 149.8, 149.6, 146.2, 146.0, 143.7, 138.3, 137.0, 136.9, 132.3, 129.3, 127.8, 126.2, 122.6, 119.1, 119.0, 69.0, 38.7, 35.2, 35.0, 29.9, 25.1, 24.0, 19.7; m/z MS (TOF ES$^+$) 430.3 [MH]$^+$; HRMS - $C_{25}H_{28}N_5O_2$ [MH]$^+$ calcd 430.2243; found 430.2244; LC-MS t_R: 3.24 min; $[\alpha]_D^{27}$ = +6.11° (0.67, DMSO).

*3-((1S,2S)-2-Hydroxycyclohexyl)-7,8-dimethyl-6-((6-(1-methyl-1H-pyrazol-4-yl)pyridin-3-yl)methyl)quinazolin-4(3H)-one (**6**) and 3-((1S,2S)-2-Hydroxycyclohexyl)-7,8-dimethyl-6-(pyridin-3-ylmethyl)quinazolin-4(3H)-one (**7**).* 6-((6-Chloropyridin-3-yl)-methyl)-3-((1*S*,2*S*)-2-hydroxycyclohexyl)-7,8-dimethylquinazolin-4(3*H*)-one (**36**) (61 mg, 0.15 mmol) underwent Suzuki coupling according to General Procedure C. The crude product was purified by PLC (MeOH/EtOAc 5:95, plate run three times). The higher running band was found to be dehalogenated starting material: 3-((1*S*,2*S*)-2-Hydroxycyclohexyl)-7,8-dimethyl-6-(pyridin-3-ylmethyl)quinazolin-4(3*H*)-one (**7**), isolated as 5 mg (9%) of an off-white solid. ^{1}H NMR ($CDCl_3$) δ 8.45 (s, 2H), 8.10 (s, 1H), 7.90 (s, 1H), 7.46 (d, J = 7.9 Hz, 1H), 7.33−7.19 (m, 1H), 4.53 (s, 1H), 4.13 (s, J = 7.5 Hz, 2H), 3.97 (s, 1H), 3.82−2.86 (m, 1H), 2.52 (s, 3H), 2.33−2.13 (m, 4H), 2.03−1.69 (m, 4H), 1.61−1.33 (m, 3H); ^{13}C NMR ($CDCl_3$) δ 162.3, 148.3, 146.1, 145.1, 143.3, 142.1, 137.7, 136.6, 134.9, 129.0, 125.3, 124.2, 119.7, 72.0, 37.7, 35.7, 31.0, 25.5, 24.6, 17.0, 13.7; m/z MS (TOF ES$^+$) 364.2 [MH]$^+$; HRMS - $C_{22}H_{26}N_3O_2$ [MH]$^+$ calcd 364.2025; found 364.2031; LC-MS t_R: 2.90 min; $[\alpha]_D^{27}$ = +13.87° (0.18, DMSO).

The lower running band was found to be 3-((1*S*,2*S*)-2-hydroxycyclohexyl)-7,8-dimethyl-6-((6-(1-methyl-1*H*-pyrazol-4-yl)-pyridin-3-yl)methyl)quinazolin-4(3*H*)-one (**6**), isolated as 10 mg (15%) of white solid. ^{1}H NMR ($CDCl_3$) δ 8.20 (s, 1H), 8.08−7.93 (m, 2H), 7.83 (s, 1H), 7.81 (s, 1H), 7.48−7.32 (m, 2H), 4.35 (s, 1H), 4.05 (s, 2H), 4.01−3.73 (m, 4H), 2.43 (s, 3H), 2.17 (s, 3H), 2.07 (d, J = 10.1 Hz, 1H), 1.97−1.58 (m, 4H), 1.48−1.21 (m, 3H); ^{13}C NMR ($CDCl_3$) δ 162.1, 151.6, 146.8, 144.9, 143.5, 142.2, 139.5, 137.6, 136.6, 134.6, 133.9, 129.9, 124.9, 120.6, 119.5, 112.1, 70.6, 38.9, 37.1, 35.1, 31.0, 25.2, 24.3, 16.7, 13.4; m/z MS (TOF ES$^+$) 444.3 [MH]$^+$; HRMS - $C_{26}H_{30}N_5O_2$ [MH]$^+$ calcd 444.2400; found 444.2411; LC-MS t_R: 3.01 min; $[\alpha]_D^{27}$ = +6.44° (0.16, DMSO).

*3-((1S,2S)-2-Hydroxycyclohexyl)-6-((6-(1-methyl-1H-pyrazol-4-yl)pyridin-3-yl)methyl)pyrido[2,3-d]pyrimidin-4(3H)-one (**8**).* 6-((6-Chloropyridin-3-yl)methyl)-3-((1*S*,2*S*)-2-hydroxycyclohexyl)pyrido-[2,3-*d*]pyrimidin-4(3*H*)-one (**40**) (33 mg, 0.09 mmol) underwent Suzuki coupling according to General Procedure C. The crude product was purified by PLC (MeOH/EtOAc 7:93, plate run six times) to give 9 mg (24%) of white solid. ^{1}H NMR (CD_3OD) δ 8.88 (d, J = 2.4 Hz, 1H), 8.52 (s, 1H), 8.49−8.40 (m, 2H), 8.12 (s, 1H), 7.99 (d, J = 0.5 Hz, 1H), 7.70 (dd, J = 8.2/2.3 Hz, 1H), 7.62 (d, J = 8.2 Hz, 1H), 4.44 (s, 1H), 4.23 (s, 2H), 4.18−3.98 (m, 1H), 3.94 (s, 3H), 2.29−1.69 (m, 5H), 1.56−1.37 (m, 3H); ^{13}C NMR (CD_3OD) δ 163.1, 157.4, 157.2, 151.6, 150.4, 150.3, 139.3, 138.5, 137.3, 137.1, 134.6, 130.9, 123.9, 121.5, 118.0, 71.1, 39.1, 36.2, 36.0, 30.8, 26.4, 25.4; m/z MS (TOF ES$^+$) 417.3 [MH]$^+$; HRMS- $C_{23}H_{25}N_6O_2$ [MH]$^+$ calcd 417.2039; found 417.2025; LC-MS t_R: 3.16 min; $[\alpha]_D^{27}$ = −4.86° (0.20, DMSO).

*6-([1,1′-Biphenyl]-4-ylmethyl)-3-((1S,2S)-2-hydroxycyclohexyl)-thieno[2,3-d]pyrimidin-4(3H)-one (**9**).* 5-([1,1′-Biphenyl]-4-ylmethyl)-2-amino-*N*-((1*S*,2*S*)-2-hydroxycyclohexyl)thiophene-3-carboxamide (**49**) (91 mg, 0.22 mmol) was dispersed in formamide (20 mL), before heating at 180 °C for 4 h. LC-MS analysis indicated conversion was complete. TLC analysis (EtOAc/PE 1:1, plate run twice) indicated the starting material and product both had an R_f ∼ 0.4, with only the starting material staining positive with ninhydrin. The mixture was cooled, then poured onto ice/water, and the resulting precipitate collected by filtration (vacuum), and further washed with water. The crude product was purified by FCC (eluent EtOAc/PE 0:100 to 60:40, wet load in DCM), to give 52 mg (56%) of an off-white solid. ^{1}H NMR (DMSO-d_6) δ 8.39 (s, 1H), 7.75−7.56 (m, 4H), 7.50−7.42 (m, 2H), 7.42−7.31 (m, 3H), 7.21 (s, 1H), 4.92 (s, 1H), 4.41 (s, 1H), 4.25 (s, 2H), 3.91 (s, 1H), 2.15−1.50 (m, 4H), 1.48−1.11 (m, 4H); ^{13}C NMR (DMSO-d_6) δ 162.0, 156.8, 145.9, 142.1, 139.8, 138.9, 138.6, 129.2, 128.9, 127.4, 127.0, 126.6, 123.7, 119.6, 69.1, 35.3, 35.2, 30.6, 25.1, 23.9; m/z MS (TOF ES$^+$) 417.3 [MH]$^+$; HRMS - $C_{25}H_{25}N_2O_2S$ [MH]$^+$ calcd 417.1637; found 417.1613; LC-MS t_R: 3.98 min; $[\alpha]_D^{27}$ = +17.77° (0.35, DMSO).

*Methyl 2-Amino-3,4-dimethylbenzoate (**15**).*[12] 2-Amino-3,4-dimethylbenzoic acid (**14**) (4.92 g, 29.8 mmol) and conc. H_2SO_4 (3 mL) were dissolved in MeOH (50 mL) and boiled under reflux for 48 h. LC-MS analysis indicated approximately half of the starting material had been converted. Additional H_2SO_4 (1 mL) was added, and heating continued. After a total of 6 days, the mixture was cooled to RT, and concentrated under reduced pressure. The residue was neutralized with sat. $NaHCO_{3(aq)}$, and the resulting precipitate collected by filtration (vacuum), and washed with water. After drying, 4.452 g (83%) of an off-white solid was obtained. ^{1}H NMR ($CDCl_3$) δ 7.69 (d, J = 8.2 Hz, 1H), 6.58 (d, J = 8.2 Hz, 1H), 6.18 (s, 2H), 3.86 (s, 3H), 2.30 (s, 3H), 2.13 (s, 3H); ^{13}C NMR ($CDCl_3$) δ 169.2, 147.8, 142.8, 128.4, 122.0, 119.4, 109.5, 51.7, 21.3, 13.0; m/z MS (TOF ES$^+$) 180.2 [MH]$^+$; LC-MS t_R: 3.48 min.

*Methyl 2-Amino-5-bromo-3,4-dimethylbenzoate hydrobromide (**16**).* Methyl 2-amino-3,4-dimethylbenzoate (**15**) (3.40 g, 19.0 mmol) was dissolved in 1,4-dioxane/CCl_4 (1:1, 100 mL), and cooled to 0 °C

DOI: 10.1021/acschemneuro.6b00018
ACS Chem. Neurosci. 2016, 7, 647−661

over an ice bath, after wrapping the flask in aluminum foil to exclude light. To the cooled mixture, was added a solution of bromine (3.03 g, 18.97 mmol, 1.0 equiv) in 1,4-dioxane/CCl_4 (1:1, 20 mL) in a dropwise fashion. The mixture was stirred for 2 h at 0 °C, before addition of Et_2O, and collection of the resulting precipitate by filtration (vacuum). After washing with further Et_2O and drying, 5.96 g (93%) of an off-white solid was obtained. ^{1}H NMR (DMSO-d_6) δ 7.79 (s, 1H), 4.40 (s, 3H), 3.79 (s, 3H), 2.33 (s, 3H), 2.10 (s, 3H); ^{13}C NMR (DMSO-d_6) δ 167.2, 148.7, 140.7, 130.7, 123.8, 109.7, 108.3, 51.7, 20.5, 14.4; m/z MS (TOF ES$^+$) 258.0 $[MH]^+$; LC-MS t_R: 3.71 min.

*Ethyl 2-Amino-4-methylbenzoate (**18**).*[10] 2-Amino-4-methylbenzoic acid (**17**) (2.10 g, 13.9 mmol) was dissolved in EtOH (50 mL) with conc. H_2SO_4 (1 mL), before boiling under reflux for 2 h. LC-MS analysis indicated little progression, so further conc. H_2SO_4 (1 mL) was added, and heating continued for 65 h. The mixture was cooled, then concentrated under reduced pressure. The resulting residue was neutralized with sat. $NaHCO_{3(aq)}$, then extracted with DCM (3 × 30 mL). The combined organic layers were concentrated to give a brown oil, which was further purified by FCC (eluent EtOA/PE 0:100 to 10:90), to give 1.87 g (75%) of pale yellow oil. ^{1}H NMR ($CDCl_3$) δ 7.85 (d, J = 8.1 Hz, 1H), 6.96 (s, 1H), 6.77 (d, J = 8.1 Hz, 1H), 4.36 (q, J = 7.2 Hz, 2H), 2.34 (s, 3H), 1.39 (t, J = 7.1 Hz, 3H); ^{13}C NMR (101 MHz, $CDCl_3$) δ 168.2, 147.7, 145.2, 131.3, 119.8, 118.5, 110.5, 60.6, 21.8, 14.5; ^{1}H NMR; m/z MS (TOF ES$^+$) $C_{10}H_{14}NO_2$ 180.1 $[MH]^+$; LC-MS t_R: 3.82 min.

*Ethyl 2-Acetamido-4-methybenzoate (**19**)..*[10,11] Ethyl 2-amino-4-methylbenzoate (**18**) (1.87 g, 10.4 mmol) and TEA (1.74 mL, 12.5 mmol, 1.2 equiv) were dissolved in DCM (50 mL) and cooled to 0 °C under an atmosphere of nitrogen. Acetyl chloride (0.81 mL, 11.5 mmol, 1.1 equiv) was added and then the mixture was allowed to warm to RT, before stirring overnight. LC-MS analysis indicated incomplete conversion after this time, so further TEA (1.74 mL, 12.5 mmol, 1.2 equiv) and acetyl chloride (0.81 mL, 11.5 mmol, 1.1 equiv) were added and stirring continued for a further 4 h. The mixture was washed with water (50 mL), then sat. $NaHCO_{3(aq)}$ (50 mL), then concentrated under reduced pressure, to give 2.56 g of yellow solid (quantitative). ^{1}H NMR ($CDCl_3$) δ 11.10 (s, 1H), 8.53 (s, 1H), 7.92 (d, J = 8.2 Hz, 1H), 6.88 (ddd, J = 8.2/1.7/0.6 Hz, 1H), 4.35 (q, J = 7.1 Hz, 2H), 2.39 (s, 3H), 2.22 (s, 3H), 1.40 (t, J = 7.1 Hz, 3H); ^{13}C NMR ($CDCl_3$) δ 169.2, 168.5, 145.9, 141.7, 130.8, 123.5, 120.7, 112.6, 61.3, 25.7, 22.3, 14.4; m/z MS (TOF ES$^+$) 176.2 $[M\text{-}OEt]^+$; LC-MS t_R: 3.79 min.

*Ethyl 2-Acetamido-5-bromo-4-methylbenzoate (**20**).* Ethyl 2-acetamido-4-methybenzoate (**19**) (2.55 g, 11.5 mmol) was dissolved in acetic acid (8 mL) at RT, with stirring. A solution of bromine (1.84 g, 11.5 mmol, 1.0 equiv) in acetic acid (2 mL) was added in a dropwise fashion. After 48 h of stirring, LC-MS indicated partial progression, therefore another portion of bromine (0.30 mL, 921 mg, 5.76 mmol, 0.5 equiv) was added. After a further 72 h of stirring, further progression was evident, with the appearance of a minor peak indicating formation of the dibromo product. The mixture was stirred with 5% $Na_2S_2O_{3(aq)}$ (20 mL) for 30 min, then sat. $NaHCO_3$ (150 mL) added. This was extracted with DCM (3 × 50 mL), and the combined organic extracts washed further with sat. $NaHCO_{3(aq)}$ (50 mL), before concentration under reduced pressure. Purification of the crude material was attempted by FCC (eluent DCM), however, both starting material and product were found to coelute. FCC was reattempted (eluent DCM/PE 50:50 to 70:30, then 100:0) to give 687 mg of yellow solid (23%, brsm) and a further 995 mg of mixture containing starting material and desired product. ^{1}H NMR ($CDCl_3$) δ 10.99 (s, 1H), 8.65 (s, 1H), 8.16 (s, 1H), 4.37 (q, J = 7.1 Hz, 2H), 2.43 (s, 3H), 2.22 (s, 3H), 1.42 (t, J = 7.1 Hz, 3H); ^{13}C NMR (101 MHz, $CDCl_3$) δ 169.2, 167.4, 145.4, 140.7, 134.1, 122.3, 117.6, 114.5, 61.8, 25.7, 23.8, 14.3; m/z MS (TOF ES$^+$) 300.2 $[MH]^+$; LC-MS t_R: 4.11 min.

*2-Amino-5-bromo-3-methylbenzoic Acid Hydrobromide (**22**).*[29] 2-Amino-3-methylbenzoic acid (**13**) (2.08 g, 13.8 mmol) was dissolved in acetic acid (8 mL) and stirred at RT. A solution of bromine (2.20 g, 13.8 mmol, 1.0 equiv) in acetic acid (2 mL) was added in a dropwise fashion, followed by washings of DCM (5 mL). The mixture was stirred at RT for 1 h, then diluted with Et_2O. The resulting precipitate was collected by filtration (vacuum) and washed with Et_2O. After drying, 4.07 g (95%) of a pale beige solid was obtained as the hydrobromide salt. ^{1}H NMR (DMSO-d_6) δ 9.19 (s, 3H), 7.68 (dd, J = 2.5/0.4 Hz, 1H), 7.33 (dd, J = 2.5/0.8 Hz, 1H), 2.10 (s, 3H); ^{13}C NMR (DMSO-d_6) δ 168.9, 148.8, 136.4, 130.6, 126.4, 111.0, 104.8, 17.3; m/z MS (TOF ES$^+$) 230.0 $[MH]^+$; LC-MS t_R: 3.62 min.

*2-Amino-5-bromo-4-methylbenzoic Acid (**23**).*[30] Ethyl 2-acetamido-5-bromo-4-methylbenzoate (**20**) (672 mg, 2.24 mmol) was dissolved in 5 M $NaOH_{(aq)}$ (20 mL) and EtOH (30 mL). The resulting mixture was heated at 90 °C under a reflux condenser for 20 h. LC-MS analysis at this indicated hydrolysis was complete. The mixture was cooled to RT, then concentrated under reduced pressure to remove EtOH. The aqueous slurry was acidified with 2 M $HCl_{(aq)}$, to pH 2 resulting in formation of a precipitate. This was collected by filtration (vacuum), then washed with water and dried, to give 415 mg (81%) of a beige solid. ^{1}H NMR (DMSO-d_6) δ 7.77 (s, 1H), 11.41−6.62 (m, 2H), 6.72 (d, J = 0.6 Hz, 1H), 2.22 (s, 3H); ^{13}C NMR (DMSO-d_6) δ 168.3, 150.7, 142.8, 133.7, 118.3, 109.4, 107.8, 22.7; m/z MS (TOF ES$^+$) 230.1 $[MH]^+$; LC-MS t_R: 3.56 min.

*2-Amino-5-bromo-3,4-dimethylbenzoic Acid (**24**).*[13] Methyl 2-amino-5-bromo-3,4-dimethylbenzoate hydrobromide (**16**) (5.93 g, 17.5 mmol) was dispersed in THF/water (1:1, 100 mL), and the flask atmosphere purged with nitrogen. To this was added LiOH·H_2O (3.67 g, 87.4 mmol, 5.0 equiv), and the mixture stirred at RT for 24 h. LC-MS analysis after this time indicated complete hydrolysis had occurred. The mixture was concentrated under reduced pressure to remove THF and MeOH, and then acidified with excess 2 M $HCl_{(aq)}$. The resultant precipitate was collected by filtration (vacuum), and washed with water, before allowing to dry on the filter bed overnight. This was then taken up in EtOAc (300 mL) and washed with brine (80 mL), before drying over $MgSO_4$. Concentration of dried organic layer under reduced pressure gave 4.00 g (94%) of a pale brown solid. ^{1}H NMR (DMSO-d_6) δ 7.78 (br s, 2H), 7.78 (s, 1H), 2.32 (s, 3H), 2.09 (s, 3H); ^{13}C NMR (DMSO-d_6) δ 168.9, 149.0, 140.3, 131.2, 123.5, 109.3, 109.1, 20.4, 14.3; m/z MS (TOF ES$^+$) 244.1 $[MH]^+$; LC-MS t_R: 3.33 min.

*2-Amino-5-bromo-N-((1S,2S)-2-hydroxycyclohexyl)benzamide (**25**).* 2-Amino-5-bromobenzoic acid (**21**) (1.08 g, 5.00 mmol) and (1*S*,2*S*)-2-aminocyclohexanol hydrochloride (834 mg, 1.1 equiv) were coupled according to General Procedure A, to give 1.21 g (77%) of precipitate as a yellow solid, requiring no further purification. ^{1}H NMR (DMSO-d_6) δ 8.02 (d, J = 8.1 Hz, 1H), 7.70 (d, J = 2.4 Hz, 1H), 7.24 (dd, J = 8.8/2.4 Hz, 1H), 6.64 (d, J = 8.8 Hz, 1H), 6.47 (s, 2H), 4.65 (d, J = 5.2 Hz, 1H), 3.63−3.49 (m, 1H), 3.46−3.36 (m, 1H), 2.02−1.72 (m, 2H), 1.71−1.43 (m, 2H), 1.19 (d, J = 6.6 Hz, 4H); ^{13}C NMR (DMSO-d_6) δ 167.3, 148.6, 133.8, 130.5, 118.2, 117.2, 105.0, 71.0, 54.9, 34.6, 31.3, 24.6, 24.2; m/z MS (TOF ES$^+$) 313.1 $[MH]^+$; LC-MS t_R: 3.17 min.

*2-Amino-5-bromo-N-((1S,2S)-2-hydroxycyclohexyl)-3-methylbenzamide (**26**).* 2-Amino-5-bromo-3-methylbenzoic acid hydrobromide (**22**) (2.00 g, 6.43 mmol) and (1*S*,2*S*)-2-aminocyclohexanol hydrochloride (1.07 g, 1.1 equiv) were coupled according to General Procedure A, to give 2.00 g (95%) of precipitate as a pale yellow solid, requiring no further purification. ^{1}H NMR (DMSO-d_6) δ 8.03 (d, J = 8.1 Hz, 1H), 7.58 (d, J = 2.3 Hz, 1H), 7.22 (d, J = 1.7 Hz, 1H), 6.24 (s, 2H), 4.64 (d, J = 5.2 Hz, 1H), 3.68−3.47 (m, 1H), 3.46−3.34 (m, 1H), 2.07 (s, 3H), 1.98−1.71 (m, 2H), 1.72−1.51 (m, 2H), 1.34−1.06 (m, 4H); ^{13}C NMR (DMSO-d_6) δ 167.7, 146.6, 134.1, 128.2, 125.7, 117.2, 105.1, 70.9, 54.9, 34.6, 31.3, 24.5, 24.2, 17.3; m/z MS (TOF ES$^+$) 327.1 $[MH]^+$; LC-MS t_R: 3.62 min.

*2-Amino-5-bromo-N-((1S,2S)-2-hydroxycyclohexyl)-4-methylbenzamide (**27**).* 2-Amino-5-bromo-4-methylbenzoic acid (**23**) (386 mg, 1.68 mmol) and (1*S*,2*S*)-2-aminocyclohexanol hydrochloride (281 mg, 1.1 equiv) were coupled according to General Procedure A, to give 508 mg (92%) of precipitate as a beige solid, requiring no further purification. ^{1}H NMR (DMSO-d_6) δ 7.95 (d, J = 8.0 Hz, 1H), 7.74 (s, 1H), 6.64 (d, J = 0.5 Hz, 1H), 6.43 (s, 2H), 4.62 (d, J = 5.2 Hz, 1H), 3.68−3.45 (m, 1H), 3.45−3.34 (m, 1H), 2.20 (s, 3H), 1.97−1.71 (m,

DOI: 10.1021/acschemneuro.6b00018
ACS Chem. Neurosci. 2016, 7, 647−661

2H), 1.70−1.49 (m, 2H), 1.36−1.06 (m, 4H); ^{13}C NMR (DMSO-d_6) δ 167.2, 148.9, 140.0, 131.2, 118.1, 115.0, 108.0, 70.9, 54.83, 34.6, 31.3, 24.5, 24.2, 22.4; m/z MS (TOF ES$^+$) 327.1 [MH]$^+$; LC-MS t_R: 3.57 min.

*2-Amino-5-bromo-N-((1S,2S)-2-hydroxycyclohexyl)-3,4-dimethylbenzamide (**28**).* 2-Amino-5-bromo-3,4-dimethylbenzoic acid (**24**) (1.00 g, 4.10 mmol) and (1*S*,2*S*)-2-aminocyclohexanol hydrochloride (684 mg, 1.1 equiv) were coupled according to General Procedure A, to give 1.32 g (94%) of precipitate as an off-white solid, requiring no further purification. ^{1}H NMR (DMSO-d_6) δ 7.99 (d, J = 8.0 Hz, 1H), 7.66 (s, 1H), 6.27 (s, 2H), 4.62 (d, J = 5.2 Hz, 1H), 3.66−3.49 (m, 1H), 3.46−3.34 (m, 1H), 2.31 (s, 3H), 2.06 (s, 3H), 1.97−1.73 (m, 2H), 1.73−1.50 (m, 2H), 1.34−1.08 (m, 4H); ^{13}C NMR (DMSO-d_6) δ 167.8, 146.7, 137.5, 128.7, 123.1, 115.4, 109.7, 70.9, 54.9, 34.6, 31.3, 24.5, 24.2, 20.1, 14.3; m/z MS (TOF ES$^+$) 341.1 [MH]$^+$; LC-MS t_R: 3.31 min.

*6-Bromo-3-((1S,2S)-2-hydroxycyclohexyl)quinazolin-4(3H)-one (**29**).* 2-Amino-5-bromo-*N*-((1*S*,2*S*)-2-hydroxycyclohexyl)benzamide (**25**) (1.18 g, 3.8 mmol) was dispersed in DMF-DMA (12 mL) and heated, with stirring at 85 °C for 3 h. LC-MS analysis indicated that the dimethylamine addition product was the major component of the reaction mixture, with elimination to the desired product progressing slowly. Further DMF-DMA (5 mL) was added, and the reaction temperature was increased to 115 °C, with heating continued for 72 h (progress monitored by LC-MS). The mixture was cooled to RT and carefully quenched with water (very exothermic), and the resulting precipitate collected by filtration (vacuum) before washing with water. After drying under air, the crude precipitate was recrystallized from EtOH to 767 mg (63%) of a yellow solid. ^{1}H NMR ($CDCl_3$) δ 8.69 (s, 1H), 8.38 (d, J = 2.2 Hz, 1H), 7.83 (dd, J = 8.7/2.3 Hz, 1H), 7.70 (d, J = 8.7 Hz, 1H), 4.81−4.43 (m, 1H), 4.14−3.91 (m, 1H), 2.30−2.16 (m, 1H), 2.11−1.97 (m, 1H), 1.96−1.65 (m, 3H), 1.63−1.32 (m, 3H); ^{13}C NMR ($CDCl_3$) δ 160.6, 148.9, 144.7, 137.8, 129.7, 128.7, 123.4, 121.3, 61.5, 35.7, 31.1, 25.4, 24.5; m/z MS (TOF ES$^+$) 323.1 [MH]$^+$; LC-MS t_R: 3.21 min.

*6-Bromo-3-((1S,2S)-2-hydroxycyclohexyl)-8-methylquinazolin-4(3H)-one (**30**).* 2-Amino-5-bromo-*N*-((1*S*,2*S*)-2-hydroxycyclohexyl)-3-methylbenzamide (**26**) (1.50 g, 4.58 mmol) was dispersed in triethylorthoformate (30 mL) under an atmosphere of nitrogen. The mixture was heated under a reflux condenser, under nitrogen at 100 °C for 19 h. LC-MS analysis indicated partial conversion had occurred, so the temperature was increased to 150 °C for 96 h and monitored by LC-MS. The mixture was cooled to RT before quenching with a small amount of water (with care). On addition of water, a biphasic mixture was formed, so EtOAc was added, and the water layer decanted. The organic layer was then dried over $MgSO_4$, before concentration under reduced pressure to dryness. The crude residue was purified by FCC (eluent EtOAc/PE 0:100 to 100:0), to give 996 mg (65%) of a pale yellow solid. ^{1}H NMR (DMSO-d_6) δ 8.48 (s, 1H), 8.06 (dd, J = 2.4/0.5 Hz, 1H), 7.87 (dd, J = 2.3/0.9 Hz, 1H), 4.95 (d, J = 5.3 Hz, 1H), 4.38 (s, 1H), 3.94 (s, 1H), 2.53 (s, 3H), 2.14−1.56 (m, 5H), 1.47−1.20 (m, 3H); ^{13}C NMR (DMSO-d_6) δ 159.6, 148.3, 145.0, 138.4, 136.8, 125.9, 121.8, 118.8, 67.9, 35.1, 29.7, 25.0, 23.9, 16.7; m/z MS (TOF ES$^+$) 337.1 [MH]$^+$; LC-MS t_R: 3.77 min.

*6-Bromo-3-((1S,2S)-2-hydroxycyclohexyl)-7-methylquinazolin-4(3H)-one (**31**).* 2-Amino-5-bromo-*N*-((1*S*,2*S*)-2-hydroxycyclohexyl)-4-methylbenzamide (**27**) (481 mg, 1.46 mmol) was dispersed in formamide (4 mL) in a 10 mL microwave vial, before sealing and heating at 120 °C with stirring. LC-MS analysis after this time indicated no reaction progression, so the temperature was increased to 150 °C, and stirring continued for 4 h. LC-MS analysis indicated the reaction was complete, so the mixture was cooled to RT overnight, before diluting with water (30 mL), then extracting with EtOAc (3 × 30 mL). The combined organic layers were washed with water (30 mL) and brine (30 mL), before concentration under reduced pressure. The crude residue was recrystallized from EtOH, to give 339 mg (69%) of pale brown solid. Concentration of the mother liquor gave 141 mg of impure product. ^{1}H NMR ($CDCl_3$) δ 8.50 (s, 1H), 8.32 (s, 1H), 7.60−7.51 (m, 1H), 4.61 (s, 1H), 4.04 (s, 1H), 2.50 (s, 3H), 2.33−2.17 (m, 1H), 2.10−1.68 (m, 4H), 1.67−1.30 (m, 3H); ^{13}C NMR ($CDCl_3$) δ 160.4, 145.6, 145.5, 145.1, 130.3, 128.3, 123.8, 121.1, 72.1, 35.7, 31.0, 25.4, 24.5, 23.8; m/z MS (TOF ES$^+$) 337.1 [MH]$^+$; LC-MS t_R: 3.64 min.

*6-Bromo-3-((1S,2S)-2-hydroxycyclohexyl)-7,8-dimethylquinazolin-4(3H)-one (**32**).* 2-Amino-5-bromo-*N*-((1*S*,2*S*)-2-hydroxycyclohexyl)-3,4-dimethylbenzamide (**28**) (1.28 g, 3.75 mmol) was dispersed in DMF-DMA (12 mL) under an atmosphere of nitrogen, and heated at 85 °C for 6 h, before LC-MS analysis indicated conversion was complete. The mixture was cooled to RT, and carefully quenched with water. The resulting precipitate was collected by filtration (vacuum), washed further with water, and dried to give 1.25 g (95%) of an off-white solid. ^{1}H NMR (DMSO-d_6) δ 8.46 (s, 1H), 8.14 (s, 1H), 4.93 (d, J = 5.4 Hz, 1H), 4.36 (s, 1H), 3.94 (s, 1H), 2.59 (s, 3H), 2.49 (s, 3H), 2.17−1.54 (m, 5H), 1.52−1.06 (m, 3H); ^{13}C NMR (DMSO-d_6) δ 159.6, 147.9, 144.7, 141.5, 136.0, 126.3, 122.9, 120.8, 68.7, 35.1, 26.8, 25.0, 23.9, 20.4, 14.1; m/z MS (TOF ES$^+$) 351.1 [MH]$^+$; LC-MS t_R: 3.51 min.

*6-((6-Chloropyridin-3-yl)methyl)-3-((1S,2S)-2-hydroxycyclohexyl)-quinazolin-4(3H)-one (**33**).* 6-Bromo-3-((1*S*,2*S*)-2-hydroxycyclohexyl)quinazolin-4(3*H*)-one (**29**) (170 mg, 0.53 mmol) underwent Negishi coupling according to General Procedure B, to give 129 mg (66%) of a pale yellow solid. ^{1}H NMR (DMSO-d_6) δ 8.40 (d, J = 2.1 Hz, 1H), 8.37 (s, 1H), 8.01 (d, J = 1.8 Hz, 1H), 7.74 (dd, J = 8.2/2.5 Hz, 1H), 7.70 (dd, J = 8.4/2.1 Hz, 1H), 7.61 (d, J = 8.3 Hz, 1H), 7.44 (dd, J = 8.2/0.5 Hz, 1H), 4.91 (d, J = 5.3 Hz, 1H), 4.39 (s, 1H), 4.15 (s, 2H), 3.94 (s, 1H), 2.12−1.57 (m, 5H), 1.48−1.20 (m, 3H); ^{13}C NMR (DMSO-d_6) δ 160.3, 149.9, 148.8, 148.3, 146.0, 140.1, 139.0, 136.1, 134.9, 127.4, 125.7, 124.2, 121.7, 68.9, 36.6, 35.2, 27.6, 25.0, 23.9; m/z MS (TOF ES$^+$) 370.2 [MH]$^+$; LC-MS t_R: 3.18 min; $[\alpha]_D^{27}$ = +7.78° (0.43, DMSO).

*6-((6-Chloropyridin-3-yl)methyl)-3-((1S,2S)-2-hydroxycyclohexyl)-8-methylquinazolin-4(3H)-one (**34**).* 6-Bromo-3-((1*S*,2*S*)-2-hydroxycyclohexyl)-8-methylquinazolin-4(3*H*)-one (**30**) (462 mg, 1.37 mmol) underwent Negishi coupling according to General Procedure B, to give 390 mg (74%) of pale yellow solid. ^{1}H NMR (DMSO-d_6) δ 8.40 (d, J = 2.2 Hz, 1H), 8.39 (s, 1H), 7.85 (d, J = 1.4 Hz, 1H), 7.73 (dd, J = 8.2/2.5 Hz, 1H), 7.58 (s, 1H), 7.44 (d, J = 8.2 Hz, 1H), 4.91 (d, J = 5.4 Hz, 1H), 4.38 (s, 1H), 4.10 (s, 2H), 3.93 (s, 1H), 2.50 (s, 3H), 2.21−1.53 (m, 5H), 1.51−1.12 (m, 3H); ^{13}C NMR (DMSO-d_6) δ 160.5, 149.9, 148.2, 144.9, 144.5, 140.1, 138.4, 136.2, 135.6, 135.2, 124.2, 123.4, 121.6, 68.6, 36.6, 35.2, 30.5, 25.0, 24.0, 17.0; m/z MS (TOF ES$^+$) 384.2 [MH]$^+$; LC-MS t_R: 3.63 min.

*6-((6-Chloropyridin-3-yl)methyl)-3-((1S,2S)-2-hydroxycyclohexyl)-7-methylquinazolin-4(3H)-one (**35**).* 6-Bromo-3-((1*S*,2*S*)-2-hydroxycyclohexyl)-7-methylquinazolin-4(3*H*)-one (**31**) (328 mg, 0.97 mmol) underwent Negishi coupling according to General Procedure B, to give 334 mg (90%) of an off-white solid. ^{1}H NMR (DMSO-d_6) δ 8.35 (s, 1H), 8.31 (d, J = 2.1 Hz, 1H), 7.84 (s, 1H), 7.59 (dd, J = 8.2/2.5 Hz, 1H), 7.50 (s, 1H), 7.48−7.38 (m, 1H), 4.90 (d, J = 5.4 Hz, 1H), 4.37 (s, 1H), 4.15 (s, 2H), 3.93 (s, 1H), 2.35 (s, 3H), 2.07−1.48 (m, 5H), 1.47−1.14 (m, 3H); ^{13}C NMR (DMSO-d_6) δ 160.2, 150.0, 148.2, 146.4, 146.3, 143.6, 140.0, 137.6, 135.1, 128.0, 126.4, 124.2, 119.7, 68.9, 35.2, 34.4, 30.4, 25.1, 24.0, 19.7; m/z MS (TOF ES$^+$) 384.2 [MH]$^+$; LC-MS t_R: 3.55 min.

*6-((6-Chloropyridin-3-yl)methyl)-3-((1S,2S)-2-hydroxycyclohexyl)-7,8-dimethylquinazolin-4(3H)-one (**36**).* 6-Bromo-3-((1*S*,2*S*)-2-hydroxycyclohexyl)-7,8-dimethylquinazolin-4(3*H*)-one (**32**) (250 mg, 0.71 mmol) underwent Negishi coupling according to General Procedure B. After stirring for 24 h, LC-MS analysis indicated only partial conversion had occurred. Further $Pd(P(^tBu)_3)_2$ (11 mg, 0.02 mmol, 0.03 equiv) were added and stirring continued for a further 24 h. After this time the mixture was heated to 55 °C for an additional 24 h. After this time, the reaction had not progressed any further, so the mixture was cooled over an ice bath and quenched with a small amount of water, before dilution with water (20 mL). The aqueous slurry was extracted with EtOAc (3 × 20 mL), and the combined organic layers washed with brine (20 mL) before concentration under reduced pressure. The crude product was purified by FCC (eluent EtOAc/PE 60:40 to 100:0), to give 164 mg of the starting material (**36**) and 73 mg (75% brsm) of the desired product as an off-white

DOI: 10.1021/acschemneuro.6b00018
ACS Chem. Neurosci. 2016, 7, 647−661

glassy solid. ^{1}H NMR ($CDCl_3$) δ 8.19 (d, J = 2.1 Hz, 1H), 8.11 (s, 1H), 7.81 (s, 1H), 7.27 (dd, J = 8.6/2.8 Hz, 1H), 7.17 (d, J = 8.2 Hz, 1H), 4.49 (s, 1H), 4.16−3.85 (m, 3H), 3.10 (s, 1H), 2.47 (s, 3H), 2.21 (d, J = 15.6 Hz, 4H), 2.00−1.70 (m, 4H), 1.61−1.29 (m, 3H); ^{13}C NMR ($CDCl_3$) δ 162.1, 149.7, 149.5, 144.5, 143.6, 142.1, 139.0, 136.8, 134.6, 134.3, 125.1, 124.2, 119.5, 71.6, 37.0, 35.5, 31.0, 25.4, 24.5, 16.9, 13.7; m/z MS (TOF ES$^+$) 398.2 [MH]$^+$; LC-MS t_R: 3.41 min.

*2-Amino-5-bromo-N-((1S,2S)-2-hydroxycyclohexyl)nicotinamide (**38**).* 2-Amino-5-bromopyridine-3-carboxylic acid (**37**) (1.09 g, 5.00 mmol) and (1*S*,2*S*)-2-aminocyclohexanol hydrochloride (834 mg, 1.1 equiv) were coupled according to General Procedure A, to give 1.47 g (94%) of precipitate as an off-white solid, requiring no further purification. ^{1}H NMR (DMSO-d_6) δ 8.22 (d, J = 8.2 Hz, 1H), 8.14 (d, J = 2.4 Hz, 1H), 8.12 (d, J = 2.4 Hz, 1H), 7.17 (s, 2H), 4.70 (d, J = 5.0 Hz, 1H), 3.71−3.46 (m, 1H), 3.48−3.21 (m, 1H), 2.01−1.72 (m, 2H), 1.72−1.46 (m, 2H), 1.41−0.99 (m, 4H); ^{13}C NMR (DMSO-d_6) δ 166.0, 157.5, 150.9, 138.4, 111.8, 104.0, 71.0, 55.1, 34.4, 31.2, 24.5, 24.2; m/z MS (TOF ES$^+$) 314.1 [MH]$^+$; LC-MS t_R: 3.32 min.

*6-Bromo-3-((1S,2S)-2-hydroxycyclohexyl)pyrido[2,3-d]pyrimidin-4(3H)-one (**39**).* 2-Amino-5-bromo-*N*-((1*S*,2*S*)-2-hydroxycyclohexyl)-nicotinamide (**38**) (515 mg, 1.64 mmol) was suspended in formamide (4.5 mL) in a 10 mL microwave vial, before sealing the tube. The mixture was heated to 180 °C for 1.5 h, then allowed to stir at RT overnight, before a further period of heating at 180 °C for 2 h. The mixture was cooled to RT, then quenched with water. The resulting precipitate was collected by filtration (vacuum) to give 168 mg of brown solid. The aqueous filtrate was extracted with EtOAc (3 × 30 mL), and the combined organic extracts washed with brine (30 mL). TLC analysis (EtOAc) indicated that product was still trapped in the aqueous layer. The aqueous layer was saturated with NaCl, before re-extraction with EtOAc (2 × 30 mL) then MeOH/EtOAc (1:9, 30 mL). The combined organic layers were washed with brine (30 mL), then dried over Na_2SO_4 before concentrating under reduced pressure, to give an additional 366 mg of yellow solid. The crude solids were combined, and purified by FCC (eluent MeOH/DCM 0:100 to 6:94), to give 233 mg (44%) of pale yellow solid. ^{1}H NMR (DMSO-d_6) δ 9.05 (d, J = 2.6 Hz, 1H), 8.68 (s, 1H), 8.65 (d, J = 2.6 Hz, 1H), 5.01 (d, J = 5.0 Hz, 1H), 4.35 (s, 1H), 3.96 (s, 1H), 2.12−1.50 (m, 5H), 1.49−1.10 (m, 3H); ^{13}C NMR (DMSO-d_6) δ 160.2, 156.4, 156.0, 149.3, 137.5, 118.1, 117.3, 68.3, 34.9, 30.1, 25.0, 23.9; m/z MS (TOF ES$^+$) 324.1 [MH]$^+$; LC-MS t_R: 3.35 min.

*6-((6-Chloropyridin-3-yl)methyl)-3-((1S,2S)-2-hydroxycyclohexyl)-pyrido[2,3-d]pyrimidin-4(3H)-one (**40**).* 6-Bromo-3-((1*S*,2*S*)-2-hydroxycyclohexyl)pyrido[2,3-*d*]pyrimidin-4(3*H*)-one (**39**) underwent Negishi coupling according to General Procedure B. After quenching, the reaction mixture was concentrated under reduced pressure (prior LC-MS analysis indicated extractive workup was not suitable, due to solubility of the product in the aqueous layer). The crude product was purified by FCC (eluent MeOH/DCM 0:100 to 6:94, slow gradient over 20 column volumes) to give 33 mg (14%) of an off-white glassy solid. An additional 107 mg (37%) of yellow glassy solid was also isolated form the column, eluting before the desired product, and found to be 6-bromo-7-((6-chloropyridin-3-yl)methyl)-3-((1*S*,2*S*)-2-hydroxycyclohexyl)-7,8-dihydropyrido[2,3-*d*]pyrimidin-4(3*H*)-one. This was the major product of the reaction, resulting from nucleophilic attack by the zincate 7-position of the pyrido[2,3-*d*]pyrimidin-4(3*H*)-one ring system. ^{1}H NMR (CD_3OD) δ 8.90 (s, 1H), 8.58 (s, 1H), 8.49 (d, J = 2.4 Hz, 1H), 8.36 (d, J = 2.2 Hz, 1H), 7.74 (dd, J = 8.3/2.5 Hz, 1H), 7.42 (d, J = 8.2 Hz, 1H), 4.46 (s, 1H), 4.25 (s, 2H), 4.08 (s, 1H), 3.35 (s, 3H), 2.27−1.66 (m, 5H), 1.63−1.31 (m, 3H); ^{13}C NMR (CD_3OD) δ 162.7, 157.2, 156.7, 151.0, 150.8, 150.8, 141.5, 137.9, 137.0, 136.3, 125.8, 118.5, 70.6, 36.2, 35.4, 30.9, 26.4, 25.3; m/z MS (TOF ES$^+$) 371.2 [MH]$^+$; LC-MS t_R: 3.36 min.

*Ethyl 3-([1,1′-Biphenyl]-4-yl)acrylate (**44**).*[6] Phenylboronic acid (**41**) (2.47 g, 20.3 mmol, 1.25 equiv), 4-bromobenzaldehyde (**42**) (3.00 g, 16.2 mmol), (ethoxycarbonylmethylene)-triphenylphosphorane (**43**) (8.47 g, 24.3 mmol, 1.5 equiv), $PdCl_2(PPh_3)_2$ (398 mg 0.57 mmol, 0.035 equiv), and PPh_3 (298 mg, 1.13 mmol, 0.07 equiv) were dispersed in degassed DME (64 mL) and degassed 2 M $Na_2CO_{3(aq)}$ (32 mL). The mixture was heated at 70 °C for 22.5 h, then at 100 °C for 3 h, followed by 85 °C overnight. LC-MS analysis over this time indicated the Wittig reaction progressed at a faster rate than the Suzuki coupling. The mixture was cooled, then dilute with water (200 mL), before extracting with Et_2O (3 × 100 mL). The combined organic layers were washed with brine (100 mL), before concentration under reduced pressure. The residue was diluted with Et_2O/PE to effect precipitation of triphenylphosphine oxide, the majority of which was removed by filtration (vacuum). The resulting filtrated was reconcentrated under reduced pressure, and purified by FCC (eluent Et_2O/PE 0:100, followed by 8:92, then 10:90) to give ethyl (*Z*)-3-([1,1′-biphenyl]-4-yl)acrylate as 677 mg (17%) of a clear colorless oil and ethyl (*E*)-3-([1,1′-biphenyl]-4-yl)acrylate as 2.78 g (68%) of a white solid. Total yield 3.46 g (84%, *E*/*Z* 4:1).

E-isomer.[14] ^{1}H NMR ($CDCl_3$) δ 7.73 (d, J = 16.0 Hz, 1H), 7.67−7.56 (m, 6H), 7.52−7.42 (m, 2H), 7.42−7.34 (m, 1H), 6.48 (d, J = 16.0 Hz, 1H), 4.28 (q, J = 7.1 Hz, 2H), 1.36 (t, J = 7.1 Hz, 3H); ^{13}C NMR ($CDCl_3$) δ 167.2, 144.3, 143.1, 140.3, 133.6, 129.0, 128.7, 128.0, 127.7, 127.2, 118.3, 60.7, 14.5; m/z MS (TOF ES$^+$) 253.2 [MH]$^+$; LC-MS t_R: 3.83 min.

Z-isomer.[15] ^{1}H NMR ($CDCl_3$) δ 7.71 (d, J = 8.3 Hz, 2H), 7.65−7.55 (m, 4H), 7.49−7.40 (m, 2H), 7.40−7.31 (m, 1H), 6.97 (d, J = 12.7 Hz, 1H), 5.97 (d, J = 12.7 Hz, 1H), 4.21 (q, J = 7.1 Hz, 2H), 1.28 (t, J = 7.1 Hz, 3H); ^{13}C NMR ($CDCl_3$) δ 166.4, 142.9, 141.9, 140.7, 133.9, 130.6, 129.0, 127.7, 127.2, 126.8, 119.8, 60.5, 14.3; m/z MS (TOF ES$^+$) 253.1 [MH]$^+$; LC-MS t_R: 3.83 min.

*Ethyl 3-([1,1′-Biphenyl]-4-yl)propanoate (**45**).*[14,16] Ethyl 3-([1,1′-biphenyl]-4-yl)acrylate (**44**) (3.39 g, 13.4 mmol, *E*/*Z* isomers recombined) was dissolved in EtOAC (150 mL). Pd/C (10%, 300 mg, 0.1 wt eq) as a slurry in water (0.5 mL) was added and the mixture degassed by sonication. The vessel was evacuated and filled with hydrogen three times, then stirred under an atmosphere of hydrogen (balloon) for 4 h at RT. LC-MS analysis indicated complete consumption of starting material. The reaction mixture was filtered through a bed of Celite, with washings of EtOAc, before concentrating the filtrate under reduced pressure, to give 3.40 g (99%) of clear colorless oil. ^{1}H NMR ($CDCl_3$) δ 7.60−7.55 (m, 2H), 7.52 (d, J = 8.1 Hz, 2H), 7.43 (dd, J = 7.5 Hz, 2H), 7.37−7.30 (m, 1H), 7.28 (d, J = 8.0 Hz, 2H), 4.15 (q, J = 7.1 Hz, 2H), 3.00 (t, J = 7.8 Hz, 2H), 2.75−2.54 (m, 2H), 1.25 (t, J = 7.1 Hz, 3H); ^{13}C NMR ($CDCl_3$) δ 173.1, 141.1, 139.8, 139.4, 128.9, 127.4, 127.3, 127.2, 60.6, 36.0, 30.8, 14.4; m/z MS (TOF ES$^+$) 255.2 [MH]$^+$; LC-MS t_R: 3.78 min.

*3-([1,1′-Biphenyl]-4-yl)propanal (**46**).*[16] Ethyl 3-([1,1′-biphenyl]-4-yl)propanoate (**45**) (2.18 g, 8.57 mmol) was dissolved in dry toluene (35 mL) under an atmosphere of nitrogen. The solution was degassed under a stream of nitrogen, before cooling to −78 °C in a dry ice/acetone bath. A solution of 1 M DIBALH in toluene (17 mL, 17 mmol, 2.0 equiv) was added in dropwise, and the mixture stirred at −78 °C for 1.25 h. TLC analysis (DCM) indicated disappearance of the starting material, so the mixture was quenched with care, with dropwise addition of MeOH, while maintaining the temperature at −78 °C. Once quenched, the mixture was allowed to warm to RT, and stirred for 15 min, before addition of sat. Rochelle's solution (50 mL) and stirring for 30 min. The resulting mixture was then extracted with Et_2O (3 × 50 mL), and the combined organic layers washed with brine (50 mL). On concentration under reduced pressure, 2.01 g of milky white oil was obtained with an odor reminiscent of cinnamaldehyde. The crude product was purified by FCC (eluent EtOAc/PE 0:100 to 30:70), to give 1.58 g (88%) of a white solid. ^{1}H NMR ($CDCl_3$) δ 9.86 (t, J = 1.3 Hz, 1H), 7.61−7.55 (m, 2H), 7.55−7.50 (m, 2H), 7.47−7.40 (m, 2H), 7.38−7.31 (m, 1H), 7.28 (d, J = 8.4 Hz, 2H), 3.01 (t, J = 7.5 Hz, 2H), 2.89−2.78 (m, 2H); ^{13}C NMR ($CDCl_3$) δ 201.7, 141.0, 139.6, 139.5, 128.9, 128.9, 127.5, 127.3, 127.2, 45.4, 27.9; m/z MS (TOF ES$^+$) no mass peaks observed; LC-MS t_R: 3.95 min.

*2-Cyano-N-((1S,2S)-2-hydroxycyclohexyl)acetamide (**48**).* Cyanoacetic acid (**47**) (419 mg, 4.92 mmol) and (1*S*,2*S*)-2-aminocyclohexanol hydrochloride (821 mg, 5.41 mmol) were coupled according to General Procedure A. After stirring in water/sat. $NaHCO_{3(aq)}$, no precipitate was evident, and the organic extracts of this aqueous slurry contained mainly 1,1,3,3-tetramethylurea by-product. The aqueous layer was concentrated to dryness under

DOI: 10.1021/acschemneuro.6b00018
ACS Chem. Neurosci. 2016, 7, 647−661

reduced pressure, and the resulting residue taken up in MeCN, and stirred at RT for 30 min. The inorganic solid mass was removed by filtration (vacuum) and the resulting filtrate concentrated under reduced pressure to give 1.60 g of yellow solid. This was recrystallized from EtOAc to give 400 mg of a yellow crystalline solid. The mother liquor was reconcentrated and purified by FCC (eluent EtOAc/PE 50:50 to 100:0) to give a further 237 mg of an off-white solid. Total yield 637 mg (71%). ^{1}H NMR (DMSO-d_6) δ 8.07 (d, J = 7.9 Hz, 1H), 3.57 (d, J = 0.7 Hz, 2H), 3.45−3.28 (m, 1H), 3.26−3.13 (m, 1H), 1.93−1.70 (m, 2H), 1.69−1.46 (m, 2H), 1.35−0.94 (m, 4H); ^{13}C NMR (DMSO-d_6) δ 161.6, 116.4, 71.0, 54.9, 33.9, 30.8, 25.5, 24.1, 23.7; m/z MS (TOF ES$^-$) 181.1 [M − H]$^-$; LC-MS t_R: 2.40 min.

*5-([1,1′-Biphenyl]-4-ylmethyl)-2-amino-N-((1S,2S)-2-hydroxycyclohexyl)thiophene-3-carboxamide (**49**).* 3-([1,1′-Biphenyl]-4-yl)propanal (**46**) (334 mg, 1.59 mmol), 2-cyano-*N*-((*1S,2S*)-2-hydroxycyclohexyl)acetamide (**48**) (289 mg, 1.59 mmol, 1.0 equiv), sulfur (51 mg, 1.59 mmol, 1.0 equiv) and TEA (0.22 mL, 1.59 mmol, 1.0 equiv) were dispersed in EtOH (1.6 mL) in a 10 mL microwave vial. The mixture was sonicated at RT for 5 min, before flushing the atmosphere with nitrogen and sealing the vial. The mixture was heated at 60 °C for 6 h, at which time LC-MS analysis indicated the reaction was complete. The mixture was cooled to RT, before pouring onto ice/water. The resulting brown solid was collected by filtration (vacuum) and washed with water, then air-dried. The crude product was purified by FCC (eluent EtOAc/PE 10:90 to 100:0) to give 367 mg (57%) of red solid. ^{1}H NMR (DMSO-d_6) δ 7.80−7.56 (m, 4H), 7.53−7.40 (m, 2H), 7.40−7.28 (m, 3H), 7.24 (d, J = 7.9 Hz, 1H), 7.05 (s, 2H), 6.97 (s, 1H), 4.54 (s, 1H), 3.92 (s, 2H), 3.67−3.43 (m, 1H), 3.33 (s, 1H), 1.96−1.71 (m, 2H), 1.70−1.48 (m, 2H), 1.45−0.97 (m, 4H); ^{13}C NMR (DMSO-d_6) δ 165.4, 160.2, 134.0, 139.9, 138.2, 128.9, 128.9, 127.3, 126.8, 126.6, 122.4, 122.0, 106.9, 71.4, 54.3, 34.9, 34.6, 31.6, 24.6, 24.2; m/z MS (TOF ES$^+$) 407.2 [MH]$^+$; HRMS $C_{24}H_{27}N_2O_2S$ [MH]$^+$ calcd 407.1793; found 407.1797; LC-MS t_R: 3.92 min; $[\alpha]_D^{27}$ = +20.58° (0.14, DMSO).

Intact Cell Radioligand Binding Assays. Flp-In Chinese hamster ovary (CHO) cells expressing the human muscarinic acetylcholine M_1 (hM_1 mAChR) were grown in Dulbecco's modified Eagle's medium (DMEM) (Invitrogen, Carlsbad, CA) supplemented with fetal bovine serum (FBS) (ThermoTrace (Melbourne, Australia) and 0.2 mg/mL hygromycin-B (Roche, Mannheim, Germany). The cells were plated at 10^4 cells per well in 96-well Isoplates (PerkinElmer). Prior to assay the growth medium was removed and the attached cells were used to perform radioligand binding studies in the presence of 0.2 nM [^{3}H]NMS and varying concentrations of acetylcholine (Sigma, St. Louis, MO) and PAMs in a total volume of 200 μL of binding buffer (10 mM HEPES, 145 mM NaCl, 1 mM $MgSO_4{\cdot}7H_2O$, 10 mM glucose, 5 mM KCl, 2 mM $CaCl_2$, 1.5 mM $NaHCO_3$, pH 7.4). The binding reaction mixtures were incubated for 1 h at 37 °C, in a humidified incubator and terminated by rapid removal of radioligand followed by two 100 μL washes with ice-cold 0.9% NaCl buffer. Radioactivity was determined by addition of 100 μL Microscint scintillation liquid (PerkinElmer Life Sciences) to each well and counting in a MicroBeta plate reader (PerkinElmer Life Sciences).

IP-One Accumulation Assays. The IP-One assay kit (Cisbio, France) was used for the direct quantitative measurement of myoinositol 1 phosphate (IP_1) in FlpIn CHO cells stably expressing the hM_1 mAChR. The cells were detached and resuspended in IP_1 stimulation buffer (10 mM Hepes, 1 mM $CaCl_2$, 0.5 mM $MgCl_2$, 4.2 mM KCl, 146 mM NaCl, 5.5 mM glucose, 50 mM LiCl, pH 7.4). The stimulations were performed in 384-well Proxy-plates (PerkinElmer) in a total volume of 14 μL, in the absence or presence of increasing concentrations of ACh and the PAMs, at cell density of 10^6 million cells/ml for 1 h at 37 °C, 5% CO_2. The reactions were terminated by addition of 6 μL of lysis buffer containing HTRF reagents (the anti-IP1 Tb cryptate conjugate and the IP1-D2 conjugate), followed by incubation for 1 h at RT. The emission signals were measured at 590 and 665 nm after excitation at 340 nm using an Envision multilabel plate reader (PerkinElmer), and the signal was expressed as the HTRF ratio: F = ((fluorescence$_{665nm}$/fluorescence$_{590nm}$) × 10^4).

Data Analysis. All data were analyzed using Prism 6.01 (GraphPad Software, San Diego, CA). Binding-interaction studies with allosteric ligands were fitted to the following allosteric ternary complex model (eq 1):[31]

$$Y = \frac{B_{max}[A]}{[A] + \left(\frac{K_A K_B}{\alpha'[B] + K_B}\right)\left(1 + \frac{[I]}{K_I} + \frac{[B]}{K_B} + \frac{\alpha[I][B]}{K_I K_B}\right)} \quad (1)$$

where Y is percentage (vehicle control) binding, B_{max} is the total number of receptors, [A], [B], and [I] are the concentrations of radioligand, allosteric modulator, and the orthosteric ligand, respectively, K_A, K_B, and K_I are the equilibrium dissociation constants of the radioligand, allosteric modulator, and orthosteric ligand, respectively. α' and α are the binding cooperativities between the allosteric ligand and [^{3}H]NMS and the allosteric modulator and the agonist acetylcholine, respectively. Saturation binding experiments were used to determine the value of pK_A for [^{3}H]NMS (pK_A = 9.70 ± 0.01, K_A = 0.2 nM). Values of α (or α') > 1 denote positive cooperativity; values < 1 (but > 0) denote negative cooperativity, and value = 1 denotes neutral cooperativity. For the majority of compounds, a complete inhibition of [^{3}H]NMS binding by the allosteric modulator was observed, consistent with a very high level of negative cooperativity. In these cases to allow fitting of the data, logα' was fixed to −3 to reflect this high negative cooperativity. The dissociation constant of ACh (K_I) was not fixed in these analyses but rather determined for each separate experiment. No difference was observed in the value of K_I between experiments.

Concentration−response curves for the interaction between the allosteric ligand and the orthosteric ligand in the IP-One accumulation assays were globally fitted to the following operational model of allosterism and agonism (eq 2):[32]

$$E = \{E_m(\tau_A[A](K_B + \alpha\beta[B]) + \tau_B[B]K_A)^n\} / \{([A]K_B + K_A K_B + [B]K_A + \alpha[A][B])^n + (\tau_A[A](K_B + \alpha\beta[B]) + \tau_B[B]K_A)^n\} \quad (2)$$

where E_m is the maximum possible cellular response, [A] and [B] are the concentrations of orthosteric and allosteric ligands, respectively, K_A and K_B are the equilibrium dissociation constant of the orthosteric and allosteric ligands, respectively, τ_A and τ_B are operational measures of orthosteric and allosteric ligand efficacy, respectively, α is the binding cooperativity parameter between the orthosteric and allosteric ligand, β denotes the magnitude of the allosteric effect of the modulator on the efficacy of the orthosteric agonist, and n denotes the transducer slope that describes the underlying stimulus-response coupling of the ligand-occupied receptor to the signal pathway. This parameter was constrained to be shared between all curves within a fitted data set for each interaction study, and in all instances was not significantly different from unity. In many instances, the individual model parameters of eq 2 could not be directly estimated via the nonlinear regression algorithm by analysis of the functional data alone due to parameter redundancy. To facilitate model convergence, therefore, we fixed the equilibrium dissociation constant of each ligand to that determined from the whole cell binding assays. For compounds where no agonism was observed, logτ_B was fixed to −3.

All affinity, potency, and cooperativity values were estimated as logarithms, and statistical comparisons between values were by one-way analysis of variance using a Tukey's multiple comparison post test to determine significant differences between mutant receptors and the WT M_1 mAChR. A value of $p < 0.05$ was considered statistically significant.

AUTHOR INFORMATION

Corresponding Authors

*(P.J.S.) Phone: +61 (0)3 9903 9542. E-mail: Peter.Scammells@monash.edu.

*(J.R.L.) Phone: +61 (0)3 9903 9095. E-Mail: Rob.Lane@monash.edu.

DOI: 10.1021/acschemneuro.6b00018
ACS Chem. Neurosci. 2016, 7, 647−661

Present Address

(S.N.M.) School of Pharmacy, Centre for Biomolecular Sciences, University of Nottingham, University Park, Nottingham, NG7 2RD, UK.

Author Contributions

[§]S.N.M. and H.L. These authors contributed equally to this work. The manuscript was written through contributions of all authors, and all authors have given approval to the final version of the manuscript.

Funding

This research was supported by Discovery Grant DP110100687 of the Australian Research Council as well as Program Grant APP1055134 and Project Grant APP1049564 of the National Health and Medicinal Research Council (NHMRC) of Australia. J.R.L. is a R.D. Wright Biomedical Career Development Fellow and a Larkin's Fellow (Monash University, Australia), while A.C. is a Senior Principal Research Fellow of the NHMRC.

Notes

The authors declare no competing financial interest.

■ ABBREVIATIONS

brsm, based on recovery of starting material; DCM, dichloromethane; DIPEA, diisopropylethylamine; DMF-DMA, *N*,*N*-dimethylformamide, dimethylacetal; FCC, flash column chromatography; HCTU, *O*-(1*H*-6-chlorobenzotriazole-1-yl)-1,1,3,3-tetramethyluronium hexafluorophosphate; min, minutes; PE, petroleum spirits 40−60; TEA, triethylamine

■ REFERENCES

(1) Ferri, C. P., Prince, M., Brayne, C., Brodaty, H., Fratiglioni, L., Ganguli, M., Hall, K., Hasegawa, K., Hendrie, H., Huang, Y., Jorm, A., Mathers, C., Menezes, P. R., Rimmer, E., and Scazufca, M. (2005) Global prevalence of dementia: a Delphi consensus study. *Lancet 366*, 2112−7.

(2) van Duijn, C. M., Clayton, D., Chandra, V., Fratiglioni, L., Graves, A. B., Heyman, A., Jorm, A. F., Kokmen, E., Kondo, K., Mortimer, J. A., Rocca, W. A., Shalat, S. L., and Soininen, H. (1991) Familial aggregation of Alzheimer's disease and related disorders: a collaborative re-analysis of case-control studies. *Int. J. Epidemiol. 20* (Suppl 2), S13−20.

(3) Gao, S., Hendrie, H. C., Hall, K. S., and Hui, S. (1998) The relationships between age, sex, and the incidence of dementia and Alzheimer disease: a meta-analysis. *Arch. Gen. Psychiatry 55*, 809−15.

(4) Lanctot, K. L., Rajaram, R. D., and Herrmann, N. (2009) Therapy for Alzheimer's Disease: How Effective are Current Treatments? *Ther. Adv. Neurol. Disord. 2*, 163−80.

(5) Osborn, G. G., and Saunders, A. V. (2010) Current treatments for patients with Alzheimer disease. *J. Am. Osteopath. Assoc. 110*, S16−26.

(6) Geula, C., and Mesulam, M. M. (1995) Cholinesterases and the pathology of Alzheimer disease. *Alzheimer Dis. Assoc. Disord. 9* (Suppl 2), 23−8.

(7) Clader, J. W., and Wang, Y. (2005) Muscarinic receptor agonists and antagonists in the treatment of Alzheimer's disease. *Curr. Pharm. Des. 11*, 3353−3361.

(8) Koch, H. J., Haas, S., and Juergens, T. (2005) On the physiological relevance of muscarinic acetylcholine receptors in Alzheimer's disease. *Curr. Med. Chem. 12*, 2915−2921.

(9) Birks, J. (2006) Cholinesterase inhibitors for Alzheimer's disease. *Cochrane Database Syst. Rev.*, CD005593.

(10) Wess, J., Eglen, R. M., and Gautam, D. (2007) Muscarinic acetylcholine receptors: mutant mice provide new insights for drug development. *Nat. Rev. Drug Discovery 6*, 721−733.

(11) Christopoulos, A. (2002) Allosteric binding sites on cell-surface receptors: novel targets for drug discovery. *Nat. Rev. Drug Discovery 1*, 198−210.

(12) Conn, P. J., Christopoulos, A., and Lindsley, C. W. (2009) Allosteric modulators of GPCRs: a novel approach for the treatment of CNS disorders. *Nat. Rev. Drug Discovery 8*, 41−54.

(13) Conn, P. J., Lindsley, C. W., Meiler, J., and Niswender, C. M. (2014) Opportunities and challenges in the discovery of allosteric modulators of GPCRs for treating CNS disorders. *Nat. Rev. Drug Discovery 13*, 692−708.

(14) Decker, M., and Holzgrabe, U. (2012) M1 muscarinic acetylcholine receptor allosteric modulators as potential therapeutic opportunities for treating Alzheimer's disease. *MedChemComm 3*, 752−762.

(15) Ma, L., Seager, M., Wittmann, M., Jacobson, M., Bickel, D., Burno, M., Jones, K., Graufelds, V. K., Xu, G., Pearson, M., McCampbell, A., Gaspar, R., Shughrue, P., Danziger, A., Regan, C., Flick, R., Pascarella, D., Garson, S., Doran, S., Kreatsoulas, C., Veng, L., Lindsley, C. W., Shipe, W., Kuduk, S., Sur, C., Kinney, G., Seabrook, G. R., and Ray, W. J. (2009) Selective activation of the M1 muscarinic acetylcholine receptor achieved by allosteric potentiation. *Proc. Natl. Acad. Sci. U. S. A. 106*, 15950−15955 S15950/1-S15950/9..

(16) Shirey, J. K., Brady, A. E., Jones, P. J., Davis, A. A., Bridges, T. M., Kennedy, J. P., Jadhav, S. B., Menon, U. N., Xiang, Z., Watson, M. L., Christian, E. P., Doherty, J. J., Quirk, M. C., Snyder, D. H., Lah, J. J., Levey, A. I., Nicolle, M. M., Lindsley, C. W., and Conn, P. J. (2009) A selective allosteric potentiator of the M1 muscarinic acetylcholine receptor increases activity of medial prefrontal cortical neurons and restores impairments in reversal learning. *J. Neurosci. 29*, 14271−14286.

(17) Kuduk, S. D., and Beshore, D. C. (2012) Novel M1 allosteric ligands: a patent review. *Expert Opin. Ther. Pat. 22*, 1385−1398.

(18) Yang, F. V., Shipe, W. D., Bunda, J. L., Nolt, M. B., Wisnoski, D. D., Zhao, Z., Barrow, J. C., Ray, W. J., Ma, L., Wittmann, M., Seager, M. A., Koeplinger, K. A., Hartman, G. D., and Lindsley, C. W. (2010) Parallel synthesis of N-biaryl quinolone carboxylic acids as selective M1 positive allosteric modulators. *Bioorg. Med. Chem. Lett. 20*, 531−536.

(19) Mistry, S. N., Valant, C., Sexton, P. M., Capuano, B., Christopoulos, A., and Scammells, P. J. (2013) Synthesis and Pharmacological Profiling of Analogues of Benzyl Quinolone Carboxylic Acid (BQCA) as Allosteric Modulators of the M1Muscarinic Receptor. *J. Med. Chem. 56*, 5151−5172.

(20) Kuduk, S. D., Beshore, D. C., Di Marco, C. N., and Greshock, T. J. (2010) Benzoquinazolinone derivatives as M1 receptor positive allosteric modulators and their preparation, pharmaceutical compositions and use in the treatment of diseases. PatentWO2010059773A1.

(21) Abdul-Ridha, A., Lane, J. R., Lopez, L., Sexton, P. M., Christopoulos, A., Canals, M., Mistry, S. N., and Scammells, P. J. (2014) Mechanistic insights into allosteric structure-function relationships at the m1 muscarinic acetylcholine receptor. *J. Biol. Chem. 289*, 33701−11.

(22) Rescifina, A., Zagni, C., Varrica, M. G., Pistara, V., and Corsaro, A. (2014) Recent advances in small organic molecules as DNA intercalating agents: Synthesis, activity, and modeling. *Eur. J. Med. Chem. 74*, 95−115.

(23) Veber, D. F., Johnson, S. R., Cheng, H.-Y., Smith, B. R., Ward, K. W., and Kopple, K. D. (2002) Molecular properties that influence the oral bioavailability of drug candidates. *J. Med. Chem. 45*, 2615−23.

(24) Lin, H., Schulz, M. J., Xie, R., Zeng, J., Luengo, J. I., Squire, M. D., Tedesco, R., Qu, J., Erhard, K., Mack, J. F., Raha, K., Plant, R., Rominger, C. M., Ariazi, J. L., Sherk, C. S., Schaber, M. D., McSurdy-Freed, J., Spengler, M. D., Davis, C. B., Hardwicke, M. A., and Rivero, R. A. (2012) Rational Design, Synthesis, and SAR of a Novel Thiazolopyrimidinone Series of Selective PI3K-beta Inhibitors. *ACS Med. Chem. Lett. 3*, 524−529.

(25) Zhang, M., Tamiya, J., Nguyen, L., Rowbottom, M. W., Dyck, B., Vickers, T. D., Grey, J., Schwarz, D. A., Heise, C. E., Haelewyn, J., Mistry, M. S., and Goodfellow, V. S. (2007) Thienopyrimidinone bis-

DOI: 10.1021/acschemneuro.6b00018
ACS Chem. Neurosci. 2016, 7, 647−661

aminopyrrolidine ureas as potent melanin-concentrating hormone receptor-1 (MCH-R1) antagonists. *Bioorg. Med. Chem. Lett. 17*, 2535−2539.
(26) Mandal, S., Li, W. T., Bai, Y., Robertus, J. D., and Kerwin, S. M. (2008) Synthesis of 2-substituted 9-oxa-guanines {5-aminooxazolo-[5,4-d]pyrimidin-7(6H)-ones} and 9-oxa-2-thioxanthines {5-mercaptooxazolo[5,4-d]pyrimidin-7(6H)-ones}. *Beilstein J. Org. Chem. 4*, 26.
(27) Christopoulos, A., and Kenakin, T. (2002) G protein-coupled receptor allosterism and complexing. *Pharmacol. Rev. 54*, 323−374.
(28) Christopoulos, A. (1998) Assessing the distribution of parameters in models of ligand-receptor interaction: to log or not to log. *Trends Pharmacol. Sci. 19*, 351−357.
(29) Hua, X., Mao, W., Fan, Z., Ji, X., Li, F., Zong, G., Song, H., Li, J., Zhou, L., Zhou, L., Liang, X., Wang, G., and Chen, X. (2014) Novel Anthranilic Diamide Insecticides: Design, Synthesis, and Insecticidal Evaluation. *Aust. J. Chem. 67*, 1491−1503.
(30) Rewcastle, G. W., Denny, W. A., and Baguley, B. C. (1987) Potential antitumor agents. 51. Synthesis and antitumor activity of substituted phenazine-1-carboxamides. *J. Med. Chem. 30*, 843−51.
(31) May, L. T., Leach, K., Sexton, P. M., and Christopoulos, A. (2007) Allosteric modulation of G protein-coupled receptors. *Annu. Rev. Pharmacol. Toxicol. 47*, 1−51.
(32) Leach, K., Sexton, P. M., and Christopoulos, A. (2007) Allosteric GPCR modulators: taking advantage of permissive receptor pharmacology. *Trends Pharmacol. Sci. 28*, 382−389.

DOI: 10.1021/acschemneuro.6b00018
ACS Chem. Neurosci. 2016, 7, 647−661

Journal of Pharmaceutical Sciences 105 (2016) 1858–1866

Contents lists available at ScienceDirect

Journal of Pharmaceutical Sciences

journal homepage: www.jpharmsci.org

Pharmaceutics, Drug Delivery and Pharmaceutical Technology

Survival of the Fittest: Time-To-Event Modeling of Crystallization of Amorphous Poorly Soluble Drugs

Katarzyna Nurzyńska [1,*], Rupert P. Austin [1], Peter M. Fischer [2], Jonathan Booth [3], Frank Gommer [4]

[1] BAST Inc. Ltd., Holywell Park, Ashby Road, Loughborough, UK LE11 3AQ
[2] School of Pharmacy and Centre for Biomolecular Sciences, The University of Nottingham, Nottingham, UK NG7 2RD
[3] Pharmaceutical Development, AstraZeneca, Macclesfield, UK SK10 2NA
[4] Composites Research Group, Faculty of Engineering, The University of Nottingham, Nottingham, UK NG7 2RD

ARTICLE INFO

Article history:
Received 24 October 2015
Revised 6 March 2016
Accepted 11 March 2016

Keywords:
amorphous
crystallization
stability
poorly soluble drug
prediction

ABSTRACT

The objective of this study was to gain a quantitative understanding of the link between physicochemical properties and long-term and time-censored amorphous stability of poorly water-soluble drugs using parametric time-to-event modeling. Previously published data on amorphous stability and physicochemical properties of 25 structurally diverse neutral, poorly soluble compounds were used. To describe the general shape of the survival curve (probability of event at time > t), Constant, Gompertz, and Weibull hazard functions and their linear combinations were tested. For a selected Weibull hazard base model, the effect of each physicochemical covariate was investigated, with combined influence of enthalpy of fusion (H_f) and molecular weight (M_r) showing the highest statistical significance. The covariate model was used to simulate survival curves and calculate the median survival time for different values of H_f and M_r. It was found that a decrease in H_f or an increase in M_r contribute to longer survival times. The derived model equation was validated against external data sets consisting of 11 compounds. It showed better predictive ability than a previously published multiple linear regression model incorporating H_f and M_r. The proposed Weibull covariate model may assist in faster and more cost-effective decision making in the pre-formulation phase of drug development, where compound properties and appropriate drug formulation strategies are investigated.

Introduction

Small-molecule drug candidates with good pharmacological properties frequently suffer from low aqueous solubility. For oral drug products, this can lead to insufficient and erratic bioavailability of the active pharmaceutical ingredient (API), and for that reason, lipophilic APIs with limiting aqueous solubility are often formulated in the amorphous state, typically as solid dispersions in polymer matrices.[1] This approach is favorable because the amorphous solid state of a molecule is at a higher energy level compared with its crystalline state, giving rise to higher dissolution rates and solution concentrations of poorly soluble APIs from amorphous versus crystalline formulations.[2] However, on account of the comparatively disordered and mobile nature of amorphous solids, APIs can crystallize from amorphous formulations on storage or on contact with gastrointestinal fluids after administration. Such instability is a significant hurdle in the development of new medicines, and it would be highly desirable to be able to predict the inherent amorphous stability of poorly soluble APIs and the stability of such molecules in amorphous solid dispersions.

One physical stability classification methodology assesses the glass-forming ability of APIs after rapid solvent evaporation from a solution or cooling from a melt,[3,4] whereas in a different method the phase transition from the amorphous to a crystalline state is observed directly as a function of time.[5,6] In the former method, the assumption is that some compounds have an inherent ability to form amorphous solids from liquids, whereas others more readily assume a crystalline state on transition from the liquid to the solid state. It has been observed that the crystallization classification of model APIs is similar, independent, however, of methodology. From the limited data published to date, it would appear that the

Conflicts of interest: The authors declare no competing financial interest.
This article contains supplementary material available from the authors by request or via the Internet at http://dx.doi.org/10.1016/j.xphs.2016.03.014.

* *Correspondence to:* (Telephone: 01509222908).
E-mail address: knurzynska@bastinc.eu (K. Nurzyńska).

http://dx.doi.org/10.1016/j.xphs.2016.03.014

crystallization behavior of APIs depends predominantly on the properties of the API and other formulation components, rather than the amorphization methodology itself.[4,7] However, environmental conditions, for example, humidity and temperature, can also affect amorphous drug stability[8] and can, therefore, lead to different results reported by different laboratories. Although the intrinsic factors affecting ease of compound crystallization from the amorphous state, such as molecular mobility and thermodynamic properties of the amorphous state,[9] remain poorly understood, efforts have been underway to correlate observed glass-forming ability or physical stability of amorphous APIs with physicochemical and other properties of the APIs. Some progress has been made in the prediction of the physical stability of amorphous APIs.[6,10-13]

The framework developed on pure APIs in this work can be used as a preliminary risk assessment for the development of their solid dispersion formulations. It is expected that the amorphous stability of solid dispersions will be improved in comparison with pure drugs due to the dilution effect and the presence of specific interactions between a drug and a polymer. Amorphous compounds that are shown to have good amorphous stability should also be stable in their solid dispersions. Conversely, compounds that have poor stability may still be formulated as viable solid dispersions, but the products are likely to have higher risk of crystallization.

In a previous study,[6] the amorphous stability of 25 diverse neutral poorly soluble drug compounds were investigated. Principal component analysis and clustering methods were used to select 25 compounds with diverse physicochemical properties and chemical structures from the database of 533 marketed poorly soluble drugs. The selected sample set was shown to be representative for the calculated and predicted variables as side-by-side histograms for both distributions showed the same mean location and variance.[6] Several multiple linear regression (MLR) models were proposed to predict long-term amorphous drug stability using only easily accessible physicochemical drug properties as covariates. Due to practical limitations, continuous crystallization records during the approximately 6-month period of the experiment were not obtained. Instead, amorphous drug stability was measured at defined time points, with some compounds remaining stable at the end of the experiment. Time-to-event (TTE) modeling, also known as survival analysis,[14,15] is particularly suited to this type of data and was applied in the present study to the previously published data on 25 diverse compounds. Here we present the new application of TTE modeling to more accurately determine the influence of physicochemical parameters on the long-term amorphous stability of poorly soluble compounds.

A central concept in TTE modeling is the survival function $S(t)$, which describes the probability that an event will occur at a time greater than t. The survival function is related to the hazard function $h(t)$, which can be understood as the instantaneous failure rate (onset of amorphous to crystalline transition in this study) given that the compound has survived to that point in time. The survival and hazard functions are related through Equation 1.

$$S(t) = \exp\left(-\int_0^t h(t)\,\mathrm{d}t \right) \quad (1)$$

In parametric TTE modeling, a base model is first derived using a process in which various hazard functions $h(t)$ are proposed, and estimates of the parameters of the hazard functions are determined using maximum likelihood estimation. This involves integration of the hazard function from zero to the time of each crystallization event, giving the contribution of each event to the total likelihood, where the parameter estimates are derived by maximizing the sum of all likelihood contributions with respect to the parameter values. This estimation process is applied to each of the candidate hazard functions, and the best function is selected based on model selection criteria and graphical comparison of observed and predicted data. Once a hazard function has been selected, a covariate analysis is performed where the physicochemical properties of the compounds are allowed to influence the parameters within the hazard function. Model selection criteria are then used to select a final covariate model where the included covariates produce a statistically significant improvement compared with the base model. The model can then be used to simulate the expected behavior of new compounds with different values of the included covariates.

Methods

Software

The TTE models were developed using NONMEM software,[16] version 7.3 (Icon Development Solutions, Ellicott City, MD). All other analyses and visualization of data were implemented using R software[17] and use of the "survival" library, version 2.38,[18] and the "deSolve" library, version 1.11.[19]

Database Preparation

Previously published data of physicochemical properties and amorphous stability of 25 compounds[6] were used to derive a TTE model. For 17 of the compounds, the precise time of detectable transition from amorphous to crystalline structure is unknown. It was only recorded that the transition took place between 2 observation times. Such data are called interval-censored and were flagged on both sides of the interval within the database used for modeling (Supplementary Material A). For the remaining 8 compounds, observations were flagged as right-censored because crystallization was not observed during the 168 days of experiment. This vector of flag values was used as a dependent variable. The elapsed time of the interval and right-censored observations were included as main independent variable. The following measured, calculated, and predicted physicochemical properties of the 25 compounds[6] were also tested during development of the covariate model: enthalpy of fusion (H_f), glass transition temperature (T_g), melting temperature (T_m), configurational entropy (S_c), enthalpy (H_c) and free energy (G_c), relaxation time (τ), molecular weight (M_r), hydrogen bond donors and acceptors, rotatable bonds (rotB), number of rings, aromatic rings, aliphatic rings, heavy atom count, ratio of carbon to heteroatoms, polar surface area, lipophilicity (clogP), and water solubility ($\log S_w$) predicted both with CLab[6,20] and ALOGPS[21] (www.vcclab.org). These descriptors have been shown in the literature to have an impact on the glass-forming ability and amorphous stability,[3,11] drug bioavailability,[22] and the stability of compounds formulated as solid dispersions.[23]

Model Building and Selection Criteria

For selection of an appropriate base model, 8 different hazard functions were evaluated (Table 1).[24] The hazard functions are defined with parameters λ and β which determine the shape of the hazard function (Supplementary Material B). Because hazard functions must always be positive, the lambda parameters (λ_c, λ_1, and λ_2) were constrained to positive values during parameter estimation, whereas positive or negative estimates of the beta parameters (β_c and β_1) were permitted. The parameter values in the TTE models were estimated using the first-order conditional estimation method,

Table 1
Hazard Functions Tested During Selection of the Base Model

Hazard Function	Definition
Constant	$h(t) = \lambda_c$
Gompertz	$h(t) = \lambda_1 \cdot \exp(\beta_1 \cdot t)$
Weibull	$h(t) = \lambda_1 \cdot \exp(\beta_1 \cdot \ln(t))$
Constant + Gompertz	$h(t) = \lambda_c + \lambda_1 \cdot \exp(\beta_1 \cdot t)$
Constant + Weibull	$h(t) = \lambda_c + \lambda_1 \cdot \exp(\beta_1 \cdot \ln(t))$
Gompertz + Gompertz	$h(t) = \lambda_1 \cdot \exp(\beta_1 \cdot t) + \lambda_2 \cdot \exp(\beta_2 \cdot t)$
Weibull + Weibull	$h(t) = \lambda_1 \cdot \exp(\beta_1 \cdot \ln(t)) + \lambda_2 \cdot \exp(\beta_2 \cdot \ln(t))$
Gompertz + Weibull	$h(t) = \lambda_1 \cdot \exp(\beta_1 \cdot t) + \lambda_2 \cdot \exp(\beta_2 \cdot \ln(t))$

which uses maximum likelihood estimate to minimize the objective function value (OFV) and, thus, obtain the best model fit to the data.[25] The direction in which the OFV decreases to find the global minimum was determined in an iterative process using the gradient method.[26] To ensure convergence to the global minima, models were run repetitively, each time starting from different initial parameter estimates. The global minimum was considered to be reached when all repetitive runs resulted in the same final parameter estimates and OFVs. Estimates of parameter uncertainty (standard error) were generated using the NONMEM covariance procedure.[16]

Models were first required to pass the following acceptance criteria[27]:

1. At the last iteration, the values of the gradients have to be between 10^{-6} and 10 to indicate that the OFV successfully converged to its minimum.
2. The covariance step, where uncertainty in parameter estimates is determined, has to complete successfully.
3. The number of significant digits of parameter estimates has to be $\geq$3.
4. The correlation between estimated parameters, cp, has to be $-0.95 \leq \text{cp} \leq 0.95$. This criterion will reject models that are overparametrized.
5. The ratio of maximum to minimum eigenvalues of the correlation matrix of parameter estimates (condition number) has to be $\leq$1000. This criterion will reject models that are overparametrized.
6. The standard error of each parameter estimate is required to be <50% of the estimated parameter value. This ensures that the 95% confidence interval for the parameter estimate excludes zero.

For those models that passed the acceptance criteria, the base model (Table 1) was then selected using Akaike information criterion (AIC). This criterion is used to compare nonnested models, where fixing one parameter in the first model to its null value is not leading to the second model. According to this criterion (Eq. 2), a model (A) is statistically superior to a model (B) if AIC <0.

$$\text{AIC} = \text{OFV}_{\text{model A}} - \text{OFV}_{\text{model B}} + 2(n_{\text{model A}} - n_{\text{model B}}) \quad (2)$$

where n is the number of model parameters.

The influence of covariates on the parameters of the selected base model was then tested using the forward inclusion method. Covariate effects were assessed one by one followed by evaluation of the combined effect of significant covariates. The effect of each covariate, COV, was modeled relative to the median value of that covariate, $\text{COV}_{\text{median}}$, in the sample set[28] according to Equation 3.

$$\text{COV}_m = \text{COV} - \text{COV}_{\text{median}} \quad (3)$$

Covariate models of 2 different types were tested. When testing the influence of a covariate on a λ parameter, λ as given by the equations in Table 1 was replaced by λ_{cov} as defined by Equation 4

$$\lambda_{\text{cov}} = \lambda \cdot \exp(\theta \cdot \text{COV}_m) \quad (4)$$

where θ is a new parameter, estimated by the modeling software, which quantitatively describes the influence of the covariate on the hazard function. The functional form of Equation 4 enables the possibility that an increase in the covariate can increase or decrease the magnitude of the hazard function (positive or negative estimate of θ) while satisfying the constraint that the hazard function should always be positive. When testing the influence of a covariate on a β parameter, a different functional form of the covariate model was used as defined by Equation 5.

$$\beta_{\text{cov}} = \beta \cdot (1 + \theta \cdot \text{COV}_m) \quad (5)$$

This different functional form allows the possibility of changes in the covariate influencing the magnitude and sign of the original β parameter because both positive and negative values of β_{cov} are permitted (they both lead to a positive hazard function). The forms of Equations 4 and 5 also ensure that if the covariate parameter θ is zero, then the hazard function reduces to that of the base model.

The significance of the covariate models was assessed using the likelihood ratio test (LRT).[14] The covariate was considered to have a significant effect if the decrease in the OFV of the covariate model from that of the base model was >6.63 (p value < 0.01). This stringent p value was used due to the inflated type I error that occurs during multiple testing (testing of many possible covariate relationships). For the final covariate model, the estimates of parameter uncertainty produced by the NONMEM covariance procedure were supplemented by a more thorough bootstrap procedure implemented using PsN software.[29] This involved taking the structure of the final covariate model and repeatedly fitting it to 1000 data sets, each produced by sampling with replacement from the original data set of 25 compounds. This provided 1000 estimates of each model parameter. Then 95% nonparametric confidence intervals were generated from the 2.5 and 97.5 percentiles of the 1000 parameter estimates.

Model Qualification

The final covariate model was qualified using a visual predictive check (VPC), which involves assessment of the concordance between the observed crystallization events and repeated simulations of crystallization events from the selected model.[30-32] To generate the VPC, the selected covariate model was used to simulate 1000 sets of event times for the 25 compounds. Then, using the survival library in R, Kaplan–Meier survival curves with 95% confidence intervals were plotted for the observed events and for the 2.5, 50, and 97.5 percentiles. A good model should show extensive overlap of the confidence intervals derived from the observed and simulated event data with little evidence of bias. The simulated event times were generated through numerical integration (using R library deSolve) of $h(t)$ to give $S(t)$. This was followed by repeated sampling of random numbers from a uniform distribution in the interval 0 to 1 (because $S(t)$ is uniformly distributed on the interval 0 to 1)[24] and finding corresponding times at which the survival function became less than or equal to the sampled random number. Adjustment of the simulated event times according to the scheduled experimental measurement times (1 hour, 3 hours, 1 day, 7 days, 1 month, 2 months, 4 months, and 6 months)[6] was necessary to allow correct comparison with the interval-censored nature of the observed data. For example, if a particular simulated event time was 4.63 days, it would be adjusted to 7 days because that is the first point in time where the crystallization event could have been observed according to the experimental schedule.

Results and Discussion

Selection of the Base Model

The 8 hazard functions tested for selection as base model were Constant, Gompertz, and Weibull functions and their linear combinations (Table 1). Parameter estimates, OFV, and selection criteria status for the 8 candidate base models are given in Table 2. The last 4 models were immediately rejected due to failure of acceptance criteria. Failure was either due to an unacceptably wide standard error in one or more parameter estimates or to unsuccessful completion of the NONMEM covariance procedure that generates the standard errors. The latter occurred due to numerical instability with the Constant + Weibull model where the parameter λ_c optimized to a vanishingly small value. Figure 1 shows the 4 models that passed the acceptance criteria, where the estimated survival curves derived from the models are shown superimposed on the Kaplan–Meier plot of the observed crystallization events. The Weibull and Constant + Gompertz models clearly match the observed Kaplan–Meier curve better than the Constant and Gompertz models. The 2 former models have OFVs that are lower than the latter 2; therefore, a selection between the Weibull and Constant + Gompertz model was the only decision required.

Selection of the base model from the 2 remaining models was initially performed using a consideration of AIC alone. The Constant + Gompertz model has an OFV that is 2.8 units lower than the Weibull model (Table 2) but has 1 additional parameter (Table 1). This leads to an AIC of −0.8 in favor of the Constant + Gompertz model. It should be noted from Table 2 that the standard errors of all 3 parameter estimates in the Constant + Gompertz model are close to 50% of the parameter estimates, whereas the precision of parameter estimates in the Weibull model is considerably better. During early attempts to build covariate models using the initially selected Constant + Gompertz base model, it was soon found that the additional complexity arising from incorporation of covariate models caused all parameters to have standard errors that were >50% of the associated parameter estimate. Due to its additional complexity, the Constant + Gompertz model appears to be less stable than the Weibull model and is likely to be overparameterized when covariates are added. Hence, the selection of the most appropriate base model was reassessed, and the Weibull model was chosen on the basis that it has an OFV only 2.8 units higher than the Constant + Gompertz model. It leads to a similar visual concordance with the observed Kaplan–Meier curve (Fig. 1) but with the advantage of one fewer parameter and more precise parameter estimates.

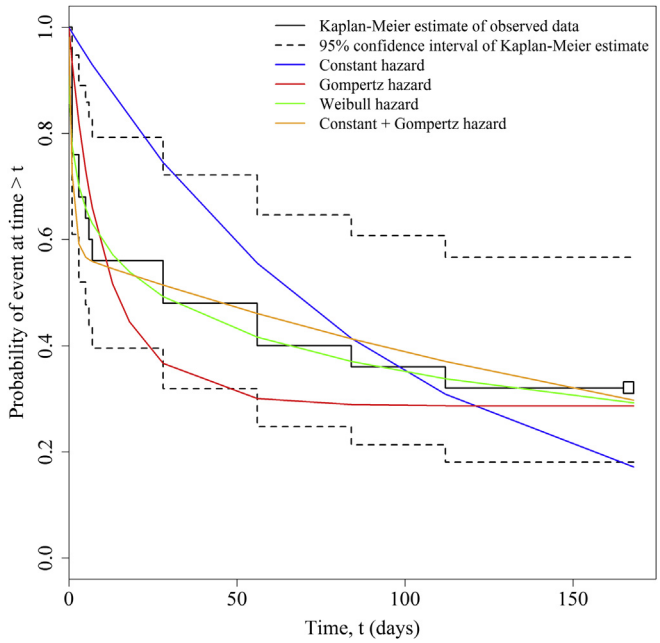

Figure 1. Visual assessment of candidate base models. Kaplan–Meier curve of observed data is shown as continuous black line with 95% confidence intervals shown as black dashed lines. Kaplan–Meier curves of estimated survival functions derived from 4 candidate base models are shown as colored lines.

Selection of the Covariate Model

The individual and combined effects of calculated, predicted, and measured compound properties[6] on the parameters λ_1 and β_1 in the Weibull hazard function were investigated. The LRT was used to decide if incorporation of a particular covariate led to a significant improvement in the model, with the requirement of a decrease in the OFV of the covariate model with respect to the base model of >6.63. Based on this criterion, none of the covariates were found to have a significant effect on β_1 and 4 covariates were found to have a significant effect on λ_1 when tested independently: H_f (ΔOFV = −13.46), M_r (ΔOFV = −10.33), heavy atom count (ΔOFV = −9.79), and number of rings (ΔOFV = −7.84). Furthermore, a model involving the influence of both H_f and M_r on λ_1 gave a further significant decrease in OFV (ΔOFV = −23.91). Additional inclusion of a multiplicative interaction term between H_f and M_r to the latter model did not further improve this model significantly given the use of an additional estimated parameter (ΔOFV = −26.14). Attempts to include either heavy atom count or number of rings as an additional covariate in this model did not lead to a further significant reduction in OFV according to the LRT. This is likely due to heavy atom count and number of rings being significantly correlated with M_r; hence, they are unable to contribute significantly to further explanation of variability in the data. The correlation matrix for all variables used in model selection is shown in Supplementary Material C. The final selected covariate

Table 2
Parameter Estimates and OFV From Base Models

Hazard Function	OFV	10^3 λ_c (d^{-1})	10^3 λ_1 (d^{-1})	10^3 β_1 (d^{-1})	10^3 λ_2 (d^{-1})	10^3 β_2 (d^{-1})	Acceptance Criteria Met
Constant	410142.8	10.5 (2.55)[a]	–	–	–	–	Yes
Gompertz	410107.9	–	72.3 (24.8)[a]	−57.8 (16.5)[a]	–	–	Yes
Weibull	410096.5	–	78.2 (19.4)[a]	−692 (68.5)[a]	–	–	Yes
Constant + Gompertz	410093.7	3.91 (1.60)[a]	475 (227)[a]	−854 (361)[a]	–	–	Yes
Constant + Weibull[b]	410096.5	$<5\times10^{-6}$	78.2	−692	–	–	No
Gompertz + Gompertz	410089.9	–	472 (235)[a]	−926 (415)[a]	13.2 (8.69)[a]	−20.7 (12.3)[a]	No
Weibull + Weibull	410096.5	–	34.8 (3200)[a]	−692 (132)[a]	43.4 (3200)[a]	−692 (114)[a]	No
Gompertz + Weibull	410091.4	–	342 (245)[a]	−847 (457)[a]	36.3 (25.1)[a]	−578 (180)[a]	No

[a] Standard errors of parameter estimates, derived using NONMEM covariance method.
[b] Covariance procedure did not complete successfully.

model, therefore, included the influence of H_f and M_r on λ_1. The hazard function for this model is given in Equation 6 (where 72.92 is the median H_f and 406.56 is the median M_r), the parameter estimates are given in Table 3, and the NONMEM control file is shown in Supplementary Material D.

$$h(t) = \lambda_1 \cdot \exp(\beta_1 \cdot \ln(t)) \cdot \exp\Big(\theta_1\left(H_f - 72.92\right) + \theta_2(M_r - 406.56)\Big) \quad (6)$$

The estimate of parameter θ_1 is positive which indicates that an increase in H_f leads to an increase in $h(t)$ and, hence, a decrease in stability of amorphous compounds. This directional influence is entirely consistent with a larger enthalpy of fusion leading to a greater thermodynamic driving force toward crystallization. Contrarily, θ_2 has a negative estimate such that an increase in M_r leads to an increase in amorphous drug stability. The positive effects of high M_r and low H_f on amorphous stability determined here are consistent with the earlier MLR analysis of the same data set[6] and also with other literature reports.[3,9,10] The MLR study found that both M_r and H_f were individually correlated with amorphous stability ($R = 0.59$ and $R = -0.73$, respectively) and the model equation involving both covariates is given by Equation 7.

$$\log(\text{Stability}) = 0.00309M_r - 0.0265H_f + 1.92. \quad (7)$$

It was previously reported that molecules with high M_r often have a complex structure that impedes orientation in a crystal lattice, which leads to higher stability in a disordered, amorphous state.[3] Molecules with high H_f require more energy to disrupt the crystalline lattice during melting. As melting precedes the formation of the amorphous material, the energy supplied during melting increases the internal energy of the system and, thus, lowers its physical stability.[6]

The 95% confidence intervals around the parameter estimates in Table 3 were derived from a nonparametric bootstrap procedure which involved fitting of the model to 1000 different data sets of 25 compounds, each sampled (with replacement) from the original data set.[29] The distributions of parameter estimates for the 4 model parameters, derived from the bootstrap procedure, are shown in Figure 2, and the 95% confidence intervals in Table 3 were derived from the 2.5 and 97.5 percentiles of each distribution. The 95% confidence intervals around the estimates of λ_1, β_1, and θ_1 all exclude the null value of zero, but the confidence interval around θ_2 does include zero by a small margin. However, the inclusion of θ_2 in the model does satisfy the requirement of the LRT because the OFV reduces by 10.45 on addition of the influence of M_r to a simpler model that only includes the influence of H_f. It is likely that adding more compounds to the sample set for a future analysis would lead to a more precise estimate of θ_2.

It is important to recognize that the generation of events using a TTE model is a stochastic process and repeated simulations of event times from the model will be different and will encompass a range of values.[24] A suitable method for qualification of such a model is the VPC, which involves repeated simulations of the model followed by a visualization (using Kaplan–Meier curves) of the observed events and the range of simulated events.[30] This diagnostic plot helps to ensure that repeated simulations of event times from the model are consistent with the observed event times, without evidence of significant bias. A VPC of the selected Weibull covariate model was generated using 1000 repeated simulations of event times for the set of 25 compounds. The results are shown in Figure 3, which indicates a very good concordance between the Kaplan–Meier curve (and associated 95% confidence interval) of the observed crystallization events and the median of the 1000 Kaplan–Meier curves (and associated 95% confidence interval) derived from simulated data. There is substantial overlap between the 2 sets of confidence intervals, and there is no indication of any significant bias, which could be observed in different relative positions of observed and simulated Kaplan–Meier curves over long periods of time. This confirms that the selected Weibull covariate model gives a good description of the experimental data.

Table 3
Parameter Estimates of the Selected Weibull Covariate Model

Parameter	Estimate	95% Confidence Interval From Bootstrap
λ_1 (1/d)	0.0630	0.0246: 0.110
β_1 (1/d)	−0.458	−0.574: −0.181
θ_1 (g/J)	0.0560	0.0381: 0.0999
θ_2 (mol/g)	−0.00771	−0.0148: 0.00341

Sensitivity Analysis

A sensitivity analysis was performed to investigate and visualize the effect of the selected covariates on the expected median event time for crystallization. The Weibull covariate model hazard function (Eq. 6) was analytically integrated to generate the associated survival function (Eq. 1).[24] The resulting survival function is given by Equation 8

$$S(t) = \exp\left(-\frac{K \cdot t^{\beta_1+1}}{\beta_1 + 1}\right) \quad (8)$$

where K is given by Equation 9

$$K = \lambda_1 \cdot \exp\Big(\theta_1\left(H_f - 72.92\right) + \theta_2(M_r - 406.56)\Big). \quad (9)$$

The expression for $S(t)$ given by Equation 8 can now be plotted for different values of H_f and M_r to explore the sensitivity of $S(t)$ to ±20% changes in H_f and M_r around values of 100 J/g and 500 g/mol, respectively. Given that the model contains significant uncertainty in the estimates of the 4 parameters in Equation 6, it was decided that parameter uncertainty should be incorporated into the sensitivity analysis. Hence, for each fixed pair of M_r and H_f values, $S(t)$ was calculated 1000 times using the 1000 sets of parameter estimates derived from the bootstrap procedure. At each time point, the median of the 1000 $S(t)$ values was calculated along with 80% confidence intervals leading to the plots shown in Figure 4. These plots indicate that 20% changes in both H_f and M_r lead to highly significant changes in the survival curves for amorphous stability. The sensitivity to changes in H_f is greater than changes in M_r such that the example ±20% changes in H_f lead to 7.9-fold changes in median crystallization time, whereas ±20% changes in M_r lead to 4.1-fold changes in median crystallization time. Note that Figure 4b contains significantly wider confidence bands than Figure 4a, and this is related to the greater uncertainty in estimation of θ_2 compared with θ_1 (Table 3).

If parameter uncertainty is neglected, the sensitivity analysis can be reduced to a simpler format by taking the expression for $S(t)$ in Equation 8, setting it equal to 0.5, and then solving the equation for t, which is equivalent to finding the median crystallization time rather than the entire survival curve including parameter uncertainty for a particular combination of both H_f and M_r. This leads to Equation 10

$$t = \exp\left(\left(\frac{1}{\beta_1 + 1}\right) \cdot \ln\left(\frac{-(\beta_1 + 1) \cdot \ln(0.5)}{K}\right)\right) \quad (10)$$

The median crystallization time for various combinations of H_f and M_r was calculated using Equation 10 and is shown in Table 4. The explored ranges of H_f and M_r led to a 17,000-fold range in

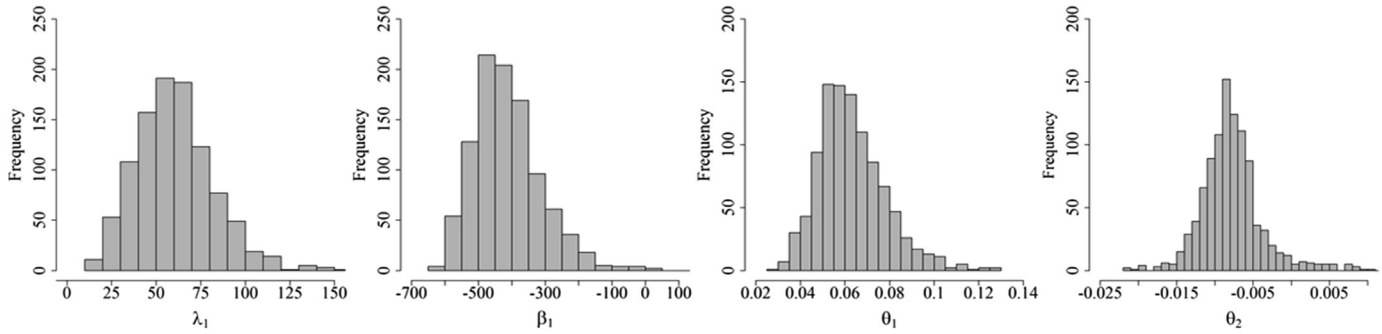

Figure 2. Distributions of parameter estimates derived from bootstrap analysis of Weibull covariate model.

amorphous stability. These results further demonstrate the large influence that H_f and M_r are expected to have on the amorphous stability of compounds with different properties.

It should be remembered that the generation of predictions using a TTE model is a stochastic process (even when parameter estimates are very precise), and once a model has been derived, the process of predicting event times involves the drawing of samples from a probability distribution. Hence, the crystallization times listed in Table 4 represent the median expected crystallization times that might be observed for large populations of compounds representing each of the combinations of H_f and M_r. There will be considerable variation in the predicted crystallization times of particular compounds around each of the median values. This is consistent with reports in the literature that compounds with similar physicochemical properties and chemical structure can demonstrate very different amorphous stability.[8] This is also true for the data set studied here, for example, celecoxib (H_f = 72.2 J/g, M_r = 358.8 g/mol, stable for 6 days) and etoricoxib (H_f = 84.1 J/g, M_r = 381.4 g/mol, stable for 84 days).

Validation on External Data Sets

A test set of 11 compounds, obtained from the literature[3] and from AstraZeneca,[6] was used to validate the derived Weibull covariate model. The observed crystallization times of the 11 test set compounds are given in Table 5. Because only the time of first detection of crystallization was known for these compounds, without knowledge of the time of the previous observation where crystallization was not detected, the crystallization times are less informative than the interval-censored data used for building the model. The Weibull covariate model was used to predict 1000 sets of crystallization times for the 11 compounds, and the observed and simulated events are displayed in Figure 5 using the same display format as that used for the VPC in Figure 3. This shows considerable overlap of the 95% confidence intervals derived from the observed and predicted data and exhibits a very similar shape of the observed and median predicted Kaplan–Meier curves. Therefore, the range of crystallization event times predicted by the Weibull covariate model are consistent with the observed event times, which indicates that the model has the ability to generate useful quantitative predictions

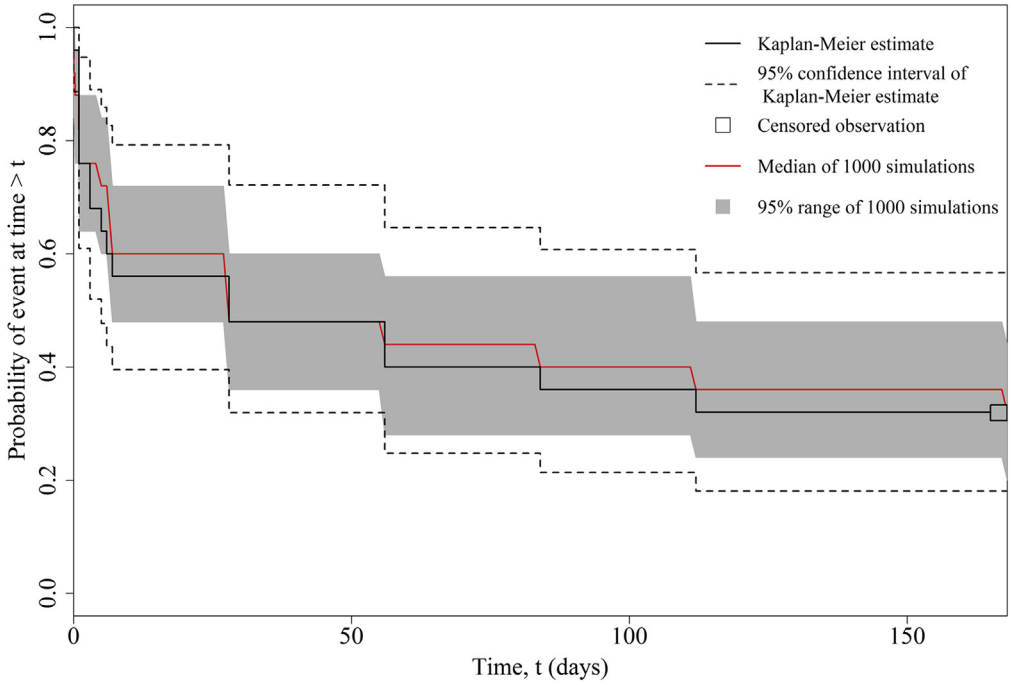

Figure 3. VPC of the selected covariate model showing Kaplan–Meier curves of observed events (black line) and median of simulated events (red line). The dashed lines indicate the 95% confidence intervals of observed events and the gray shading show the 95% confidence interval of the simulated events.

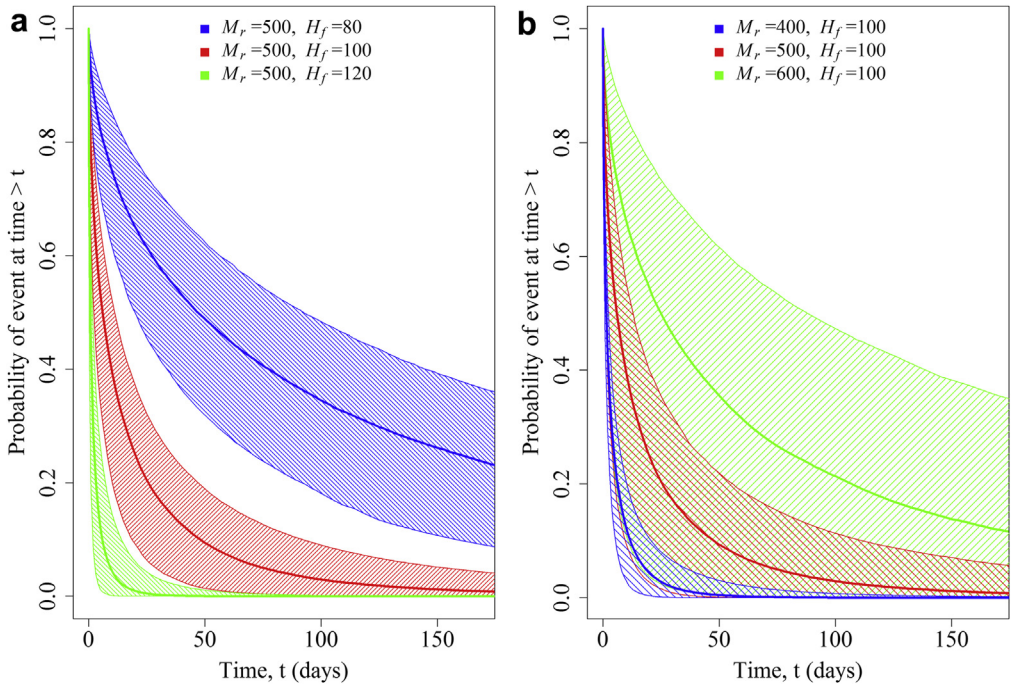

Figure 4. Sensitivity analysis showing differences in survival curves on changes in the model covariates. (a) M_r is constant and H_f changes by ±20%. (b) H_f is constant and M_r changes by ±20%. The colored areas show 80% confidence intervals based on percentiles.

for compounds outside the original 25 compound training set. Further details of the distributions of predicted crystallization event times are given in Supplementary Material E. We have previously correlated our experimentally observed amorphous stability values with those observed elsewhere using a range of different methodologies.[6] Furthermore, the relative amorphous stability ranges for the compounds in our validation data set (Table 5) are in line with the high (indoprofen[3,20,26]), intermediate (droperidol[3,26,33] and nifedipine[3,26,34]), and low (clotrimazole[3,26,34,35] and felodipine[3,26,34]) crystallization tendencies reported in the literature.

Although the representation of the model's predictive power given in Figure 5 indicates that the overall predictive performance is about as good as it could be expected, some of the individual predictions in Table 5 have large discrepancies. These discrepancies may be related to differences in preparation methods and storage conditions for the test set compounds compared with the compounds used in model building. For instance, felodipine was a member of the 25 compound training set[6] and classified as an unstable compound (measured crystallization within 5 days of storage) and was also a member of the test set where it had been assessed as a fairly stable compound (crystallization within 84 days).[3] It may be possible to further improve the model by including additional covariates in the future which have not yet been explored in the present study.

We should note that each of the 11 test set molecules represents a single sample from a corresponding large population of possible molecules, with each population having the appropriate pair of H_f and M_r values. Each of those populations will exhibit a range of amorphous stability. Furthermore, given the earlier discussion of the stochastic nature of TTE models, we can understand that the predicted crystallization times arise from distributions of values.

Table 4
Median Crystallization Times (days) for Different Combinations of H_f (J/g) and M_r (g/mol) Calculated Using Equation 10 and Parameter Estimates From Table 3

H_f \ M_r	300	350	400	450	500	550
50	63.2	128.8	262.3	534.1	1088	2215
60	22.5	45.8	93.3	190.1	387.1	788.3
70	8.01	16.31	33.21	67.6	137.7	280.5
80	2.85	5.80	11.82	24.07	49.02	99.83
90	1.01	2.07	4.21	8.57	17.4	35.53
100	0.36	0.74	1.50	3.05	6.21	12.64
110	0.13	0.26	0.53	1.09	2.21	4.50

Median crystallization times longer than 168 days are shaded in green (very stable compounds) and shorter than 1 week are shaded in red (very unstable compounds).

Table 5
Amorphous Stability Data for 11 Compounds Along With Prediction From MLR and TTE Models. Amorphous Stability Predicted With TTE Is Represented as the Median of the Simulated Event Times. Event Times Were Generated Up to 168 Days

Compound	Stability (d)		
	Observed	Predicted With MLR	Predicted With TTE
Indoprofen	0.004	1.63	0.02
Droperidol	1	5.13	0.7
Nifedipine	1	3.87	0.3
Clotrimazole	84	6.25	1
Felodipine	84	12.7	8
1	<14	12	16
2	5-14	8.3	11
3	<1	1	0.3
4	>40	1806.9	168
5	168	11.2	18
6	<1	123.6	168

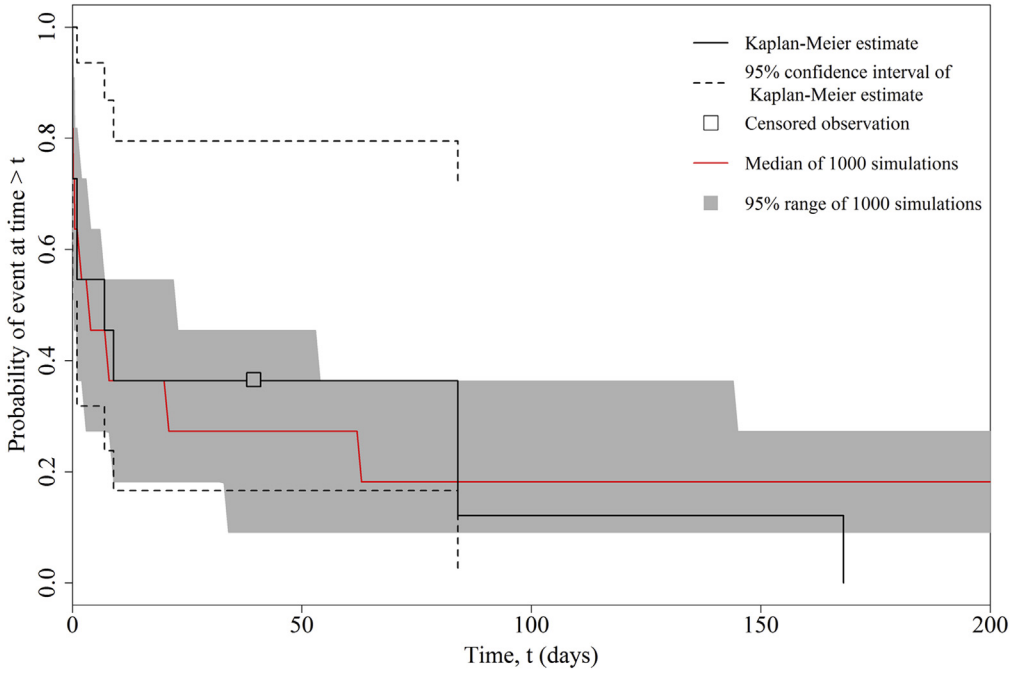

Figure 5. Assessment of predictive performance of the Weibull covariate model on 11 test set compounds.

Therefore, both, the observed and predicted crystallization times, should be viewed as having significant variability. The presence of some test set compounds with large discrepancy between the 2 times is to be expected. The variability in the predictions is tolerable as the derived model is not intended to replace the need for empirical drug stability studies and it would not be used in isolation to make critical decisions related to product development. The model should be rather viewed as a "risk assessment" tool to rank the relative amorphous stability of compounds, for example, in a discovery or early development setting, where there is a requirement from a biopharmaceutical or solid-state consideration for an amorphous drug formulation.

To compare the predictive abilities of the TTE model (Eq. 6) and the published MLR model (Eq. 7), the values of geometric mean-fold error (GMFE) and bias[36] were calculated for both models. These model predictivity metrics are listed in Table 6. The GMFE of the MLR model was 33% higher than the GMFE of the Weibull covariate model, and the bias was lower for the TTE model. This indicates that the predictive performance of the TTE model is better than the MLR model. This is consistent with the fact that a TTE analysis is, for several theoretical reasons, better suited to analysis of event versus time data (particularly given the interval-censored and right-censored nature of the data) than MLR.

Concluding Remarks

In this work, we discussed a novel application of TTE modeling to better understand the influence of physicochemical parameters on measured long-term amorphous stability with censored observations. This study used a previously published set of 25 representative poorly soluble compounds. The best description of the shape of the survival curve for the measured data was obtained with a Weibull hazard model consisting of 2 structural parameters, λ_1 and β_1. After investigating the effect of different physicochemical properties on λ_1 and β_1, the enthalpy of fusion (H_f) and molecular weight (M_r) significantly improved the model statistics. Using sensitivity analysis, it was shown that a decrease in H_f and an increase in M_r contribute to longer survival times of amorphous compounds and that amorphous stability depends more strongly on H_f than on M_r. The Weibull covariate model was used to calculate the median survival times for different values of H_f and M_r. The resulting survival times can serve as a useful indication of how amorphous drug stability typically responds to changes in H_f and M_r but with the realization that significant discrepancies are to be expected. Finally, the Weibull covariate model was tested on an external data set of 11 compounds and showed superior predictive power compared with a previously published MLR model, which also has a dependence on H_f and M_r. Because the 2 used covariates are readily accessible, through calculation and by means of differential scanning calorimetry, they may be of interest to the pharmaceutical industry in time- and cost-effective assessment of compound stability on storage and development of amorphous products. However, it will be beneficial to study additional compounds in the future to increase the data set and consequently reduce the uncertainty in the model parameter estimates.

Table 6
Metrics Comparing Predictive Performance of TTE and MLR Models When Tested on 11 External Compounds

Model	GMFE	Bias
MLR	10.10	1.63
TTE	6.73	−0.30

References

1. Newman A, Nagapudi K, Wenslow R. Amorphous solid dispersions: a robust platform to address bioavailability challenges. *Ther Deliv*. 2015;6(2):247-261.
2. Murdande SB, Pikal MJ, Shanker RM, Bogner RH. Solubility advantage of amorphous pharmaceuticals, part 3: is maximum solubility advantage experimentally attainable and sustainable? *J Pharm Sci*. 2011;100(10):4349-4356.
3. Baird JA, Van Eerdenbrugh B, Taylor LS. A classification system to assess the crystallization tendency of organic molecules from undercooled melts. *J Pharm Sci*. 2010;99(9):3787-3806.
4. Van Eerdenbrugh B, Raina S, Hsieh YL, Augustijns P, Taylor LS. Classification of the crystallization behavior of amorphous active pharmaceutical ingredients in aqueous environments. *Pharm Res*. 2014;31(4):969-982.

5. Graeser KA, Patterson JE, Zeitler JA, Gordon KC, Rades T. Correlating thermodynamic and kinetic parameters with amorphous stability. *Eur J Pharm Sci*. 2009;37(3-4):492-498.
6. Nurzyńska K, Booth J, Roberts CJ, McCabe J, Dryden I, Fischer PM. Long-term amorphous drug stability predictions using easily calculated, predicted and measured parameters. *Mol Pharm*. 2015;12:3389-3398.
7. Karmwar P, Graeser K, Gordon KC, Strachan CJ, Rades T. Investigation of properties and recrystallisation behaviour of amorphous indomethacin samples prepared by different methods. *Int J Pharm*. 2011;417(1-2):94-100.
8. Marsac PJ, Konno H, Taylor LS. A comparison of the physical stability of amorphous felodipine and nifedipine systems. *Pharm Res*. 2006;23(10):2306-2316.
9. Bhugra C, Pikal MJ. Role of thermodynamic, molecular, and kinetic factors in crystallization from the amorphous state. *J Pharm Sci*. 2008;97(4):1329-1349.
10. Mahlin D, Bergström CA. Early drug development predictions of glass-forming ability and physical stability of drugs. *Eur J Pharm Sci*. 2013;49(2):323-332.
11. Mahlin D, Ponnambalam S, Hockerfelt MH, Bergstrom CAS. Toward in silico prediction of glass-forming ability from molecular structure alone: a screening tool in early drug development. *Mol Pharm*. 2011;8(2):498-506.
12. Habgood M, Lancaster RW, Gateshki M, Kenwright AM. The amorphous form of salicylsalicylic acid: experimental characterization and computational predictability. *Cryst Growth Des*. 2013;13(4):1771-1779.
13. Ito A, Watanabe T, Yada S, et al. Prediction of recrystallization behavior of troglitazone/polyvinylpyrrolidone solid dispersion by solid-state NMR. *Int J Pharm*. 2010;383(1-2):18-23.
14. Hosmer DW, Lemeshow S, May S. *Applied Survival Analysis*. Hoboken, NJ: Wiley; 2008.
15. Holford N. A time to event tutorial for pharmacometricians. *CPT Pharmacometrics Syst Pharmacol*. 2013;2(5):1-8.
16. Owen JS, Fiedler-Kelly J. *Introduction to Population Pharmacokinetic/pharmacodynamic Analysis with Nonlinear Mixed Effects Models*. New York, NY: John Wiley & Sons; 2014.
17. Team RC. *R: A Language and Environment for Statistical Computing*. Vienna, Austria: R Foundation for Statistical Computing; 2014:2012. ISBN 3-900051-07-0.
18. Therneau T. *A Package for Survival Analysis in S. version 2.38*; 2013. Available at: http://CRAN.R-project.org/package=survival. Accessed April 10, 2016.
19. Soetaert K, Petzoldt T, Setzer RW. Solving differential equations in R. *RJ*. 2010;2:5-15.
20. Ueda H, Muranushi N, Sakuma S, et al. A strategy for co-former selection to design stable co-amorphous formations based on physicochemical properties of non-steroidal inflammatory drugs. *Pharm Res*. 2016;33(4):1018-1029.
21. Balakin KV, Savchuk NP, Tetko IV. In silico approaches to prediction of aqueous and DMSO solubility of drug-like compounds: trends, problems and solutions. *Curr Med Chem*. 2006;13(2):223-241.
22. Veber DF, Johnson SR, Cheng H-Y, Smith BR, Ward KW, Kopple KD. Molecular properties that influence the oral bioavailability of drug candidates. *J Med Chem*. 2002;45(12):2615-2623.
23. Taylor LS, Zografi G. Spectroscopic characterization of interactions between PVP and indomethacin in amorphous molecular dispersions. *Pharm Res*. 1997;14(12):1691-1698.
24. Bender R, Augustin T, Blettner M. Generating survival times to simulate Cox proportional hazards models. *Stat Med*. 2005;24(11):1713-1723.
25. Mould D, Upton R. Basic concepts in population modeling, simulation, and model-based drug development—Part 2: introduction to pharmacokinetic modeling methods. *CPT Pharmacometrics Syst Pharmacol*. 2013;2(4):1-14.
26. Baird JA, Thomas LC, Aubuchon SR, Taylor LS. Evaluating the non-isothermal crystallization behavior of organic molecules from the undercooled melt state using rapid heat/cool calorimetry. *Cryst Eng Comm*. 2013;15(1):111-119.
27. Byon W, Smith M, Chan P, et al. Establishing best practices and guidance in population modeling: an experience with an internal population pharmacokinetic analysis guidance. *CPT Pharmacometrics Syst Pharmacol*. 2013;2(7):1-8.
28. Mandema JW, Verotta D, Sheiner LB. Building population pharmacokinetic-pharmacodynamic models. I. Models for covariate effects. *J Pharmacokinet Biopharm*. 1992;20(5):511-528.
29. Lindbom L, Ribbing J, Jonsson EN. Perl-speaks-NONMEM (PsN)—a Perl module for NONMEM related programming. *Comput Methods Programs Biomed*. 2004;75(2):85-94.
30. Vu TC, Nutt JG, Holford NH. Disease progress and response to treatment as predictors of survival, disability, cognitive impairment and depression in Parkinson's disease. *Br J Clin Pharmacol*. 2012;74(2):284-295.
31. Karlsson M, Savic R. Diagnosing model diagnostics. *Clin Pharmacol Ther*. 2007;82(1):17-20.
32. Holford N. The visual predictive check—Superiority to standard diagnostic (Rorschach) plots. Conference abstract 738. Pamplona, Spain; 2005; 14. Available at: http://www.page-meeting.org/?abstract=738. Accessed April 21, 2016.
33. Trasi NS, Baird JA, Kestur US, Taylor LS. Factors influencing crystal growth rates from undercooled liquids of pharmaceutical compounds. *J Phys Chem B*. 2014;118(33):9974-9982.
34. Alhalaweh A, Alzghoul A, Mahlin D, Bergström CA. Physical stability of drugs after storage above and below the glass transition temperature: relationship to glass-forming ability. *Int J Pharm*. 2015;495(1):312-317.
35. Pajula K, Taskinen M, Lehto V-P, Ketolainen J, Korhonen O. Predicting the formation and stability of amorphous small molecule binary mixtures from computationally determined Flory–Huggins interaction parameter and phase diagram. *Mol Pharm*. 2010;7(3):795-804.
36. Lombardo F, Waters NJ, Argikar UA, et al. Comprehensive assessment of human pharmacokinetic prediction based on in vivo animal pharmacokinetic data, part 2: clearance. *J Clin Pharm*. 2013;53(2):178-191.

Mathematical Biosciences 276 (2016) 101–113

Contents lists available at ScienceDirect

Mathematical Biosciences

journal homepage: www.elsevier.com/locate/mbs

Modelling the role of CtfA/B in reverse shift continuous culture experiments of *Clostridium acetobutylicum*

Graeme J. Thorn[1,*], John R. King

School of Mathematical Sciences, Mathematical Sciences Building, University of Nottingham, University Park, Nottingham NG7 2RD, UK

ARTICLE INFO

Article history:
Received 10 January 2014
Revised 7 November 2015
Accepted 4 March 2016
Available online 18 March 2016

Keywords:
AB fermentation
Clostridium acetobutylicum
Systems biology
ODE modelling

ABSTRACT

In continuous phosphate-limited conditions, under pH control from high pH (pH $\gtrsim$ 5.2) to low pH (pH $\lesssim$ 5.2), the metabolism of the Gram-positive bacterium *Clostridium acetobutylicum,* switches from acid to solvent production. Three main enzymes are responsible for the shift, acetoacetate decarboxylase (Adc), alcohol dehydrogenase (AdhE1/2) and a CoA-transferase (CtfA/B), which are produced in increased quantities during solventogenesis. A two-population model, Millat et al. (2013) and fitted to such 'forward'-shift data, can explain this, as well as observed changes in optical density immediately following the shift: an acidogenic subpopulation is washed out and a solventogenic subpopulation grows in its place, each with distinct physiologies and proteomes. We fit this model to a 'reverse'-shift experiment, where the pH is increased from solventogenic to acidogenic conditions. We find corresponding changes in reaction rates, with AdhE1 and Adc production falling, as in the 'forward' experiments; however, for CtfA/B, the best fit surprisingly arises from the same level of production in both conditions. We propose experiments that would test whether this is a model artefact or accurately reflects cultures shifted in this reverse direction, and, if true, may suggest that over-expressing CtfA/B in both solventogenic and acidogenic conditions could improve the efficiency of fermentation.

1. Introduction

The acetone–butanol–ethanol (ABE) fermentation process [9] uses the Gram-positive anaerobic bacterium *Clostridium acetobutylicum* to produce the three solvents from sugars. The use of ABE fermentation in the production of butanol for biofuels has led to recent work aiming to increase the efficiency of this process. The metabolism of *C. acetobutylicum* proceeds through two main stages in batch culture, namely an initial acidogenic phase followed by a later solventogenic phase, with the primary driver of the shift being the external pH (for pH $\gtrsim$ 5.2, acidogenesis is prevalent with acetate and butyrate being produced with little acetone and butanol, below this pH, $\lesssim$ 5.2, solventogenesis is prevalent with acetone and butanol being produced with little acetate and butyrate). Ethanol is produced during both phases in small amounts. In such batch culture, acids build up before the pH falls, triggering the shift to solventogenesis as the acids are reabsorbed. In a phosphate-limited continuous culture, the transition between the two states can be directly induced by a change of external pH [2], without needing acid or solvent build-up. In this case, a change in the internal clostridial pH is effected in order to maintain a constant pH gradient across the cell membrane of approximately 1 pH unit [6].

A simplified version of the *C. acetobutylicum* metabolism is shown in Fig. 1 (after Millat et al. [10]), which merges intermediate reactions between the metabolic branch points and between the branch points and products of the full metabolism [9]. Glycolysis of glucose (or other hexose sugar) occurs after phosphoenolpyruvate-dependent phosphotransferase mediated transport into the cell, leaving pyruvate [9]. Further steps (not shown in the figure) convert this into acetyl coenzyme A (acetyl-CoA), which forms the first important branch point in the network. The C_2 products (acetate and ethanol) are formed from this intermediate, with C_3 products (butyrate, acetone and butanol) produced from further metabolism of acetyl-CoA into acetoacetyl-CoA and butyryl-CoA, the three CoA compounds forming the important (pH-independent) metabolic backbone of the organism.

* Corresponding author. Tel.: +44 115 951 3423; fax: +44 115 846 8002.
E-mail addresses: graeme.thorn@nottingham.ac.uk (G.J. Thorn), john.king@nottingham.ac.uk (J.R. King).
[1] Present address: School of Pharmacy, University of Nottingham, University Park, Nottingham NG7 2RD, UK.

http://dx.doi.org/10.1016/j.mbs.2016.03.003
0025-5564/

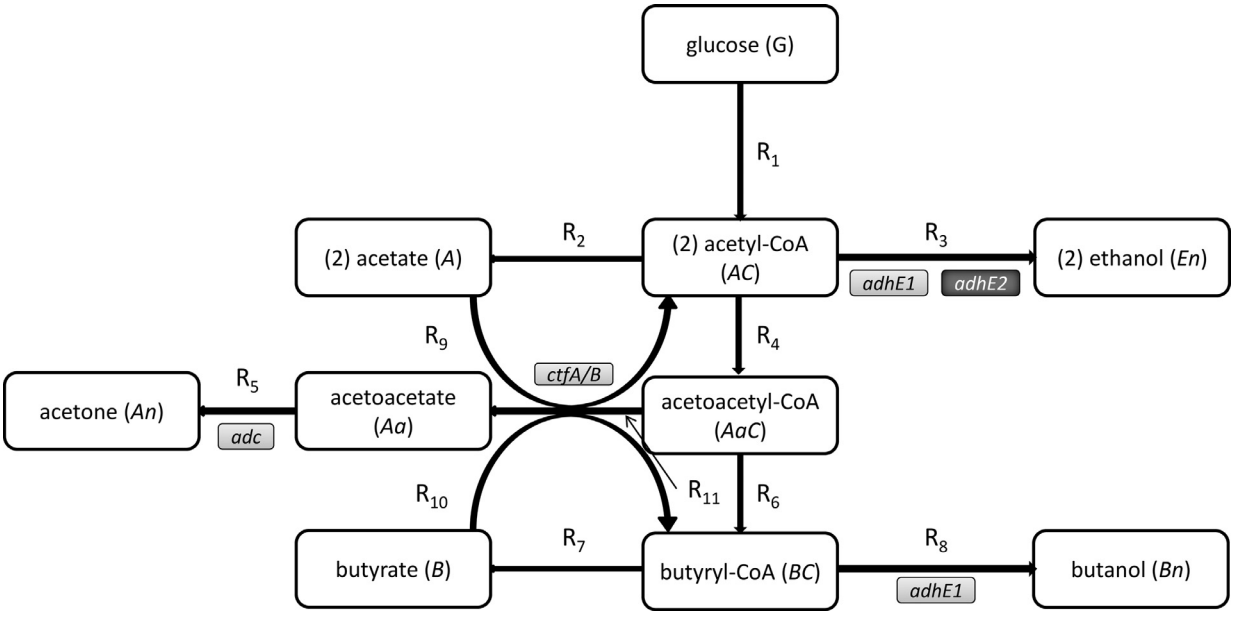

Fig. 1. Simplified metabolic pathway of ABE fermentation used in this paper (adapted from Millat et al. [10]). In phosphate-limited continuous culture, acetate and butyrate are produced during acidogenesis (pH $\gtrsim$ 5.2), whereas the solvents acetone and butanol are produced during solventogenesis (pH $\lesssim$ 5.2). Ethanol is produced in both sets of conditions. Reactions labelled R_i are modelled directly, with enzymes induced during solventogenesis or acidogenesis highlighted in light grey and dark grey, respectively.

In the initial stages of culture, phosphate groups are added to acetyl-CoA and butyryl-CoA, which are then converted further into the acids acetate and butyrate and then excreted. Post-metabolic shift, the acids are reabsorbed, reversing the above reactions (in Ping-Pong-Bi-Bi reactions) back into butyryl-CoA and acetyl-CoA (mediated by a CoA transferase (CtfA/B)), whilst converting acetoacetyl-CoA to acetoacetate, which acetoacetate decarboxylase (Adc) in turn converts into acetone. Finally, acetyl-CoA and butyryl-CoA are converted into acetaldehyde and butyraldehyde, and then into ethanol and butanol. Both reactions are mediated by an acetaldehyde dehydrogenase (AdhE1), which is only active during solventogenesis. A second acetaldehyde dehydrogenase (AdhE2), which converts acetyl-CoA to ethanol is active, during acidogenesis [4,8]. The enzymes CtfA/B and Adc are produced in higher quantities during solventogenesis compared to acidogenesis [9], measured in both steady-state and forward shift experiments.

Recent developments of the metabolic model for the COSMIC strain (namely *C. acetobutylicum* ATCC842) have led to a model consisting of two subpopulations (an acidogenic and solventogenic subpopulation) [10], each with distinct proteomic composition. This is a development of earlier kinetic models of the fermentation (including Shinto et al. [12]) in continuous culture [7,13]: the earlier of the two recent models [7] considers the continuous culture to be a single homogeneous population that modifies its proteome in order to react to changing pH conditions in phosphate-limited continuous culture, whereas the latter [13] considers a non-metabolising spore fraction to arise post-shift. A lack of experimental evidence for the presence of spores in continuous culture has meant that this latter model has not developed further.

In this work, we apply the two-population model of Millat et al. [10] to both forward (pH decreasing) and reverse (pH increasing) shift continuous phosphate-limited chemostat metabolic experiments using the *C. acetobutylicum* strain ATCC842 (COSMIC strain). In order to do this, we modify the model as published in order to model the two populations in reverse shift experiments. We estimate the parameters in the two separate cases and find that in the forward experiments, the fitted enzyme production rate parameters are as we expect from experimental investigations in steady states (with Adc, AdhE1 and CtfA/B produced in higher quantities during solventogenesis), whereas for the reverse experiment, the fitted enzyme production rate parameters are significantly different, in that Adc and AdhE1 production falls when passing from solventogenesis back to acidogenesis, but, more unexpectedly, CtfA/B production remains constant in both metabolic phases. Finally, we discuss possible experiments which could be performed to check whether this potentially important phenomenon is a real one, possibly due to cell adaptation in the culture, or whether it is an artefact arising from the limited data or the limitations of the model. If the findings hold true after experimental investigation, this could be used to improve the efficiency of fermentation by engineering strains which over-express CtfA/B.

2. Method

The reduced metabolism we model in this paper is given in Fig. 1, and is taken from Millat et al. [10]. We model the continuous *Clostridium* culture as two separate subpopulations: an acidogenic and solventogenic population, each with distinct physiologies, and separate reaction rates. As Millat et al. [10] only considered the forward shift (acidogenesis to solventogenesis), we need to modify the model used there in order to apply it to the reverse shift experimental data. In this section, we will discuss the common aspects of the model for the forward and reverse shift, before discussing how the model was modified for the reverse shift.

2.1. Overall metabolic model

Below, we summarise the main reactions (R_1–R_{11}) in Fig. 1 (the superscripts A and S denote acidogenic or solventogenic subpopulations, respectively):

Reaction i	Description	Acidogenic reaction rate R_i^A	Solventogenic reaction rate R_i^S
1	glucose → acetyl-CoA	$\frac{2V_1 G}{K_1 + G}$	$\frac{2V_1 G}{K_1 + G}$
2	acetyl-CoA → acetate	$\frac{V_2}{}\frac{AC}{K_2 + AC}$	$\frac{V_2}{f_2}\frac{AC}{K_2 + AC}$
3	acetyl-CoA → ethanol	$\alpha_{32}\, AC\, AdhE2$	$\alpha_{31}\, AC\, AdhE1$
4	acetyl-CoA → acetoacetyl-CoA	$\frac{V_4 AC}{2(K_4 + AC)}$	$\frac{V_4 AC}{2(K_4 + AC)}$
5	acetoacetate → acetone	$\alpha_5\, Aa\, Adc^{\mathrm{A}}$	$\alpha_5\, Aa\, Adc^{S}$
6	acetoacetyl-CoA → butyryl-CoA	$\frac{V_6 AaC}{K_6 + AaC}$	$\frac{V_6 AaC}{K_6 + AaC}$
7	butyryl-CoA → butyrate	$\frac{V_7}{}\frac{BC}{K_7 + BC}$	$\frac{V_7}{f_7}\frac{BC}{K_7 + BC}$
8	butyryl-CoA → butanol	0	$\alpha_{81}\, BC\, AdhE1$
9	acetate → acetyl-CoA	$\alpha_9\, A\, AaC\, Ctf^{\mathrm{A}}$	$\alpha_9\, A\, AaC\, Ctf^{S}$
10	butyrate → butyryl-CoA	$\alpha_{10}\, B\, AaC\, Ctf^{\mathrm{A}}$	$\alpha_{10}\, B\, AaC\, Ctf^{S}$
11	acetoacetyl-CoA → acetoactate	$\alpha_{11}\, Adc^{\mathrm{A}}\, AaC$	$f_{11}\, \alpha_{11}\, Adc^{S}\, AaC$

(2.1)

The metabolites all satisfy a differential equation consisting of a linear combination of the above reactions and a decay term (representing dilution):

$$\frac{dZ}{dt} = \sum_i \delta_i R_i - D \cdot Z \tag{2.2}$$

where δ_i represents whether R_i produces metabolite Z ($\delta_i = 1$), consumes metabolite Z ($\delta_i = -1$) or leaves Z unchanged ($\delta_i = 0$); the symbols for the metabolites are defined in Fig. 1. The enzyme concentrations (symbols *AdhE1, AdhE2,* Adc^{A}, Ctf^{A}, Adc^{S}, Ctf^{S}) are considered to be steady state, with a lower (acidogenic) production rate and an increased (solventogenic) production rate where stated (as in Millat et al. [10]). In particular:

$$AdhE1 = \frac{1}{D} r_{Ah1} \quad AdhE2 = \frac{1}{D} r_{Ah2} \tag{2.3}$$

$$Adc^{A} = \frac{1}{D} r_{Ad} \quad Adc^{S} = \frac{1}{D}\left(r_{Ad} + r_{Ad}^{+}\right) \tag{2.4}$$

$$Ctf^{A} = \frac{1}{D} r_{Cf} \quad Ctf^{S} = \frac{1}{D}\left(r_{cf} + r_{cf}^{+}\right) \tag{2.5}$$

The extra factors f_2 f_7 and f_{11} arise from the pH-dependent change in the specific activity of the respective enzymes [1,9,14]. The total reaction rates R_i for each reaction i are given by a sum over acid- and solvent-forming cells

$$R_i = R_i^{\mathrm{A}} \cdot OD^{\mathrm{A}}(t) + R_i^{S} \cdot OD^{S}(t) \tag{2.6}$$

where OD^{A} and OD^{S} are the sizes of the two populations, here given in terms of the optical density at 600 nm. In effect this means that the reactions in the individual populations $R_i^{\{A,S\}}$ are given as reactions per OD unit.

2.2. Forward shift model for pH and population sizes

The population model for the forward shift experiments is identical to that in [10], with an exponential decrease in the acidogenic population, and a sigmoidal function for the solventogenic population, both after a short delay following the shift initiation. The pH is also given by an exponential function following the shift, with the pH function applied for the relevant dataset as follows:

$$\mathrm{pH}(t) = \begin{cases} 5.7 & \text{for } t < \beta, \\ 1.2\, \mathrm{e}^{-\alpha\,(t-\beta)} + 4.5 & \text{for } t \geq \beta. \end{cases} \tag{2.7}$$

with the parameters α and β fitted to the overall shifted and stretched pH measurements in the dataset: α measures the rate of pH change while β represents the time at which the pH control is switched off. In the present case, the parameters are set to $\alpha = 0.135\,\mathrm{h}^{-1}$ and $\beta = 140\,\mathrm{h}$.

The population functions for this dataset are fitted to the optical density measurements from the experimental data, and are given as follows:

$$OD^{\mathrm{A}}(t) = \begin{cases} \mathrm{OD}^{\mathrm{A}} & \text{for } t < \beta_{\mathrm{A}}^{F}, \\ \mathrm{OD}^{\mathrm{A}}\, \mathrm{e}^{-\alpha_{\mathrm{A}}^{F}\,(t-\beta_{\mathrm{A}}^{F})} & \text{for } t \geq \beta_{\mathrm{A}}^{F}. \end{cases} \tag{2.8}$$

for the acidogenic population, and

$$OD^{S}(t) = \frac{\mathrm{OD}^{S}}{2}\left(\tanh\left[\frac{\alpha_S^F}{2}(t - \beta_S^F)\right] + 1\right), \tag{2.9}$$

for the solventogenic population. In the acidogenic case, there is a short delay of 6 h post-shift initiation (i.e. $\beta_{\mathrm{A}}^{F} = 146$ h), followed by a decay at a rate of $\alpha_{\mathrm{A}}^{F} = 0.07\ \mathrm{h}^{-1}$. In the solventogenic case, the parameters $\alpha_S^F = 0.175\,\mathrm{h}^{-1}$ and $\beta_S^F = 178\,\mathrm{h}$ denote the initial growth rate, and the time at which half-saturation of the logistic model is reached respectively. The steady state population sizes are given by $\mathrm{OD}^{\mathrm{A}} = 5.5$ and $\mathrm{OD}^{S} = 5.0$, reflecting the smaller solventogenic population (as measured by optical density) in [10]. The fitting of these parameters to the measured optical density is explained in [10]: we do not perform any more optimisation over these values in the present work, although we do note that the functional forms of the populations can instead be derived by solving differential equations with pH-dependent growth rates.

2.3. Reverse shift model for pH and population sizes

In order to model the reverse shift experiments, we require a population model that allows for the solventogenic population to die away as the pH is shifted back to acidogenic conditions, and for the acidogenic population to grow in the elevated pH conditions.

In this experiment the pH is forced using the automatic addition of KOH to induce a reverse transition from solventogenesis to acidogenesis so we use the hyperbolic tangent function to model the pH, as originally in [7], instead of an exponential function as in the forward shift:

$$\mathrm{pH}(t) = 5.1 + 0.6 \tanh\left[1.6507(t - 137.4886)\right] \tag{2.10}$$

which is fitted using `nlinfit` in Matlab to the pH values from the reverse experiment.

Table 1
Estimated parameters (from [10]) in Eq. (2.7) for the forward shift experiments, along with the parameters for the combined forward shift data set.

Experiment number	α [h^{-1}]	β [h]
1	0.162	136.9
2	0.110	136.9
3	0.134	120.8
Combined	0.135	140

Table 2
Lower and upper bounds for the optimisation of different parameters. These bounds are taken from both [7] and [13] and are therefore thought plausible.

Parameter group	Lower bound	Upper bound	Log-transformed?
V_i	0	400	No
K_i	0	5	No
$r_X^{\{A,S\}}$	0	5	No
f_i	1	10^2	Yes
α_i	10^{-6}	10^6	Yes

In the absence of optical density data for the reverse experiment, we again take the values $OD^A = 5.5$ and $OD^S = 5.0$, that is the steady state population sizes are the same in the respective conditions, and take the reverse population growth and decay parameters (for the acidogenic population) to be equal to the forward population growth and decay parameters (for the solventogenic population) and vice versa, i.e. $\alpha_A^R = \alpha_S^F$, $\beta_A^R = \beta_S^F$ for the acidogenic population in the reverse population and $\alpha_S^R = \alpha_A^F$, $\beta_S^R = \beta_A^F$ for the solventogenic population in the reverse population.

The equivalents of Eqs. (2.8) and (2.9) for the reverse shift are:

$$OD^A(t) = \frac{OD^A}{2}\left(\tanh\left[\frac{\alpha_A^R}{2}(t-\beta_A^R)\right]+1\right), \tag{2.11}$$

for the acidogenic population (note that this represents logistic growth of the population post-shift-initiation), and

$$OD^S(t) = \begin{cases} OD^S & \text{for } t < \beta_S^R, \\ OD^S\, e^{-\alpha_S^R (t-\beta_S^R)} & \text{for } t \geq \beta_S^R. \end{cases}, \tag{2.12}$$

for the solventogenic population (note that this is exponential decay post-shift-initiation), with the parameters $\alpha_A^R = 0.175\,h^{-1}$, $\beta_A^R = 164.735\,h$, $\alpha_S^R = 0.07\,h^{-1}$ and $\alpha_S^R = 137.085\,h$, i.e., as noted above, the reverse population growth and decay parameters (for the acidogenic population) are equal to the forward population growth and decay parameters (for the solventogenic population) and vice versa.

We fit the characteristic times (of population change) $\beta_{\{A,S\}}^R$ by matching the pH values at which significant population changes occur in the forward experiments, and then inverting the pH function (2.10) to find the relevant times. This ensures that population changes occur at the same pH values in both the reverse and forward experiments.

2.4. Experimental data

The raw untransformed data for the three forward shift experiments and the reverse shift experiment are available in the supplementary data in [13]. We combine the forward shift data experiments with slightly different pH control into a single experimental dataset for optimisation by following the procedure in [10] to transform the times in order that the pH curves match exactly between the three experiments. The procedure for this matching is described in detail in that reference, but we briefly revisit the main points here:

- The continuous-culture pH was kept at 5.7 by automatic addition of 2M KOH. This control was removed, the pH falls as acids are generated. Once pH reached 4.5, the pH was controlled using 2M KOH as in the solventogenic phase.
- For each experiment, the time at the start of the pH shift was noted, and the rate at which the pH decreased over time was fitted to a shifted-exponential function of the form in Eq. (2.7). The three sets of α and β are given in Table 1.
- Each experiment was translated by its parameter β so that the time at which pH-shift initiation matched at time $t^* = 0$, followed by non-dimensionalising t by the constant α.
- Each non-dimensionalised time series was then redimensionalised to give a decay constant $\alpha = 0.135\,h^{-1}$, and then shifted so that pH shift starts at $t = 140$ h.
- Finally, the three shifted and rescaled time series were combined into a single forward dataset.

For the reverse experiment: instead of the pH control moving from pH 5.7 to 4.5, the pH was shifted, after time $t = 129$ h from the 4.5 solventogenic steady state to 5.7 acidogenic steady state by the addition of KOH. As this experiment runs contrary to the direction of the metabolic shift in batch cultures, the pH is modelled by a hyperbolic tangent function, representing the forcing of the pH in the opposite direction.

The shifted, scaled pH data (along with the single fit) is shown in Fig. 2 (left); the reverse pH data and fit is shown in the right of the same figure.

2.5. Parameter fitting method

The method we use for parameter estimation in this paper is the hybrid simplex/simulated annealing method described by Cardoso et al. [3] and used in [10] for other work using the two-populations model. This general method combines the two optimisation methods of the simplex algorithm and simulated annealing (for examples of both, see [11]). The main improvement over the simplex method is the introduction of an extra parameter T (analogous to the temperature in simulated annealing) such that uphill steps are taken in simplex method with a probability $\propto \exp(-1/T)$. As T is reduced, the probability of an uphill step is also reduced by that factor, and when T is reduced to zero, the method becomes a local Nelder–Mead simplex search. Our implementation of this approach scales the parameters such that they all lie between 0 and 1 (and hence can be treated as of the same order of magnitude), by providing plausible bounds based on the values of parameters given elsewhere [7,13] (furthermore, the parameters α_i^X and f_i are log-transformed before scaling): these are given in Table 2. The objective function we use is the squared differences between the predictions from the model and the experimental outputs:

$$S(\mathbf{x}) = \sum_{\text{data points}} \left[\tilde{y}_i - y_i(t)\right]^2 \tag{2.13}$$

with the data points being from $t > 100$ for the forward experiments (as in [10]).

3. Results

The 500 best-scoring scaled parameters fitted to the forward and the reverse models separately are given in Fig. 3 (note that the best-performing parameters are also given in [10] – in order to facilitate comparison with the reverse-fitted parameters these are included here). In general, the sets of parameters are very similar, but there are a few exceptions: most notably, for the reverse parameters, the level of CtfA/B is approximately constant in both acidogenic and solventogenic phases (indicated by $r_{Cf}^+ \approx 0$). There are also other significant differences between the parameters: V_1,

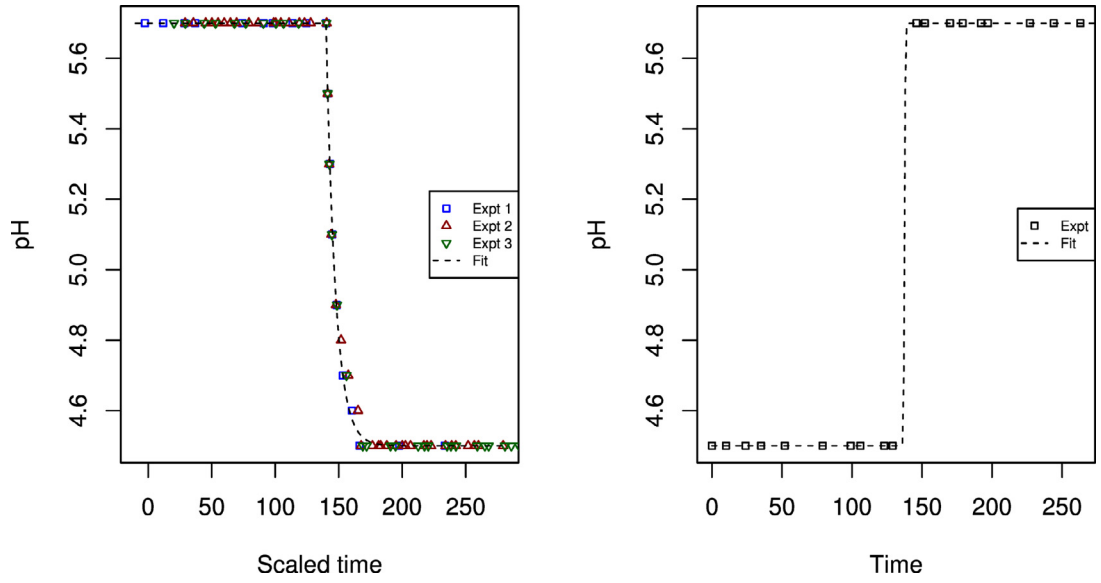

Fig. 2. Plots of the time-scaled, time-shifted forward pH data against the modelled pH (left); plot of the reverse pH data against the modelled pH (right).

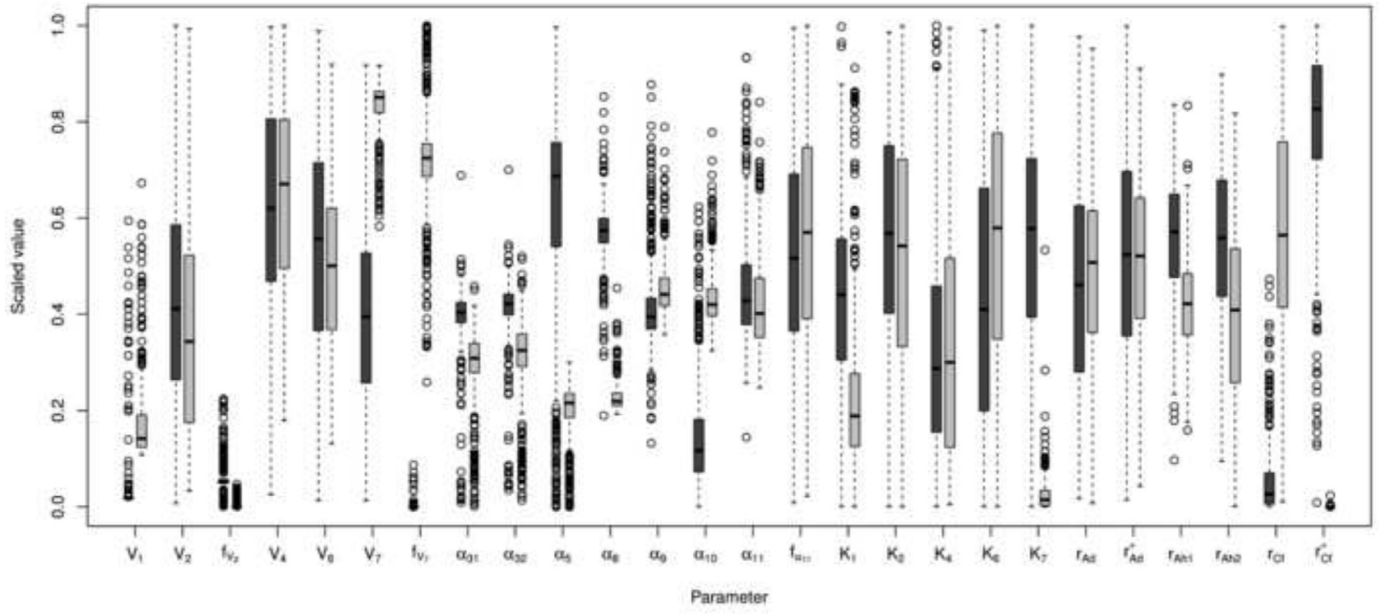

Fig. 3. Boxplot of the best scoring 500 sets of parameters, fitted to the forward data (left boxes) and the reverse data (right boxes), with no restrictions on the r_{cf} and r^{+}_{Cf} parameters. Note the significant differences in the K_7 and the r_{Cf} and r^{+}_{Cf} parameters, amongst others.

V_7 and f_{V_7} are all increased for the forward model compared to the reverse model, whereas f_{V_2} and α_{10} move in the opposite direction. K_7 by comparison drops close to zero in the reverse representing the half-saturation constant of the butyryl-CoA to butyrate reaction, perhaps as the model compensates for CtfA/B remaining constant. Figs. 4 and 5 show how the best fit forward parameters perform against the forward data and how the reverse parameters perform against the reverse data (for the forward experiments this has been shown elsewhere [10], but the figure is included here for completeness.) The ethanol profile in the reverse experiments (Fig. 5) shows some curious behaviour. This is consistent with ethanol production only occurring in the solventogenic population pre-reverse-shift, with little or no ethanol produced in the acidogenic population. Following the reverse-shift, ethanol begins to be produced in the acidogenic population, but this is not enough to compensate for the solventogenic population decrease over the period 130–170 h. The overall dynamic is reflective of ethanol concentrations reaching saturation in the individual dominant populations during the two metabolic phases, with dynamics around the shift dominated by changes in population level.

To test the general applicability of the parameters to each experiments, we show how the best-fit parameters perform against the opposite dataset, i.e. plots of the acid and solvent concentrations of reverse data for the best-fit forward parameters are shown in Fig. 6, and plots of the forward data for the best-fit reverse parameters are shown in Fig. 7. For the 'cross' fittings (reverse data, forward parameters and forward data, reverse parameters) there is a delay of approximately 40 h in the modelled response relative to the data in both cases. This lag appears to be an intrinsic part of the fits from the metabolic model, and could represent the characteristic timescale over which the metabolism shifts from acidogenesis to solventogenesis, or indeed could indicate other important

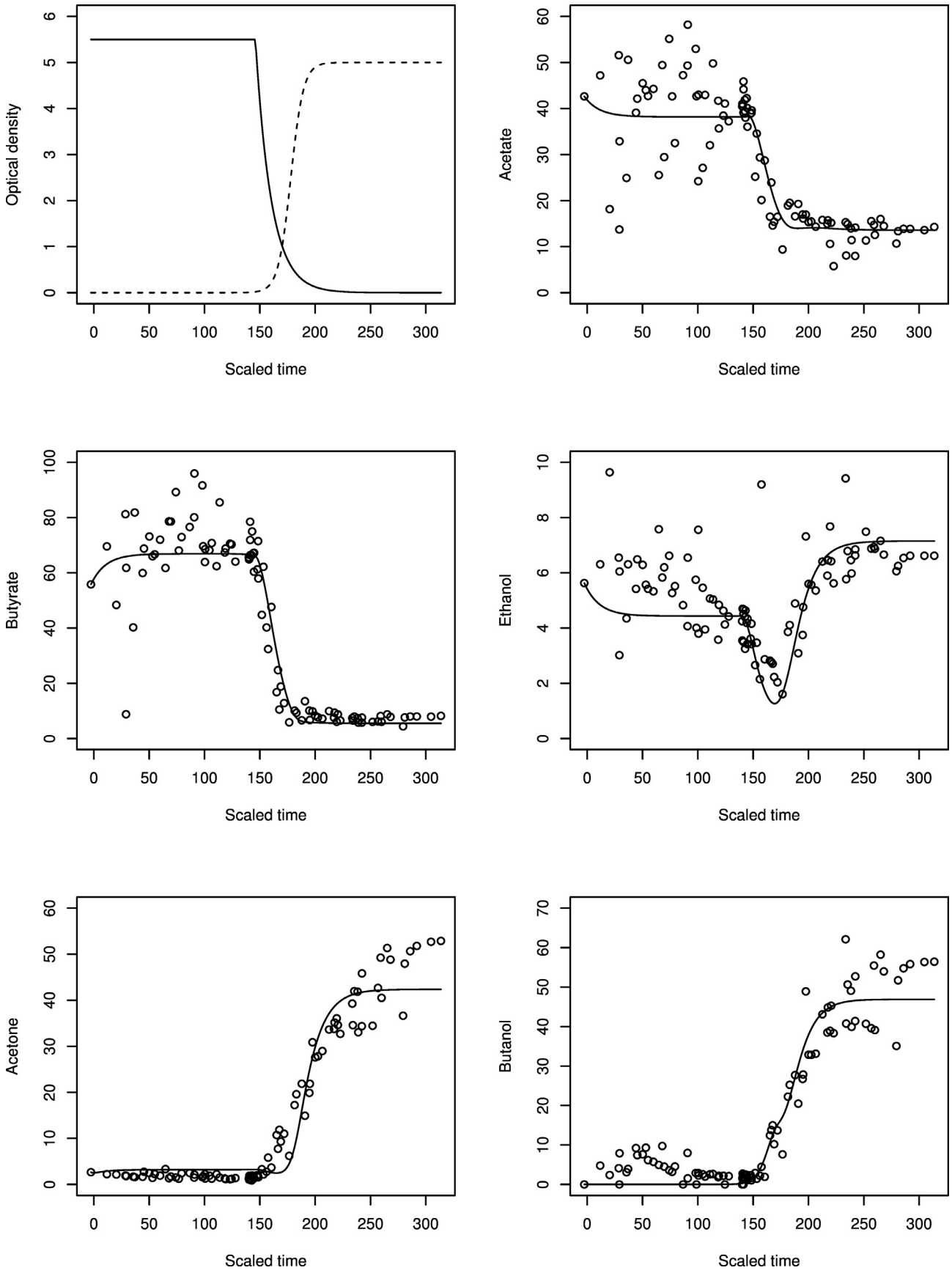

Fig. 4. Plot of the acid and solvent concentrations for the best-fit forward parameters against the data for the forward experiment with unrestricted CtfA/B concentration with the modelled optical density in the top-left: solid line acidogenic population, dashed line solventogenic population.

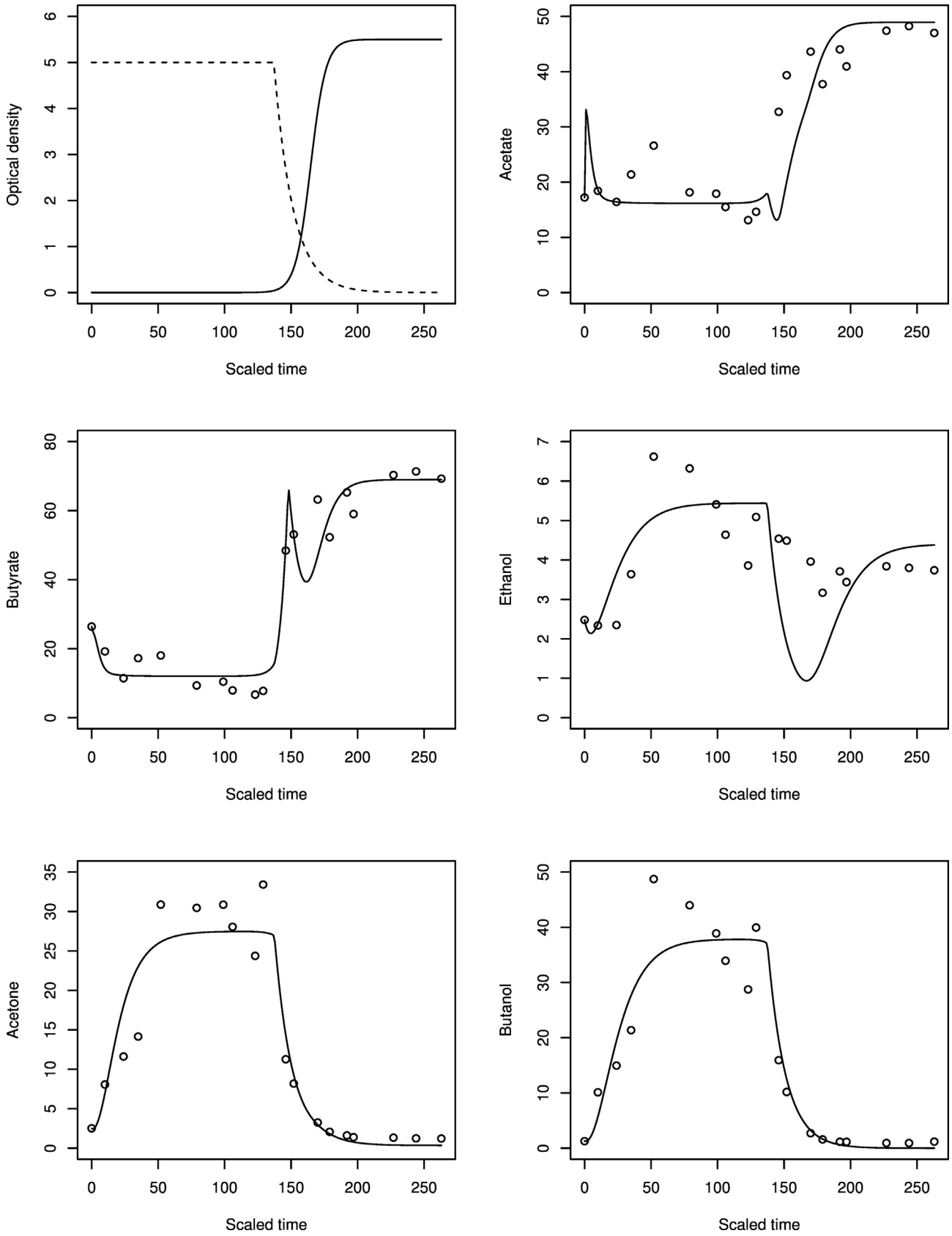

Fig. 5. Plot of the acid and solvent concentrations for the best-fit reverse parameters against the data for the reverse experiments with unrestricted CtfA/B concentration with the modelled optical density in the top-left: solid line acidogenic population, dashed line solventogenic population.

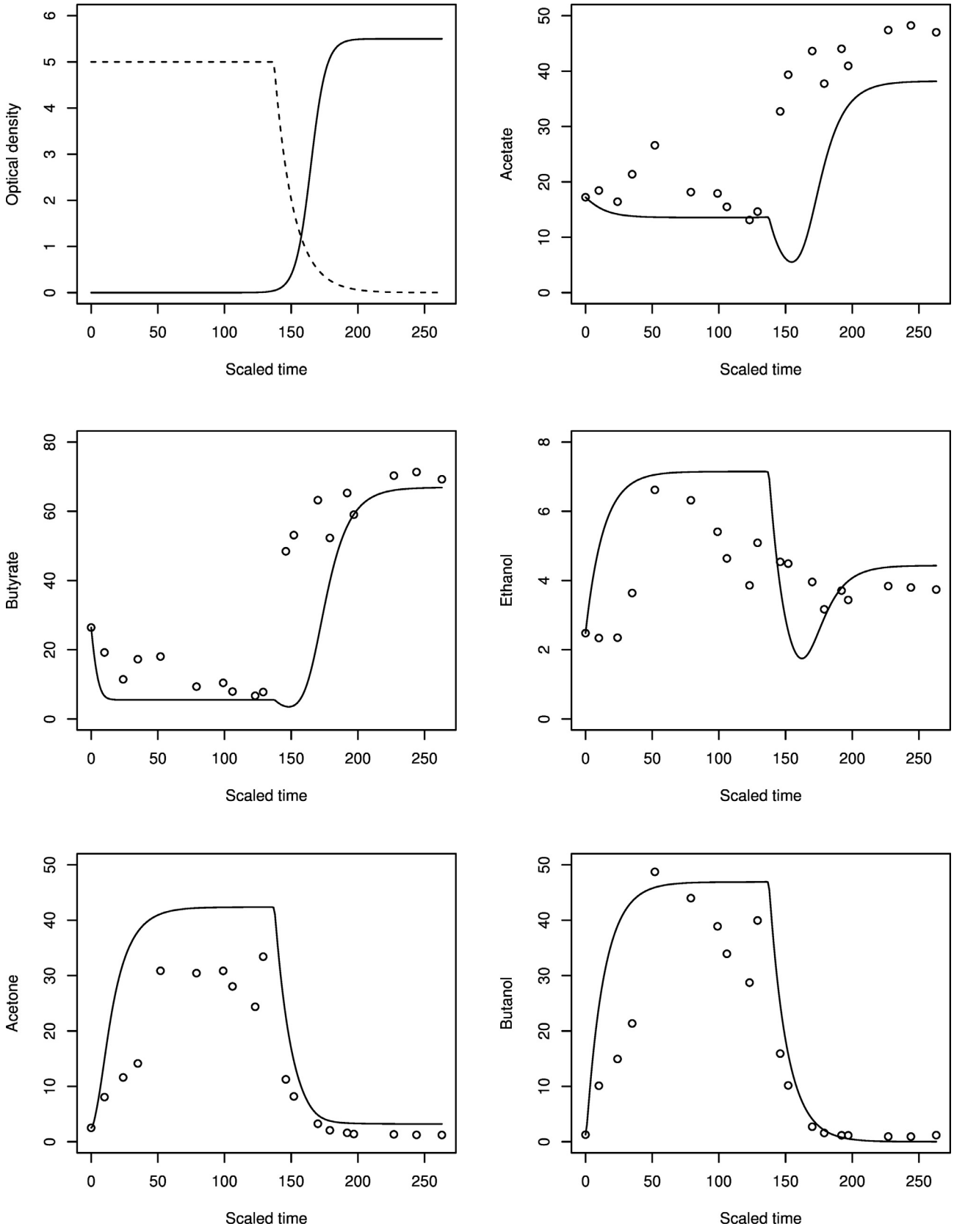

Fig. 6. Plot of the acid and solvent concentrations for the best-fit forward parameters against the data for the reverse experiment with unrestricted CtfA/B concentration with the modelled optical density in the top-left: solid line acidogenic population, dashed line solventogenic population. Note the delay in the modelled metabolic response, which is particularly noticeable in the butyrate concentration.

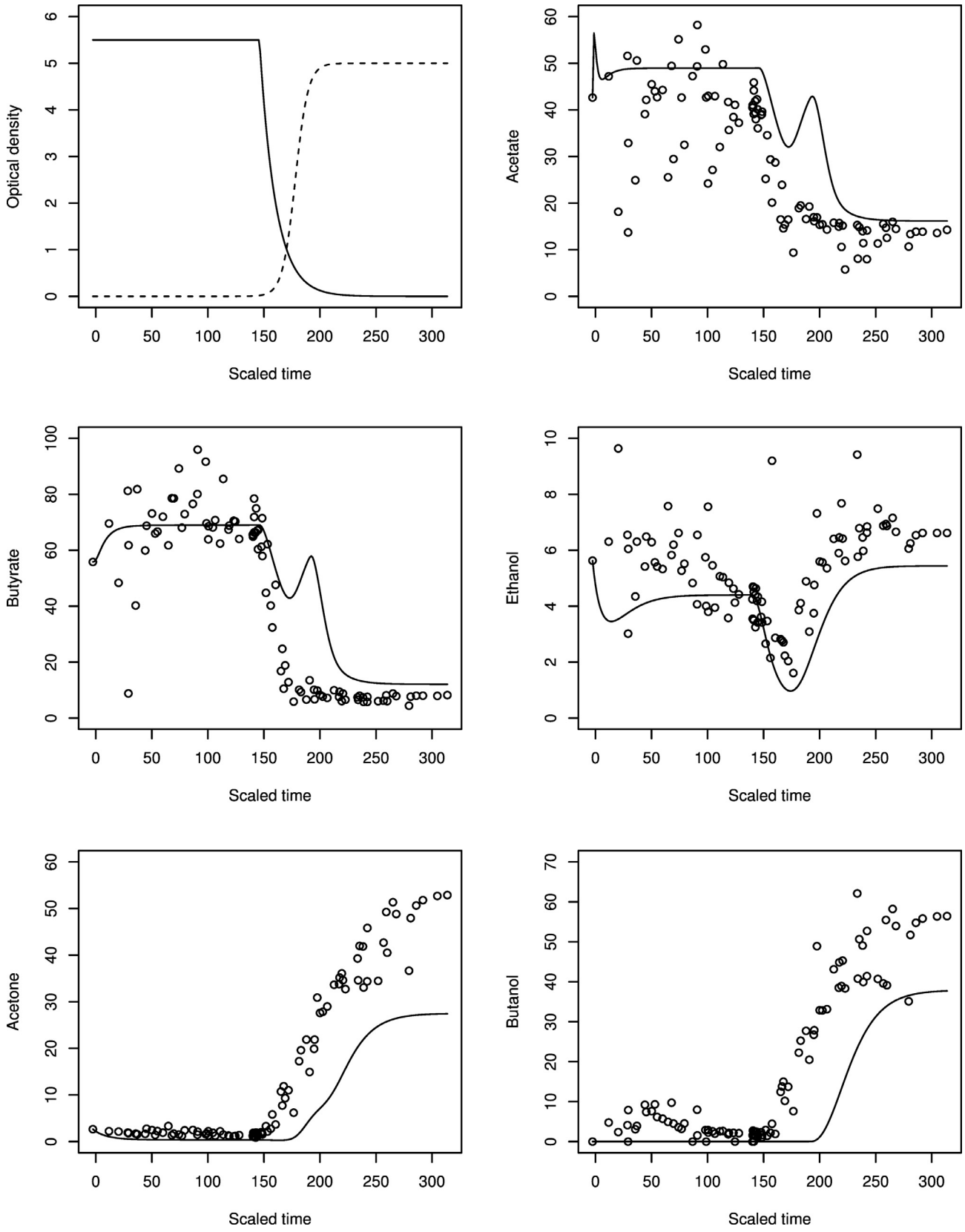

Fig. 7. Plot of the acid and solvent concentrations for the best-fit reverse parameters against the data for the forward experiments with unrestricted CtfA/B concentration with the modelled optical density in the top-left: solid line acidogenic population, dashed line solventogenic population. Note, as in Fig. 6, there is a delay in the modelled metabolic response of approximately 40 h, as well as a bump in acetate and butyrate concentrations around 200 h from the start of the experiment.

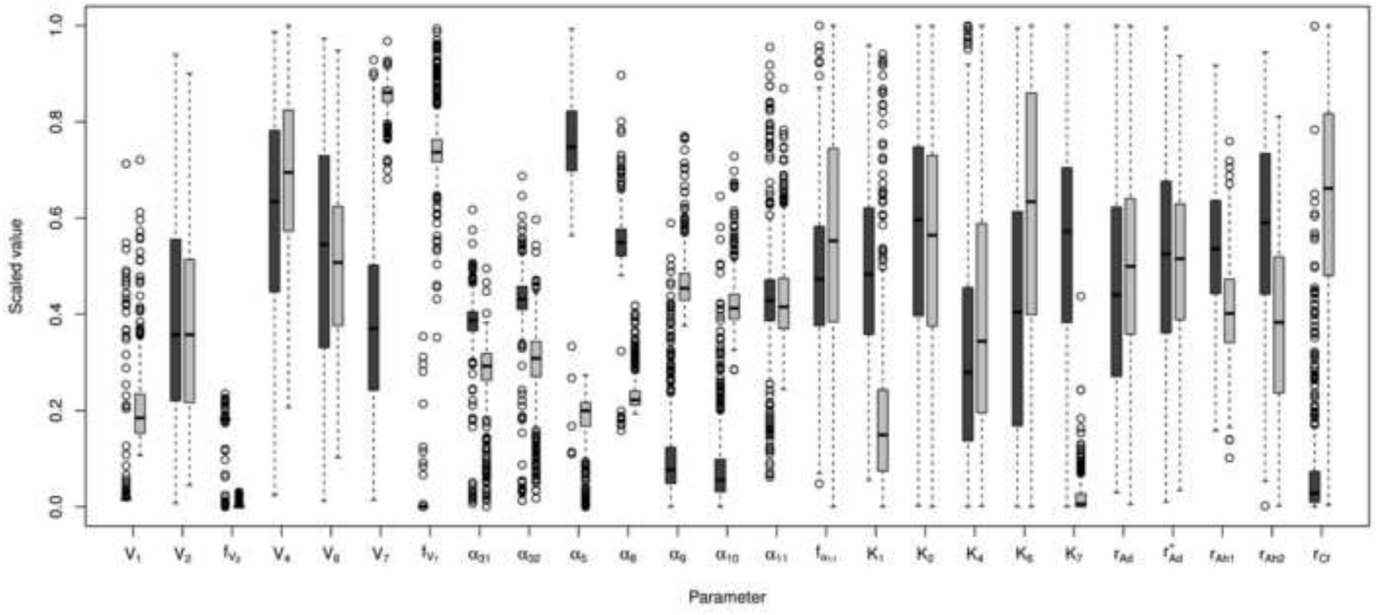

Fig. 8. Boxplot of the best scoring 500 sets of parameters, fitted to the forward data (left boxes) and the reverse data (right boxes), with the concentration of CtfA/B prescribed to be the same in acidogenic and solventogenic phases. Note how the non-r_{Cf} parameters follow the same pattern as for the unrestricted CtfA/B concentration plot in Fig. 3.

reactions which are missed in the model. One other interesting feature which appears is a second peak in the acetate and butyrate concentrations post-shift. This is related to the half-saturation K_7 in the butyrate production reaction – a lower value of this will boost production of butryate for lower concentrations of butyrate-CoA as the metabolism switches from acidogenic to solventogenic.

Repeating the same optimisations for the metabolic model (2.1) in which the CtfA/B concentration is constant in both phases shows a similar pattern in the parameters for forward and reverse data fitted parameters (Fig. 8), and with the 40 h delay in the forward parameters against reverse data plot (Fig. 9) and reverse parameters against forward data plot (Fig. 10), showing the consistency of this potentially characteristic metabolic remodelling time.

4. Discussion

The two population model developed in [10] has been fitted to both forward and reverse shift data for *Clostridium aceotbutylicum* in continuous phosphate-limited culture: in both cases the pH of the solution is controlled by the automatic addition of KOH, which allows the system to be shifted in both directions as desired. Due to the lack of optical density data for the reverse experiment, an estimate of the relative population sizes has been used to model the two populations in reverse data, using plausible values for the steady-state sizes derived from the forward experiment acidogenic and solventogenic population sizes and population growth rates.

The parameters for the model were fitted with the level of CtfA/B allowed to vary between acidogenic and solventogenic phases and with CtfA/B constant between the two phases. In both cases, the best-fit parameters behaved the same way: the relative levels of the limiting glucose intake velocity V_1, the glucose intake half-saturation constant K_1, the maximum butyryl-CoA conversion into butyrate rate V_7 and the Michaelis–Menten constant for the butyryl-CoA to butyrate reaction K_7 were all higher for parameters fitted to the forward data than for the reverse: indeed the constant K_7 drops almost to zero when fitted to the reverse data. This is unexpected, but could be due to the unchanging nature of the CtfA/B concentration in the reverse model. The parameter α_{10}, which is involved in the re-uptake of butyrate back into butyryl-CoA is also reduced when moving from forward-fitted parameters to reverse-fitted parameters, which maintains the overall equilibrium of the interconversion of butyrate and butyryl-CoA. The surprising parameter fit is that of the increase in CtfA/B production during solventogenesis, r_{Cf}^{+}, which is optimised to zero when fitted to reverse data (with a corresponding increase in the basal production rate r_{Cf}). Restricting CtfA/B to a constant concentration in both phases of the metabolism does not change the fit too much in both phases, nor does it change the distributions of the other parameters. This is highly suggestive that the network includes some redundancy which allows other parameters to shift their relative values to account for the unchanging level of CtfA/B, causing the knock-on effects on the parameters for the butyrate and butyryl-CoA interconversion. A consequence of the change in these parameters is the appearance of a brief peak of butyrate and acetate production post-shift when plotted against the forward data (Fig. 10).

A similar round of parameter-fitting with different limits on r_{Cf}^{+}, so that the change in CtfA/B is restricted to be significantly greater than zero between acidogenesis and solventogenesis is shown in Fig. 11. In the figure, the distribution of the other parameters is near-identical to that of the previous two cases, but the parameter r_{Cf}^{+} is minimised for the reverse-fitted parameters so that the overall change in CtfA/B is reduced.

Since this result could be highly significant, the question of whether this is a real effect or whether this is an artefact of the model is an important one. CtfA/B concentration remaining constant during a reverse shift is contradictory to the expectation implicit in nearly all previous experimental work on clostridial metabolism: it is generally considered that CtfA/B is at a lower concentration in acidogenic phase than in solventogenic phase. However, most of this experimental work is performed either in steady state conditions or during a forward shift (acidogenic-to-solventogenic transition) [1,5,6,9], with relatively little experimental work performed during reverse shift [7], with no measurements of relative levels of this enzyme. Experimental measurements of this enzyme CtfA/B, perhaps from a proteomic study, during a

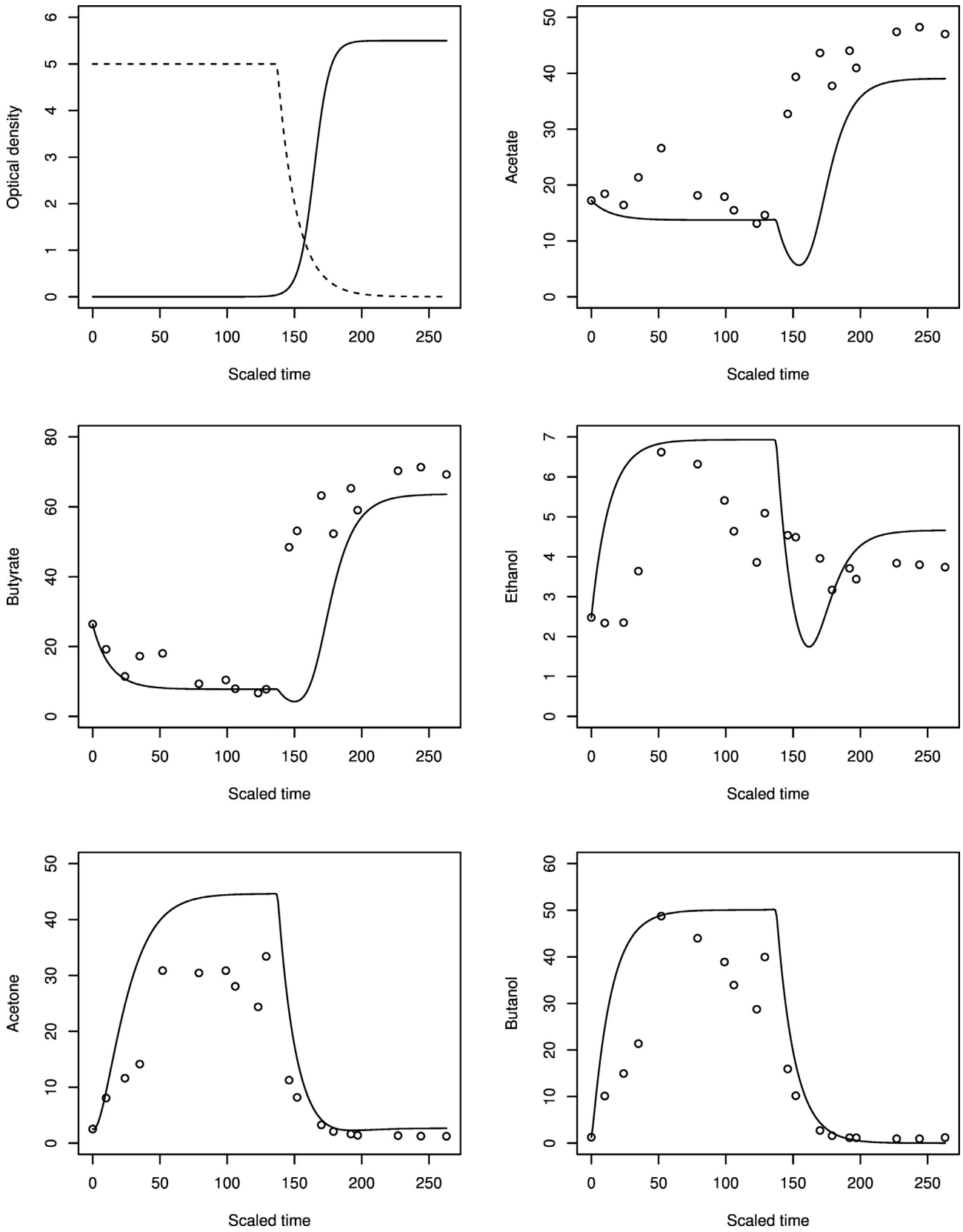

Fig. 9. Plot of the acid and solvent concentrations for the best-fit forward parameters against the data for the reverse experiment with CtfA/B concentration assumed constant in both acidogenic and solventogenic phases: with the modelled optical density in the top-left: solid line acidogenic population, dashed line solventogenic population. Note, as in Fig. 6, there is a delay in the modelled metabolic response.

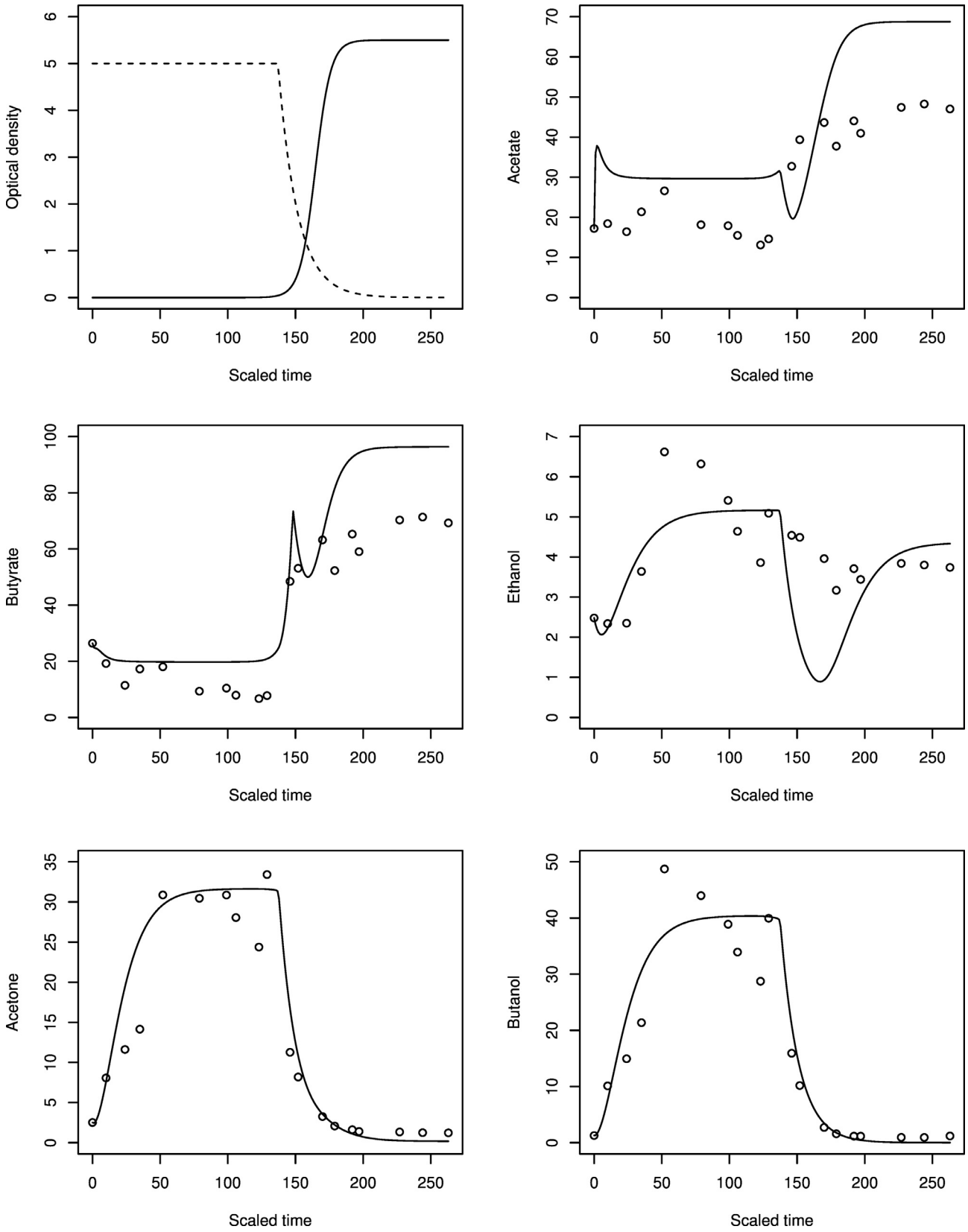

Fig. 10. Plot of the acid and solvent concentrations for the best-fit reverse parameters against the data for the forward experiment with CtfA/B concentration assumed constant in both acidogenic and solventogenic phases: with the modelled optical density in the top-left: solid line acidogenic population, dashed line solventogenic population. Again, note the delayed modelled metabolic response, and the bump in acetate and butyrate concentrations around 180–200 h from the start of the experiment.

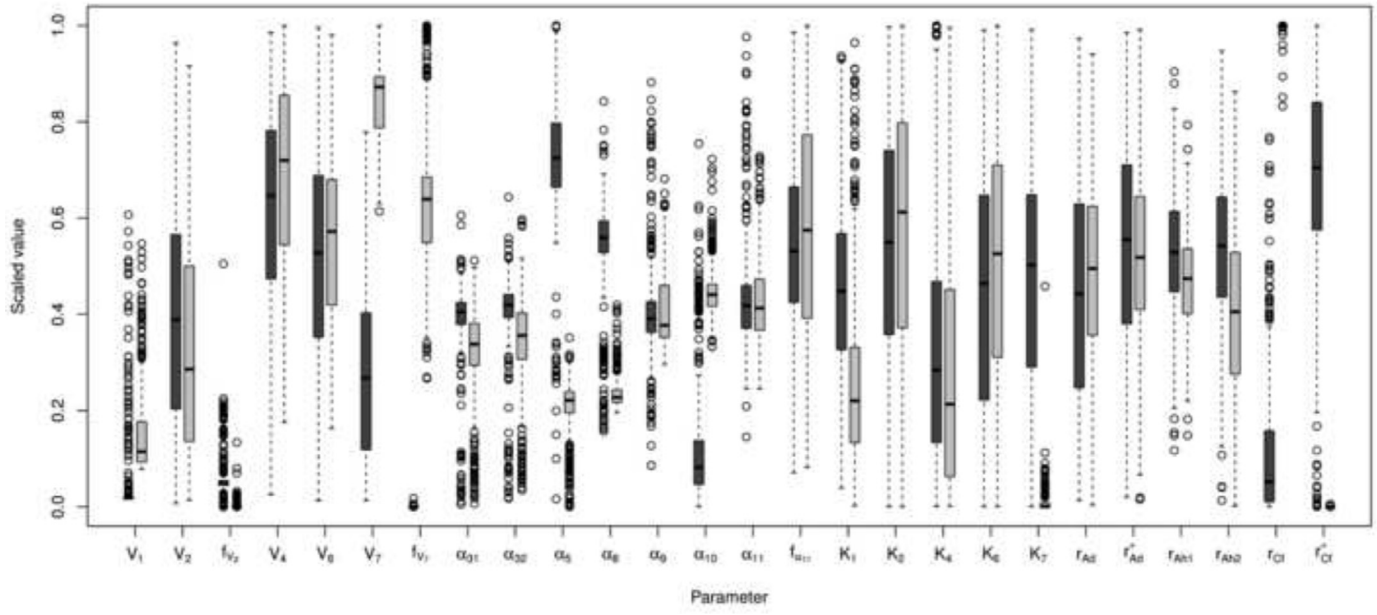

Fig. 11. Boxplot of the best scoring 500 sets of parameters, fitted to the forward data (left boxes) and the reverse data (right boxes), where the increase in CtfA/B when passing from acidogenic to solventogenic phases is restricted to being significantly nonzero. Notice that the overall distribution of parameters is similar to that for unrestricted CtfA/B levels 3, and for constant CtfA/B levels 8, and that the change in CtfA/B production between acidogenic and solventogenic phases, represented by r_{Cf}^{+} is at the bottom of its scaled interval, minimising the change in concentration.

reverse shift would answer the question as to whether this is real (and due to cell adaptation to the reverse shift conditions), or due to overfitting of the model from the data. Previous work by the authors Thorn et al. [15] on an earlier version of the metabolism model shows that there were a number of correlations between parameters, representing multiple paths to the same overall external metabolite concentrations, suggests that the latter may be true. A metabolomic study to determine the relative concentrations of the important metabolites acetyl-CoA, acetoacetyl-CoA and butyryl-CoA would restrict the potential values of the parameters further, and along with measurements of population sizes (optical densities), would determine the question one way or another. If indeed the findings are confirmed by experiments, then this could lead to an improvement in the efficiency of solventogenesis by engineering the organism to over-express the vital solventogenic enzyme CtfA/B.

Acknowledgements

The authors acknowledge support by the Biotechnology and Biological Sciences Research Council (BBSRC Grant no. BB/I004513/1) as part of the European Transnational Network Systems Biology of Microorganisms (SysMO) – within the COSMIC2 consortium. JRK also acknowledges the funding of the Royal Society and Wolfson Foundation. We are also grateful for fruitful discussions with other members of the COSMIC2 consortium, and for the use of the University of Nottingham High Performance Computing facility, in order to run multiple numerical parameter fits in parallel on multiple cores.

References

[1] W. Andersch, H. Bahl, G. Gottschalk, Level of enzymes involved in acetate, butyrate, acetone and butanol formation by clostridium acetobutylicum, Appl. Microbiol. Biotechnol. 18 (6) (1983) 327–332.

[2] H. Bahl, W. Andersch, K. Braun, G. Gottschalk, Effect of pH and butyrate concentration on the production of acetone and butanol by clostridium acetobutylicum grown in continuous culture, Eur. J. Appl. Microbiol. Biotechnol. 14 (1982) 17–20.

[3] M. Cardoso, R. Salcedo, S.F. de Azevedo., The simplex-simulated annealing approach to continuous non-linear optimization, Comput. Chem. Eng. 20 (9) (1996) 1054–1080.

[4] P. Dürre (Ed.), Handbook on Clostridia, Taylor & Francis, 1995.

[5] P. Dürre, R.-J. Fischer, A. Kuhn, K. Lorenz, W. Schreiber, B. Stürzenhofecker, S. Ullmann, K. Winzer, U. Sauer, Solventogenic enzymes of clostridium acetobutylicum: catalytic properties, genetic organization, and transcriptional regulation, FEMS Microbiol. Rev. 17 (1995) 251–262.

[6] M. Gottwald, G. Gottschalk, The internal pH of clostridium acetobutylicum and its effect on the shift from acid to solvent formation, Arch. Microbiol. 143 (1985) 42–46.

[7] S. Haus, S. Jabbari, T. Millat, H. Janssen, R.-J. Fisher, H. Bahl, O. Wolkenhauer, A systems biology approach to investigate the effect of pH-induced gene regulation on solvent production by clostridium acetobutylicum in continuous culture, BMC Syst. Biol. 5 (2011) 10.

[8] H. Janssen, C. Döring, A. Ehrenreich, B. Voigt, M. Hecker, H. Bahl, R.J. Fischer, A proteomic and transcriptional view of acidogenic and solventogenic steady-state cells of clostridium acetobutylicum in a chemostat culture, Appl. Microbiol. Biotechnol. 87 (2010) 2209–2226.

[9] D.T. Jones, D.R. Woods, Acetone-butanol fermentation revisited, Microbiol. Rev. 50 (1986) 484–524.

[10] T. Millat, H. Janssen, G.J. Thorn, J.R. King, H. Bahl, R.-J. Fischer, O. Wolkenhauer, A shift in the dominant phenotype governs the pH-induced metabolic switch of clostridium acetobutylicum in phosphate-limited continuous cultures, Appl. Microbiol. Biotechnol. 97 (2013) 6451–6466.

[11] W.H. Press, S.A. Teukolsky, W.T. Vetterling, B.P. Flannery, Numerical Recipes in C: The Art of Scientific Computing, second, ed. Cambridge University Press, 1992.

[12] H. Shinto, Y. Tashiro, M. Yamashita, G. Kobayashi, T. Sekiguchi, T. Hanai, Y. Kuriya, K. Okamoto, M. Sonamoto, Kinetic modeling and sensitivity analysis of acetone-butanol-ethanol production, J. Biotechnol. 131 (2007) 45–56.

[13] G.J. Thorn, J.R. King, S. Jabbari, pH-induced gene regulation of solvent production by clostridium acetobutylicum in continuous culture: parameter estimation and sporulation modelling, Math. Biosci. 242 (1) (2013) 51–58.

[14] D.P. Wiesenborn, F.B. Rudolph, E.T. Papoutsakis, Phosphotransbutyrylase from Clostridium acetobutylicum ATCC 824 and its role in acidogenesis, Appl. Microbiol. Biotechnol. 55 (2) (1989) 317–322.

[15] G.J. Thorn, J.R. King, The metabolic network of *Clostridium acetobutylicum*: Comparison of the approximate Bayesian computation via sequential Monte Carlo (ABC-SMC) and profile likelihood estimation (PLE) methods for determinability analysis, Math. Biosci. 271 (2016) 62–79.

Methods 104 (2016) 101–110

Contents lists available at ScienceDirect

Methods

journal homepage: www.elsevier.com/locate/ymeth

Investigating MALDI MSI parameters (Part 1) – A systematic survey of the effects of repetition rates up to 20 kHz in continuous raster mode

Rory T. Steven [a], Alex Dexter [a,b], Josephine Bunch [a,c,*]

[a] National Centre of Excellence in Mass Spectrometry Imaging (NiCE-MSI), National Physical Laboratory (NPL), Teddington TW11 0LW, UK
[b] University of Birmingham, School of Chemistry, B15 2TT, UK
[c] School of Pharmacy, University of Nottingham, NG7 2RD, UK

ARTICLE INFO

Article history:
Received 30 November 2015
Received in revised form 15 March 2016
Accepted 8 April 2016
Available online 11 April 2016

Keywords:
MALDI MSI
Mass spectrometry imaging
High repetition rate lasers
Lipid analysis
Continuous raster imaging

ABSTRACT

Recent developments in laser performance, combined with the desire for increases in detected ion intensity and throughput, have led to the adoption of high repetition-rate diode-pumped solid-state (DPSS) lasers in matrix-assisted laser desorption/ionization (MALDI) mass spectrometry imaging (MSI). Previous studies have demonstrated a more complex relationship between detected ion intensity, stage raster speed and laser pulse repetition rate than the simple linear relationship between number of pulses and detected ion intensity that might be expected. Here we report, for the first time, the interrelated influence of varying laser energy, repetition rate and stage raster speed on detected ion intensity. Thin films of PC 34:1 lipid standard and murine brain tissue with CHCA are analysed by continuous stage raster MALDI MSI. Contrary to previous reports, the optimum laser repetition rate is found to be dependent on both laser energy and stage raster speed and is found to be as high as 20 kHz under some conditions. The effects of different repetition rates and raster speeds are also found to vary for different ion species within MALDI MSI of tissue and so may be significant when either targeting specific molecules or seeking to minimize bias. A clear dependence on time between laser pulses is also observed indicating the underlying mechanisms may be related to on-plate hysteresis-exhibiting processes such as matrix chemical modification.

1. Introduction

The N_2 laser operating at around 20 Hz was, until relatively recently, standard within UV matrix-assisted laser desorption/ionization (MALDI) mass spectrometry (MS) applications. More recently the desire for improvements in pulse-to-pulse stability, laser lifetime and repetition rate has led to a widespread uptake in the standard employment by manufacturers of diode pumped solid state (DPSS) lasers. UV DPSS lasers used within MALDI MS are typically variations of neodymium doped lasers including: Nd:YAG [1–3], Nd:YLF [4,5] and Nd:YVO_4 [6] with a variety of repetition rate, temporal pulse width and energy characteristics.

The desire for increased laser pulse repetition rate is driven primarily by the need in MALDI mass spectrometry imaging (MSI) for increased throughput when imaging over larger tissue areas or with smaller pixel sizes and is considered to be of great importance for the next-generation instrumentation. Within MALDI MS it is generally understood that there will be a trade-off between the time spent interrogating a given region and the detected ion intensity achieved for a given analyte of interest; notwithstanding the complete removal of available matrix-analyte crystal in that region. Therefore, the ability to increase the rate of sampling, typically necessitating an increase in repetition rate, is needed.

The benefit of increased repetition rate for faster data acquisition has been demonstrated for spot data acquisition [3,7] and has also been shown in conjunction with improvements in detected ion intensity over a standard N_2 laser at atmospheric pressure [8]. More recently Bruker Daltonics have developed a new high-throughput MALDI-TOF imaging platform with a 10 kHz Nd:YAG laser enabling the acquisition of 50 pixels per second. This platform was recently employed to demonstrate the use of low vapour-pressure matrices within high-vacuum systems for MALDI MSI [9].

In order to access the fastest image acquisition times it may also be considered necessary to apply these high-repetition rate lasers to MALDI MSI utilising continuous raster mode. This provides throughput benefits over spot mode image acquisition due to the

* Corresponding author at: National Centre of Excellence in Mass Spectrometry Imaging (NiCE-MSI), National Physical Laboratory (NPL), Teddington TW11 0LW, UK; School of Pharmacy, University of Nottingham, NG7 2RD, UK.
E-mail address: josephine.bunch@npl.co.uk (J. Bunch).

http://dx.doi.org/10.1016/j.ymeth.2016.04.010
1046-2023/

continuous movement of the laser over the sample. The performance of high-repetition rate lasers in MALDI MSI in raster mode was the topic of three recent publications [6,10,11]. These studies show that high-repetition rate lasers can provide high-quality tissue imaging data in short timeframes but also suggest that there is an optimum repetition rate for use in raster imaging below or above which a decrease in detected ion intensity may be observed. An early adoption of a DPSS high-repetition rate laser, similar to the one used within this study, was reported by Trim et al. where the most effective repetition rates were found to be at around 5 kHz, coinciding with the highest energy-per-pulse emitted by the laser in question [6]. Mass spectra from tissue were also shown within this study using 15 kHz repetition rate which was the highest reported repetition rate used for tissue imaging within MALDI MSI. Interestingly, Spraggins et al., when investigating peptides in α-cyano-4-hydroxycinnamic acid (CHCA) thin films, reported that a reduction in detected ion intensity was observed at higher repetition rates or at lower stage raster speeds, stating that this was due to excessive laser pulse-to-pulse overlap and that a limit of 50 laser pulses per unit area should be observed for optimum performance [10].

Porta et al. [12] investigated the effect of altering a number of variables including laser repetition rate between (50–1000 Hz) and stage raster speed (1–4 mm/s) on quantification in MALDI MSI by single reaction monitoring (SRM). Within their work it was observed that an increased ion intensity was observed where faster raster speeds or higher repetition rates were employed.

The interrelated influence of stage raster speed, laser repetition rate and varying laser energy has never previously been studied, particularly in a tissue imaging context. With the continuing progression of MSI systems toward high-throughput performance, this knowledge is increasingly important to best understand and optimise experiments within MALDI MSI. Within this study, the influence of laser pulsed repetition rate, energy and stage raster speed in continuous stage raster MALDI MSI are studied using both thin-film CHCA preparations of PC 34:1 lipid standard and CHCA-coated murine brain tissue sections. For thin-film studies the repetition rate is varied between 100 Hz and 20 kHz for stage raster speeds between 0.2 and 2.8 mm/s at four different single pulse energy values between 1.7 and 6.4 μJ. For tissue imaging studies repetition rates of 2 and 20 kHz, raster speeds of 0.5 and 2.8 mm/s and energies of 1 and 3 μJ are assessed.

2. Methods

2.1. Materials

Methanol (HPLC grade) used in preparation of all matrix solutions was purchased from Fisher Scientific (Leicestershire, UK). The water used was purified by an ELGA Purelab Option system (Marlow, UK). Trifluoroacetic acid (TFA, 99.9% purity) and CHCA (99% purity) were purchased from Sigma Aldrich (Dorset, UK). MALDI MS stainless steel imaging plates from Sciex (Ontario, Canada) were used for all experiments. The lipid standard PC 34:1 (18:1/16:0) with mass of 759.578 Da was purchased from Avanti Polar Lipids Incorporated (Delf Zyl, Netherlands).

2.2. Tissue preparation and sectioning

Mice were sacrificed humanly at the School of Cancer Sciences, University of Birmingham, in accordance with the Home Office Animals (Scientific Procedures) Act 1986 [13]. Mouse brain was flash frozen in liquid nitrogen immediately after excision. Four serial sections (10 μm thick) were collected and thaw-mounted onto a single MALDI imaging plate. Sectioning was performed on a Leica CM 1850 Cryostat (Milton Keynes, UK).

2.3. Matrix application

For the thin-film experiments using the lipid standard, a PC 34:1 solution (0.04 mg/mL in 80% CH_3OH) was mixed 1:1 (v:v) with a CHCA solution (10 mg/mL in 80% CH_3OH, 0.2% TFA) and for tissue imaging a CHCA solution at 5 mg/mL in 80% CH_3OH, 0.1% TFA was used. A MALDI imaging plate was used in the case of the thin–film measurements of the lipid standard. The solution, in either case, was then applied to the imaging plate using a TM Sprayer (HTX Technologies, Carrboro, NC) with a nebulizer temperature of 90 °C, a solvent flow rate of 0.115 mL/min, a gas pressure of 10 psi, and a spray head speed of 1333 mm/min. Eight sequential passes across the whole plate were used, each with a spacing of 3 mm between lines, even passes were performed horizontally, and odd passes vertically, and an offset of 1.5 mm was used on passes 3, 4, 7, and 8. This gave a density of matrix and lipid on the plate of 0.115 mg/cm^2 and 0.0005 mg/cm^2, respectively, resulting in an even distribution of matrix/analyte across the whole plate.

2.4. Mass spectrometry

The laser energy per pulse was measured using a pyroelectric sensor (PD10-C, Ophir Photonics). Further details and a schematic of the laser delivery setup are shown in the supplementary information (SI) Fig. S1 and associated text.

MALDI-TOF MS analysis was carried out on a QSTAR XL QqTOF instrument using Analyst QS 1.1 with oMALDI server 5.1 (Sciex). A Nd:YVO_4 (SPOT-10-100-355; Elforlight, Daventry, UK) DPSS laser with a wavelength of 355 nm, a repetition rate of <40 kHz and a pulse length of <1.5 ns was used in this study. The Nd:YVO_4 laser was continuously triggered by a function generator (TTi – TG2000 20 MHz DDS) during all analyses whilst the path of the laser was blocked by a shutter system triggered by the QSTAR oMALDI software to 'turn the laser on and off', rather than triggering the laser directly, ensuring a greater degree of pulse-to-pulse laser stability. The laser was coupled to the MALDI source via a 100 μm core diameter fiber optic patch cord of 4 m (Fiberguide Industries via AMS Technologies, Leicestershire, UK; NA = 0.22) for the tissue imaging experiments and a 105 μm core diameter fiber optic patch cord (Thorlabs Ltd; NA = 0.22) for the thin-film experiments. The raster speeds employed were dictated by the preset software speed values available within the oMALDI (Sciex) software named slowest, slower, slow, medium and fast and correspond to 0.2, 0.3, 0.5, 1.0 or 2.8 mm/s respectively. An m/z range of 50–1000 was used for all experiments. All data were acquired in positive ion mode.

For the thin-film lipid standard analysis the Nd:YVO_4 laser was operated at repetition rates of 100, 500, 1000, 2500, 5000, 7500, 10,000, 12,500, 15,000 and 20,000 Hz, at raster speeds of either 0.2, 0.3, 0.5, 1.0 or 2.8 mm/s and at single-pulse energies of either 1.7, 2.8, 4.2 or 6.4 μJ. A table of parameter combinations is shown in Table S1. The irradiated area on the sample as measured by the fluorometric method [14] was 2.8×10^{-8} m^2 giving fluence values of 225.7, 148.1, 98.8 and 60.0 J/m^2. One raster line of 56 pixels (360 μm diameter per pixel) in length was acquired for each variable combination. The energy of the laser was measured before each of these acquisitions. The average of these values are discussed in the text and used in the fluence calculation.

Tissue MSI data were acquired at stage speeds of 0.3 and 2.8 mm/s ('slower' and 'fast' as labeled within the oMALDI software) at repetition rates of 2 and 20 kHz, and energies of 3 and 1 μJ per pulse. The irradiated area on the sample as measured by the fluorometric method [14] was 2.05×10^{-8} m^2 giving fluence

values of 146.4 and 48.8 J/m^2. All images were acquired in a random order and each half of the coronal section was acquired separately to provide comparison and control during the course of the experiment. These images were acquired with pixel sizes of 360 μm in x and 50 μm in y and took between approximately 10 and 30 min to acquire per section hemisphere.

2.5. Processing of MALDI MSI data

The data were converted from AB Sciex proprietary file format (.wiff) to .mzML using AB MS Data Converter (version 1.3; Sciex) and then converted to imzML using imzMLConverter [15] and processed in MatLab (version R2014b; Math Works Inc, USA). The mean ion counts (peak areas) for selected mass-to-charge values were calculated along with the standard deviation and are plotted as mean value ± expanded uncertainty (k = 2, giving a 95% confidence interval). The image colour scheme was chosen to align with mass spectrometric best practice guidelines [16]. No detector saturation was observed in any data presented within this study. Pulse-normalized data were calculated by dividing mean ion intensity values by the number of laser pulses incident per pixel (Table S1) for each given combination of variables.

3. Results and discussion

3.1. On the alteration of laser repetition rate in MALDI MS

The use of DPSS lasers is now common within the field of MALDI MS and MSI. In the majority of cases these lasers are embedded within commercially supplied MS instrumentation and therefore inaccessible to the user beyond the minimal control given within the software. When the operational repetition rate of the laser is altered, the energy per pulse emitted by the laser may vary depending upon the triggering frequency (repetition rate). This may be due to thermal equilibration phenomena or lasing material excited state lifetime-related effects, for example. In addition, a phenomenon called 'spiking' may occur, depending upon the laser design, whereby the first number of triggered laser pulses, after a longer period without triggering, will have significantly higher energy until a steady state is reached. This phenomenon could be present at the initiation of laser sampling of each pixel or raster line within a MALDI MSI experiment. A shutter triggering system was used within this study to help ensure the absence of these and other laser instabilities. A manuscript on the use of a shuttered triggering system within MALDI MS is currently in preparation. The energy output from the laser over the relevant range of repetition rates used within this study is shown in Fig. 1. The repetition rate

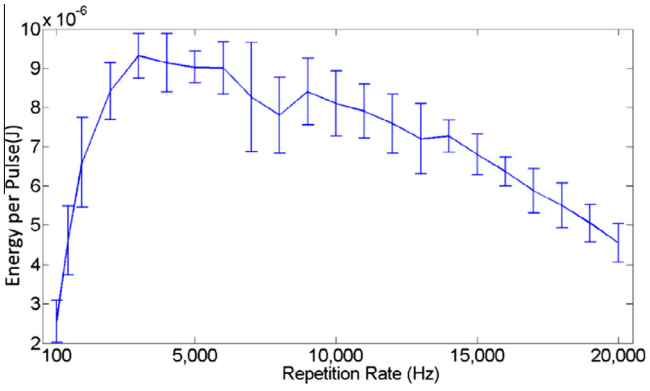

Fig. 1. Laer energy output (mean ± 1 standard deviation) over the experimental range of repetition rates without any alteration in the level of attenuation.

at which the highest output energy is emitted is observed to be in the region of ~3–6 kHz.

In order to better study the influence of laser pulse repetition rate within MALDI MSI this changing energy with repetition rate needs to be accounted for. Typical commercial MALDI MSI instruments do not enable energy measurement or uninhibited control of the repetition rate. Therefore, we implemented an improved laser delivery system to enable on-line energy monitoring and control, thus allowing the attenuation to be altered so that a constant energy was delivered to the sample regardless of the repetition rate employed. A schematic of this setup is shown in Fig. S1.

3.2. Variation of repetition rate and raster speed in continuous raster sampling MALDI MS

To study the interrelating influences of laser pulse repetition rate, energy and stage raster speed a thin-film sample of CHCA and the lipid standard PC 34:1 was interrogated in continuous raster sampling mode. The ion intensities for the three detected intact adducts ($[M+H]^+$, $[M+Na]^+$ and $[M+K]^+$) of PC 34:1 were summed and the results for raster speeds of 0.2, 0.5, 1.0 and 2.8 mm/s are shown below in Fig. 2. These three adducts were combined in this way to account for any change in the ratio of these species over the experimental range of variables. The equivalent graph for the 0.3 mm/s raster speed, omitted from Fig. 2, is shown in Fig. S2.

A number of broad trends are evident within these data. Firstly, the detected ion intensity clearly increases with increasing fluence as a global trend, an observation that is in agreement with other research [17,18]. The highest ion intensities were detected at 0.2 mm/s, 2.5 kHz and 6.4 μJ. However, the impact of changing fluence varies dramatically depending upon the chosen repetition rate and raster speed employed. For example, at 500 Hz, 0.2 mm/s, 6.4 and 4.2 μJ (Fig. 2 – A) there is a marked difference in the detected intact lipid ion intensity. However, at 15 kHz with the same speed there is little difference between the detected ion intensity at these two energies. Similar observations are also evident across the raster speeds investigated whereby the differences in the detected ion intensity at different energies (and so fluences) are enhanced or reduced depending upon the laser pulse repetition rate. Secondly, the relationship between detected ion intensity and repetition rate, for a given raster speed, is dependent upon the laser energy employed. For example, at 0.2 mm/s raster speed the optimum repetition rate is 2.5 kHz for 6.4 μJ, whereas it is 7.5 kHz for 4.2 μJ and 10 kHz at 2.8 μJ (Fig. 2 – A), a shift to higher optimum repetition rates with decreasing energy. This shift of optimum repetition rate across energies is evident across the different raster speeds e.g. at 2.8 mm/s the 6.4 μJ data shows an optimum repetition rate at 10 kHz whereas the 4.2 μJ data arguably shows an optimum at 20 kHz. Thirdly, the optimum repetition rate for a given energy broadly follows an upward trend where the raster speed increases and/or the energy decreases. For example, the 6.4 μJ data shows an optimum repetition rate of 2.5 kHz at 0.2 mm/s whereas it is 10 kHz at 2.8 mm/s and for the 4.2 μJ data the optimum repetition rate is 7.5 kHz at 0.2 mm/s whereas it is 20 kHz at 2.8 mm/s. Finally, the above discussed trends appear to be less evident as the energy is decreased, *i.e.* the impact of repetition rate at a given raster speed is considerably lessened at lower energies and at the lowest energies within Fig. 2 the repetition rate used results in little difference. Rearranged bar chart versions of these same data are shown in Fig. S3. In addition to the summed intact lipid ions shown in Fig. 2, the total ion counts (TIC) per pixel were plotted in the same manner as was the TIC-normalized version of Fig. 2 (Figs. S4 and S5). Further to the extracted ion intensity data the spectral information also provides an additional perspective on the relationship between energy, stage raster speed and laser pulse repetition rate. Example mean spectra

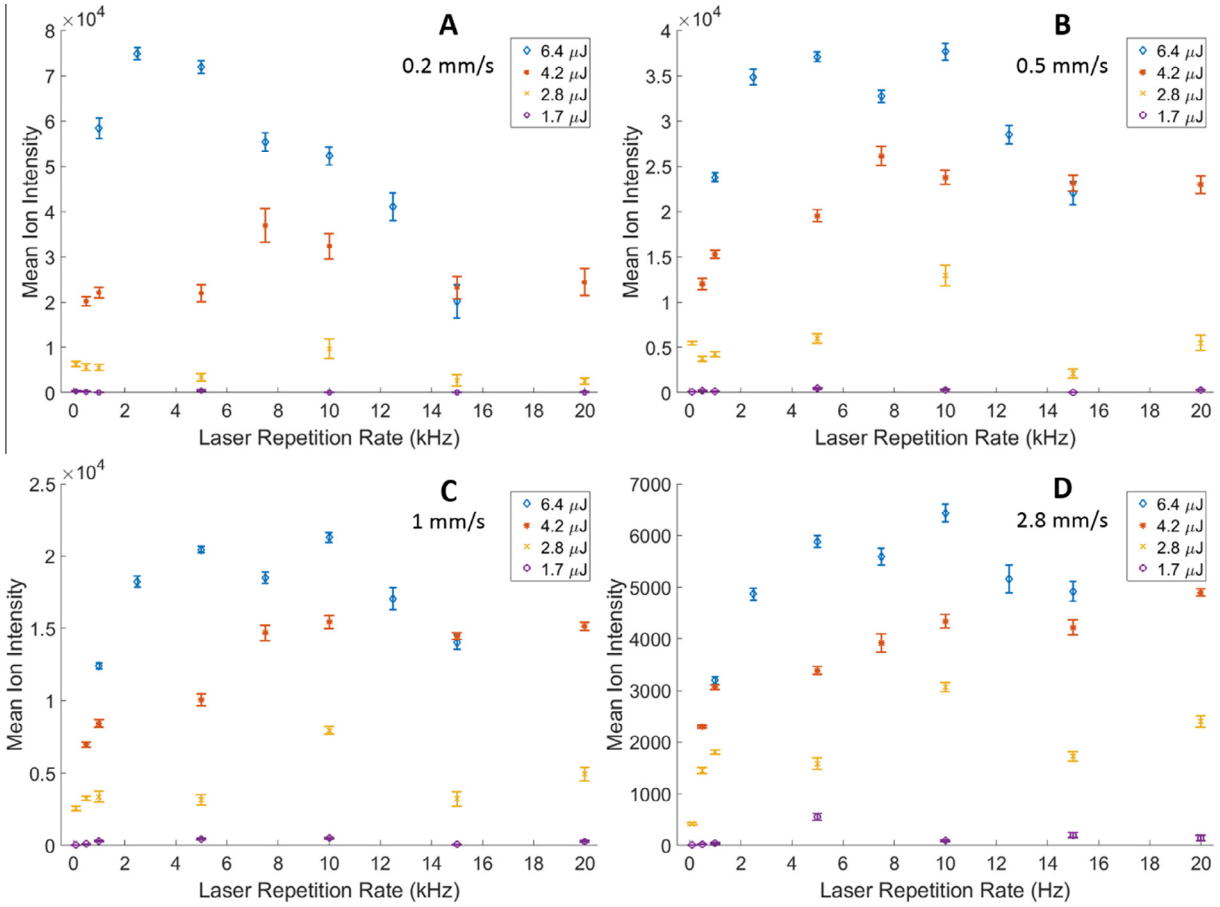

Fig. 2. Mean detected ion intensity per pixel for the sum of the intact adduct ion signals of the PC 34:1 lipid standard ($[M+H]^+$, $[M+Na]^+$, $[M+K]^+$) with varying laser pulse repetition rate, energy and raster speed. Energies of 6.4, 4.2, 2.8 and 1.7 μJ at a range of laser pulse repetition rates from 100 to 20,000 at raster speeds of 0.2 mm/s (A), 0.5 mm/s (B), 1 mm/s (C), and 2.8 mm/s (D). Errors are expressed as k = 2 expanded uncertainty giving a 95% confidence interval.

for some pertinent variable combinations are displayed within Fig. 3.

The alteration of repetition rate and raster speed across several laser pulse energies provides the opportunity to compare data from pixels which have received the same number of pulses but at different temporal rates. Each pixel within the data acquired at 6.4 μJ with raster speed and repetition rate of 0.2 mm/s and 1 kHz, 0.5 mm/s and 2.5 kHz or 1 mm/s and 5 kHz all received 1800 pulses per pixel at this same fixed energy. The mean spectra from these respective experiments are shown in Fig. 3 A, B and C. It is clear that despite the same number of pulses at the same energy there is an increase in detection of the protonated PC 34:1 lipid ion ($[M+H]^+$ at m/z 760.6) with decreasing raster speed and repetition rate. In addition, the intensity of the sodiated ion ($[M+Na]^+$ at m/z 782.6) and the phospholipid head-group fragment ion at m/z 184.1 [19] (proposed structure for these and other fragment ions shown in Fig. S6) increase relative to the $[M+H]^+$ peak as the raster speed and repetition rate are increased (Fig. 3, A–C). Graphs displaying these changes across all variable combinations for m/z 184.1 are displayed in Fig. S7. Further, the (lack of) influence of increased pulses per pixel (under certain circumstances) due to increasing repetition rate are shown in Fig. 3D–F where increasing repetition rate (and so pulses per pixel), at a fixed energy, appears to have little significant effect on the intensity of peaks within the detected mass spectra. Additionally, at lower energies, the raster speed employed (and again the number of pulses per pixel) at a fixed energy and repetition rate may have little influence over the detection ion intensity and spectral profile (Fig. 3G–I).

The number of pulses per pixel, whilst not causing linear variation in the detected ion intensities, can be used to normalize the data displayed within Fig. 2. Graphs showing these normalized data are shown in Fig. 4.

In all cases, for a given energy, the lower the repetition rate used, a trend towards a higher detected ion intensity per pixel and laser pulse is observed. This may be related to the fact that the time period between laser pulses increases with decreasing repetition rate and so, for a specific stage speed, the area of sample irradiated by each new laser pulse will also increase. This increasing area of fresh sample irradiated by each new laser pulse is not, however, the sole reason for the trends seen within Figs. 2–4. For example, the pulse normalized data show similar ion intensity per pixel and laser pulse across all raster speeds investigated (Fig. 4). Additionally, the trends between each energy data set alter across the different raster speeds, whereby, the difference between detected ion intensity per pixel and laser pulse, at each laser energy, reduces as the raster speed increases. This is particularly evident at the lower repetition rates. For instance at 0.2 mm/s and 1 kHz the ion intensity at 6.4 μJ is ~3 times that of 4.2 μJ. This ratio then decreases to less than 2 at 0.5 and 1 mm/s and further decreases a roughly equal value at 2.8 mm/s (Fig. 4). The changing trends of the pulse-normalized data at different energies are further exemplified when displayed as graphs of single energy data as oppose to the single raster speed data shown above (SI Fig. S8). Here the changing trends at different energies can clearly be seen across the varying raster speed for a given energy.

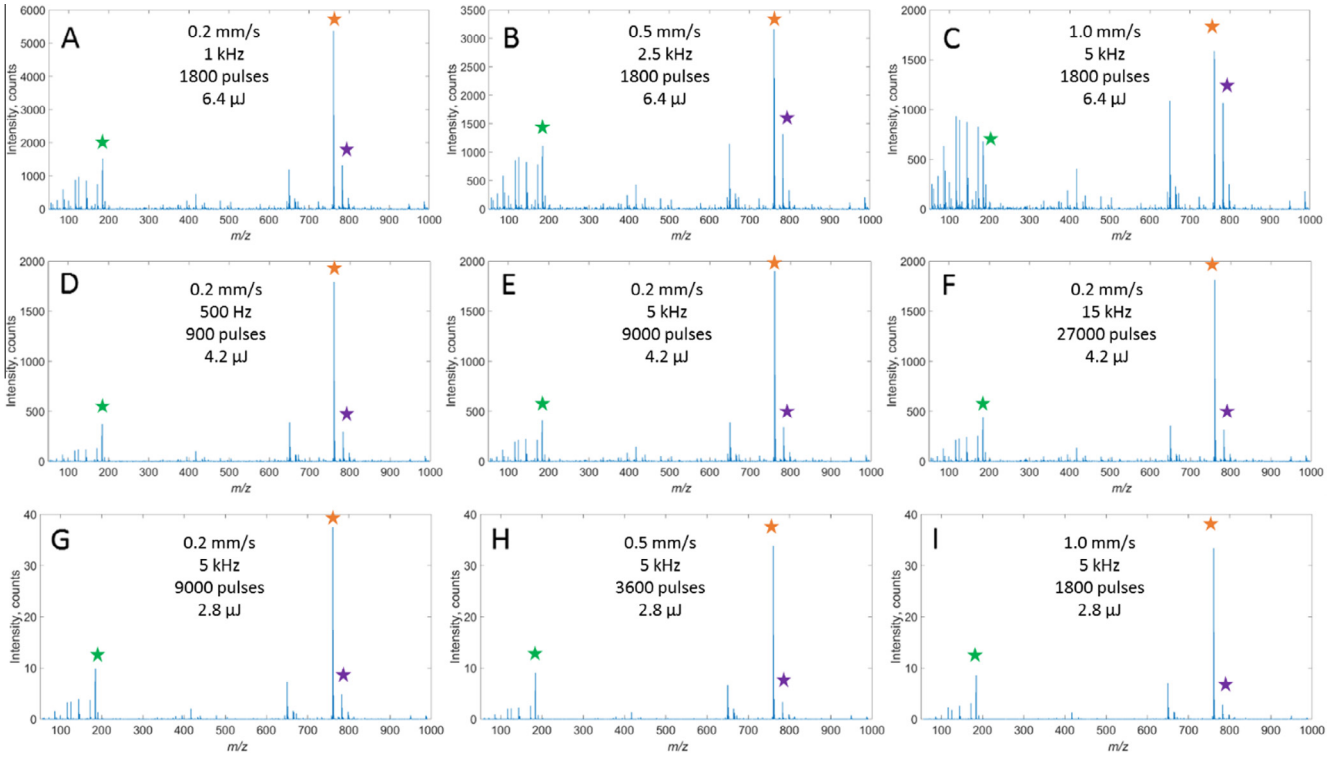

Fig. 3. Example mean spectra from the lipid standard PC 34:1 in CHCA thin films acquired with varying laser pulse repetition rate, energy and stage raster speed from the data shown in Fig. 2. The green star (left), orange star (middle) and purple star (right) in each spectra indicate peaks at *m*/*z* 184.1, 760.6 and 782.6 respectively.

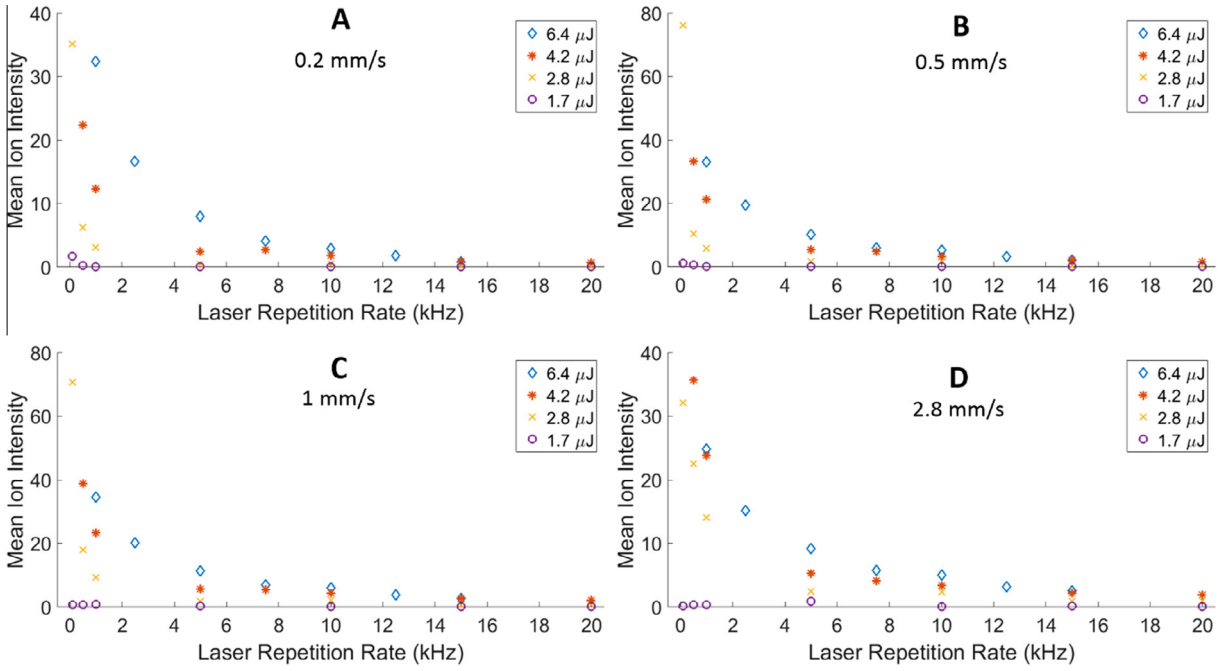

Fig. 4. Mean ion intensity per pixel and laser pulse. Data displayed within Fig. 2 divided by the number of laser pulses incident per pixel for each given variable combination. An increase in average detected ion intensity per pixel and laser pulse is observed with decreasing laser repetition rate.

The change in the ratio of ion signals detected at *m*/*z* 760.6 and at *m*/*z* 782.6 or 184.1 can also be illustrated by plotting these ratios in the same form as Fig. 2. These ratio graphs for $[M+H]^+/[M+Na]^+$ are displayed in Fig. S9 and those for $[M+H]^+/m/z$ 184.1 in Fig. S10. Evident within these figures is the decreasing ratio for $[M+H]^+/[M+Na]^+$ with increasing energy across all raster speeds. Across almost all energies and raster speeds aside from 2.8 mm/s and 1.7 µJ, the $[M+H]^+/[M+Na]^+$ ratio also generally decreases with increasing repetition rate until some minima at which the ratio increases again, for a given raster speed and energy. For the ratio of $[M+H]^+$ to the ion detected at *m*/*z* 184.1 the variation is less significant but there is again a reduction in this ratio with increasing energy.

In summary, the major trends observed within these analyses are: the optimum repetition rate for increased detected ion intensity varies considerably depending upon the stage raster speed and laser energy used within the experiment; there are differential effects on different detected ions as a result of varying laser repetition rate, fluence and stage raster speed; there is a clear dependence of the detected ion intensity on the time period between incident laser pulses where the same number of laser pulses are incident per pixel under different raster speed and repetition rate combinations (Fig. 3A–C).

It is worth, at this point, commenting briefly on the workings of the mass spectrometer used within this study, though far more detailed descriptions are available [20]. The QSTAR XL instrument is a quadrupole time-of-flight instrument which, in single MS mode (full mass range TOF analysis), operates the quadrupoles as ion guides only. Consequently the collisional cooling of the ions, at the repetition rates employed within this study, will result in a quasi-continuous beam of ions through the quadrupole regions to the TOF pusher region. The mass spectrum recorded for each pixel is the sum of hundreds or thousands of TOF cycles (depending upon the pixel acquisition time) – the TOF effectively samples from this continuous beam of ions. As the mass range is fixed within this study, the TOF pusher frequency is also fixed. Therefore, the number of TOF cycles summed on average for the ions resulting from one laser pulse will vary, depending upon the repetition rate. One can further normalize the data shown in Fig. 4 to the number of TOF cycles, resulting in values of mean ion signal intensity per laser pulse, per TOF cycle. However, as the number of TOF cycles per laser pulse is inversely proportional to the laser pulse repetition rate used, the trends seen simply revert back to the exact shapes seen in Fig. 2 with an associated scaling of the y-axis.

3.3. Variation of laser pulse repetition rate and raster speed in continuous raster sampling MALDI MSI of murine brain tissue

The complex interrelation of spectral information as a result of varying laser pulse energy, repetition rate and stage raster speed for the analysis of the thin-film lipid standard samples strongly implies that these variables will also show complex interrelated behavior when investigated in the context of MALDI MSI analysis. Continuous stage raster MALDI MSI data at 0.3 and 2.8 mm/s, 2 and 20 kHz and 1 and 3 μJ were acquired from eight serial sections of murine brain tissue. Image data were acquired in a random order from section hemispheres. The corresponding hemispheres from a single brain section were analysed with a single set of variables but at different time points to act as an internal temporal control. Selected ion images and mean on-tissue spectra from these analyses are shown in Figs. 5 and 6. Detected peaks, tentatively assigned from literature, corresponding to PC 16:0/16:0 $[M+K]^+$ at m/z 772.5, PC 18:0/18:1 $[M+K]^+$ at m/z 826.6, unknown tissue related molecule at m/z 868.5 (tentative assignment of PI 37:6, PA 35:2 or DG 42:11 based on LIPID MAPS (http://www.lipidmaps.org/) database search; the lower mass resolving power of this instrument prevents a more accurate match) and the PC lipid headgroup fragment at m/z 184.1 [21–23].

As was observed from the analysis of thin films, the analyses at the slower raster speed and higher energy give the highest detected ion intensities for intact lipid species (Fig. 5 and 0.3 mm/s, 3 μJ, 2 and 20 kHz). Despite this energy and raster speed clearly giving the highest detected ion intensities, the optimum repetition rate appears to vary depending upon the peak chosen for display where, in this example, 20 kHz is more appropriate for the ion at m/z 868.5 but 2 kHz shows higher intensity for m/z 826.6, 772.5 and 184.1. This phenomenon of differential optimum repetition rate is also evident in the 0.3 mm/s μJ data set but is not evident in quite the same way for the 2.8 mm/s data, where there is either little difference between the 2 and 20 kHz data or 20 kHz is slightly superior overall. This echoes the findings for the high raster speed data acquisition in the thin-film samples discussed above, where the impact of repetition rate decreased as the raster speed is increased with a general trend to higher optimum repetition rates at certain energies.

In all cases the detected ion intensities are higher for the higher laser pulse energy, an observation that would likely be expected based upon existing literature but one which has not been studied within the context of MALDI MSI studies before. It is clear from several of the images that there is a noticeable degree of leeching of endogenous molecules from the tissue, a result of the slightly overly 'wet' sample preparation employed, creating the halo effect observed before in the literature and is particularly evident for the m/z = 184[21]. This is not an issue for the conclusions presented in this study and can even be considered useful with regards to providing insight into the effects of laser pulse repetition rate, energy and stage raster speed. Foremost, the relative levels of fragmentation on tissue and in the halo vary depending upon the energy, repetition rate and raster speed. Typically an increase in fragmentation, for a given laser energy, is to be expected in the halo due to the lower energy requirement for desorption/ionization from stainless steel as compared to the tissue surface. Though, it is also possible that already formed PC headgroup fragments are preferentially solubilized and therefore leached from the tissue, causing a similar visible effect. This is clear from Fig. 5 in all cases apart from at 2.8 mm/s^3 μJ and 20 kHz where the level of fragmentation on tissue is approximately equal to that of the halo region. These and other trends observed within this tissue image data set are evident within the mean on-tissue spectra shown within Fig. 6.

The general optimum ion intensity at 0.3 mm/s^3 μJ and 2 kHz is again evident within Fig. 6 B but it remains clear that the higher repetition rate (20 kHz) data can provide an increased detected ion intensity for some peaks observed in the mass spectrum (Fig. 6D). For example, the peak at m/z 868.5 is more intense in Fig. 6D as compared to 6 B. Further MS/MS studies are required to better assign these enhanced ions. Also clear within the spectra is the large increase in intensity for the peak at m/z 184.1 (likely PC lipid head-group fragment [19]) relative to the mostly intact lipid species detected within the m/z 700–900 region in the high-energy, high-raster speed data shown in Fig. 6F and H. Despite this the highest intensity detected for m/z 184.1 is observed at 0.3 mm/s and 2 kHz (Fig. 6B) where it has increased in line with a global ion intensity increase rather than relative to intact lipid peaks. In addition to this relative increase of m/z 184 in Fig. 6F and H, there is also an increase in other lipid fragment and matrix-related ions below m/z 600 relative to the intensity of the intact species when compared to the other spectra. The spectrum which stands out the most is Fig. 6D where, as well as the above mentioned increase in detected ion intensity for a number of peaks, there is also an almost global increase in the detected ion intensity for typically low intensity peaks throughout the majority of the mass spectrum above m/z 300. The display of this spectrum in Fig. 6D initially gives the impression that an increase in noise baseline is observed using these parameters but this is not, in fact, the case and when zooming into view smaller m/z regions within this spectrum one can see this is actually an increase in fully resolved low intensity peaks compared to the other spectra (see Figs. S11 and S12 for zoomed regions of spectra shown in Fig. 6D and B respectively). More work is, however, required to confirm whether these ions are intact species detected with a greater intensity or the result of other processes such as changing adduct formation or increased ion fragmentation and meta-stable decay, for example.

Again, the trends observed within the data presented can be summarized as follows: the optimum repetition rate for highest detected ion intensity depends upon the stage speed and laser

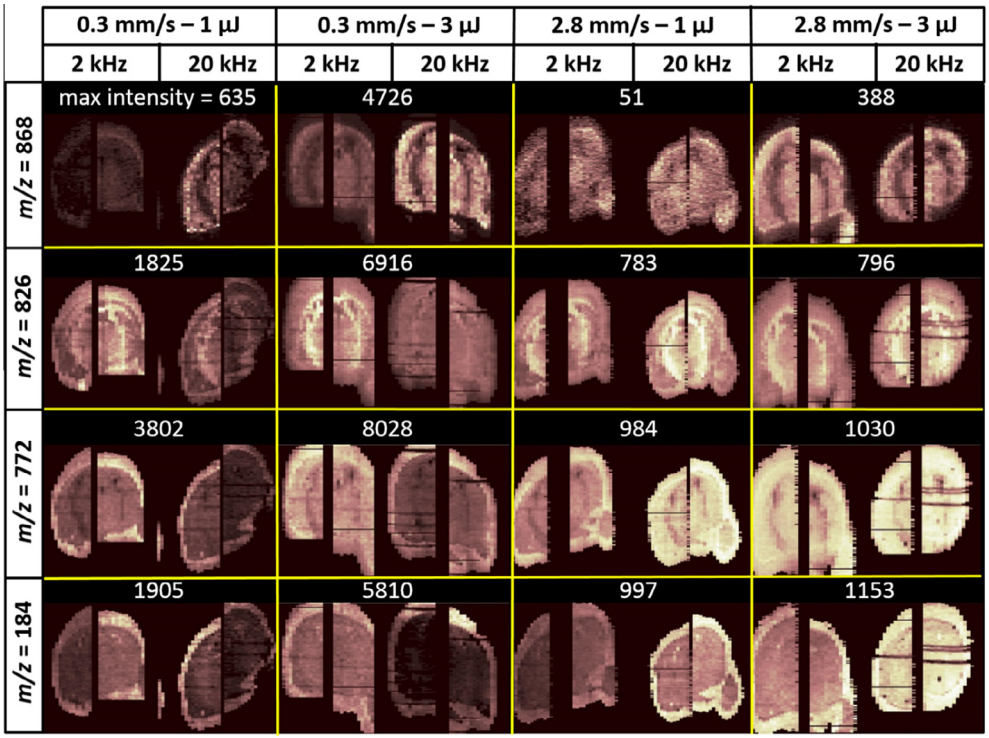

Fig. 5. Selected ion intensity images from murine brain tissue sections for varying laser pulse energy, repetition rate and stage raster speed. Columns of single ion images are shown from the same tissue section. Each pair of single ion images at a given raster speed and energy are on the same intensity scale and the maximum ion intensity of this scale is displayed as a number above the corresponding pair. Intensity scales progress from low to high intensity. The low intensity raster lines (dark rows of pixels) are areas where the laser triggering did not activate during data acquisition.

pulse energy used, with increasing benefit of higher repetition rates evident at higher raster speeds and lower energies. The extent to which these variables enhance the detection of a specific ion depend upon the ion in question and this must be considered in targeted analysis to select variables most appropriate but should also be considered in un-targeted experiments where effects may be more severe for some ions and not uniform over the spectral range. There is also a clear dependence of detected ion intensity on the time period between incident laser pulses where the same or very similar numbers of laser pulses are incident per pixel at different repetition rate and raster speed combinations (Figs. 3A–C and 6B and H).

Although the trends observed from the analysis of the lipid standard and tissue (Figs. 2–6) provide strong evidence that the relationship between fluence, raster speed and repetition rate is highly complex, and serve to direct researchers seeking to optimise their experiments, they do not in themselves reveal the underlying mechanisms causing these phenomena. Changing intensity of different lipid peaks in MALDI MSI of tissue and changing intensity of lipid adduction and alteration of fragmentation levels are evident but do not appear to be the primary cause of the observed trends, though these two phenomena are likely products of the underlying mechanism(s).

Research on the variation of raster speed and laser pulse repetition rate by Spraggins et al. showed a decrease in ion yield when approximately 50 pulses per unit area were exceeded [10]. Whilst this study does, in places, broadly support their conclusions, only in the minority of cases here were less than 50 pulses per unit area employed and in most cases this number was vastly exceeded (Table S1). At all lower fluences, repetition rates of above 5 kHz were often found to be optimum and higher repetition rates as well as higher raster speeds were also often found to be beneficial. This suggests the picture is more complex than a simple pulse per unit area limit above which performance is reduced.

Investigations by Fournier et al. in a single large protein doped sinapinic acid (SA) crystal revealed pulse number and energy related effects on detected ion intensity [24]. Ion yield per pulse was observed to halt after ~30 pulses at energy of 1.5–2 µJ but several 8–9 µJ pulses allowed further subsequent ion acquisition at the lower energy again. Structural changes to the crater surface, as well as decarboxylation of the matrix and the effect of this on the UV absorption were thought to be the cause; it was further mentioned that a similar effect was also observed in CHCA [24]. Aspects of this phenomenon were further investigated by Tarzi et al. who studied the effects of heating on various UV MALDI MS matrices [25]. It was shown that heating of CHCA and SA led to chemical changes in the matrix. Decarboxylation of these matrices was again found to be present though to a much greater extent in CHCA than in SA. It was proposed that the observed thermochemical degradation of SA and CHCA was likely to blame for the phenomenon seen by Fournier et al. [24,26].

Qiao et al. investigated issues relating to the number of laser pulses and fluence for spot mode analysis using Nd:YAG and N_2 lasers [27]. They found that the ion yield of substance P (1347 Da) with CHCA as matrix at a laser pulse fluence of 560 J/m^2 reached its maximum of $\sim 1.4 \times 10^4$ after ~150 laser pulses and the sample was visibly depleted. At 320 J/m^2 the maximum ion yield of $\sim 4 \times 10^4$ was reached after ~300 laser pulses but there was no accompanying visible depletion of the sample. It was suggested that the decay of the ion signal at lower fluences, despite the remaining visible sample, could be due to surface modification/heating/hysteresis effects [24,26,28]. Recently, Wiegelmann et al. observed similar phenomena when studying detected ion intensity at various laser wavelengths for CHCA, 2,5-dihydroxybenzoic acid (DHB) and fluorinated and chlorinated CHCA derivatives (DiFCCA and ClCCA) [29]. The ion intensity per laser pulse for 900 successive pulses showed an initial increase followed by a subsequent decrease, where it was stated that changes

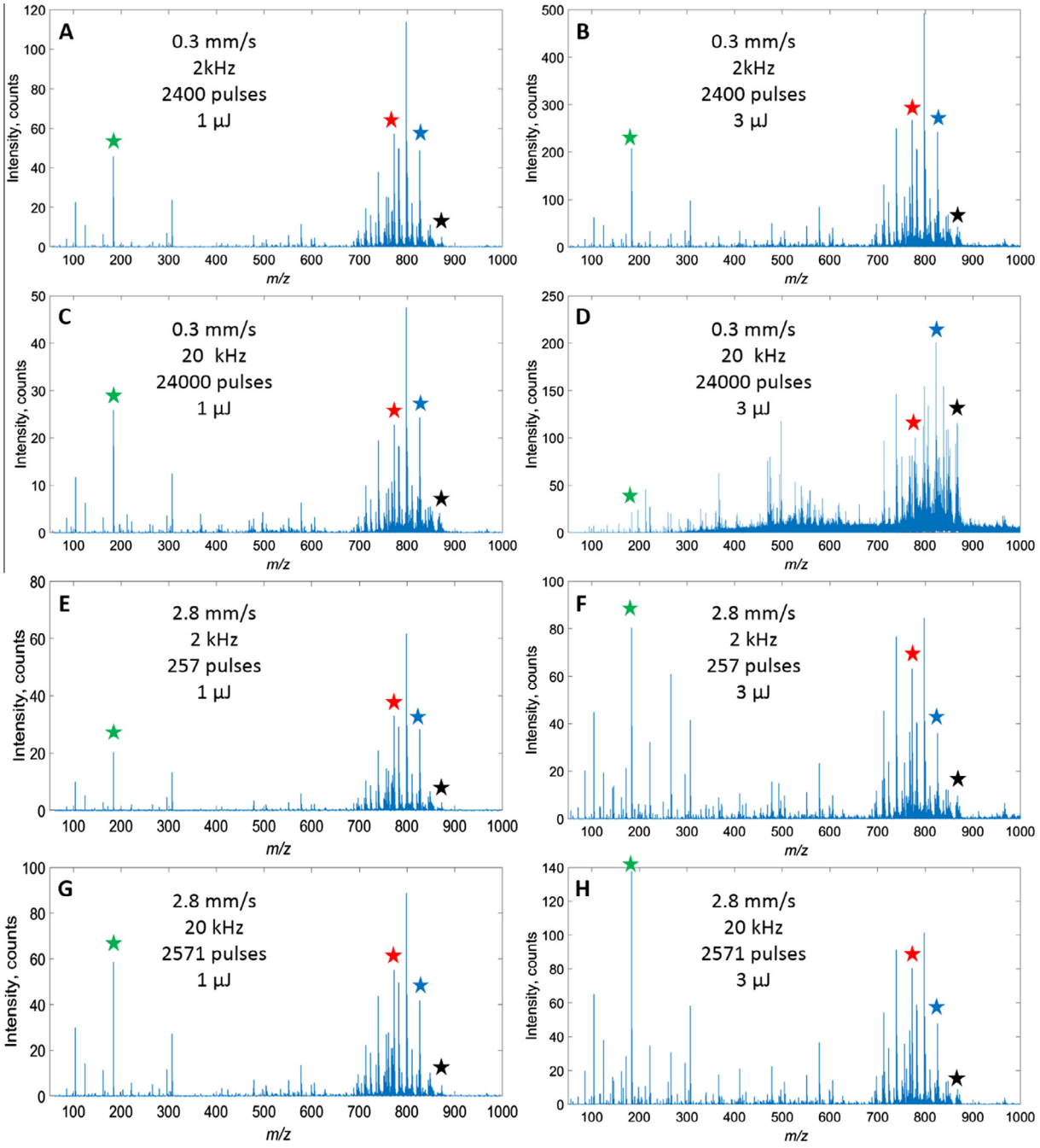

Fig. 6. Mean on-tissue spectra from murine brain tissue acquired with varying laser pulse repetition rate, energy and stage raster speed from data shown in Fig. 5. The green star (left side on each spectrum), red star (left middle), blues star (right middle) and black star (right) in each spectra indicate peaks shown as images in Fig. 5 at *m*/*z* 184.1, 772.5 and 826.6 and 868.5 respectively.

in the optical absorption profile of pre-irradiated matrix layers could be responsible for this overall chronogram shape.

Evidence obtained by the Zenobi group [30], amongst others, shows that matrices such as DHB and nicotinic acid will experience temperatures as high as 1000 K during MALDI MS analyses. Furthermore, matrix dimerization was observed in CHCA crystals for up to several hours after laser irradiation and the dynamics of this formation process was observed to depend upon crystal morphological properties and the laser energy [31]. Additionally, it is known in certain laser ablation scenarios that the threshold fluence of ablation can have a dependence on the laser repetition rate due to accumulation of thermal energy on these timescales [32].

The above mentioned phenomena may help to explain the trends observed within this study. The apparent influence of pulse-to-pulse delay and stage movement imply that phenomena occurring on the plate on timescales of $\sim 10^{-5}$–10^{-2} s or longer, are potential causes of the observed trends. Therefore, the structural modifications observed by Fournier et al., the deposition and subsequent dissipation of thermal energy and dimerization (or even multimerization) could all contribute to these observations. For example, a decreased pulse-to-pulse delay time would potentially result in an increase in local temperature on average, altering the morphology of the sample left behind on the sample plate and causing further decarboxylation of this matrix material

and differing dimerization properties. Consequently the material ablated by subsequent laser pulses would exhibit different mass spectral properties to those acquired under a different repetition rate. As the stage speed dictates the number of laser pulses incident on a particular area this rationale also covers the alteration of raster speed and its effect upon the mass spectra observed within this study.

It is worth noting that due to the variation of photon density across the laser beam profile used in this study, there may be similar low/high energy variation analogous to that used by Fournier et al. and thus varying surface modification and hysteresis effects may well be occurring naturally within this and other MALDI MSI studies for this reason also.

This implies that very different relationships between laser pulse energy, repetition rate and stage raster speed would be observed if similar studies to this were carried out with other matrices and possibly even with different sample preparations of the same matrix where crystal size and morphology differ substantially.

4. Conclusions

A Nd:YVO_4 laser with high repetition rate (up to 20 kHz) was used in conjunction with a hybrid orthogonal MALDI QqToF mass spectrometer to probe the relationship between beam profile, repetition rate, raster speed and fluence within raster mode MSI of lipids.

Analysis of thin-layer CHCA/lipid standard preparations show complex relationships with several underlying trends evident within the data. Similarly complex relationships are also shown to be present in tissue data sets. A fluence dependence of the relationship between repetition rate and raster speed was shown. A repetition rate of 20 kHz was, for the first time within MALDI MSI, employed to acquire tissue image data and observed to provide optimum ion yield under certain scenarios in tissue with continuous raster mode analysis.

This study provides new and detailed information into the interplay of these important variables within MALDI MSI studies. Particularly with regards to the differential detection of certain lipid species, ion adduct variation and fragmentation processes at different repetition rates and the dependence of MS data on the pulse-to-pulse delay time. Though these features are not the sole causes of the observed trends they are instead likely to be symptoms of on-plate, thermally driven, hysteresis-exhibiting processes such as matrix chemical and structural modification as well as sample heating. The extent to which this is the case is not totally clear, however, and further work investigating these phenomena in other matrix–sample systems is required.

The influence of both laser pulse repetition rate and raster speed is shown to be extremely important when optimizing raster imaging experiments for increased detected ion intensity and/or throughput. These considerations are also crucial for the improved understanding and implementation of high-repetition rate lasers, high-throughput and high-ion yield MALDI MSI. Once the operator or experimenter understands the role these variables play in influencing the detected ion intensity of MALDI MS, this knowledge can be implemented in applications such as tissue imaging. In addition, a better understanding of these variables allow one to move their investigations into other important areas of MALDI MS, such as studying the influence of new matrices, with a better overall understanding of the influence of these variables on the data obtained.

Acknowledgements

Thanks to Keith Oakes for useful discussion. Funding was provided by NPL strategic research program 'NiCE MSI' project SR 116301 and Innovate UK (formerly TSB) award 101788.

AD is in receipt of an EPSRC studentship via the PSIBS doctoral training centre (EP/F50053X/1), in collaboration with AstraZeneca and the National Physical Laboratory.

Appendix A. Supplementary data

Supplementary data associated with this article can be found, in the online version, at http://dx.doi.org/10.1016/j.ymeth.2016.04.010.

References

[1] N. Zaima, T. Sasaki, H. Tanaka, X.W. Cheng, K. Onoue, T. Hayasaka, et al., Imaging mass spectrometry-based histopathologic examination of atherosclerotic lesions, Atherosclerosis 217 (2011) 427–432.
[2] G.A. Amadei, C.F. Cho, J.D. Lewis, L.G. Luyt, A fast, reproducible and low cost method for sequence deconvolution of 'on bead' peptides via 'on target' maldi TOF/TOF mass spectrometry, J. Mass Spectrom. 45 (2010) 241–251.
[3] J.J. Corr, P. Kovarik, B.B. Schneider, J. Hendrikse, A. Loboda, T.R. Covey, Design considerations for high speed quantitative mass spectrometry with MALDI ionization, J. Am. Soc. Mass Spectrom. 17 (2006) 1129–1141.
[4] S.N. Jackson, B. Colsch, T. Egan, E.K. Lewis, J.A. Schultz, A.S. Woods, Gangliosides' analysis by MALDI-ion mobility MS, Analyst 136 (2010) 463–466.
[5] S. Sundarapandian, J.C. May, J.A. McLean, Dual source ion mobility-mass spectrometer for direct comparison of electrospray ionization and MALDI collision cross section measurements, Anal. Chem. 82 (2010) 3247–3254.
[6] M.R. Clench, P.J. Trim, M.C. Djidja, S.J. Atkinson, K. Oakes, L.M. Cole, et al., Introduction of a 20 kHz Nd:YVO_4 laser into a hybrid quadrupole time-of-flight mass spectrometer for MALDI-MS imaging, Anal. Bioanal. Chem. 397 (2010) 3409–3419.
[7] E. Moskovets, J. Preisler, H.S. Chen, T. Rejtar, V. Andreev, B.L. Karger, High-throughput axial MALDI-TOF MS using a 2-kHz repetition rate laser, Anal. Chem. 78 (2006) 912–919.
[8] J.A. McLean, W.K. Russell, D.H. Russell, A high repetition rate (1 kHz) microcrystal laser for high throughput atmospheric pressure MALDI-quadrupole-time-of-flight mass spectrometry, Anal. Chem. 75 (2003) 648–654.
[9] N. Ogrinc Potočnik, T. Porta, M. Becker, R. Heeren, S.R. Ellis, Use of advantageous, volatile matrices enabled by next-generation high-speed matrix-assisted laser desorption/ionization time-of-flight imaging employing a scanning laser beam, Rapid Commun. Mass Spectrom. 29 (2015) 2195–2203.
[10] R. Caprioli, J.M. Spraggins, High-Speed MALDI-TOF imaging mass spectrometry: rapid ion image acquisition and considerations for next generation instrumentation, J. Am. Soc. Mass Spectrom. 22 (2011) 1022–1031.
[11] B.M. Prentice, C.W. Chumbley, R.M. Caprioli, High-speed MALDI MS/MS imaging mass spectrometry using continuous raster sampling, J. Mass Spectrom. 50 (2015) 703–710.
[12] T. Porta, A. Lesur, E. Varesio, G. Hopfgartner, Quantification in MALDI-MS imaging: what can we learn from MALDI-selected reaction monitoring and what can we expect for imaging?, Anal Bioanal. Chem. 407 (2015) 2177–2187.
[13] C. Hollands, The animals (scientific procedures) act 1986, The Lancet 328 (1986) 32–33.
[14] R.T. Steven, A.D. Palmer, J. Bunch, Fluorometric beam profiling of UV MALDI lasers, J. Am. Soc. Mass Spectrom. 24 (2013) 1146–1152.
[15] A.M. Race, I.B. Styles, J. Bunch, Inclusive sharing of mass spectrometry imaging data requires a converter for all, J. Proteomics 75 (2012) 5111–5112.
[16] A.M. Race, J. Bunch, Optimisation of colour schemes to accurately display mass spectrometry imaging data based on human colour perception, Anal. Bioanal. Chem. 407 (2015) 2047–2054.
[17] K. Dreisewerd, The desorption process in MALDI, Chem. Rev. 103 (2003) 395–425.
[18] J. Soltwisch, T.W. Jaskolla, F. Hillenkamp, M. Karas, K. Dreisewerd, Ion yields in UV-MALDI mass spectrometry as a function of excitation laser wavelength and optical and physico-chemical properties of classical and halogen-substituted MALDI matrixes, Anal. Chem. 84 (2012) 6567–6576.
[19] R.T. Steven, J. Bunch, Repeat MALDI MS imaging of a single tissue section using multiple matrices and tissue washes, Anal. Bioanal. Chem. 405 (2013) 4719–4728.
[20] I.V. Chernushevich, A.V. Loboda, B.A. Thomson, An introduction to quadrupole–time-of-flight mass spectrometry, J. Mass Spectrom. 36 (2001) 849–865.
[21] R.T. Steven, A.M. Race, J. Bunch, Para-nitroaniline is a promising matrix for MALDI-MS imaging on intermediate pressure MS systems, J. Am. Soc. Mass Spectrom. 24 (2013) 801–804.
[22] H.Y.J. Wang, C.B. Liu, H.W. Wu, J.S. Kuo, Direct profiling of phospholipids and lysophospholipids in rat brain sections after ischemic stroke, Rapid Commun. Mass Spectrom. 24 (2010) 2057–2064.
[23] K. Shrivas, T. Hayasaka, N. Goto-Inoue, Y. Sugiura, N. Zaima, M. Setou, Ionic matrix for enhanced MALDI imaging mass spectrometry for identification of phospholipids in mouse liver and cerebellum tissue sections, Anal. Chem. 82 (2010) 8800–8806.

[24] I. Fournier, J.C. Tabet, G. Bolbach, Irradiation effects in MALDI and surface modifications. Part I. Sinapinic acid monocrystals, Int. J. Mass Spectrom. 219 (2002) 515–523.
[25] O.I. Tarzi, H. Nonami, R. Erra-Balsells, The effect of temperature on the stability of compounds used as UV-MALDI-MS matrix: 2,5-dihydroxybenzoic acid, 2,4,6-trihydroxyacetophenone, α-cyano-4-hydroxycinnamic acid, 3,5-dimethoxy-4-hydroxycinnamic acid, nor-harmane and harmane, J. Mass Spectrom. 44 (2009) 260–277.
[26] I. Fournier, R. Beavis, J. Blais, J. Tabet, G. Bolbach, Hysteresis effects observed in MALDI using oriented, protein-doped matrix crystals, Int. J. Mass Spectrom. Ion Process. 169 (1997) 19–29.
[27] H. Qiao, V. Spicer, W. Ens, The effect of laser profile, fluence, and spot size on sensitivity in orthogonal-injection matrix-assisted laser desorption/ionization time-of-flight mass spectrometry, Rapid Commun. Mass Spectrom. 22 (2008) 2779–2790.
[28] I. Fournier, C. Marinach, J.C. Tabet, G. Bolbach, Irradiation effects in MALDI, ablation, ion production, and surface modifications. Part II. 2,5-dihydroxybenzoic acid monocrystals, J. Am. Soc. Mass Spectrom. 14 (2003) 893–899.
[29] M. Wiegelmann, J. Soltwisch, T.W. Jaskolla, K. Dreisewerd, Matching the laser wavelength to the absorption properties of matrices increases the ion yield in UV-MALDI mass spectrometry, Anal. Bioanal. Chem. 405 (2013) 6925–6932.
[30] A. Koubenakis, V. Frankevich, J. Zhang, R. Zenobi, Time-resolved surface temperature measurement of MALDI matrices under pulsed UV laser irradiation, J. Phys. Chem. A 108 (2004) 2405–2410.
[31] T. Hoyer, W. Tuszynski, C. Lienau, Ultrafast photodimerization dynamics in α-cyano-4-hydroxycinnamic and sinapinic acid crystals, Chem. Phys. Lett. 443 (2007) 107–112.
[32] F. Brygo, A. Semerok, R. Oltra, J.-M. Weulersse, S. Fomichev, Laser heating and ablation at high repetition rate in thermal confinement regime, Appl. Surf. Sci. 252 (2006) 8314–8318.

Methods 104 (2016) 111–117

Contents lists available at ScienceDirect

Methods

journal homepage: www.elsevier.com/locate/ymeth

Investigating MALDI MSI parameters (Part 2) – On the use of a mechanically shuttered trigger system for improved laser energy stability

Rory T. Steven [a], Alex Dexter [a,b], Josephine Bunch [a,c,*]

[a] National Centre of Excellence in Mass Spectrometry Imaging (NiCE-MSI), National Physical Laboratory (NPL), Teddington TW11 0LW, UK
[b] University of Birmingham, School of Chemistry, B15 2TT, UK
[c] School of Pharmacy, University of Nottingham, NG7 2RD, UK

ARTICLE INFO

Article history:
Received 30 November 2015
Received in revised form 1 March 2016
Accepted 13 April 2016
Available online 16 April 2016

Keywords:
MALDI MSI
Laser
Shutter
Mass spectrometry imaging
Lipid imaging
Multivariate analysis

ABSTRACT

Matrix-assisted laser desorption/ionization (MALDI) mass spectrometry imaging (MSI) is now widely used to desorb, ionize and detect molecules from complex samples and tissue sections. The detected ion intensity within MALDI MS and MSI is intimately linked to the laser energy per pulse incident upon the sample during analysis. Laser energy/power stability can be significantly affected by the manner in which the laser is operated. High-repetition rate diode-pumped solid-state (DPSS) lasers are being increasingly adopted to enable high-throughput MALDI MSI analysis. Within this work two different laser-triggering setups are used to demonstrate the effect of laser energy instabilities due to spiking and thermal control phenomena and a setup with a shutter to remove these effects. The effect of non-equilibrium laser operation on MALDI MSI data versus the more stable laser pulse energy of the shutter-triggered system is demonstrated in thin films of α-cyano-4-hydroxycinnamic acid (CHCA) and for imaging of murine brain tissue sections. Significant unwanted variations in absolute and relative detected ion intensity are shown where energy variation is introduced by these phenomena, which return to equilibrium within the setup employed here over timescales relevant to MALDI MS analysis.

1. Introduction

The intensity of detected ions within matrix-assisted laser desorption/ionization (MALDI) mass spectrometry (MS) is intimately linked to the incident number of laser photons per unit area on the sample. This relationship is typically described by the power law relationship $I \propto H^m$ where I is the detected ion intensity, H is the laser fluence and m is the fitting parameter [1]. Consequently, fluctuations in incident laser energy may have a large effect on the detected ion intensity, potentially giving a false value for the sample being analysed or introducing a larger variation in the detected number of ions than may be desired. The energy output of a laser can vary for a number of reasons including: long term depletion due to damage of optical components, short time scale high-energy pulses due to spiking and wandering behaviors due to thermal control and equilibration of the laser and/or the room in which the laser is housed. Potentially significant causes of energy variation within MALDI MS experimentation, where the laser needs to be repeatedly triggered for relatively short time periods (*i.e.* for the ablation of material from a pixel or row of pixels), are spiking and the thermal equilibration of the lasing components during those intermittent periods of triggering. Spiking is caused when resonator losses are suddenly reduced after some time of extended pumping of the gain medium, such as Q-switching, causing a series of high-energy pulses to be emitted prior to the lasing process reaching a steady-state and energy-per-pulse stabilisation. Spiking is commonly observed within laser systems in which the upper state lifetime is much larger than the cavity damping time, *i.e.* if the time period between triggered laser pulses is shorter than the upper state lifetime of the gain medium, as is common in some high-repetition rate DPSS lasers used in MALDI mass spectrometry imaging (MSI). One way to ensure steady state, equilibrium-operation of a laser within a system such as a MALDI mass spectrometer is to continuously trigger the laser at the desired repetition rate to ensure steady-state operation. Then, during analysis, turn the laser 'on' and 'off' by opening and closing a mechanical shutter placed in the path of the beam.

* Corresponding author at: National Centre of Excellence in Mass Spectrometry Imaging (NiCE-MSI), National Physical Laboratory (NPL), Teddington TW11 0LW, UK; School of Pharmacy, University of Nottingham, NG7 2RD, UK.
E-mail address: josephine.bunch@npl.co.uk (J. Bunch).

http://dx.doi.org/10.1016/j.ymeth.2016.04.013
1046-2023/

Laser-based systems in fields other than MALDI MS have utilised shutter systems to minimise laser energy variability due to spiking and other non-equilibrium energy variations as well as to allow greater control over pulse timing. Shutters have been used in femtosecond laser desorption and ionisation setups to better control the timing of laser pulses arriving at the sample [2,3]. A shutter systems was used by Bradshaw et al. within their combined laser desorption ionisation (LDI) and atomic force microscopy (AFM) system to enable laser control for desired pulse timing [4]. In laser ablation inductively coupled plasma (LA-ICP) MS it is considered good practice to include a shutter system to remove pulse-to-pulse variability, as well as inclusion of an energy meter to monitor the delivery as it occurs [5].

Shutter systems have been used explicitly on a few occasions within the field of MALDI MS and MSI. Zavalin et al. allowed single laser shots to be transmitted to their sample for analysis at a rate of 100 Hz for transmission mode MALDI MSI [6]. Westmacott et al. made use of a mechanical shutter system to improve pulse-to-pulse stability of their laser in fundamentals studies of the influence of laser fluence in MALDI MS [7]. No data, however, in either of these examples, was presented on the effect of these shutter systems on the MALDI MS data obtained.

The intimate link between detected ion intensity and laser energy coupled with the clear need in all analytical techniques to reduce instrument induced variance within the data demonstrates the need to inform researchers of the effects of laser instability and its mitigation by the use of shutters. Particularly within a field where modification of existing and building of new ion sources and their accompanying laser optics is relatively common.

Within this study we demonstrate the presence of energy spiking phenomena in a MALDI MS relevant triggering setup. The mitigation of this effect under the same analytical conditions is then demonstrated. Data is acquired under both of these setups using thin films of α-cyano-4-hydroxycinnamic acid (CHCA) and CHCA-coated murine brain tissue samples by MALDI MSI. Multivariate analyses are also implemented to further probe the spectral differences resulting from MALDI MSI analyses under these two triggering regimes.

2. Methods

2.1. Materials

Methanol (HPLC grade) was purchased from Fisher Scientific (Leicestershire, UK). Water was purified by an ELGA Purelab Option system (Marlow, UK). Trifluoroacetic acid (TFA; 99.9% purity) and CHCA were purchased from Sigma Aldrich (Dorset, UK). MALDI MS stainless steel imaging plates from Sciex (Ontario, Canada) were used for all samples.

2.2. Tissue preparation and sectioning

Mice were sacrificed humanly at the School of Cancer Sciences, University of Birmingham in accordance with the Home Office Animals (Scientific Procedures) Act 1986 [8]. Mouse brain was flash frozen in liquid nitrogen immediately after excision. Two serial sections (10 μm thick) were collected and thaw mounted onto a single MALDI imaging plate. Sectioning was performed on a CM 1850 Cryo-microtome (Leica, Milton Keynes, UK).

2.3. Matrix application

For the thin-film and tissue experiments, a CHCA solution (5 mg/mL in 80% CH_3OH, 0.1% TFA) was deposited onto the MALDI imaging plate by a TM Sprayer (HTX Technologies, Carrboro, NC) at a nebuliser temperature of 90 °C, a solvent flow rate of 0.115 mL/min, a gas pressure of 10 psi, and a nebuliser speed of 1333 mm/min. Eight sequential passes across the whole plate were used, each with a track spacing of 3 mm, an offset of 1.5 mm was applied on every other pass with alternating horizontal and vertical path direction. This gave a density of matrix on the plate of 0.115 mg/cm^2.

2.4. Mass spectrometry

MALDI-TOF MS analysis was carried out on a QSTAR XL QqTOF instrument using Analyst QS 1.1 with oMALDI server 5.1 (Sciex). A Nd:YAG (FQS-100-1-Y-355; Elforlight, Daventry, UK) DPSS laser with a wavelength of 355 nm, a repetition rate of ⩽10 kHz and a pulse length of <4 ns was used in this study. In all cases the laser was triggered directly by a function generator (TTi – TG2000 20 MHz DDS). For the shutter-triggered data acquisition the QSTAR oMALDI software-controlled trigger signal was coupled to a shutter (2.5 cm diaphragm shutter, 10 ms full aperture opening time; Thorlabs Ltd, Ely, UK), which was placed in the path of the laser beam prior to the fibre coupling (see Fig. 1 for schematic of the optics setup used within this study). Therefore, the laser remained on continuously whilst the shutter, as triggered by the QSTAR software, allowed or prevented the laser ablation on the sample itself. For the non-shutter-controlled sample analysis, the shutter was set continuously to open and the function generator was triggered directly from the QSTAR instead. All MALDI MSI analyses were carried out in continuous raster mode. Consequently, the laser triggering was initiated (by either method) at the beginning of each raster line and the laser fired continuously until the end of the raster line when the triggering ceased. Therefore, the shutter was opened (or the pulse generator began its trigger pulse train) at the start of each raster line and was closed (the trigger pulse train was stopped) at the end of each raster line.

The laser was coupled to the MALDI source via a 100 μm core diameter fibre optic patchcord of 4 m (Fiberguide Industries via AMS Technologies, Leicestershire, UK; NA = 0.22). The raster speed used was dictated by the preset speed values available within the oMALDI (Sciex) software and the speed corresponding to 0.3 mm/s (named slower in the oMALDI software) was used within this study. An m/z range of 50–1000 was used for all experiments. All data were acquired in positive ion mode.

For the CHCA thin-film analysis the Nd:YAG laser was operated at 3.3 kHz at a raster speed of 0.3 mm/s. Laser energies used are displayed within the main body of this article. MS data from four raster lines of 126 pixels (each 100 μm wide) in length were acquired for each variable combination in continuous stage raster imaging mode.

Tissue MSI data were acquired at a stage speed of 0.3 mm/s and a laser pulse repetition rate of 4 kHz. The same half of each coronal section was analysed. These images were acquired with pixel sizes of 100 × 100 μm and took approximately 20 min to acquire per image.

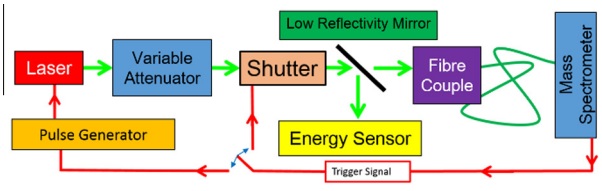

Fig. 1. Schematic of optics setup used within these studies.

2.5. Laser beam profiling and energy measurement

The irradiated area on the sample as measured by the fluorometric method utilising the fluorescence from CHCA at low (non-ablating) energies [9] was 2.05×10^{-8} m^2. The laser energy per pulse was measured using a pyro-electric sensor (PD10-C, Ophir Photonics) both post fibre and from the beam sampler prior to the experiment, and later from the beam sampler during the experiment allowing the energy incident to be calculated from the earlier calibration. A Watt Pilot (Altechna, Lithuania) computer-controlled half-wave plate and Brewster-angle filter attenuation setup was used to attenuate the beam. A schematic of the laser delivery setup is shown in Fig. 1.

2.6. Processing of MALDI MSI data

The data was converted from AB Sciex proprietary file format (.wiff) to .mzML using AB MS Data Converter (version 1.3; Sciex) and then converted to imzML using imzMLConverter [10]. Further processing was carried out on in-house software running from MatLab (version R2014b; Math Works Inc, USA). The mean ion counts (peak areas) for selected mass-to-charge values were calculated along with the standard deviation and are plotted as mean value ± standard variation. The image colour scheme was chosen to align with mass spectrometric best practice guidelines [11]. Multivariate analyses (MVA) were carried out with the following pre-processing: zero filling, 3× sequential Savitzky-Golay smoothing, window size 7, polynomial order 2, negatives removed, TIC-normalized where stated, gradient peak picked with top 2000 peaks retained for multivariate analyses. PCA was carried out according to the memory efficient method [12] and non-negative matrix factorisation (NMF) by using the MATLAB function nnmf with k = 5.

3. Results and discussion

3.1. On laser stability in MALDI MS and MSI

Triggering of the laser within the setup employed for these studies (and other studies with similarly triggered MALDI laser systems involves the active release of the 1062-nm photons from the diode-pumped lasing medium. These photons go on to pass through the frequency doubling and tripling portions of the laser prior to exiting the laser. During MALDI MS analysis the lasing media and associated optics, if repeatedly triggered at the same frequency, will operate at an equilibrium state where the emitted 355-nm photons exhibit optimal energy/power stability. However, within MALDI MS and MSI experiments the laser triggering will typically only occur in this fashion for a short time during the analysis of each pixel or row of pixels. Outside of this time the primary lasing medium will still typically be pumped and lasing but the downstream optics may not be active. There are a number of issues related to this repeated pausing of triggering: the thermal stability of the downstream optical elements of the laser are only ever approaching an equilibrium state and spiking may occur at the beginning of each pixel or raster line whereby a number of higher energy pulses are emitted until a steady-state is reached. Spiking results from the sudden reduction in resonator loss (triggered Q-switching of the laser for example) after a suitably long time where the gain medium was pumped. This may happen particularly if the trigger frequency (repetition rate) provides only a short pump time between switching in comparison to the upper-state lifetime of the lasing media. Thus, the stored energy prior to triggering may be large compared to that emitted during continuous triggering (normal continuous operation).

The continuous variation between constant triggering and no triggering within MALDI MS experiments can, therefore, lend itself to the consistent presence of these potentially deleterious phenomena, the result of which may be seen with the detected mass spectra themselves due to the well-known relationship between laser energy/fluence and detected ion intensity within MALDI MS [13].

3.2. Investigation into the use of a mechanical shutter in MALDI MSI of a thin matrix film

In order to investigate the effect of continuous laser operation with shutter triggering versus the direct triggering of the laser, the optics setup coupling the laser to the QSTAR instrument was modified slightly to enable manual switching between these modes (Fig. 1).

In initial investigations into the effect on MALDI MS-derived spectra, experiments were carried out in thin films of CHCA matrix. Continuous raster mode MSI data was acquired at a fixed attenuation whilst simultaneously recording the laser energy from the laser beam-sampling mirror to provide on-line energy measurement. Data from these analyses are presented within Fig. 2.

The energy measurements from the non-shutter-triggered and shutter-triggered experiments show the considerable increase in initial energy due to some combination of spiking and thermal equilibration type phenomenon within the non-shutter-triggered data (Fig. 2A and B). The values shown have been calibrated to show the value incident upon the sample itself within the ion source. The energy for the non-shutter-triggered data only relaxes to the equilibrium level of the laser, at the repetition rate used, by the end of the raster line. The total ion count (TIC) detected per pixel for the concomitantly acquired MALDI MSI data from the thin-layer CHCA sample is displayed as an average ± standard deviation from the four horizontal raster lines acquired (Fig. 2C and D). It is clear that the TIC correlates with the increased energy per pulse emitted due to the spiking/thermal phenomena caused by the direct triggering of the laser at the beginning of each raster line (Fig. 2C), whereas the continuously operated shutter-triggered laser shows a much more stable TIC across the four raster lines (Fig. 2D), giving a value equal to that reached at the end of the line in Fig. 2C throughout the acquisition. Despite the effect of these energy instabilities clearly showing within the TIC data, the effect on the MS data is more complex than a global intensity increase across all peaks within the mass spectra, as may be assumed. Principal component analysis (PCA) was carried out on the un-normalized and TIC-normalized data to give further insight into the spectral effects of the energy differences afforded by these two triggering setups (Fig. 2E and F). The un-normalized PCA score plot and loading spectrum for principal component (PC) 1 shows what appears to be mostly global intensity changes due to the varying incident energy causing the desorption and ablation from the sample; whereby the top half of the image (where the shutter was employed) correlates with only very minor variation in small scale peaks and the lower half of the image (without shutter and so with considerable energy variation across the image) shows correlation with a substantial change in the detection of many peaks across the mass spectrum. If linear intensity changes across all peaks in the mass spectrum were the only result of the energy variation resulting from these two trigger setups then TIC-normalizing prior to carrying out PCA should show the shuttered and non-shuttered pixels to have much more similar scores within the subsequent PCA score plot. These data are shown in Fig. 2F and it is evident within the TIC-normalized PC 1 score plot and loadings spectrum that the shuttered and non-shuttered data are still showing substantial differences. Therefore, within these analyses, rather than what look like global intensity differences, there

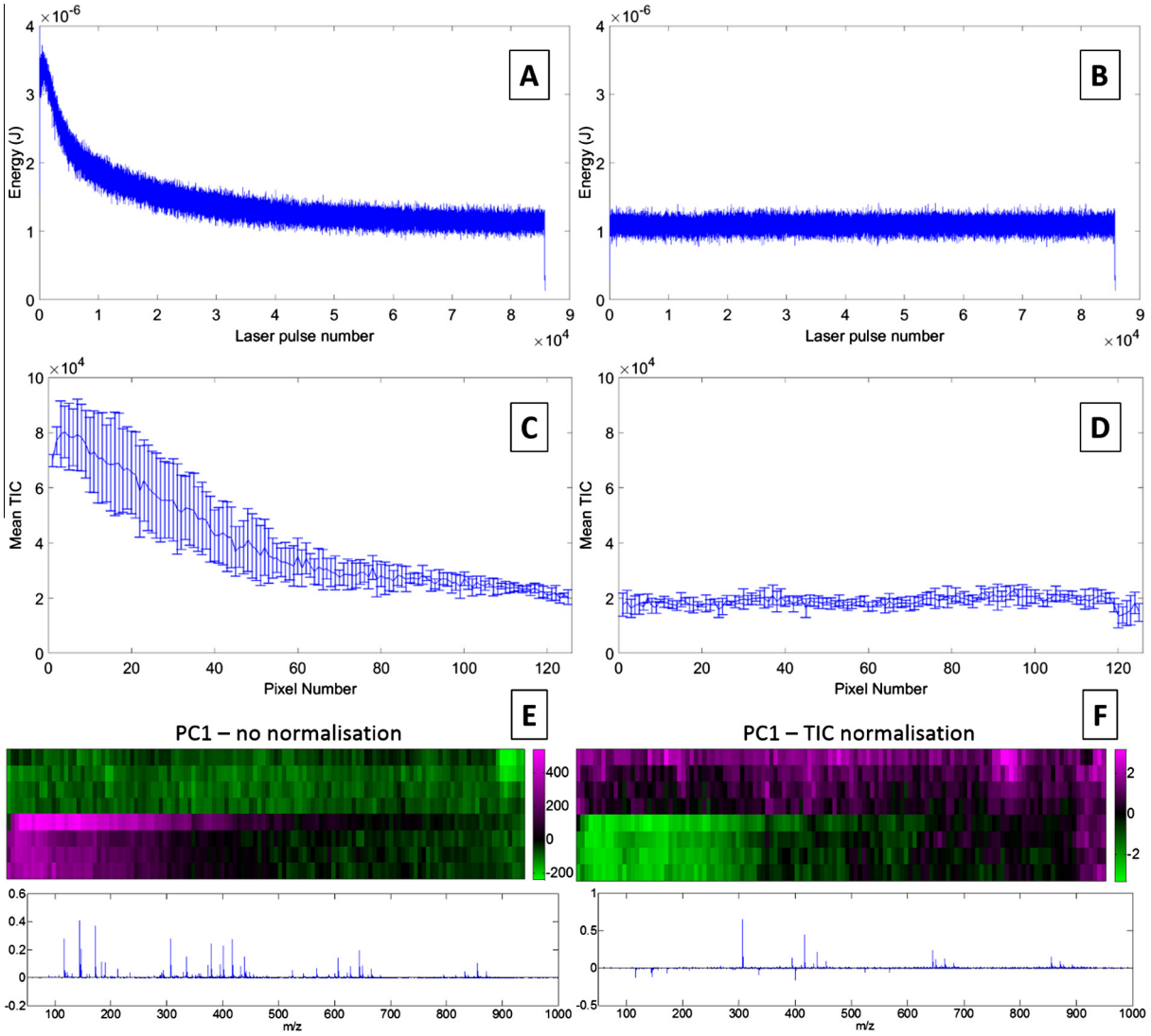

Fig. 2. MALDI MSI data acquired from a thin film of CHCA under two different trigger regimes. Raw single-pulse on-line energy and mean total ion count (TIC) data for non-shutter- (A, C) and shutter- (B, D) triggered data, respectively. Data derived from principle component analysis of these images is shown for raw (E) and TIC-normalized (F) data. The top half of the data within the images in E and F were acquired with the shutter and the bottom half without. Significant variation in energy-per-pulse, total-ion-intensity and spectral complexity are evident depending upon the laser-triggering method used with the shutter method providing improved stability.

is more complex chemical variation between the two data sets corresponding to a reduced correlation to commonly observed high-mass matrix cluster peaks in the non-shutter-triggered data. The correlation of changing detected TIC and shifting spectral nature with the reduced energy stability, resulting from the non-shutter-based laser-triggering method, clearly demonstrate the potential issues which can arise from poor laser stability due to this type of triggering method.

3.3. Investigation into the use of a mechanical shutter in MALDI MSI of murine brain tissue

To further study these phenomena and their influence within MALDI MSI the same shutter-triggered and non-shutter-triggered systems were employed to acquire data from the right hemisphere of each of two coronal serial sections of murine brain tissue coated with CHCA. Images and other analyses from these image datasets are shown in Fig. 3.

The laser energy per pulse within these tissue MSI experiments followed the same shape and magnitude of trend as displayed in Fig. 2A and B and so is not included here but displayed in the Supplementary Information (SI) Figs. S1 and S2. Tissue images acquired using the shuttered trigger setup or with the non-shuttered, directly triggered setup are displayed for the TIC (Fig. 3A and B), PC 34:1 ($[M+K]^+$, tentatively assigned from the literature [14–17]) at m/z 798.5 (Fig. 3C and D) and PC lipid head-group fragment ($[C_5H_{14}NO_4P+H]^+$, tentatively assigned from the literature [18,19]) at m/z 184.1 (Fig. 3E and F). The lipid ion PC 34:1 ($[M+K]^+$) at m/z 798.5 was chosen for display here due to its relatively homogenous detection within MALDI MSI of murine tissue [16], meaning it will better exemplify changes in the detected ion intensity within this tissue imaging context. The PC lipid head-group fragment at m/z 184.1 is chosen for display here as fragmentation of detected species within MALDI MS is intimately linked to the incident laser energy [20]. Consequently, the image of this fragment, a fragment from a commonly observed abundant class of lipids, is highly relevant to the study of varying laser energy in MALDI MSI. In the four single ion images (Fig. 3C–F) there is a clearly visible halo around the tissue section itself resulting from an overly 'wet' matrix deposition, a common

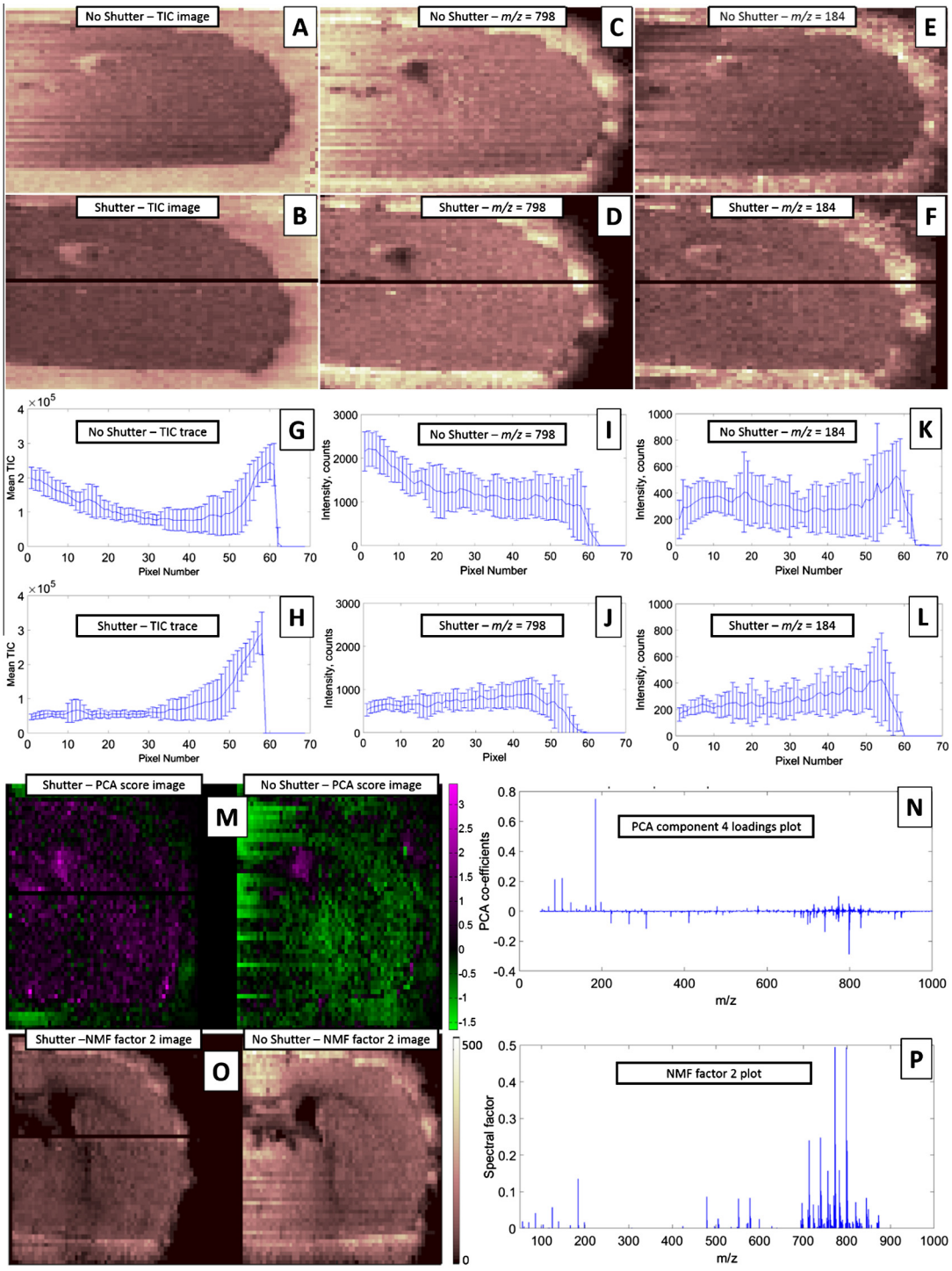

Fig. 3. Effect of shutter-triggering in tissue MALDI MSI. Images of TIC, PC 34:1 ($[M+K]^+$) at m/z 798.5 and PC lipid head-group fragment at m/z 184.1 for both shutter-triggered and non-shutter-triggered data sets are shown in A through F, respectively. Corresponding traces for these images showing mean values ± standard deviation from each column of pixels in the image are shown in G through L. PCA and NMF plots are shown in M, N, O and P to help summarize aspects of the spectral changes caused by the different trigger setups. Images A–F are images taken from regions that are ~6 mm wide and ~5.3 mm high and images M and O are based on PAC and NMF data for these same images, slightly resized for display purposes.

feature of solvent-based matrix deposition within MALDI MSI. Whilst this creates an obvious undesirable feature within these images it is not problematic for this type of study and can even be taken advantage of when forming conclusions regarding the changing stability of the laser due to the differing ablation threshold of on-tissue vs. on-plate desorption/ablation behaviors. In all three of these image pairs, the effect of the more stable laser energy resulting from the shutter-triggering (Fig. 3B, D and F) and the (initially high) decreasing laser energy resulting from the direct non-shutter triggering (Fig. 3A, C and E), are clear in the more consistent ion intensities across the tissue section seen in Fig. 3B, D and F. In line with the elevated energy at the beginning of each raster line, more intense regions are clear to the left of the TIC and m/z 798.6 images. Interestingly, there is a reduction in the

intensity of m/z 184.1 resulting from these higher energies which may appear counter intuitive to the idea that increased internal energy results from increased laser energy. However, this appears to be due to these high energies (and so fluences – 293 J/m^2 at the most intense) causing the PC lipid species to fragment into smaller structures than m/z 184.1. For example, the tissue images of a smaller component of the PC headgroup detected at m/z 56 show an increase to the left hand side of the image in accordance with the increased energies of the non-shutter data (SI Figs. S3 and S4). The increase or decrease of various ion intensities across each raster line in the non-shutter data (from left to right), in response to the decreasing energy per pulse, all show greatest similarity in on-tissue ion intensities to the shutter-triggered image in the rightmost tissue region. This is also the region in which the laser energy finally decreases back to the level set by the attenuator for the equilibrium operation demonstrated in the shutter-triggered data set (SI Figs. S1 and S2). These changes are further demonstrated in the graphs within Fig. 3G through L in which the intensities in each column of the corresponding tissue images are plotted as mean value ± standard deviation. Again, the influence of the varying energy is clear in the increased mean ion intensity for the TIC and m/z 798.6 and the decrease in m/z 184.1 to the left of their corresponding non-shutter-triggered traces (Fig. 3G, I and K). It also appears that there is less variation in the ion intensity detected within the shutter-triggered data (as demonstrated by the smaller error bars) as compared to the corresponding non-shuttered-triggered data.

As with the thin-film CHCA investigation MVA were carried out on this tissue imaging data. Both shutter and non-shutter images were combined into a single image prior to MVA. Again PCA was performed and an example score image and loadings plot is shown in Fig. 3M and N, respectively. Here PC 4 shows the shutter-triggered, on-tissue, portion of the image grouping together in a clear and relatively homogenous manner and the off-tissue halo portion of this image correlates with the majority of the non-shutter-triggered image, with only some tissue features correlating with those of the shutter image. The corresponding loadings plot clearly shows that these differences are not only due to the intensity differences shown within the single ion analyses (Fig. 3A–L) but result from a more complex change in detected ion intensity across the whole mass spectrum, both within the matrix and lipid fragment-dominated regions of low m/z and the mostly intact lipid ions above approximately m/z 700. This further demonstrates that varying detected ion intensities, resulting from the non-shutter-triggered laser energy decrease across each raster line, are not accounted for by a typical univariate normalization such as TIC normalization, as the changes in chemistry caused by this energy change are complex and variable. In addition to the PCA, non-negative matrix factorization was also applied to these image data. NMF is often applied within MSI to provide data reduction and chemical interpretation of variance contributions in a way that is similar to PCA but avoids the negative loadings and factors in a way that potentially makes the data easier to interpret [21]. Here the score image and loadings plot of the second NMF factor are shown (Fig. 3O and P, respectively). The differential weightings of the detected ions within the factor 2 loadings plot (Fig. 3P) may, at first, look like a fairly typical MALDI MSI spectrum from murine brain, which would lead one to conclude that this factor was describing only global intensity differences. However, when compared to a mean on-tissue mass spectrum (SI Fig. S5), considerable differences are evident in the relative intensities of different ions across the m/z range. Also, clear within these mean spectra is the increased intensity of the majority of peaks within the non-shutter spectrum. This is due to the high energy of the laser at the beginning of each raster line increasing the detected ion intensity within these regions as shown in Fig. 3A–F. This is also the case for other NMF factors resulting from this analysis (SI Fig. S6). The corresponding NMF factor 2 image (Fig. 3O) shows the correlation with the m/z loadings shown in Fig. 3 P as being relatively even across the tissue spectrum, for the shuttered data, as compared to the intense correlation with these factors to the left of the non-shuttered NMF image, which fades to an intensity similar to that of the shutter-triggered data to the right hand side of the tissue. This is similar to the intensity variations seen in the single ion images, where the detected intensity in the non-shutter-triggered data reduces to the level of the shutter-triggered data to the right hand side of the image, in line with the reducing energy per pulse (SI Figs. S1 and S2) as the laser equilibrates over the course of each raster line acquisition. These NMF factor loadings and image plots further demonstrate the complexity of the spectral variations across the non-shuttered image due to this changing energy per pulse.

The relationship between detected ion intensity and laser energy or fluence has been studied a number of times by different groups [1,7,13,22–24]. Within a given fluence range the ion signal intensity, I, is observed to increase according to the power law relationship $I \propto H^m$ where H is the fluence and m is the fitting parameter. Beyond this exponential like increase there will be a plateau in the detected ion intensity and a further increase in fluence will not lead to a further increase in detected ions and may even lead to a decrease. This relationship clearly explains the increase in ion intensity observed in correlation with the increased energy per pulse within the non-shutter-triggered data sets within this study and reaffirms the need for stable laser energy within MALDI MS and MSI experiments. What is not obvious from the literature and remains a topic ripe for further study, is the effect of laser energy within more complex systems such as tissue imaging studies. The results here suggest that aside from the anticipated variation in ion intensity with laser energy there are more complex phenomena occurring, where relative amounts of different intact lipid species are detected and differing levels of fragmentation seen depending upon the incident laser energy.

4. Conclusions

The detected ion intensity was observed to vary due to energy ‘spiking’ and temperature equilibration effects when triggering the laser directly from the function generator. These effects can be removed by continuous triggering of the laser in conjunction with a separate mechanical shutter system being used to ‘trigger’ the laser for MS analysis. This allows the laser to operate continuously at equilibrium, even when no MS data is being acquired, ensuring the emitted pulse-to-pulse energy is stable when the MALDI MS analyses are carried out. The shutter system used here provides a cheap and easy-to-install solution to non-equilibrium operation laser stability issues, which may be encountered by MALDI MS researchers and practitioners.

The consequence of energy variation as a result of non-equilibrium laser operation demonstrated here is not only observed to cause differences in detected ion intensity for single ions, but also to result in differing relative abundances of detected lipid ions and their characteristic fragments. Commercial MALDI MS systems to not provide for true laser energy control and monitoring, making knowledge of the behavior of one’s laser system difficult to obtain. It is therefore recommended that researchers within MALDI MS and MSI are aware of the behavior of their laser system under different operational conditions, in order to best adjust or account for any laser energy drift due to spiking and short term thermal control effects such as those observed here, or due to longer term drifts in energy due to thermal changes in the lab or damage within the laser optics. A shutter system or another

compensatory attenuation feedback setup is recommended for systems in which these phenomena are likely to occur.

Acknowledgments

Thank you to Keith Oakes for very helpful discussion. Funding was provided by NPL strategic research program 'NiCE MSI' (project 116301) and Innovate UK (formerly TSB) award 101788. AD is in receipt of an EPSRC studentship via the PSIBS doctoral training centre (EP/F50053X/1), in collaboration with AstraZeneca and the National Physical Laboratory.

Appendix A. Supplementary data

Supplementary data associated with this article can be found, in the online version, at http://dx.doi.org/10.1016/j.ymeth.2016.04.013.

References

[1] K. Dreisewerd, The desorption process in MALDI, Chem. Rev. 103 (2003) 395–425.
[2] J.I. Berry, S. Sun, Y. Dou, A. Wucher, N. Winograd, Laser desorption and imaging of proteins from ice via UV femtosecond laser pulses, Anal. Chem. 75 (2003) 5146–5151.
[3] C.L. Kalcic, G.E. Reid, V.V. Lozovoy, M. Dantus, Mechanism elucidation for nonstochastic femtosecond laser-induced ionization/dissociation: from amino acids to peptides, J. Phys. Chem. A 116 (2012) 2764–2774.
[4] J.A. Bradshaw, O.S. Ovchinnikova, K.A. Meyer, D.E. Goeringer, Combined chemical and topographic imaging at atmospheric pressure via microprobe laser desorption/ionization mass spectrometry-atomic force microscopy, Rapid Commun. Mass Spectrom. 23 (2009) 3781–3786.
[5] J.T. Westheide, J.S. Becker, R. Jäger, H.-J. Dietze, J.A. Broekaert, Analysis of ceramic layers for solid oxide fuel cells by laser ablation inductively coupled plasma mass spectroscopy, J. Anal. At. Spectrom. 11 (1996) 661–666.
[6] A. Zavalin, E.M. Todd, P.D. Rawhouser, J. Yang, J.L. Norris, R.M. Caprioli, Direct imaging of single cells and tissue at sub-cellular spatial resolution using transmission geometry MALDI MS, J. Mass Spectrom. 47 (2012) 1473–1481.
[7] G. Westmacott, W. Ens, F. Hillenkamp, K. Dreisewerd, M. Schurenberg, The influence of laser fluence on ion yield in matrix-assisted laser desorption ionization mass spectrometry, Int. J. Mass Spectrom. 221 (2002) 67–81.
[8] C. Hollands, The animals (scientific procedures) act 1986, Lancet 328 (1986) 32–33.
[9] R.T. Steven, A.D. Palmer, J. Bunch, Fluorometric beam profiling of UV MALDI lasers, J. Am. Soc. Mass Spectrom. 24 (2013) 1146–1152.
[10] A.M. Race, I.B. Styles, J. Bunch, Inclusive sharing of mass spectrometry imaging data requires a converter for all, J. Proteomics 75 (2012) 5111–5112.
[11] A.M. Race, J. Bunch, Optimisation of colour schemes to accurately display mass spectrometry imaging data based on human colour perception, Anal. Bioanal. Chem. 407 (2015) 2047–2054.
[12] A.M. Race, R.T. Steven, A.D. Palmer, I.B. Styles, J. Bunch, Memory efficient principal component analysis for the dimensionality reduction of large mass spectrometry imaging data sets, Anal. Chem. 85 (2013) 3071–3078.
[13] S. Guenther, M. Koestler, O. Schulz, B. Spengler, Laser spot size and laser power dependence of ion formation in high resolution MALDI imaging, Int. J. Mass Spectrom. 294 (2010) 7–15.
[14] S.N. Jackson, M. Ugarov, J.D. Post, T. Egan, D. Langlais, J.A. Schultz, et al., A study of phospholipids by ion mobility TOFMS, J. Am. Soc. Mass Spectrom. 19 (2008) 1655–1662.
[15] H.Y.J. Wang, C.B. Liu, H.W. Wu, J.S. Kuo, Direct profiling of phospholipids and lysophospholipids in rat brain sections after ischemic stroke, Rapid Commun. Mass Spectrom. 24 (2010) 2057–2064.
[16] R.T. Steven, A.M. Race, J. Bunch, Para-Nitroaniline is a promising matrix for MALDI-MS imaging on intermediate pressure MS systems, J. Am. Soc. Mass Spectrom. 24 (2013) 801–804.
[17] K. Shrivas, T. Hayasaka, N. Goto-Inoue, Y. Sugiura, N. Zaima, M. Setou, Ionic matrix for enhanced MALDI imaging mass spectrometry for identification of phospholipids in mouse liver and cerebellum tissue sections, Anal. Chem. 82 (2010) 8800–8806.
[18] K.A. Zemski Berry, J.A. Hankin, R.M. Barkley, J.M. Spraggins, R.M. Caprioli, R.C. Murphy, MALDI Imaging of lipid biochemistry in tissues by mass spectrometry, Chem. Rev. 111 (2011) 6491–6512.
[19] X. Wang, J. Han, A. Chou, J. Yang, J. Pan, C.H. Borchers, Hydroxyflavones as a new family of matrices for MALDI tissue imaging, Anal. Chem. 85 (2013) 7566–7573.
[20] G. Luo, I. Marginean, A. Vertes, Internal energy of ions generated by matrix-assisted laser desorption/ionization, Anal. Chem. 74 (2002) 6185–6190.
[21] E.A. Jones, A. van Remoortere, R.J. van Zeijl, P.C. Hogendoorn, J.V. Bovée, A.M. Deelder, et al., Multiple statistical analysis techniques corroborate intratumor heterogeneity in imaging mass spectrometry datasets of myxofibrosarcoma, PLoS One 6 (2011) e24913.
[22] J. Soltwisch, T.W. Jaskolla, K. Dreisewerd, Color matters—material ejection and ion yields in UV-MALDI mass spectrometry as a function of laser wavelength and laser fluence, J. Am. Soc. Mass Spectrom. 24 (2013) 1477–1488.
[23] K. Dreisewerd, M. Schurenberg, M. Karas, F. Hillenkamp, Influence of the laser intensity and spot size on the desorption of molecules and ions in matrix-assisted laser-desorption ionization with a uniform beam profile, Int. J. Mass Spectrom. 141 (1995) 127–148.
[24] H. Qiao, V. Spicer, W. Ens, The effect of laser profile, fluence, and spot size on sensitivity in orthogonal-injection matrix-assisted laser desorption/ionization time-of-flight mass spectrometry, Rapid Commun. Mass Spectrom. 22 (2008) 2779–2790.

The influence of nanotexturing of poly(lactic-co-glycolic acid) films upon human ovarian cancer cell attachment

2016 Nanotechnology 27 255102

(http://iopscience.iop.org/0957-4484/27/25/255102)

IOP Publishing Nanotechnology
Nanotechnology 27 (2016) 255102 (9pp) doi:10.1088/0957-4484/27/25/255102

The influence of nanotexturing of poly(lactic-co-glycolic acid) films upon human ovarian cancer cell attachment

Gökçen Yaşayan[1,2], Xuan Xue[1], Pamela Collier[3], Philip Clarke[3], Morgan R Alexander[4] and Maria Marlow[1]

[1] University of Nottingham, School of Pharmacy, Division of Drug Delivery and Tissue Engineering, Boots Science Building, University Park, Nottingham, NG7 2RD, UK
[2] Marmara University, Faculty of Pharmacy, Department of Pharmaceutical Technology İstanbul, 34668, Turkey
[3] University of Nottingham, School of Medicine, Division of Cancer and Stem Cells, Nottingham, NG7 2UH, UK
[4] University of Nottingham, School of Pharmacy, Laboratory of Biophysics and Surface Analysis, Boots Science Building, University Park, Nottingham, NG7 2RD, UK

E-mail: Maria.Marlow@nottingham.ac.uk

Received 17 September 2015, revised 25 February 2016
Accepted for publication 28 April 2016
Published 17 May 2016

Abstract

In this study, we have produced nanotextured poly(lactic-co-glycolic acid) (PLGA) films by using polystyrene (PS) particles as a template to make a polydimethylsiloxane mould against which PLGA is solvent cast. Biocompatible, biodegradable and nanotextured PLGA films were prepared with PS particles of diameter of 57, 99, 210, and 280 nm that produced domes of the same dimension in the PLGA surface. The effect of the particulate monolayer templating method was investigated to enable preparation of the films with uniformly ordered surface nanodomes. Cell attachment of a human ovarian cancer cell line (OVCAR3) alone and co-cultured with mesenchymal stem cells (MSCs) was evaluated on flat and topographically nano-patterned surfaces. Cell numbers were observed to increase on the nanotextured surfaces compared to non-textured surfaces both with OVCAR3 cultures and OVCAR3-MSC co-cultures at 24 and 48 h time points.

S Online supplementary data available from stacks.iop.org/NANO/27/255102/mmedia

Keywords: nanotexturing, films, poly(lactic-co-glycolic acid), human ovarian cancer cell

(Some figures may appear in colour only in the online journal)

Introduction

Nanotexturing of biomaterials has been widely used to mimic the extracellular matrix and is currently an approach used to modulate, isolate and optimize the response of the cells for multiple applications in regenerative medicine and cancer therapeutics (Zhang and Webster 2012).

Previous studies of the topographical influence of cell-material attachment have been carried out with geometries including grooves, wells, pits, and protrusions on a diverse range of materials. The results for mature cells including cancer cells show that they respond to nano- and micro-textured biomaterial surfaces, where changes in cell adhesion, proliferation, orientation, alignment, migration and morphology were all observed. (Curtis and Wilkinson 1997, Flemming *et al* 1999, Andersson *et al* 2003, Matsuzaka *et al* 2003, Recknor *et al* 2004, Hsu *et al* 2005, Falconnet *et al* 2006, Miller *et al* 2007, Martinez *et al* 2009, Sarna *et al* 2009, Lamers *et al* 2010, Zhang and Webster 2012). These textured biomaterials may mimic *in vivo* microenvironments, and thus enable modeling of cell–cell and cell–extracellular matrix interactions and modulation of cell-surface interactions

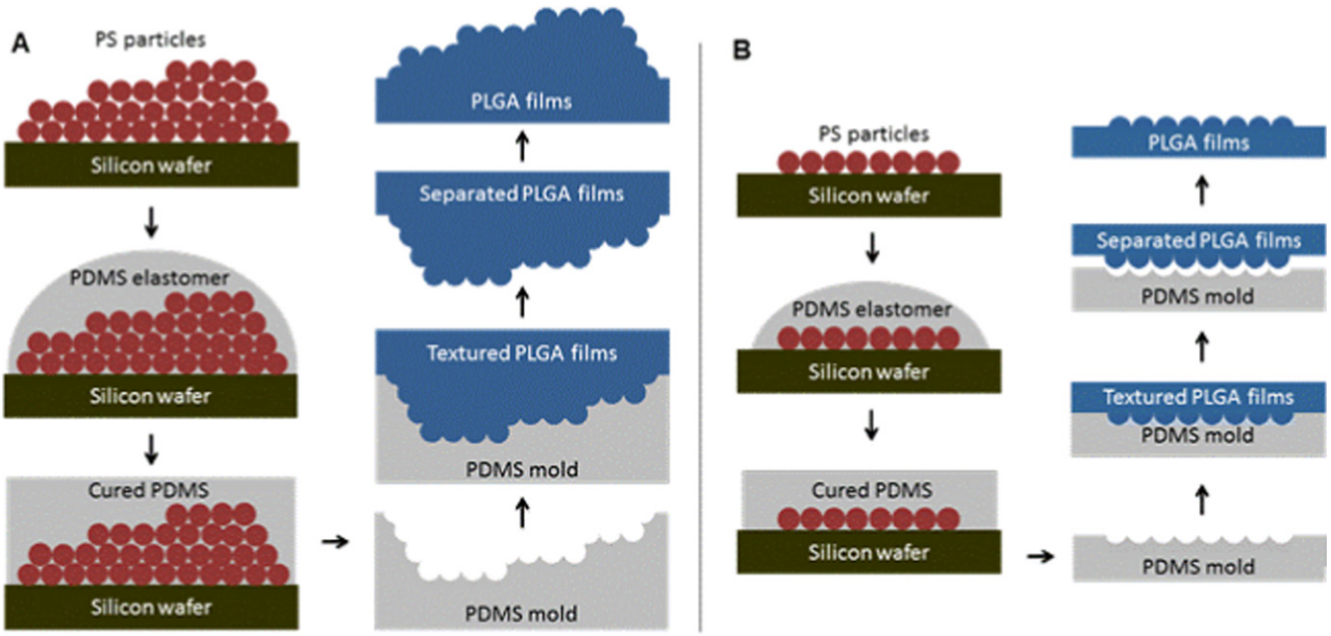

Figure 1. A schematic representation for preparation of the PLGA films. Surface morphologies of the PS particles were transferred to PDMS templates as inverse moulds. By using PDMS moulds, PLGA films were obtained. (A) Preparation of multi-layered PLGA films. With this method, step edges on the surface between areas of disorder were observed. (B) Preparation of mono-layered PLGA films. With this method, no other surface morphology was observed other than nanotexturing.

(Craighead *et al* 1998, Dalby *et al* 2004, Martinez *et al* 2009, Ng *et al* 2012).

Although there are numerous studies on textured materials, the complexity of their role in controlling cell interactions and cell responses is still yet not fully understood and hence is impossible to predict without carrying out the individual cell studies. Also the response mechanisms of different cell lines to textured surfaces are not well defined (Andersson *et al* 2003, Hsu *et al* 2005, Miller *et al* 2007, Martinez *et al* 2009, Lamers *et al* 2010, Zhang and Webster 2012). Hence in this study, we have focused on fabrication, characterization and cell culture studies of hemispherical protrusions to provide nanotextured biodegradable biomaterials to characterize the ovarian cancer cell response to this surface topography. We have focused on fabrication of large scale (1 cm × 1 cm), defect-free textured surfaces with various protrusion dimensions, and their impact on ovarian cancer cell attachment.

Hemispherical protrusion shaped nanotextured materials were manufactured using a colloidal particle lithography technique employing polystyrene (PS) particles with the diameters from 57 to 280 nm. The PS templates were prepared by using two methods, the first as described in Zhang and Webster's study (Zhang and Webster 2012) which enabled formation of a multi-layered templates, and a second approach (Ogaki *et al* 2010) by using self-assembly of PS particles at an air–water interface which produced mono-layered particles reducing the occurrence of step edges in the nano imprinted polymer surfaces. The latter method has not been used before to prepare biomaterial surfaces. The PS templates were used to form a negative relief in polydimethylsiloxane (PDMS) from which replication of the particulate topography was obtained in the biodegradable poly(lactic-co-glycolic acid) (PLGA) films (figure 1).

Atomic force microscopy (AFM) was used to characterize the topography, x-ray photoelectron spectroscopy (XPS) to analyze surface chemistry, and contact angle to measure the surface wettability.

Cell attachment on PLGA films was evaluated with an ovarian cancer cell line, OVCAR3, and OVCAR3 co-cultured with mesenchymal stem cells (MSCs). Specifically, the cell responses to non-textured PLGA films and nanotextured PLGA films were compared. With ovarian and other cancer types, the presence of a viable stem cell niche i.e. MSCs is critical to tumor growth and invasion, conferring a metastatic phenotype and chemo- and radio-resistance. Indeed, co-culturing the OVCAR3s with MSCs provides more disease relevance and appropriate cell:cell interactions. Specifically MCSs will differentiate into fibroblasts, thereby providing increased opportunity for cancer cell anchorage (Haller *et al* 2000, Lehmann *et al* 2011, Touboul *et al* 2013).

Materials and methods

Preparation of PS templates

Multi-layer PS templates. Multi-layer PS templates were prepared as described previously (Carpenter *et al* 2008, Zhang and Webster 2012); borosilicate glass coverslips (18 mm in diameter, Fisher) were cleaned and degreased by acetone, ethanol (70%) and dH_2O. Then PS suspensions (300 μl, 10 wt%, Bangs Labs) with the diameters of 57, 99,

210 or 280 nm were pipetted onto the coverslips, and vacuum desiccated to remove the solvent (~2 days).

Mono-layer PS templates. Mono-layer PS templates were prepared as described previously (Rybczynski *et al* 2003, Ogaki *et al* 2010). Silicon wafers (Sigma-Aldrich) were cut to small (~1 × 1 cm^2) and large (~1 × 3 cm^2) sizes and sonicated with ethanol. Afterwards they were washed several times with Milli-Q water (Millipore, resistibility of 18.2 MΩ cm^{-1} at 25 °C), and blown dry with nitrogen at room temperature. After drying, the silicon wafers were exposed to UV to increase wafer hydrophilicity for 20 min (UV/Ozone ProCleaner, BioForce Nanosciences, Inc.). The large silicon wafer was placed in a petri dish at an inclined plane, and the Petri dish was filled with Milli-Q water. PS particle suspension (100 μl, 10 wt%) was mixed with an equal amount of ethanol. This mixture was applied slowly over the large silicon wafer to water surface using an Eppendorf pipette, the silicon wafer was then slowly submerged in the water. To obtain hexagonal close packed particles, a dodecylsodiumsulfate (SDS) solution (2%, ~10 μl) was added to Petri dish. The PS mono-layers on the water–air interface were then lifted off from the water surface by using the small-size silicon wafer, and were dried at room temperature. The surfaces were prepared by using PS particles with the diameters of 99, 210 or 280 nm.

Preparation of PDMS templates

PDMS (Sylgard 184 silicone elastomer, Dow Corning) was mixed thoroughly (curing agent: base, 3.5 ml: 26.5 ml), and then centrifuged for 15 min at 2000 rpm. It was poured over the PS coated coverslips (or silicon wafers) placed in a borosilicate glass Petri dish, residual bubbles were removed by vacuum extraction and the wafer was heated to 40 °C for 2 h to accelerate the curing process. Once cooled, the PDMS template was separated from PS template. The PDMS template was washed with acetone to remove the remaining PS particles on the surface.

Preparation of PLGA films

PLGA (1g, 50:50 PLA/PGA, 7000-17000; Sigma Aldrich) was dissolved in chloroform (10 ml), and poured over the PDMS moulds, then placed into a vacuum desiccator to avoid bubble formation. After allowing evaporation of the solvent for 48 h, PLGA films were peeled off from the moulds and placed on glass coverslips. To remove the residual PDMS, PLGA films were washed with hexane (Sigma-Aldrich). For control studies, non-textured PDMS and PLGA films were prepared without PS beads following the procedure described above.

AFM studies

Topography images and analysis (section and bearing) of PS, PDMS and PLGA films were obtained in air using a D3000 AFM instrument with a NanoScope IIIa controller (Bruker) operating in Tapping™ mode. RTESPA AFM probes (nominal resonant mechanical frequency: 300 kHz, spring constant: 40 N m^{-1}, Bruker) were used, and images were acquired using an E-scanner, at scan rates between 0.6 and 1 Hz, with a resolution of 512 × 512 pixels. Image data was analyzed, section and bearing analysis were carried by NanoScope Analysis software-Version 1.20 (Bruker).

Optical microscopy studies

The samples were viewed using an optical microscope (Prior Scientific Instruments Ltd) equipped with a digital camera (QICAM Fast 1394, QImaging).

Water contact angle measurements

Water contact angle measurements of the films were measured by a Krüss DSA 100 instrument by dispersing an ultrapure Milli-Q water droplet (Millipore, resistibility of 18.2 MΩ cm^{-1} at 25 °C) with a volume of ~400 pl.

XPS measurements

The samples were analyzed using XPS in order to determine surface elemental composition using a Kratos AXIS Ultra Spectrometer (Kratos Analytical, Manchester, UK) with a mono-chromatic Al Kα x-ray source (1486.6 eV) operated at 10 mA emission current and 12 kV anode potential. The ULTRA was used in fixed analyzed transmission mode, a pass energy of 80 eV was used for the wide scans, and 20 eV for the high resolution scans. Data analysis was carried out using CASAXPS software with empirically derived sensitivity factors to determine the composition (atomic percent) from the peak areas. The photoelectrons were collected normal to the sample surface. The measurements were carried only with a mono-layer textured 280 nm films and non-textured films which had been cast against a flat PDMS mold.

The residual PDMS layer thickness over the mono-layered 280 nm textured PLGA films and the non-textured films were calculated by using the silicon signal in the XPS data. Topofactors for hemispheres were used to calculate the equivalent conformal PDMS thickness of the textured surfaces (Shard *et al* 2009, Shard 2012).

Human ovarian carcinoma cell and MSC adhesion assay

Human ovarian carcinoma cell line, OVCAR3 (US National Cancer Institute) was cultured only/or co-cultured with MSC line, hm-MSC-bm (Sciencell Research Laboratories, CA, US) in Dulbecco's modified eagles medium (DMEM, Sigma, UK) with 10% fetal bovine serum (FBS, Sigma, UK).

For sterilization of the films, PLGA films were removed from the coverslips by soaking in 70% ethanol for approximately 4 h, and later soaking in clean 70% ethanol for approximately 20 min. The surfaces were sterilized by UV light for 5 min in ethanol, and later 5 min, without ethanol. After rinsing with media the films were placed in 3 ml of DMEM + 10% FBS.

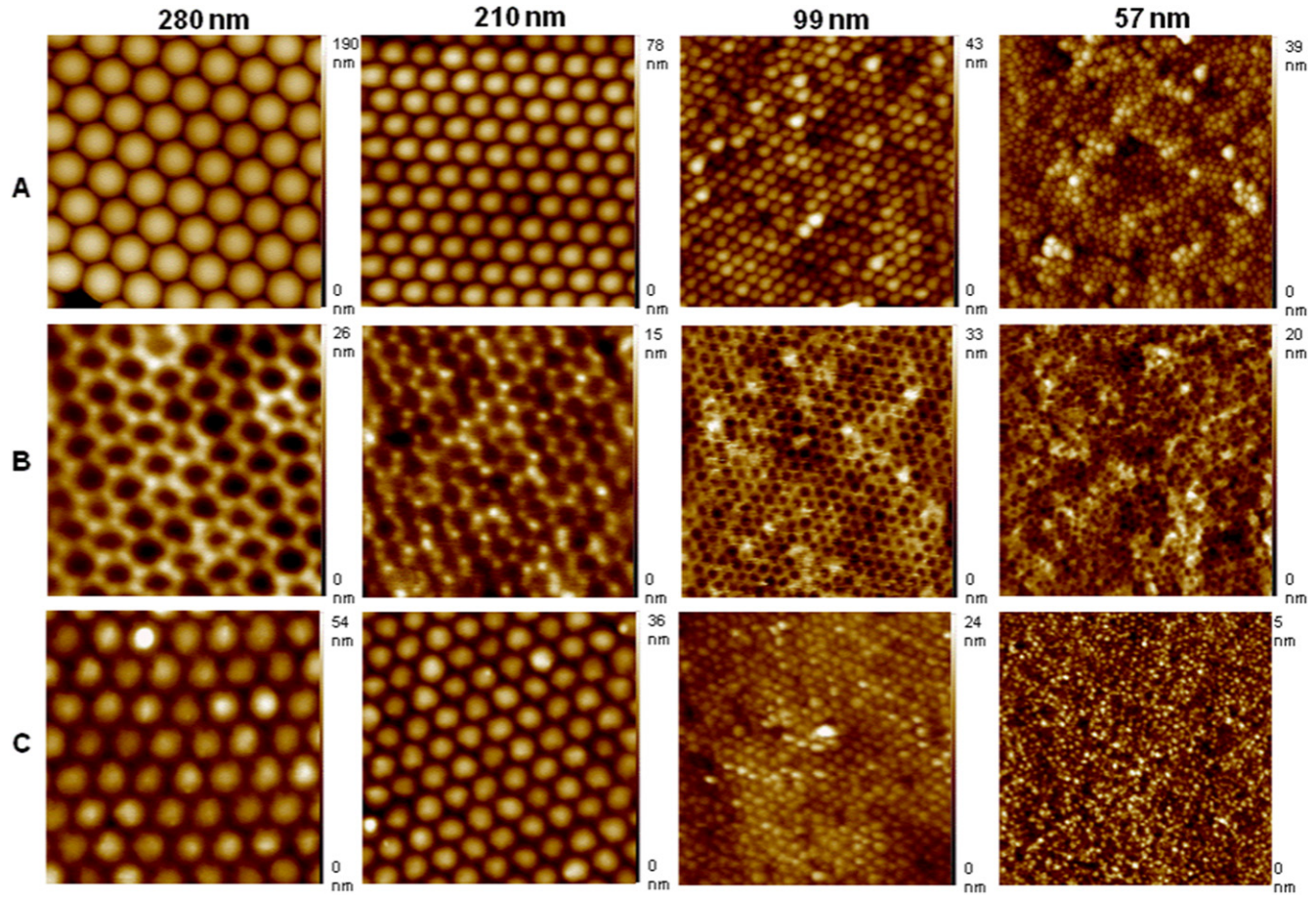

Figure 2. AFM topography images of PS surfaces (A), PDMS surfaces (B), and PLGA films (C) prepared from multi-layer PS templates. The surfaces were prepared by use of 280, 210, 99, and 57 nm PS beads. All images were 2 μm $\times$ 2 μm.

OVCAR3 cells were labeled with Cell tracker™ CM-DiI red fluorescent protein reporter (Life Technologies, UK) and cultured on three different surfaces including a control well of a six well plate (flat plastic), non-textured PLGA films, and textured PLGA films prepared from mono-layered 280 nm PS templates for 48 h. For each condition the cells were plated (OVCAR3 only, OVCAR3 and MSC's combined at a 1:1 ratio) on duplicate wafers (one per well, six well plates) with a final density of 6×10^5 and monitored over 48 h for cell attachment. Three plates, one for each time point were set up (4, 24 and 48 h) and in each case the wafers were removed for counting.

At 4, 24 and 48 h, the cells in all conditions were counted manually over three regions of interest (ROI) for each duplicate well where possible. Cells emitting red light were photographed at 10X objective magnification in three areas of each well (duplicate wells). Each image was divided into four equal (dimensions) ROI's and the cells counted. In this study, number of cells attached to the films at the 4th hour, 24th hour, and 48th hour were studied.

Statistical analysis

The validation and analysis of cell attachment data was carried out in SPSS 21, (IBM) using Wilcoxon signed ranks test. Other statistical analysis was performed by a two sample t-test assuming both equal and unequal variances. Statistical significance was accepted at $p < 0.05$.

Results

In these studies we have focused on fabricating regular nanotextured and defect-free materials over large lengths scales compatible with the cell culture experiments (1 cm $\times$ 1 cm).

Nanotextured surfaces prepared from multi-layer PS templates

Utilizing the Zhang and Webster method (Zhang and Webster 2012), we successfully produced PDMS templates from multi-layers of PS spheres. Using AFM imaging, we determined that the form of the PS templates were transferred to PDMS templates and then to the PLGA films (figure 2). This data also indicated that the diameters of the features in PS templates and PLGA films remained unchanged during the fabrication process of the films. (See also figure S3, ESI.)

From the AFM images of the PS particles, the PDMS mould and the PLGA surfaces presented in figure 2, hexagonal close packing of the particles is evident for the 210

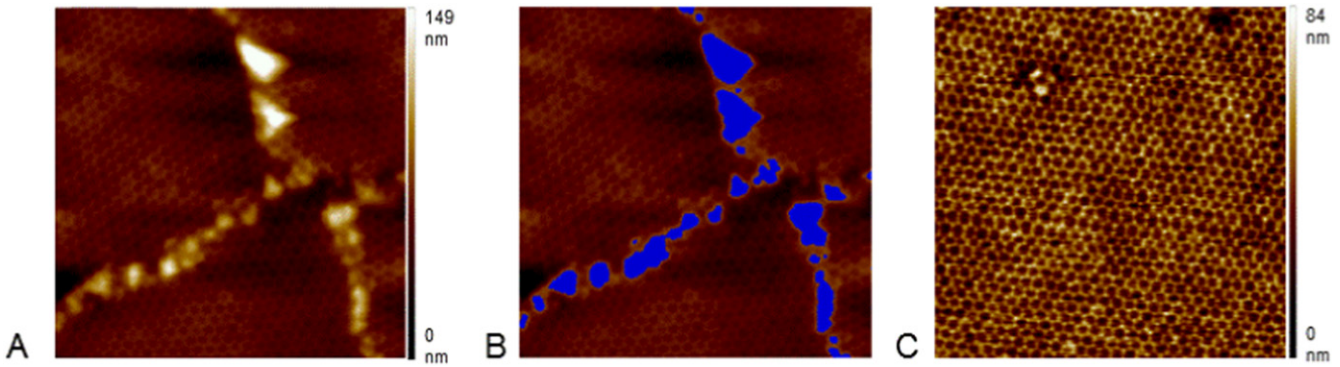

Figure 3. Representative AFM images of multi-layered and mono-layered silicone mould surfaces. For multilayered surfaces (A), surface irregularities on the surface were observed. For the PDMS surfaces prepared from 280 nm multi-layer templates, the area occupied by boundary structures ((B), the area in blue) was 7.1%. No boundary structures were observed for the PDMS surfaces prepared from 280 nm mono-layer templates (C). 8 μm $\times$ 8 μm scan.

and 280 nm assemblies, but this was accompanied by retention of PS particles in the structure imprinted in to the silicone mould for the 99 nm surface and the order was not present in the 57 nm beads.

AFM studies with larger scan areas (8 μm $\times$ 8 μm) indicated the presence of flat layers of particles, separated by step edges between areas of disorder in the PLGA films (figure 3). These step edges were attributed to the formation of multi-layers during PS template preparation (figure S4, ESI). By analysis of the AFM images, the percentage of the protrusions by boundary structures in the PDMS surfaces was found to be up to ~7% of the overall scan area.

Nanotextured surfaces prepared from mono-layer PS templates

In an alternative method, adapted from Ogaki *et al* (Ogaki *et al* 2010), PS templates were prepared by self-assembly of the PS beads on the water–air interface; a single layer of PS particles were spread on the wafer during the preparation of the templates. Mono-layered PS templates were prepared from beads with the diameters of 280, 210 and 99 nm, but 57 nm particles did not prove effective (figure S5, ESI). For the templates prepared from 280 to 210 nm, AFM results indicated that PS mono-layer templates were prepared successfully, without the retained particles as found in the multilayer moulding, and the nanotexturing was again transferred to PDMS and PLGA films. For 99 nm templates prepared by this new method, multi-layers were observed and surface regularity was disrupted compared to larger particle diameters (figure 4). For 210 and 280 nm PS particles, step edges were not observed on the surfaces (figure S6, ESI). Optical microscopy images have also confirmed the elimination of the macroscopic defects (figure S7).

When AFM data obtained from both methods with different PS particle diameters were considered, the films prepared from mono-layer 280 nm particles formed defect free highly ordered hexagonal packing both over small and large scales. The presence of step edges and nano-grooves were fully eliminated, as well as macroscopic non-ordered cracks. For these reasons, PLGA surfaces prepared from mono-layered 280 nm templates were selected for further characterization.

XPS and water contact angle measurements

Since chemistry, as well as topography, effect cell response to materials, XPS studies were carried out with the PLGA samples to determine whether the samples have similar chemistries after a hexane wash to reduce PDMS residuals. The studies were undertaken with textured and non-textured PLGA surfaces as well as a PLGA powder reference. XPS data indicated the presence of silicon at a similar thickness in textured (1.2 $\pm$ 0.3 nm) and non-textured (1.0 $\pm$ 0.1 nm) surfaces (table 1). This was assigned to PDMS oligomers carried over from the silicone mould. All other spectral features where equivalent in the textured and non-textured surfaces indicating chemical equivalence.

Overlayer PDMS thickness on PLGA particles were calculated from XPS data with the method described previously (Shard *et al* 2009). By using the topofactors given for the hemispheres, the equivalent conformal thickness was calculated via the thickness of PDMS as for a flat sample. According to the calculations, both flat samples and topofactor corrected textured surfaces have ~1 nm overlayer PDMS remaining. A two sample t-test was carried on the film PDMS film thicknesses and the *P* value was found to be 0.09, indicating that there was no statistical significance between the textured and non-textured films.

Contact angle measurements indicated that the wettability values of the surfaces were similar. In both surfaces, contact angle values were found higher than 90°, which indicates that the wetting of the surfaces were poor, and the surfaces were hydrophobic (table 1).

Cell culture studies

OVCAR3 cells were studied in monoculture and in co-culture with MSC's in order to assess their response to 280 nm hemispherical topographies. Cell culture studies were carried out with PLGA surfaces prepared from mono-layered

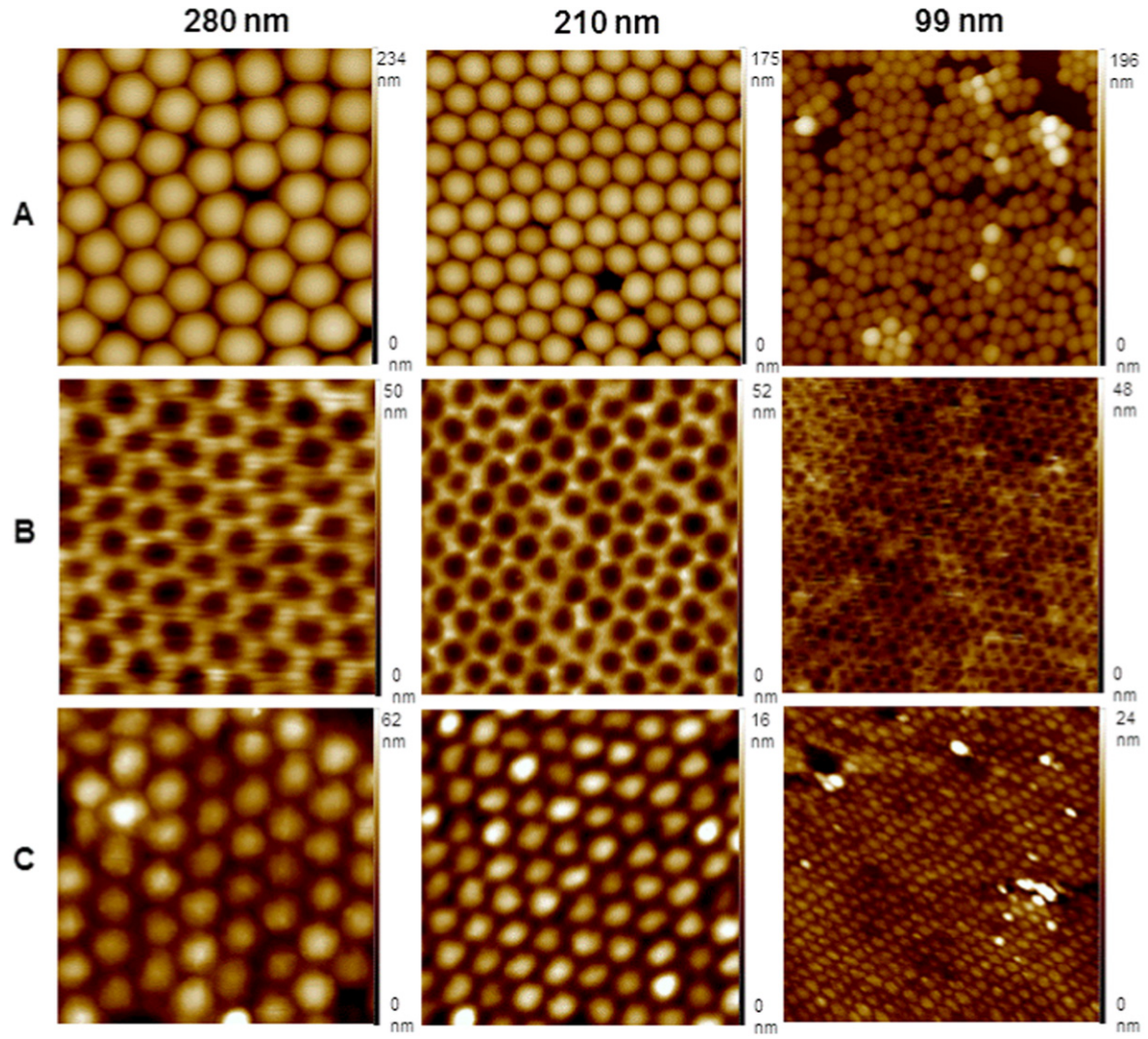

Figure 4. AFM topography images of PS surfaces (A), PDMS surfaces (B), and PLGA films (C) prepared from mono-layered PS templates. The surfaces were prepared by use of 280, 210, and 99 nm PS beads. All images were 2 μm × 2 μm.

Table 1. XPS results, PDMS thickness calculations with and without topofactor correction, and contact angle measurements of the samples. The studies carried out with nanotextured PLGA films prepared from mono-layered 280 nm templates, and non-textured PLGA films after a hexane wash of the samples. For XPS studies, PLGA powder was also analyzed as a reference. The conformal coating thickness of PDMS was calculated using the stoichiometry of PDMS and a topofactor correction for the particle topography developed by Shard. (Shard *et al* 2009, Shard 2012).

	XPS results			PDMS thickness (nm)		
Samples	C 1s %	O 1s %	Si 2p %	Non-corrected	Topofactor corrected	Contact angle (θ)
PLGA powder	62.9 ± 0.28	37.1 ± 0.28	—	—	—	—
Textured films	58.7 ± 2.44	33.1 ± 0.78	8.2 ± 1.9	1.6 ± 0.5	1.2 ± 0.3	104.4 ± 0.5
Non-textured films	63.2 ± 0.52	31.2 ± 0.51	5.6 ± 0.37	1.0 ± 0.1	—	107.9 ± 0.8

280 nm templates and non-textured flat PLGA surfaces. Flat plate wells (tissue culture plastic only with no other added matrix/wafer/gel) were used for control studies. OVCAR3, and OVCAR3 seeded with MSCs at a 1:1 ratio were cultured onto the surfaces. In the study, attachment of the cells to the films at 4th hour, 24th hour and 48th hour were studied.

OVCAR3 alone

It was observed that OVCAR3 cells were adhered to the surfaces by 4 h and the mean number of cells attached per wafer were similar for both textured and non-textured surfaces but less than the flat plate well, cell culture plastic control (figure 5, figure S8, ESI).

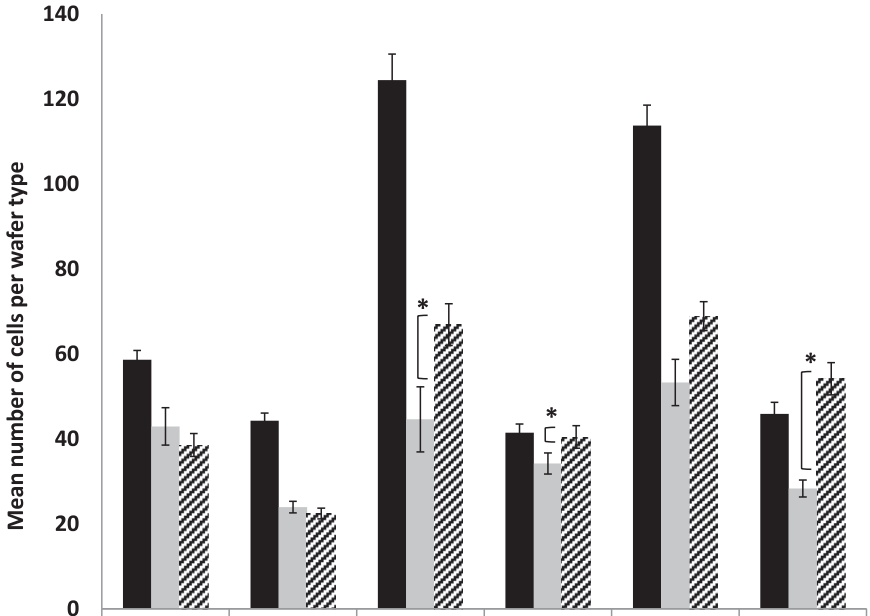

	4hrs OVCAR3	4hrs OVCAR3 with MSCs	24hrs OVCAR3	24hrs OVCAR3 with MSCs	48hrs OVCAR3	48hrs OVCAR3 with MSCs
flat plate well	58.63	44.27	124.46	41.42	113.75	45.88
non-textured surface	42.92	23.92	44.58	34.18	53.25	28.30
textured surface	38.54	22.42	66.88	40.43	68.89	54.13

Figure 5. Mean number of cells in OVCAR3 monocultures, and OVCAR3-MSC co-cultures per wafer type at 4, 24, and 48 h. Flat well plates, non-textured PLGA surfaces, and PLGA surfaces prepared from mono-layered 280 nm templates were used as a substrate. Data are expressed as a mean ± SD *: $p < 0.05$ compared to non-textured surfaces.

The mean number of cells per wafer increased for both textured and non-textured surfaces over time, however in the flat plate well cell culture control, a decrease was observed after 24 h with OVCAR3s probably due to having reached confluency and then overgrowth of the cells on the well plate. The mean number of cells per wafer were higher on textured surfaces as compared to non-textured surfaces at the 24 and 48 h time points and were significantly greater ($p < 0.05$) at the 24 h time point. Also the cells at these time points were clustered in islets on the tissue culture plate control and wafers indicative of proliferation (figure S8).

OVCAR3 co-cultured with MSCs

In the studies with OVCAR3 seeded 1:1 with MSC cell lines, again it was found that the cells were adhered to all surfaces by 4 h and that the mean number of cells adhered per wafer were similar for both textured and non-textured surfaces but less than the flat plate well (figure S9, ESI). Again, a decrease in the mean number of cells for the flat well plate at 24 h was observed (figure 5). The mean number of cells per wafer were significantly greater ($p < 0.05$) on textured surfaces as compared to the non-textured surface at 24 and 48 h time points. Again, our results demonstrate that textured surfaces promote cell attachment compared to non-textured surfaces beyond the 4th hour and also the cells at these time points were clustered in islets on the tissue culture plate control and wafers indicative of proliferation (figure S9).

Discussion

There has been recent interest in the use of biomaterials to modulate cancer cell adhesion (Hartman *et al* 2010, Wan *et al* 2012, Kim *et al* 2013, Sharma *et al* 2014, Islam *et al* 2015) motivated by the few studies in this area and to our knowledge none with ovarian cancer cells, we investigated the modulation of ovarian cancer cell adhesion fabricating novel regularly nanotextured and defect-free materials over large lengths scales. Indeed, neither of these factors has been explored to date. Our first method of nanotexturing was to use a colloidal lithography approach similar to that reported by Zhang and Webster (Zhang and Webster 2012) where we observed with AFM, step edges in PLGA films as a result of formation of multi-layers during PS template preparation (figures 2 and 3). These step-edges appear to be points of weakness in the interparticulate bonding, and resulted in PS particulate transfer to PDMS along these edges and subsequently PLGA films. Since it has been reported that cells can be aligned with surface features (known as 'contact guidance') (Curtis and Wilkinson 1997, Rajnicek *et al* 1997, Flemming *et al* 1999, Wilkinson *et al* 2002), we then sort to find another colloidal lithography that could remove these features in the topography. Eliminating this response of the cells to non-ordered topography, allows study of cell response to nanotextured substrates only and to achieve this monolayer PS templates were prepared. Monolayers of PS particles

have been reported previously (Ogaki *et al* 2010), however here for the first time we used these to template nanotexture into PLGA surfaces for a biomaterial application. We found that we could create defect free nanotextured surfaces with nanotextured domes either 210 or 280 nm in diameter. However when smaller PS particle diameters were used in template preparation (99 and 57 nm), the order of small scale nanotexturing was disrupted. With this method, hexagonal packing is achieved by addition of SDS and indeed the particle diameters and SDS solution concentrations are crucial. Hence only the nanotextured surfaces with 280 nm nanotextured domes were progressed further where these films and a flat surface control were rigorously characterized using XPS and contact angle measurements. These measurements proved chemical equivalence in surface chemistry and hence we can be certain that any difference in cell response is due to topography i.e. nanotexturing.

Using these 280 nm nanotextured defect free films and a flat surface control of chemical equivalence, we then progressed to evaluating OVCAR3 cell adhesion on these films, in monoculture and in co-culture with MSCs. Our data shows that OVCAR3 cell adhesion, whether in monoculture or co-cultured with MSCs, to all surfaces and similarities between textured and non-textured surfaces at the four hour time point as also reported by Zhang and Webster (Zhang and Webster 2012) for breast cancer cells. It should also be noted that these cell attachment studies are also the first to our knowledge using a co-culture with MSCs.

However at 24 and 48 h time points, our results demonstrated that textured surfaces have more cells attached compared to non-textured surfaces when alone or co-cultured with MSCs. Our data is in agreement with previous studies with cell lines where reported changes in cell attachment were observed compared to non-textured surfaces. In some papers, a decrease in cell adhesion/proliferation was reported due to texturing (Curtis *et al* 2001, Wilkinson *et al* 2002), and oppositely some reported an increase in cell adhesion/proliferation (Miller *et al* 2007, Carpenter *et al* 2008) as was observed in our studies.

Conclusions

In this study, we aimed to investigate the effect of hemispherical protrusion surface topographies on ovarian cancer cell adhesion. For this purpose, flat and nanotextured PLGA films obtained from (1) mono-layered and (2) multi-layered PS templates were characterized by AFM and optical microscope.

According to our results:

- Films obtained from multi-layered templates had non-ordered, uncontrolled surface topographies (macroscopic structures and step edges).
- Films obtained from monolayered templates were defect-free at large length scales, and demonstrated nanotexturing in small scale. However it was found that when the PS particle diameters for template preparation decreased to 99 nm and 57 nm, the order of small scale nanotexturing was disrupted.
- Whilst in the cancer cell adhesion studies, OVCAR3 seeded alone, and seeded with MSCs, cancer cells adhered to all surfaces, and increased cell numbers on textured surfaces compared with the non-textured surfaces was observed at 24 and 48 h time points.

Acknowledgments

Thanks to Dr Ryosuke Ogaki for his help in preparation of mono-layer PS templates, Taranjit Singh for water contact angle measurements. Thanks to Dr Emily Smith at the Nottingham Nanotechnology and Nanoscience Centre for performing the XPS analysis and EPSRC for funding the XPS instrument, Grant EP/K005138/1. Thanks go to Alex G Shard at the National Physical Laboratory for his help on the XPS topofactor analysis. This research is funded by EPSRC Research Development Fund, Grant: Call–RDF-PP-0313.

References

Andersson A S, Backhed F, von Euler A, Richter-Dahlfors A, Sutherland D and Kasemo B 2003 Nanoscale features influence epithelial cell morphology and cytokine production *Biomaterials* **24** 3427–36

Carpenter J, Khang D and Webster T J 2008 Nanometer polymer surface features: the influence on surface energy, protein adsorption and endothelial cell adhesion *Nanotechnology* **19** 505103

Craighead H G *et al* 1998 Chemical and topographical surface modification for control of central nervous system cell adhesion *Biomed. Microdevices* **1** 49–64

Curtis A and Wilkinson C 1997 Topographical control of cells *Biomaterials* **18** 1573–83

Curtis A S G, Casey B, Gallagher J O, Pasqui D, Wood M A and Wilkinson C D W 2001 Substratum nanotopography and the adhesion of biological cells. Are symmetry or regularity of nanotopography important? *Biophys. Chem.* **94** 275–83

Dalby M J, Giannaras D, Riehle M O, Gadegaard N, Affrossman S and Curtis A S G 2004 Rapid fibroblast adhesion to 27 nm high polymer demixed nano-topography *Biomaterials* **25** 77–83

Falconnet D, Csucs G, Grandin H M and Textor M 2006 Surface engineering approaches to micropattern surfaces for cell-based assays *Biomaterials* **27** 3044–63

Flemming R G, Murphy C J, Abrams G A, Goodman S L and Nealey P F 1999 Effects of synthetic micro- and nano-structured surfaces on cell behavior *Biomaterials* **20** 573–88

Haller D, Bode C, Hammes W P, Pfeifer A M A, Schiffrin E J and Blum S 2000 Non-pathogenic bacteria elicit a differential cytokine response by intestinal epithelial cell/leucocyte co-cultures *Gut* **47** 79–87

Hartman O, Zhang C, Adams E L, Farach-Carson M C, Petrelli N J, Chase B D and Rabolt J E 2010 Biofunctionalization of electrospun PCL-based scaffolds with perlecan domain IV peptide to create a 3D pharmacokinetic cancer model *Biomaterials* **31** 5700–18

Hsu S H, Chen C Y, Lu P S, Lai C S and Chen C J 2005 Oriented Schwann cell growth on microgrooved surfaces *Biotechnol. Bioeng.* **92** 579–88

Islam M, Sajid A, Mahmood M A I, Bellah M M, Allen P B, Kim Y T and Iqbal S M 2015 Nanotextured polymer substrates show enhanced cancer cell isolation and cell culture *Nanotechnology* **26** 225101

Kim H N, Jiao A, Hwang N S, Kim M S, Kang D H, Kim D H and Suh K Y 2013 Nanotopography-guided tissue engineering and regenerative medicine *Adv. Drug Deliv. Rev.* **65** 536–58

Lamers E, Walboomers X F, Domanski M, te Riet J, van Delft F, Luttge R, Winnubst L, Gardeniers H and Jansen J A 2010 The influence of nanoscale grooved substrates on osteoblast behavior and extracellular matrix deposition *Biomaterials* **31** 3307–16

Lehmann A D, Daum N, Bur M, Lehr C-M, Gehr P and Rothen-Rutishauser B M 2011 An *in vitro* triple cell co-culture model with primary cells mimicking the human alveolar epithelial barrier *Eur. J. Pharmaceutics Biopharmaceutics* **77** 398–406

Martinez E, Engel E, Planell J A and Samitier J 2009 Effects of artificial micro- and nano-structured surfaces on cell behaviour *Ann. Anat.—Anatomischer Anz.* **191** 126–35

Matsuzaka K, Walboomers X F, Yoshinari M, Inoue T and Jansen J A 2003 The attachment and growth behavior of osteoblast-like cells on microtextured surfaces *Biomaterials* **24** 2711–9

Miller D C, Haberstroh K M and Webster T J 2007 PLGA nanometer surface features manipulate fibronectin interactions for improved vascular cell adhesion *J. Biomed. Mater. Res.* A **81** 678–84

Ng R, Zang R, Yang K K, Liu N and Yang S-T 2012 Three-dimensional fibrous scaffolds with microstructures and nanotextures for tissue engineering *RSC Adv.* **2** 10110–24

Ogaki R, Lyckegaard F and Kingshott P 2010 High-resolution surface chemical analysis of a trifunctional pattern made by sequential colloidal shadowing *ChemPhysChem* **11** 3609–16

Rajnicek A M, Britland S and McCaig C D 1997 Contact guidance of CNS neurites on grooved quartz: influence of groove dimensions, neuronal age and cell type *J. Cell Sci.* **110** 2905–13

Recknor J B, Recknor J C, Sakaguchi D S and Mallapragadaa S K 2004 Oriented astroglial cell growth on micropatterned polystyrene substrates *Biomaterials* **25** 2753–67

Rybczynski J, Ebels U and Giersig M 2003 Large-scale, 2D arrays of magnetic nanoparticles *Colloids Surf.* A **219** 1–6

Sarna M, Wybieralska E, Miekus K, Drukala J and Madeja Z 2009 Topographical control of prostate cancer cell migration *Mol. Med. Rep.* **2** 865–71

Shard A G 2012 A straightforward method for interpreting XPS data from core–shell nanoparticles *J. Phys. Chem.* C **116** 16806–13

Shard A G, Wang J and Spencer S J 2009 XPS topofactors: determining overlayer thickness on particles and fibres *Surf. Interface Anal.* **41** 541–8

Sharma A, Sharma N L, Lavy C B, Kiltie A E, Hamdy F C and Czernuszka J 2014 Three-dimensional scaffolds: an *in vitro* strategy for the biomimetic modelling of *in vivo* tumour biology *J. Mater. Sci.* **49** 5809–20

Touboul C, Lis R, Al Farsi H, Raynaud C M, Warfa M, Althawadi H, Mery E, Mirshahi M and Rafii A 2013 Mesenchymal stem cells enhance ovarian cancer cell infiltration through IL6 secretion in an amniochorionic membrane based 3D model *J. Transl. Med.* **11** 28

Wan Y, Mahmood M A I, Li N, Allen P B, Kim Y T, Bachoo R, Ellington A D and Iqbal S M 2012 Nanotextured substrates with immobilized aptamers for cancer cell isolation and cytology *Cancer* **118** 1145–54

Wilkinson C D W, Riehle M, Wood M, Gallagher J and Curtis A S G 2002 The use of materials patterned on a nano- and micro-metric scale in cellular engineering *Mater. Sci. Eng.* C **19** 263–9

Zhang L and Webster T J 2012 Poly-lactic-glycolic-acid surface nanotopographies selectively decrease breast adenocarcinoma cell functions *Nanotechnology* **23** 155101

Neuroscience Letters 626 (2016) 164–173

Contents lists available at ScienceDirect

Neuroscience Letters

journal homepage: www.elsevier.com/locate/neulet

Research paper

Interfering with the CCL2–glycosaminoglycan axis as a potential approach to modulate neuroinflammation

Martha Gschwandtner[a], Anna Maria Piccinini[b,1], Tanja Gerlza[b], Tiziana Adage[b], Andreas J. Kungl[a,b,*]

[a] Institute of Pharmaceutical Sciences, University of Graz, Schubertstraße 1/1, A- 8010 Graz, Austria
[b] ProtAffin Biotechnologie AG, A- 8020 Graz, Austria

HIGHLIGHTS

- CCL2 decoy with enhanced GAG binding properties and knocked-out GPCR activation.
- Decoy shows anti-migratory activity towards inflammatory monocytes and therefore anti-inflammatory properties.
- Ameliorating effect was shown in an experimental autoimmune encephalitis, a model of Multiple Sclerosis.

GRAPHICAL ABSTRACT

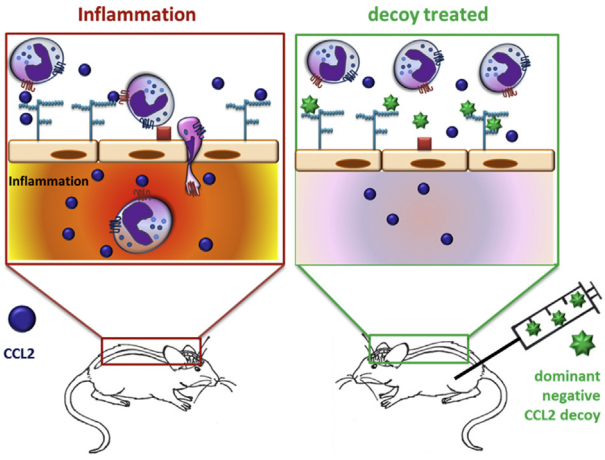

ARTICLE INFO

Article history:
Received 5 February 2016
Received in revised form 3 May 2016
Accepted 18 May 2016
Available online 19 May 2016

Keywords:
CCL2 decoy
Glycosaminoglycans
Anti-inflammatory
Multiple sclerosis

ABSTRACT

Multiple Sclerosis, a chronic inflammatory demyelinating disease of the central nervous system, involves an increased expression of monocyte chemotactic protein 1 MCP1-/CCL2. For exerting its chemotactic effects, chemokine binding to glycosaminoglycans (GAGs) is required and therefore this interaction represents a potential target for therapeutic intervention. We have designed an anti-inflammatory decoy variant, Met-CCL2 (Y13A S21K Q23R), embodying increased affinity for GAGs as well as knocked-out GPCR activation properties. This non-signalling dominant-negative mutant is shown here to be able to displace wild type CCL2 from GAGs by which it is supposed to interfere with the chemokine-related inflammatory response. *In vivo*, the anti-inflammatory properties were successfully demonstrated in a murine model of zymosan-induced peritonitis as well as in an experimental autoimmune encephalomyelitis, a model relevant for multiple sclerosis, where the compound lead to significantly reduced clinical scores due to

Abbreviations: MCP-1/CCL2, monocyte chemoattractant protein-1/; GPCR, G-protein coupled receptor; GAG, glycosaminoglycan ECM extracellular matrix; EAE, experimental autoimmune encephalomyelitis; MS, multiple sclerosis; CNS, central nervous system; MOG, myelin-oligodendrocyte-glycoprotein.

* Corresponding author at: Institute of Pharmaceutical Sciences, Department of Pharmaceutical Chemistry, University of Graz, Schubertstraße 1/1, 8010, Graz, Austria.
E-mail address: andreas.kungl@uni-graz.at (A.J. Kungl).
[1] Present address: School of Pharmacy, University of Nottingham, University Park, Nottingham, NG7 2RD, UK.

http://dx.doi.org/10.1016/j.neulet.2016.05.037

Experimental autoimmune encephalomyelitis

reduction of cellular infiltrates and demyelination in spinal cord and cerebellum. These findings indicate a promising potential for future therapeutic development.

1. Introduction

Chemokines are small secreted proteins that direct leukocyte trafficking from the lumen of blood vessels into the inflamed surrounding tissue [1]. Bound to glycosaminoglycans (GAGs, see below) on the endothelium, chemokines are retained at the site of action and are presented in their active conformation towards the attracted leukocytes [2]. Once activated *via* chemokine-specific GPCRs, the target blood cells migrate through the endothelial blood vessel cell layer to enter the site of tissue inflammation and to further induce and to boost the host immune response [3].

Monocyte chemoattractant protein-1 (MCP-1/CCL2) is a member of the chemokine-β family (CC chemokines), specifically activates monocytes and lymphocytes and is found in a variety of diseases that feature a monocyte-rich inflammatory component, such as atherosclerosis [4], rheumatoid arthritis [5] and congestive heart failure [6]. Most notably, there is also evidence that CCL2 plays a crucial role in the disease pathogenesis of Multiple Sclerosis (MS) [7,8].

MS is an inflammatory disease of the central nervous system (CNS). It is caused by infiltrating leukocytes damaging myelin and axons, ultimately leading to extensive and chronic neurodegeneration [9,10]. In this context, CCL2 is described to be responsible for CCR2-bearing leukocyte infiltration into the MS lesions of the CNS, but also for T-cell and monocyte migration within the CNS parenchyma. Moreover, CCL2 expression is altered depending on disease activity [11]. Particularly important is the reported observation that in active demyelinating as well as in chronic active MS lesions, reactive hypertrophic astrocytes are strongly immunoreactive for CCL2, suggesting a significant role for CCL2 in the recruitment and activation of myelin-degrading macrophages and thereby contributing to the evolution of MS [12]. Perivascular and parenchymal foamy macrophages do not express CCL2 protein and are likely to contribute to resolution of inflammation by inhibiting further lesion development and promoting lesion repair [13,14]. On this line of evidence it has recently been reported that in a murine model of experimental autoimmune encephalomyelitis, mice with conditional astroglial ablation of CCL2 showed a reduced severity of pathology due to less spinal cord axonal loss [15]. Additionally, CCL2 significantly increases the permeability of the blood-brain barrier *in vivo* and thereby facilitates leukocyte migration during inflammation [16].

As mentioned above, chemokine activity *in vivo* was shown to be dependent on the interaction with glycosaminoglycans (GAGs) [2]. This means, that only the triple complex consisting of chemokine, chemokine-specific GPC receptor, and GAG co-receptor gives the fully functional entity for chemotaxis *in vivo*. These particular glycans are linear, negatively charged polysaccharides which consist of repeating disaccharide units of an amino sugar and a uronic acid [17]. Most of them are covalently attached to a core protein to form the so-called proteoglycans localized in the cell membrane or in the extracellular matrix [18]. The physiologically most relevant GAG types on cell surfaces and in the extracellular matrix are heparan sulfate and chondroitin sulfate which differ from one another in the disaccharide unit composition, the chain length and the degree of sulfation [19]. In fact, post-polymerization modifications, which include N-, 2-O, and 6-O sulfation as well as epimerization of GlcA into IdoA, provide high structural complexity within GAGs and allow the generation of particular oligosaccharide sequences that are supposed to be specific for their protein ligands, as it has been shown for antithrombin [20] and for basic fibroblast growth factor [21]. The sulfation patterns are cell type and tissue specific and are tightly regulated developmentally and pathophysiologically [22–24]. In the CNS GAGs/proteoglycans can be found as ECM components and in the basement membrane [25,26]. Although specificity/selectivity in the chemokine/GAG interaction has not been fully elucidated so far, the great variety in GAG structures on the one side and the reported different affinities for GAGs displayed towards chemokines on the other side, suggest that chemokines interact with disease specific GAG structures *in vivo* [27,28].

Applying a rational design approach based the CellJammer® Technology [29] human pro-inflammatory CCL2 was altered to an anti-inflammatory chemokine decoy protein with increased glycan binding affinity, as previously reported by Piccinini et al. [30] and was shown to limit neointima formation and myocardial ischemia/reperfusion injury in mice [31].

In this letter we describe the investigation of the anti-inflammatory activity of Met-CCL2 (Y13A S21K Q23R) in animals using the mechanistic inflammatory model of zymosan-induced peritonitis as well as a disease relevant model of Multiple Sclerosis, the experimental autoimmune encephalomyelitis (EAE).

2. Materials and methods

2.1. Design, expression and purification

The CCL2 decoy Met-CCL2 (Y13A S21K Q23R) was designed on the basis of human mature CCL2 (1–76) (Swiss-Prot # P13500) by introducing 3 mutations in order to abolish receptor binding (Y13A) as well as to increase the affinity for its glycan ligand with additional positive amino acids (S21K Q23R) on both sides of the known GAG binding motif. Furthermore, Met-CCL2 constructs were generated in the background of a M64I mutation, which alters neither binding nor activity, however improves homogeneity of the mutants by eliminating the possibility of methionine sulfoxide species on position 64 [32]. The leading N-terminal Met residue is a result of the recombinant protein expression in *E. coli*. It was not cleaved off after expression since it did not compromise the heparan sulfate binding properties of the protein [30].

Met-CCL2 and Met-CCL2 (Y13A S21K Q23R) were expressed and purified as described previously [30]. During the purification process, good lab standard practices were applied to reduce endotoxin contents of protein samples by working with endotoxin-free plastic ware and by rinsing glass ware and chromatographic equipment with concentrated NaOH. The final bacterial endotoxin content of the chemokine mutant samples was determined by the limulus amebocyte lysate test (BioWhittaker, Cambrex). Typical values obtained were in the < 0.18 EU/ml range.

2.2. ELISA-like competition (ELICO)

2.5 μg GAG/250 nM biotinylated Met-CCL2 was diluted in PBS and coated onto Iduron (Manchester, UK) GAG-binding plates over night at RT. A washing step was performed to remove unbound biotinylated chemokine and GAG, followed by a 2 h incubation with different Met-CCL2 (Y13A S21K Q23R) concentrations diluted in

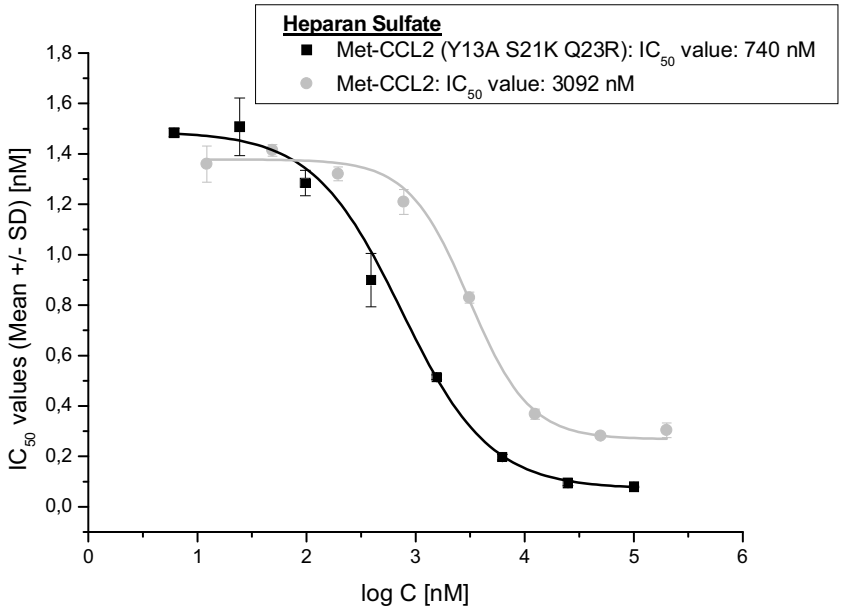

Fig. 1. ELICO displacement assay of Met-CCL2 (Y13A S21K Q23R) (black) in comparison to Met-CCL2 (grey) competing with biotinylated Met-CCL2 for binding to heparan sulfate. The normalized absorption values (mean+/−SD) at 450 nm (TMB) were plotted against the concentration of the proteins. IC_{50} values were determined by competition analysis of the displacement curves. (For interpretation of the references to colour in this figure legend, the reader is referred to the web version of this article.)

PBS starting from 100 μM to 6 nM measuring each concentration in triplicates. To detect the remaining biotinylated Met-CCL2 we used an ELISA-like setup, therefore after another washing step we incubated the plates with high sensitivity Streptavidin HRP (Thermo Scientific, Waltham, MA, USA) diluted in 0.2% dry milk that binds to the non-displaced biotinylated chemokine on the plate. After another hour incubation at RT and removal of unbound Streptavidin by a washing step, we analysed the plate by adding the substrate Tetramethylbenzidine (TMB), resulting in a blue colour change. After stopping the reaction with sulphuric acid the absorbance at 450 nm was read in a Beckman Coulter DTX 800 Multimode Detector (Beckman Coulter, Austria). The reference (OD620) values were subtracted from the sample values (OD450) and the Mean and Standard Deviation was calculated. Data analysis was performed using specialized statistical software Origin® (GE Healthcare, Chalfont St Giles, UK).

2.3. Animal experiments

Animal care and handling procedures were performed in accordance with the European guidelines and all the experiments received prior approval from the local ethics committees.

2.3.1. Met-CCL2 (Y13A S21K Q23R) pharmacokinetics

Male C57BL/6 mice (SIPPR-BK Laboratory, Shanghai) were group housed under a 12:00 h light/dark cycle, provided with food and water *ad libitum* and allowed to acclimatize for at least 1 week before the experiment. Animals were treated with Met-CCL2 (Y13A S21K Q23R) at a dose of 40 μg/kg intravenously (i.v.) or at 40 μg/kg and 400 μg/kg intrapritoneally (i.p.). At prefixed times post administration approximately 200 μL blood was collected *via* retro-orbital from deeply isoflurane anesthetized mice (n = 3/time/dose) and transferred to a centrifuge tube and kept on wet ice for 30 min. Serum was separated by centrifugation at 5000 rpm for 15 min at 4 °C. The resulting serum was stored at −80 °C until subjected to ELISA for quantification. The ELISA (h-MCP-1, Anogen Cat. No.:EL0009) was validated for cross reactivity with Met-CCL2 (Y13A S21K Q23R) and performed according to the manufacturer's instructions. The lower limit of detection was 50 pg/ml.

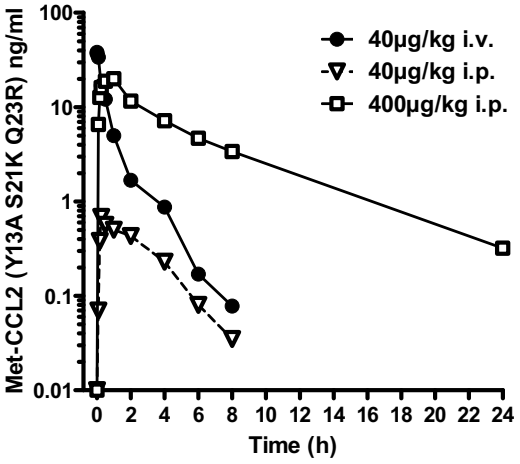

Fig. 2. Pharmacokinetic profiles of Met-CCL2 (Y13A S21K Q23R) administered at the dose of 40 μg/kg i.v. or 40 and 40 μg/kg i.p. in male C57BL/6 mice. Serum levels were evaluated using a commercial h-MCP-1 ELISA validated to recognize our protein.

2.3.2. Zymosan-induced peritonitis

Male C57BL/6 mice (Charles River, UK) were group housed under a 12:00 h light/dark cycle, provided with food and water *ad libitum* and allowed to acclimatize for at least 1 week before the experiment. On the experiment day, all the animals were injected with 0.2 mg of zymosan (Sigma-Aldrich) intraperitoneally (time 0) to induce peritonitis. Pharmacological treatments with vehicle (sterile PBS i.v. n = 8), with dexamethasone (1 mg/kg s.c. n = 8)or with Met-CCL2 (Y13A S21K Q23R) (40 μg/kg i.v. n = 8) were performed 1 h and 6 h post zymosan injection. Sham animals (intraperitoneal treatment with saline n = 3) were used as controls. 24 h post zymosan intraperitoneal administration, the peritoneal cavities were washed with 3 mL of PBS containing 3 mM EDTA and the number of total leukocytes was determined by staining with Turk's solution (0.01% crystal violet in 3% acetic acid) and counting using

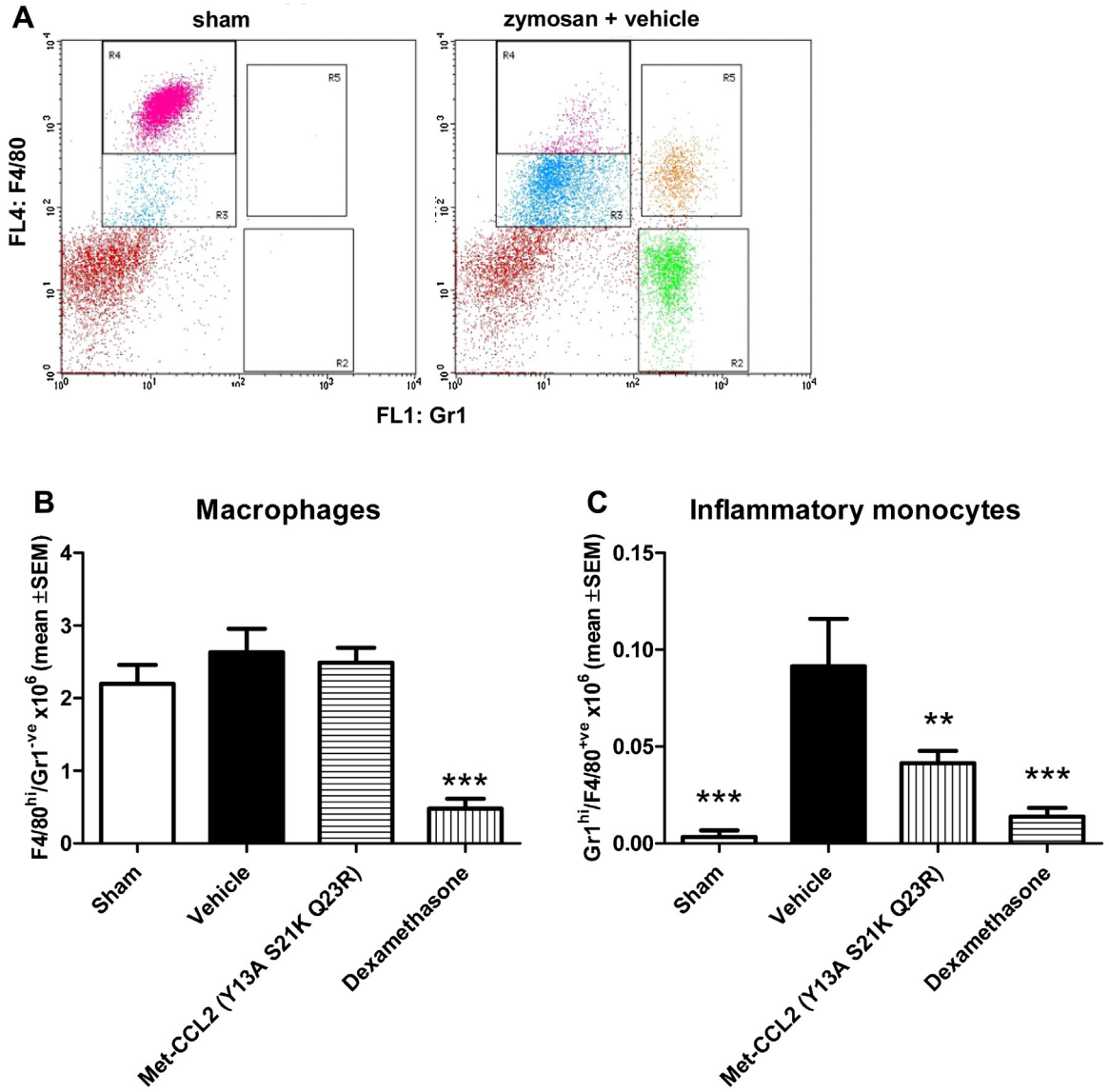

Fig. 3. Zymosan-induced peritonitis in C57BL/6 male mice caused a strong infiltration of cells, which were characterized by FACS using the forward and side scatter characteristics. Further gating criteria were set using cells collected in sham (panel A left) and zymosan + vehicle (panel A right). FL1 channel on x axis (Gr-1), FL4 on y axis (F4/80). $Gr1^{high}/F4/80^{-ve}$: granulocyte population (R2); $F4/80^{high}/Gr1^{-ve}$: macrophage (R3 + R4); Cells positive for both antigens indicated the inflammatory monocyte population (R5). $Gr1^{high}/F4/80^{+ve}$ inflammatory monocytes. Based on this gating, dexamethasone showed activity on all cell types (B,C), while Met-CCL2 (Y13A S21K Q23R) showed specific activity on the inflammatory monocytes (C). Anova followed by ANOVA followed by Dunnett's multiple comparison. $^{**}p < 0.01$; $^{***}p < 0.001$.

a Neubauer hemocytometer and a light microscope. Appropriate aliquots were then stained using specific antibodies (FITC GR-1 (Ly6 G and Ly6C), clone RB6-8C5; APC F4/80; eBioscience) and flow cytometric analysis was performed using a FACScan analyzer (Becton Dickinson). Cells were initially characterized using the forward and side scatter characteristics, to distinguish between the three distinct cell populations (lymphocytes, monocytes/macrophages and granulocytes). Further gating was performed using cells collected in sham and zymosan + vehicle. Cells positive for Gr1 and negative for F4/80 determined the granulocyte population. Cells positive for F4/80 and negative for Gr1 determined the macrophage population. Cells positive for both antigens indicated the inflammatory monocyte population. Determination of positive and negative populations was performed based on the control staining with an irrelevant IgG isotype labeled with FITC or APC (both from eBioscience). Once determined, gating quadrants were rigorously maintained for the analyses of the cells all the groups. The experiment was repeated twice, and data from one experiment are presented.

2.3.3. MOG-induced experimental autoimmune encephalomyelitis (EAE)

Ten-week old, female C57BL/6 mice (Charles River, NL,) were group housed under a 12:00 h light/dark cycle, provided with food and water *ad libitum* and allowed to acclimatize for at least 2 weeks before the experiment. During the experiment additional mixture of powder food and water was given into the animal's cage. On day 0 and day 7 the mice were immunized with 200 μg MOG(35–55) (Isogen life science) in an emulsion of PBS and complete Freund's adjuvant supplemented with *M. tuberculosis* H37RA (both Difco Laboratories) administered subcutaneously in both flanks. On day 0 and on day 2 the mice additionally received i.v. 300 ng Pertussis toxin (Calbiochem). Pharmacological interventions were administered from day from day 7 post immunization (n = 10/group) when no clinical signs of the pathology are present, but an increase in circulating chemokines (including murine CCL2, also known as JE) is already reported, and was continued once daily for 21 days (day 28 post immunization) The mice were treated with vehicle i.p., dexamethasone 1 mg/kg i.p., and 40, 200 and

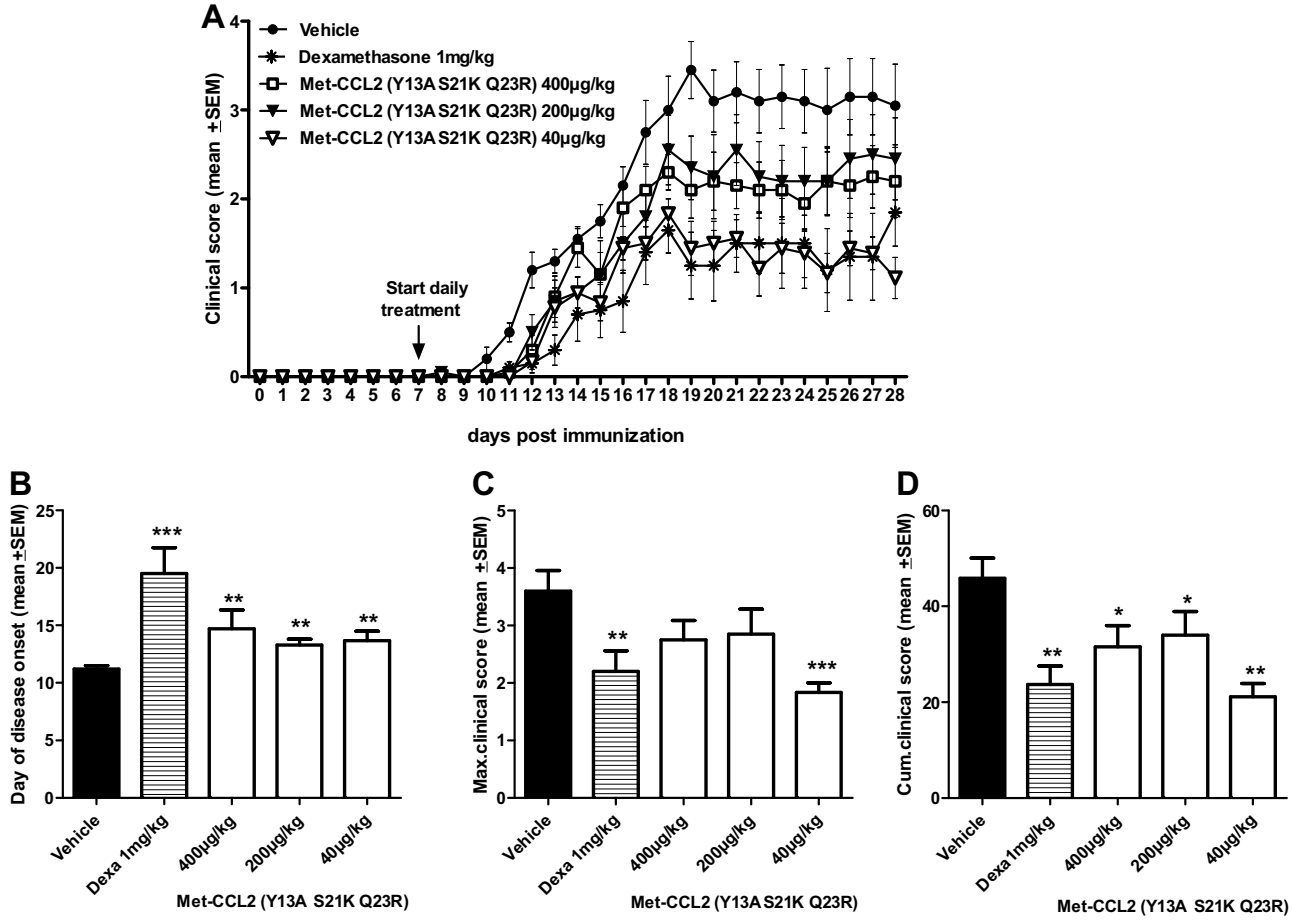

Fig. 4. MOG(35–55) EAE was induced in C57BL/6 female mice (n = 10/group). Main parameters for disease severity are reported as follows, (A) daily clinical score; data were analysed using repeated-measures ANOVA ($p < 0.001$), followed by LSD: dexamethasone $p < 0.001$, Met-CCL2 (Y13A S21K Q23R) 40 μg/kg $p < 0.001$, 200 μg/kg and 400 μg/kg$p < 0.05$ vs vehicle treatment; (B) day of disease onset; (C) maximal clinical score, and (D) cumulative clinical score. Kruskal-Wallis followed by Mann-Whitney *U* test. $^{*}p < 0.05$; $^{**}p < 0.01$; $^{***}p < 0.001$ vs Vehicle.

400 μg/kg Met-CCL2 (Y13A S21K Q23R) i.p. During the experiment mice were monitored daily and body weight was recorded. EAE score was assessed daily using the following scoring system: 0 = no disease, 0.5 = tail paresis or partial paralysis, 1 = complete tail paralysis, 2 = paraparesis:limb weakness and tail paralysis, 2.5 = partial limb paralysis, 3 = complete hind- or front limb paralysis, 3.5 = paraplegia, 4 = quadriplegia, moribund, 5 = death due to EAE. These data were used also to determine the day of onset, defined as the first of three consecutive days on which a cumulative clinical score of at least three was reached, the maximum clinical score and the cumulative clinical score. On day 28 mice were euthanized and the central nervous system collected, fixed and stored in formaldehyde. Spinal cord and cerebellum of each mouse in the vehicle, dexamethasone and Met-CCL2 (Y13A S21K Q23R) 40 μg/kg groups were embedded in paraffin. Sections (5 μm, separated by 50 μm) were generated and stained using Hematoxylin/Eosin and scored for cellular infiltrates or stained using Kluver-Barrera and assessed for demyelinization. In both cases a minimum of three slides/animals/tissue were quantified using a qualitative scale of 0–4.

2.4. Statistical analysis

All data are reported as means + standard errors of the means (SEM). Pharmacokinetic profiles of Met-CCL2 (Y13A S21K Q23R) were evaluated with WinNonLin using non-compartment model. For the zymosan-induced peritonitis, statistical analysis was performed using ANOVA followed by Dunnett's multiple comparison using GraphPad Prism software. The EAE data were analysed using the Kruskal-Wallis test followed by the Mann-Whitney *U* test. The significance of differences between the treatment groups in the time-dependent outcome parameters (daily clinical score and body weight) were tested using repeated-measures ANOVA, followed by LSD post hoc. Analysis was performed using SPSS17 for Windows. In both cases, the significance level was set at $p < 0.05$. Significance is reported as follows: $^{*}p < 0.05$; $^{**}p < 0.01$; $^{***}p < 0.01$.

3. Results

3.1. ELISA-like competition assay

Since our mutant proteins were designed in a way to displace the corresponding wild type chemokine from its GAG co-receptor, we have developed a novel competition assay which gives IC_{50} values derived from displacement curves rather than K_d values obtained from bi-molecular binding isotherms [33] . In our assay we have tried to mimic the glycocalyx of cell surfaces by coating heparan sulfate onto specially prepared microtiter plates. We then added biotinylated Met-CCL2 which was, after washing, displaced either by unmodified Met-CCL2 or by Met-CCL2 (Y13A S21K Q23R) in a concentration-dependent manner (Fig. 1). The IC_{50} values derived from these experiments clearly show that the mutant chemokine is a much better competitor for bound Met-CCL2 (giving an IC_{50} value of 740 nM) than unmodified Met-CCL2 (IC_{50} = 3092 nM).

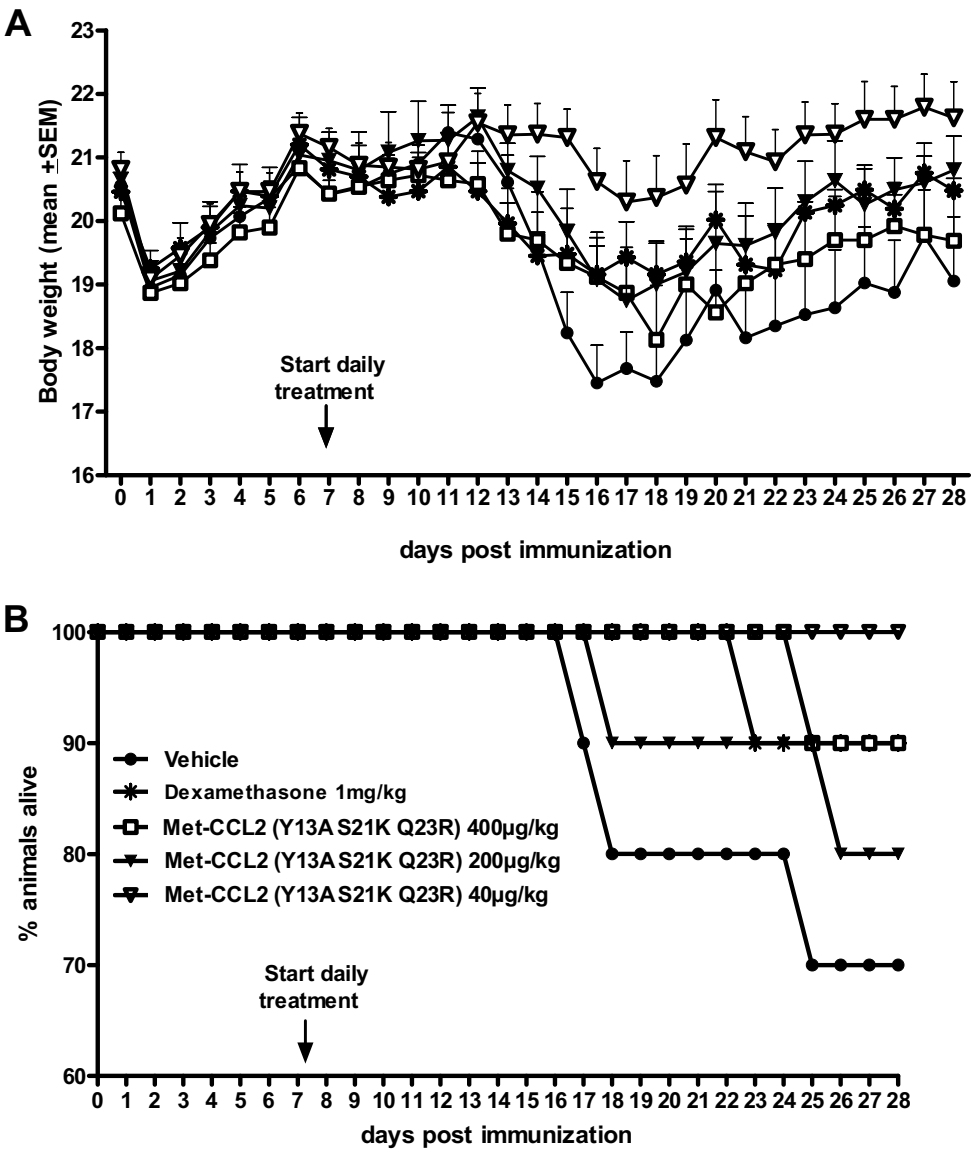

Fig. 5. MOG(35–55) EAE was induced in C57BL/6 female mice. (A) survival curves show up to a 30% mortality in the vehicle group, that was reduced by Met-CCL2 (Y13A S21K Q23R) treatment, with no dead animals in the 40 μg/kg group. (B) daily body weight data were analysed using repeated-measures ANOVA ($p < 0.001$), followed by LSD: Met-CCL2 (Y13A S21K Q23R) 40 μg/kg $p < 0.001$.

3.2. Met-CCL2 (Y13A S21K Q23R) pharmacokinetics

Pharmacokinetic profiles of Met-CCL2 (Y13A S21K Q23R) after i.v. and i.p. administration are shown in Fig. 2. After i.v. administration the protein was eliminated, as expected, relatively fast, with a serum half-life ($t_{1/2}$) of 1.08 h, and an area under the curve ($AUC_{0\text{-last}}$) of 22.3 h ng/mL. After i.p. administration at 40 μg/kg the protein was absorbed with a time of maximal concentration (T_{max}) of 15 min, the maximal serum concentration (C_{max}) of 0.69 ng/ml and the $AUC_{0\text{-last}}$ of 4.86 h ng/mL, the $t_{1/2}$ was of 1.75 h. After i.p. administration at 400 μg/kg the protein was absorbed with T_{max} of 1 h at a C_{max} of 19.9 ng/ml and the $AUC_{0\text{-last}}$ of 473 h ng/mL, the $t_{1/2}$ was of 4.13 h. No levels were detectable in the 24 h samples of mice treated i.v. or i.p. at the dose of 40 μg/kg.

3.3. Zymosan-induced peritonitis

In this study Met-CCL2 (Y13A S21K Q23R) at a concentration of 40 μg/kg i.v. was directly compared to the immunosuppressant dexamethasone at a dose of 1 mg/kg s.c. While the latter reduced the total cell infiltrate (data not shown), Met-CCL2 (Y13A S21K Q23R) effects were specifically observed on a particular subset of monocytes expressing F4/80 as well as Gr1 (Ly6C and Ly6G) marker, and considered to be a pro-inflammatory subset of monocytes (Fig. 3A R5 and 3C), while not affecting the number of residential macrophages ($F4/80^{high}/Gr1^{-ve}$, Fig. 3A R3-4 and 3B), that are thought to contribute to the pathology resolution [34].

3.4. MOG-induced experimental autoimmune encephalomyelitis (EAE)

Immunization with the MOG(35–55) protein successfully induced EAE in vehicle treated animals, with an incidence of 100%. In our study, administration of 40, 200 and 400 μg/kg of Met-CCL2 (Y13A S21K Q23R) i.p. from day 7 post immunization onwards significantly delayed the day of onset of the disease independently of the dose (Fig. 4B) and resulted in an overall better clinical score (Fig. 4A), a reduced maximal disease severity (Fig. 4C), and a cumulative clinical score (Fig. 4D). Additionally, Met-CCL2 (Y13A S21K Q23R) promoted preservation of body weight (Fig. 5A) and

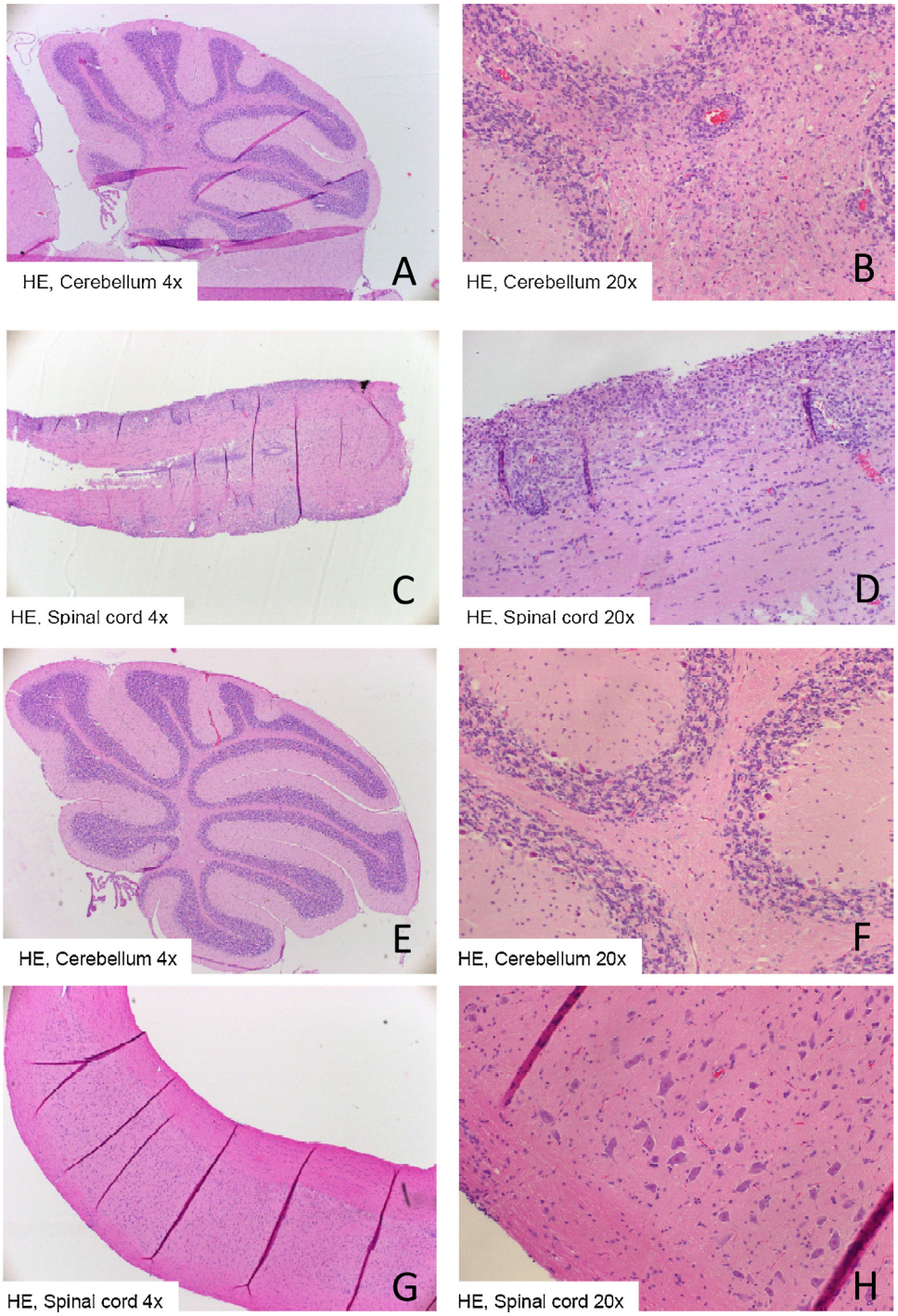

Fig. 6. Histological analysis of the MOG(35–55)-induced EAE C57BL/6 female mice euthanized at day 28 post immunization. Spinal cord and cerebellum of each mouse in the vehicle, dexamethasone and Met-CCL2 (Y13A S21K Q23R) 40 μg/kg groups were embedded in paraffin. Sections (5 μm, separated by 50 μm) were generated and stained using Hematoxylin/Eosin and scored for cellular infiltrates. Representative images at two different magnifications: (A) vehicle cerebellum 4 x; (B) vehicle cerebellum 20 x; (C) vehicle spinal cord 4x; (D) vehicle spinal cord 20x; (E) Met-CCL2 (Y13A S21K Q23R) 40 μg/kg cerebellum 4x; (F) Met-CCL2 (Y13A S21K Q23R) 40 μg/kg cerebellum 20x; (G) Met-CCL2 (Y13A S21K Q23R) 40 μg/kg spinal cord 4x; (H) Met-CCL2 (Y13A S21K Q23R) 40 μg/kg spinal cord 4x. Animals in the dexamethasone groups presented similar features as animals in the Met-CCL2 (Y13A S21K Q23R) 40 μg/kg group.

increased survival (Fig. 5B). In EAE animals, where progressive paralysis reduces animal motility and impacts the ability of the animals to feed, even if food if provided into the cage, a diminished loss of body weight is considered to reflect an index of animal general well-being.

Histological analysis showed that compared to the vehicle-treated control group Met-CCL2 (Y13A S21K Q23R) and dexamethasone significantly reduced the influx of inflammatory cells to the cerebellum and the spinal cord, (cerebellum: vehicle 1.55 + 0.3, Met-CCL2 (Y13A S21K Q23R) 0.35 + 0.1***, dexamethasone 0.1 + 0.2***; spinal cord: vehicle 1.81 + 0.4, Met-CCL2 (Y13A S21K Q23R) 0.33 + 0.1***, dexamethasone0.37 + 0.17*** see Fig. 6A–H) as well as demyelination (cerebellum: vehicle 1.33 + 0.4, Met-CCL2 (Y13A S21K Q23R) 0.44 + 0.2, dexamethasone 0.08 + 0.03; spinal cord: vehicle 3.3 + 0.3, Met-CCL2 (Y13A S21K Q23R) 0.63 + 0.2, dexamethasone 0.63 + 0.3 see Fig. 7A–H).

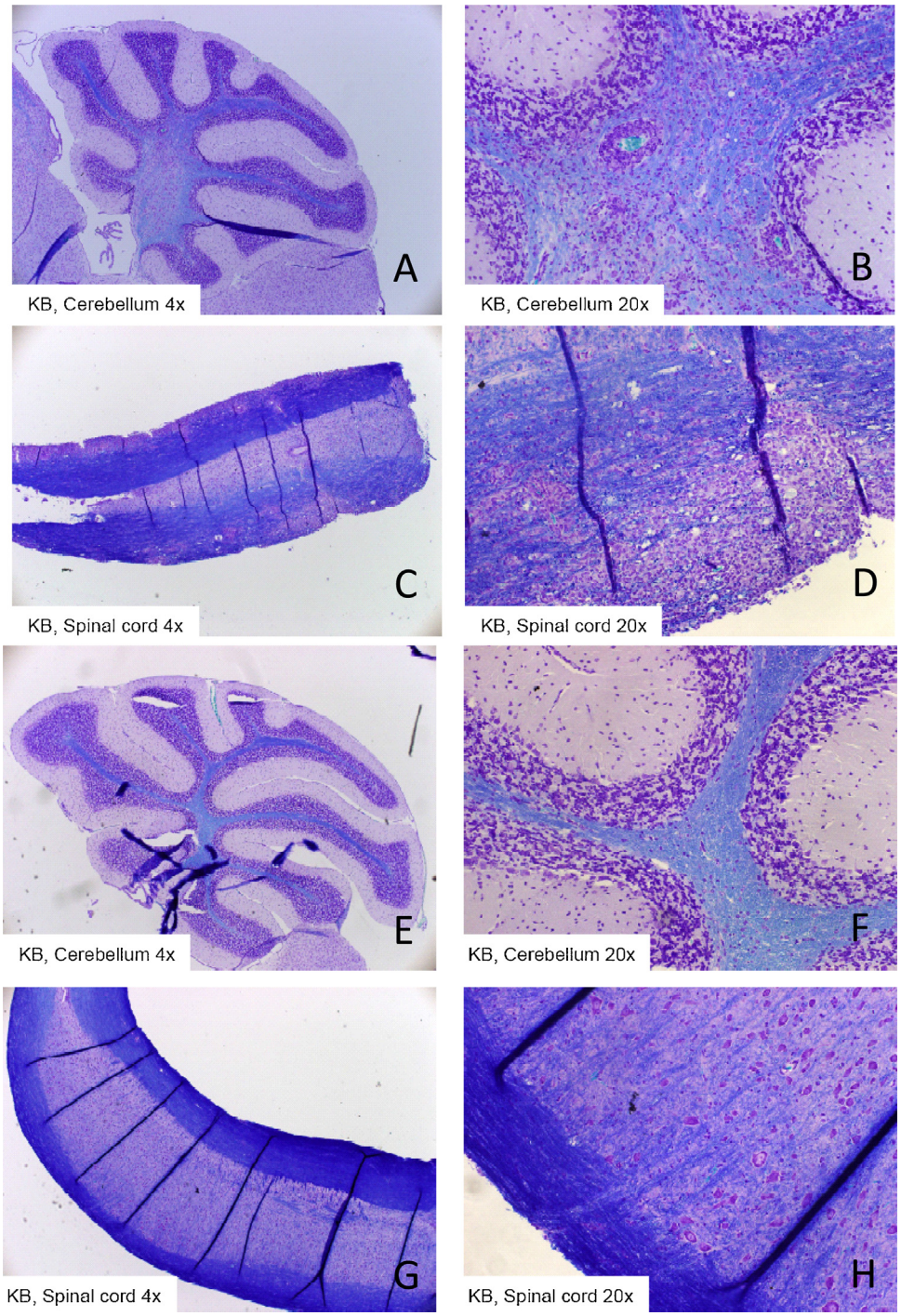

Fig. 7. Histological analysis of the MOG(35–55)-induced EAE C57BL/6 female mice euthanized at day 28 post immunization. Spinal cord and cerebellum of each mouse in the vehicle, dexamethasone and Met-CCL2 (Y13A S21K Q23R) 40 μg/kg groups were embedded in paraffin. Sections (5 μm, separated by 50 μm) were generated and stained using Kluver-Barrera and assessed for demyelinization. Representative images at two different magnifications: (A) vehicle cerebellum 4 x; (B) vehicle cerebellum 20 x; (C) vehicle spinal cord 4x; (D) vehicle spinal cord 20x; (E) Met-CCL2 (Y13A S21K Q23R) 40 μg/kg cerebellum 4x; (F) Met-CCL2 (Y13A S21K Q23R) 40 μg/kg cerebellum 20x; (G) Met-CCL2 (Y13A S21K Q23R) 40 μg/kg spinal cord 4x; (H) Met-CCL2 (Y13A S21K Q23R) 40 μg/kg spinal cord 4x. Animals in the dexamethasone groups presented similar features as animals in the Met-CCL2 (Y13A S21K Q23R) 40 μg/kg group.

4. Discussion

Met-CCL2 (Y13A S21K Q23R) shows higher GAG binding affinity compared to Met-CCL2 but shows impaired CCR2 receptor activation [30]. Here we show that, in addition, the mutant is able to displace the wild type chemokine efficiently from HS chains (see Fig. 1). Since it is proposed that CCL2 *in vivo* is mainly displayed to approaching monocytes/macrophages in a GAG-bound form, the competitive potency (expressed in the IC_{50} value) of a CCL2 mutant is much more relevant parameter than the direct binding of chemokine to its GAG ligand. This relates directly to the proposed mode of action of the CCL2 mutant, namely that it acts like a protein-based GAG antagonist.

The proposed anti-inflammatory effect of the mutant was subsequently tested *in vivo* in a mechanistic model of zymosan- induced peritonitis [35] to allow initial assessment of the dose *in vivo* and

anti-inflammatory/anti-migratory properties, and only then in an animal model of multiple sclerosis, EAE.

In the zymosan- induced peritonitis model we could show that we are able to retain selectivity for the specific cell populations *in vivo*, thereby selectively inhibiting the recruitment of Gr1 and F4/80 double positive cells, considered to be newly recruited inflammatory monocytes, while not affecting macrophages. Moreover, this finding implies that the mutant has found its appropriate endothelial GAG target and gained the energetically preferred active form.

MOG-induced EAE in mice is recognized to be a good experimental model of human MS pathogenesis [7,36,37], and in the present study MOG (35–55) successfully induced EAE in all vehicle treated animals. The severity of the pathology caused death in some animals. By administering the decoy molecule the disease onset could be delayed significantly. Furthermore, the maximal clinical score was significantly decreased showing differences in the maximal disease severity that are particularly relevant in terms of quality of life when translated to the human situation. The efficacy of the decoy molecule observed at clinical score level correlated, as expected, with changes at histological level in which vehicle-treated animals showed massive infiltration of inflammatory cells in the spinal cord and in the perivascular region of the cerebellum, whereas almost no inflammatory cell infiltrates were present in decoy treated animals. Moreover, the myelin exhibited normal features in decoy treated animals in contrast to pronounced demyelination in the spinal cord of vehicle-treated animals.

The observed effect could not be due to inhibition of bone marrow cell mobilization, as has been reported for inhibitors of the GPC receptor CCR2 [38,39], since we have already shown that Met-CCL2 (Y13A S12K Q23R) does not bind or activate, CCR2 [30]. Surprisingly, Met-CCL2 (Y13A S12K Q23R) activity on the different parameters measured was not dose-dependent, with the lowest dose administered being the most effective. This is not due to a non-linear exposure, since the PK profile for the protein seems to be linear in this range (at least in term of AUC). The binding affinities of chemokines to GAGs are known to not be dose dependent [40] with loss of affinity at too high concentrations, therefore, even if it seems unlikely from the plasma concentration measured during the PK assessment, we cannot exclude that at the two higher doses the binding equilibrium at the GAG target was moving toward dissociation. Alternatively, it is possible that the apparent differences observed between doses are due to the limited number of animals used in the experiment, in which even the survival of one more animal in a treatment group may affect the overall clinical score profile, suggesting that plateau activity is already achieved at a dose of 40 μg/kg. This aspect should be further analysed using a broader range of doses and in a time-course experiment, with direct assessment of cell type infiltrates in the CNS of the animals by either immunohistochemistry, or FACs analysis.

However, the clinical development of a protein requesting daily administration is not foreseeable (and already difficult to assess preclinically, since twice a day chronic treatment is not feasible in mice), and strategies to extend its exposure, such as by conjugation with carrier proteins (*e.g.* human serum albumin) are currently under evaluation [41] and will be further tested in MS animal models.

What we can state from the current data is that the dose of 40 μg/kg Met-CCL2 (Y13A S12K Q23R) was, in both the experimental peritonitis and in the EAE model, at least as effective as dexamethasone in reducing inflammation and consequent demyelination. It has to be considered that dexamethasone was administered in this study at a dose highly effective in mice, but toxic if translated to a human dose.

In conclusion, we have confirmed that the engineered increased GAG binding affinity of Met-CCL2 (Y13A S21K Q23R), which was measured *in vitro*, can be translated into anti-inflammatory activities *in vivo*. Our approach of targeting glycans for interfering with CCL2 signalling in CNS inflammation is completely unique, and opens a possible new avenue for therapeutic intervention that may be applicable to MS treatment.

Acknowledgments

We would like to thank M. Perretti, T. Montero-Melendez and V. Brancaleone from William Harvey Research Institute (London UK), and F. Tielen from TNO (Leiden, The Netherlands). M. Gschwandtner is recipient of a DOC Fellowship of the Austrian Academy of Sciences at the Institute of Pharmaceutical Sciences, University of Graz.

References

[1] M. Baggiolini, Chemokines and leukocyte traffic, Nature 392 (1998) 565–568.
[2] A.E.I. Proudfoot, T.M. Handel, Z. Johnson, E.K. Lau, P. LiWang, I. Clark-Lewis, F. Borlat, T.N.C. Wells, M.H. Kosco-Vilbois, Glycosaminoglycan binding and oligomerization are essential for the in vivo activity of certain chemokines, Proc. Natl. Acad. Sci. U. S. A. 100 (2003) 1885–1890.
[3] C.R. Parish, Heparan sulfate and inflammation, Nat. Immunol. 6 (2005) 861–862.
[4] J.R. Harrington, The role of MCP-1 in atherosclerosis, Stem Cells 18 (2000) 65–66.
[5] M. Harigai, M. Hara, T. Yoshimura, E.J. Leonard, K. Inoue, S. Kashiwazaki, Monocyte chemoattractant protein-1 (MCP-1) in inflammatory joint diseases and its involvement in the cytokine network of rheumatoid synovium, Clin. Immunol. Immunopathol. 69 (1993) 83–91.
[6] P. Aukrust, T. Ueland, F. Müller, A.K. Andreassen, I. Nordøy, H. Aas, J. Kjekshus, S. Simonsen, S.S. Frøland, L. Gullestad, Elevated circulating levels of CC chemokines in patients with congestive heart failure, Circulation 97 (1998) 1136–1143.
[7] L. Izikson, R.S. Klein, I.F. Charo, H.L. Weiner, A.D. Luster, Resistance to experimental autoimmune encephalomyelitis in mice lacking the CC chemokine receptor (CCR2), J. Exp. Med. 192 (2000) 1075–1080.
[8] D.J. Mahad, R.M. Ransohoff, The role of MCP-1 (CCL2) and CCR2 in multiple sclerosis and experimental autoimmune encephalomyelitis (EAE), Semin. Immunol. (2003) 23–32, Elsevier.
[9] A. Compston, A. Coles, Multiple sclerosis, Lancet 372 (2008) 1502–1517.
[10] C.M. Poser, V.V. Brinar, Diagnostic criteria for multiple sclerosis, Clin. Neurol. Neurosurg. 103 (2001) 1–11.
[11] D. Mahad, S. Howell, M. Woodroofe, Expression of chemokines in the CSF and correlation with clinical disease activity in patients with multiple sclerosis, J. Neurol. Neurosurg. Psychiatry 72 (2002) 498–502.
[12] R.-N.E. Dogan, A. Elhofy, W.J. Karpus, Production of CCL2 by central nervous system cells regulates development of murine experimental autoimmune encephalomyelitis through the recruitment of TNF-and iNOS-expressing macrophages and myeloid dendritic cells, J. Immunol. 180 (2008) 7376–7384.
[13] P. Van Der Voorn, J. Tekstra, R.H. Beelen, C.P. Tensen, P. Van Der Valk, C.J. De Groot, Expression of MCP-1 by reactive astrocytes in demyelinating multiple sclerosis lesions, Am. J. Pathol. 154 (1999) 45–51.
[14] C. McManus, J.W. Berman, F.M. Brett, H. Staunton, M. Farrell, C.F. Brosnan, MCP-1, MCP-2 and MCP-3 expression in multiple sclerosis lesions: an immunohistochemical and in situ hybridization study, J. Neuroimmunol. 86 (1998) 20–29.
[15] M. Moreno, P. Bannerman, J. Ma, F. Guo, L. Miers, A.M. Soulika, D. Pleasure, Conditional ablation of astroglial CCL2 suppresses CNS accumulation of M1 macrophages and preserves axons in mice with MOG peptide EAE, J. Neurosci. 34 (2014) 8175–8185.
[16] S.M. Stamatovic, P. Shakui, R.F. Keep, B.B. Moore, S.L. Kunkel, N. Van Rooijen, A.V. Andjelkovic, Monocyte chemoattractant protein-1 regulation of blood–brain barrier permeability, J. Cereb. Blood Flow Metab. 25 (2005) 593–606.
[17] J.D. Esko, U. Lindahl, Molecular diversity of heparan sulfate, J. Clin. Invest. 108 (2001) 169.
[18] J.R. Bishop, M. Schuksz, J.D. Esko, Heparan sulphate proteoglycans fine-tune mammalian physiology, Nature 446 (2007) 1030–1037.
[19] J.D. Esko, K. Kimata, U. Lindahl, Proteoglycans and Sulfated Glycosaminoglycans. Essentials of Glycobiology, Cold Spring Harbor Laboratory Press, 2009.
[20] L. Jin, J.P. Abrahams, R. Skinner, M. Petitou, R.N. Pike, R.W. Carrell, The anticoagulant activation of antithrombin by heparin, Proc. Natl. Acad. Sci. 94 (1997) 14683–14688.
[21] J.E. Turnbull, D. Fernig, Y. Ke, M.C. Wilkinson, J.T. Gallagher, Identification of the basic fibroblast growth factor binding sequence in fibroblast heparan sulfate, J. Biol. Chem. 267 (1992) 10337–10341.
[22] E. Feyzi, T. Saldeen, E. Larsson, U. Lindahl, M. Salmivirta, Age-dependent modulation of heparan sulfate structure and function, J. Biol. Chem. 273 (1998) 13395–13398.
[23] N.M. Carter, S. Ali, J.A. Kirby, Endothelial inflammation: the role of differential expression of *N*-deacetylase/*N*-sulphotransferase enzymes in alteration of the

immunological properties of heparan sulphate, J. Cell Sci. 116 (2003) 3591–3600.
[24] R. Sasisekharan, Z. Shriver, G. Venkataraman, U. Narayanasami, Roles of heparan-sulphate glycosaminoglycans in cancer, Nat. Rev. Cancer 2 (2002) 521–528.
[25] E. Ruoslahti, Brain extracellular matrix, Glycobiology 6 (1996) 489–492.
[26] J. Van Horssen, C.D. Dijkstra, H.E. De Vries, The extracellular matrix in multiple sclerosis pathology, J. Neurochem. 103 (2007) 1293–1301.
[27] G.S. Kuschert, F. Coulin, C.A. Power, A.E. Proudfoot, R.E. Hubbard, A.J. Hoogewerf, T.N. Wells, Glycosaminoglycans interact selectively with chemokines and modulate receptor binding and cellular responses, Biochemistry 38 (1999) 12959–12968.
[28] J.D. Esko, S.B. Selleck, Order out of chaos: assembly of ligand binding sites in heparan sulfate, Annu. Rev. Biochem. 71 (2002) 435–471.
[29] T. Adage, A.-M. Piccinini, A. Falsone, M. Trinker, J. Robinson, B. Gesslbauer, A.J. Kungl, Structure-based design of decoy chemokines as a way to explore the pharmacological potential of glycosaminoglycans, Br. J. Pharmacol. 167 (2012) 1195–1205.
[30] A.M. Piccinini, K. Knebl, A. Rek, G. Wildner, M. Diedrichs-Möhring, A.J. Kungl, Rationally evolving MCP-1/CCL2 into a decoy protein with potent anti-inflammatory activity in vivo, J. Biol. Chem. 285 (2010) 8782–8792.
[31] E.A. Liehn, A.-M. Piccinini, R.R. Koenen, O. Soehnlein, T. Adage, R. Fatu, A. Curaj, A. Popescu, A. Zernecke, A.J. Kungl, A new monocyte chemotactic protein-1/chemokine CC motif ligand-2 competitor limiting neointima formation and myocardial ischemia/reperfusion injury in mice, J. Am. Coll. Cardiol. 56 (2010) 1847–1857.
[32] C.D. Paavola, S. Hemmerich, D. Grunberger, I. Polsky, A. Bloom, R. Freedman, M. Mulkins, S. Bhakta, D. McCarley, L. Wiesent, B. Wong, K. Jarnagin, T.M. Handel, Monomeric monocyte chemoattractant protein-1 (MCP-1) binds and activates the MCP-1 receptor CCR2B, J. Biol. Chem. 273 (1998) 33157–33165.
[33] T. Gerlza, B. Hecher, D. Jeremic, T. Fuchs, M. Gschwandtner, A. Falsone, B. Gesslbauer, A.J. Kungl, A combinatorial approach to biophysically characterise chemokine-glycan binding affinities for drug development, Molecules 19 (2014) 10618–10634.
[34] M.N. Ajuebor, A.M. Das, L. Virág, R.J. Flower, C. Szabó, M. Perretti, Role of resident peritoneal macrophages and mast cells in chemokine production and neutrophil migration in acute inflammation: evidence for an inhibitory loop involving endogenous IL-10, J. Immunol. 162 (1999) 1685–1691.
[35] J.L. Cash, G.E. White, D.R. Greaves, Zymosan-induced peritonitis as a simple experimental system for the study of inflammation, Methods Enzymol. 461 (2009) 379–396.
[36] M.K. Racke, Experimental autoimmune encephalomyelitis (EAE), Curr. Protoc. Neurosci. (2001) 9.7.1–9.7.11.
[37] K.J. Kennedy, R.M. Strieter, S.L. Kunkel, N.W. Lukacs, W.J. Karpus, Acute and relapsing experimental autoimmune encephalomyelitis are regulated by differential expression of the CC chemokines macrophage inflammatory protein-1α and monocyte chemotactic protein-1, J. Neuroimmunol. 92 (1998) 98–108.
[38] H. Jung, D.S. Mithal, J.E. Park, R.J. Miller, Localized CCR2 activation in the bone marrow niche mobilizes monocytes by desensitizing CXCR4, PLoS One 10 (2015) e0128387.
[39] Y. Wang, L. Cui, W. Gonsiorek, S.-H. Min, G. Anilkumar, S. Rosenblum, J. Kozlowski, D. Lundell, J.S. Fine, E.P. Grant, CCR2 and CXCR4 regulate peripheral blood monocyte pharmacodynamics and link to efficacy in experimental autoimmune encephalomyelitis, J. Inflamm. (London) 6 (2009) 32.
[40] B. Goger, Y. Halden, A. Rek, R. Mösl, D. Pye, J. Gallagher, A.J. Kungl, Different affinities of glycosaminoglycan oligosaccharides for monomeric and dimeric interleukin-8: a model for chemokine regulation at inflammatory sites, Biochemistry 41 (2002) 1640–1646.
[41] T. Gerlza, S. Winkler, A. Atlic, C. Zankl, V. Konya, N. Kitic, E. Strutzmann, K. Knebl, T. Adage, A. Heinemann, R. Weis, A.J. Kungl, Designing a mutant CCL2-HSA chimera with high glycosaminoglycan-binding affinity and selectivity, Protein Eng. Des. Sel. 28 (2015) 231–240.

5450–5456 *Nucleic Acids Research, 2016, Vol. 44, No. 11* *Published online 20 April 2016*
doi: 10.1093/nar/gkw293

Structure and dynamics of DNA loops on nucleosomes studied with atomistic, microsecond-scale molecular dynamics

Marco Pasi and Richard Lavery*

MMSB, University Lyon I/CNRS UMR 5086, Institut de Biologie et Chimie des Protéines, 7 passage du Vercors, 69367 Lyon, France

Received February 18, 2016; Revised April 08, 2016; Accepted April 08, 2016

ABSTRACT

DNA loop formation on nucleosomes is strongly implicated in chromatin remodeling and occurs spontaneously in nucleosomes subjected to superhelical stress. The nature of such loops depends crucially on the balance between DNA deformation and DNA interaction with the nucleosome core. Currently, no high-resolution structural data on these loops exist. Although uniform rod models have been used to study loop size and shape, these models make assumptions concerning DNA mechanics and DNA–core binding. We present here atomic-scale molecular dynamics simulations for two different loop sizes. The results point to the key role of localized DNA kinking within the loops. Kinks enable the relaxation of DNA bending strain to be coupled with improved DNA–core interactions. Kinks lead to small, irregularly shaped loops that are asymmetrically positioned with respect to the nucleosome core. We also find that loop position can influence the dynamics of the DNA segments at the extremities of the nucleosome.

INTRODUCTION

Nucleosomes are the fundamental building blocks of eukaryotic chromatin. They consist of a protein core of eight histones (two copies of H2A, H2B, H3 and H4), surrounded by 147 base pairs (bp) of double-stranded DNA. Electrostatic interactions between the dominantly cationic histones and the anionic DNA overcome the bending strain of the double helix and the electrostatic repulsion between adjacent turns (or 'spires'), enabling DNA to be wrapped around the core, forming a left-handed superhelix with an average radius of 41.4 Å and an average pitch of 22.2 Å (using the helical axis calculated with Curves+ (1) and the PDB structure 1KX5 (2,3)). The principal DNA–histone contacts occur in phase with the helical pitch of DNA (roughly every 10 bp within the nucleosome), where cationic arginine side chains penetrate the minor groove of DNA. These 14 contact points are numbered $+1 \rightarrow +7$ and $-1 \rightarrow -7$ in opposite directions leading away from the pseudodyad of the nucleosome (corresponding to the position of the central base pair of the wrapped DNA, see Supplementary Figure S1). The 147 base pairs are similarly numbered $-73 \rightarrow 0 \rightarrow +73$.

Since nucleosome-wrapped DNA is not easily accessible to proteins, nucleosome positioning within eukaryotic chromatin is a crucial element of gene regulation. Under normal physiological conditions, nucleosomes are relatively stable, although they will spontaneously migrate on the timescale of hours, and considerably faster at higher temperatures, or at lower salt concentrations (4–6). Such spontaneous movement (at least of some nucleosomes) may explain the intrinsic 'fuzziness' in mapping nucleosome positioning within chromatin (7). However, to carry out controlled nucleosome movements, cells contain chromatin remodelers, multi-protein complexes that bind and move nucleosomes, while consuming large quantities of ATP (8–11). Although the detailed mechanism of spontaneous, or controlled, nucleosome repositioning is not clear, global rotation of the histone core or global screw rotation of DNA around its superhelical axis can be excluded due to the large activation energies involved in simultaneously breaking all DNA–histone contacts (12). In the case of the SWI/SNF and RSC family of remodelers, there is strong evidence in favor of DNA loop formation during remodeling (13,14). Recent experiments have notably shown that RSC can release stable intermediates, termed 'remosomes', that are nucleosomes containing 30–40 bp of additional DNA, drawn into the nucleosome symmetrically from both ends (15). Remosomes have irregular shapes compatible with the formation of loops at various positions around the histone core. DNA loops are also probably involved in spontaneous nucleosome migration, and can be induced by superhelical stress (16).

*To whom correspondence should be addressed. Tel: +33 4 7272 2637; Fax: +33 4 7272 2604; Email: richard.lavery@ibcp.fr
Present address: Marco Pasi, Centre for Biomolecular Sciences and School of Pharmacy, University of Nottingham, Nottingham NG7 2RD, UK.

Until now, DNA loops on nucleosomes have been studied with uniform elastic rod models of DNA that cannot treat breakdowns in elastic behavior and also require some assumptions about how DNA–histone interaction energy is distributed around the nucleosome core (17–19). These models try to limit the elastic deformation of DNA by avoiding small radii of curvature while, at the same time, minimizing the loss of stabilizing DNA–histone interactions. While long loops, typically beyond the persistence length of DNA (≈ 500 Å, 150 bp), can preferentially form plectonemic (interwound) structures, short loops involving a few turns of DNA cannot. These loops, which are our current target, are termed planar loops. In passing, we note that Wiggins et al. have included the notion of local breakdowns in uniform elastic behavior (i.e. kink formation) (20), but, to our knowledge, these models have not yet been applied to studying nucleosome loops.

Here, we use atomistic molecular dynamics (MD) simulations to investigate the detailed structure and dynamics of loops containing either two- (21 bp) or four- (42 bp) helical turns of inserted DNA, increasing the nucleosome-wrapped DNA from 147 bp to either 168 or 189 bp. The lengths of the DNA inserts were chosen to minimize any torsional stress within the looped DNA (given an average helical pitch in solution of 10.5 bp).

MATERIALS AND METHODS

Simulation protocol

MD simulations were performed using the GROMACS 5 package (21–24) with the Amber 99SB-ILDN force field for proteins (25–27) and the recent PARMBSC1 modifications (28) that have been specifically developed for DNA and shown to accurately reproduce its conformational and dynamic behavior. The modified nucleosomes, IN21 and IN42, were placed in a truncated octahedral box, solvated with SPC/E water molecules (29) to a depth of at least 10 Å and neutralized with potassium cations. K^+Cl^- ion pairs (30) were then added to reach a physiological salt concentration of 0.15 M. After energy minimization of the solvent, and careful thermalization of the system, following a standard protocol described elsewhere (31), we began simulations under controlled temperature (298 K) and pressure (1 bar) conditions using the Bussi thermostat (32) and the Berendsen barostat (33), both with a 5 ps coupling constant. Long-range electrostatic interactions were treated using the particle mesh Ewald method (34) with a real-space cutoff of 10 Å. Bond lengths involving hydrogen atoms were restrained using P-LINCS (35,36), allowing a time step of 2 fs. Translational movement of the solute was removed every 5000 steps to avoid any kinetic energy build up (37). Simulations were carried out typically using between 240 and 480 computer cores depending on the system size, which allowed a production rate of ∼50 ns/day for both systems. The solvated system with the 21 bp insert (IN21) contained 256 K atoms, while the system with the 42 bp insert (IN42) contained a total of 470 K atoms.

Conformational analysis

Conformations were extracted from the MD simulation every ps and DNA conformations were analyzed using Curves+ (1). As well as defining helical, backbone and groove variables, this analysis also determines an optimal curvilinear helical axis. DNA bending was subsequently described with the variable 'axis bend' that quantifies the angle between the helical axis segments associated with successive base pairs. The time evolution of axis bend during the simulations (see Figure 3) provides a concise picture of the changing conformation of the DNA loops, and notably makes it easy to identify the appearance and the location of the local conformational disruptions termed kinks. Although the exact nature of DNA kinks is still actively studied (38), molecular dynamics simulations currently suggest that they can adopt different structures including unstacking at a single step (termed Type I and originally proposed by molecular model building in 1975 (39)) or unstacking at two consecutive steps with a central broken base pair (Type II) (40,41). However, we should stress that the kinks discussed here are major local disruptions of the double helix, well beyond the smaller 'kinking' seen within DNA bound to unperturbed nucleosomes (3,42,43). We locate kinks, as in our earlier work, by using the inter-BP variables roll and propeller. These variables are presented in Supplementary Figures S2 and S3 of the supplementary material accompanying this article. Average axis bend values also enable us to quantify the overall bending within the DNA loops. Such averages exclude any broken base pairs within the kinks and one flanking base pair on either side (see panels D and E of Figure 2).

In order to define which segment of DNA belongs to the loop at any given moment, we rely on the interactions between DNA and the 14 arginine side chains that are distributed regularly around the histone core and that usually bind in the minor groove once every turn of the double helix (see Supplementary Figure S1). In order to locate each arginine side chain with respect to DNA, we use the curvilinear helicoidal coordinate analysis recently developed for locating ions around DNA (44,45). This enables us to calculate the distance R between the central carbon of each arginine head group and the helical axis of DNA. We have analyzed the distance R in MD simulations of an unperturbed nucleosome (28) (data kindly provided by P.D. Dans and F. Battistini, IRB Barcelona). The results presented in Supplementary Figure S5 show that, in this case, the arginine head groups lie either within the DNA minor groove at $R \leq$ 10.25 Å or at the level of the backbone phosphate groups at $10.25 < R \leq 15$ Å (which also corresponds to the distance for an optimal salt bridge between phosphate and arginine). We have consequently chosen $R > 15$ Å as a cutoff to indicate unbound arginine side chains and indeed unbound arginines in our loop simulations typically occur around $R = 25$ Å. In analyzing the extent of the loop region during simulations (Figure 4), short-lived binding/unbinding events were filtered out by using 25 ns sliding-window averaging.

Elastic rod calculations

We use the worm-like chain (WLC) loop model proposed by Schiessel *et al.* (17). This model describes the total loop length L as the sum of the length of the inserted DNA ΔL and the length of DNA detached from the nucleosome core L^*,

$$L^* = \left(\frac{20\,\pi^4\kappa}{\lambda\,R_0^2}\right)^{1/6}\left(\frac{\Delta L}{R_0}\right)^{1/3} R_0$$

where $\kappa = l_P k_B T$, l_P is the persistence length of DNA (taken as 500 Å), k_B is Boltzmann's constant and T the temperature is taken as 300 K. R_0 is the radius of DNA on the nucleosome (41.1 Å) and the λ is the adsorption energy of DNA on the nucleosome core per unit length (taken as the upper limit of the experimental estimates, 0.1 kcal mol^{-1} Å^{-1}) (17,46–48). Using these criteria, and taking the average rise/bp of DNA to be 3.4 Å, for $\Delta L = 21$ bp, $L^* = 62$ bp and $L = 83$ bp, while for $\Delta L = 42$ bp, $L^* = 78$ bp and $L = 120$ bp.

Graphics

All molecular graphics were obtained using Chimera v1.11 (49,50). Raw data was analyzed using numpy v1.10 (51) and pandas v0.15, and visualized using matplotlib v1.5 (52) within IPython v4.0 (53).

RESULTS AND DISCUSSION

Loop construction

The DNA to be inserted into the nucleosome was built with a repeating tetranucleotide sequence ATGC. This sequence was chosen to have a balanced AT/GC content and to be free of backbone conformational oscillations observed with some other sequences (31). To construct the initial loops with either 21 or 42 bp inserts (termed hereafter IN21 and IN42), we began with a high-resolution structure of the nucleosome from the Protein Data Bank 1KX5 (2,3). The unstructured histone tails were removed since they cannot be correctly conformationally sampled on the timescale of our simulations. We chose to insert the loops at the pseudodyad position of the nucleosome. In line with earlier coarse-grain loop models, we assumed that sharp DNA bending should be avoided. This was achieved by removing an entire superhelical turn of DNA, centered on the pseudodyad position, building a new superhelical turn incorporating the extra base pairs and then linking this turn back into the nucleosome structure with energy minimization, using the internal coordinate program JUMNA (54). Energy minimization used the same force field as the subsequent MD simulations, coupled with a simple continuum solvent and salt model. The resulting structures contain large epicyclic loops, namely loops that are tangential to the nucleosome core (Figure 1). This initial conformation favors low curvature (large radius of curvature), at the cost of lost DNA–histone contacts.

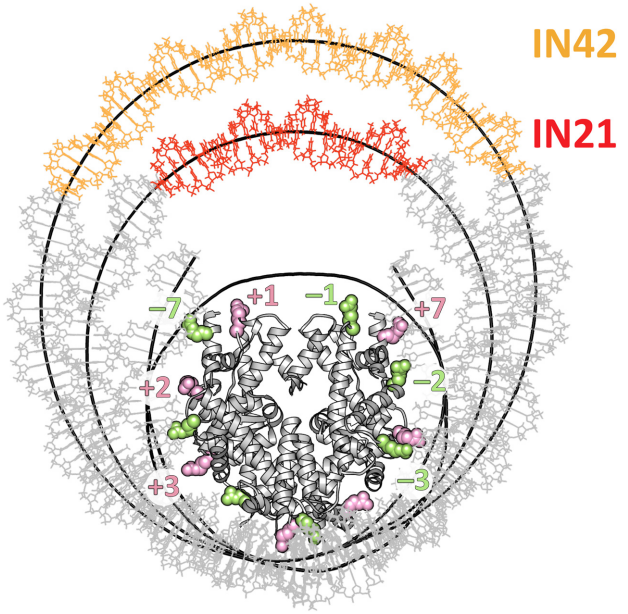

Figure 1. Epicyclic DNA loop constructions on the nucleosome core. Superposed structures of the IN42 and IN21 loops (with inserted DNA in orange and red, respectively). The helical axes of the loops and of the native nucleosome are shown as thick black lines. Histones are shown in grey and the arginines contacting the DNA minor groove are shown as green spheres (−1 → −7) and pink spheres (+1 → +7). Following the numbering of PDB entry 1KX5, arginines, from +1 to +7 are H4.R45, H3.R63, H3.R83, H2A.R42, H2A.R29, H2A.R77, H3.R49. See also Supplementary Figure S1.

Molecular dynamics simulations

Simulations were performed using the GROMACS 5 package (21–24) with the recent PARMBSC1 force field (28). Trajectories of the IN21 and IN42 nucleosomes were obtained in an aqueous environment, with a physiological salt concentration (yielding a total of 256 K atoms for IN21 and of 470 K atoms for IN42), for durations of 1.0 and 0.5 μs, respectively. See the Materials and Methods section for further details of the simulation and conformational analysis protocols.

We begin by considering the larger IN42 structure (Figure 1). Creating the initial epicyclic loop involved cutting the nucleosomal DNA at positions −37 and +37 (opposite the pseudodyad) and replacing the existing 73 bp superhelical turn with a 115 bp fragment containing the centrally positioned 42 bp insert. This leads to a change in superhelical radius from 41.4 to 72.6 Å. The creation of this loop results in breaking six minor groove arginine contact points, −3 → +3. As soon as the MD simulation begins, the loop begins to distort, losing its regular superhelical shape and moving towards the closest contact points. After a few nanoseconds (ns) of simulation, histone contacts −3 and +3 are reestablished (Figure 2a), thanks to an increase in DNA bending at symmetric positions −69 and 69, respectively towards the minor and major grooves (see Figure 3 top and Supplementary Figure S2). This effectively reduces the loop size to 95 bp. By 30 ns, contact −2 is transiently reformed and around 80 ns, contacts at −2 and −1 are both stably reestablished (Figure 4 top). Beyond this point, the distortion of the 74

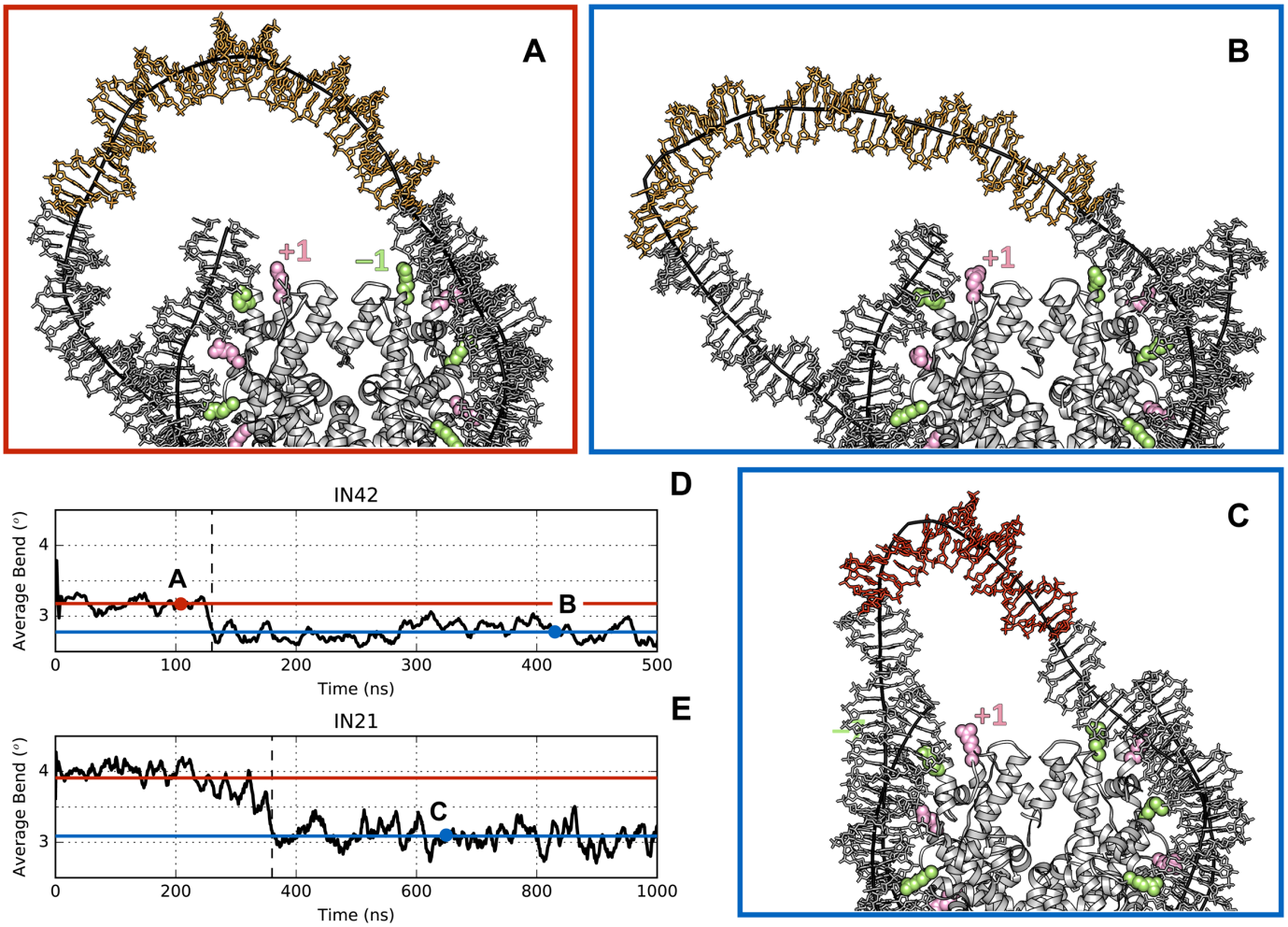

Figure 2. Kink formation and average DNA bending. Snapshots along the MD trajectories of IN42 (A and B) and IN21 (C). Plots (D) and (E) show 10 ns sliding-window averages of the DNA axis bend for IN42 and IN21 respectively (calculated excluding 1 bp on either side of DNA kinks). The red and blue horizontal lines show the average axis bend before and after kink formation (indicated by the vertical dashed lines). The position of the snapshots (A), (B) and (C) are indicated by the letters on the time axis. See the Supplementary Information for further details of the analyses.

bp remaining in the loop results in the formation of a kink toward the minor groove within the 42 bp insert (Figure 3 top). This kink belongs to the family termed Type II (Figure 5, left), implying a strong roll at two adjacent base pair steps (i.e. bending of the double helix towards the minor groove, see Supplementary Figure S2) and disruption of the central base pair (40,55,56). The appearance of a localized kink allows the rest of the DNA loop to relax, as evidenced by a decrease in the average axis bend (Figure 2d). Note that a 1° decrease in average axis bend with respect to its average value for the nucleosome (4.7°) corresponds to an increase in radius of 11 Å. After 0.5 μs of simulation, the IN42 loop has adopted a 'V-like' shape with the kink at its apex, flanked by weakly curved DNA arms (Figure 2b). Note that because kinks involve sharp bending in a fixed direction (toward the local minor groove), the kink location will reflect the need to avoid further straining the loop by induced writhe (40).

We now consider the smaller IN21 insert. The nucleosomal DNA is again cut out between positions −37 and +37 and the intervening 73 bp are replaced with a 94 bp superhelical fragment containing the centrally placed 21 bp insert, leading to a superhelical radius of 59.7 Å. However, this loop remains close enough to the histone core to only truly break minor groove histone contacts −2 → +2, reducing the effective loop size to 73 bp. During energy minimization the loop again becomes asymmetric, leaning towards the histone core on the side of the negative contact points and early in the MD trajectory contacts −2 and −1 are reformed, reducing the effective loop to 53 bp (Figure 4 bottom). This distortion is accompanied by the formation of a Type II kink within the 21 bp insert (Figure 3 bottom, Figure 2c). After 170 ns, the +2 contact is recovered, while the 45 bp remaining in the loop continue to distort and the kink moves one turn towards the positive contact points around 300 ns (Figure 3 bottom). After 800 ns, the kink moves again slightly and leads to two successive broken base pairs. The two purines from these base pairs stack on the flanking base pairs, while the pyrimidines form an unusual, offset pairing interaction (Figure 5). We term this previously unseen kink conformation Type III. As in the case of IN42, kink for-

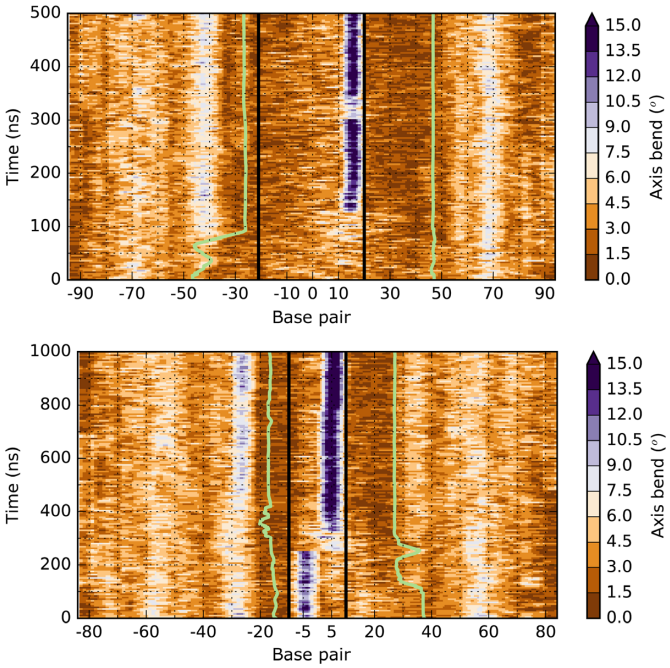

Figure 3. Time evolution of the DNA axis bend. Axis bend values at each base-pair step along the MD trajectories of IN42 (top) and IN21 (bottom). Black lines delimit the DNA inserts and green lines indicate loop DNA that is detached from the protein core. White and blue regions indicate increasing DNA bending.

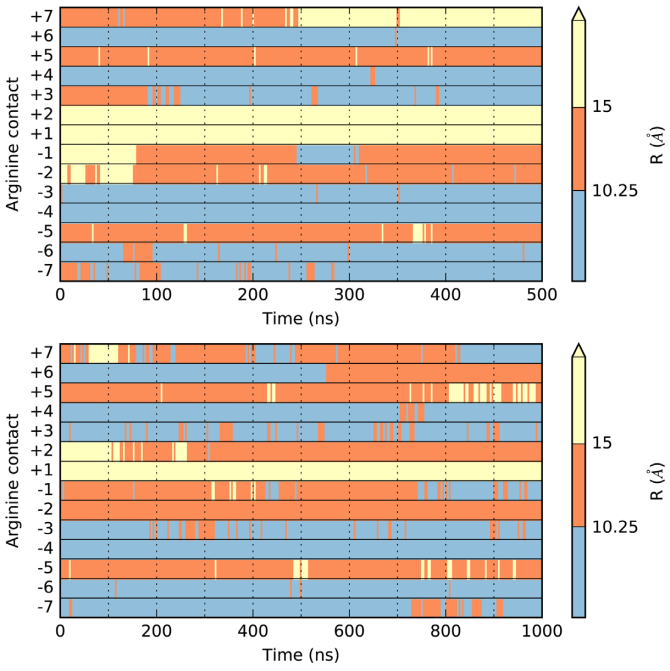

Figure 4. Time evolution of minor groove arginine contacts. Distance R of the 14 arginine head groups from the DNA helical axis along the MD trajectories of IN42 (top) and IN21 (bottom). Each row refers to one of the 14 arginines contact points, numbered $-7 \rightarrow +7$. Distances are color-coded according to whether the arginine is within the groove ($R \leq 10.25$ Å), bound to phosphates (10.25 Å $< R \leq 15$ Å) or unbound ($R > 15$ Å).

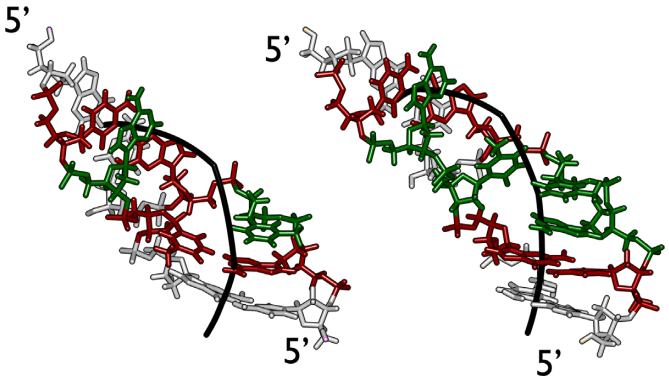

Figure 5. Kinked structures. Structures of Type II (left) and Type III (right) kinks extracted from the simulation of the IN21 structure. DNA is shown as grey sticks; base pairs are colored green if they are broken and red if they are intact but feature large negative values of roll with one of their neighbors. The Curves+ helical axis is shown as a thick black line.

mation reduces the bending strain in the rest of the loop (Figure 2e).

A last interesting point concerns the ends of the nucleosomal DNA that, both experimentally (57) and during simulations (58–60), have been shown to sporadically detach from the histone core. During the IN42 simulation, this only occurs for the end held by the +7 histone contact and only after 250 ns when the IN42 loop has reformed the −1 and −2 contacts in the neighboring spire (Figure 4 top and Supplementary Figure S5). Similarly, we see a brief detachment of the +7 contact at the beginning of the IN21 simulation when this loop has also formed the −1 and −2 contacts (see Figure 4 bottom and Supplementary Figure S5). These observations suggest that inter-spire electrostatic repulsion is an important factor in destabilizing the DNA termini of nucleosomes.

CONCLUSIONS

Atomistic, microsecond-scale MD trajectories, using the latest BSC1 DNA force field, have been used to study two differently sized DNA loops formed on the nucleosome core. Despite building both loops with smooth 'epicyclic' conformations, our study shows that nucleosomal DNA loops attempt to establish maximal contacts with the histone core. This leads to small effective loop sizes with high bending strain that can only be relaxed by localized kink formation. We have modeled loops involving the insertion of either two or four helical turns of DNA into a native nucleosome. Restablishing DNA–histone contacts reduces the final lengths of loop DNA to only two to three turns more than the length of the insert, namely 45 and 74 bp respectively, with the loss of only one or two DNA–arginine interactions in the minor groove compared to native nucleosomes. This finding is compatible with the observed stability of isolated 'remosomes' (nucleosomes containing three to four turns of additional DNA) created and then released by the RSC remodeler. It could also explain the accessibility of the DNA in remosomes to attack by restriction enzymes (DNase I and ExoIII) (15), if we assume that loops can occur at any position around the histone core. Although

the limited timescale of our simulations may preclude any observation of spontaneous movement of loops around the core once they are formed, kink formation coupled with extensive DNA–core interactions suggests these movements may not occur easily.

The small loops that result from atomistic simulations can be compared with a simple worm-like chain (WLC) model of DNA loops (17), although, as it has been pointed out (61), WLC models are likely to overestimate elastic bending energy for small loops. Such a model indeed predicts much larger loop sizes, with 83 bp for IN21 and of 120 bp for IN42 (see Materials and Methods section). These loops are somewhat larger than our initial epicyclic loop constructions and would imply that either six or eight DNA–core contacts would be broken.

In contrast to smoothly curved elastic rod models, the kinked DNA loops adopt very irregular shapes and are asymmetrically positioned with respect to the histone core. An analysis of the kinks shows that the longer 74 bp loop of the IN42 insert contains a kink (Type II) that involves perturbing the stacking at two consecutive base pair steps and breaking the intervening base pair. This type of kink has already been seen in earlier simulation studies of small minicercles (40,62). In contrast, the final state of the smaller and, consequently, more strained 45 bp loop of the IN21 insert brings to light a new kink (now termed Type III) involving two broken base pairs and the formation of an unusual offset pyrimidine-pyrimidine base pairing interaction. While a number of experimental studies support the formation of kinks in strongly bent DNA (38,63,64), their exact structure remains unclear. This uncertainty may in part be due to the existence of a number of distinct kink families such as those found here. It should also be remarked that kinks can affect not only local bending, but also, as a function of their type, put different constraints on bending direction (40), a fact that is worth considering when developing more sophisticated rod models of DNA.

Finally, these simulations suggest that electrostatic repulsion between the adjacent spires of DNA wrapped around the nucleosome core is a significant factor in facilitating the detachment of the DNA termini, since no detachment occurs when the position of a DNA loop increases the distance separating the spires.

SUPPLEMENTARY DATA

Supplementary Data are available at NAR Online.

ACKNOWLEDGEMENTS

The authors wish to acknowledge GENCI for a generous allocation of computer time on the CINES supercomputer OCCIGEN and K. Zakrzewska for assistance in developing computer code for constructing DNA loops and for helpful discussions.

FUNDING

Agence Nationale de la Recherche (ANR) Project CHROME [ANR-12-BSV5-0017-01]. Funding for open access charge: Project CHROME [ANR-12-BSV5-0017-01]

Conflict of interest statement. None declared.

REFERENCES

1. Lavery,R., Moakher,M., Maddocks,J.H., Petkeviciute,D. and Zakrzewska,K. (2009) Conformational analysis of nucleic acids revisited: Curves+. *Nucleic Acids Res.*, **37**, 5917–5929.
2. Davey,C.A., Sargent,D.F., Luger,K., Maeder,A.W. and Richmond,T.J. (2002) Solvent mediated interactions in the structure of the nucleosome core particle at 1.9 a resolution. *J. Mol. Biol.*, **319**, 1097–1113.
3. Richmond,T.J. and Davey,C.A. (2003) The structure of DNA in the nucleosome core. *Nature*, **423**, 145–150.
4. Beard,P. (1978) Mobility of histones on the chromosome of simian virus 40. *Cell*, **15**, 955–967.
5. Spadafora,C., Oudet,P. and Chambon,P. (1979) Rearrangement of chromatin structure induced by increasing ionic strength and temperature. *Eur. J. Biochem.*, **100**, 225–235.
6. Pennings,S., Meersseman,G. and Bradbury,E.M. (1991) Mobility of positioned nucleosomes on 5 S rDNA. *J. Mol. Biol.*, **220**, 101–110.
7. Deniz,Ö,, Flores,O., Aldea,M., Soler-López,M. and Orozco,M. (2016) Nucleosome architecture throughout the cell cycle. *Sci. Rep.*, **6**, 19729.
8. Becker,P.B. (2002) Nucleosome sliding: facts and fiction. *EMBO J.*, **21**, 4749–4753.
9. Flaus,A. and Owen-Hughes,T. (2003) Mechanisms for nucleosome mobilization. *Biopolymers*, **68**, 563–578.
10. Bowman,G.D. (2010) Mechanisms of ATP-dependent nucleosome sliding. *Curr. Opin. Struct. Biol.*, **20**, 73–81.
11. Mueller-Planitz,F., Klinker,H. and Becker,P.B. (2013) Nucleosome sliding mechanisms: new twists in a looped history. *Nat. Struct. Mol. Biol.*, **20**, 1026–1032.
12. Flaus,A. and Owen-Hughes,T. (2003) Dynamic properties of nucleosomes during thermal and ATP-driven mobilization. *Mol. Cell. Biol.*, **23**, 7767–7779.
13. Zhang,Y., Smith,C.L., Saha,A., Grill,S.W., Mihardja,S., Smith,S.B., Cairns,B.R., Peterson,C.L. and Bustamante,C. (2006) DNA translocation and loop formation mechanism of chromatin remodeling by SWI/SNF and RSC. *Mol. Cell*, **24**, 559–568.
14. Lia,G., Praly,E., Ferreira,H., Stockdale,C., Tse-Dinh,Y.C., Dunlap,D., Croquette,V., Bensimon,D. and Owen-Hughes,T. (2006) Direct observation of DNA distortion by the RSC complex. *Mol. Cell*, **21**, 417–425.
15. Shukla,M.S., Syed,S.H., Montel,F., Faivre-Moskalenko,C., Bednar,J., Travers,A., Angelov,D. and Dimitrov,S. (2010) Remosomes: RSC generated non-mobilized particles with approximately 180 bp DNA loosely associated with the histone octamer. *Proc. Natl. Acad. Sci. U.S.A.*, **107**, 1936–1941.
16. Bussiek,M., Tóth,K., Brun,N. and Langowski,J. (2005) DNA-loop formation on nucleosomes shown by in situ scanning force microscopy of supercoiled DNA. *J. Mol. Biol.*, **345**, 695–706.
17. Schiessel,H., Widom,J., Bruinsma,R.F. and Gelbart,W.M. (2001) Polymer reptation and nucleosome repositioning. *Phys. Rev. Lett.*, **86**, 4414–4417.
18. Kulić,I.M. and Schiessel,H. (2003) Nucleosome repositioning via loop formation. *Biophys. J.*, **84**, 3197–3211.
19. Biswas,M.-R., Voltz,K., Smith,J.C. and Langowski,J. (2011) Role of histone tails in structural stability of the nucleosome. *PLoS Comput. Biol.*, **7**, e1002279.
20. Wiggins,P.A., Phillips,R. and Nelson,P.C. (2005) Exact theory of kinkable elastic polymers. *Phys. Rev. E Stat. Nonlin. Soft Matter Phys.*, **71**, 021909.
21. Hess,B., Kutzner,C., van der Spoel,D. and Lindahl,E. (2008) Gromacs 4: algorithms for highly efficient, load-balanced, and scalable molecular simulation. *J. Chem. Theory Comput.*, **4**, 435–447.
22. Van Der Spoel,D., Lindahl,E., Hess,B., Groenhof,G., Mark,A.E. and Berendsen,H.J. (2005) GROMACS: fast, flexible, and free. *J. Comput. Chem.*, **26**, 1701–1718.
23. Lindahl,E., Hess,B. and van der Spoel,D. (2001) GROMACS 3.0: a package for molecular simulation and trajectory analysis. *J. Mol. Model.*, **7**, 306–317.

24. Berendsen,H.J.C., Van der Spoel,D. and Van Drunen,R. (1995) GROMACS: a message-passing parallel molecular dynamics implementation. *Comput. Phys. Commun.*, **91**, 43–56.
25. Lindorff-Larsen,K., Piana,S., Palmo,K., Maragakis,P., Klepeis,J.L., Dror,R.O. and Shaw,D.E. (2010) Improved side-chain torsion potentials for the Amber ff99SB protein force field. *Proteins*, **78**, 1950–1958.
26. Hornak,V., Abel,R., Okur,A., Strockbine,B., Roitberg,A. and Simmerling,C. (2006) Comparison of multiple Amber force fields and development of improved protein backbone parameters. *Proteins*, **65**, 712–725.
27. Wang,J.M., Cieplak,P. and Kollman,P.A. (2000) How well does a restrained electrostatic potential (RESP) model perform in calculating conformational energies of organic and biological molecules? *J. Comput. Chem.*, **21**, 1049–1074.
28. Ivani,I., Dans,P.D., Noy,A., Pérez,A., Faustino,I., Hospital,A., Walther,J., Andrio,P., Goñi,R. and Balaceanu,A. (2016) Parmbsc1: a refined force field for DNA simulations. *Nat. Methods*, **13**, 55–58.
29. Berendsen,H.J.C., Grigera,J.R. and Straatsma,T.P. (1987) The missing term in effective pair potentials. *J. Phys. Chem.*, **91**, 6269–6271.
30. Dang,L.X. (1995) Mechanism and thermodynamics of ion selectivity in aqueous-solutions of 18-crown-6 ether - A molecular dynamics study. *J. Am. Chem. Soc.*, **117**, 6954–6960.
31. Pasi,M., Maddocks,J.H., Beveridge,D., Bishop,T.C., Case,D.A., Cheatham,T., Dans,P.D., Jayaram,B., Lankas,F. *et al.* (2014) μABC: a systematic microsecond molecular dynamics study of tetranucleotide sequence effects in B-DNA. *Nucleic Acids Res.*, **42**, 12272–12283.
32. Bussi,G., Donadio,D. and Parrinello,M. (2007) Canonical sampling through velocity rescaling. *J. Chem. Phys.*, **126**, 014101.
33. Berendsen,H.J.C., Postma,J.P.M., van Gunsteren,W.F., DiNola,A. and Haak,J.R. (1984) Molecular dynamics with coupling to an external bath. *J. Chem. Phys.*, **81**, 3684–3690.
34. Essmann,U., Perera,L., Berkowitz,M.L., Darden,T., Lee,H. and Pedersen,L.G. (1995) A smooth particle mesh Ewald method. *J. Chem. Phys.*, **103**, 8577–8593.
35. Hess,B., Bekker,H., Berendsen,H.J. and Fraaije,J.G. (1997) LINCS: a linear constraint solver for molecular simulations. *J. Comput. Chem.*, **18**, 1463–1472.
36. Hess,B., Kutzner,C., van der Spoel,D. and Lindahl,E. (2008) Gromacs 4: algorithms for highly efficient, load-balanced, and scalable molecular simulation. *J. Chem. Theory Comput*, **4**, 435–447.
37. Harvey,S.C., Tan,R.K.Z. and Cheatham,T.E. III (1998) The flying ice cube: velocity rescaling in molecular dynamics leads to violation of energy equipartition. *J. Comput. Chem.*, **19**, 726–740.
38. Vologodskii,A. and Maxim,M. (2013) Strong bending of the DNA double helix. *Nucleic Acids Res.*, **41**, 6785–6792.
39. Crick,F.H. and Klug,A. (1975) Kinky helix. *Nature*, **255**, 530–533.
40. Lankas,F., Lavery,R. and Maddocks,J.H. (2006) Kinking occurs during molecular dynamics simulations of small DNA minicircles. *Structure*, **14**, 1527–1534.
41. Curuksu,J., Zacharias,M., Lavery,R. and Zakrzewska,K. (2009) Local and global effects of strong DNA bending induced during molecular dynamics simulations. *Nucleic Acids Res.*, **37**, 3766–3773.
42. Mukherjee,R. and Bishop,T.C. (2011) Nucleosomal DNA: kinked, not kinked, or self-healing material. In: Richard,D, Sheardy, Stephen,A and Winkle (eds). *Frontiers in Nucleic Acids*. pp. 69–92.
43. Olson,W.K. and Zhurkin,V.B. (2011) Working the kinks out of nucleosomal DNA. *Curr. Opin. Struct. Biol.*, **21**, 348–357.
44. Lavery,R., Maddocks,J.H., Pasi,M. and Zakrzewska,K. (2014) Analyzing ion distributions around DNA. *Nucleic Acids Res.*, **42**, 8138–8149.
45. Pasi,M., Maddocks,J.H. and Lavery,R. (2015) Analyzing ion distributions around DNA: sequence-dependence of potassium ion distributions from microsecond molecular dynamics. *Nucleic Acids Res.*, **43**, 2413–2423.
46. Polach,K.J. and Widom,J. (1995) Mechanism of protein access to specific DNA sequences in chromatin: a dynamic equilibrium model for gene regulation. *J. Mol. Biol.*, **254**, 130–149.
47. Polach,K.J. and Widom,J. (1996) A model for the cooperative binding of eukaryotic regulatory proteins to nucleosomal target sites. *J. Mol. Biol.*, **258**, 800–812.
48. Schiessel,H., Widom,J., Bruinsma,R.F. and Gelbart,W.M. (2002) Erratum: polymer reptation and nucleosome repositioning. *Phys Rev Lett*, **88**, 129902.
49. Goddard,T.D., Huang,C.C. and Ferrin,T.E. (2007) Visualizing density maps with UCSF chimera. *J. Struct. Biol.*, **157**, 281–287.
50. Pettersen,E.F., Goddard,T.D., Huang,C.C., Couch,G.S., Greenblatt,D.M., Meng,E.C. and Ferrin,T.E. (2004) UCSF Chimera–a visualization system for exploratory research and analysis. *J. Comput. Chem.*, **25**, 1605–1612.
51. Oliphant,T.E. (2007) Python for scientific computing. *Comput. Sci. Eng.*, **9**, 10–20.
52. Hunter,J.D. (2007) Matplotlib: A 2D graphics environment. *Comput. Sci. Eng.*, **9**, 90–95.
53. Pérez,F. and Granger,B.E. (2007) IPython: a system for interactive scientific computing. *Comput. Sci. Eng.*, **9**, 21–29.
54. Lavery,R., Zakrzewska,K. and Sklenar,H. (1995) JUMNA (Junction Minimization of Nucleic-Acids). *Comput. Phys. Commun.*, **91**, 135–158.
55. Du,Q., Kotlyar,A. and Vologodskii,A. (2008) Kinking the double helix by bending deformation. *Nucleic Acids Res.*, **36**, 1120–1128.
56. Harris,S.A., Laughton,C.A. and Liverpool,T.B. (2008) Mapping the phase diagram of the writhe of DNA nanocircles using atomistic molecular dynamics simulations. *Nucleic Acids Res.*, **36**, 21–29.
57. Li,G., Levitus,M., Bustamante,C. and Widom,J. (2005) Rapid spontaneous accessibility of nucleosomal DNA. *Nat. Struct. Mol. Biol.*, **12**, 46–53.
58. Ramaswamy,A., Bahar,I. and Ioshikhes,I. (2005) Structural dynamics of nucleosome core particle: comparison with nucleosomes containing histone variants. *Proteins: Struct. Funct. Bioinf.*, **58**, 683–696.
59. Roccatano,D., Barthel,A. and Zacharias,M. (2007) Structural flexibility of the nucleosome core particle at atomic resolution studied by molecular dynamics simulation. *Biopolymers*, **85**, 407–421.
60. Kono,H., Sakuraba,S. and Ishida,H. (2015) Free energy profiles for nucleosomal DNA unwrapping. *Biophys. J.*, **108**, 73a.
61. Schiessel,H. (2003) The physics of chromatin. *J. Phys. Condens. Matter*, **15**, R699–R774.
62. Mitchell,J.S., Laughton,C.A. and Harris,S.A. (2011) Atomistic simulations reveal bubbles, kinks and wrinkles in supercoiled DNA. *Nucleic Acids Res.*, **39**, 3928–3938.
63. Fields,A.P., Meyer,E.A. and Cohen,A.E. (2013) Euler buckling and nonlinear kinking of double-stranded DNA. *Nucleic Acids Res.*, **41**, 9881–9890.
64. Lionberger,T.A., Demurtas,D., Witz,G., Dorier,J., Lillian,T., Meyhöfer,E. and Stasiak,A. (2011) Cooperative kinking at distant sites in mechanically stressed DNA. *Nucleic Acids Res.*, **39**, 9820–9832.

Pharm Res (2016) 33:1671–1681
DOI 10.1007/s11095-016-1908-2

RESEARCH PAPER

Synthesis and In Vitro Evaluation of Polyethylene Glycol-Paclitaxel Conjugates for Lung Cancer Therapy

Tian Luo[1,2] • Johannes Magnusson[2] • Véronique Préat[1] • Raphael Frédérick[3] • Cameron Alexander[2] • Cynthia Bosquillon[2] • Rita Vanbever[1]

Received: 18 December 2015 / Accepted: 9 March 2016 / Published online: 16 March 2016

ABSTRACT

Purpose Pulmonary drug delivery is considered an attractive route of drug administration for lung cancer chemotherapy. However, fast clearance mechanisms result in short residence time of small molecule drugs in the lung. Therefore, achieving a sustained presence of chemotherapeutics in the lung is very challenging. In this study, we synthesized two different polyethylene glycol-paclitaxel ester conjugates with molecular weights of 6 and 20 kDa in order to achieve sustained release of paclitaxel in the lung.

Methods One structure was synthesized with azide linker using "click" chemistry and the other structure was synthesized with a succinic spacer. The physicochemical and biological properties of the conjugates were characterized *in vitro*.

Results Conjugation to polyethylene glycol improved the solubility of paclitaxel by up to four orders of magnitude. The conjugates showed good stability in phosphate buffer saline pH 6.9 (half-life ≥72 h) and in bronchoalveolar lavage (half-life of 3 to 9 h) at both molecular weights, but hydrolyzed quickly in mouse serum (half-life of 1 to 3 h). The conjugates showed cytotoxicity to B16-F10 melanoma cells and LL/2 Lewis lung cancer cells but less than free paclitaxel or Taxol, the commercial paclitaxel formulation.

Conclusions These properties imply that the conjugates have the potential to retain paclitaxel in the lung for a prolonged duration and to sustain its release locally for a better efficacy.

✉ Rita Vanbever
rita.vanbever@uclouvain.be

[1] Advanced Drug Delivery & Biomaterials, Louvain Drug Research Institute, Université catholique de Louvain, Avenue E. Mounier, 73 1200 Brussels, Belgium

[2] School of Pharmacy, University of Nottingham, Nottingham, UK

[3] Medicinal Chemistry, Louvain Drug Research Institute, Université catholique de Louvain, Brussels, Belgium

KEY WORDS drug conjugate · lung cancer · paclitaxel · polyethylene glycol · pulmonary drug delivery

ABBREVIATIONS

BAL	Bronchoalveolar lavage
DIC	N,N'-Diisopropylcarbodiimide
DMAP	4-Dimethylaminopyridine
DMEM	Dulbecco's modified eagle medium
DMF	Dimethylformamide
DMSO	Dimethyl sulfoxide
DPBS	Dulbecco's phosphate-buffered saline
FBS	Fetal bovine serum
FT-IR	Fourier transform infrared spectroscopy
HBSS	Hank's balanced salt solution
HPLC	High performance liquid chromatography
MEM-Alpha	Minimum essential medium eagle alpha
MTT	3-(4,5-Dimethylthiazol-2-yl)-2,5-Diphenyltetrazolium bromide
MW	Molecular weight
NMR	Nuclear magnetic resonance
PEG	Polyethylene glycol
PTX	Paclitaxel
R.T.	Room temperature
$t_{1/2}$	Half-life
TEA	Triethylamine
TLC	Thin layer chromatography
TOF-ES-MS	Time-of-flight electrospray mass spectrometry

INTRODUCTION

Lung cancer is the most common cancer worldwide and caused 1.6 million deaths in 2012 (1). Systemic chemotherapy is widely used in the treatment of lung cancer, but the clinical efficacy is unsatisfactory as a result of the low local drug concentrations in

the lung tumors and the severe dose-limiting side effects. Pulmonary delivery of chemotherapeutic agents is considered an attractive route of administration, with the advantages of high drug concentrations locally and low side effects systemically. However, small molecules have very short half-lives of absorption from the lung to the systemic circulation (2). In general, small hydrophilic compounds (log $P<0$) have a half-life to absorption of approximately 1 h, whereas lipophilic small molecules (log $P>0$) are absorbed in approximately 1 min. This rapid systemic absorption results in a short residence time of chemotherapeutics in the lung. In addition, inhalation of chemotherapeutics alone would lead to transient peaks in drug concentrations locally and unacceptable toxicity to the lung tissue (3). Therefore, drug carriers could provide promising application for the pulmonary administration of anti-cancer agents in lung cancer with prolonged drug retention and sustained drug release locally as well as with reduced lung toxicity compared to the pulmonary delivery of the free drug (4).

Several nanocarrier-based pulmonary delivery systems have been developed and evaluated as potential treatment for lung cancer after inhalation, such as polymeric nanoparticles of doxorubicin and liposomes of paclitaxel (PTX) (5, 6). However, the control of the release kinetics is difficult to achieve with these delivery systems. Moreover, the absorption of the therapeutics across pulmonary epithelia to lung tumors and the drug distribution in tumors are expected to be decreased due to the relatively large size and surface charges of these nanocarrier systems (7, 8).

Conjugation of drugs to macromolecules by means of esterification provides a possible mechanism by which drugs could be retained in the lung due to the long residence times of macromolecules in the airspaces (2). Polyethylene glycol (PEG) is widely used in drug delivery and it has been shown that PEG with large molecular weight (MW >5 kDa) can be retained in the lung for up to 7 days (9). This could enable a sustained release of a drug conjugated to PEG by hydrolysis of the ester bond between the polymer and the drug (9–11). Moreover, the polymer-drug conjugates will be taken into the cells by endocytosis (12, 13), which could possibly avoid multi-drug resistance mediated by efflux pumps (14, 15). As compared to carrier particles and micelles, drug loading is relatively high for conjugates (10–30%) (16). In addition, as the conjugates will be delivered in solution, the size of this carrier will be very small (<10 nm), which will not generate the problem of tumor access.

PTX is a first-line drug for lung cancer treatment but it is poorly water soluble. Taxol®, the commercial formulation of PTX, contains Cremophor EL to increase the drug solubility. However, Cremophor EL is well-known for its severe toxicity and its impact on PTX pharmacokinetics. Cremophor EL alters PTX pharmacokinetic behaviour to a non-linear profile (17–19). Conjugation to highly hydrated PEG could largely increase PTX solubility without inducing unexpected toxicity (20, 21). In fact, PEG is nontoxic and it can be eliminated by mucociliary clearance and by renal and hepatic pathways (10). It has already been approved for human use in dosage forms for intravenous, oral and inhalation applications (22). Several studies have reported the synthesis of polymer-PTX conjugates in the literature. For instance, poly (L-glutamic acid)-PTX (Opaxio™) has already reached phase III clinical trials for ovarian cancer (23) and this conjugate showed reduced toxicity when locally delivered to the lung of mice (24). There are also various studies on PEG-PTX conjugates in the literature (25–29). However, the pulmonary application of PEGylated PTX for lung cancer and the evaluation of its properties for lung cancer therapy both *in vitro* and *in vivo* have not been explored.

Therefore, the aim of this study was to develop water soluble and stable PEG-PTX conjugates for pulmonary application in lung cancer. Two conjugates with either an azide linker (PEG-N_3-PTX) or a succinic linker (PEG-suc-PTX) were designed with 6 and 20 kDa MW PEG (Fig. 1). Linear PEGs were modified with PTX at both hydroxyl ends to increase the drug load in the final products. PTX was linked to the PEG molecule *via* an ester bond at the C-2′ position on PTX side chain. Although the hydroxyl on the C-2′ is necessary for PTX activity, the chemical and enzymatic hydrolysis of the conjugate in the lung could offer a progressive release of active PTX with free C-2′ hydroxyl. Moreover, the C-2′ position on PTX does not present steric hindrance as the hydroxyl 1-OH and 7-OH on the taxane ring do and could permit a high conversion rate. We used "click" chemistry in one of the synthetic routes because of the high efficiency of the azide and alkyne reaction. Moreover, the triazole formed between alkyne and PEG-azide is very stable and cannot hydrolyse before the ester bond. Consequently, the free PTX will release from the conjugate in an active form. All the conjugates were characterized physically and chemically and stability as well as cytotoxicity were evaluated *in vitro*.

MATERIALS AND METHODS

Materials and Instruments

PEG with two hydroxyl terminals and MW of 6 and 20 kDa were purchased from Iris Biotech (Marktredwitz, Germany). Paclitaxel was purchased from Chemieliva (Chongqing, China). Taxol was obtained from Brystol-Myers Squibb. N, N'-diisopropylcarbodiimide (DIC), 4-dimethylaminopyridine (DMAP), tysol chloride, triethylamine (TEA), dichloromethane, dimethyl sulfoxide (DMSO), acetonitrile, dimethylformamide (DMF), and Cremophor EL (Kolliphor® EL) were all purchased from Sigma Aldrich (Gillingham, UK). Hank's balanced salt solution (HBSS) and

Dulbecco's phosphate-buffered saline (DPBS) were purchased from Life Technologies (Paisley, UK). The thiazolyl blue tetrazolium bromide (MTT) was from Sigma Aldrich (St. Louis, MO, USA).

Spectra/Por® 7 Tubing (Spectrum Laboratories, Inc, Rancho Dominguez, CA, US) was used to carry out all the dialysis work.

Nuclear magnetic resonance (NMR) spectra were recorded on a Bruker 400 MHz spectrometer. Chemical shifts are reported in ppm (δ units) downfield from internal tetramethylsilane.

Time-of-flight electrospray mass spectrometry (TOF-ES-MS) was performed by WATERS-2795 (Waters, UK) and analyzed by MassLynx software.

Chemistry

Synthesis of PEG-N_3 6 and 20 kDa

PEG-N_3 was obtained by tosylation followed by azidation. PEG 6 kDa (1 g, 0.167 mmol, 1.0 equiv.) was dissolved in 5 mL toluene and evaporated to dry for 3 cycles to remove water. The dried PEG was dissolved in 5 mL dichloromethane under Argon. The solution was cooled to 0°C, then tosyl chloride (0.191 g, 1 mmol, 6 equiv.) and triethylamine (0.139 mL, 1 mmol, 6.0 equiv.) were added. The solution was kept at 0°C for 2 h and then warmed up to room temperature and stirred overnight. The reaction solution was poured into cool diethyl ether three times to

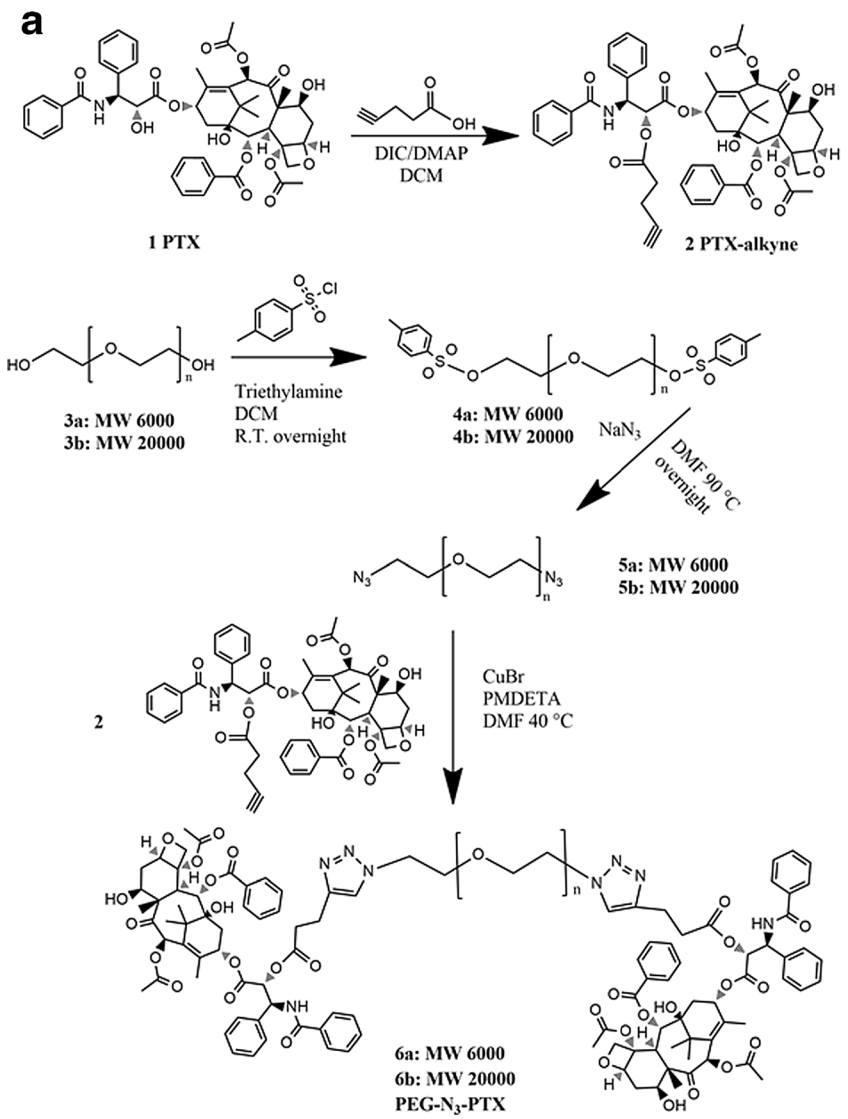

Fig. 1 Synthetic routes of PEG-PTX conjugates. (**a**). "**Click**" **chemistry route:** PTX (compound 1) was modified with pentynoic acid at C-2′ group to obtain PTX-alkyne (compound 2). PEG-N_3 6 and 20 kDa (compounds 5a and 5b) were synthesized from PEG with 2 hydroxyl ends by tosylation followed by azidation. PTX-alkyne was then conjugated to PEG-N_3 6 and 20 kDa *via* "click" chemistry respectively to obtain the final conjugates PEG-N_3-PTX 6 and 20 kDa (compounds 6a and 6b). (**b**)**. Succinic spacer route:** succinic acid was linked to PEG 6 and 20 kDa *via* esterification to obtain PEG-suc 6 and 20 kDa (compounds 7a and 7b). PEG-suc-PTX 6 and 20 kDa (compounds 8a and 8b) were then obtained by esterification of PEG-suc and PTX at C-2′ position.

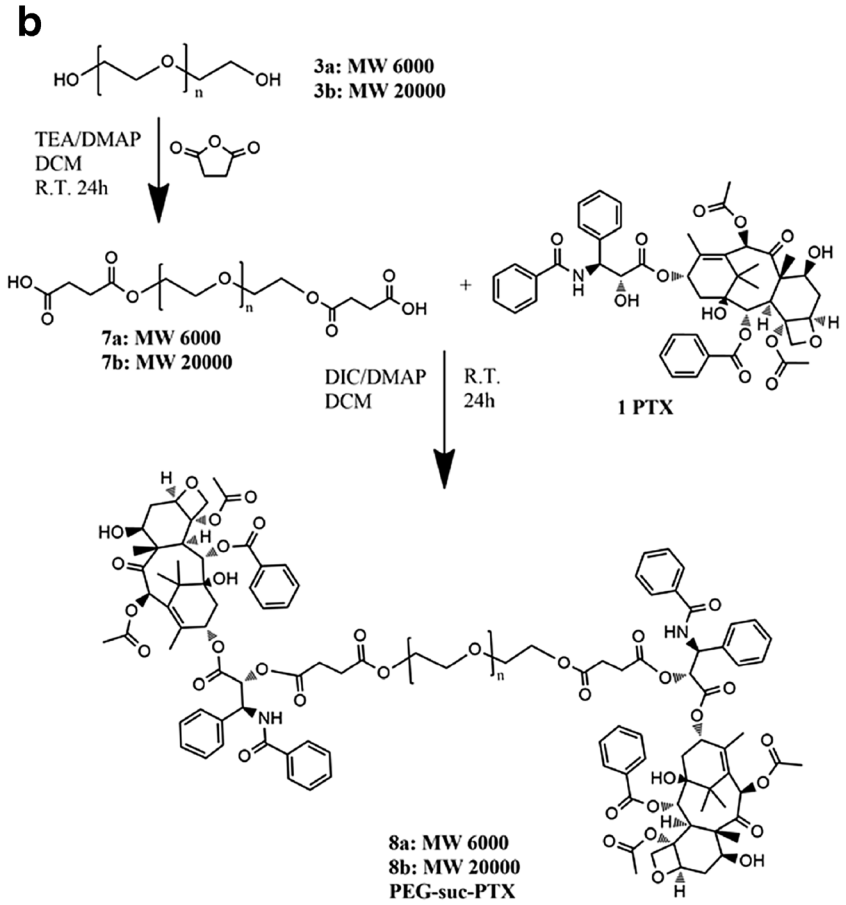

Fig. 1 (continued)

precipitate PEG-tosyl. The product was then filtrated and dried under vacuum overnight. The same method and reaction scale were applied for PEG 20 kDa. The yield was 80% at both PEG MW. Compounds 4a and 4b: ^{1}H NMR (400 MHz, D_2O, δ in ppm) δ 7.79 (d, $\mathcal{J}$ = 8.5 Hz, 4H), 7.45 (d, $\mathcal{J}$ = 7.9 Hz, 4H), 4.20 (d, $\mathcal{J}$ = 4.4 Hz, 4H), 3.62 (m, PEG), 2.39 (s, 6H, -CH_3).

PEG-tosyl 6 kDa (1.0 g, 0.167 mmol, 1.0 equiv.) and NaN_3 (0.106 g, 1.67 mMol, 10.0 equiv.) were dissolved in 5 mL DMF. The mixture was stirred at 90°C under argon atmosphere overnight. The product was precipitated in diethylether to remove DMF. Precipitates were dissolved in 10 mL water, and transferred to pre-wetted dialysis bags MW cut-off 2000 Da. Dialysis was carried out against deionized water overnight under stirring to remove excess sodium azide and DMF. The product was finally freeze dried. The same method and reaction scale were applied to PEG-tosyl 20 kDa. The yield was 80% at both PEG MW. Compounds **5a** and **5b**: ^{1}H NMR ($CDCl_3$, δ in ppm) δ 3.77–3.58 (m, PEG backbone), 3.41 (t, $\mathcal{J}$ = 5.0 Hz, 4H, PEG-O-CH_2-CH_2-N_3). FT-IR (Perkin Elmer, US) (cm^{-1}): 2916.74, 2113.73, 1644.69, 1469.55, 1349.95, 1297.95, 1251.61, 1097.31, 949.52, 840.07.

Synthesis of PTX Alkyne

The synthesis of PTX alkyne has previously been described (30). PTX (50 mg, 0.059 mmol, 1.0 equiv.) was dissolved in 5.0 mL anhydrous dichloromethane under Argon. 4-Pentynoic acid (6.9 mg, 0.07 mmol, 1.2 equiv.), DIC (11.1 mg, 0.08 mmol, 1.5 equiv.) and DMAP (3.5 mg, 0.03 mmol, 0.5 equiv.) were dissolved in dichloromethane under nitrogen. The resulting solution was left to stir under Argon at room temperature overnight. The product was purified using a silica gel column, and hexane/ethyl acetate 1:1 was used as eluent. Thin layer chromatography was used to track the product. Samples containing PTX were combined and the solvent was removed by vacuum. The product was dried under vacuum overnight. The yield was 65%. Compound **2**: ^{1}H NMR ($CDCl_3$, δ in ppm) δ 8.19 (d, $\mathcal{J}$ = 7.4 Hz, 2H, 2-OBz), 7.79 (d, $\mathcal{J}$ = 7.5 Hz, 2H, 3′-NBz), 7.68 (t, $\mathcal{J}$ = 7.4 Hz, 1H, 2-OBz), 7.58–7.51 (m, 3H, 2-OBz, 3′-NBz), 7.47–7.35 (m, 7H, 2-OBz, 3′-ph, 3′-NBz), 6.32 (s, 1H, C10-H), 6.28 (t, $\mathcal{J}$ = 8.9 Hz, 1H, C13-H), 6.00 (dd, $\mathcal{J}$ = 9.2, 3.0 Hz, 1H, C3′-H), 5.71 (d, $\mathcal{J}$ = 7.1 Hz, 1H, C2-H), 5.55 (d, $\mathcal{J}$ = 3.1 Hz, 1H, C2-H), 5.00 (d, $\mathcal{J}$ = 7.7 Hz, 1H, C5-H), 4.51–4.43 (m, 1H, C7-

H), 4.34 (t, J = 7.1 Hz, 1H, C20-H_a), 4.26–4.20 (m, 1H, C20-H_b), 3.84 (d, J = 7.1 Hz,1H, C3-H), 2.71 (m, 2H, HC≡C-CH_2-CH_2-COO-PTX), 2.60 (m, 2H, HC≡C-CH_2-CH_2-COO-PTX), 2.53 (m, 1H, C6-H_a), 2.51 (m, 1H 7-OH), 2.48(s, 3H, C4-OAc), 2.39 (m, 1H, C14-H_a), 2.26 (s, 3H, C10-OAc), 2.20 (m, 1H, C14-H_b), 1.97 (s, 3H, C18-Me), 1.94 (m, 1H, C6-H_b), 1.91 (s, 1H, *H*C≡C-CH_2-CH_2-COO-PTX), 1.68 (s, 3H, C19-Me), 1.26 (s, 3H, C17-Me) 1.15 (s, 3H, C16-Me). MS m/z (ES+) calculated from $C_{52}H_{55}NO_{15}$: 934.4 ($M+H^+$) (PTX-alkyne + H^+), 856.3 (fragment of PTX).

Synthesis of PEG-N_3-PTX Conjugates 6 and 20 kDa

PEG-N_3 6 kDa (100 mg, 0.016 mmol, 1.0 equiv.), PTX alkyne (39 mg, 0.04 mmol, 2.5 equiv.) and N,N,N′,N″,N″-Pentamethyldiethylenetriamine (10 μL, 0.05 mmol, 3.0 equiv.) were dissolved in 4 mL DMF under nitrogen, and then degassed for 10 min. Copper bromide (7 mg, 0.1 mmol, 3.0 equiv.) and sodium ascorbate (19.5 mg, 0.2 mmol, 6.0 equiv.) were dissolved in 1 mL DMF in another vial under nitrogen and degassed for 10 min. The mixture of coper bromide and sodium ascorbate were added into the reaction flask under nitrogen and degassed for another 10 min. The reaction was stirred at 45°C overnight. The conjugate was first purified by precipitation in cold diethylether to remove PTX and catalysts, and then by dialysis against water to remove copper bromide. The 20 k conjugate was produced with the same method. The yield was 70% at both PEG MW. Compounds **6a** and **6b**: ^{1}H NMR ($CDCl_3$, δ in ppm) δ 8.14 (d, J = 7.4 Hz, 4H, 2-OBz), 7.82 (d, J = 7.5 Hz, 4H, 3′-NBz), 7.62 (t, J = 7.4 Hz, 4H, 2-OBz), 7.56–7.45 (m, 10H, 2-OBz, 3′-NBz, 3′-ph), 7.42–7.33 (m, 12H, triazole, 2-OBz, 3′-ph, 3′-NBz), 6.28 (s, 2H, C10-H), 6.19 (t, J = 8.9 Hz, 2H, C13-H), 5.94 (dd, J = 8.6, 3.7 Hz, 2H, C3′-H), 5.67 (d, J = 7.0 Hz, 2H, C2-H), 5.44 (d, J = 3.7 Hz,, 2H, C2′-H), 4.96 (d, J = 8.5 Hz, 2H, C5-H), 4.53–4.39 (m, 6H, PEG-O-CH2-CH_2-triazole, C7-H), 4.31 (d, J = 8.5 Hz, 2H, C20-H_a), 4.19 (d, J = 8.5 Hz, 2H, C20-H_b), 3.80(m, 6H, C3-H, PEG-O-CH_2-CH_2-triazole), 3.55–3.75 (m, PEG), 3.03 (m, 4H, PEG-triazole-CH_2-CH2-CO-PTX), 2.85 (m, 4H, PEG-triazole-CH_2-CH_2-CO-PTX), 2.60–2.52 (m, 2H, C6-H_a), 2.50 (d, J = 3.9 Hz, 2H, 7-OH), 2.42 (s, 6H, C4-OAc), 2.29 (dd, J = 15.4, 9.4 Hz, 2H, C14-H_a), 2.23 (s, 6H, C10-OAc), 2.06 (dd, J = 15.4, 8.9 Hz, 2H, C14-H_b), 1.92 (s, 6H, C18-Me), 1.86 (m, 2H, C6-H_b), 1.68 (s, 6H, C-19), 1.22 (s, 6H, C17-Me), 1.13 (s, 6H, C16-Me).

Synthesis of PEG-suc 6 and 20 kDa

PEG 6 kDa (1.0 g, 0.167 mmol, 1.0 equiv.) was dissolved in 5 mL toluene and evaporated three times to remove water. The dried PEG was dissolved in dichloromethane under Argon. The solution was cooled to 0°C, succinic anhydride was added (100 mg, 1 mmol, 6.0 equiv.). TEA (0.14 mL, 1 mmol, 6.0 equiv.) was dropped with a syringe. The reaction was then kept on ice for 1 h and was stirred at room temperature overnight. The PEG-suc was purified by precipitation in cold diethylether three times. The precipitates were dried under vacuum at room temperature overnight. The same method and reaction scale were applied to PEG 20 kDa. The yield was 80% at both PEG MW. Compounds **7a** and **7b**: ^{1}H NMR ($CDCl_3$, δ in ppm) δ 4.22 (t, J = 25.0 Hz, 4H, PEG-O-CH_2-CH_2-O-succinic acid), 3.94–3.36 (m, PEG backbone), 2.71 (m, 8H, PEG-COO-CH_2-CH_2-COOH).

Synthesis of PEG-suc-PTX Conjugates 6 and 20 kDa

PEG-suc 6 kDa (100 mg, 0.017 mmol, 1.0 equiv.), PTX (37 mg, 0.04 mmol, 2.5 equiv.) and DMAP (5 mg, 0.04 mmol, 2.5 equiv.) were dissolved in 1.5 mL dichloromethane under nitrogen. The reaction flask was placed on ice and DIC (2.0 μL, 0.04 mmol, 2.5 equiv.) was added into the flask. The reaction was then stirred overnight at room temperature. The conjugate was purified by precipitation in cold diethylether three times and dried under vacuum. The 20 k conjugate was produced with the same method but with higher PTX ratio (equiv. 4.0). The yield was 70% at both PEG MW. Compounds **8a** and **8b**: ^{1}H NMR ($CDCl_3$, δ in ppm) δ 8.10 (m, 4H, 2-OBz), 7.85 (m, 4H, 3′-NBz), 7.62 (t, J = 7.4 Hz, 4H, 2-OBz), 7.56–7.45 (m, 10H, 2-OBz, 3′-NBz, 3′-ph), 7.42–7.33 (m, 10H, 2-OBz, 3′-ph, 3′-NBz), 7.33 (t, J = 6.8 Hz, 2H, 3′-NBz), 7.07 (t, J = 9.0 Hz, 2H, 3′-NH), 6.29 (s, 2H, C10-H), 6.23 (t, J = 8.7 Hz, C13-H, 1H), 5.97 (dd, J = 9.1, 3.0 Hz, 2H, C3′-H), 5.68 (d, J = 7.1 Hz, 2H, C2-H), 5.49 (d, J = 5.5 Hz, 2H, C2′-H), 4.97 (d, J = 7.9 Hz, 2H, C5-H), 4.45 (m, 2H, C7-H), 4.32 (d, J = 8.4 Hz, 2H, C20-H_a), 4.20 (d, J = 8.5 Hz, 2H, C20-H_b), 4.10 (m, 4H, PEG-O-CH_2-CH_2-O-succinic) 3.51–3.80 (m, PEG backbone), 2.80–2.69 (m, 4H, PEG-COO-CH_2-CH_2-COO-PTX), 2.64 (m, 4H, PEG-COO-CH_2-CH_2-COO-PTX), 2.56 (m, 2H, C6-H_a), 2.50 (d, J = 3.9 Hz, 2H, 7-OH), 2.44 (s, 6H, C4-OAc), 2.36 (dd, J = 15.4, 9.3 Hz, 2H, C14-H_a), 2.23 (s, 6H, C10-OAc), 2.15 (dd, J = 15.4, 8.9 Hz, 2H, C14-H_b), 1.98 (s, 6H, C18-Me), 1.86 (m, 2H, C6-H_b), 1.68 (s, 6H, C19-Me), 1.24 (s, 6H, C17-Me), 1.13 (s, 6H, C16-Me).

Solubility

The solubility of the conjugates was estimated by adding increasing amounts of conjugates to 0.1 mL ultrapure water at room temperature until saturation (29, 31). Solubility was estimated by the weights added in three parallel experiments.

Stability of Conjugates in PBS, BAL and Serum of Mice

The conjugates were dissolved in 5 mL PBS at pH 6.9 and pH 7.4 respectively (final concentration of PTX 20 μg/mL). The solutions were incubated at 37°C in a water bath with shaking. 200 μL samples were withdrawn at pre-determined time points. The samples were then diluted with acetonitrile and centrifuged at 15,000×*g* for 10 min before High Performance Liquid Chromatography (HPLC) analysis.

Female NMRI mice (6 to 8 week-old; Elevage Janvier, Le Genest-St-Isle, France) were used to collect serum and bronchoalveolar lavage (BAL). Blood samples were collected from the orbital sinus of the mice. The blood samples were kept in the fridge (4°C) overnight and centrifuged at 12,000×*g*. The serum supernatant was then taken and stored at −20°C. BAL was performed after euthanizing the mice by cervical dislocation. One ml of HBSS was injected into the trachea and left for 15 s. 0.5 mL of the fluid was then withdrawn and re-injected into the lung. All the BAL liquid was removed from the lung afterwards. This procedure was repeated twice until a total of 3 mL HBSS was injected. The BAL was then centrifuged at 4500×*g* for 10 min to remove the cells. The supernatant was collected and stored at −20°C. All experimental procedures were performed in compliance with guidelines of the Institutional Animal Care and Use Committee of the Université catholique de Louvain (Permit number: 2012/UCL/MD/006). Animals were anesthetized before manipulation and efforts were made to minimize animal suffering.

The 6 and 20 kDa conjugates were dissolved in 200 μL BAL in Eppendorf tubes at the concentration of 50 and 35 μg/mL (PTX equiv.). Conjugates were also dissolved in 40 μL serum at the same concentrations as above. All the samples were then incubated at 37°C. These tubes were taken out for analysis at different time points. 200 μL acetonitrile were added into the samples which were then centrifuged at 15,000×*g* for 10 min before HPLC analysis. The percentages of conjugates remaining in BAL or serum over time were calculated by comparing with the amount recovered at 0 h. The degradation half-lives of the conjugates were calculated from time *vs.* residual amount curves by assuming first-order kinetics.

HPLC was carried out using the Hewlett Packard series 1100 system (Agilent Technologies, Palo Alto, CA) using a reverse phase C_{18} column (NUCLEOSIL® 300–5 C18 5 μm particles 300 Å pores, 250 × 4.6 mm, MACHEREY-NAGEL GmbH & Co. KG, Düren, Germany). The mobile phase was acetonitrile and water eluted at 1 mL/min using a gradient protocol as follows: a linear gradient from acetonitrile 40 to 60% for 20 min, a linear gradient from acetonitrile 60 to 40% for 5 min. Absorbance of the column effluent was monitored at 227 nm (29). A standard curve was established in the range of 5–100 μg/mL of PTX dissolved in acetonitrile (correlation coefficient of $R^2 = 0.9995$, LOD = 1.52, LOQ = 5.01 μg/ml). Samples of 20 μL were injected. The areas under the peaks of conjugates and paclitaxel were monitored. The retention time of paclitaxel was 13 min according to this analytical method. PEG chain does not have a significant UV absorbance. After conjugation with paclitaxel, the PEG-PTX conjugates had retention times of 19–20 min for 6 k and 15–16 min for 20 k. The peaks of the mono- and di-conjugates were not separated in the method.

Cytotoxicity

The *in vitro* cytotoxicity of the conjugates was tested on LL/2 Lewis lung carcinoma cell line (ATCC® CRL-1642™) and B16-F10 melanoma cell line (ATCC® CRL-6475™) using the MTT assay. LL/2 cells were cultured in Dulbecco's Modified Eagle Medium (DMEM, Life Technologies, Belgium) and B16-F10 melanoma cells were cultured in Minimum Essential Medium Eagle Alpha (MEM Alpha, Life Technologies, Belgium). Both media were supplemented with 10% fetal bovine serum and 1% antibiotics (Pen Strep, Life Technologies, Belgium). The cells were maintained in a 5% CO_2 humidified atmosphere at 37°C.

Cells were seeded in 96 plates at a density of 100 cells/well for LL/2 and 1000 cells/well for B16-F10. Cells were then incubated with the 4 conjugates, and Taxol dissolved in 100 μL full culture medium at different concentrations (6×10^{-6}–2.5 μg/mL, PTX equivalent) for 72 h. PTX was also tested at the same concentrations by diluting PTX stock solution in DMSO (500 μg/mL) with culture medium. Less than 0.5% of DMSO was present in the final culture medium. Then, the medium was removed and the cells were incubated with MTT 0.5 mg/mL in culture medium without FBS for 3 h. MTT was aspirated off and DMSO was added to dissolve the formazan crystal. The absorbance was then measured at 560 nm with the spectrophotometer Multiskan EX (Thermo Scientific, US). Untreated cells were taken as control with 100% metabolic activity and cells incubated with Triton X-100 1% were used as positive control. The toxicity of PEG reagents (PEG, PEG-N_3 6 and 20 kDa, PEG-suc 6 and 20 kDa) was evaluated on LL/2 cells at a concentration corresponding to 2.5 μg/mL PTX in the conjugates. Cremophor EL/ethanol was also tested on LL/2 cells at a concentration corresponding to 2.5 μg/mL PTX in Taxol®. DMSO 0.5% in culture medium (corresponding to 2.5 ug/mL PTX) was tested on LL/2 cells as a control. The IC_{50} was calculated using the regression equation from the plot showing the cell metabolic activity *versus* the log of concentration.

Statistics

All the results were shown as mean ± standard deviation. Mann–Whitney test was conducted to demonstrate statistical differences ($p < 0.05$). The Pearson correlation coefficient was

calculated using the Excel function CORREL. Graphpad Prism as well as Microsoft Excel 2010 were used for data processing.

RESULTS AND DISCUSSION

Chemistry

PEG-N_3-PTX conjugates 6 and 20 kDa were obtained using "click" chemistry. PTX was first modified by pentynoic acid to obtain an alkyne group, while PEG was activated to PEG-azide by tosylation followed by azidation. DMF was chosen as the solvent because of the satisfactory solubilities of PTX, PEG as well as copper bromide in this solvent. As shown in Fig. 2, C2′-H on PTX shifted from δ 4.8 (a, Fig. 2) to δ 5.5 (a', Fig. 2) in ^{1}H NMR spectra, which indicates the formation of the ester bond.

PEG-suc-PTX conjugates 6 and 20 kDa were obtained using a typical method of esterification. First, succinic acid was added to the PEG backbone to introduce carboxyl groups and also to act as a spacer between PTX and PEG. PTX was then conjugated to PEG under the catalysts DIC/DMAP in dichloromethane. As shown in Fig. 2, C2′-H shifted from δ 4.8 (a, Fig. 2) to δ 5.5 (a", Fig. 2). No downfield shift was observed in ^{1}H-NMR for either of the C2 (i, Fig. 2) or C7 (e, Fig. 2) protons in both PEG-N_3-PTX and PEG-suc-PTX structures, which indicates that PTX was conjugated to PEG on the C2′. Therefore, the data confirm that it was not necessary to protect the 7-OH and 1-OH on PTX because the steric hindrance makes these two hydroxyls not easy to access for esterification (32). On the contrary, if the goal was to modify the 7-OH, the protection of 2′-OH on the side chain of PTX would be necessary (33). The PTX substitution reached 90% for both structures at both molecular weights.

The drug loading in the conjugates was calculated by dividing PTX mass by the whole molecule mass according to the ratio of PTX substitution calculated with ^{1}H NMR. It reached 20 and 7% (w/w) in all the structures of 6 and 20 kDa conjugates, respectively. The molecular ratio of PTX in PEG-PTX conjugates was approximately 1.8 PTX for 1 PEG molecule in both structures and both molecular weights.

The structure of the azide conjugate is novel with a hydrolysable ester bond and a stable triazole link between PEG and PTX. The ester bond ensures that paclitaxel can be released in an intact form and the triazole link enhances the stability of the conjugate. Although various polymer-paclitaxel conjugates have been prepared, few studies have been performed in the field of pulmonary drug delivery. In the case of the pulmonary delivery of polymer-drug conjugates, a long residence time of the conjugates in the lung is crucial for attaining sustained local drug concentrations. Herein, we used high molecular weight PEG in the conjugates, with the expectation that it should contribute to a long drug residency in the lung (9). Then, the progressive release of paclitaxel by hydrolysis of the ester bond should result in sustained local drug concentrations.

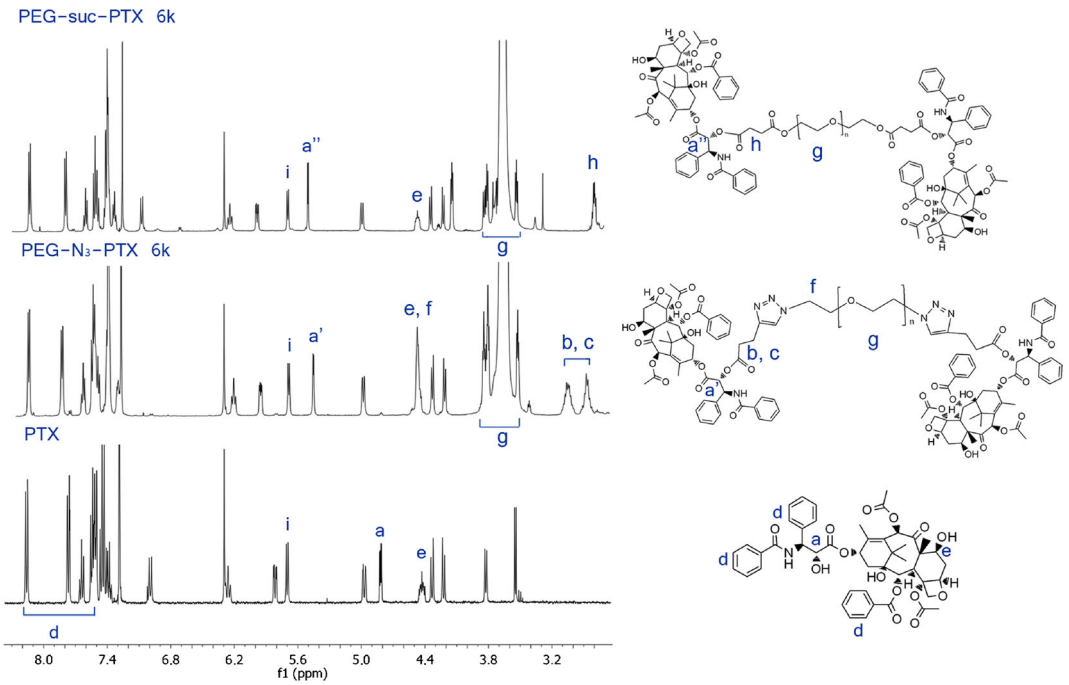

Fig. 2 ^{1}H NMR spectrum of PEG-suc-PTX, PEG-N_3-PTX 6 kDa and PTX.

Table I Half-Lives of Conjugates in Different Media

Conjugates	t ½ PBS pH 6.9 (h)	t ½ PBS pH 7.4 (h)	t½ BAL (h)	t ½ Serum (h)
PEG-N_3-PTX 6 k	>72	>72	8.6 ± 1.1	3.2 ± 0.8
PEG-N_3-PTX 20 k	>72	>72	7.2 ± 1.0	3.5 ± 0.6
PEG-suc-PTX 6 k	>72	10.0 ± 2.5*	2.5 ± 0.1*	1.1 ± 0.2*
PEG-suc-PTX 20 k	>72	36.1 ± 4.1	4.0 ± 0.4	1.0 ± 0.1

Means ± SD are given, $n = 3$. * $p < 0.05$, PEG-suc-PTX 6 k *versus* 20 k (Mann–Whitney)

Aqueous Solubility and *In Vitro* Stability of PEG-PTX Conjugates

The PEGylation of PTX greatly increased the aqueous solubility of PTX. The reported solubility of PTX in water in the literature is 0.3 μg/mL (34). PEG-N_3-PTX and PEG-suc-PTX 6 kDa conjugates showed a highly increased solubility of 30 and 25 mg/mL PTX equivalent (*i.e.*, 145 and 118 mg/mL conjugates). Although PEG is a hydrophilic molecule, the solubilities of the 20 kDa conjugates were lower (73 mg/mL for PEG-N_3-PTX 20 kDa and 61 mg/mL for PEG-suc-PTX 20 kDa, or 5.8 and 4.9 mg/mL PTX equivalent, respectively). Conjugation therefore increased the solubility of paclitaxel in pure water by 3–4 orders of magnitude. The solvation of the PEG chain probably decreases with the increase of PEG molecular weight, due to the crystalline structure of the polymer chain. The lower solubility with higher PEG molecular weight was also found in previous reports on PEG-PTX prodrugs (27, 29).

The *in vitro* stability tests were performed in PBS at pH 6.9 and 7.4, BAL and mouse serum. All the conjugates showed better stability in PBS pH 6.9 than in PBS pH 7.4. The pH of 6.9 is the pH of the lung lining fluid in humans (35), while the pH of 7.4 is the physiological pH of human blood. As shown in Table I and Fig. 3, the half-lives of these conjugates were longer than 72 h in PBS pH 6.9, but decreased significantly in BAL and serum. The PEG-N_3-PTX conjugates were more stable than the PEG-suc-PTX conjugates. In our strategy, PEG-N_3-PTX was designed due to the superiority of the stability of the triazole ring over the ester bond. The triazole ring is very stable and could not hydrolyse before the ester bond. Thus, free PTX will be released from the conjugate in an active form. However, there are two ester bonds between PTX and PEG in the structure of PEG-suc-PTX, which leads to increased possibilities for hydrolysis. As a result, the stability of the PEG-N_3-PTX conjugates should increase compared with the PEG-suc-PTX conjugates, which is consistent with the results obtained.

In BAL and PBS pH 7.4, the 20 kDa succinic conjugate presented longer half-life than the 6 kDa ($p < 0.05$ Mann–Whitney). However, for the azide conjugates, increased stability was not observed for the 20 kDa conjugate. In serum, all conjugates had short half-lives. The PEG-N_3-PTX azide conjugates showed better stability than the PEG-suc-PTX succinic conjugates at both MW in serum. Both 6 and 20 k molecular weights of conjugates presented similar stability in serum for both structures. Although in the literature, the hydrolysis rate of conjugates does not correlate with MW (25, 27, 29), the stability of PEG-suc-PTX conjugates at pH 7.4 and in

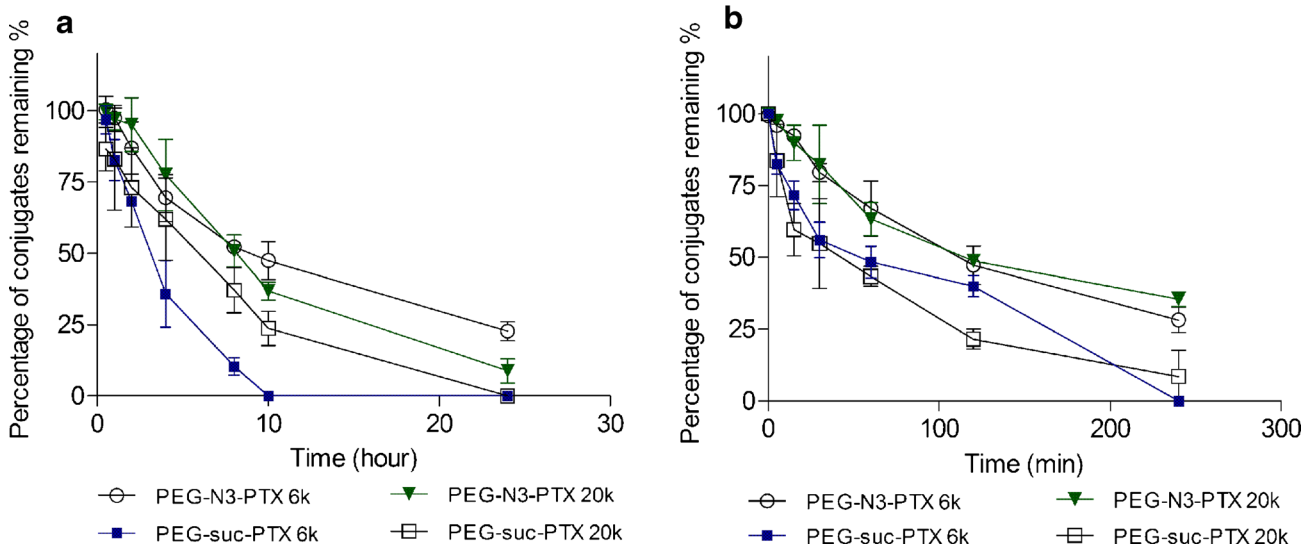

Fig. 3 Stability profiles of conjugates in bronchoalveolar lavage (**a**) and serum of mouse (**b**).

Table II IC_{50} Values of all the Conjugates Calculated Based on the Data of MTT Test

IC_{50} of conjugates on different cancer cells (μg/mL)		
	LL/2	B16-F10
PEG-N_3-PTX 6 k	0.0203 ± 0.0064 *	0.0567 ± 0.0110 *
PEG-N_3-PTX 20 k	0.0286 ± 0.0058 *	0.0521 ± 0.0134 *
PEG-suc-PTX 6 k	0.1789 ± 0.0551 *	0.3050 ± 0.0363 *
PEG-suc-PTX 20 k	0.0226 ± 0.0039 *	0.0809 ± 0.0083 *
Taxol	0.0039 ± 0.0006 *	0.0100 ± 0.0005 *
PTX	0.0022 ± 0.0005	0.0069 ± 0.0009

Means ± SD are given, $n = 3$, 8 measurements each test. * $p < 0.05$, conjugates or Taxol *versus* PTX group, respectively (Mann–Whitney)

BAL was dependent on MW in our study. The increased stability of the 20 kDa PEG-suc-PTX might result from the increased steric hindrance created by PEG and thereby, decreased accessibility of esterases for hydrolysis.

Cytotoxicity

The cytotoxicity of the conjugates was evaluated on LL/2 Lewis lung carcinoma cells and B16-F10 melanoma cells, which are widely used cell lines to establish a lung cancer model or a lung metastasis model in mice (36–38). The conjugates and Taxol® were incubated at 37°C with the cells for 72 h in order to provide enough time for PTX release. Free PTX was also tested as a control. All the conjugates showed cytotoxicity on both cell lines but lower than Taxol® and free PTX. Taxol had a similar cytotoxic profile as free PTX but with higher IC_{50}. The IC_{50} of all the conjugates were 5-fold higher compared with Taxol® and more than 7-fold higher compared with free PTX (Table II, Fig. 4). This is likely due to the slow release of PTX from the conjugates. However, the statistical test was not able to show a correlation between the *in vitro* release of the four conjugates in all the media tested and the cytotoxicity (Pearson correlation, $p > 0.05$ for all). The sensitivity of these two cell lines to PTX cannot be compared because the numbers of cells seeded were different in the tests in order to reach the linear detection range of the UV absorbance.

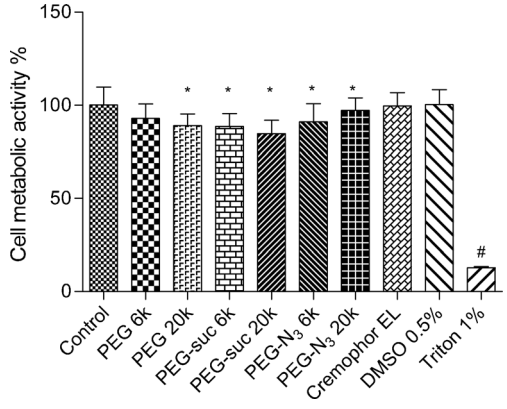

Fig. 5 Cytotoxicity of PEG reagents on LL/2 cells after 72 h incubation at the concentration of 2.5 μg/mL (PTX equiv.). Results are shown as the mean of three independent tests (8 measurements per test) and standard deviation. * $p < 0.05$, when compared with control group. # $p < 0.05$, when compared with triton 1% (Mann–Whitney).

The cellular internalization process is supposed to be different for free paclitaxel and Taxol®, which comprises nanomicelles. Taxol showed a slightly increased IC50 value compared with free paclitaxel. In the case of the 4 conjugates, as molecular mass of conjugates increased, the cellular internalization likely involved endocytosis instead of diffusion of free PTX. This change of mechanism along with the slow release of PTX from the conjugates might lead to the increase of IC_{50}. An increase of the IC_{50} after conjugation of anticancer drugs to polymers has previously been reported (25).

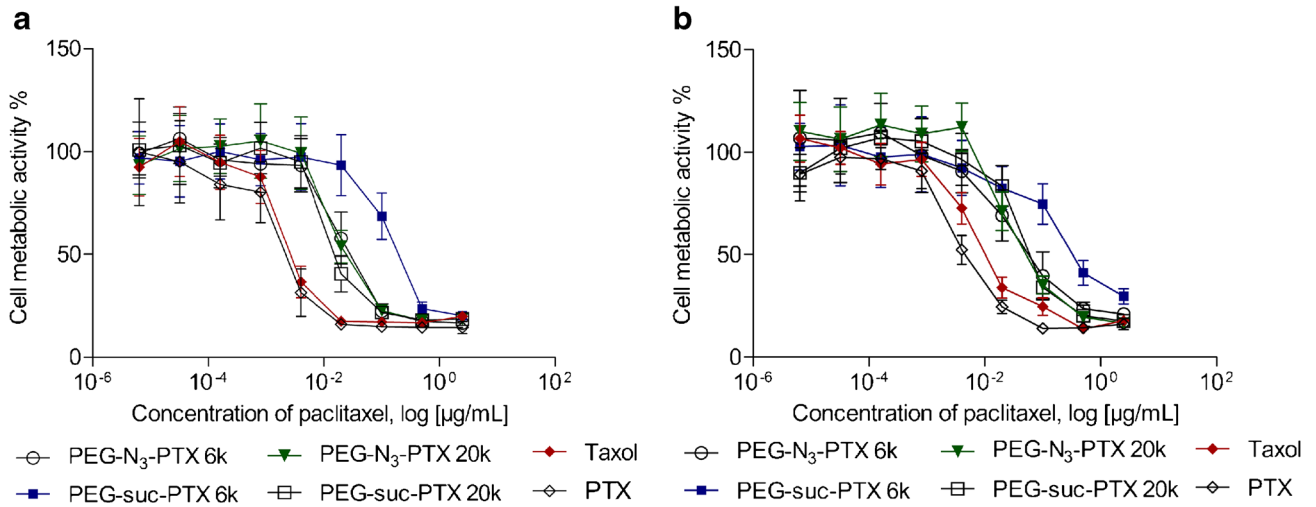

Fig. 4 Cell metabolic activities of PEG-PTX conjugates and Taxol® on LL/2 Lewis lung cancer cells (**a**) and B16-F10 melanoma cells (**b**). Results are shown as the mean of 3 independent tests (8 measurements each test) and standard deviation.

PTX was turned to a prodrug by PEGylation at the 2′-OH which is a necessary group for cytotoxicity (39). Thus the prodrug temporally lost cytotoxicity. After the hydrolysis of the ester bond between PTX and PEG, PTX was released in a non-conjugated form and began to interfere with the cell cycle and led to cell death.

We assessed the cytotoxicity of the PEG reagents, PEG-suc and PEG-N_3, on LL/2 cells because as PTX was released, PEG reagents were simultaneously released. The results showed that all the PEG reagents were very slightly toxic to LL/2 cells at the concentration of 2.5 μg/mL (PTX equiv.; Fig. 5), which was the highest concentration used in the cytotoxicity assay for LL/2 cells (Fig. 4). In particular, PEG-suc 20 k was slightly toxic to LL/2 cells, with a 15% loss of viability after 72 h of contact. In Taxol®, paclitaxel is dissolved in Cremophor EL and ethanol (1:1 v/v). Because Cremophor EL is involved in the side effects induced by Taxol®, we also tested the cytotoxicity of Cremophor EL with ethanol on LL/2 cells. Results showed that Cremophor EL did not inhibit the growth of LL/2 cells at the concentration of 2.5 μg/mL (PTX equiv.; Fig. 5). This could come from the low concentration of Cremophor EL tested. Therefore, the decrease in cell viability induced by Taxol® (Fig. 4) was caused by paclitaxel itself, and not the excipients Cremophor EL and ethanol. To exclude the interference of DMSO used in the stock solution of free PTX, the cytotoxicity of 0.5% DMSO was also tested on LL/2 cells. This amount of DMSO in culture medium corresponded to the highest PTX concentration 2.5 μg/mL used in this test. Results showed DMSO below this level did not interfere with the cell viability (Fig. 5).

To have an idea of the PTX concentrations in the cell culture medium after 72 h of incubation of the conjugates, we extracted PTX from the supernatant of the incubation medium of PEG-N_3-PTX 6 kDa (200 μg/mL PTX equiv.) in a separate experiment and assayed it by HPLC. We found that the concentration of PTX was 23 ± 4 μg/mL, which is only 12% of the total amount of PTX in the conjugate. In addition, there was only 11% of intact PEG-N_3-PTX 6 kDa conjugate remaining in the incubation medium. The low level of PTX detected may be due to the uptake and metabolism of PTX by the cells. We suggest that the conjugates were taken up by the cells through endocytosis and then that PTX was released in the cytoplasm and had its cytotoxic effect. This hypothesis might explain the lack of correlation between cytotoxicity and drug release in acellular media. On the other hand, a study in the literature investigated the intracellular fate of polymer-bound anticancer agents and showed that the toxicity of conjugates might appear against the cytoplasmic, endosomal or lysosomal membranes. Then, the disintegration of the cell organization preceded apoptosis (40). Therefore, conjugates themselves could present cytotoxicity without the release of the anticancer drug. In the case of our PEG-PTX conjugates, the results imply that the toxicity of the conjugates was mainly caused by the released PTX or the conjugates themselves, but not by the PEG reagents.

CONCLUSION

Two structures of PEG-PTX conjugates with ester bond as linkage have been produced. Large PEGs with MW of 6 and 20 kDa have been employed for the purpose of sustaining the presence of PTX in the lungs. The conjugates developed by click chemistry demonstrated good stability at the pH of the lung lining fluid and in murine BAL, which is essential for sustaining drug release in the lungs. *In vitro* cytotoxicity studies on two types of cancer cells showed that the IC_{50} of all the conjugates were increased due to the formation of the prodrugs at 2′-OH on PTX. To conclude, the delivery system of PEG-PTX conjugates shows the potential to sustain the release of PTX in the lungs. The sustained drug release and the anti-tumor efficacy of the conjugates are currently investigated *in vivo* in the Lewis lung cancer murine model. If efficacy and safety are demonstrated in animal models, these conjugates could possibly be administrated to patients using a nebulizer and a mouthpiece in a cytotoxic chamber in the hospital in preliminary clinical trials.

ACKNOWLEDGMENTS AND DISCLOSURES

This work was a thesis project funded by the European Commission, Education, Audiovisual and Culture Executive Agency (EACEA), Erasmus Mundus programme, NanoFar doctorate. This work was also supported by the Fonds de la Recherche Scientifique Médicale, Belgium (Grant 3.4503.12). Rita Vanbever is Maître de Recherches of the Fonds National de la Recherche Scientifique (Belgium). The author would like to thank Dr. Cecil Le Duff, Department of chemistry, Université catholique de Louvain, for helping with detection and analysis of NMR data.

REFERENCES

1. Torre LA, Bray F, Siegel RL, Ferlay J, Lortet-Tieulent J, Jemal A. Global cancer statistics, 2012. CA Cancer J Clin. 2015;65:87–108.
2. Patton JS, Fishburn CS, Weers JG. The lungs as a portal of entry for systemic drug delivery. Proc Am Phorac Soc. 2004;1:338–44.
3. Zarogoulidis P, Giraleli C, Karamanos NK. Inhaled chemotherapy in lung cancer: safety concerns of nanocomplexes delivered. Ther Deliv. 2012;3:1021–3.
4. Loira-Pastoriza C, Todoroff J, Vanbever R. Delivery strategies for sustained drug release in the lungs. Adv Drug Deliv Rev. 2014;75:81–91.
5. Roa WH, Azarmi S, Al-Hallak MH, Finlay WH, Magliocco AM, Lobenberg R. Inhalable nanoparticles, a non-invasive approach to

treat lung cancer in a mouse model. J Control Release. 2011;150: 49–55.
6. Garbuzenko OB, Saad M, Betigeri S, Zhang M, Vetcher AA, Soldatenkov VA, *et al.* Intratracheal versus intravenous liposomal delivery of siRNA, antisense oligonucleotides and anticancer drug. Pharm Res. 2009;26:382–94.
7. Waiteand CL, Roth CM. Nanoscale drug delivery systems for enhanced drug penetration into solid tumors: current progress and opportunities. Crit Rev Biomed Eng. 2012;40:21–41.
8. Jain RK. Transport of molecules in the tumor interstitium: a review. Cancer Res. 1987;47:3039–51.
9. Gursahani H, Riggs-Sauthier J, Pfeiffer J, Lechuga-Ballesteros D, Fishburn CS. Absorption of polyethylene glycol (PEG) polymers: the effect of PEG size on permeability. J Pharm Sci. 2009;98:2847–56.
10. Koussoroplis SJ, Paulissen G, Tyteca D, Goldansaz H, Todoroff J, Barilly C, *et al.* PEGylation of antibody fragments greatly increases their local residence time following delivery to the respiratory tract. J Control Release. 2014;187:91–100.
11. Bayard FJ, Thielemans W, Pritchard DI, Paine SW, Young SS, Backman P, *et al.* Polyethylene glycol-drug ester conjugates for prolonged retention of small inhaled drugs in the lung. J Control Release. 2013;171:234–40.
12. Duncan R, Vicent MJ, Greco F, Nicholson RI. Polymer-drug conjugates: towards a novel approach for the treatment of endrocine-related cancer. Endocr Relat Cancer. 2005;12 Suppl 1:S189–199.
13. Vicent MJ. Polymer-drug conjugates as modulators of cellular apoptosis. AAPS J. 2007;9:E200–207.
14. Krishnaand R, Mayer LD, Multidrug resistance (MDR) in cancer. Mechanisms, reversal using modulators of MDR and the role of MDR modulators in influencing the pharmacokinetics of anticancer drugs. Eur J Pharm Sci. 2000;11:265–83.
15. Cole SP, Bhardwaj G, Gerlach JH, Mackie JE, Grant CE, Almquist KC, *et al.* Overexpression of a transporter gene in a multidrug-resistant human lung cancer cell line. Science. 1992;258:1650–4.
16. Danhier F, Danhier P, De Saedeleer CJ, Fruytier AC, Schleich N, Rieux A, *et al.* Paclitaxel-loaded micelles enhance transvascular permeability and retention of nanomedicines in tumors. Int J Pharm. 2015;479:399–407.
17. Sparreboom A, van Tellingen O, Nooijen WJ, Beijnen JH. Nonlinear pharmacokinetics of paclitaxel in mice results from the pharmaceutical vehicle Cremophor EL. Cancer Res. 1996;56: 2112–5.
18. Gelderblom H, Verweij J, Nooter K, Sparreboom A. Cremophor EL: the drawbacks and advantages of vehicle selection for drug formulation. Eur J Cancer. 2001;37:1590–8.
19. Kiss L, Walter FR, Bocsik A, Veszelka S, Ozsvari B, Puskas LG, *et al.* Kinetic analysis of the toxicity of pharmaceutical excipients Cremophor EL and RH40 on endothelial and epithelial cells. J Pharm Sci. 2013;102:1173–81.
20. Chen S, Li L, Zhao C, Zheng J. Surface hydration: principles and applications toward low-fouling/nonfouling biomaterials. Polymer. 2010;51:5283–93.
21. Brancaand C, Magazu S. Hydration study of PEG/water mixtures by quasi elastic light scattering, acoustic and rheological measurements. J Phys Chem B. 2002;106:10272–6.
22. Navath RS, Wang B, Kannan S, Romero R, Kannan RM. Stimuli-responsive star poly(ethylene glycol) drug conjugates for improved intracellular delivery of the drug in neuroinflammation. J Control Release. 2010;142:447–56.
23. Li C, Price JE, Milas L, Hunter NR, Ke S, Yu DF, *et al.* Antitumor activity of poly(L-glutamic acid)-paclitaxel on syngeneic and xenografted tumors. Clin Cancer Res. 1999;5:891–7.
24. Zou Y, Fu H, Ghosh S, Farquhar D, Klostergaard J. Antitumor activity of hydrophilic Paclitaxel copolymer prodrug using locoregional delivery in human orthotopic non-small cell lung cancer xenograft models. Clin Cancer Res. 2004;10:7382–91.
25. Greenwald RB. PEG drugs: an overview. J Control Release. 2001;74:159–71.
26. Greenwald RB, Choe YH, McGuire J, Conover CD. Effective drug delivery by PEGylated drug conjugates. Adv Drug Deliv Rev. 2003;55:217–50.
27. Greenwald RB, Gilbert CW, Pendri A, Conover CD, Xia J, Martinez A. Drug delivery systems: water soluble taxol 2′-poly(ethylene glycol) ester prodrugs-design and in vivo effectiveness. J Med Chem. 1996;39:424–31.
28. Khandare JJ, Jayant S, Singh A, Chandna P, Wang Y, Vorsa N, *et al.* Dendrimer versus linear conjugate: influence of polymeric architecture on the delivery and anticancer effect of paclitaxel. Bioconjug Chem. 2006;17:1464–72.
29. Arpicco S, Stella B, Schiavon O, Milla P, Zonari D, Cattel L. Preparation and characterization of novel poly(ethylene glycol) paclitaxel derivatives. Int J Pharm. 2013;454:653–9.
30. Pilkington-Miksa M, Arosio D, Battistini L, Belvisi L, De Matteo M, Vasile F, *et al.* Design, synthesis, and biological evaluation of novel cRGD-paclitaxel conjugates for integrin-assisted drug delivery. Bioconjug Chem. 2012;23:1610–22.
31. Greenwald RB, Pendri A, Bolikal D. Highly water soluble taxol derivatives: 7-polyethylene glycol carbamates and carbonates. J Org Chem. 1995;60:331–6.
32. Deutsch HM, Glinski JA, Hernandez M, Haugwitz RD, Narayanan VL, Suffness M, *et al.* Synthesis of congeners and prodrugs. 3. Water-soluble prodrugs of taxol with potent antitumor activity. J Med Chem. 1989;32:788–92.
33. de Groot FM, van Berkom LW, Scheeren HW. Synthesis and biological evaluation of 2′-carbamate-linked and 2′-carbonate-linked prodrugs of paclitaxel: selective activation by the tumor-associated protease plasmin. J Med Chem. 2000;43:3093–102.
34. Lee J, Lee SC, Acharya G, Chang CJ, Park K. Hydrotropic solubilization of paclitaxel: analysis of chemical structures for hydrotropic property. Pharm Res. 2003;20:1022–30.
35. Ng AW, Bidani A, Heming TA. Innate host defense of the lung: effects of lung-lining fluid pH. Lung. 2004;182:297–317.
36. Rocks N, Bekaert S, Coia I, Paulissen G, Gueders M, Evrard B, *et al.* Curcumin–cyclodextrin complexes potentiate gemcitabine effects in an orthotopic mouse model of lung cancer. Br J Cancer. 2012;107:1083–92.
37. Sorrentino R, Morello S, Luciano A, Crother TR, Maiolino P, Bonavita E, *et al.* Plasmacytoid dendritic cells alter the antitumor activity of CpG-oligodeoxynucleotides in a mouse model of lung carcinoma. J Immunol. 2010;185:4641–50.
38. Yoshiura K, Nishishita T, Nakaoka T, Yamashita N, Yamashita N. Inhibition of B16 melanoma growth and metastasis in C57BL mice by vaccination with a syngeneic endothelial cell line. J Exp Clin Cancer Res. 2009;28:13.
39. Li W, Zhang P, De Clercq E, Lou H, Liu X. Current drug research on PEGylation with small molecular agents. Prog Polym Sci. 2013;38:421–44.
40. Hovorka O, St'astny M, Etrych T, Subr V, Strohalm J, Ulbrich K, *et al.* Differences in the intracellular fate of free and polymer-bound doxorubicin. J Control Release. 2002;80:101–17.

Volume 7 | Number 28 | 28 July 2016 | Pages 4577–4704

Polymer Chemistry

www.rsc.org/polymers

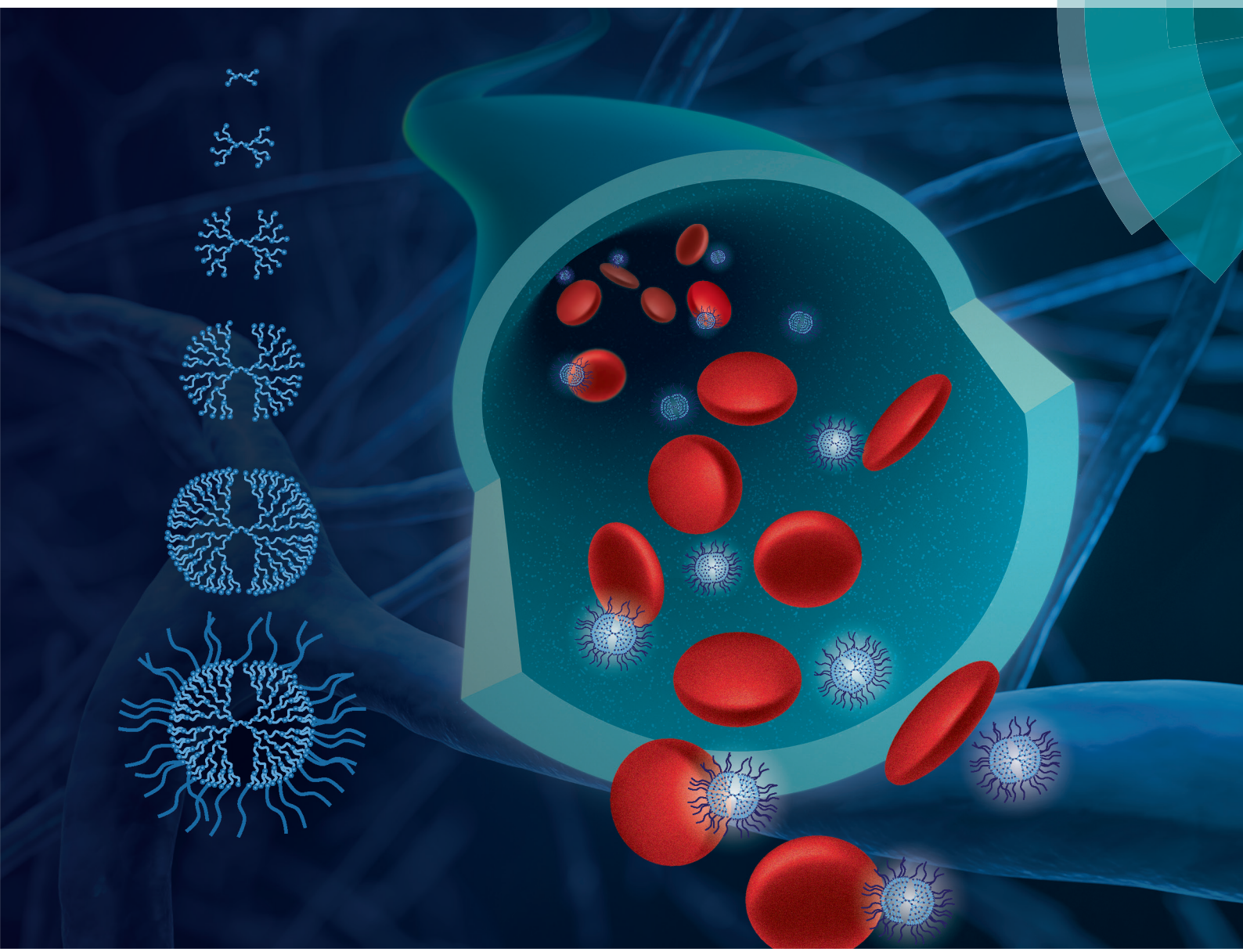

ISSN 1759-9954

ROYAL SOCIETY OF CHEMISTRY

PAPER
R. M. England *et al.*
Enhanced cytocompatibility and functional group content of poly(L-lysine) dendrimers by grafting with poly(oxazolines)

175 YEARS

Polymer Chemistry

PAPER

View Article Online
View Journal | View Issue

Cite this: *Polym. Chem.*, 2016, **7**, 4609

Enhanced cytocompatibility and functional group content of poly(L-lysine) dendrimers by grafting with poly(oxazolines)†

R. M. England,*[a,b] J. I. Hare,[a] P. D. Kemmitt,[a] K. E. Treacher,[c] M. J. Waring,[a] S. T. Barry,[a] C. Alexander[d] and M. Ashford[b]

Received 17th March 2016,
Accepted 18th May 2016

DOI: 10.1039/c6py00478d

www.rsc.org/polymers

When considering the design of an advanced drug delivery system, a common desirable attribute is to have a prolonged residence time in blood circulation so that accumulation and localised payload release may occur at the site of interest (*e.g.* a tumour). Polyethylene glycol (PEG) has been a gold standard for fulfilling this requirement, and consequently has been well investigated as a material for surface modification of dendrimers. As an alternative, we have explored the use of polyoxazolines (POZ)s as materials for modifying the surface of a generation 5 L-lysine dendrimer and found that there was a significant improvement in the biocompatibility properties over the unmodified dendrimer. One particularly useful advantage of POZ over PEG lies in the main-chain pendant groups available that we were able to exploit to impart functionality. Modifying the POZ to have pendant carboxyl groups led to a novel modified dendrimer with significantly more sites for conjugation. With this, we have demonstrated a sixfold increase in the loading of coumarin (our model compound) when compared to a non-functional POZ equivalent.

Introduction

Dendrimer-drug conjugates, typically in the range of 2–25 nm in size, are increasingly popular as drug delivery systems because they are water soluble, have near-monomodal molecular weight distributions, reproducible synthesis steps and have large numbers of surface groups available for drug conjugation. In addition, these accessible functional groups can be easily modified for property enhancement, for example by substitution with PEG chains to reduce cytotoxicity and systemic clearance. PEGylation has been widely employed with polyamidoamine (PAMAM)[1–4] and poly(L-lysine) dendrimers.[5–8] The circulation time of these cationic dendrimers is significantly improved when modified with PEG as the surface charge is neutralised and PEG tends to have low reticuloendothelial system uptake and low immunogenicity. These types of drug delivery systems can also benefit from accumulation at the site of interest (*e.g.* a tumour *via* the Enhanced Permeation and Retention (EPR) effect) allowing for desirable localised drug delivery.[9] However, the relative inertness of PEG can also be disadvantageous, as it is difficult to functionalise PEG itself with components like targeting ligands. To improve the diversity and functionality of these derivatised poly(amine) dendrimer systems we chose to use POZs as an alternative material to modify the dendrimer surface. POZs have become popular alternatives to PEG, in-part owing to the diversity offered by the pendant group that could in turn be derivatised to a wide range of different functionalities with many different resulting polymer properties.[10–12] Furthermore, the implementation of microwave synthesis for POZs has significantly improved reaction rates whilst maintaining living polymerisation, leading to well-defined polymers with facile introduction of chain-end functionality.[13–15] POZs have been reported to have similar stealth and biocompatibility properties to PEG[16–18] and thus have been widely used in the field of investigational polymer therapeutics.[19–22] With this in mind we considered two of the most widely used types of POZ for bioapplications; poly(2-methyl-2-oxazoline) (PMOx) and poly(2-ethyl-2-oxazoline) (PEOx) for the surface modification of a generation 5 L-lysine dendrimer. The attraction of this system lies in the fine-tuning of the properties that could be achieved by using POZ through main-chain and end group variation *e.g.* improved water solubility and improved viscosity properties. In this manuscript, the most important main-chain variation that we have explored is a POZ with a pendant ester group that was synthesized and used to modify pre-formed

[a]*AstraZeneca, Oncology iMed, Alderley Park, Macclesfield, Cheshire SK10 4TG, UK. E-mail: Richard.England@astrazeneca.com*
[b]*AstraZeneca, Pharmaceutical Science, Innovative Medicines, Silk Court Business Park, Macclesfield, Cheshire SK10 2NA, UK*
[c]*AstraZeneca, Pharmaceutical Technology and Development, Silk Court Business Park, Macclesfield, Cheshire SK10 2NA, UK*
[d]*School of Pharmacy, University of Nottingham, UK*
† Electronic supplementary information (ESI) available: Additional GPC chromatograms, Fig. 25–27. See DOI: 10.1039/c6py00478d

lysine dendrimers. Subsequent deprotection of the ester groups yielded carboxyl functionalities along the backbone and therefore significantly more sites for drug conjugation than currently available using existing PEG and PMOx/PEOx modified dendrimers. Without these additional conjugation sites these types of dendrimers are limited to the remaining (lysine) functional groups from the dendrimer scaffold. These novel dendrimer types have been explored for properties which would underlie their potential application as drug delivery systems using a model compound (coumarin) to conjugate to the dendrimers as a proof-of-principle experiment to test drug loading and cytocompatibility.

Materials and methods

Materials

All reagents and solvents were purchased from Sigma Aldrich with exception of MeO-PEG-COOH (2000 Da) (Iris Biotech GMBH), Boc-L-Lys(Boc)-ONp & 2-chloro-4,6-dimethoxy-1,3,5-triazine (Chem-Impex International), 2-chloroethylamine hydrochloride (Fluorochem Inc.), sodium methoxide 5.4 M (Acros Organics), Fetal calf serum (PAA), NucView™ (Biotium). Sartorius AG Viva-Flow® 50 cassettes (30 kDa MWCO) were purchased from VWR. Polyethylene oxide standards were purchased from Agilent Technologies as a kit. Wistar rat heparinized whole blood was ordered fresh from Harlan Laboratories UK Ltd and used the same day.

Equipment

^{1}H NMR analysis was performed on a Bruker AV400. Gel Permeation Chromatography-Refractive Index (GPC)-RI was performed on a Malvern TDA302 with either an Agilent Technologies aquagel-OH-20 column running 50/50 MeOH/40 : 10 mM $NaNO_3$: NaH_2PO_4 as the eluent or a Tosoh Bioscience TSKgel GMPWxl column with 40 : 10 mM $NaNO_3$: NaH_2PO_4 as the eluent. The system calibration was performed using a single poly(ethylene oxide) standard (16 100 g mol^{-1}) and absolute molecular weights determined using the refractive index and light scattering signals. Organic GPC was performed with DMF (0.05 M LiBr) and a universal calibration using PEG/PEO narrow standards ranging from 194 g mol^{-1} to 16 100 g mol^{-1}. GPC-UV was performed on a Waters HP1100 fitted with a Tosoh Bioscience TSKgel GMPWxl column with PBS as the eluent and UV detection at 220 nm. Haemoglobin levels were recorded using a HemoCue® Hb210 and HemoCue plasma/low Hb system for high and low hemoglobin concentration measurements. Samples were centrifuged in a Eppendorf™ MiniSpin™ microcentrifuge. Dynamic light scattering was performed on a Malvern Zetasizer® Nano ZS instrument with back scattering detector (173°, 633 nm laser wavelength). The dispersant RI and viscosity were assumed to be that of water (n = 1.59 and η = 0.888 mPa·s). The sample RI was 1.59 and the temperature was set at 25 °C. The hydrodynamic diameter (D_H) was reported as the volume-weighted average after a minimum of twelve measurements per sample and was calculated by the software. Samples were made to concentrations of 5 mg mL^{-1} in 10 mMolar NaCl solution or a 40 : 10 mMolar ratio of $NaNO_3$: NaH_2PO_4 at pH 7.4 and were filtered using a 0.2 μm syringe filter prior to measurement. Data was obtained using Malvern Zetasizer software version 6.21J. Haemoaggregation was measured on a Zeiss Axio Scope. A1 at 40× magnification. Images were taken with an integrated Zeiss Axio Cam ERc 5 s camera and manipulated with Zeiss ZEN Lite 2011 software.

Methods

4-(4,6-Dimethoxy-1,3,5-triazin-2-yl)-4-methylmorpholinium chloride and tetrafluoroborate. DMTMM·Cl[23] and DMTMM·BF_4 [24] were synthesised according to methods reported previously.

***N*-(2-Aminoethyl)-2-oxo-2*H*-chromene-3-carboxamide (coumarin-NH_2).** Coumarin-3-carboxylic acid (200 mg, 1.05 mmol) and DMTMM·BF_4 (518 mg, 1.58 mmol) were weighed into a reaction vial. DMF (5 mL) was added, followed by *tert*-butyl (2-aminoethyl)carbamate (253 mg, 1.58 mmol) dissolved in anhydrous DMF (0.5 mL). The reaction was followed to completion by UPLC-MS (approximately 30 min). The reaction mixture was diluted with EtOAc (20 mL), and washed with saturated $NaHCO_3$ (2 × 10 mL) and saturated brine (2 × 10 mL). The organic layer was dried over $MgSO_4$, filtered and evaporated to afford crude product, which was purified by flash silica chromatography, elution gradient 20 to 70% 3 : 1 EtOAc/EtOH in heptane to give *tert*-butyl (2-(2-oxo-2*H*-chromene-3-carboxamido)ethyl)carbamate (264 mg, 76%). The boc-deprotecting group was removed by stirring the solid in DCM (7.5 mL) and TFA (1 mL, 16 eq.) for 4 h and removing the solvents under vacuum at room temperature overnight to give the title compound. Yield = 275 mg, 100% (TFA salt). MS ES$^+$ = 333.3 (analytical ESI S2 Fig. 1–4†).

Generation 5 L-lysine dendrimer. The dendrimer was synthesised to generation 2 according to a literature method.[25] Successive generations were synthesised from repetitive steps involving the deprotection of the previous generation's lysine boc-protecting groups using trifluoroacetic acid (50 eq. to boc groups) in DCM (10× volume) followed by partial evaporation and precipitation into 20× excess of diethyl ether. A white solid was obtained through filtration and overnight drying in a vacuum oven. Further reaction with Boc-L-Lys(Boc)-Onp in the presence of triethylamine produced the next generation boc-protected dendrimer. Reaction times, equivalents of reagents and yields are summed up in ESI S1 Table 1.† ^{1}H NMR and MALDI-TOF-MS ESI S2 Fig. 5.†

HOOC-poly(2-methyl-2-oxazoline)-OMe (1a). Freshly distilled 2-methyl-2-oxazoline (2 g, 23.5 mmol) (over CaH_2, N_2) was added to an oven-dried, nitrogen-purged microwave tube fitted with a septum. Anhydrous acetonitrile (4 mL) was added *via* syringe, followed by *tert*-butyl bromoacetate (0.195 g, 1 mmol). The reaction mixture was transferred to a microwave reactor and heated to 140 °C for 30 min. The solution was cooled to 0 °C using an ice bath and then sodium methoxide solution (2 M, 2.5 mL, 5 eq.) was added dropwise and then stirred for 10 minutes at 0 °C. Sodium hydroxide solution (2 M, 2 mL) was added and the reaction mixture was stirred overnight at rt. The reaction mixture was acidified to pH 5 using HCl (2 M)

and then the solvents were removed by rotary evaporation. Anhydrous ethanol (dried over 3A molecular sieves) (15 mL) was added and the flask agitated under a nitrogen blanket until the polymer had dissolved leaving behind the NaCl salts which were filtered off. The ethanol was evaporated and the process repeated. The polymer was dissolved in a minimum volume of anhydrous ethanol and was added to a large volume of diethyl ether (400 mL), filtered and dried under vacuum. To remove traces of ethanol the polymer was freeze-dried to obtain the title compound as a white solid. Yield = 1.9 g, 89%. ^{1}H NMR ESI S2 Fig. 6.†

HOOC-poly(2-ethyl-2-oxazoline)-OMe (1b). This compound was synthesised following the method for **1a**, but in place of anhydrous ethanol, anhydrous DCM was used to remove the unwanted NaCl salts. The polymer was obtained as a white solid after precipitation into diethyl ether, filtering and drying overnight under vacuum at 40 °C. Yield = 1.74 g, 83%. ^{1}H NMR ESI S2 Fig. 7.†

MeO-PEG-COOH (2000 Da) (1c). This polymer was purchased from Iris Biotech GMBH. ^{1}H NMR ESI S2 Fig. 8.†

Methyl 4-(2-chloroethyl)amino)-4-oxobutanoate. This compound was synthesised according to the literature[26] using methyl 4-chloro-4-oxobutyrate (8 g, 53.13 mmol) to give the title compound (6.92 g, 67.3%) as a yellow oil. The crude product was used without further purification.

Methyl 3-(4,5-dihydrooxazol-2-yl)propanoate. Methyl 4-((2-chloroethyl)amino)-4-oxobutanoate (6.9 g, 35.64 mmol) and anhydrous sodium carbonate (2.83 g, 26.73 mmol) were mixed under vacuum at 0.5 mbar and gradually heated to 157 °C in a Kugelrohr apparatus. The title compound distilled off as a colourless oil and was collected and used immediately. Yield = 2.70 g, 48.2%.

HOOC-poly(methyl-4-oxobutanoate-2-oxazoline)-ethyl-2-thioethanoate (HOOC-PEsterOx-COOMe) (1d). Methyl 3-(4,5-dihydrooxazol-2-yl)propanoate (2.7 g, 17.18 mmol) was added to an oven-dried, nitrogen-purged microwave tube fitted with a stirrer bar and septum. Anhydrous acetonitrile (5 mL) was added, followed by *tert*-butyl bromoacetate (0.181 mL, 1.23 mmol). The reaction mixture was transferred to a Biotage microwave and heated to 140 °C for 30 min. After cooling to rt, ethyl thioglycolate (2 eq.) was added followed by anhydrous triethylamine (2 eq.) and stirred overnight. The reaction mixture was added dropwise to rapidly stirring diethyl ether (250 mL) to form a white precipitate that was filtered and dried under vacuum. The solid was then taken up in DCM (100 mL) and washed with saturated $NaHCO_3$ (3 × 30 mL) before washing with saturated brine (2 × 30 mL). The organic layer was dried over magnesium sulphate, filtered and the solvents evaporated. The film was taken up in DCM (25 mL) and TFA (4 mL) was added dropwise and stirred for 5 h. The solvents were removed under vacuum and the film was taken up in deionised water (50 mL) before freeze-drying to give the title compound as a white solid. Yield = 2.8 g, 90% ^{1}H NMR ESI S2 Fig. 9.†

G5-PLL[PMOx-OMe]$_x$[NH$_2$]$_y$ (2a). The generation 5 L-lysine dendrimer (100 mg, 6.53 μmol) and **1a** (667 mg, 0.31 mmol, 48 eq.) were dissolved together in deionised water (5 mL). DMTMM·Cl (174 mg, 0.63 mmol, 96 eq.) was added as a solid and after dissolution the pH of the solution was adjusted to ~8 using saturated $NaHCO_3$ solution. The reaction mixture was stirred at rt for **4d**. The pH of the reaction was monitored and maintained at 8. Afterwards, the reaction mixture was acidified to pH 5 using HCl (2 M) and purified using a Viva-Flow® cassette in deionised water (30 kDa MWCO) connected to a peristaltic pump. Removal of unreacted POZ and DMTMM·Cl was monitored by SEC-UV (220 nm) and the reaction was typically free of low molecular weight impurities after 1–2 hours. The title compound was obtained as a white solid after freeze-drying. Yield = 348 mg, 70%. (Yield calculated according to a desired 50% modified polymer.)

G5-PLL[PEOx-OMe]$_x$[NH2]$_y$ (2b). The method above was used but with **1b** in place of **1a**. Yield = 343 mg, 69% ^{1}H NMR ESI S2 Fig. 10.†

G5-PLL[PEG-OMe]$_x$[NH2]$_y$ (2c). The method for **2a** was used but with commercially available HOOC-PEG-OMe (**1c**). Yield = 373 mg, 79% ^{1}H NMR ESI S2 Fig. 11.†

G5-PLL[P(2-ester-2-oxazoline)]$_x$[NH$_2$]$_y$ (2d). The generation 5 L-lysine dendrimer (100 mg, 6.53 μmol) and **1d** (697 mg, 0.31 mmol, 48 eq.) were dissolved together in anhydrous DMF (5 mL). DMTMM·BF_4 (206 mg, 0.63 mmol, 96 eq.) was added as a solid and after dissolution *N*-methyl morpholine (~20 μL) was added. The reaction was then stirred for 48 h at rt. The reaction mixture was diluted with ethyl acetate (3 mL) and the solution added to rapidly stirring diethyl ether (250 mL) to form a white precipitate. The precipitate was filtered, dried under vacuum and then taken up in deionised water (50 mL). The pH was adjusted to 5 with HCl (2 M) and the polymer purified similarly to **2a**. The title compound was obtained as a white solid. Yield = 425 mg, 82%. ^{1}H NMR ESI S2 Fig. 12.†

G5-PLL[PMOx-OMe]$_x$[COOH]$_y$ (3a) and G5-PLL[P(2-ester-2-oxazoline)]$_x$[COOH]$_y$ (3d). The residual amine groups on **2a** and **2d** were modified to acids using succinic anhydride. Briefly, the dendrimer (200 mg, 0.08 mmol (NH_2)) was dissolved in anhydrous methanol (4 mL). Succinic anhydride (50.1 mg, 0.50 mmol, 6 eq. to NH_2) was added as a solid, followed by triethylamine (23 μL, 0.17 mmol, 64 eq.). The reaction mixture was stirred at rt for 5 h before diluting with deionised water (40 mL) and acidifying to pH 5 with HCl (0.1 M) and purifying using VivaFlow® (30 kDa MWCO) for 1 hour. Both polymers were obtained as white solids after freeze-drying. Yield **3a** = 174 mg, 74%. **3d** = 195 mg, 94%. ^{1}H NMR ESI S2 Fig. 13† (**3a**).

G5-PLL[P(2-acid-2-oxazoline)]$_x$[COOH]$_y$ (4d). Polymer **3d** (150 mg, 1.70 mmol (ester repeat unit)) was dissolved in methanol (3 mL). LiOH (42 mg, 2 eq. to each repeat unit) dissolved in deionised water (1 mL) was added dropwise and the reaction mixture was stirred overnight at rt. The pH was adjusted to 8 before removing the solvent under vacuum. The solid was taken up in deionised water (20 mL) and the pH adjusted to 4–5 to form a white precipitate that became a gum on stirring. The water was decanted to waste and the gum washed with deionised water (20 mL) before freeze-drying the gum to obtain the title compound as a white solid. Yield = 111 mg, 89%. ^{1}H NMR ESI S2 Fig. 14.†

G5-PLL[PMOx-OMe]$_x$[coumarin]$_y$ (4a). Polymer **3a** (50 mg, 0.62 μmol) was dissolved in anhydrous DMF (2 mL) in a nitrogen purged reaction tube fitted with a stirrer bar and septum. DMTMM·BF_4 (9.8 mg, 0.03 mmol) was added and the solution stirred for 5 min. A preprepared solution of coumarin-NH_2 (8.62 mg, 0.02 mmol, 40 eq.) in anhydrous DMF (0.5 mL) was added *via* syringe. Triethylamine (3.5 μl, 0.02 mmol) in DMF (0.2 mL) was added and the reaction mixture was stirred at rt for 24 hours. The solution was then diluted with EtOAc (2 mL) and precipitated into diethyl ether (200 mL). The precipitate was collected, dried under vacuum and then dissolved in a 50/50 MeOH/water mixture (25 mL). The solution was passed through a 0.45 μm filter and then purified by VivaFlow® (30 kDa MWCO) gradually changing the eluent to pure deionised water. The title compound was obtained as a white solid after freeze-drying. Yield = 46 mg, 81%. ^{1}H NMR ESI S2 Fig. 15.†

G5-PLL[P(2-acid-2-oxazoline)]$_x$[coumarin]$_y$ (5d). This polymer was prepared in a similar method as for **5a**. Polymer **4c** 50 mg, 0.56 μmol was dissolved in anhydrous DMF (2 mL) in a nitrogen purged reaction tube fitted with stirrer bar and septum. DMTMM·BF_4 (35 mg, 0.11 mmol) was added and the solution stirred for 5 min. **Coumarin-NH_2** (34 mg, 0.10 mmol) was added as a solid directly and after dissolution, triethylamine (14 μl, 0.10 mmol) in DMF (0.2 mL) was added slowly drop-wise to avoid precipitation. The reaction mixture was stirred at rt for 24 h before diluting with EtOAc (2 mL) and precipitating the product by addition to rapidly stirring diethyl ether (200 mL). The precipitate was collected, dried under vacuum and then dissolved initially in a small volume of $NaHCO_3$ solution (2 mL) and then diluted in a 50/50 MeOH/water mixture (25 mL). The solution was passed through a 0.45 μm filter and then purified by VivaFlow® (30 kDa MWCO) gradually changing the eluent to pure deionised water. The title compound was obtained as a white solid after freeze-drying. Yield = 54 mg, 78%. ^{1}H NMR ESI S2 Fig. 16.†

Methodology for the cell viability and blood compatibility

Cell viability and proliferation assays. NIH 3T3 mouse fibroblasts were obtained from the Albert Wong Jefferson Cancer Institute. Cells were cultured at 37 °C/5% CO_2 in RPMI-1640, supplemented with 10% fetal calf serum and 2 mM glutamine, in the presence of penicillin–streptomycin. Cells were not used beyond passage number 10 for these experiments. Cells were seeded into 96-well plates at 5000 cells per well, in the presence of 1 μM NucView™ to enable the detection of apoptosis. Seeded cells were allowed to adhere overnight. In triplicate, the cells were treated with the modified dendrimers (except dendrimer **2d** which was not soluble enough to make a stock solution) & unmodified L-lysine dendrimer at 0.5 mg mL^{-1} (final concentration) in full media. Plates were incubated at 37 °C in an IncuCyte™ FLR (Essen BioScience) and were scanned every 4 hours for NucView™ fluorescence (apoptosis) and cell confluence. The apoptosis induced by each dendrimer was calculated relative to untreated controls and a maximum value obtained from the unmodified L-lysine dendrimer at 96 hours.

Blood compatibility studies. The blood compatibility studies were performed using Wistar rat blood collected in lithium heparinised tubes. 250 μl of lithium heparinised whole blood was placed in to a 1 ml Eppendorf tube and 250 μl of the sample (4 mg ml^{-1} to measure at 2 mg ml^{-1}) was added and mixed gently for 45 seconds. 500 μl of physiological saline was added to quench haemolysis and gently mixed. The tube was placed into a centrifuge and spun at 600*g* for 5 minutes. A sample of the supernatant was taken with a capillary stick, and placed at the top of a micro-cuvette (plasma/low Hb) allowing 20 μl to be automatically drawn up by capillary action. The cuvette was transferred to a Hemocue photometer (plasma/low photometer) and the haemolysis measurement (released haemoglobin, g dl^{-1}) was taken. To measure the haemoaggregation, 100 μL of lithium heparinised whole blood was diluted with 100 μL of sample in physiological saline (4 mg ml^{-1}) and gently mixed for 30 seconds. 20 μL of the mixture was transferred to a microscopy slide and a cover carefully placed on top. The red blood cells were inspected at 40× magnification and images were captured using the integrated Zeiss Axio camera.

Results and discussion

PMOx, PEOx and PEsterOx synthesis

POZs **1a** and **1b** (Scheme 1) were synthesised to have similar chain end functional groups and molecular weight profiles to the commercially available methoxy-poly(ethylene glycol) (2000 g mol^{-1}), which was used as a comparison in the dendrimer modifications.

Here we have compared polymers with average molecular weights of ~2000 g mol^{-1}, but it is important to note that the number of repeat units is different for each polymer at this same molecular weight. The theoretical number of repeat units for each polymer at this molecular weight decrease in the order PEG > PMOx > PEOx > PEsterOx (n = 44, 23, 20, 14). The use of PEG and POZ at ~2000 g mol^{-1} was largely decided from the literature where PEG has been extensively studied, and comprehensively summarised by Kaminskas, Boyd and Porter.[6] Increasing the molecular weight beyond this would lead to a reduction in the maximum drug loading (weight%) and make purification by ultrafiltration more difficult. The POZs were all polymerized from freshly distilled monomer, under anhydrous conditions to maintain a living polymerisation and have low polydispersity. Sodium methoxide was used to quench the polymerizations of PMOx and PEOx under conditions designed not to cleave the amide bonds. Loss of the *tert*-butyl ester protecting group at the initiator end after treating with sodium methoxide indicated transesterification had taken place as an unwanted side-reaction. Sodium hydroxide solution was added after quenching to deprotect the newly formed methyl ester. Full conversion of the monomer and proof of the initiation from *tert*-butyl bromoacetate is demonstrated in the ^{1}H NMR spectra of the reaction mixture before quenching (ESI S2 Fig. 17†) showing the *tert*-butyl ester peak at 1.49 ppm and oxazolinium protons at 4.59 ppm and 5.01 ppm, which disappeared after addition of sodium methoxide.

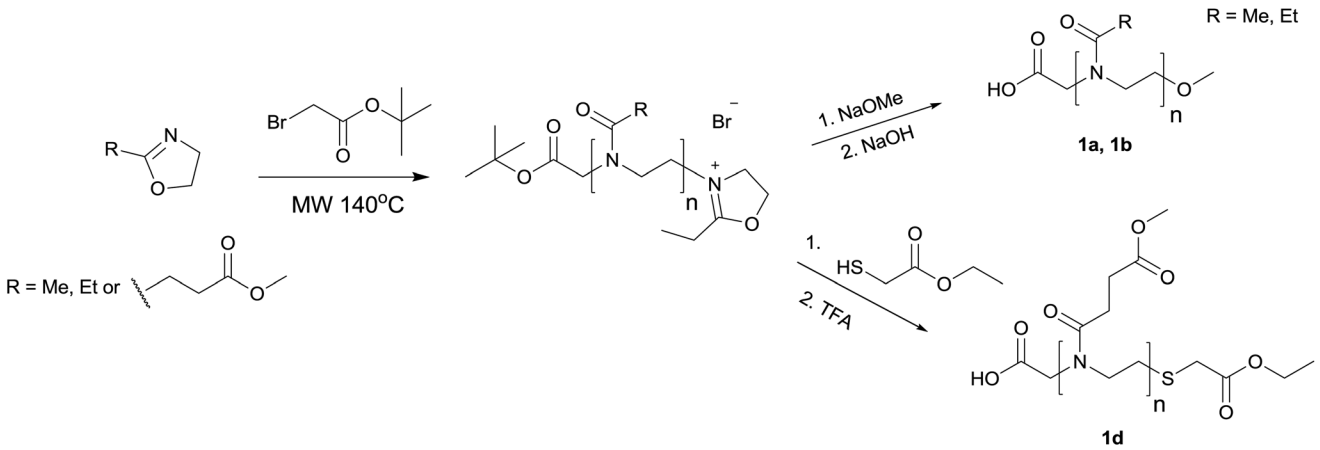

Scheme 1 Polyoxazoline synthesis route.

The ester POZ was not quenched with sodium methoxide because the resulting methyl ester at the α-chain end could not be hydrolysed without backbone esters also being cleaved. Instead, ethyl thioglycolate was used to quench the chain-end providing an ethyl ester terminal group and preserving the *tert*-butyl ester at the α-chain end. Ultimately the ethyl ester provided another carboxyl group at the terminal chain-end and yet another site for conjugation of coumarin. The synthetic routes to the POZs are summarized in Scheme 1 and the characteristics are summarized in Table 1.

POZ and PEG coupling to G5-PLL dendrimer. Polymers **1a–d** were used to modify the surface of the generation 5 L-lysine dendrimer using the coupling agent 4-(4,6-dimethoxy-1,3,5-triazin-2-yl)-4-methylmorpholinium (DMTMM) in a random modification *i.e.* some chains may have substituted onto α-amines and others onto ε-amines. For PMOx, PEOx and PEG the modifications were performed in aqueous conditions using DMTMM chloride, which has been reported to be stable in water for several days[23] and a good option in sterically hindered systems for which slow coupling is problematic. The ester POZ (**1d**) had limited water solubility and the coupling had to be performed in DMF with the tetrafluoroborate salt of DMTMM, which is reported to be stable in organic solvent.[24] VivaFlow® cassettes proved to be an efficient way to purify the dendrimers and gave good yields (69–85%). The removal of the excess linear POZ could be followed using HPLC-SEC-UV at 220 nm (example in ESI Fig. 18†). Following purification, the removal of linear material was also confirmed by GPC (ESI Fig. 19† showing an overlay of the linear PMOx and PMOx-modified dendrimer). Previous attempts using dialysis (25 kDa MWCO) for several days did not yield material free of linear POZ or PEG (data not shown). When purified, the POZ coated dendrimers had hydrodynamic diameters in the region of 8–10 nm as measured by DLS and high molecular weights (79.5 kg mol^{-1} & 100.0 kg mol^{-1}) with narrow polydispersities (<1.1). The PEG modified dendrimer (**2c**) was found to be slightly larger at 14 nm, which might be explained by the longer chain length of PEG compared to the POZs (see Table 2). Another explanation could be that there are more bound water molecules to PEG than POZ given the differences in structure. The polydispersity indices of the sub-9 nm particles were not accurately determined due to interference in the intensity signal on the DLS instrument which was not thought to be polymer related. An interesting observation from the DLS data was that the zeta potentials for **2a–c** were almost neutral despite the residual amines from the unmodified lysines of the dendrimer. This suggests that the dendrimer surface was shielded by the presence of the POZ and PEG. However, in the case of the **2d** there was a positive zeta potential measured that then became negative after reacting the amines with succinic anhydride (Table 2). This could be explained by the relatively poor solubility of the polymer driving a compacted conformation as well as a shorter chain length (n = 16) compared to PEG (n = 44) and PMOx (n = 24). The result is that the coverage was likely insufficient to mask the surface charge.

Table 1 Polyethylene glycol and polyoxazoline characteristics

Sample	Yield [%]	DP (theor.)	DP (NMR)	M_n (GPC) kDa	PDI (GPC)
HOOC-PMOx-OMe (**1a**)	89	23	24	2.2	1.09
HOOC-PEOx-OMe (**1b**)	83	20	23	2.1	1.08
HOOC-PEG-OMe[a] (**1c**)	—	45	44	2.1	1.06
HOOC-PEsterOx-COOMe (**1d**)[b]	90	14	16	3.1	1.12

[a] Commercially available PEG (Iris Biotech). [b] Bimodal by aqueous GPC.

Biocompatibility studies. The cytotoxicity studies were performed in the presence of a fluorescent marker to measure apoptosis. The fluorescence intensities indicated that at the various time points of incubation, the POZ and PEG modified dendrimers were undergoing much less apoptosis that the unmodified dendrimer. For example, at 24 h there was 2–3% of the cells undergoing apopotosis compared to 36% for the unmodified dendrimer at a concentration of 0.5 mg mL^{-1} (mouse endothelial cells NIH-3T3) (Fig. 1). This was largely seen across all of the time points measured, with some small

Table 2 Unmodified and modified dendrimer characteristics

Sample description	Yield [%]	Estimated no. of substituted amines (^{1}H NMR)	M_n (kg mol^{-1}) (GPC)	PDI (GPC)	D_H (nm) (GPC)	D_H (nm) (DLS)[a]	Zeta potential (DLS)
G5-PLL-NH_2	—	—	ND	ND	ND	ND	32.1 ± 5.07
G5-PLL[PMOx]$_x$[NH_2]$_y$ (**2a**)	70	35	79.5	1.06	10.9	9.04	3.2 ± 6.80
G5-PLL[PEOx]$_x$[NH_2]$_y$ (**2b**)	69	38	100.0	1.05	11.8	10.24	2.76 ± 4.26
G5-PLL[PEG]$_x$[NH_2]$_y$ (**2c**)	79	30	80.7	1.09	14.0	14.54	−0.514 ± 3.92
G5-PLL[PEster]$_x$[NH_2]$_y$ (**2d**)	82	28	ND	ND	ND	8.56	10.3 ± 5.41
G5-PLL[PEster]$_x$[COOH]$_y$ (**3d**)	94	64[c]	ND	ND	ND	7.87	−12.1 ± 5.63
G5-PLL[PAcid]$_x$[COOH]$_y$ (**4d**)	89	64[c]	117.2	1.04	12.6	6.73 (8.93[b])	−36 ± 12.2

ND = not determined. [a] Volume average. [b] Measured in GPC eluent (40 : 10 mM $NaNO_3$: NaH_2PO_4 in water). [c] Remaining amines were modified with succinic anhydride.

variations at 96 h. The images captured reflected what was measured by the fluorescence, with large numbers of the cells undergoing apoptosis for the unmodified dendrimer, whilst the cells incubated with the modified dendrimers were similar in appearance to the saline control. The modification of the dendrimer with POZ and PEG had removed and masked some of the cationic charge from the surface of the dendrimer and provided a barrier to membrane disruption, which was consistent with previously reported studies.[27]

Blood compatibility studies were performed on the various modified dendrimers. Firstly, haemolysis experiments were performed, which was a measurement of the haemoglobin (Hb) released by the red blood cells after rupture of the cell. The results showed that the PEG and POZ modified dendrimers were found to be non-haemolytic (ESI Fig. 20†) where the haemoglobin measured was lower than the limit of detection for the instrument (<0.3 g dl^{-1}). Only a small amount of haemolysis (2.45 g dl^{-1}) was observed for the unmodified dendrimer but this was mainly due to the aggregation of the blood cells. The second experiment for blood compatibility was red blood cell aggregation, and was determined though microscopy. The unmodified lysine dendrimer caused severe

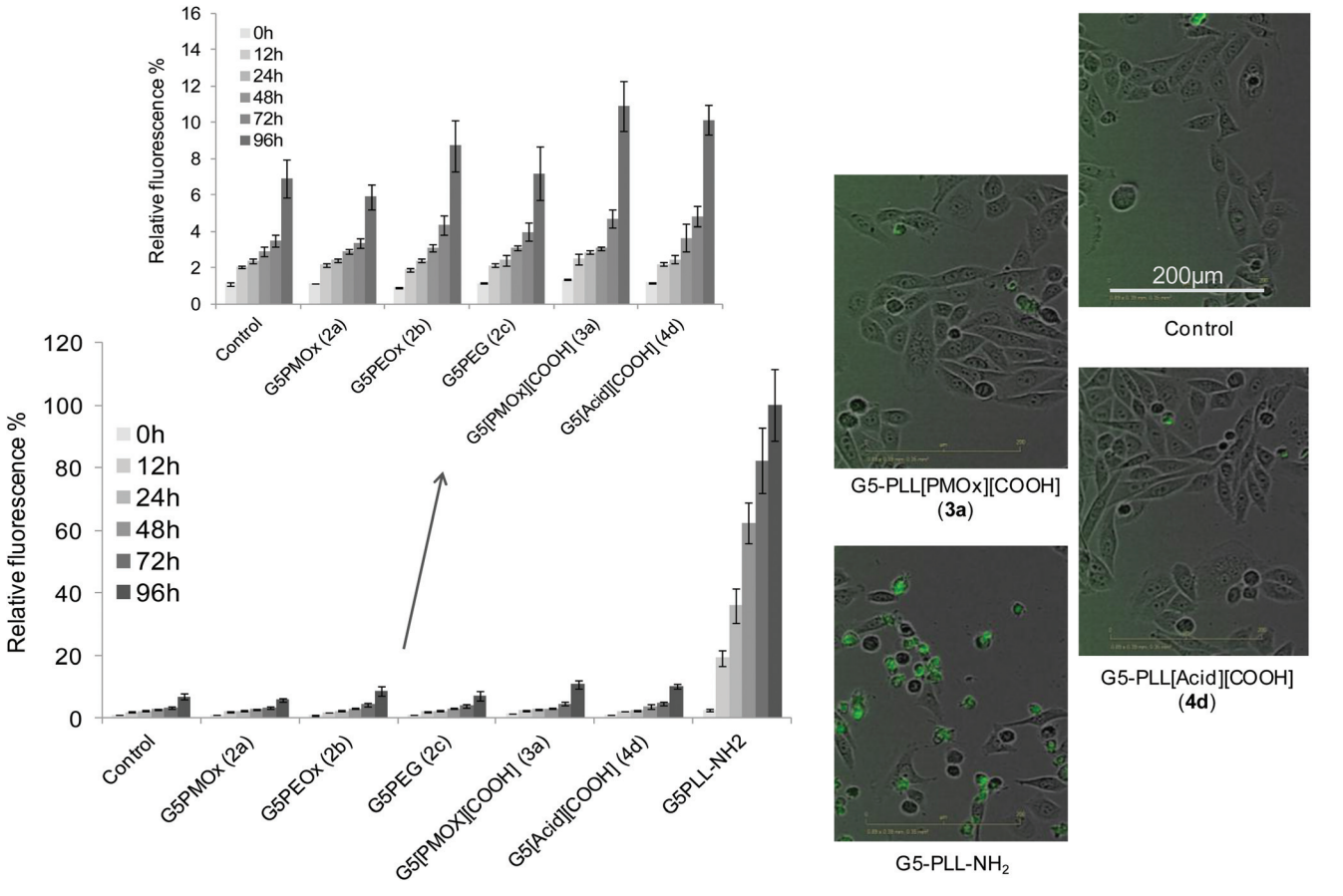

Fig. 1 Cell apoptosis studies. Graph showing relative apoptosis (measured by fluorescence and compared to unmodified dendrimer at 96 h over various time points). Right showing representative images of the cells at 24 h.

aggregation of the red blood cells forming a continous network of red blood cells (Fig. 2). The POZ and PEG modified dendrimers did not cause any observable aggregation of the red blood cells and looked consistent with the saline control.

The concentrations for the blood compatibility and cytotoxicity were chosen to reflect a scenario of an IV administered dendrimer at a reasonable dose of 50 mg kg^{-1} in mouse. The hypothesis being that a mouse weighing 30 g would receive approximately 1.5 mg of polymer per dose and therefore initial concentrations would be highest in plasma followed by dilution and distribution/clearance to give lower final tissue concentrations.

Coumarin loading onto POZ modified dendrimers. A derivative of coumarin with a primary amine attachment point was used as a model compound to conjugate to the dendrimers. This compound offered the benefit of a stable amide bond to the dendrimer to aid with the purification and analysis. The aromatic protons made the quantification of the loading straightforward by ^{1}H NMR since there are no other interfering signals from the dendrimer in this region. Here we wanted to show that by adapting the main-chain functionality of the POZ from a simple alkyl group into a useful moiety (carboxyl groups) there could be significantly more sites available for conjugation and significantly higher loading could be achieved. The remaining lysine amines on the POZ modified dendrimers (**2a** and **2d**) were reacted with succinic anhydride to convert them into carboxyl groups (dendrimers **3a** and **3d**). Polymer 3d then underwent a mild methyl ester deprotection step using LiOH in MeOH/H_2O overnight to convert the main-chain esters into carboxyl groups to generate further sites for conjugation of the coumarin (polymer **4d**). Whilst the PMOx modified dendrimer (**3a**) had ~32 theoretical sites on the dendrimer for conjugation of courmarin, the carboxyl-functional POZ dendrimer (**4d**) had ~576 (18× more). However, it is well known in a drug delivery scenario that overloading polymeric carriers with hydrophobic species can lead to solubility problems/aggregation in solution. Therefore, we aimed to modify a conservative 30% of the carboxyl groups (173 sites). The conjugation of coumarin to the dendrimers was performed using DMTMM·BF_4 in anhydrous DMF using a slight excess of the coumarin for polymer **3a** 40 molecules per dendrimer, 1.25 eq.) and the intended 173 molecules per dendrimer for polymer **4d**. The loadings of coumarin were measured using ^{1}H NMR (Fig. 3).

The loadings were found to be 6.4 wt% (25 molecules per dendrimer) for the PMOx modified dendrimer and 31 wt% (166 molecules per dendrimer) for the carboxyl-functionalized dendrimer (6.6× more loading). To determine whether the high coumarin loading on **4d** (resultant polymer **5d**) had induced the formation of aggregates or micellar structures,

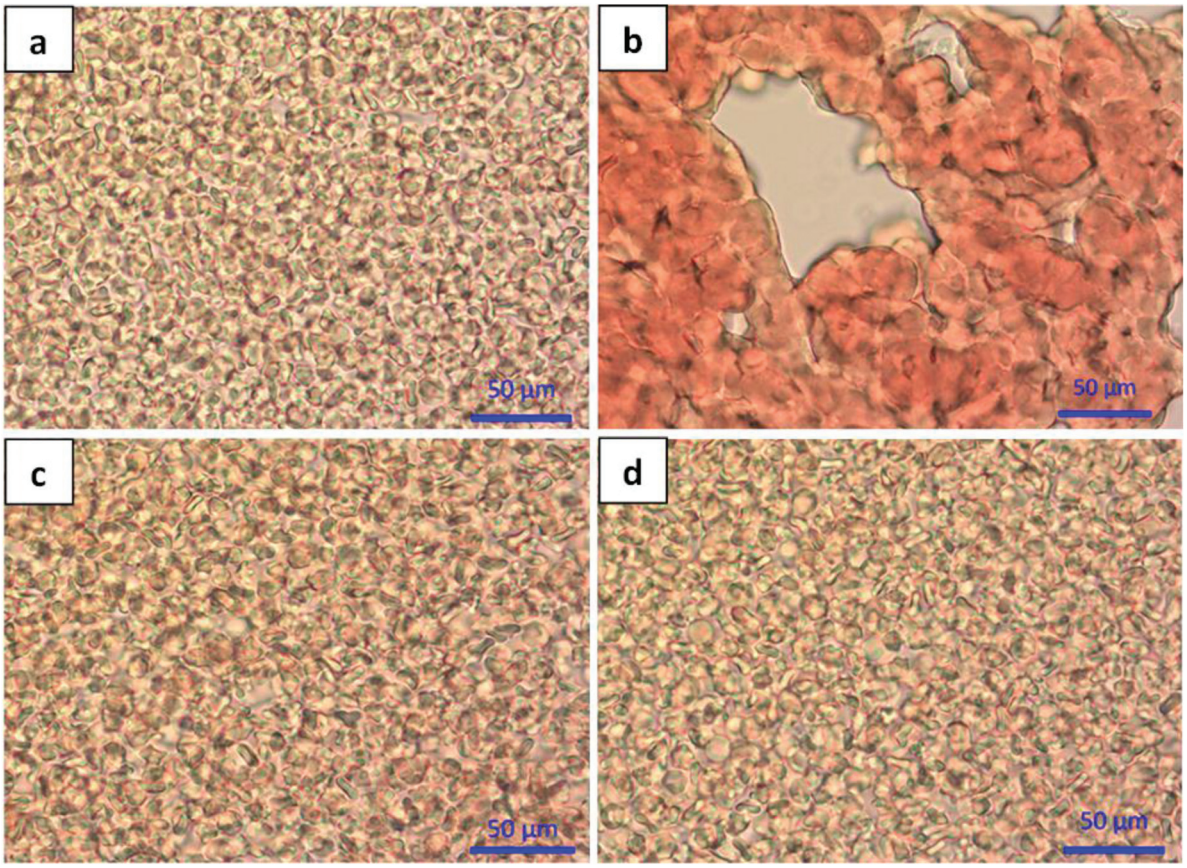

Fig. 2 Blood compatibility aggregation study of unmodified *versus* PEG and PEOx modified dendrimers (a = saline, b = unmodified dendrimer, c = PEG modified and d = PEOx modified).

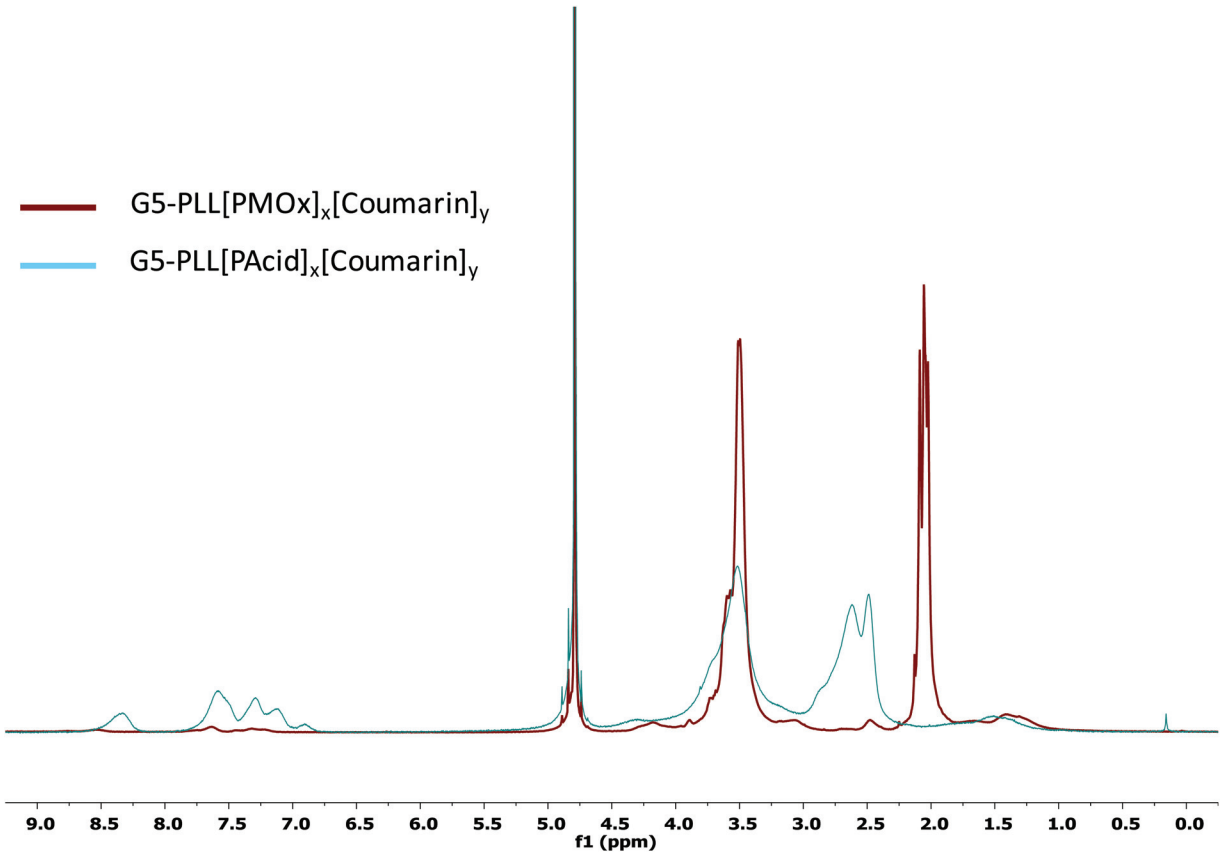

Fig. 3 ^{1}H NMR (400 MHz, D_2O) spectra for the coumarin conjugated POZ dendrimers showing 6.4 wt% loading for PMOx modified dendrimer and 31 wt% loading for the carboxyl functional POZ dendrimer.

DLS was performed. For the polymer conjugate derived from the PMOx modified dendrimer **4a** (25 coumarin molecules) there was no observable change to the size distribution (ESI Fig. 21†). For the coumarin loaded carboxyl-functional dendrimer, **5d** there was a small reduction in hydrodynamic volume accompanied with a tail of larger particle sizes observed in the size distribution when compared to the precursor (ESI Fig. 22†). However, when repeated in a more appropriate buffer (as for GPC) this was not observed (ESI Fig. 23†). The absence of higher molecular weight species was strengthened from the GPC data where no aggregation or larger particles were observed in the light scattering (ESI Fig. 24†).

Clinically, high drug loading on drug delivery systems is desirable. Historically many polymer-drug conjugates have suffered from low drug loading and typically have less than 10% by weight active compound (*e.g.* HPMA-Doxorubicin, PK1 and PEG-Camptothecin, PROTHECAN).[28] Low drug loading drives the need for very potent drug molecules, which are not always possible or desirable. Alternatively, large amounts of the nano-carrier are required often resulting in high number of nanoparticles dosed per injection. Both the quantity of nano-carrier and the number of particles being dosed carry a toxicity risk, either from the material itself or excessively large numbers of nanoparticles. More extensive pre-clinical toxicity studies will be required if a clinically unprecedented concentration of materials is dosed and regulatory hurdles will be higher. Additionally, from a practical perspective, in pre-clinical development where injection volume is limited to 5 mL kg^{-1} in many species, doses may be limited due to solubility or physical stability issues. Similarly in the clinic, low drug loading can result in large volumes or a large number of vials with additional challenges to patient, clinical staff and costs. Many of the polymers used in polymer therapeutics are bespoke and are therefore expensive with often non-standard and extensive characterisation requirements to ensure quality and reproducible *in vivo* performance, thus, minimising quantities from a cost of goods perspective will be desirable. Therefore nano-carriers such as the dendrimers described in this paper with the capacity for considerably higher drug loading provide a more efficient delivery system and therefore have benefits in terms of development and commercialisation and patient/clinician acceptability.

Conclusions

Polyoxazolines have already shown great promise in the field of polymer therapeutics and we wanted to extend their use to coating materials for L-lysine dendrimers. Three different polyoxazolines were synthesised with average molecular weights in

the region of 2000 g mol^{-1} to compare with a commercial methoxy-PEG. A generation 5 L-lysine dendrimer was then modified with these chain-end functional POZs and PEG though an amide coupling step. We demonstrated that the PMOx and PEOx coated lysine dendrimers have similar properties to the PEG coated equivalent but with slightly lower hydrodynamic diameters. We imagined that one major benefit of POZ over PEG came from the mainchain functionality that it could offer and therefore a POZ with main-chain ester functionalities was synthesized and used to modify the dendrimer, which were subsequently deprotected to give carboxyl groups. Whilst the PEG and PMOx dendrimers with 50% coating modification were limited to ~32 coumarin molecules per dendrimer, the novel carboxyl functional POZ coating had the potential to hold up to ~576, albeit that a rational choice to prevent aggregation was to conjugate coumarin to only 30% of these (173 molecules). The use of a carboxyl-functional POZ has provided a novel approach for generating large numbers of conjugation sites for drug molecules to improve the loading, whilst other approaches have been limited by the residual surface functional groups from the ultimate generation of the dendrimer itself.

Acknowledgements

We thank the AstraZeneca PLC iMed Postdoctoral Research Scheme. We also thank the UK Engineering and Physical Sciences Research Council (EPSRC) for financial support (Leadership Fellowship to CA and Grants EP/H005625/1, and EP/J021180/1).

Notes and references

1 D. Bhadra, S. Bhadra, S. Jain and N. K. Jain, *Int. J. Pharm.*, 2003, **257**, 111–124.
2 D. Luo, K. Haverstick, N. Belcheva, E. Han and W. M. Saltzman, *Macromolecules*, 2002, **35**, 3456–3462.
3 H. Namazi and M. Adeli, *Biomaterials*, 2005, **26**, 1175–1183.
4 P. Singh, U. Gupta, A. Asthana and N. K. Jain, *Bioconjugate Chem.*, 2008, **19**, 2239–2252.
5 L. M. Kaminskas, B. D. Kelly, V. M. McLeod, G. Sberna, B. J. Boyd, D. J. Owen and C. J. Porter, *Mol. Pharm.*, 2011, **8**, 338–349.
6 L. M. Kaminskas, B. J. Boyd and C. J. Porter, *Nanomedicine*, 2011, **6**, 1063–1084.
7 L. M. Kaminskas, B. J. Boyd, P. Karellas, G. Y. Krippner, R. Lessene, B. Kelly and C. J. Porter, *Mol. Pharm.*, 2008, **5**, 449–463.
8 T. Okuda, S. Kawakami, T. Maeie, T. Niidome, F. Yamashita and M. Hashida, *J. Controlled Release*, 2006, **114**, 69–77.
9 H. Maeda, J. Wu, T. Sawa, Y. Matsumura and K. Hori, *J. Controlled Release*, 2000, **65**, 271–284.
10 E. Rossegger, V. Schenk and F. Wiesbrock, *Polymers*, 2013, **5**, 956–1011.
11 A. C. Rinkenauer, L. Tauhardt, F. Wendler, K. Kempe, M. Gottschaldt, A. Traeger and U. S. Schubert, *Macromol. Biosci.*, 2015, **15**, 414–425.
12 L. Tauhardt, D. Pretzel, K. Kempe, M. Gottschaldt, D. Pohlers and U. S. Schubert, *Polym. Chem.*, 2014, **5**, 5751–5764.
13 F. Wiesbrock, R. Hoogenboom, C. H. Abeln and U. S. Schubert, *Macromol. Rapid Commun.*, 2004, **25**, 1895–1899.
14 F. Wiesbrock, R. Hoogenboom, M. A. M. Leenen, M. A. R. Meier and U. S. Schubert, *Macromolecules*, 2005, **38**, 5025–5034.
15 K. P. Luef, R. Hoogenboom, U. S. Schubert and F. Wiesbrock, *Microwave-Assisted Cationic Ring-Opening Polymerization of 2-Oxazolines*, Springer, Berlin, Heidelberg, 2015, pp. 1–26, DOI: 10.1007/12_2015_340.
16 M. Bauer, C. Lautenschlaeger, K. Kempe, L. Tauhardt, U. S. Schubert and D. Fischer, *Macromol. Biosci.*, 2012, **12**, 986–998.
17 T. X. Viegas, M. D. Bentley, J. M. Harris, Z. Fang, K. Yoon, B. Dizman, R. Weimer, A. Mero, G. Pasut and F. M. Veronese, *Bioconjugate Chem.*, 2011, **22**, 976–986.
18 R. Hoogenboom, *Angew. Chem., Int. Ed.*, 2009, **48**, 7978–7994.
19 R. Luxenhofer, Y. Han, A. Schulz, J. Tong, Z. He, A. V. Kabanov and R. Jordan, *Macromol. Rapid Commun.*, 2012, **33**, 1613–1631.
20 M. Bauer, S. Schroeder, L. Tauhardt, K. Kempe, U. S. Schubert and D. Fischer, *J. Polym. Sci. Part A: Polym. Chem.*, 2013, **51**, 1816–1821.
21 O. Sedlacek, B. D. Monnery, S. K. Filippov, R. Hoogenboom and M. Hruby, *Macromol. Rapid Commun.*, 2012, **33**, 1648–1662.
22 V. R. de la Rosa, *J. Mater. Sci.: Mater. Med.*, 2013, **25**, 1211–1225.
23 M. Kunishima, C. Kawachi, J. Monta, K. Terao, F. Iwasaki and S. Tani, *Tetrahedron*, 1999, **55**, 13159–13170.
24 S. A. Raw, *Tetrahedron Lett.*, 2009, **50**, 946–948.
25 M. E. Fox, S. Guillaudeu, J. M. Frechet, K. Jerger, N. Macaraeg and F. C. Szoka, *Mol. Pharm.*, 2009, **6**, 1562–1572.
26 M. T. Zarka, O. Nuyken and R. Weberskirch, *Chemistry*, 2003, **9**, 3228–3234.
27 R. Duncan and L. Izzo, *Adv. Drug Delivery Rev.*, 2005, **57**, 2215–2237.
28 R. Duncan, *Nat. Rev. Drug Discovery*, 2003, **2**, 347–360.

SCIENTIFIC REPORTS

OPEN

Transcriptome analysis of *Streptococcus pneumoniae* treated with the designed antimicrobial peptides, DM3

Received: 11 February 2016
Accepted: 09 May 2016
Published: 26 May 2016

Cheng-Foh Le[1,2], Ranganath Gudimella[3], Rozaimi Razali[3], Rishya Manikam[4] & Shamala Devi Sekaran[1]

In our previous studies, we generated a short 13 amino acid antimicrobial peptide (AMP), DM3, showing potent antipneumococcal activity *in vitro* and *in vivo*. Here we analyse the underlying mechanisms of action using Next-Generation transcriptome sequencing of penicillin (PEN)-resistant and PEN-susceptible pneumococci treated with DM3, PEN, and combination of DM3 and PEN (DM3PEN). DM3 induced differential expression in cell wall and cell membrane structural and transmembrane processes. Notably, DM3 altered the expression of competence-induction pathways by upregulating CelA, CelB, and CglA while downregulating Ccs16, ComF, and Ccs4 proteins. Capsular polysaccharide subunits were downregulated in DM3-treated cells, however, it was upregulated in PEN- and DM3PEN-treated groups. Additionally, DM3 altered the amino acids biosynthesis pathways, particularly targeting ribosomal rRNA subunits. Downregulation of cationic AMPs resistance pathway suggests that DM3 treatment could autoenhance pneumococci susceptibility to DM3. Gene enrichment analysis showed that unlike PEN and DM3PEN, DM3 treatment exerted no effect on DNA-binding RNA polymerase activity but observed downregulation of RpoD and RNA polymerase sigma factor. In contrast to DM3, DM3PEN altered the regulation of multiple purine/pyrimidine biosynthesis and metabolic pathways. Future studies based on *in vitro* experiments are proposed to investigate the key pathways leading to pneumococcal cell death caused by DM3.

Streptococcus pneumoniae represents one of the major bacterial pathogens heavily affecting human health worldwide causing severe life-threatening infections particularly pneumonia, meningitis, and bacteremia[1,2]. Pneumococcal disease is the leading cause of vaccine-preventable deaths among children aged less than five with 0.7–1 million cases every year worldwide[3,4]. Treatment options are further reduced by the increasingly prevalent antibiotic-resistant *S. pneumoniae* particularly the multidrug-resistant strains in infections, inversely affecting the mortality and morbidity of patients[5–8]. Continued reduction in conventional antibiotic efficiency is inevitable and development of new classes of antibiotics as alternative antimicrobial agents is highly demanded.

Antimicrobial Peptides (AMPs) are characterized by short chain length (5–50 amino acids), polycationic, and amphipathic produced naturally by various organisms as effector defence molecules against bacteria, fungi, viruses, eukaryotic parasites, and others[9–12]. In line with new AMPs discovery from natural sources, researchers have been actively developing engineered AMPs with enhanced antimicrobial and reduced cytotoxicity as potential antibiotic candidates[13–16]. AMPs induced strong non-receptor mediated membrane lytic mechanism as the primary microbicidal strategy[17,18]. Three principal membrane disruption machineries have been described[19]. Toroidal pore (e.g. lacticin Q)[20], barrel-stave (e.g. Alamethicin)[21] and carpet models (e.g. cecropin P1)[22], Aggregation of peptide monomers to form transmembrane channels or insertion of the peptides into the cell membrane to disrupt the native integrity of cell membrane eventually lead to direct cellular leakage and cell death.

[1]Department of Medical Microbiology, Faculty of Medicine, University of Malaya, Kuala Lumpur, Malaysia. [2]School of Pharmacy, Faculty of Science, University of Nottingham Malaysia Campus, Semenyih, Selangor, Malaysia. [3]Sengenics Sdn Bhd, High Impact Research Building, University of Malaya, 50603, Kuala Lumpur, Malaysia. [4]Department of Trauma and Emergency Medicine, University Malaya Medical Centre, 50603 Kuala Lumpur, Malaysia. Correspondence and requests for materials should be addressed to S.D.S. (email: shamala@um.edu.my)

AMPs possessing non-membrane targeting activity have also been increasingly documented[19,23,24]. Indolicidin, a Trp-rich polycationic peptide belongs to the cathelicidin family of polypeptides interacts with bacterial nucleic acids to interfere with cell replication or transcriptional processes leading to cell death[25]. Buforin II derived from the parent peptide buforin I inhibited cellular functions by binding exclusively to DNA and RNA without disturbing membrane integrity[26]. Histatin-5 is a mitochondrion inhibitor causing loss of transmembrane potential and generates reactive oxygen species which damages the cells[27,28]. Altogether, this indicates that the intracellular acting AMPs are able to traverse across cell wall and cell membrane efficiently and bind to the targeted macromolecules to exert inhibitory effects. Besides, peptides with multiple inhibitory effects have also been reported. CP10A, an indolicidin derivative was able to induce membrane lysis and inhibit DNA, RNA, and protein synthesis simultaneously[29]. PR-39 is another class of AMP interrupts with both protein and DNA synthesis pathways leading to metabolic cessation[30]. In addition, AMPs could produce varying inhibitory effects at different concentration. Lethal dose of pleurocidin would produce similar antimicrobial effects as CP10A as mentioned above, however, at sublethal dose the peptide was able to only inhibit protein synthesis by reducing histidine, uridine, and thymidine incorporations in *E. coli*[31].

Advancement in Next Generation Sequencing platform for transcriptome analysis enables genome-wide expression studies on the cellular components and pathways affected by drug treatments via differential gene expression profiling. This includes previously known genes and novel expression systems, for example, the finding of two novel putative ABC transporters in *Streptomyces coelicolor* A3 (2) strain treated with vancomycin, bacitracin, and moenomycin A[32]. Qin *et al.* employed RNA sequencing (RNA-seq) to study the biofilm-inhibition potential of ursolic acid and resveratrol in methicillin-resistant *Staphylococcus aureus* (MRSA)[33]. Furthermore, specific gene expression can be identified by comparative analysis. For instance, the glyoxylate-bypass genes of the citrate cycle was upregulated in ampicillin-treated *Acinetobacter oleivorans* DR1 strain while norfloxacin induced significant SOS response[34].

Our previous work had designed DM3, a water-soluble 13 amino acids cationic AMP generated based on hybridization of lead peptide fragments selected from the indolicidin-derivative peptide CP10A[35] and the antibacterial peptide aurein 1.2[36]. DM3 showed potent antipneumococcal activity against both PEN-susceptible and nonsusceptible clinical isolates with greater killing kinetics as compared to PEN. In addition, DM3 is broad spectrum against common bacterial pathogens of both gram types. Combination with PEN synergized the antipneumococcal effect *in vitro*. Interestingly, DM3-PEN synergism was able to be translated into therapeutic improvement as shown in a lethal pneumococcal infection model using the non-toxic dose of the pair. Although the cell wall and cell membrane disruption potential of DM3 was evident, however, the detailed antipneumococcal actions of DM3 remain largely unclear. Here we aim at investigating the mechanisms of actions of DM3 in standalone and in synergistic formulation with PEN against *S. pneumoniae* via differential gene expression analysis using the high-throughput Illumina RNA-seq platform to identify the differentially expressed genes and the pathways involved.

Results

Transcriptomic analysis of PRSP and PSSP treated with standalone DM3 and in combination with PEN. In this study, both PEN-resistant *S. pneumoniae* (PRSP) and PEN-susceptible *S. pneumoniae* (PSSP) were treated with DM3, PEN, and DM3PEN (combination treatment) to determine the underlying differential expression of genes and associated pathways following the drug treatment. This allows us to better understand the mechanism of actions of DM3 and the synergistic effect of DM3PEN. Heatmaps showing the differential gene expression for both untreated and treated cells against PRSP and PSSP are shown in Figs 1 and 2, respectively. As compared to PSSP, sharp differences in the number of differentially expressed genes and enrichment pathways was observed. For PRSP, there are a total of 682, 721, and 695 differentially expressed genes for DM3-, PEN-, and DM3PEN-treated groups, respectively. Gene annotations (as well as statistical analysis) of the enrichment pathways can be found in supplementary Tables S1–S3. In contrast, there are only a small set of differentially expressed genes 18, 65, and 20 for DM3-, PEN-, and DM3PEN-treated PSSP, respectively. Pathway enrichment was only determined for PEN-treated group (Table S4) but not for groups treated with DM3 and DM3PEN.

Effects of DM3 and combination treatment on amino acid metabolism. Transcriptomic analysis on both PRSP and PSSP showed that DM3 and PEN have predominant effects on pneumococcal amino acids biosynthesis processes. From the gene enrichment analyses, the precursory pathways responsible for amino acids biosynthesis were noted. These include amine (GO:0009309), nitrogen compound (GO:0044271), carboxylic acid (GO:0046394), and aromatic compound (GO:0019438) biosynthesis processes. Although the differentially expressed genes encoded for a number of amino acids were reported including glycine, alanine, glutamate, and aspartate, the aromatic and branched chain family amino acids were most affected. The branched chain amino acids were valine, leucine, and isoleucine while aromatic amino acids included phenylalanine, tyrosine, and tryptophan. Tryptophan represented the most affected amino acids among the aromatic group as the expression of high number of genes associated with tryptophan precursor anthranilate biosynthesis and metabolisms were altered. Moreover, the specific downregulation of tryptophan biosynthesis (GO:0000162) and tryptophan metabolic process (GO:6568) were due to PEN as seen in both PEN- and DM3PEN-treated groups. For alanine biosynthesis, one unique gene (SP_1671, D-alanyl-alanine synthetase A) was downregulated in both DM3 and DM3PEN-treated PRSP but not in PEN-treated group (Tables S1–S3).

PEN-treated cells observed greater pathway differences as seen with the doubling of the number of enriched pathways found as compared to the DM3-treated cells (Tables S1 and S2). Several of these were associated with indolalklyamine, indole, and indole derivatives-related pathways, heterocycle biosynthesis, chorismate metabolic process, lyase, dicarboxylic acid metabolic and biosynthetic processes. Similar results were observed in DM3PEN

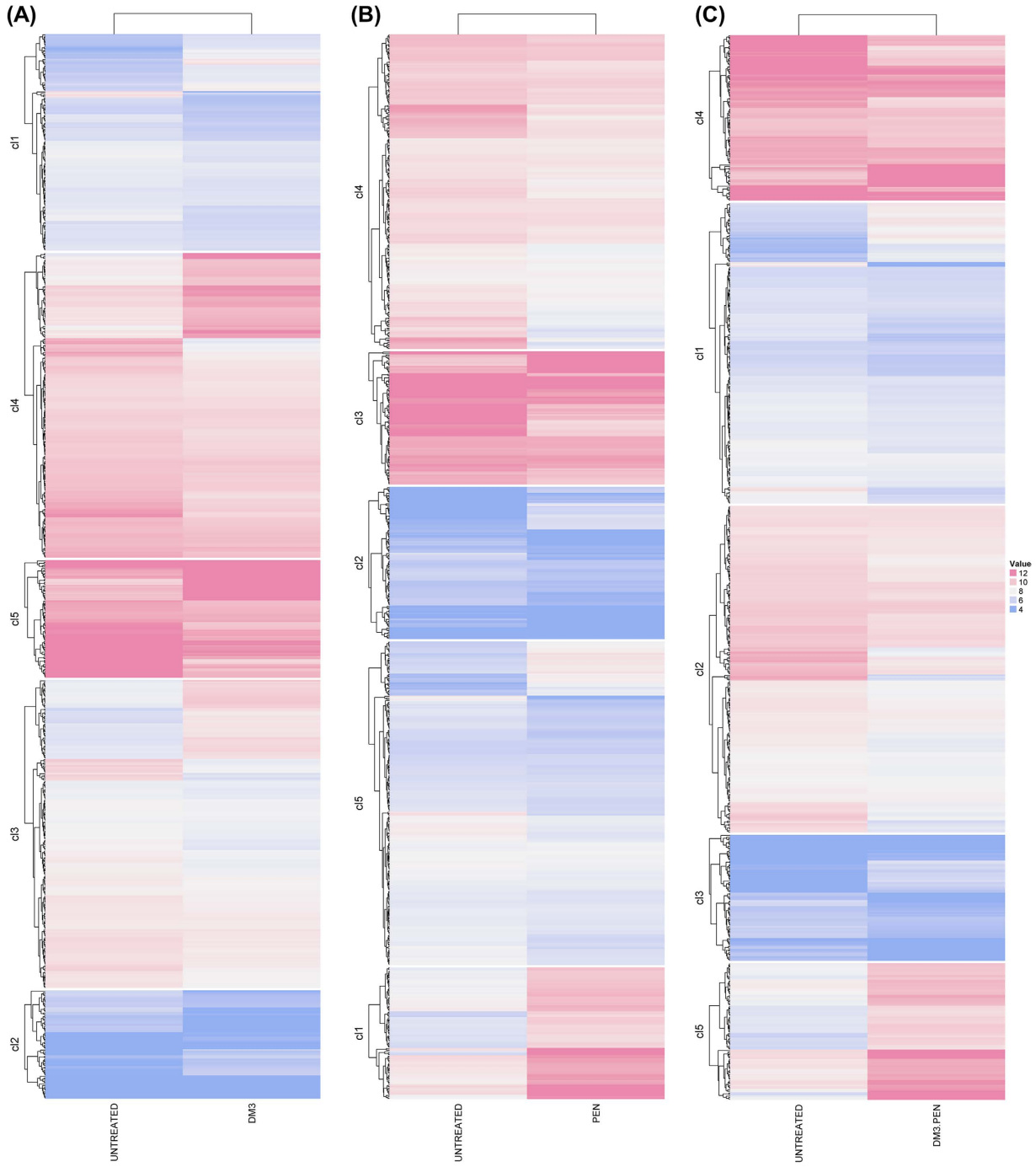

Figure 1. Heatmaps showing expression level of clustered genes of PRSP. Each group is classified into five clusters. (**A**) untreated versus DM3, (**B**) untreated versus PEN, and (**C**) untreated versus DM3PEN.

and this was likely be due to presence of PEN in the combination treatment which produced such effects in the cells.

For PSSP, the set of differentially expressed genes in all three groups were similar, observing predominant effect against the 30S small ribosomal subunit involving significant upregulation of the genes *rrnaB16S*, *rrnaC16S*, *rrnaC23S*, and *rrnaD23S*. Upregulation of *rrnaC16S* and 23S *rrnaD23S* rRNA genes were particularly drastic with more than 32-fold change as compared to the untreated cells except the lower upregulation fold-change in rrnaB16S of DM3PEN group.

Effects of DM3 and combination treatment on nucleic acid metabolism. Results showed significant differential expression associated with genes related to DNA replication and transcription mechanisms. Notably, genes encoded for DNA helicase, gyrase, and topoisomerases subunits were differentially expressed. Different subunits of the DNA-directed RNA polymerase were found to be differentially expressed with

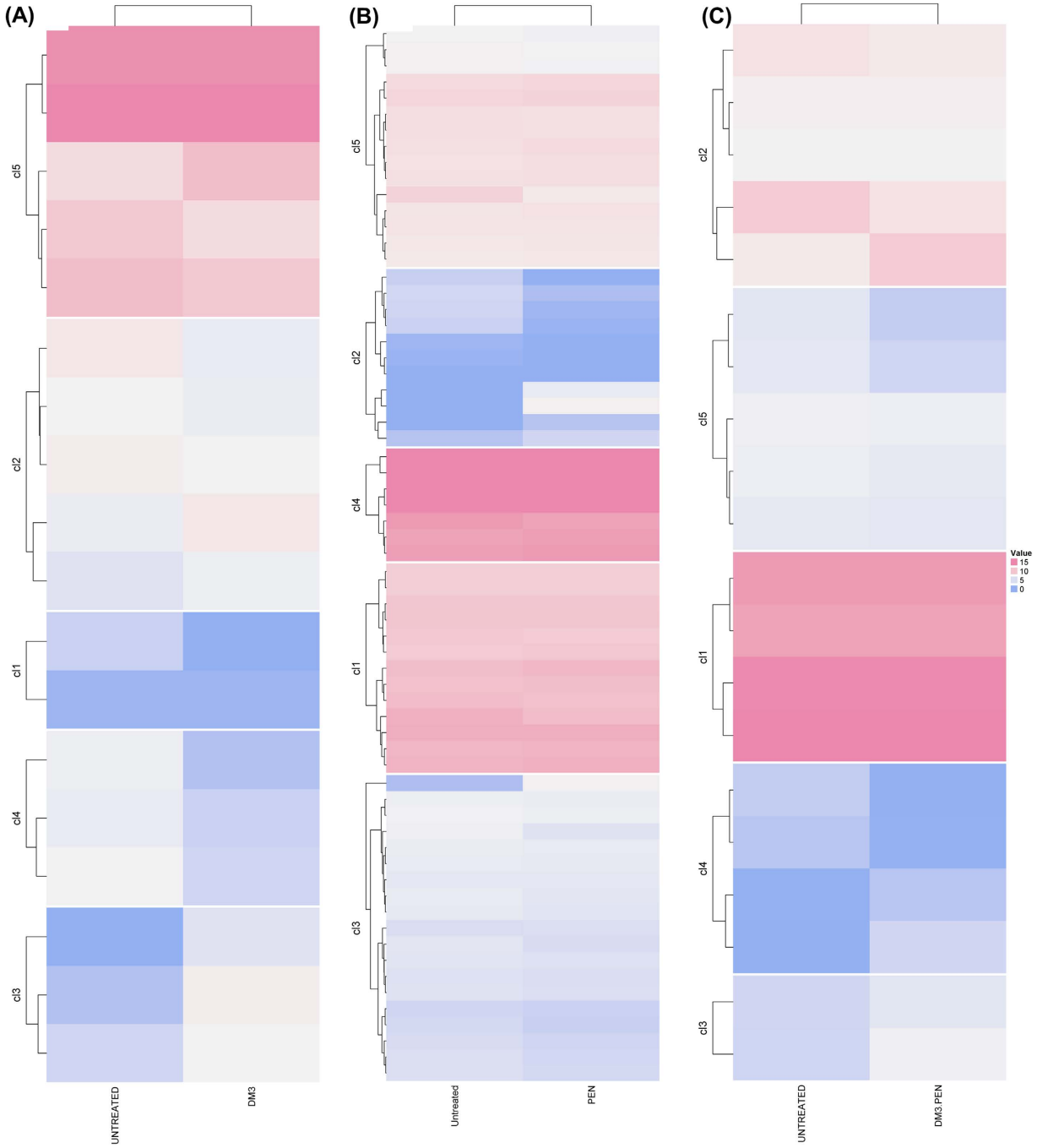

Figure 2. Heatmaps showing expression level of clustered genes of PSSP. Each group is classified into five clusters. (**A**) untreated versus DM3, (**B**) untreated versus PEN, and (**C**) untreated versus DM3PEN.

PEN-treatment; while both alpha- and beta-subunits were upregulated, the delta-subunit was downregulated. This is accompanied by upregulation of RNA polymerase sigma factor RpoD. Conversely, RpoD was downregulated in DM3-treated cells and no differential expression was observed with DNA-binding RNA polymerase subunits indicating that DM3 has no inhibitory activity on RNA polymerase. In the combination treatment, the collective effects were noted with upregulation of DNA-directed RNA-polymerase beta subunit while both alpha- and delta were downregulated accompanied by upregulation of RpoD. Besides, all three translation-initiation factor-1 (IF-1), IF-2, and IF-3 were differentially expressed but only IF-3 was reported in DM3 treatment.

Downregulation of the alpha- and beta subunits in DNA topoisomerase IV was found in both DM3- and PEN-treatment, however, the expression of topoisomerase I was increased in DM3 but decreased in PEN-treated cells. Unlike PEN which caused increased expression in DNA gyrase, DM3 exerted no effect on this enzyme. Such differential expressions were observed in combination treatment whereby topoisomerase I was downregulated. In addition, gene enrichment performed showed transposase activity with differential expression of the IS4-like protein.

A number of unique enrichment pathways associated with nucleic acids (purine and pyrimidine) biosynthesis and metabolisms were noted with combination treatment. These were not found in the standalone DM3 and PEN treatments against pneumococci. The pathways reported in PEN were of purine nucleotide binding. Conversely, many pathways associated with nucleoside/ribonucleoside triphosphate biosynthetic/metabolic processes were observed. Examples include purine nucleoside triphosphate metabolic/biosynthetic process (GO:0009144/5), purine ribonucleoside triphosphate metabolic/biosynthetic process (GO:0009205/6), purine nucleotide metabolic/biosynthetic process (GO:0009150/2), ribonucleotide metabolic/biosynthetic process (GO:0009259/60), and others.

In addition, the downstream processes following amino acids biosynthesis leading to the generation of peptides/proteins were affected by the treatments as well. Differential RNA expressions associated with aminoacyl-tRNA biosynthesis, tRNA ligase activity, 30S and 50S ribosomal proteins, and ribosomal large subunit assembly. The translation-initiation factors (IFs) were differentially expressed in the treatment groups where (1) in DM3 treatment group, only IF3 was differentially expressed with upregulation, (2) PEN treatment group noted upregulation of IF-1 and IF-2, while IF-3 was downregulated and (3) DM3PEN was observed with IF-2 upregulation and IF-3 downregulation.

Effects of DM3 and combination treatment on pneumococcal cell wall, pathogenesis, and competence induction. Gene enrichment analyses highlighted that genes encoding for cell membrane and transmembrane pathways were clearly impacted in DM3-treated pneumococci. More than 20 genes were differentially expressed in these pathways and represented the largest gene sets as compared to any other pathways. Such effects were similarly observed in DM3PEN group but not in PEN treatment alone. Moreover, DM3PEN-treated group was reported with changes in a number of transmembrane transport associated pathways and these include the cation transmembrane transport (GO:0034220), monovalent inorganic cation transmembrane transporter activity (GO:0015077), hydrogen ion transmembrane transporter activity (GO:0015078), and others.

In DM3-treated pneumococci, a total of eight genes were differentially expressed which included the response regulator CiaR, sensor histidine kinase CiaH, and six competence-induced proteins Ccs16, CelA, CelB, CglA, ComF, Ccs4. Among these genes, Ccs16, ComF, Ccs4, CiaR, and CiaH were downregulated. For PEN-treated group, only five differentially expressed genes (CelB, CglA, Ccs4, CiaR, CiaH) were noted at which all were downregulated. Only three genes (CelB, CglA, Ccs4, with an addition of one unique entry CoiA) were differentially expressed in the DM3PEN-treatment group. CoiA was upregulated in the combination treatment. Cells treated with DM3 alone could have greater alteration in competence regulatory activity than PEN or the combination treatment.

S. pneumoniae has capsular polysaccharide (CPS) covering the outer surface of the cell wall. Unlike PEN which caused downregulation in three genes CPS4A, CPS4C, CPS4D and upregulation in CPS4B, all four genes were downregulated in DM3-treated group. This CPS4B downregulatory activity was not seen in the combination treatment and is specific to the standalone DM3 treatment. Hence, DM3 could exert specific inhibitory activity against CPS4B. Suppression of both hemolysin and exfoliative toxin in *S. pneumoniae* were seen in both standalone DM3 and PEN groups, however, combination of both drugs lead to upregulation of hemolysin in the pneumococcal cells.

DM3 has no significant effect on the major protein pneumococcal autolysin but upregulation was observed in combination treatment despite being downregulated in PEN-treated group. Notably, only standalone DM3 treatment resulted in downregulation of the serine protease (SP-2239) linked to the cationic AMP resistance pathway (CAMP). This is rather unusual as conventional antibiotics would eventually select, induce, and eventually lead to expansion of the antibiotic-resistance clones of bacterial cells. Interestingly, DM3 appeared to reduce pneumococcal CAMP resistance by decreasing the expression of SP-2239, a gene responsible for cationic antimicrobial peptide resistance in pneumococcal cells.

Discussion

Novel AMPs drug discovery have received much attentions in recent years with increasing number of engineered AMPs variants documented with potent and broad spectrum antimicrobial activity. These short peptides could be the future alternative or supportive treatment to conventional antibiotics where usage have been heavily complicated by reports of multidrug-resistance and high-level resistance microbial strains. Our previous work had designed DM3 which exhibited strong *in vitro* antipneumococcal activity against *S. pneumoniae* including the PRSP strain[37]. Subsequent *in vivo* murine infection model testing showed promising therapeutic efficacy particularly using combination treatment[38]. To further investigate the mechanism of actions of DM3, we perform high-throughput Next-generation sequencing platform using RNA-seq to study the transcriptomic profile of DM3 treatment. Differential expression profiles and gene enrichment analyses allow the statistically significant affected pathways and genes to be compared and shortlisted to investigate the treatment effects.

Pneumococcal virulence factors include a set of cell wall- or surface anchor proteins to achieve efficient colonization, invasion, and establishment. One of these is autolysin , a N-acetylmuramoyl L-alanine amidase that cleaves lactyl-amide bond linking the peptide-glycan components of peptidoglycan causing cell wall hydrolysis of the producer host. Autolysin has been described in PEN-induced lysis[39,40]. Increased expression of autolysin in combination treatment could have induced the autolytic mechanism in pneumococci leading to cell death. This is opposed to PEN treatment where autolysin expression was downregulated and thus suggests a different cell lysis mechanism. Our previous result based on transmission electron micrograph reported extensive cell wall and cell membrane lysis processes in DM3-treated pneumococcal cells. Together with the absence of differential autolysin expression in DM3-treated group in this study, it is suggested that other lytic mechanisms could be involved. In addition, membrane and cell wall associated structural components and transport mechanisms were greatly affected particularly in combination treatment. One example is downregulation of the transmembrane water channel protein aquaporin in both DM3 and PEN treatments, however, combination of both drugs produced synergism which observed opposing effects and caused upregulation in aquaporin gene expression.

Pneumococcal CPS differs in the chemical compositions thus giving rise to the serogroups/serotypes antigen-antisera based classification. CPS is a virulence factor that covers the outermost layer of pneumococcal cell wall serving multiple functions particularly in protection against host immune responses following invasion and protects against transport of harmful molecules into pneumococcal cells. In this study, all four subunits of CPS4ABCD were downregulated in DM3-treated cells while only CPS4ACD, but not CPS4B were downregulated in PEN and combination treatments. Standalone DM3 may have profound effects in suppressing all CPS4ABCD subunits and thus the inhibition could be of higher efficiency as compared to PEN- and DM3PEN treatments. Reduction in CPS gene expression may impair pneumococcal cell's host immune evasion resulting in higher susceptibility to phagocytosis and greater clearance efficiency[41]. Besides, DM3 showed predominant cell wall and cell membrane regulatory effects and could partly contribute to explain its lytic activity in pneumococcal cells.

CAMP resistance mechanism downregulation induced by DM3 is of interest. It is hypothesized that DM3 could reduce the CAMP resistance mechanism to enhance its antimicrobial activity on the target cells. Additionally, downregulation of CAMP resistance mechanism suggests that the AMP-defense mechanism in pneumococci could have been compromised leading to increased susceptibility of *S. pneumoniae* against other AMPs classes. However, further investigations are needed to support the hypothesis.

DM3 treatment was found to alter competence regulatory activity in *S. pneumoniae*. The number of differentially expressed genes in DM3 treated cells were higher than PEN treated cells. Natural competence induction in *S. pneumoniae* is a quorum-sensing regulated transient mechanism encoded by *comCDE* and *comAB* regulons in allowing the cells to undergo genetic transformation by uptake of foreign DNA[42]. *comCDE* is responsible for induction of genetic competence *comC* encodes for the pheromone-like competence-stimulating peptide (CSP) which is exported using the ComAB transporter[43]. The CSP stimulation signal will be captured by the ComD/ComE signal transduction system[44]. Another gene, *endA*, is also a membrane-bound DNA-entry nuclease important in pneumococcal transformation. However, DM3 as well as the combination treatment DM3PEN showed no significant effect on these fundamental competence genes responsible for competent induction. Significant changes in expression are reported with *celA*, *celB*, *cglA*, *ccs4* and others exhibiting important roles in DNA transport, processing, and recombination; CelA and Cel B are both DNA transformation transporter CglA while *ccs4* and *ccs16* are competence-induced proteins. Competence regulation was not the primary target of DM3 in standalone or in combination with PEN. Of note, CoiA, which functions to promote genetic recombination during transformation[45], was only found in cells treated with DM3PEN suggesting the unique effect of the synergistic treatment in enhancing transformational recombination. Additionally, it is possible that the current experimental design could have undermined the effect of DM3 on competence induction and represents one of the limitation of the current study. This is because the pneumococcal culture used was in mid-log phase rather than at the beginning of log phase to which pneumococcus is at the highest competence capacity[46]. Although current study was not directed at investigating the role of DM3 in regulation of transformation in *S. pneumoniae*, this could be an aspect to study about DM3 in the future.

D-alanine metabolism was only found in cells treated with DM3 whether in standalone or combination, hence DM3 is hypothesized to exert inhibitory effect on the processing of D-alanine which is an important intermediate in cell wall biosynthesis. The lower expression of this component could result in cell wall lysis and cell death.

There are many heavily affected genes and pathways which are common to all three treatments. These include specific pathways collected under purine and pyrimidine biosynthesis and metabolisms, aminoacyl-tRNA biosynthesis, rRNA, ribosomal proteins, ATP biosynthesis and metabolisms, ABC transport system, and the phophotransferase (PTS) system. One potential explanation is these pathways constitute the common sets of genes and pathways in response to antimicrobial treatment. Replication, transcription, and translation mechanisms have seen a number of changes arising from the treatments as well. For example, RpoD was downregulated in the DM3-treated cells but otherwise no effect on RNA polymerase. On the contrary, combination treatment using both DM3 and PEN caused downregulation of RNA polymerase accompanied by RpoD upregulation which was in part due to the combination effect from PEN-treatment. While PEN increased DNA gyrase expression in pneumococcal cells, this was not the target of DM3. Notably, DM3PEN caused downregulation of topoisomerase I which could affect the mechanism of DNA replication and transcription.

From the study, several important genes and its associated pathways affected by DM3 and DM3PEN have been highlighted. This provides a better understanding of the drug effects at the genomic level. Together with our previous study, it is becoming clearer that DM3 exerts multiple inhibitory mechanisms by direct cell wall or cell membrane lysis killing of the target bacterial cells enhanced with disruption mechanisms to inhibit cell wall biosynthetic processes. In addition, DM3 antibacterial activity is supported by metabolic disruption activities to produce higher antibacterial efficiency. The two main metabolic processes affected are nucleic acid and amino acid biosynthesis activities. Thus, DM3 is a potent antibacterial targeting multiple cellular targets to exert killing effects. Moreover, it is important to state that the greater extent of differentially expressed genes and pathways involved due to DM3PEN-treatment may be the main reason why DM3-PEN combination showed better therapeutic efficiency in an *in vivo* infection model[38].

One interesting point to highlight is the higher susceptibility of PRSP than PSSP to DM3. This is essentially one of our main objectives in designing DM3 – a novel drug possessing high antibacterial activity against the antibiotic-resistance strains. The gene expression profile of SP17 (PRSP strain used in this study) was heavily affected by DM3 and DM3PEN which was in sharp contrast to the gene expression profile of SP27 (PSSP strain used in this study). This strongly suggests that DM3 could have higher inhibitory effect against PRSP than PSSP but it is unclear of why such differences exists whether it is due to PEN-susceptibility of the strains alone or involve other factors including serotype variation, thickness of cell wall, pathogenicity of strain, and others. We are unclear of how these complex interactions (up or downregulation) occur in the pneumococcal cells at this stage. Therefore, further studies to determine the key mechanisms causing cell death based on *in vitro* experiments is proposed in subsequent investigations.

Methods

Peptide Synthesis. DM3 was synthesized by Genscript Inc. (USA) using Fluorenylmethyloxycarbonyl chloride (Fmoc) chemistry to >90% purity and validated using High Performance Liquid Chromatography and Mass Spectrometry.

Pneumococcal cultures and assay media. One PSSP (SP17, $MIC_{PEN} = 0.06\,\mu g/ml$) and –resistant (SP27, $MIC_{PEN} = 4\,\mu g/ml$) isolates were selected from the previous collection maintained in the laboratory. The isolates were stored in multiple vials in BHI supplemented with 10% glycerol at −80 °C to avoid repeated freeze-thaw cycles. The isolates were passaged twice prior to experimentation. All experimental were carried out in accordance with approved guidelines and were approved by the University Malaya Biosafety & Biosecurity Committee.

Cell treatment and RNA extraction. Overnight bacterial cultures on defibrinated sheep blood agar (Oxoid, UK) were inoculated into Mueller-Hinton Broth (MHB) broth using direct colony suspension method and incubated at 37 °C with 5% CO_2 and shaked at 200 rpm for 4–6 hrs to mid-log phase growth (approx. OD_{600} 0.35–0.5). Aliquot equivalent to 2×10^9 CFU was transferred into a fresh tube and make up to 10 ml with fresh MHB. Both PRSP (SP17, serotype 19F) and PSSP (SP27, serogroup 18) strains used were treated at the respective MIC levels for 60 min: SP17, DM3 (31.25 μg/ml), PEN (4 μg/ml), and DM3 + PEN (7.81 μg/ml, 0.5 μg/ml); SP27, DM3 (31.25 μg/ml), PEN (0.06 μg/ml), and DM3 + PEN (7.81 μg/ml, 0.015 μg/ml). The 60 min treatment duration was chosen as it was found that prolonged treatment for 120 min or more caused low yield and poor quality of RNA obtained probably due to direct lysis of cells by DM3 and hence release of cellular contents including RNA to the medium before RNA extraction. The short treatment duration would still allow substantial interruption of expression changes in the cells. Untreated cells was served as control. Subsequently, the suspensions were washed twice and resuspended in one volume of PBS followed by addition of two volumes of RNAprotect Bacteria reagent (Qiagen, Germany), immediately vortex mixed for 5 s and incubated at room temperature for 5 min before centrifuge pelleting at 5000× g for 10 min and discarded the supernatant. The pellets were lysed with 20 μl Proteinase K (Qiagen, Germany) and 200 μl bacterial lysis mix consisting of mutanolysin (M9901, Sigma, US) and lysozyme to final concentrations of 15 mg/ml and 15 U/ml, respectively made up to 200 μl using Tris-EDTA buffer. The suspensions were vortexed for 10 s and incubated at room temperature for 10 min with 2 min mixing interval. RNA extraction of the treated cells was performed using RNeasy Plus Mini kit (Qiagen, Germany) according to manufacturer's guidelines and eluted in DEPC water (Bioline, UK). A total of three biological replicates were included for each treatment group and an untreated control group for comparison analysis.

RNA-Seq library preparation and analysis. Quality of RNA was verified using Bioanalyzer (Agilent Technologies, Santa Clara, CA, USA) and NanoDrop spectrometer. Samples that passes quality control (minimum RNA integrity number (RIN) of 7, absorbance ratios A260/280 in the range 2.0–2.2 and A260/230 above 1.8), a non-normalized cDNA library was constructed. Barcoded libraries were multiplexed by 12 in each lane and sequenced on an Illumina HiSeq 2000 system using the single-end mode. The length of the reads was around 100 bp. Quality control of the RNA-Seq data was performed using FastQC and detailed information about the quality of reads in each replicate is provided in Additional file (xx_). Sequence reads have been deposited in the NCBI Sequence Read Archive (SRA) under accession number PRJNA308880 (www.ncbi.nlm.gov/bioproject/PRJNA308880).

Quality check (QC) with FastQC. Adapters from the fastQ file were removed using Cutadapt (https://code.google.com/p/cutadapt/). Removal of reads with phred score below 20 were performed using fastx-toolkit (http://hannonlab.cshl.edu/fastx_toolkit/).

Mapping and Expression analysis. Raw reads in fastq format from illumina sequencing were used to map against *streptococcus pneumoniae* TIGR4 genome (NC_003028) by TopHat v2.0.10 program[47]. To compare expression analysis among samples output bam file from TopHat and GFF file from gene prediction were used as input to cuffdiff v2.1.1 program[48] with classic method of normalization with FPKM to identify the differentially expressed genes between all the samples.

Gene clustering and Heat map. Differentially expressed genes were clustered using K-means clustering algorithm using ComplexHeatmap[41] package from Bioconductor in R. Clusters generated by K-means were submitted to DAVID 6.7 web server[40] for gene enrichment studies. Annotations from various databases such as KEGG pathways, gene ontology (GO), and swissprot were also retrieved from DAVID 6.7 server[40].

References

1. Gillespie, S. H. Aspects of pneumococcal infection including bacterial virulence, host response and vaccination. *J Med Microbiol* **28,** 237–248 (1989).
2. Musher, D. M. Infections caused by *Streptococcus pneumoniae*: clinical spectrum, pathogenesis, immunity, and treatment. *Clin Infect Dis* **14,** 801–807 (1992).
3. World Health Organization. *Pneumococcal conjugate vaccine for childhood immunization–WHO position paper*. 93–104 (2007).
4. MMWR Morb Mortal Wkly Rep. Vaccine preventable deaths and the Global Immunization Vision and Strategy, 2006–2015. *MMWR Morb Mortal Wkly Rep* **55,** 511–515 (2006).
5. Garcia-Vidal, C. & Carratala, J. Early and late treatment failure in community-acquired pneumonia. *Semin Respir Crit Care Med* **30,** 154–160 (2009).
6. Lynch, J. P., 3rd & Zhanel, G. G. *Streptococcus pneumoniae*: does antimicrobial resistance matter? *Semin Respir Crit Care Med* **30,** 210–238 (2009).
7. Menendez, R. & Torres, A. Treatment failure in community-acquired pneumonia. *Chest* **132,** 1348–1355 (2007).

8. Schrag, S. J. *et al.* Emergence of *Streptococcus pneumoniae* with very-high-level resistance to penicillin. *Antimicrob Agents Chemother* **48,** 3016–3023 (2004).
9. Epand, R. M. & Vogel, H. J. Diversity of antimicrobial peptides and their mechanisms of action. *Biochim Biophys Acta* **1462,** 11–28 (1999).
10. Hancock, R. E. Cationic peptides: effectors in innate immunity and novel antimicrobials. *Lancet Infect Dis* **1,** 156–164 (2001).
11. Hancock, R. E., Falla, T. & Brown, M. Cationic bactericidal peptides. *Adv Microb Physiol* **37,** 135–175 (1995).
12. Nizet, V. *et al.* Innate antimicrobial peptide protects the skin from invasive bacterial infection. *Nature* **414,** 454–457 (2001).
13. Wu, X. *et al. In vitro* and *in vivo* activities of antimicrobial peptides developed using an amino acid-based activity prediction method. *Antimicrob Agents Chemother* **58,** 5342–5349 (2014).
14. Jiang, Z. *et al.* Effects of net charge and the number of positively charged residues on the biological activity of amphipathic alpha-helical cationic antimicrobial peptides. *Biopolymers* **90,** 369–383 (2008).
15. Jindal, H. M. *et al.* Antimicrobial Activity of Novel Synthetic Peptides Derived from Indolicidin and Ranalexin against *Streptococcus pneumoniae*. *PLoS One* **10,** e0128532 (2015).
16. Lum, K. Y. *et al.* Activity of Novel Synthetic Peptides against Candida albicans. *Sci Rep* **5,** 9657 (2015).
17. Shai, Y. Mode of action of membrane active antimicrobial peptides. *Biopolymers* **66,** 236–248 (2002).
18. Yeaman, M. R. & Yount, N. Y. Mechanisms of antimicrobial peptide action and resistance. *Pharmacol Rev* **55,** 27–55 (2003).
19. Brogden, K. A. Antimicrobial peptides: pore formers or metabolic inhibitors in bacteria? *Nat Rev Microbiol* **3,** 238–250 (2005).
20. Yoneyama, F. *et al.* Peptide-lipid huge toroidal pore, a new antimicrobial mechanism mediated by a lactococcal bacteriocin, lacticin Q. *Antimicrob Agents Chemother* **53,** 3211–3217 (2009).
21. Yang, L., Harroun, T. A., Weiss, T. M., Ding, L. & Huang, H. W. Barrel-stave model or toroidal model? A case study on melittin pores. *Biophys J* **81,** 1475–1485 (2001).
22. Gazit, E., Boman, A., Boman, H. G. & Shai, Y. Interaction of the mammalian antibacterial peptide cecropin P1 with phospholipid vesicles. *Biochemistry* **34,** 11479–11488 (1995).
23. Hale, J. D. & Hancock, R. E. Alternative mechanisms of action of cationic antimicrobial peptides on bacteria. *Expert Rev Anti Infect Ther* **5,** 951–959 (2007).
24. Nguyen, L. T., Haney, E. F. & Vogel, H. J. The expanding scope of antimicrobial peptide structures and their modes of action. *Trends Biotechnol* **29,** 464–472 (2011).
25. Subbalakshmi, C., Krishnakumari, V., Nagaraj, R. & Sitaram, N. Requirements for antibacterial and hemolytic activities in the bovine neutrophil derived 13-residue peptide indolicidin. *FEBS Lett* **395,** 48–52 (1996).
26. Park, C. B., Kim, H. S. & Kim, S. C. Mechanism of action of the antimicrobial peptide buforin II: buforin II kills microorganisms by penetrating the cell membrane and inhibiting cellular functions. *Biochem Biophys Res Commun* **244,** 253–257 (1998).
27. Helmerhorst, E. J. *et al.* The cellular target of histatin 5 on Candida albicans is the energized mitochondrion. *J Biol Chem* **274,** 7286–7291 (1999).
28. Helmerhorst, E. J., Troxler, R. F. & Oppenheim, F. G. The human salivary peptide histatin 5 exerts its antifungal activity through the formation of reactive oxygen species. *Proc Natl Acad Sci USA* **98,** 14637–14642 (2001).
29. Friedrich, C. L., Rozek, A., Patrzykat, A. & Hancock, R. E. Structure and mechanism of action of an indolicidin peptide derivative with improved activity against gram-positive bacteria. *J Biol Chem* **276,** 24015–24022 (2001).
30. Boman, H. G., Agerberth, B. & Boman, A. Mechanisms of action on Escherichia coli of cecropin P1 and PR-39, two antibacterial peptides from pig intestine. *Infect Immun* **61,** 2978–2984 (1993).
31. Patrzykat, A., Friedrich, C. L., Zhang, L., Mendoza, V. & Hancock, R. E. Sublethal concentrations of pleurocidin-derived antimicrobial peptides inhibit macromolecular synthesis in Escherichia coli. *Antimicrob Agents Chemother* **46,** 605–614 (2002).
32. Hesketh, A. *et al.* Genome-wide dynamics of a bacterial response to antibiotics that target the cell envelope. *BMC Genomics* **12,** 226 (2011).
33. Qin, N. *et al.* RNA-Seq-based transcriptome analysis of methicillin-resistant Staphylococcus aureus biofilm inhibition by ursolic acid and resveratrol. *Sci Rep* **4,** 5467 (2014).
34. Heo, A., Jang, H. J., Sung, J. S. & Park, W. Global transcriptome and physiological responses of Acinetobacter oleivorans DR1 exposed to distinct classes of antibiotics. *PLoS One* **9,** e110215 (2014).
35. Friedrich, C. L., Moyles, D., Beveridge, T. J. & Hancock, R. E. Antibacterial action of structurally diverse cationic peptides on gram-positive bacteria. *Antimicrob Agents Chemother* **44,** 2086–2092 (2000).
36. Wang, G., Li, Y. & Li, X. Correlation of three-dimensional structures with the antibacterial activity of a group of peptides designed based on a nontoxic bacterial membrane anchor. *J Biol Chem* **280,** 5803–5811 (2005).
37. Le, C. F., Yusof, M. Y., Hassan, H. & Sekaran, S. D. *In vitro* properties of designed antimicrobial peptides that exhibit potent antipneumococcal activity and produces synergism in combination with penicillin. *Sci. Rep.* **5,** 9761 (2015).
38. Le, C. F. *et al. In vivo* efficacy and molecular docking of designed peptide that exhibits potent antipneumococcal activity and synergises in combination with penicillin. *Sci. Rep.* **5,** 11886 (2015).
39. Tomasz, A., Albino, A. & Zanati, E. Multiple antibiotic resistance in a bacterium with suppressed autolytic system. *Nature* **227,** 138–140 (1970).
40. Tomasz, A. & Waks, S. Mechanism of action of penicillin: triggering of the pneumococcal autolytic enzyme by inhibitors of cell wall synthesis. *Proc Natl Acad Sci. USA* **72,** 4162–4166 (1975).
41. O'Riordan, K. & Lee, J. C. Staphylococcus aureus capsular polysaccharides. *Clin Microbiol Rev* **17,** 218–234 (2004).
42. Cheng, Q., Campbell, E. A., Naughton, A. M., Johnson, S. & Masure, H. R. The com locus controls genetic transformation in *Streptococcus pneumoniae*. *Mol Microbiol* **23,** 683–692 (1997).
43. Hui, F. M., Zhou, L. & Morrison, D. A. Competence for genetic transformation in *Streptococcus pneumoniae*: organization of a regulatory locus with homology to two lactococcin A secretion genes. *Gene.* **153,** 25–31 (1995).
44. Pestova, E. V., Havarstein, L. S. & Morrison, D. A. Regulation of competence for genetic transformation in *Streptococcus pneumoniae* by an auto-induced peptide pheromone and a two-component regulatory system. *Mol Microbiol.* **21,** 853–862 (1996).
45. Desai, B. V. & Morrison, D. A. Transformation in *Streptococcus pneumoniae*: formation of eclipse complex in a coiA mutant implicates CoiA in genetic recombination. *Mol Microbiol* **63,** 1107–1117 (2007).
46. Berge, M., Langen, H., Claverys, J. P. & Martin, B. Identification of a protein that inactivates the competence-stimulating peptide of *Streptococcus pneumoniae*. *J Bacteriol* **184,** 610–613 (2002).
47. Trapnell, C., Pachter, L. & Salzberg, S. L. TopHat: discovering splice junctions with RNA-Seq. *Bioinformatics* **25,** 1105–1111 (2009).
48. Trapnell, C. *et al.* Transcript assembly and quantification by RNA-Seq reveals unannotated transcripts and isoform switching during cell differentiation. *Nat Biotechnol* **28,** 511–515 (2010).

Acknowledgements

This study was supported by University of Malaya High Impact Research grant (reference number: UM.C/HIR/MOHE/MED/40, account number: H-848 20001-E000079) and University of Malaya Research Grant (UMRG Project no. RP020C-14AFR and RP001C-13ICT).

Author Contributions

S.D.S. and C.F.L. designed and carried out the experiments, C.F.L., R.G. and R.R. performed the analysis and methods used in the analysis, C.F.L., S.D.S. and R.M. wrote the manuscript and S.D.S. and R.M. funded the project.

Additional Information

Supplementary information accompanies this paper at http://www.nature.com/srep

Competing financial interests: The authors declare no competing financial interests.

How to cite this article: Le, C.-F. *et al.* Transcriptome analysis of *Streptococcus pneumoniae* treated with the designed antimicrobial peptides, DM3. *Sci. Rep.* **6**, 26828; doi: 10.1038/srep26828 (2016).

Regular Article

THROMBOSIS AND HEMOSTASIS

A novel DFP tripeptide motif interacts with the coagulation factor XI apple 2 domain

Szu S. Wong,[1,2] Søren Østergaard,[2] Gareth Hall,[1] Chan Li,[1] Philip M. Williams,[1] Henning Stennicke,[2] and Jonas Emsley[1]

[1]Centre for Biomolecular Sciences, School of Pharmacy, University of Nottingham, Nottingham, United Kingdom; and [2]Novo Nordisk, Måløv, Denmark

Key Points

- A novel FXI binding tripeptide motif has sequence Asp-Phe-Pro (DFP).
- FXI complex crystal structures reveal DFP peptides bound to the apple 2 domain.

Factor XI (FXI) is the zymogen of FXIa, which cleaves FIX in the intrinsic pathway of coagulation. FXI is known to exist as a dimer and interacts with multiple proteins via its 4 apple domains in the "saucer section" of the enzyme; however, to date, no complex crystal structure has been described. To investigate protein interactions of FXI, a large random peptide library consisting of 10^6 to 10^7 peptides was screened for FXI binding, which identified a series of FXI binding motifs containing the signature Asp-Phe-Pro (DFP) tripeptide. Motifs containing this core tripeptide were found in diverse proteins, including the known ligand high-molecular-weight kininogen (HK), as well as the extracellular matrix proteins laminin and collagen V. To define the binding site on FXI, we determined the crystal structure of FXI in complex with the HK-derived peptide NPISDFPDT. This revealed the location of the DFP peptide bound to the FXI apple 2 domain, and central to the interaction, the DFP phenylalanine side-chain inserts into a major hydrophobic pocket in the apple 2 domain and the isoleucine occupies a flanking minor pocket. Two further structures of FXI in complex with the laminin-derived peptide EFPDFP and a DFP peptide from the random screen demonstrated binding in the same pocket, although in a slightly different conformation, thus revealing some flexibility in the molecular interactions of the FXI apple 2 domain. (*Blood*. 2016;127(23):2915-2923)

Introduction

The physiological function of coagulation factor XI (FXI) is poorly understood compared with the vitamin K–dependent coagulation proteases; people deficient in FXI do not show the strong bleeding phenotypes observed for FVIII and FIX deficiency.[1] From a structural perspective, FXI is unique among the coagulation factors because it circulates as a disulfide-linked dimer.[2-4] Each subunit has 607 amino acids, with four 90–amino acid apple domains (A1-A4) that, in the FXI monomer, assemble into a saucer-shaped disc, with the protease domain resting on top in an arrangement that we have described as a cup and saucer.[5] Biochemical data have mapped protein interactions to the apple domains for diverse ligands, including substrate FIX,[6] thrombin,[7] platelet glycoprotein Ib,[8] and high-molecular-weight kininogen (HK),[9] but to date, no complex crystal structures have been determined to define the molecular basis of these interactions.[10] FXI circulates in complex with cofactor HK.[9] A close homolog of FXI is plasma coagulation factor prekallikrein (PK), which has the same domain structure, with 4 apple domains at the N-terminus. In common with FXI, PK also binds HK, but unlike FXI, PK is a monomeric protein.[11]

The 2 pathways contributing to blood coagulation in humans are the intrinsic pathway, which can be activated by FXIa cleaving FIX, and the extrinsic pathway, which is activated by tissue factor. In addition to the principal substrate FIX, FXIa has also been shown to cleave and inactivate tissue factor pathway inhibitor, promoting a pathway of intravascular thrombus formation.[12] Several lines of evidence suggest that therapeutic intervention targeting FXI and HK has the potential for providing medicines with a safer anticoagulation profile than those currently available.[1,13,14]

Random combinatorial peptide libraries based on the one-bead-one-compound method have proved successful in identifying ligands for various macromolecular targets.[15] By screening a random peptide library comprising 10^6 to 10^7 peptides, we have identified FXI binding peptides that all share the core motif Asp-Phe-Pro (DFP). Of importance, this motif can also be found in the cofactor HK, laminin, and collagen V. By determining 3 FXI-DFP peptide ligand complex structures, we show how synthetic DFP peptides interact with a pocket in the apple 2 domain and how the dimeric FXI orients 2 bound DFP peptides onto the same surface.

Methods

Synthesis and screening of peptide libraries

The one-bead-one-compound libraries were synthesized on TentaGel S-NH_2 resin (Rapp Polymere, Tübingen, Germany) using the split-mix method.[15,16] Two unbiased libraries (libraries 1 and 2) where screened against biotinylated FXI. Library 1 was fixed at 12 residues in length; library 2 had varying lengths. The format for library 1 was O_{12}-resin, whereby O was D,N,2Q,A,S,T,G,P,H,K,R,Y,W,F,L,I,V and M and C were omitted. The format for library 2 was OO-Ψ-$O_{0,1,2}$-Ψ-$O_{0,1,2}$-Ψ-$O_{0,1,2}$-Ψ-OO-resin, whereby O was D,N,E,Q,A,S,T,G,P,H,K,R,V and Ψ (only hydrophobic) was W,F,Y,L,V; the residues M and C were

Submitted October 19, 2015; accepted March 17, 2016. Prepublished online as *Blood* First Edition paper, March 22, 2016; DOI 10.1182/blood-2015-10-676122.

The online version of this article contains a data supplement.

The publication costs of this article were defrayed in part by page charge payment. Therefore, and solely to indicate this fact, this article is hereby marked "advertisement" in accordance with 18 USC section 1734.

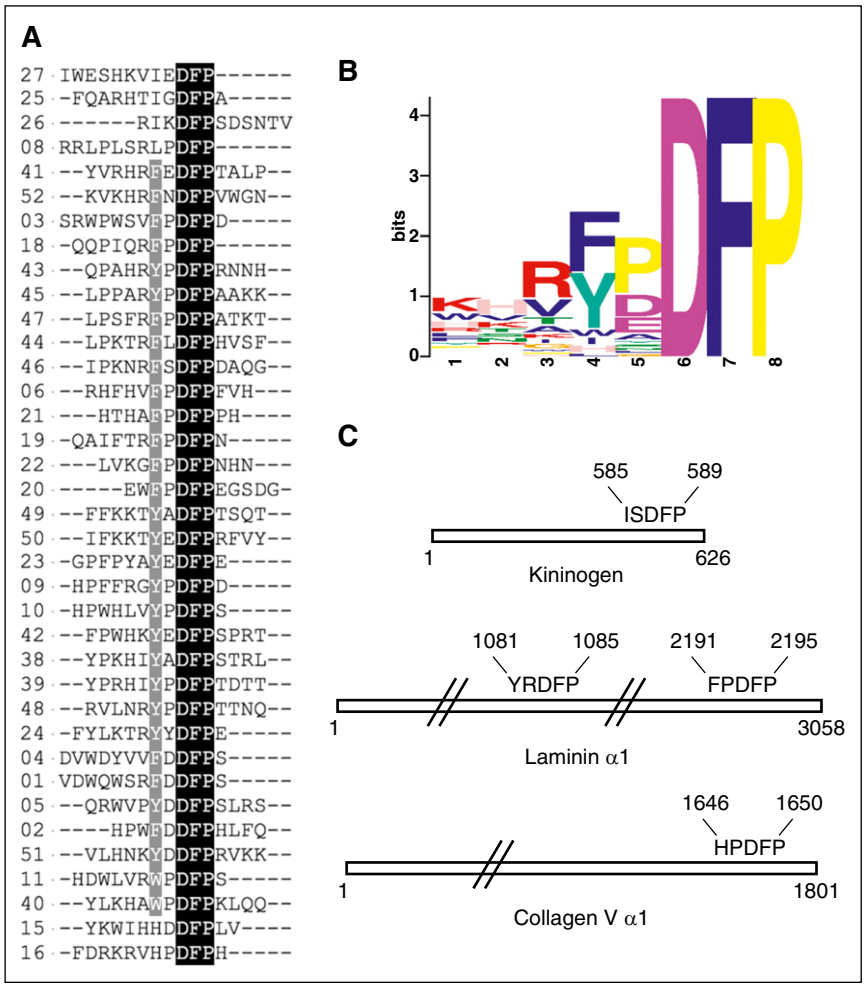

Figure 1. FXI binding peptides with the DFP motif. (A) Alignment of peptide sequences from the random screen, with 37 peptides shown containing the DFP tripeptide. (B) Peptide motif overview calculated using MEME software for the 37 FXI-binding DFP peptide sequences. (C) Location of DFP pentapeptide sequences in the proteins HK (KNG1_HUMAN), laminin (LAMA1_HUMAN), and collagen V (CO5A1_HUMAN) identified using PROSITE software.

omitted. A total of 1 g of resin was used in a 5-mL syringe with filter frit. The resin was washed 5 times with 15 mM Tris pH 7.4, 150 mM sodium chloride (NaCl), 0.5% bovine serum albumin, and 0.05% Tween 20 (incubation buffer). For prescreening of libraries against streptavidin-alkaline phosphatase (Strep-AP; stock 1 mg/mL; Sigma), Strep-AP alone was added to the library to a final dilution of 1:10 000 and incubated for 30 minutes. This library was then washed 4 times with washing buffer (15 mM Tris pH 7.4, 150 mM NaCl, and 0.05% Tween 20) and washed twice with staining buffer (50 mM Tris pH 8.8, 0.15 M NaCl, 0.05% Tween 80, and 15 mM magnesium chloride). The substrate 6-chloro-3-indoxyl-phosphate (50 mg/mL in *N*-methyl-2-pyrrolidone; Biosynth AG) was added, and the reaction was allowed to proceed for 30 to 45 minutes. For screening of libraries against FXI, the resins were washed with 6 M guanidinium chloride pH 3.0 for 20 minutes, washed with washing buffer, and lastly washed twice with incubation buffer. Biotinylation of FXI was performed using 200 μg of FXI, which was gel filtrated using a NAP5 column equilibrated with 1% sodium bicarbonate pH 8. Added to this solution (500 μL) was 4 μL of a 7 mM solution of biotin *N*-hydroxysuccinimide ester (Sigma) in DMSO, and the reaction was allowed to proceed for 3 hours at 4°C. The FXI was then gel filtrated using a NAP5 column against 100 mM NaCl and Tris buffer pH 7.4 and stored in aliquots (30 μL) at −25°C. A total of 4 μL of biotinylated FXI (stock concentration 1.2 μM) plus 1 μL of Strep-AP was added to the library in 2 mL of incubation buffer and allowed to incubate for 2 hours. The resin was washed 3 times with washing buffer and then staining buffer, and 5-bromo-4-chloro-3-indolyl phosphate with nitro blue tetrazolium was added. After 1 hour, the reaction was stopped and the most intense blue beads were removed for sequencing. For the sequence determination, blue beads were removed under a microscope and sequenced by an Edman sequencer (Procise, Applied Biosystems). Peptide sequences were aligned using the program MEME[17] to produce Figure 1B, and database searches for DFP motifs were performed using PROSITE.[18] In Figure 3A, HK protein sequences were aligned with National Center for Biotechnology Information HOMOLOGENE server and shaded with the BOXSHADE server.

Protein crystallization and structure determination

Recombinant human untagged FXI was expressed and purified from Chinese hamster ovary cells as previously described.[19] All synthetic peptides used for crystallization experiments were purchased from GenScript. FXI was concentrated to 8 mg/mL and added to an equal volume of peptide sequence YPRHIYPDFPTDTT (P39), FNPISDFPDTTS (HKP), or RLEFPDFPIDD (LP2) to achieve a 1:5 protein-to-peptide molar ratio for P39 and a 1:6 ratio for peptides HKP and LP2. The resulting solution was 4 mg/mL FXI in 50 mM Tris-HCl pH 7.6 and 75 mM NaCl. Crystals were grown in sitting drop from conditions of 0.1 M 2-(*N*-morpholino)ethanesulfonic acid pH 6.5 and 20% polyethylene glycol 4000 for the FXI-P39 complex and 0.1 M *N*-2-hydroxyethylpiperazine-*N*′-2-ethanesulfonic acid pH 7.5 and 20% polyethylene glycol 1500 for the FXI-HKP and FXI-LP2 complexes. Data were collected from 2 crystals for FXI-P39 and on a single crystal for FXI-HKP and FXI-LP2 at the Diamond Light Source synchrotron using beamline I04. Data were processed with XDS[20] and reduced in space group $P4_32_12$ using the CCP4 software suite[21] (Table 1). The structures were solved by molecular replacement using Phaser,[22] with the crystal structure of FXI (Protein Data Bank code 2F83)[5] as a search model. High-quality $2mF_o - DF_c$ and $mF_o - DF_c$ electron density maps enabled direct location of the bound peptides (supplemental Figure 2, available on the *Blood* Web site). Manual rebuilding was performed using the program Coot,[23] and refinement was performed using REFMAC, with statistics shown in Table 1. Protein structures in Figures 2A-B,D,F and 4 were generated using PyMOL, and those in Figure 2C,E used LIGPLOT.[24]

Table 1. Crystallographic data collection and refinement statistics

	FXI-HKP	FXI-P39	FXI-LP2
Data collection			
Space group	$P4_32_12$	$P4_32_12$	$P4_32_12$
Cell dimensions			
a, b, c, Å	80.6, 80.6, 251.8	81.3, 81.3, 252.2	81.1, 81.1, 253.0
α, β, γ, °	90, 90, 90	90, 90, 90	90, 90, 90
Resolution, Å	39.8-2.85 (2.92-2.85)	77.4-2.80 (2.90-2.80)	77.3-3.0 (3.08-3.0)
R_{sym}*	0.083	0.094	0.158
I/sig*I*	16.0 (3.0)	17.1 (2.8)	12.5 (3.1)
Completeness, %	99.9 (100.0)	95.1 (71.9)	97.8 (97.2)
Redundancy	6.0 (6.2)	8.3 (3.5)	9.8 (9.1)
Refinement			
Number of reflections	20 319	19 565	23 419
R_{work} /R_{free}†	0.226/0.285	0.201/0.264	0.210/0.279
B-factors, Å^2			
Protein	81.5	74.6	80.30
Ligands	21.0	111.80	117.50
Root mean square deviations			
Bond lengths, Å	0.011	0.015	0.022
Bond angles, °	1.82	1.82	1.98
Protein Data Bank code	5I25	5EOK	5EOD

Values in parentheses are for highest-resolution shell.

*R_{sym} is Sum(h) [Sum(j) [I(hj) − <Ih>]/Sum(hj) < Ih>, where *I* is the observed intensity and <*Ih*> is the average intensity of multiple observations from symmetry-related reflections calculated with SCALA.

†R_{work} is Sum(h) ||F_o|h − |F_c||h|/Sum(h) |F_o|h, where F_o and F_c are the observed and calculated structure factors, respectively. R_{free} is computed as in R_{work}, but only for (5%) randomly selected reflections, which were omitted in refinement, calculated using REFMAC.

SPR binding studies

Plasma-purified HK was purchased from Enzyme Research Laboratories. Laminin 111, 411, and 511 were purchased from BioLamina. HK, FXI, or laminin was immobilized onto a CM5 chip using an amine coupling kit (GE Healthcare), and experiments were performed on a Biacore 3000 instrument. The running buffer used for all experiments was 10 mM *N*-2-hydroxyethylpiperazine-*N*′-2-ethanesulfonic acid pH 7.5, 140 mM NaCl, 5 μM ETDA, and 0.005% polysorbate 20. To assess any nonspecific binding, the analyte (FXI or peptide) was also injected over an empty flow cell. Collagen V peptide of sequence KDLQLCHPDFPDGEB and HK peptide of sequence INPTTQMKESYYFDLTDGLS (HKC) were purchased from Biomatik. Binding curves were analyzed on the basis of the surface plasmon resonance (SPR) response units recorded at equilibrium for each analyte protein concentration, and a Hill plot was generated using Prism 6 (GraphPad Software). Competition assays were performed with increasing concentrations of peptide P39 (6-600 nM) mixed with a fixed concentration of FXI (6 nM).

Results

Identification of peptides binding FXI

To identify peptides and novel ligands for FXI, we screened a random peptide library containing greater than 3 million peptides and identified 52 FXI binding peptides. From the sequences identified (termed P1-P52), 37 were observed to contain the tripeptide motif Asp-Phe-Pro (DFP) and 4 contained a related DFD sequence, 2 contained DFS sequences, and 1 contained the DLP sequence. Figure 1A shows the DFP-containing peptides aligned, and supplemental Figure 1 contains all 52 peptide sequences. A hydrophobic side chain F/Y/I/W located 2 amino acids before DFP is preferred across all DFP peptides, with the exception of HxDFP, and there are no examples in which a charged K/R/D/E amino acid occupies this position. The most common motif is F/YxDFP, present in 29 peptides; 3 peptides contain IxDFP and 2 contain WxDFP or HxDFP. A preference for proline occurs between F/Y/I and the DFP tripeptide, with the second preference being an acidic residue. It is also common to observe 1 or 2 basic residues N-terminal to the hydrophobic F/Y/I/W residue. By contrast, the C-terminus does not show any conserved features, and several peptides have no residues present C-terminal to the DFP motif.

A search of the Swiss-Prot database for extracellular human proteins containing the DFP motif revealed that the FxDFP sequence occurs in 13 human proteins, YxDFP in 4, HxDFP in 3, WxDFP in 2, and IxDFP in 7 (supplemental Tables 1-3). The known binding partner for FXI (cofactor HK)[25] contains the sequence ISDFP (residues 585-589; mature sequence numbering is used from the Swiss-Prot database entry name KNG1_HUMAN), which is located in the C-terminal domain 6. Other proteins that contained a close match to sequences from the screen include the extracellular matrix protein laminin α1 chain, with the sequence YRDFP (sequence LAMA1_HUMAN, residues 1081-1085, termed LP1) and FPDFP (residues 2191-2195, termed LP2). The laminin peptide LP2 most closely resembles the screen peptides, with FPDFP being the most common pentapeptide motif occurring in 8 peptides. Other proteins that closely match the pentapeptide preferences include matrix protein collagen V, with the sequence HPDFP (sequence CO5A1_HUMAN, residues 1646-1650) and collagen XI (sequence COBA1_HUMAN, residues 1614-1618) (Figure 1C).

Structures of F/YxDFP peptide FXI complexes

We next synthesized examples of peptides containing the DFP motif, including peptide P39 from the screen and DFP peptides derived from HK (HKP) and laminin (LP2), and performed cocrystallization experiments with FXI. The laminin-derived LP2 peptide with sequence RLEFPDFPIDD cocrystallized with FXI in a 1:6 molar mixture, and the structure was solved to 3.0 Å resolution, with clearly identifiable electron density for the sequence EFPDFP. The peptide forms contacts exclusively with the apple 2 domain through interactions with a major and minor pocket, burying a total surface area of 992 Å^2 (Figure 2A).

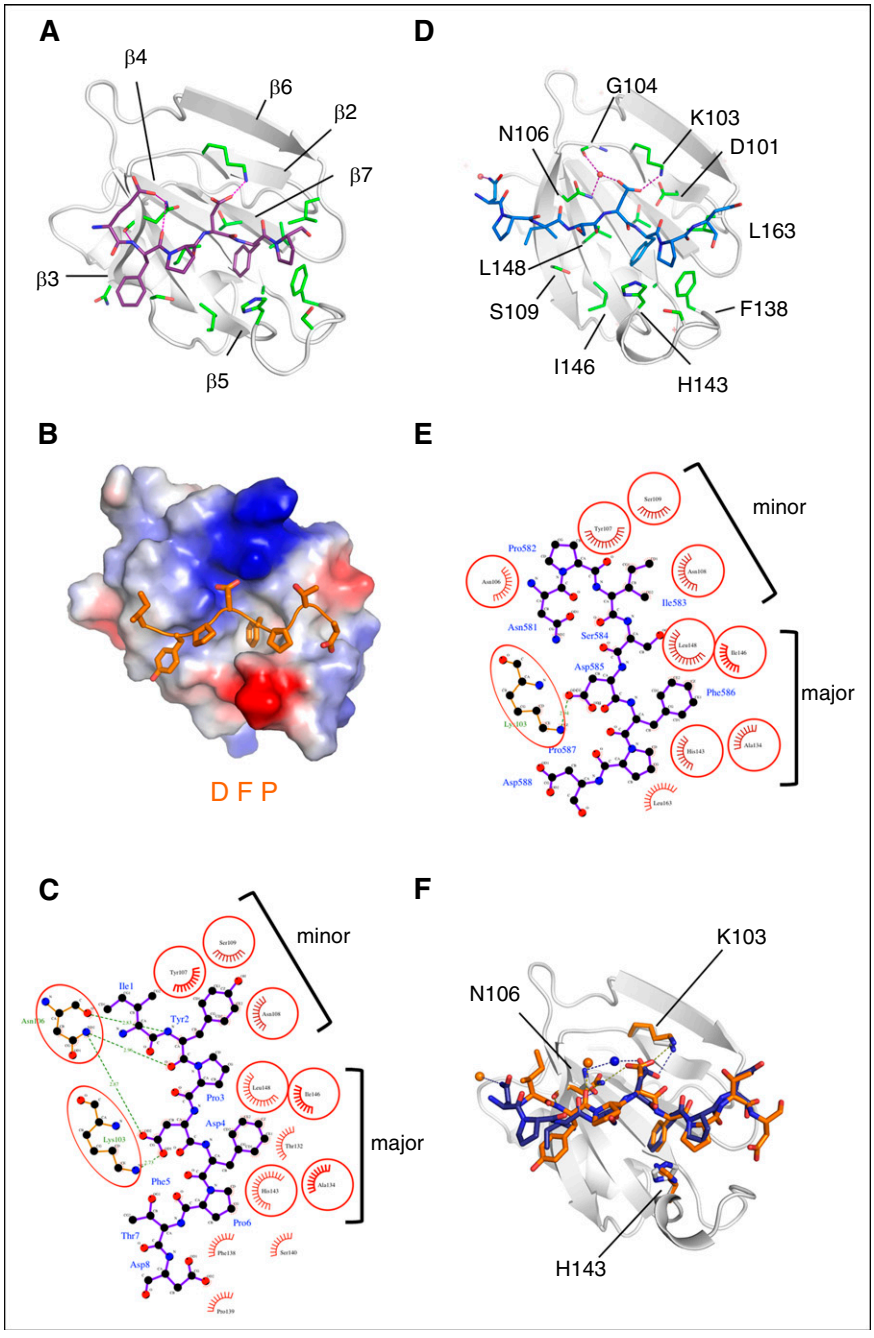

Figure 2. FXI peptide complex structures. (A) Cartoon diagram showing only the apple 2 domain in white, with laminin LP2 peptide shown as sticks in purple. Electrostatic and hydrogen bonding interactions are shown as lavender dotted lines. Residues interacting with the peptide are shown as sticks in green. (B) Charged surface representation of the apple 2 domain (blue is positive, red is negative) bound to the P39 peptide (orange) shown as sticks. (C) Schematic diagram illustrating the P39 peptide (purple) bound to the apple 2 domain, calculated using LIGPLOT software, with major and minor pockets indicated. (D) Cartoon diagram of the apple 2 domain in white, with bound HK peptide in blue shown as sticks. (E) Schematic diagram illustrating HK peptide (purple) bound to the apple 2 domain, calculated using LIGPLOT. (F) Superposition of the FXI-P39 and FXI-HKP peptide apple 2 domain structures. The apple 2 domain is shown as a cartoon in white for the FXI-P39 structure, and the P39 and HKP peptides are shown as sticks in orange and purple, respectively.

Central to the interaction is the DFP phenylalanine side chain that fits precisely into a major pocket, forming contacts with side chains from the apple domain β sheet (residues Leu148, Ile146, Thr132, and Ala134). The DFP proline ring packs against the His143 side chain from the β4-β5 loop. The DFP aspartate side chain forms a salt bridge to FXI Lys103 and a hydrogen bond to the FXI Asn106 side chain (Figure 2A). A second interaction site occurs from the peptide phenylalanine that is 2 residues N-terminal to the DFP sequence contacting a minor pocket formed by residues Tyr107, Asn108, and Ser109. For this peptide, the phenylalanine main-chain amide and carbonyl form hydrogen bonds to the FXI residue Asn106 main-chain carbonyl and side chain nitrogen, respectively. The peptide glutamate residue side chain forms a hydrogen bond to the side chain of Asn106.

In addition, we determined the 2.8-Å structure of FXI in complex with peptide P39 from the random screen using a similar protocol. Clearly identifiable electron density was observed for the 8-residue sequence IYPDFPTD (supplemental Figure 2). The peptide occupies the same elongated crevice as the laminin peptide, and the tyrosine aromatic side chain packs into the same minor pocket. At the C-terminus of the P39 structure, the Thr-Asp residues are observed to form minor van der Waals contacts with FXI, as shown in Figure 2B-C.

Structure of the HK DFP peptide FXI complex

The FXI complex structure with a 12-mer peptide containing HK amino acids 582 to 593 was solved to 2.85-Å resolution. The HK peptide HKP was also observed bound to the apple 2 domain, and the sequence NPISDFPD was successfully identified in the electron density (Figure 2D). The DFP motif occupies the same major pocket as P39 peptide, and the isoleucine side chain from HKP

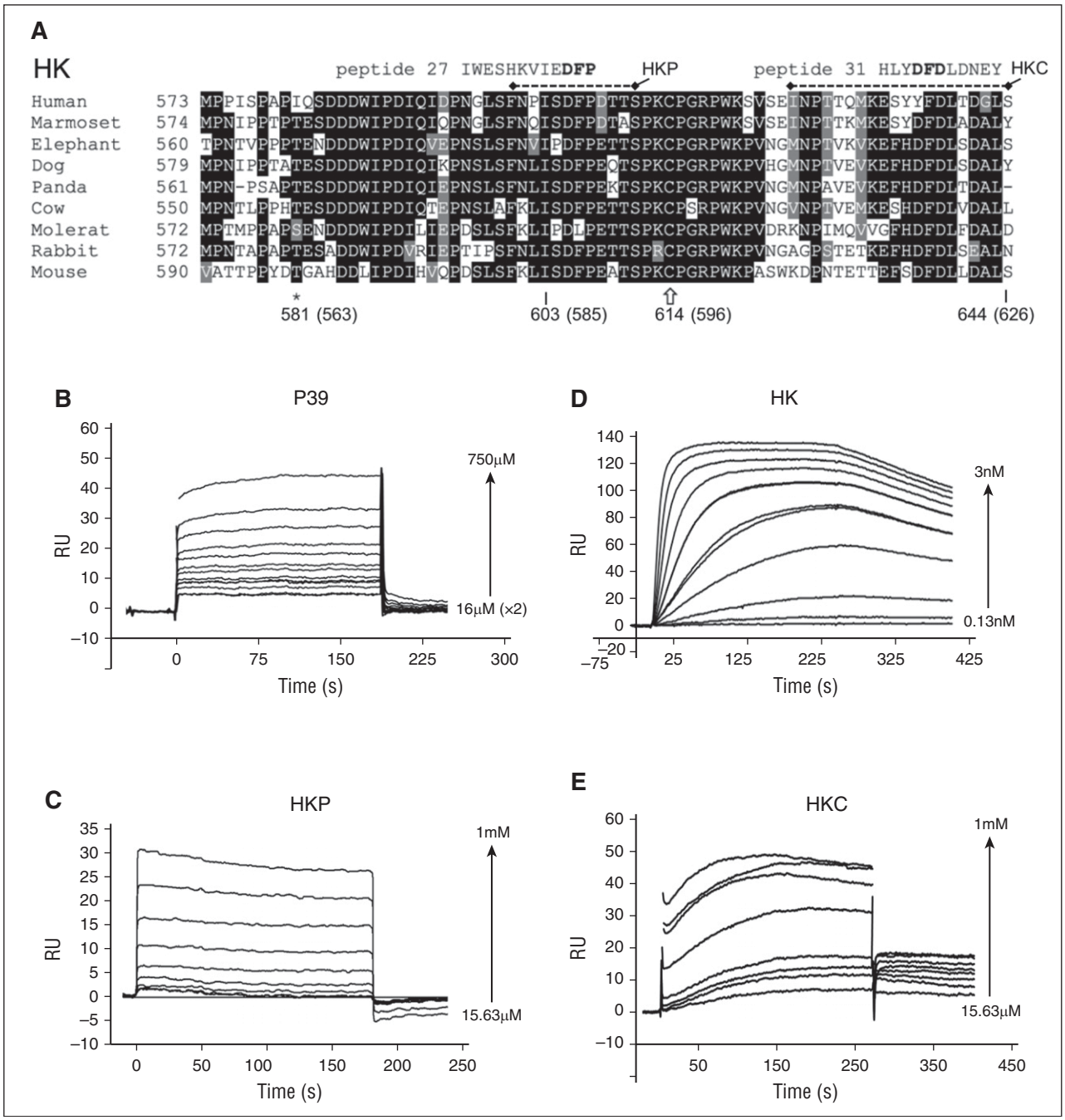

Figure 3. HK amino acid sequences and interaction with FXI. (A) The HK C-terminal domain 6 amino acid sequence alignment derived from the National Center for Biotechnology Information HOMOLOGENE server for different species is indicated. Conserved residues across >50% of the sequences are shaded black (highly conserved) or gray (weak conservation) with the program BOXSHADE. Peptides P27 and P31 from the random screen that match sequences within HK domain 6 are shown aligned. Dashed lines represent the sequence of synthetic peptides HKP and HKC. ★ indicates residue Ile563, which is the location of a venous thrombosis risk factor–associated human missense mutation Ile563Thr, located directly N-terminal to the HK ISDFP sequence. Plots of SPR sensorgrams measured in response units (RU) illustrate peptide P39 (B) and HKP (C) binding to immobilized FXI, and FXI binding to immobilized HK (D). (E) Binding of the HKC peptide to immobilized FXI.

forms an equivalent packing interaction to the tyrosine side chain from P39, contacting the FXI apple 2 domain minor pocket (Figure 2E).

Figure 2F illustrates a superposition of the FXI-P39 and FXI-HKP structures, revealing differences between IxDFP and YxDFP, whereby the DFP Phe contact with the FXI apple 2 domain major pocket is identical; however, there is some flexibility in the positioning of the N-terminal amino acids contacting the minor pocket. The P39 peptide tyrosine main-chain backbone amide forms a hydrogen bond to the main-chain carbonyl of FXI Asn140, which does not occur in the HKP complex. In contrast, both the native FXI structure and the HKP complex have a water molecule bound to the side chain of Asn140. In the HKP complex, this water molecule is also coordinated by the DFP aspartate side chain, whereas in the laminin and P39 complex structure, there is no bound water present and the DFP aspartate side chain is slightly reoriented, forming an interaction with the Asn106 side chain.

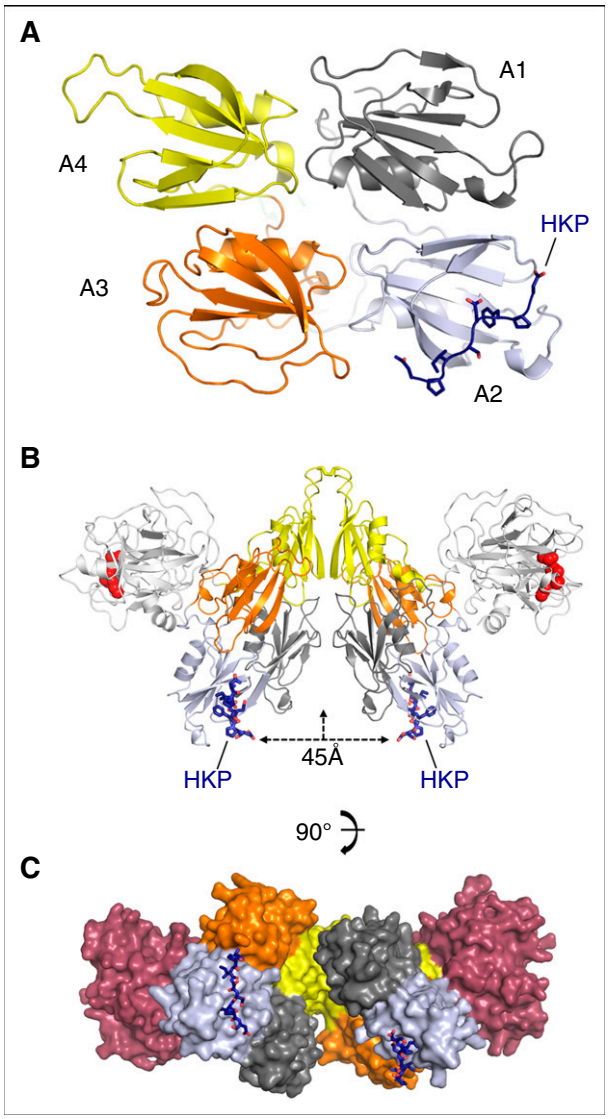

Figure 4. FXI dimer colocalization of bound HK peptides. (A) Cartoon diagram of the apple domain saucer section shown in gray, blue, orange, and yellow for the A1, A2, A3, and A4 domains, respectively. The HK peptide is colored in dark blue and shown as sticks. (B) The FXI dimer bound to the HK peptide (blue sticks) is shown with the protease domain (white) and active-site residues (red spheres) for His413, Asp462, and Ser557. The distance between the HK peptides is indicated as 45 Å, and the vertical arrow shows the dimer axis. (C) Surface representation of the FXI dimer, with each subunit colored the same as in panel A, except the protease domain is red.

Biological significance of the FXI-HKP complex structure

The FXI-HKP structure is supported by previous data: biochemical characterization of the interaction between FXI and HK has localized binding to the C-terminal portion of the HK domain 6, spanning at least 58 amino acids (HK residues 556-613) and containing the HKP sequence.[25] An alignment of the HK C-terminal region of domain 6 sequences across several species shows that the ISDFP sequence in HKP is well conserved (Figure 3A). Amino acid substitutions in the region surrounding ISDFP show similarities to the conserved features identified in the random peptide screen. In common with the FXI binding peptide sequences from the random screen, (1) the aspartate from the HKP DFP is absolutely conserved, (2) a proline residue is present directly N-terminal to the DFP in elephant and mole rat sequences, (3) a lysine residue is present 4 amino acids N-terminal to the DFP in cow, mole rat, and mouse, and (4) the mole rat IPDLP sequence is similar to the screen peptide 7, which has sequence FPDLP (supplemental Figure 1). One significant difference with the random peptide screen is that the HK sequences have a conserved isoleucine residue occurring 2 amino acids N-terminal to the DFP that is not substituted to F/Y/W/H in any species.

Previously, it had been shown that monoclonal antibodies against the FXI apple 2 domain can inhibit the FXI-HK interaction, with binding constants in the low nanomolar range.[26,27] To examine the interaction of FXI with HK and peptide P39, we developed an SPR assay (see "Methods"). Using this assay, the P39 peptide and the HKP peptide bound to immobilized FXI with a K_D of 320 μM and 324 μM, respectively, which is similar to the 150 μM value previously reported for a 13-mer peptide[25] from the HK sequence (Figure 3B-C). The binding of FXI to full-length HK resulted in a K_D of ~0.3 nM, which differs significantly from the published value of 69 nM that was measured for the isolated HK light-chain fragment in a solution-based assay.[25] Furthermore, using the same SPR assay, the homologous protein PK binding to HK resulted in a K_D of 18 nM (data not shown), which is in excellent agreement with the published value of 12 nM measuring the PK interaction with the HK light-chain fragment.[25]

Because previous data have described that at least 58 amino acids from the HK domain 6 contribute to FXI binding,[25] we examined these amino acid stretches for further matches with the FXI binding peptides. This revealed a sequence similarity with the DFD FXI binding peptides in the far C-terminal region of HK (Figure 3A shows the peptide P31 sequence aligned). To test whether this sequence binds FXI, we synthesized a peptide spanning the C-terminal residues 607 to 626 of HK (HKC) and, in an SPR experiment, recorded specific binding with a measured K_D of 90 μM.

The FXI "saucer sections" organize DFP peptides onto the same surface

The structure of the HKP peptide bound to the apple 2 domain in the FXI saucer section is shown in Figure 4A. Two FXI monomers assemble into a disulfide-linked dimer through the apple 4 domain; Figure 4B shows that the 2 HKP peptides are organized onto an opposing surface in relation to the protease domain. The peptides are facing the dimer axis in an arrangement that effectively localizes the apple 2 domain binding pockets in the same plane 45 Å apart (Figure 4B). The apple 4 domain dimer interface is offset by an angle of 90° such that the orientation of the 2 bound HK peptides is approximately at right angles (Figure 4C; supplemental Video). This arrangement raises the question as to whether, in the biological complex, 2 HK polypeptides bind FXI using both apple 2 domains.

Early studies isolated the tightly bound FXI-HK complex from plasma, describing a complex of 380 kDa characterized by gel filtration.[9] The disulfide-linked dimeric nature of FXI is well established biochemically and structurally,[5] and on gel filtration, it elutes at ~200 kDa, which is the same molecular weight described by nonreducing sodium dodecyl sulfate (SDS)–polyacrylamide gel electrophoresis (PAGE). HK, by comparison, has been previously reported as both a disulfide-linked circular monomer[28] and dimer.[29,30] We repeated these gel filtration experiments to examine the stoichiometry of binding for the FXI-HK complex using a calibrated Superdex 200 column. This revealed that FXI elutes close to the expected molecular weight of the disulfide-linked dimer at ~200 kDa (supplemental Figure 3). Gel filtration of FXI-HK mixtures with a varying ratio revealed a peak for a complex obtained with a molecular weight of ~400 kDa, consistent with previously published results.[9] SDS-PAGE of samples collected from the resulting gel filtration fractions of the FXI-HK complex revealed that both components were

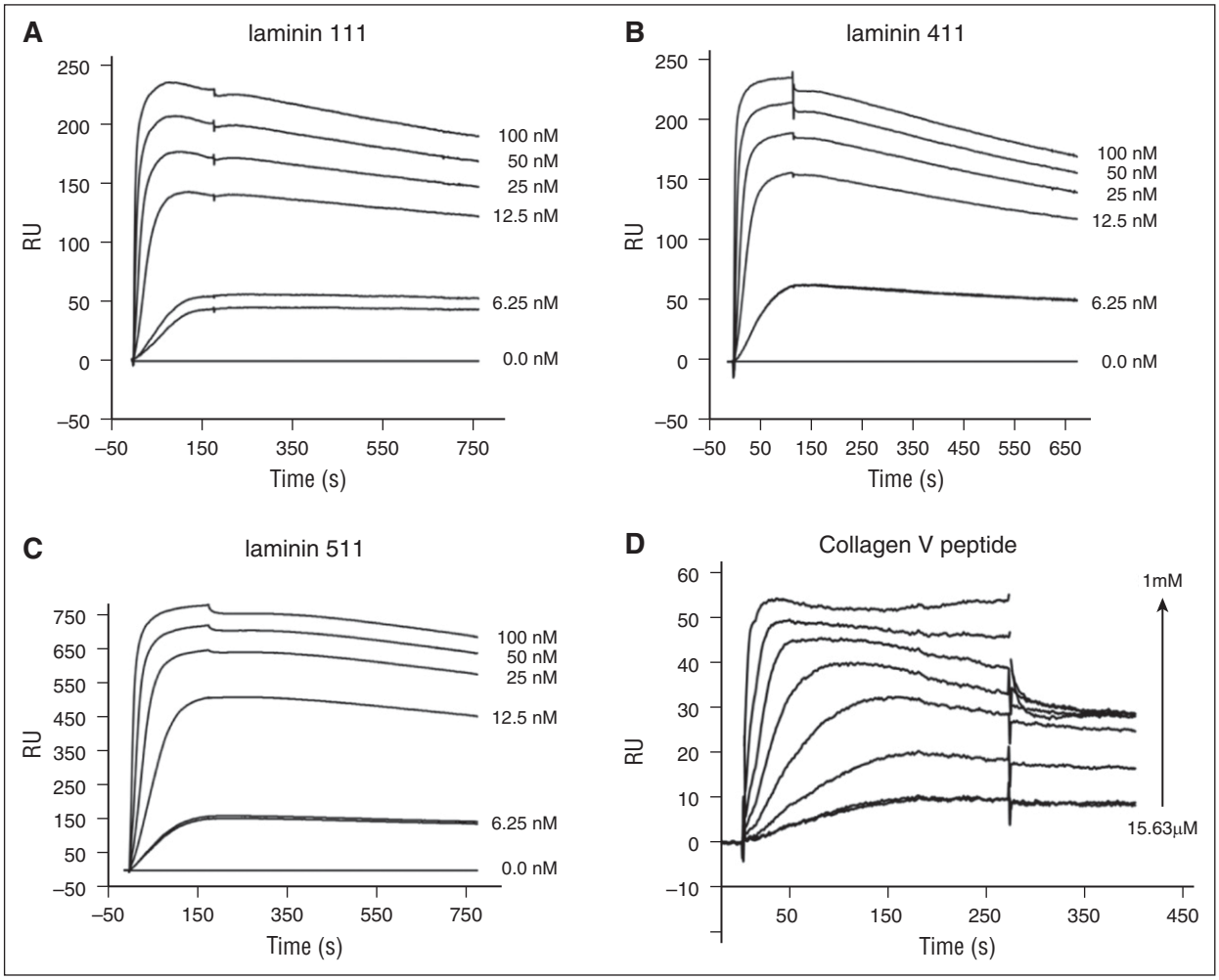

Figure 5. FXI binding to laminin and a collagen V peptide. Plots of SPR sensorgrams measured in response units (RU) illustrating FXI binding to laminin 111 (A), laminin 411 (B), or laminin 511 (C) immobilized on a CM5 sensor chip. (D) DFP peptide derived from the collagen V sequence binding to immobilized FXI.

present, and nonreducing SDS-PAGE gels revealed FXI and HK migrating at the same molecular weight of ~200 kDa (supplemental Figure 3). To quantitate FXI and HK in these experiments, a gel filtration experiment with a 1:1 molar ratio of FXI and HK was performed, and samples of the resulting single peak were analyzed by Edman degradation, confirming the equimolar presence of FXI and HK polypeptides in the 2:2 FXI-HK 400-kDa complex (supplemental Table 4). The lower plasma concentration of FXI dimer (0.031 μM) compared with HK (0.6363 μM) means that the 2:2 complex will be favored, and the structural data suggest that the 2 domains of HK domain 6 will be aligned in close proximity (Figure 4C).

FXI binding to laminin and a collagen V–derived DFP peptide

Laminins are large heterotrimeric proteins with α, β, and γ subunits and form a critical component of the basement membrane.[31] Laminin 111 is important in development and occurs in the brain, whereas laminin 411 and 511 are abundant in the extracellular matrix of blood vessels and arteries.[31] FXI has not been previously shown to bind proteins from the extracellular matrix; however, our observation that the FPDFP and YPDFP motifs are present in laminin prompted us to evaluate the binding of FXI to human laminin heterotrimers 111, 411, and 511 using SPR. These experiments demonstrated that FXI bound in a concentration-dependent manner to laminin 111, 411, and 511 with K_D values of 11.1 nM, 9.2 nM, and 8.3 nM, respectively (plots shown in Figure 5; all K_D values were determined using a Hill plot and averaged from triplicated experiments). We also found that laminin 111 purified from a native basement membrane (Engelbreth-Holm-Swarm murine sarcoma basement membrane; Sigma) bound FXI in a similar fashion to the recombinant laminins, with a K_D of 18.8 nM (data not shown).

The HPDFP motif occurs in the C-terminal noncollagenous (NC) domains of collagen V and XI α1 chains (termed α1(V)) and does not occur in the fibrillar regions. To test whether a peptide derived from the α1(V) chain could bind FXI, we synthesized a peptide of sequence KDLQLCHPDFPDGE; SPR measurements revealed that this bound with a K_D of 78 μM (Figure 5D).

Discussion

FXI contains 4 apple domains, which are members of the plasminogen, apple, and nematode family of protein folds found in the coagulation factors plasminogen, FXI, and PK, as well as in parasite cell binding proteins and hepatocyte growth factor.[32] One of the fundamental and unanswered questions is how these apple domains recognize ligands.[32] Here, we report that FXI binds peptides containing the DFP motif, with a preference for I/Y/F/W/HxDFP pentapeptides. Three complex crystal

structures describe examples of I/Y/FxDFP peptides bound to the FXI apple 2 domain that utilize a major pocket in the center of the β sheet to bind the DFP; a minor pocket is occupied by the I/Y/F amino acid side chain. A second distinct group of FXI binding peptides were identified that contained the DFD motif, and these were found to have similarity to the C-terminal region of HK.

The data are biologically significant, in that an ISDFP pentapeptide occurs in the amino acid sequence of domain 6 from HK, which is a known cofactor of FXI. HK acts as a cofactor for FXI zymogen activation by FXIIa[33,34] cleavage, and functional assays have shown that peptides derived from the HK domain 6 sequence inhibit kaolin-stimulated coagulation reactions.[25] Monoclonal antibodies that bind to the FXI apple 2 domain have been shown to inhibit HK binding in vitro, as well as thrombus formation in vivo in animal models of cardiovascular disease.[27] In addition to studies in animals, global genetic linkage analysis of mutations in humans has identified a common HK variant located in domain 6 that is linked to greater susceptibility to deep vein thrombosis and changes in coagulation.[35] This missense mutation Ile563Thr is located directly N-terminal to the HK ISDFP sequence (highlighted in Figure 3A as a star). Directly C-terminal to the HK ISDFP sequence is the Cys596 residue, which is implicated in forming a disulfide bond with Cys10 from the HK N-terminus, although the complete disulfide bonding has been reported previously only for splice variant low-molecular-weight kininogen,[36] and not for HK. The overall 3-dimensional structure of the HK domain 6 is unknown, and there are no homologous proteins in the database to allow molecular modeling.

We identified the HPDFP sequence in the C-terminal NC domain of collagen V. This sequence occurs in the α1(V) chain, and collagen V is normally present within the interiors of collagen fibers as $\alpha1(V)_2\alpha2(V)$ heterotrimers. Upon secretion, the collagen V C-terminal NC domains are cleaved off and secreted into the extracellular space.[37] Excessive amounts of α1(V) chains have been shown to be deposited in atherosclerotic lesions, although it is unknown whether the C-terminal NC domains are also deposited.[38,39]

FPDFP and YRDFP pentapeptide sequences occur within the extracellular matrix protein laminin, and we demonstrated binding of FXI to native and recombinant laminin heterotrimers. There is increasing evidence of the importance of laminins in plasma coagulation and thrombus formation, and the interaction between platelet integrins and laminins has been well characterized.[40,41] Efficient coagulation factor cleavage reactions typically take place only on a designated surface, and vitamin K–dependent coagulation factors have an N-terminal Gla domain that is capable of binding directly to negatively charged phospholipids present in activated platelets to fulfill this purpose. Laminin has been previously shown to provide a surface that can promote plasma coagulation and thrombus formation in the absence of platelets.[42] HK and coagulation FXII (which activates FXI) have both previously been reported to bind laminin.[43,44] It is notable that the substrate of FXIa is FIX which binds the basement membrane through a well-characterized interaction with collagen IV,[45] and the interaction we observe for FXI with laminin may be important for colocalization of coagulation factors from the intrinsic pathway to sites in the extracellular matrix.

Acknowledgments

The authors thank Diamond Light Source for access to beamline I04 (proposal number 10369). The authors thank Helen Phillipou (University of Leeds) for assistance with SPR data collection, Lars Thim (Novo Nordisk) for N-terminal sequencing, and Hanne Grøn (Novo Nordisk) for critical reading of the manuscript.

This work was supported by an industrial PhD studentship from the Danish Agency for Science Technology and Innovation (S.S.W.) and the British Heart Foundation Programme grant RG/12/9/29775 (J.E.).

Authorship

Contribution: S.S.W. and G.H. crystallized and determined the structures of FXI-P39, FXI-LP2, and FXI-HKP; S.Ø. performed the peptide screening experiments; S.S.W., C.L., and P.M.W. performed and analyzed the SPR experiments; and J.E. and H.S. initiated and designed the research, analyzed the results, and wrote the paper.

Conflict-of-interest disclosure: S.Ø. and H.S. are Novo Nordisk employees. The remaining authors declare no competing financial interests.

Correspondence: Jonas Emsley, Centre for Biomolecular Sciences, School of Pharmacy, University of Nottingham, Nottingham NG72RD, United Kingdom; e-mail: jonas.emsley@nottingham.ac.uk.

References

1. Gailani D, Bane CE, Gruber A. Factor XI and contact activation as targets for antithrombotic therapy. *J Thromb Haemost.* 2015;13(8):1383-1395.
2. Bouma BN, Griffin JH. Human blood coagulation factor XI. Purification, properties, and mechanism of activation by activated factor XII. *J Biol Chem.* 1977;252(18):6432-6437.
3. Fujikawa K, Chung DW, Hendrickson LE, Davie EW. Amino acid sequence of human factor XI, a blood coagulation factor with four tandem repeats that are highly homologous with plasma prekallikrein. *Biochemistry.* 1986;25(9):2417-2424.
4. McMullen BA, Fujikawa K, Davie EW. Location of the disulfide bonds in human coagulation factor XI: the presence of tandem apple domains. *Biochemistry.* 1991;30(8):2056-2060.
5. Papagrigoriou E, McEwan PA, Walsh PN, Emsley J. Crystal structure of the factor XI zymogen reveals a pathway for transactivation. *Nat Struct Mol Biol.* 2006;13(6):557-558.
6. Sun Y, Gailani D. Identification of a factor IX binding site on the third apple domain of activated factor XI. *J Biol Chem.* 1996;271(46):29023-29028.
7. Baglia FA, Walsh PN. A binding site for thrombin in the apple 1 domain of factor XI. *J Biol Chem.* 1996;271(7):3652-3658.
8. Baglia FA, Shrimpton CN, Emsley J, et al. Factor XI interacts with the leucine-rich repeats of glycoprotein Ibalpha on the activated platelet. *J Biol Chem.* 2004;279(47):49323-49329.
9. Thompson RE, Mandle R Jr, Kaplan AP. Association of factor XI and high molecular weight kininogen in human plasma. *J Clin Invest.* 1977;60(6):1376-1380.
10. Emsley J, McEwan PA, Gailani D. Structure and function of factor XI. *Blood.* 2010;115(13):2569-2577.
11. Mandle RJ, Colman RW, Kaplan AP. Identification of prekallikrein and high-molecular-weight kininogen as a complex in human plasma. *Proc Natl Acad Sci USA.* 1976;73(11):4179-4183.
12. Puy C, Tucker EI, Matafonov A, et al. Activated factor XI increases the procoagulant activity of the extrinsic pathway by inactivating tissue factor pathway inhibitor. *Blood.* 2015;125(9):1488-1496.
13. Wang X, Cheng Q, Xu L, et al. Effects of factor IX or factor XI deficiency on ferric chloride-induced carotid artery occlusion in mice. *J Thromb Haemost.* 2005;3(4):695-702.
14. Langhauser F, Göb E, Kraft P, et al. Kininogen deficiency protects from ischemic neurodegeneration in mice by reducing thrombosis, blood-brain barrier damage, and inflammation. *Blood.* 2012;120(19):4082-4092.
15. Lam KS, Salmon SE, Hersh EM, Hruby VJ, Kazmierski WM, Knapp RJ. A new type of synthetic peptide library for identifying ligand-binding activity. *Nature.* 1991;354(6348):82-84.
16. Østergaard S., inventor; Novo Nordisk, assignee. Factor XI-binding proteins. World Intellectual

Property Organization patent WO 00826, January 26, 2006.

17. Bailey TL, Boden M, Buske FA, et al. MEME SUITE: tools for motif discovery and searching. *Nucleic Acids Res.* 2009;37(Suppl 2):W202-208.
18. de Castro E, Sigrist CJ, Gattiker A, et al. ScanProsite: detection of PROSITE signature matches and ProRule-associated functional and structural residues in proteins. *Nucleic Acids Res.* 2006;34(Suppl 2):W362-365.
19. Jensen S., inventor; Novo Nordisk, assignee. Pharmaceutical formulation of factor XI. World Intellectual Property Organization patent WO 128467. June 1, 2006.
20. Kabsch W. XDS. *Acta Crystallogr D Biol Crystallogr.* 2010;66(Pt 2):125-132.
21. Winn MD, Ballard CC, Cowtan KD, et al. Overview of the CCP4 suite and current developments. *Acta Crystallogr D Biol Crystallogr.* 2011;67(Pt 4): 235-242.
22. McCoy AJ, Grosse-Kunstleve RW, Adams PD, Winn MD, Storoni LC, Read RJ. Phaser crystallographic software. *J Appl Cryst.* 2007; 40(Pt 4):658-674.
23. Emsley P, Lohkamp B, Scott WG, Cowtan K. Features and development of Coot. *Acta Crystallogr D Biol Crystallogr.* 2010;66(Pt 4): 486-501.
24. Laskowski RA, Swindells MB. LigPlot+: multiple ligand-protein interaction diagrams for drug discovery. *J Chem Inf Model.* 2011;51(10): 2778-2786.
25. Tait JF, Fujikawa K. Primary structure requirements for the binding of human high molecular weight kininogen to plasma prekallikrein and factor XI. *J Biol Chem.* 1987;262(24):11651-11656.
26. Renné T, Gailani D, Meijers JC, Müller-Esterl W. Characterization of the H-kininogen-binding site on factor XI: a comparison of factor XI and plasma prekallikrein. *J Biol Chem.* 2002;277(7): 4892-4899.
27. Cheng Q, Tucker EI, Pine MS, et al. A role for factor XIIa-mediated factor XI activation in thrombus formation in vivo. *Blood.* 2010;116(19): 3981-3989.
28. Weisel JW, Nagaswami C, Woodhead JL, DeLa Cadena RA, Page JD, Colman RW. The shape of high molecular weight kininogen. Organization into structural domains, changes with activation, and interactions with prekallikrein, as determined by electron microscopy. *J Biol Chem.* 1994; 269(13):10100-10106.
29. Higashiyama S, Ohkubo I, Ishiguro H, Kunimatsu M, Sawaki K, Sasaki M. Human high molecular weight kininogen as a thiol proteinase inhibitor: presence of the entire inhibition capacity in the native form of heavy chain. *Biochemistry.* 1986; 25(7):1669-1675.
30. Baba SP, Zehra S, Bano B. Purification and characterization of kininogens from sheep plasma. *Protein J.* 2005;24(2):95-102.
31. Hallmann R, Horn N, Selg M, Wendler O, Pausch F, Sorokin LM. Expression and function of laminins in the embryonic and mature vasculature. *Physiol Rev.* 2005;85(3):979-1000.
32. Tordai H, Bányai L, Patthy L. The PAN module: the N-terminal domains of plasminogen and hepatocyte growth factor are homologous with the apple domains of the prekallikrein family and with a novel domain found in numerous nematode proteins. *FEBS Lett.* 1999;461(1-2):63-67.
33. Wiggins RC, Bouma BN, Cochrane CG, Griffin JH. Role of high-molecular-weight kininogen in surface-binding and activation of coagulation Factor XI and prekallikrein. *Proc Natl Acad Sci USA.* 1977;74(10):4636-4640.
34. Matafonov A, Leung PY, Gailani AE, et al. Factor XII inhibition reduces thrombus formation in a primate thrombosis model. *Blood.* 2014;123(11): 1739-1746.
35. Morange PE, Oudot-Mellakh T, Cohen W, et al. KNG1 Ile581Thr and susceptibility to venous thrombosis. *Blood.* 2011;117(13):3692-3694.
36. Kellermann J, Thelen C, Lottspeich F, Henschen A, Vogel R, Müller-Esterl W. Arrangement of the disulphide bridges in human low-Mr kininogen. *Biochem J.* 1987;247(1):15-21.
37. Unsöld C, Pappano WN, Imamura Y, Steiglitz BM, Greenspan DS. Biosynthetic processing of the pro-alpha 1(V)2pro-alpha 2(V) collagen heterotrimer by bone morphogenetic protein-1 and furin-like proprotein convertases. *J Biol Chem.* 2002;277(7):5596-5602.
38. Ooshima A. Collagen alpha B chain: increased proportion in human atherosclerosis. *Science.* 1981;213(4508):666-668.
39. Katsuda S, Okada Y, Minamoto T, Oda Y, Matsui Y, Nakanishi I. Collagens in human atherosclerosis. Immunohistochemical analysis using collagen type-specific antibodies. *Arterioscler Thromb.* 1992;12(4):494-502.
40. Inoue O, Suzuki-Inoue K, McCarty OJ, et al. Laminin stimulates spreading of platelets through integrin alpha6beta1-dependent activation of GPVI. *Blood.* 2006;107(4):1405-1412.
41. Schaff M, Tang C, Maurer E, et al. Integrin $\alpha 6\beta 1$ is the main receptor for vascular laminins and plays a role in platelet adhesion, activation, and arterial thrombosis. *Circulation.* 2013;128(5): 541-552.
42. White-Adams TC, Berny MA, Patel IA, et al. Laminin promotes coagulation and thrombus formation in a factor XII-dependent manner. *J Thromb Haemost.* 2010;8(6):1295-1301.
43. Schousboe I. Endothelial cells express a matrix protein which binds activated factor XII in a zinc-independent manner. *Thromb Haemost.* 2006; 95(2):312-319.
44. Schousboe I, Nystrøm B. High molecular weight kininogen binds to laminin–characterization and kinetic analysis. *FEBS J.* 2009;276(18): 5228-5238.
45. Wolberg AS, Stafford DW, Erie DA. Human factor IX binds to specific sites on the collagenous domain of collagen IV. *J Biol Chem.* 1997; 272(27):16717-16720.

2016 127: 2915-2923
doi:10.1182/blood-2015-10-676122 originally published online March 22, 2016

A novel DFP tripeptide motif interacts with the coagulation factor XI apple 2 domain

Szu S. Wong, Søren Østergaard, Gareth Hall, Chan Li, Philip M. Williams, Henning Stennicke and Jonas Emsley

Blood (print ISSN 0006-4971, online ISSN 1528-0020), is published weekly by the American Society of Hematology, 2021 L St, NW, Suite 900, Washington DC 20036.

DIA DEVELOP INNOVATE ADVANCE

Therapeutic Innovation & Regulatory Science
2016, Vol. 50(4) 427-435

DOI: 10.1177/2168479016628301
tirs.sagepub.com

Consumer Opinions on Existing and Proposed Australian Over-the-Counter Medicine Labeling Strategies in Comparison With the Standardized US Drug Facts Label

Vivien Tong, BPharm(Hons), GradCertPharmPrac[1], David K. Raynor, BPharm, PhD[2], Kim K. Hamrosi, BPharm(Hons), PhD[1], Basoori Acharya, MPharm[3], Nisha Panchal, MPharm[3], and Parisa Aslani, BPharm(Hons), MSc, PhD, G Cert Ed Stud (Higher Ed)[1]

Abstract

Background: With common over-the-counter (OTC) medication use, OTC labels as medicine information sources must be of high quality and usability. Standardized OTC labeling has been proposed in Australia using the Medicine Information Box (MIB), modeled on the US Drug Facts label. However, limited research has explored consumer opinions on existing nonstandardized Australian OTC, US Drug Facts, and proposed MIB labels. Therefore, this study aimed to explore consumer opinions on all 3 groups of OTC labels. *Methods:* Three focus groups (N = 21 participants) were conducted in Sydney, Australia. Participants were shown existing Australian OTC labels, US Drug Facts labels, and mock MIB formats based on the Australian Therapeutic Goods Administration proposal. Discussions were audio recorded, transcribed verbatim, and thematically analyzed. *Results:* Participants expressed varying opinions regarding existing nonstandardized Australian OTC labels' content and design, from acknowledgment of positive aspects (clear headings, relevant content) to decreased perceived readability (suboptimal color use, font size) and content discrepancies. Participants identified key Drug Facts and MIB label characteristics that contributed to perceived usability and format clarity (good headings, black-and-white format). Many preferred the Drug Facts label because of its greater perceived clarity and usability. Missing content (inactive ingredients, further contact details) were identified and consequently became opportunities for MIB improvement. *Conclusions:* Most participants seemed to prefer the US Drug Facts label, partly because of its perceived completeness. These findings suggest further improvements for the proposed MIB as a step toward Australian OTC label standardization.

Keywords

drug labeling; consumers; nonprescription medicines; focus groups; consumer perspectives

Introduction

Consumer use of over-the-counter (OTC) medicines is common,[1] and the availability and provision of relevant, high-quality OTC medicine information is therefore necessary to assist consumers with safe medication use. Consumers want information on the effectiveness of the medicine, dosing, potential side effects, and possible drug interactions prior to taking an OTC medicine[2] and will read OTC labels to obtain such information.[3] As consumers recall only a proportion of spoken information provided by pharmacists,[4] written medicine information sources are critical.

Design and comprehensibility of written OTC medicine information contribute to their quality.[5] Consequently, efforts to improve the usability of OTC labels and leaflets are imperative in supporting medication safety. For example, standardization of OTC labeling in the United States (US) using the Drug Facts label format[6] was implemented to ensure format

[1] Faculty of Pharmacy, The University of Sydney, Sydney, Australia
[2] School of Healthcare, University of Leeds, Leeds, United Kingdom
[3] School of Pharmacy, The University of Nottingham, Nottingham, United Kingdom

Submitted 07-Dec-2015; accepted 30-Dec-2015

Corresponding Author:
Vivien Tong, BPharm(Hons), GradCertPharmPrac, Pharmacy and Bank Building (A15), The University of Sydney, Sydney, New South Wales 2006, Australia.
Email: vivien.tong@sydney.edu.au

consistency and increase usability. Consumers who utilized the Drug Facts label gave statistically significantly more correct responses on the whole, in relation to the appropriate action required to be taken in four different scenarios relevant to warnings information, than when using the older label format.[7] Furthermore, consumer preference ratings for the Drug Facts label for a pain reliever were statistically significantly higher than for the corresponding older label format.[7] Other studies have also noted an improved time taken to find information when using the Drug Facts label compared to older label formats.[8,9]

In contrast to the United States, OTC labels are not standardized in Australia.[10] Despite this, standardization of written medicine information in Australia is not unknown, as leaflets known as Consumer Medicine Information are available in a standardized format and are mandatory for both prescription and pharmacist only OTC medicines.[11]

In Australia, existing legislation[12] provides a comprehensive outline of the label content required.[13] However, with labeling, consumers face a number of potential problems such as impaired label readability (because of factors such as small font size and amount of content), difficulty in understanding and acting upon relevant medicine information, in addition to relating the information back to their own personal needs.[14] A 2012 consultation paper published by the Australian Therapeutic Goods Administration (TGA) implied the need to improve OTC labeling, proposing the introduction of a standardized OTC label format titled the Medicine Information Box (MIB), modeled on the US Drug Facts label format.[15]

Limited research has explored consumer opinions on the MIB in Australia. Furthermore, opinions on existing labeling standardization, namely, the US Drug Facts label, have not been explored in a consumer population such as Australia, where regulatory activities indicate that OTC label standardization may be implemented in the near future. As the MIB is based on the Drug Facts label format,[15] it is prudent to explore consumer opinions on both formats for comparison prior to the implementation of standardization. Therefore, the study aim was to explore consumers' opinions on existing Australian nonstandardized OTC labels, the US Drug Facts label, and the MIB.

Methods

This study formed part of a larger international research project exploring consumer OTC medicine information needs and use, and perspectives on OTC medicine information. The study received ethics approval from the University of Sydney Human Research Ethics Committee (project number 2013/1013). Participants provided written informed consent to participate in this study.

Participants and Setting

Three focus groups lasting approximately 1 to 1.5 hours were conducted in Sydney, Australia, in February 2014 with a total of 21 participants (Table 1). Focus groups were utilized to address the study aim, and complement a series of earlier semi-structured interviews that explored consumer perspectives on the MIB specifically.[16] The group dynamic inherent in focus groups was intended to encourage discussion about, and comparison between, all 3 label types.

Table 1. Summary of Focus Group Participant Demographics.

Demographic	Three Focus Groups (N = 21)
Gender	
Male	10
Female	11
Age, y	
18-29	7
30-49	7
50-69	6
≥70	1
Highest level of education	
School Certificate or below	1
Higher School Certificate/college qualification	15
Bachelor's degree or above	5
Main language spoken at home	
English	17
Other	4
Country of birth	
Australia	11
Overseas	10

Each focus group was conducted by 2 experienced female focus group facilitators (P.A., K.K.H.), with field notes taken by 2 researchers (N.P., B.A.). People were eligible to participate if they were aged 18 years and older, conversant in English (did not require a translator to participate in the study), and had purchased an OTC medicine in the 6 months prior to the study for personal use or for an individual under their care. All participants were identified from the consumer database of a market research company using the inclusion criteria specified. Potential participants were contacted and provided with an information sheet and consent form, and if willing to participate, were assigned to attend one of the scheduled focus groups held at various venues in Sydney. Participants were reimbursed AU$80 for their time.

Focus Group Protocol

The focus group protocol was developed to address the broader research project aims, and included specific questions regarding consumers' OTC medicine information needs, utilization of OTC medicine information, and perspectives on existing and proposed OTC labeling strategies (Australia and United States). Only findings pertaining to the study aim described here will be presented.

During the focus groups, participants were shown 3 broad groups of stimulus materials in the following order:

Table 2. Products Shown to Consumers as Stimulus Material During the Focus Groups.

Proprietary Product Label Type	Product
Existing Australian OTC product labels	• Nurofen for Children 1-5 years oral suspension (ibuprofen) • Panadol Children 5-12 years oral suspension (acetaminophen) • Bisolvon Dry oral liquid (dextromethorphan) • Children's Panadol 6 months–5 years suppositories (acetaminophen) • Earclear Earache Relief ear drops (phenazone, benzocaine) • Codral 4 Flu tablets (acetaminophen, codeine, phenylephrine, chlorpheniramine) • Gastro-Stop capsules (loperamide) • Panamax tablets (acetaminophen) • Daktarin Cream for Athlete's Foot (miconazole)
Existing US Drug Facts labels	• Up&Up naproxen sodium tablets, 220 mg (naproxen) • Advil caplets (ibuprofen) • Up&Up acetaminophen extra strength caplets, 500 mg (acetaminophen) • Natureplex Maximum Strength Hydrocortisone Cream (hydrocortisone) • Up&Up Acid Reducer Original Strength tablets (famotidine) • Children's Quick-dissolving Wal-Tussin Cough Relief tablets (dextromethorphan) • Benadryl Extra Strength Itch Stopping Cream (diphenhydramine, zinc acetate) • Up&Up Gas Relief Extra Strength chewable tablets (simethicone) • Well at Walgreens Sterile Lubricant Eye Drops (carboxymethylcellulose) • Children's Mucinex Chest Congestion Mini-melts granules (guaifenesin) • Well at Walgreens Sterile Original Prescription Strength Eye Itch Relief eye drops (ketotifen)

1. 1 product per participant from a random selection of existing Australian OTC product labels (Table 2);
2. 1 product per participant from a random selection of US OTC product labels that displayed the Drug Facts label format (Table 2); and
3. 2 mock MIB labels for exemplar study medicines diclofenac and pholcodine (developed and published previously,[16] based on the TGA consultation paper[15]) (Figure 1).

Participants were asked to review the stimulus materials provided, and participant opinions on the different labels were sought. Table 3 provides the broad, core questions included in the semistructured focus group protocol, utilized by the facilitators to help stimulate discussions.

Labels on existing products were presented as they would be available at the point of purchase, with no changes in packaging or removal of leaflets (where available). They were randomly chosen and purchased from a pharmacy in Australia and the United States to represent a range of dosage forms, potential user demographics, and labeling characteristics/conditions (for instance, total packaging size). The US products allowed participants to visualize actual OTC label standardization and its impact on overall OTC packaging.

Both MIB labels were given to the participants as paper copies, not contextualized as part of complete OTC product packaging.

Data Analysis

Thematic saturation[17] was achieved with the 3 focus groups conducted. All focus groups were audio recorded with permission from the participants and were transcribed verbatim. Transcript accuracy was verified by checking transcripts against the relevant original audio recording prior to analysis. Checked transcripts were analyzed via thematic content analysis.[18] Three researchers (V.T., B.A., and N.P.) independently analyzed the data, and themes were verified in consultation with another researcher (P.A.). Preliminary data analysis was conducted by hand on the checked transcripts. Subthemes were determined from the data, and refined and conceptually grouped under identified broad themes. One researcher (V.T.) presented the data using a matrix display,[19] which was compared with the themes and subthemes identified by the other 2 researchers.

Results

Consumer Perspectives on Existing Australian OTC labels

Positive label characteristics

Some participants appreciated the clear headings and large font size of the writing on a proportion of existing Australian OTC labels examined. The simple wording and color used on the Nurofen label were perceived positively and were believed to increase readability (see Table 4, quote 1).

Barriers contributing to perceived information retrieval difficulty

Participants noted numerous label characteristics that contributed to information retrieval difficulties. A mixed portrait and landscape headings arrangement adopted by the Codral 4 Flu label was perceived to contribute to increased time needed to read the information, in comparison to the simpler Gastro-Stop label (2-column landscape format) (Table 4, quote 2).

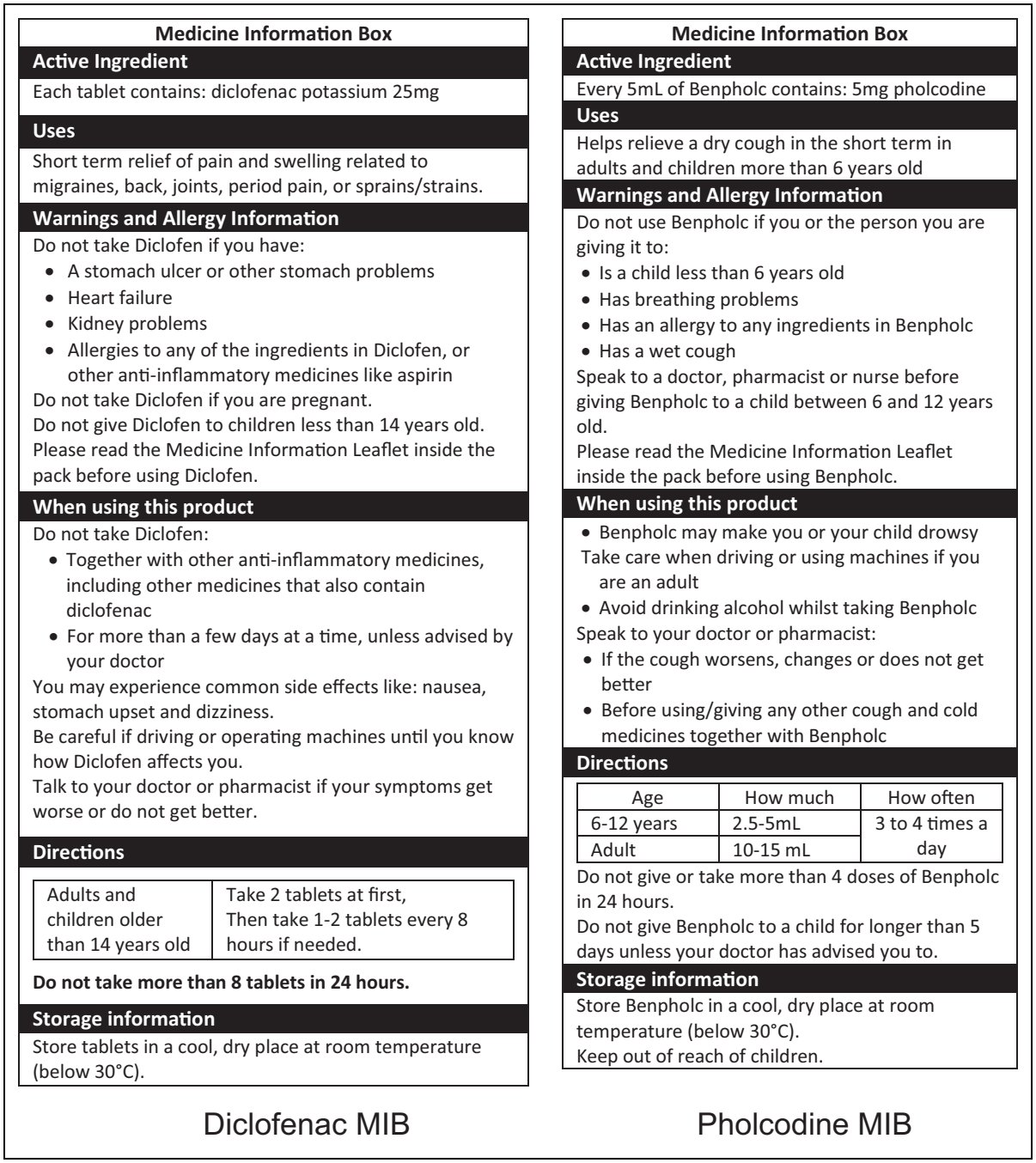

Figure 1. Mock Medicine Information Box (MIB) label formats shown to participants.
Source: Label formats reproduced from Tong et al.[16]

Small font size was an issue mentioned in every focus group. Decreased font size increased perceived consumer difficulty in reading information, but this appeared to be less if the participant thought they had good eyesight. Specifically, small font size proved problematic with the Panadol suppositories label (most label text printed in font 1 mm high), potentially contributing to self-selection errors as the dosage form was not immediately apparent (Table 4, quote 3).

Color had varying impact on readability, where the red-and-orange Nurofen label was seen as more difficult to read than a label that utilized higher contrasting colors (Table 4, quote 4). This was in contrast to an earlier comment made by participant FG2 F3 (Table 4, quote 1).

Label content: Perceptions and identified discrepancies

Overall, many thought existing Australian OTC labels included relevant key information relating to product use (such as

Table 3. Broad Questions Included in the Semistructured Focus Group Protocol.

Opinions on existing OTC medicine information	If we specifically looked at the product labels and WMI leaflets of nonprescription medicines, what are your thoughts about the quality and amount of information, as well as how easy it is to understand the information?
Suggestions for improvement of OTC medicine information	If you think about the currently available product labels and WMI leaflets for nonprescription medicines (examples provided as stimulus prompts), how do you think the format, layout, and content can be improved?
Perspectives on standardization of OTC medicine information	What are your thoughts about standardizing the WMI leaflets and product labels, so that the same type and level of information is provided with all medicines?
Perspectives on existing and proposed OTC labeling standardization strategies	What do you think about this label? (provide US OTC product label displaying Drug Facts label format, and then the 2 mock MIB labels, and state type of label appropriately)

OTC, over-the-counter; WMI, written medicine information.

directions and warnings), raised in every focus group. Despite this, the notion of content discrepancies was also discussed in every focus group, where some identified content discrepancies between different OTC products, and/or between the label and corresponding leaflet for a single product such as the Daktarin cream. For instance, contact details such as a website and/or telephone number were identified as missing from some labels. In particular, the potential safety implication for inconsistent inclusion of emergency contact information between the label and corresponding leaflet was implied by one participant (Table 4, quote 5). Another participant echoed this sentiment regarding the lack of pregnancy precaution included on the Daktarin label (Table 4, quote 6).

Suggestions for label design improvement

A few participants recommended increasing the font size to improve label design; placing small bottles in a larger box was one suggestion: ''maybe you could put it [the bottle of Panadol suppositories] in a box with big writing on it'' (FG2 F2). One participant preferred to have the active ingredient in larger font. Another recognized a potential to more effectively utilize the total packaging space to include more relevant content (such as contraindications) (Table 4, quote 7).

Consumer Perspectives on Existing and Proposed OTC Labeling Standardization Strategies

Participants from every focus group were positive toward OTC label standardization. Standardization of OTC labels (both Drug Facts label and MIB) was positively supported by most participants, with many having a more positive disposition toward the Drug Facts label in comparison to existing Australian OTC labels. Many appeared to prefer the Drug Facts label compared to the MIB, explicitly identifying that, first, it was more helpful because of reference to additional information sources such as websites and telephone numbers, allowing people to seek information beyond the label; and second, the use of additional, descriptive subheadings (corresponding to the action required to be taken) in the Drug Facts label, which helped divide the large ''Warnings'' section.

Conversely, some MIB aspects were appreciated and seen as favorable over the Drug Facts label, such as tabulated dosage and slightly clearer headings. A few did not indicate a preference, where both formats were seen as comparable regarding perceived ease of use.

Consumer perspectives on the Drug Facts label

Positive perspectives. Participants reported that the Drug Facts label had a good or clear layout, which was indicated in every focus group. It was seen as easy to navigate, and able to promote increased ease of OTC product selection. Effective subheadings helped break up larger sections such as the ''Warnings.'' A few thought that the Drug Facts label was ''perfect.'' The black-and-white format exhibited by most labels contributed to their clarity.

Participants found the inclusion of a telephone number or helpline helpful. The inclusion of both active and inactive ingredients was liked (Table 4, quote 8).

Inclusion of inactive ingredient information provided reassurance that manufacturers were not withholding information. The communication of active ingredient together with its purpose was seen to give meaning to the active ingredient.

Negative perspectives. There were very few negatives raised by participants regarding the Drug Facts label. One participant implied that there was insufficient information regarding drug interactions, where ''you would still have to jump on the Internet or ask the pharmacist to get that information'' (FG2 M2).

Consumer perspectives on the MIB

The MIB was appreciated for its bullet points, clear headings, ample white space, and plain English use.

Some liked the black-and-white format. A few participants noted that the headings stood out more clearly, compared to the Drug Facts label. Specifically, pholcodine dosage tabulation was liked (raised in each of the focus groups) and seen to help support accurate retrieval of pholcodine dosage information (Table 4, quote 9). However, a small number of consumers did not like the tabulated directions in the diclofenac MIB.

Table 4. Identified Themes/Subthemes and Relevant Illustrative Quotes.

Theme/Subtheme	Illustrative Quote
1. Consumer perspectives on existing Australian OTC labels	
Positive label characteristics	1. "Yeah really easy. . . . Like none of it [Nurofen label] is in like complicated language or anything- it's all really simple and easy visually to read because of the colors. And it's good." (FG2 F3)
Barriers contributing to perceived information retrieval difficulty	2. "They are both in a different order. Gastro-Stop is a lot easier to read and it just has the headings and tells you what's underneath them. As where Codral has, like, headings across the page and headings down the page and then, they divide the page in half. It's two sections; I'd have to keep looking around. It would take me a while to read the Codral 4 Flu [as] opposed to the Gastro-Stop." (FG1 F1)
	3. "It's very small writing. I mean my eyes are good and yeah it's [Panadol suppositories label] tiny writing, not easy to read. I mean I really would have picked this up by accident so. . . ." (FG2 F2)
	4. "You see for me that's different. That one [Nurofen label] for me is harder to read just because I have eye problems, whereas this one where it's clearly darker blue and the yellow—that's easier for me to read. Umm everyone is different but that's just me." (FG2 F4)
Label content- perceptions and identified discrepancies	5. "The thing I noticed is that this one on the box doesn't have anything about the poisons [centre] or what to call, but it has it in here [in the leaflet], so if someone goes and throws that out and it's not on the box and they can't use the Internet. . . ." (FG2 F2)
	6. "There's not much information on the [Daktarin] box as such so you really do need to take out the brochure and the brochure is really good because it has lots of clear subheadings . . . one of the sub headings is umm why not to use it and it's if you're pregnant. And I'm thinking why isn't it on the outside of the box? You wouldn't think athlete's foot cream would annoy a pregnancy but it obviously does and I think that's really important, that it's just not there." (FG3 F2)
Suggestions for label design improvement	7. "Umm yeah they, they could have done less of the blue and more you know "Don't use if" umm before I have to drag this [leaflet] out in the supermarket. It's not that easy to start reading pamphlets in the supermarket because you're always in a hurry to get home." (FG3 F2)
2. Consumer perspectives on existing and proposed OTC labeling standardization strategies	
Positive consumer perspectives on the Drug Facts label	8. "I like that it has the active ingredients as well as inactive ingredients. It has all the colorings and stuff like that so you can see if you're allergic to something." (FG2 F2)
Positive consumer perspectives on the MIB	9. "I like the line in the directions where you've got the, the children's ages and the mL's . . . there's definitely a line so it's quite easy to see and you're not going to mess up in the middle of the night when you're dealing with children's medication." (FG3 F2)

F, female; FG, focus group; MIB, Medicine Information Box; OTC, over-the-counter.

Participants identified areas for improvement, broadly regarding MIB content and title. Although content coverage was considered good, participants identified discrepancies between the Drug Facts label and MIB content. One participant felt that the MIB was not sufficiently informative. Absence of inactive ingredient information, manufacturer information (website and/or emergency contact information), and lack of active ingredient conveyed side by side with the "purpose" were identified as MIB shortcomings, which could then be inherently and/or directly linked in many cases to perceived necessary improvements.

One participant raised the issue that despite the warning to avoid use if allergic to any of the ingredients, the lack of inactive ingredient information in the MIB meant they could not satisfactorily discern if allergies were applicable.

Participants compared the 2 titles used for the standardized label formats and proposed possible variations to the title "Medicine Information Box." They preferred the term "medicine" over "drug." However, the Drug Facts title was favored by one participant, as " 'Drug Facts' is better because it sort of conveys the gravity of it a little bit more than 'medicine' " (FG2 F3).

Others suggested Medicine Facts as a potential title, regarded as "a good blend of seriousness but not using the word 'drugs'" (FG2 M2). In addition, one participant assumed that in Australia, "we preferentially used 'information' rather than 'facts' because it's less prescriptive and . . . there isn't as much weight behind information. Like not saying that it's a fact; you're just giving us information in you know good umm good . . . faith" (FG3 M4). Omission of the word "box" in "Medicine Information Box" was also proposed.

Discussion

This is the first study that has evaluated Australian consumer opinions on current Australian OTC labels, the proposed standardized OTC label format for Australia, and US standardized Drug Facts labels. The evaluation was qualitative and exploratory in nature, and has identified consumer preferences as well as recommendations to inform the standardization of OTC labeling in Australia. Participants on the whole preferred the Drug Facts label over the existing Australian OTC labels and MIB.

Despite the MIB being modeled on the Drug Facts label,[15] all aspects of the Drug Facts label appear not to have been fully adopted. Many MIB shortcomings identified by participants were in fact the preferred characteristics seen on the Drug Facts label. This, therefore, brings to the forefront the notion of whether the MIB would constitute an overall improvement over the existing Drug Facts standardized OTC label format that participants preferred. The observed preference for the Drug Facts label, also supported by previous work,[7] indicates that the MIB should incorporate more aspects of the Drug Facts label to better cater to consumers' reported needs. Interestingly, the Australian TGA released a follow-up consultation in August 2014 (after completion of this study), proposing a revised version of the MIB.[20] This revised format shares more similarities to the Drug Facts label[6] in comparison to the original proposed MIB,[15] such as the structure of the "Warnings" section and the inclusion of the "Other information" heading. However, the present study highlights some potential improvements that still remain unaddressed.

Inclusion of additional information sources, inactive ingredients, contact details, and the colocation of the active ingredient(s) and its purpose were key reported differences between the Drug Facts label and MIB. Participants preferred the Drug Facts label over the MIB, as it included content on additional information sources. Consumers do not solely rely on the label for all their OTC medicine information needs,[2] and both receive[1] and utilize[21] a variety of information sources in the context of self-management. Consumers have also previously noted that labels alone are unable to completely support safe OTC medicine use as a stand-alone information source.[22] Further contact information should therefore be included in the MIB in future.

More comprehensive inactive ingredient information inclusion in the MIB should also be considered and taken forward, similar to the conclusion of an older US study published prior to the implementation of the Drug Facts label.[23] However, a potential barrier, from a regulatory perspective within the Australian context, is that complete inactive ingredient information on Australian OTC labels is currently not legislated; only specific inactive ingredients, such as ethanol and lactose, are mandated for inclusion.[13]

Participants liked the active ingredient(s) presented alongside its purpose. Consumer focus on OTC medicine benefits[24] and the opportunity for information contextualization may explain why linking the two through effective information design is of particular importance. Consequently, adoption of this strategy in the MIB should be considered as a step to promoting safe and quality use of OTC medicines.

Existing diversity among Australian OTC packaging contributed to variations in perceived quality in the present study, where OTC label content diversity has also been previously identified.[25,26] Despite many participants indicating an overall preference for the Drug Facts label, aspects of existing Australian OTC labels and the MIB were still considered as positive. This reflected good information design principles advocated for use in written medicine information[27] and were comparable to the findings of semistructured interviews previously conducted with Australian and UK participants.[16] When comparing these study findings to the semistructured interviews,[16] participants in the group discussions focused more on identifying content discrepancies demonstrated by the MIB and on suggesting alternative titles for the MIB. This may be due to differences in stimulus material provided to participants between the 2 studies (one existing OTC label and a corresponding mock MIB label provided in the semistructured interviews[16]; various OTC label formats provided in the present study), affecting the scope of discussion. Additionally, negative emotional responses to the MIB, mentioned in the semistructured interviews,[16] were not raised in this study. This may be due in part to the black-and-white Drug Facts labels available as comparators, which may have been less daunting when presented as part of complete packaging, with color used on other panels on those packs. Consequently, future work should explore consumer opinions of alternative MIB versions, with the MIB revised in light of these study findings, as part of complete packaging to provide context for consumers. The aim should be to develop better performing labels that take into consideration characteristics relevant to both preferences and results from evaluations by consumers.[28] In addition, efforts should ensure that packaging size does not become a rate-limiting factor influencing OTC label content and design, and their ability to support safe medication use.

As OTC label standardization is currently implemented in the United States, regulatory bodies such as the Australian TGA should learn from the impact of the Drug Facts label; however, proposals put forward must remain within the Australian context. Presently, there is insufficient evidence to support the implementation of either the Drug Facts label or the MIB in an Australian context or that this strategy would be advantageous from a label usability standpoint. As this study did not aim to investigate the usability of the MIB or the Drug Facts label formats using diagnostic performance testing with consumers,[29] future research should apply the recommendations and user test standardized OTC labels to ensure that implemented labels are fit for purpose.

When examining research conducted in relation to the Drug Facts label, while evidence suggests that it was an improvement on label formats available around the time of its proposal, some evaluations[8,9] were conducted after its introduction. Unsurprisingly, issues pertinent to potentially reduced OTC label quality still exist after implementation of the Drug Facts label,[30,31] highlighting the critical role of post-implementation evaluation, in conjunction with thorough pre-implementation needs analysis and performance testing. OTC label standardization in Australia must be implemented alongside an audit process to ensure ongoing monitoring, thereby enabling

opportunities for timely optimization where necessary. Similarly, the positive impact of a US campaign that yielded an increased use of medicine information included on OTC labels, with more than half being knowledgeable of the Drug Facts label 1 year after widespread implementation,[32] indicates the potential importance of a similar, timely campaign in Australia if standardization is implemented.

Certain limitations of the present study should be acknowledged. The MIBs were presented to participants as paper copies, rather than incorporated as part of complete OTC packaging. This was due to the exploratory nature of the study, and as the MIB has not been implemented. Accordingly, this distinction among stimulus materials may have affected participant opinions of the MIB.

Conclusions

Participants appreciated characteristics of existing Australian OTC labels, Drug Facts, and MIB label formats that contributed to perceived usability and format clarity. However, many implied a broad preference for the Drug Facts label, partly because of its increased perceived completeness. The absence of inactive ingredient information, contact details, and parallel communication of the active ingredient and its purpose were identified as gaps in the MIB labels. Consideration should be given to incorporating these aspects into the MIB. Performance testing of the resultant improved label format with consumers is a key necessary next step to demonstrate the extent to which the format supports both perceived and actual OTC label quality and usability.

Author Notes

This study was presented at the International Pharmaceutical Federation (FIP) World Congress, 2015, in Düsseldorf, Germany (oral presentation): Tong V, Raynor DK, Hamrosi KK, Acharya B, Panchal N, Aslani P. Consumer perspectives on Australian and U.S. over-the-counter medicine labelling strategies: is standardisation the way forward?

Acknowledgments

The authors thank all the focus group participants for their time and invaluable input in this study.

Declaration of Conflicting Interests

The author(s) declared the following potential conflicts of interest with respect to the research, authorship, and/or publication of this article: D.K.R. is the cofounder and academic advisor for Luto Research, a company that provides performance-based testing services for health information. K.K.H. is currently employed as a Health Economics and Outcomes Consultant at Optum, which provides medical market access, health economics and outcomes research, real-world evidence generation, and pharmacoepidemiology services.

Funding

The author(s) disclosed receipt of the following financial support for the research, authorship, and/or publication of this article: Funding for the conduct of the focus groups was received from the University of Sydney's Thompson Equity Fellowship (2013) awarded to P.A.

References

1. Harris Interactive Inc. Attitudes and beliefs about the use of over-the-counter medicines: a dose of reality; a national survey of consumers and health professionals. http://www.bemedwise.org/survey/final_survey.pdf. Published 2002. Accessed December 7, 2015.
2. Blom AT, Rens JA. Information about over-the-counter medication: the role of the pharmacy. *Patient Educ Couns*. 1989;14:181-189.
3. Nabors LA, Lehmkuhl HD, Parkins IS, Drury AM. Reading about over-the-counter medications. *Issues Compr Pediatr Nurs*. 2004;27:297-305.
4. Evans SW, John DN, Bloor MJ, Luscombe DK. Use of non-prescription advice offered to the public by community pharmacists. *Int J Pharm Pract*. 1997;5:16-25.
5. Tong V, Raynor DK, Aslani P. Design and comprehensibility of over-the-counter product labels and leaflets: a narrative review. *Int J Clin Pharm*. 2014;36:865-872.
6. Over-the-counter human drugs; labeling requirements. *Federal Register*. 1999;64:13254-13303. http://www.gpo.gov/fdsys/pkg/FR-1999-03-17/pdf/99-6296.pdf. Accessed December 7, 2015.
7. Aikin KJ. *Consumer comprehension and preference for variations in the proposed over-the-counter drug labeling format: final report*. Bethesda, MD: Center for Drug Evaluation and Research, US Food and Drug Administration; 1998.
8. Mendat CC, Watson AM, Mayhorn CB, Wogalter MS. Age differences in search time for two over-the-counter (OTC) drug label formats. *Proc Hum Fact Ergon Soc Annu Meet*. 2005;49:200-203.
9. Shaver EF, Wogalter MS. A comparison of older vs. newer over-the-counter (OTC) nonprescription drug labels on search time accuracy. *Proc Hum Fact Ergon Soc Annu Meet*. 2003;47:826-830.
10. Lalor D. Medicines labelling. *Aust Prescr*. 2011;34:136-138.
11. Aslani P. Consumer medicine information conundrums. *Aust Prescr*. 2007;30:122-124.
12. Australian Government Department of Health and Ageing Therapeutic Goods Administration. Australian regulatory guideline for over-the-counter medicines. *Appendix 3: Guidelines on presentation aspects of OTC applications Version 1.0, October 2012*. Australian Capital Territory: Therapeutic Goods Administration, 2012.
13. Therapeutic Goods Order No. 69: General requirements for labels for medicines, Australia. http://www.comlaw.gov.au/Details/F2014C00926. Published July 14, 2014. Accessed December 7, 2015.
14. NPS Medicinewise. Naming, packaging and labelling of medicines: briefing prepared for the Department of Health and Ageing; quantitative and qualitative evidence and anecdotal information on the problems associated with confusing naming, packaging and labelling in Australia, November 2010. 2010.
15. Australian Government Department of Health and Ageing Therapeutic Goods Administration. *TGA medicine labelling and*

packaging review: consultation paper version 1.0, May 2012. Australian Capital Territory: Therapeutic Goods Administration, 2012. 55 p. Report No.: R12/759506.
16. Tong V, Raynor DK, Aslani P. 'It's all there in black and white'—or is it? Consumer perspectives on the proposed Australian Medicine Information Box over-the-counter label format [published online July 31, 2015]. *Health Expect*. doi: 10.1111/hex.12389.
17. Krueger RA, Casey MA. *Focus Groups: A Practical Guide for Applied Research*. Thousand Oaks, CA: Sage Publications; 2009.
18. Green J, Thorogood N. *Qualitative Methods for Health Research*. 3rd ed. London: Sage Publications; 2014.
19. Miles MB, Huberman AM. *Qualitative Data Analysis: An Expanded Sourcebook*. 2nd ed. Thousand Oaks, CA: Sage Publications; 1994.
20. Australian Government Department of Health and Ageing Therapeutic Goods Administration. *Guideline for the labelling of medicines: Draft—Version 1.0, August 2014*. Australian Capital Territory: Therapeutic Goods Administration, 2014. 39 p. Report No.: R14/643926.
21. Calamusa A, Di Marzio A, Cristofani R, et al. Factors that influence Italian consumers' understanding of over-the-counter medicines and risk perception. *Patient Educ Couns*. 2012;87:395-401.
22. Smith F, Newbould J. Perspectives of community groups on the reclassification of medicines from prescription to non-prescription. *Int J Health Promot Educ*. 2002;40:21-30.
23. Kumar A, Rawlings RD, Beaman DC. The mystery ingredients: sweeteners, flavorings, dyes, and preservatives in analgesic/antipyretic, antihistamine/decongestant, cough and cold, antidiarrheal, and liquid theophylline preparations. *Pediatrics*. 1993;91:927-933.
24. Hibbert D, Bissell P, Ward PR. Consumerism and professional work in the community pharmacy. *Sociology of Health & Illness*. 2002;24:46-65.
25. Department for Transport. Over-the-counter medicines and the potential for unwanted sleepiness (No. 24). http://webarchive.nationalarchives.gov.uk/20070206175455/http://www.dft.gov.uk/pdf/pgr/roadsafety/research/rsrr/theme3/overthecountermedicinesandth4772. Accessed December 7, 2015.
26. Joshi MP, Vaidya RX, De Sousa E, Mangaonkar S. Assessment of over-the-counter medicine labels in India for patient information. *Pharma Times*. 2012;44:20-21.
27. European Commission. *Guideline on the readability of the labelling and package leaflet of medicinal products for human use*. Revision 1, 12 January 2009. Brussels: European Commission. http://ec.europa.eu/health/files/eudralex/vol-2/c/2009_01_12_readability_guideline_final_en.pdf. Published 2009. Accessed December 7, 2015.
28. Wogalter MS, Vigilante WJ Jr. Effects of label format on knowledge acquisition and perceived readability by younger and older adults. *Ergonomics*. 2003;46:327-344.
29. Communication Research Institute of Australia. *Labelling Code of Practice: Designing Usable Non-prescription Medicine Labels for Consumers*. Canberra: Communication Research Press; 2004.
30. Trivedi H, Trivedi A, Hannan MF. Readability and comprehensibility of over-the-counter medication labels. *Ren Fail*. 2014;36:473-477.
31. Yin HS, Parker RM, Wolf MS, et al. Health literacy assessment of labeling of pediatric nonprescription medications: examination of characteristics that may impair parent understanding. *Acad Pediatr*. 2012;12:288-296.
32. National Council on Patient Information and Education. Uses and attitudes about taking over-the-counter medicines: findings of a 2003 national opinion survey conducted for the National Council on Patient Information and Education: executive summary. http://bemedwise.org/survey/summary_survey_findings.pdf. Accessed December 7, 2015.

School of Pharmacy

MENU

Home
Study with us
Research
Industry and business partnerships
News
2016
3.5m for new materials library to put UK at forefront of 3D printing
Guardian 2017 league table success
PhD student wins first prize for best poster presentation
Roger Knaggs receives the Fellowship by Election award of the Faculty of Pain Medicine
Archive
Events
Publications
People
Contact us

Postgraduate student awarded best poster prize

Engineering Research Showcase 2016

Congratulations to Adam Dundas who won the 'Best Poster on Display' award at the Engineering Research Showcase held on 10th May 2016 at the Crowne Plaza Hotel in Nottingham. Adam was also awarded 3rd place for Research Quality. Adam's poster was entitled "High Throughput Synthesis of Monomers using Microwaves".

Adam is a 2nd year postgraduate student who is supervised by Morgan Alexander and Andrew Hook from the School of Pharmacy; and Georgios Dimtrakis, Derek Irvine and Sam Kingman from the Faculty of Engineering.

Posted on Tuesday 17th May 2016

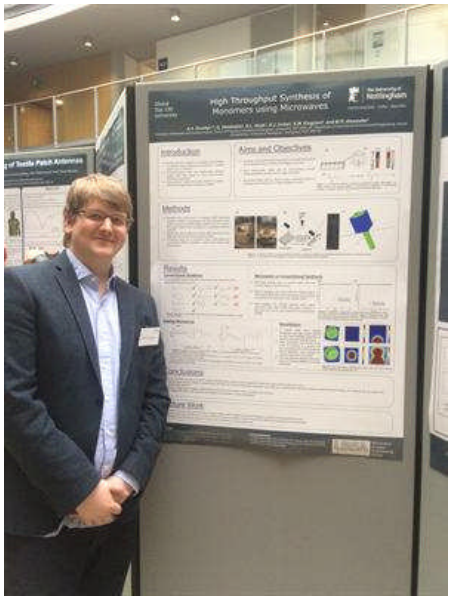

Adam Dundas with his winning poster

School of Pharmacy
University of Nottingham
University Park
Nottingham, NG7 2RD

For all enquiries please visit:
www.nottingham.ac.uk/enquiry

School of Pharmacy

MENU

Home
Study with us
Research
Industry and business partnerships
News
2016
3.5m for new materials library to put UK at forefront of 3D printing
Guardian 2017 league table success
PhD student wins first prize for best poster presentation
Roger Knaggs receives the Fellowship by Election award of the Faculty of Pain Medicine
Archive
Events
Publications
People
Contact us

School staff win a Lord Dearing Teaching Award

The Lord Dearing Award recognises outstanding achievements in enhancing the student learning experience. Matthew Boyd, Claire Anderson, Vibhu Solanki, Kimberley Sonnex and Sarah Brydges have together won for the development of our new 4th year module, **Pharmacy Leadership and Management (PLM)**, a 12 day team-based student-centred simulation of pharmacy practice delivered in a dedicated teaching suite. The module gives students the opportunity to drive forward as the future leaders of pharmacy. Designed with internal and external stakeholders to maximize learning and employability, this unique module facilitates students to be the best they can be. The awarding panel noted, in particular, the creative and innovative methods employed in designing a module that is highly relevant for students.

Posted on Thursday 19th May 2016

School of Pharmacy
University of Nottingham
University Park
Nottingham, NG7 2RD

For all enquiries please visit:
www.nottingham.ac.uk/enquiry

School of Pharmacy

MENU

Home
Study with us
Research
Industry and business partnerships
News
2016
3.5m for new materials library to put UK at forefront of 3D printing
Guardian 2017 league table success
PhD student wins first prize for best poster presentation
Roger Knaggs receives the Fellowship by Election award of the Faculty of Pain Medicine
Archive
Events
Publications
People
Contact us

Postgraduate student wins prizes.

Muna Adan is a third year PhD student working at the Division of Social Research in Medicines and Health. Muna says: "I recently submitted an abstract to the British Pain Society's Annual Scientific Conference 2016 in Harrogate, which was entitled: *'Characteristics of non-cancer pain patients prescribed long-term strong opioids in primary care: a population based study using CPRD*.' This was selected amongst the top 5 oral student presentations in the country and I was invited on the 12th of May to give a talk. To my surprise I received a prize for the top three best research presentation for the talk and it gladdened me to have represented the University and the School at the event."

The research is supervised by Professor Roger Knaggs and Professor Li-Chia Chen.

Posted on Monday 23rd May 2016

School of Pharmacy
University of Nottingham
University Park
Nottingham, NG7 2RD

School of Pharmacy

MENU

Home
Study with us
Research
Industry and business partnerships
News
2016
3.5m for new materials library to put UK at forefront of 3D printing
Guardian 2017 league table success
PhD student wins first prize for best poster presentation
Roger Knaggs receives the Fellowship by Election award of the Faculty of Pain Medicine
Archive
Events
Publications
People
Contact us

Guardian 2017 league table success

The School has been ranked as 4th in the 2017 Guardian University Guide league table for Pharmacy and Pharmacology, up one place from 2016, and remains the top school of pharmacy in England.

The Guardian rankings place particular emphasis on the quality of the student experience including the National Student Survey and graduate employment. We are delighted that this table reflects the hard work of all of our staff, and our student representatives, to make studying on our 4-year MPharm and 5-year MPharm with integrated pre-registration scheme such a brilliant experience.

Posted on Monday 6th June 2016

School of Pharmacy
University of Nottingham
University Park
Nottingham, NG7 2RD

For all enquiries please visit:
www.nottingham.ac.uk/enquiry

£3.5m for new materials library to put UK at forefront of 3D printing

MENU

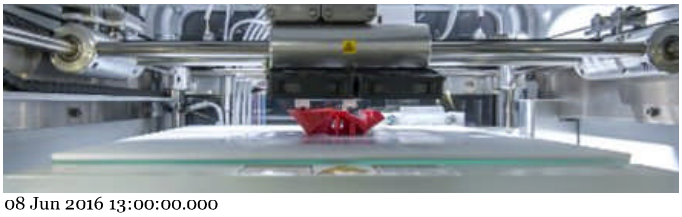

08 Jun 2016 13:00:00.000

A team of scientists at The University of Nottingham has been awarded a £3.5m grant to develop a new library of 3D printing materials which could accelerate commercial uptake of the technology.

The team aims to create 'plug and pla latf terials, material combinations and formulations which could be used to develop 3D printed products in fields as diverse as pharmaceuticals, food, agrochemicals and consumer products.

UK is already at the forefront of this rapidly develo ld, but this step will allow UK industr to leapfrog other nations in the area of multi-material, multifunctional 3D printing; the project's industrial partners - GlaxoSmithKline, Unilever, PPG, Syngenta and Malvern Instruments – have cited the current limited range of materials as an obstacle to the commercial development of 3D printing.

Click here for full story

By esta lishing a suite of new materials from which anyone can select to most appropriate 3D printa terial for their product, the limited palette o terials available to industr ll be removed and significant barrier to the wider adoption of the technology significantly reduced.

"There is considerable industrial demand for this kind of product in the 3D printing industry, which could help the technology to reach its full potential as a manufacturing platform in the UK," explains project lead, **Professor Ricky Wildman** (ht //www.nottingham.ac.uk/engineering/departments/chemenv/people/ricky.wildman) , from the Faculty of Engineering at The University of Nottingham.

The project will build on the considerable success that The University of Nottingham has had in the fields of 3D printing and high throughput pharmaceutical analysis.

The Future Formulation Plug and Pla ls for 3D Printing grant was awarded to Professor Wildman and his team by the **Engineering and Physical Sciences Research Council** (ht /w .epsrc.ac.uk/) (EPSRC).

The University of Nottingham team comprises Professor Wildman, Professor Richard Hague, Professor Ian Ashcroft, Dr Chris Tuck and Dr Derek Irvine, from the Faculty of Engineering; Professor Clive Roberts and Professor Morgan Alexander form the School o ter, Professor of Food Manufacturing and director of Centre for Innovative Food Manufacturing; and David Ambilino, Professor of Sustainable Chemistry.

Wayne Hayes, Professor of Polymer Chemistry at the University of Reading; Tom Mills, Lecturer in Food Manufacturing; Fotios Spyropoulos, Early Career Researcher in Chemical Engineering, and Professor Ian Norton, Director of Centre for Formulation Engineering; all from the University of Birmingham, also pla les in achieving the goals of the project.

The Additive Manufacturing and 3D Printing Group is currently an EPSRC Centre for Innovative Manufacturing in Additive Manufacturing (CIMAM) and also a Centre for Doctoral T (CDT) in Additive Manufacturing and 3D Printing. Professor Ricky Wildman is a Co-Investigator in both the CIMAM and CDT.

— Ends —

Our academics can now be interviewed for broadcast via our Media Hub, which offers a Globelynx fixed camera and ISDN line facilities at University Park campus. For further information please contact a member of the Communications team on +44 (0)115 951 5798, email **mediahub@nottingham.ac.uk** (mailto:mediahub@nottingham.ac.uk) or see the **Globelynx website** (http://www.globelynx.com/registration-0) for how to register for this service.

For up to the minute media alerts, **follow us on Twitter** (https://twitter.com/UoNPressOffice)

Notes to editors: The **University of Nottingham** (http://ww .nottingham.ac.uk/) has 43,000 students and is 'the nearest Britain has to a truly global university, with a "distinct" approach to internationalisation, which rests on those full-scale campuses in **China** (ht //www.nottingham.edu.c /index.aspx) and **Malaysia** (ht //www.nottingham.edu.my/index.aspx) , as well as a large presence in its home city.' (*Times Good University Guide 2016*). It is also one of the most popular universities in the UK among **graduate employers** (http://www.nottingham.ac.uk/news/pressreleases/2014/january/nottingham-is-t -number-one-target-for-graduate-employers.aspx) and the winner of 'Outstanding Support for Early Career Researchers' at the ***Times Higher Education Awards* 2015** (ht //ww .nottingham.ac.uk/news/pressreleases/2015/november/t -excellence-award-for-t -university-of-nottingham.aspx) . More than 97% of **research** (/research/research.aspx) at The University of Nottingham is recognised internationally and it is **8th in the UK** (http://www.nottingham.ac.uk/news/pressreleases/2014/december/world-class-research-recognised-at-the-university-of-nottingham.aspx) by research power according to the Research Excellence Framework 2014. It has been voted the world's greenest campus for **four years running** (http://blogs.nottingham.ac.uk/newsroom/2016/01/22/nottingham-is-number-one-in-the-world-for-sustainability-for-the-fourth-time/) , according to Greenmetrics Ranking of World Universities.

Additional r

l resources for this article

Related articles

New world-leading additive manufacturing research la (/news/pressreleases/2015/june/new-world-leading-additive-manufacturing-research-lab.aspx)

Thursday 25th June 2015

Landmark 3D printing exhibition showcases University research (/news/pressreleases/2013/october/landmark-3d-printing-exhibition-showcases-university-research.aspx)

Tuesday 8th October 2013

Scans locate historic secret room in walls o Gunpowder plo (/news/pressreleases/2016/november/scans-loc -historic-secret-room-in-walls-o -gunpowder-plot-house.aspx)

Friday 4th November 2016

Impact: The Nottingham Campaign (ht //www.nottingham.ac.uk/impactcampaign) , its biggest-ever fundraising campaign, is delivering the University's vision to change lives, tackle global issues and shape the future. **More news...** (ht //www.nottingham.ac.uk/news)

Story credits

More information is availa le from Prof Ricky Wildman, in the Department of Chemical and Environmental Engineering, at The University of Nottingham on +44 (0)115 8466893, **ricky.wildman@nottingham.ac.uk** (mailto:ricky.wildman@nottingham.ac.uk)

Emma Lowry - Media Relations Manager
Email: **emma.lowry@nottingham.ac.uk** (mailto:emma.lo)
Phone: +44 (0)115 846 7156
Location: University Park

School of Pharmacy

MENU

Home
Study with us
Research
Industry and business partnerships
News
2016
3.5m for new materials library to put UK at forefront of 3D printing
Guardian 2017 league table success
PhD student wins first prize for best poster presentation
Roger Knaggs receives the Fellowship by Election award of the Faculty of Pain Medicine
Archive
Events
Publications
People
Contact us

PhD student invited to attend BSA Masterclass: Science Communication Primer

Alshaimaa Almehmady, a Pharmacy postgraduate student in the Drug Delivery and Tissue Engineering Division, has been selected to attend a scientific communication conference next week in Manchester. The conference is the British Science Association Masterclass: Science Communication Primer. During the day, the programme will include guidance for delegates on the next steps for their career development.

After the training day, delegates will be invited to move on to the SciComm burrito, to relax with the other delegates, and meet the local science communication network in Manchester and the North West.

Alshaima also took part in a 3 minute (3MT) competition on 3 June. This competition was an academic research communication competition developed by The University of Queensland (UQ), Australia. The challenge was for researchers to explain the complexity and relevance of their research to a non-specialist audience in a concise and engaging way

Posted on Thursday 9th June 2016

School of Pharmacy
University of Nottingham
University Park
Nottingham, NG7 2RD

School of Pharmacy

MENU

Home
Study with us
Research
Industry and business partnerships
News
2016
3.5m for new materials library to put UK at forefront of 3D printing
Guardian 2017 league table success
PhD student wins first prize for best poster presentation
Roger Knaggs receives the Fellowship by Election award of the Faculty of Pain Medicine
Archive
Events
Publications
People
Contact us

PhD student wins scientific poster competition

Shehnaz Ahmed says:
"I am a PhD student based in the School of Pharmacy and supervised by Jonathan Aylott and Amir Ghaemmaghami.

I recently attended an international conference in Barcelona "Advances in Cell and Tissue Culture" (30th May-1st June) held by Kirkstall Ltd. The conference had a scientific poster competition, and I won 1st prize."

Her poster was entitled "Investigating fibroblast response in a 3D *in vitro* lung wound model exposed to interstitial flow conditions"

Congratulations Shehnaz!

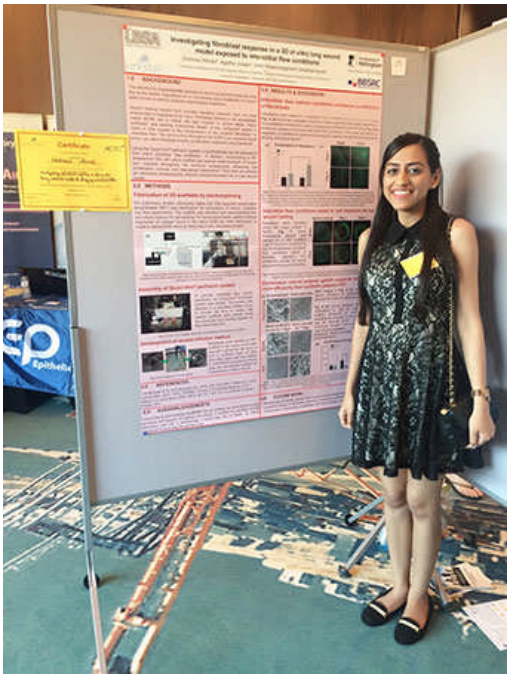

Posted on Tuesday 14th June 2016

School of Pharmacy
University of Nottingham
University Park
Nottingham, NG7 2RD

For all enquiries please visit:
www.nottingham.ac.uk/enquiry

School of Pharmacy

MENU

Home
Study with us
Research
Industry and business partnerships
News
2016
3.5m for new materials library to put UK at forefront of 3D printing
Guardian 2017 league table success
PhD student wins first prize for best poster presentation
Roger Knaggs receives the Fellowship by Election award of the Faculty of Pain Medicine
Archive
Events
Publications
People
Contact us

A new undergraduate science course to meet the future needs of pharma and biotech

A new undergraduate course is launched at the University of Nottingham to meet the current and future needs of the pharmaceutical and biotechnology sectors.

The MSci Pharmaceutical Sciences with a Year in Industry programme will be delivered by one of the world's most respected Schools of Pharmacy. The course includes a year working in the pharmaceutical, biotech or healthcare industry to help students hit the ground running in the global workplace from the day they graduate.

The course is designed together with experts from industry to prepare graduates for careers in drug discovery, medicines design and development. In addition to a strong foundation in the chemical and biological sciences, students will also learn about patients, business skills, and medicines regulation.

Professor Clive Roberts, Head of the School of Pharmacy, The University of Nottingham, said "This is an exciting and innovative course designed specifically to produce the next-generation of pharmaceutical scientists to lead research and industry in the development of new medicines."

Posted on Thursday 30th June 2016

School of Pharmacy
University of Nottingham
University Park
Nottingham, NG7 2RD

For all enquiries please visit:
www.nottingham.ac.uk/enquiry

School of Pharmacy

MENU

Home
Study with us
Research
Industry and business partnerships
News
2016
3.5m for new materials library to put UK at forefront of 3D printing
Guardian 2017 league table success
PhD student wins first prize for best poster presentation
Roger Knaggs receives the Fellowship by Election award of the Faculty of Pain Medicine
Archive
Events
Publications
People
Contact us

Roger Knaggs receives the Fellowship by Election award of the Faculty of Pain Medicine

Dr Roger Knaggs has been awarded a Fellowship by Election of the Faculty of Pain Medicine of the Royal College of Anaesthetists; the first non-medical healthcare professional to receive this award.

The Fellowship by Election is 'the highest accolade possible' given by the Faculty. It is considered for practitioners across the world who have made sustained and significant contributions to the practice of Pain Medicine at an internationally active level over at least ten years.

Roger will be formally admitted to the Fellowship at a presentation ceremony at their Annual Meeting for Fellows and Members on 2 December 2016 at Churchill House.

Posted on Monday 4th July 2016

School of Pharmacy
University of Nottingham
University Park
Nottingham, NG7 2RD

Fillings that heal your teeth – how regenerative medicine could change your visit to the dentist

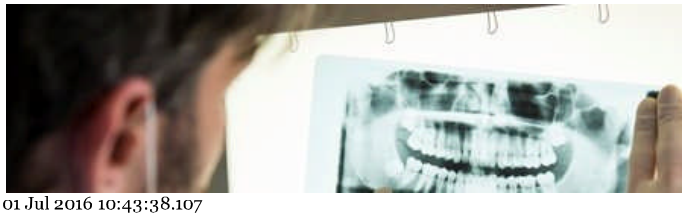

01 Jul 2016 10:43:38.107
A team behind regenerative dental fillings that could help heal teeth have been awarded a Royal Society of Chemistry prize.

Click here for full story

Researchers from the University of Nottingham and the Wyss Institute at Harvard University have developed therapeutic synthetic, light-curable, biomaterials for dental treatments that support native dental stem cells inside teeth to repair and regenerate dentin.
The approach could significantly impact millions of dental patients each year by dental fillings that help heal teeth when they are injured from dental disease or dental surgery.
The research won second prize in the materials category of the Royal Society of Chemistry's **Emerging Technologies Competition** (http://rsc.l /emerging-technologies) 2016.
Dr Adam Celiz, Marie Curie Research Fellow at the University of Nottingham, said: "Existing dental fillings are to to cells and are therefore incompatible with pulp tissue inside the tooth. In cases of dental pulp disease and injury a root c ty to remove the infected tissues.
"We have designed synthetic biomaterials that can be used similarly to dental fillings but can be placed in direct c tact with pulp tissue to stimulate the native stem cell population for repair and regeneration of pulp tissue and the surrounding dentin. Our approach has great promise to impact the dental field and this prize provides a great platform to develop this technology further with industrial partners."
David Mooney, the Pinkas Family Professor of Bioengineering at the John Paulson School of Engineering and Applied Sciences at Harvard and the Wyss Institute for Biologically Inspired Engineering, added: "These materials may provide an effective and practical approach to allow a patient to regenerate components of their own teeth."
Dr Kyle Vining, DDS, Fellow at the Wyss Institute at Harvard University said: "We are excited about the promise of therapeutic biomaterials for bringing regenerative medicine to restorative dentistry."
Applications were judged on the degree of innovation of the technology, its potential impact, and the quality of the science behind it. The group will receive tailored business support from multinational partner companies, business training, media support, and a cash prize of £3,000.
Dr Steve Pleasance, Head of Industr t the Royal Society of Chemistry said: "Increasing innovation in the chemical sciences is one of the key elements of the Royal Society of Chemistr tr trategy. "
Our Emerging Technologies competition, now in its fourth year and supported by our industr tners, is proving to be highly successful in accelerating the commercialisation of the cutting-edge research taking place in both universities and small companies."
Winning the competition gives businesses the platform they need to make the industr their technolo .
Since the initiative began in 2013, winners have gone on to raise a combined total o llion in further funding, grown their companies and entered commercial contracts.
A previous winner went on to secure US$1.7 million of funding from the Bill and Melinda Gates Foundation to develop their novel treatment for iron deficiency anaemia, whilst another received support from GSK and was awarded over £2.5 million to take their enzyme catalysis technolo .
Forty shortlisted entrants presented their ideas to a panel o t t tion final, held at the Chemistr t. The judges are industr leaders and experts in their fields, drawn from a wide range of specialisms.
— Ends —
Our academics can now be interviewed for broadcast v lobelynx fixed camera and ISDN line facilities at University Park campus. For further information please contact a member of the Communications team on +44 (0)115 951 5798, email **mediahub@nottingham.ac.uk** (mailto:mediahub@nottingham.ac.uk) or see the **Globelynx website** (ht /w .glo lynx.com/registration-0) for how to register for this service.
For up to the minute media alerts, **follow us on Twitter** (https://twitter.com/UoNPressOffice)
Notes to editors: The **University of Nottingham** (ht //ww .nottingham.ac.uk/) has 43,000 students and is 'the nearest Britain has to a truly global university, with a "distinct" approach to internationalisation, w ll-scale campuses in **China** (ht //ww .nottingham.edu.c /en/index.aspx) and **Malaysia** (ht //ww .nottingham.edu.my/index.aspx) , as well as a large presence in its home city.' (*Times Good University Guide 2016*). It is also one of the most popular universities in the UK among **graduate employers** (http://ww .nottingham.ac.uk/news/pressreleases/2014/january/nottingham-is-the-number-one-target-for-graduate-employers.aspx) and the winner of 'Outstanding Support for Early Career Researchers' at the ***Times Higher Education Awards* 2015** (http://ww .nottingham.ac.uk/news/pressreleases/2015/november/t -excellence-award-for-the-university-of-nottingham.aspx) . More than 97% of **research** (/research/research.aspx) at The University of Nottingham is recognised internationally and it is **8th in the UK** (http://ww .nottingham.ac.uk/news/pressreleases/2014/december/world-class-research-recognised-at-

Additional r

l resources for this article

Related articles

Breakthrough in scaling up life-changing stem cell production (/news/pressreleases/2016/july/breakthrough-in-scaling-up-life-changing-stem-c ll-production.aspx)

Wednesday 13th July 2016

t -university-of-nottingham.aspx) by research power according to the Research Excellence Framework 2014. It has been voted the world's greenest campus for **four years running** (ht //blogs.nottingham.ac.uk/newsroom/2016/01/22/nottingham-is-number-one-in-t -world-for-sustainability-for-the-fourth-time/) , according to Greenmetrics Ranking of World Universities. **Impact: The Nottingham Campaign** (ht //www.nottingham.ac.uk/impactcampaign) , its biggest-ever fundraising campaign, is delivering the University's vision to change lives, tackle global issues and shape the future. **More news...** (http://www.nottingham.ac.uk/news)

Story credits

Credits

Liz Cass - Head of Media Relations
Email: liz.cass@nottingham.ac.u (mailto:liz.c tingham.ac.uk)
Phone: +44 (0)115 748 4734
Location: University Park

The end of root canals? Revolutionary 'stem cell fillings' trigger teeth to repair themselves

- **Synthetic biomaterials are used in a similar way to dental fillings**
- **Material is placed in direct contact with pulp tissue**
- **This stimulates the native stem cell population for repair and regeneration**

By MARK PRIGG FOR DAILYMAIL.COM
PUBLISHED: 22:28, 5 July 2016 | **UPDATED:** 10:05, 6 July 2016

The horror of a root canal could soon be a thing of the past thanks to a radical new stem cell treatment.

Researchers say the new type of tooth filling can cause teeth to repair and regenerate themselves.

The approach could significantly impact millions of patients each year with dental fillings that help heal teeth when they are injured from dental disease or dental surgery.

Scroll down for video

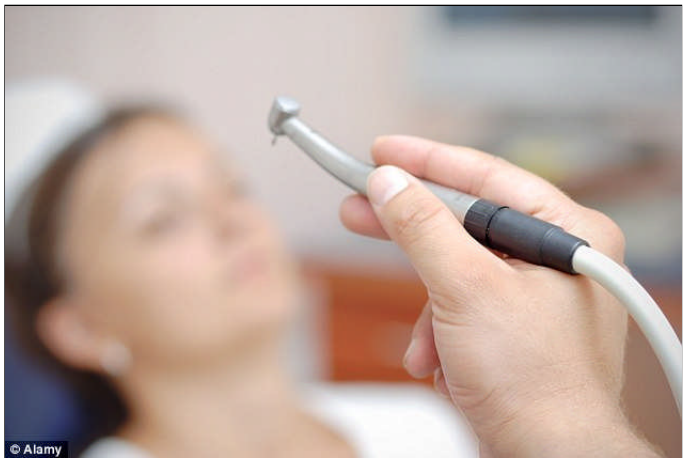

Researchers say the new type of tooth filling can cause teeth to repair and regenerate themselves.

Researchers from the University of Nottingham and the Wyss Institute at Harvard University developed the therapeutic synthetic, light-curable, biomaterials.

They allow native dental stem cells inside teeth to repair and regenerate dentin.

Dr Adam Celiz, Marie Curie Research Fellow at the University of Nottingham, said: 'Existing dental fillings are toxic to cells and are therefore incompatible with pulp tissue inside the tooth.

'In cases of dental pulp disease and injury a root canal is typically performed to remove the infected tissues.

'We have designed synthetic biomaterials that can be used similarly to dental fillings

HOW THEY WORK

The synthetic biomaterials that can be used similarly to dental fillings.

They are placed in direct contact with pulp tissue

This stimulates the native stem cell population for repair and regeneration of pulp tissue and the surrounding dentin.

We have designed synthetic biomaterials that can be used similarly to dental fillings but can be placed in direct contact with pulp tissue to stimulate the native stem cell population for repair and regeneration of pulp tissue and the surrounding dentin.

RELATED ARTICLES


Is the Large Hadron Collider set to reveal the secrets of...


Would you upload YOUR brain to a computer? Experts reveal...


Animated emoji set to come to the iPhone: Apple tests first...


Plastic waste thrown into UK seas finds its way into the...

'Our approach has great promise to impact the dental field and this prize provides a great platform to develop this technology further with industrial partners.'

The research won second prize in the materials category of the Royal Society of Chemistry's Emerging Technologies Competition 2016.

David Mooney, the Pinkas Family Professor of Bioengineering at the John Paulson School of Engineering and Applied Sciences at Harvard and the Wyss Institute for Biologically Inspired Engineering, added: 'These materials may provide an effective and practical approach to allow a patient to regenerate components of their own teeth.'

The synthetic biomaterials that can be used similarly to dental fillings.

Dr Kyle Vining, DDS, Fellow at the Wyss Institute at Harvard University said: 'We are excited about the promise of therapeutic biomaterials for bringing regenerative medicine to restorative dentistry.'

Applications were judged on the degree of innovation of the technology, its potential impact, and the quality of the science behind it.

Dr Steve Pleasance, Head of Industry at the Royal Society of Chemistry said: 'Increasing innovation in the chemical sciences is one of the key elements of the Royal Society of Chemistry's industry strategy. '

Scientists develop new human stem cells with half a genome

'Ten tiny fingers, ten tiny toes': Rochelle Humes announces she is expecting second child with Marvin... after revealing pressure from daughter for sibling

'As rumours go, it's not the worst!' Jon Hamm addresses speculation he's well endowed after THAT photo sparked discussion about his manhood

From Kate Moss's denim jacket to Taylor Swift's checked crombie and Cara's parka - 'IT' coats you need to know about right NOW
SPONSORED

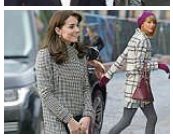

'Back in December!' Katie Price announces return to Loose Women after taking a break from the public eye to focus on her marriage... as she hits the town

'I'm very sick, I need help!' The Shining star Shelley Duvall's struggle with mental illness is revealed as she claims Robin Williams 'is not dead'

Chic Jenna Coleman stuns in a floral velvet coat and frilly white blouse as she mingles David Beckham at his fashion launch
Victoria meets Becks

'You are bang out of order!' Sam Faiers' f ly are livid with her and boyfriend Paul Knightley as they drop the bombshell that they are moving to LA

They didn't rapper very well! Iggy Azalea left in a sticky situation as boob tape FAIL leaves her looking not so fancy at GQ Awards
Major fashion faux pas

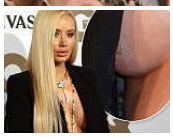

Advertisement

My drug-addled, drink-soaked affair with Harrison Ford on the Star Wars set: Carrie Fisher's denied it for years. Now she finally admits what happened

Tyre-d of the scandal? Harrison Ford forgets his troubles as he enjoys a motorbike ride in wake of Carrie Fisher Star Wars affair revelation

Braless Vogue Williams is inches from a nip-slip in an open white blazer and sexy fitted pencil skirt for charity do
Mail

lled wine, hot toddies, and honeycomb lattes! 10 deliciously

School of Pharmacy

MENU

Home
Study with us
Research
Industry and business partnerships
News
2016
3.5m for new materials library to put UK at forefront of 3D printing
Guardian 2017 league table success
PhD student wins first prize for best poster presentation
Roger Knaggs receives the Fellowship by Election award of the Faculty of Pain Medicine
Archive
Events
Publications
People
Contact us

PhD student wins first prize for best poster presentation

PhD candidate Tamara Mahmood, supervised by Professor Clive J Roberts, Professor Morgan R Alexander (The University of Nottingham), Dr. Nial Bullett and Dr. Kadem Al-Lamee (Arterius Ltd) presented a poster entitled "Characterization of a Bioresorbable Drug-Eluting Scaffold" at the UK Society for Biomaterials 15th annual conference, University of Westminster, London.

Tamara was awarded first prize for the best poster presentation. She won £200 and sponsorship in the form of a poster prize certificate and a year's free access to the Journal of Materials Chemistry B and Biomaterials Science. This excellent experience will provide Tamara with encouragement for her future research.

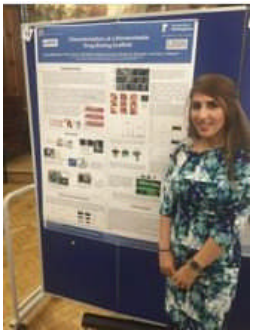

Tamara next to her winning poster

Posted on Monday 11th July 2016

School of Pharmacy
University of Nottingham
University Park
Nottingham, NG7 2RD

For all enquiries please visit:
www.nottingham.ac.uk/enquiry

Breakthrough in scaling up life-changing stem cell production

MENU

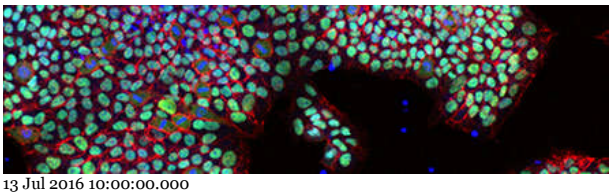

13 Jul 2016 10:00:00.000
PA 170/16

Scientists have discovered a new method of creating human stem cells which could solve the big problem of the large-scale production needed to fully realise the potential of these remarkable cells for understanding and treating disease.

The discovery has been made by a team of scientists at The University of Nottingham, Uppsala University and GE Healthcare in Sweden.

Human pluripotent stem cells are undifferentiated cells which have the unique potential to develop into all the different types of cells in the body. With applications in disease modelling, drug screening, regenerative medicine and tissue engineering, there is already an enormous demand for these cells, which will only grow as their use in the clinic and by the pharmaceutical industry increases.

Click here for full story

The production of stem cells at the scale required for optimal application in modern healthcare is currently not feasible because available culture methods are either too expensive, or reliant on substances that would not be safe for clinical use in humans.

In this new piece of research, published in ***Nature Communications*** (http://www.nature.com/ncomms/2016/160713/ncomms12170/full/ncomms12170.html) , a team combining researchers from The University of Nottingham's **Wolfson Centre for Stem Cells, Tissue Engineering and Modelling** (http://www.nottingham.ac.uk/research/groups/stemcellbiology/index.aspx) , Uppsala University and GE Healthcare has identified an improved method for human stem cell culture that could lead to quicker and cheaper large scale industrial production.

The work was started at Uppsala University in Sweden, and the first author, Dr Sara Pijuan-Galitó, is now continuing her work as a Swedish Research Council Research Fellow at Nottingham. Sara said: "By using a protein derived from human blood called Inter-alpha inhibitor, we have grown human pluripotent stem cells in a minimal medium without the need for costly and time-consuming biological substrates. Inter-alpha inhibitor is found in human blood at high concentrations, and is currently a by-product of standard drug purification schemes.

"The protein can make stem cells attach on unmodified tissue culture plastic, and improve survival of the stem cells in harsh conditions. It is the first stem cell culture method that does not require a pre-treated biological substrate for attachment, and therefore, is more cost and time-efficient and paves the way for easier and cheaper large-scale production."

Lead supervisor Dr Cecilia Annerén, who has a joint position at Uppsala University and at GE Healthcare in Uppsala, said: "As coating is a time-consuming step and adds cost to human stem cell culture, this new method has the potential to save time and money in large-scale and high-throughput cultures, and be highly valuable for both basic research and commercial applications."

Co-author on the paper **Dr Cathy Merry** (http://www.nottingham.ac.uk/medicine/about/cancerandstemcells/people/cathy.merry) added: "We now intend to combine Inter-alpha inhibitor protein with our innovative hydrogel technology to improve on current methods to control cell differentiation and apply it to disease modelling. This will help research into many diseases but our focus is on understanding rare conditions like Multiple Osteochondroma (an inherited disease associated with painful lumps developing on bones) at the cellular level. Our aim is to replicate the 3 dimensional environment that cells experience in the body so that our lab-bench biology is more accurate in modelling diseases."

Dr Sara Pijuan-Galitó has also been awarded the prestigious Sir Henry Wellcome Postdoctoral Fellowship. This will enable her to combine Inter-alpha inhibitor with improved synthetic polymers in collaboration with other regenerative medicine pioneers at the University, Professor Morgan Alexander and Professor Chris Denning. This team plans to further improve on current human stem cell culture, designing an economical and safe method that can be easily translated to large-scale production and can deliver the billions of cells necessary to start taking cellular therapeutics to the individual patients.

The full Nature Communications research paper '*Human serum-derived protein removes need for coating in novel defined human pluripotent stem cell culture*' is available **here** (http://www.nature.com/ncomms/2016/160713/ncomms12170/full/ncomms12170.html) .

The technology described in the paper is undergoing patent protection by GE Healthcare who co-funded the project at Uppsala University (WO2014158089A1).

— Ends —

Our academics can now be interviewed for broadcast via our Media Hub, which offers a Globelynx fixed camera and ISDN line facilities at University Park campus. For further information please contact a member of the Communications team on +44 (0)115 951 5798, email **mediahub@nottingham.ac.uk** (mailto:mediahub@nottingham.ac.uk) or see the **Globelynx website** (http://www.globelynx.com/registration-0) for how to register for this service.

For up to the minute media alerts, **follow us on Twitter** (https://twitter.com/UoNPressOffice)

Notes to editors: The **University of Nottingham** (http://www.nottingham.ac.uk/) has 43,000 students and is 'the nearest Britain has to a truly global university, with a "distinct" approach to internationalisation, which rests on those full-scale campuses in **China** (http://www.nottingham.edu.cn/en/index.aspx) and **Malaysia** (http://www.nottingham.edu.my/index.aspx) , as well as a large presence in its home city.' (*Times Good University Guide 2016*). It is also one of the most popular universities in the UK among **graduate**

Additional resources

No additional resources for this article

Related articles

Fillings that heal your teeth – how regenerative medicine could change your visit to the dentist (/news/pressreleases/2016/july/fillings-that-heal-your-teeth.aspx)

Friday 1st July 2016

£1.2m for injectable stem-cell carrying microspheres to regenerate bones (/news/pressreleases/2016/july/1.2m-for-injectable-stem-cell-carrying-microspheres-to-regenerate-bones.aspx)

Monday 25th July 2016

How artificially-intelligent medical devices will one day treat cancer and critical care patients (/news/pressreleases/2016/june/how-artificially-intelligent-medical-devices-will-one-day-treat-cancer-and-critical-care-patients.aspx)

Thursday 16th June 2016

£23.6 million boost for medical research in Nottingham (/news/pressreleases/2016/september/medical-research-nottingham.aspx)

Thursday 15th September 2016

'Omnigen' amniotic bandage could help save sight in trauma patients (/news/pressreleases/2016/june/'omnigen'-amniotic-bandage-could-help-save-sight-in-trauma-patients.aspx)

Tuesday 28th June 2016

Protein that protects tumour cells associated with improved survival in some breast cancer patients, study finds (/news/pressreleases/2016/june/protein-that-protects-tumour-cells-associated-with-improved-survival-in-some-breast-cancer-patients-study-finds.aspx)

Wednesday 29th June 2016

New material forges the way for 'stem cell factories' (/news/pressreleases/2015/july/new-material-forges-the-way-for-stem-cell-factories.aspx)

Wednesday 22nd July 2015

employers (http://www.nottingham.ac.uk/news/pressreleases/2014/january/nottingham-is-the-number-one-target-for-graduate-employers.aspx) and the winner of 'Outstanding Support for Early Career Researchers' at the ***Times Higher Education Awards* 2015** (http://www.nottingham.ac.uk/news/pressreleases/2015/november/the-excellence-award-for-the-university-of-nottingham.aspx) . More than 97% of **research** (/research/research.aspx) at The University of Nottingham is recognised internationally and it is **8th in the UK** (http://www.nottingham.ac.uk/news/pressreleases/2014/december/world-class-research-recognised-at-the-university-of-nottingham.aspx) by research power according to the Research Excellence Framework 2014. It has been voted the world's greenest campus for **four years running** (http://blogs.nottingham.ac.uk/newsroom/2016/01/22/nottingham-is-number-one-in-the-world-for-sustainability-for-the-fourth-time/) , according to Greenmetrics Ranking of World Universities. **Impact: The Nottingham Campaign** (http://www.nottingham.ac.uk/impactcampaign) , its biggest-ever fundraising campaign, is delivering the University's vision to change lives, tackle global issues and shape the future. **More news...** (http://www.nottingham.ac.uk/news)

Story credits

More information is available from **Dr Sara Pijuan-Galitó** in the Wolfson Centre for Stem Cells, Tissue Engineering & Modelling, Centre for Biomolecular Sciences on **+44 (0)115 823 1234**, **sara.pijuangalito@nottingham.ac.uk** (mailto:sara.pijuangalito@nottingham.ac.uk)

Emma Rayner - Media Relations Manager
Email: **emma.rayner@nottingham.ac.uk** (mailto:emma.rayner@nottingham.ac.uk)
Phone: +44 (0)115 951 5793
Location: University Park

School of Pharmacy

MENU

Home
Study with us
Research
Industry and business partnerships
News
2016
3.5m for new materials library to put UK at forefront of 3D printing
Guardian 2017 league table success
PhD student wins first prize for best poster presentation
Roger Knaggs receives the Fellowship by Election award of the Faculty of Pain Medicine
Archive
Events
Publications
People
Contact us

PhD student heads to Seattle for postdoc position

Michael Taylor, supervised by Professor Morgan Alexander, Dr Mischa Zelzer, Dr Lee Buttery (The University of Nottingham) and Professor Matthias Lutolf (Ecole Polytechnique Federale de Lausanne) becomes the third of Morgan's students to head to NESAC/BIO, the National ESCA and Surface Analysis Centre for Biomedical Problems at the University of Washington, Seattle. Michael recently obtained a postdoctoral position to work on development and analysis of functional tissue scaffolds, and Time-of-Flight Secondary Ion Mass Spectrometry (ToF-SIMS) of pancreatic tissues to aid the development of an early warning system for cancer.

NESAC/BIO provides expert information about surface properties (composition, structure, spatial distribution, and molecular orientation) needed by biomedical researchers. The research institute combines surface analysis expertise with collaborators' biomedical expertise to provide the information needed to develop new generations of biomaterials and biomedical devices. This excellent opportunity will provide Michael with a platform to continue his research career.

Posted on Tuesday 26th July 2016

Michael Taylor at the RS Summer Science Exhibition Plastic Inside Us

School of Pharmacy
University of Nottingham
University Park
Nottingham, NG7 2RD

For all enquiries please visit:
www.nottingham.ac.uk/enquiry